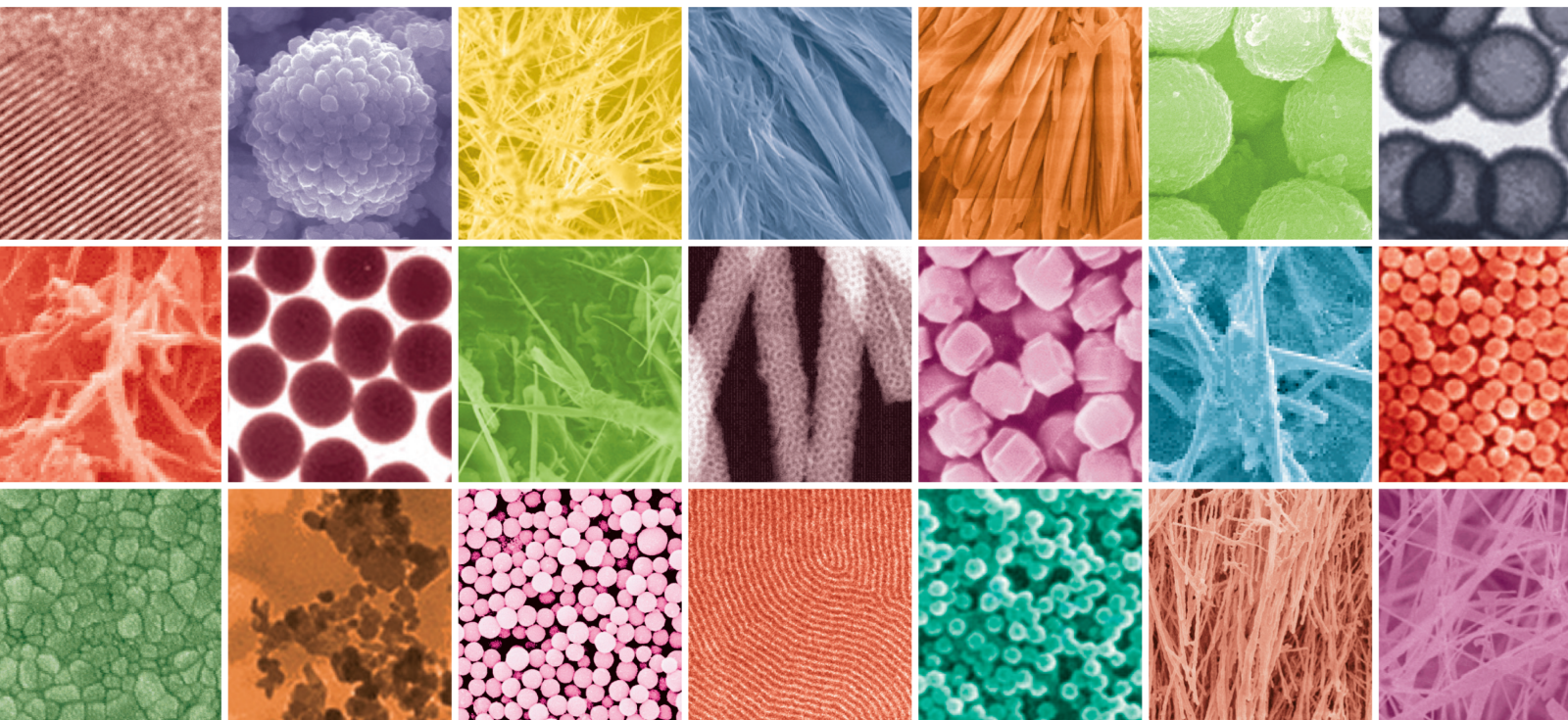



Nano Particles in Material Development and Machinability of Engineering Materials

Lead Guest Editor: V. Vijayan

Guest Editors: N. Senthilkumar and Lee Chang Chuan





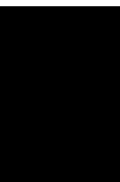
Nano Particles in Material Development and Machinability of Engineering Materials

Journal of Nanomaterials

**Nano Particles in Material Development
and Machinability of Engineering
Materials**

Lead Guest Editor: V. Vijayan

Guest Editors: N. Senthilkumar and Lee Chang
Chuan





Copyright © 2022 Hindawi Limited. All rights reserved.

This is a special issue published in "Journal of Nanomaterials." All articles are open access articles distributed under the Creative Commons Attribution License, which permits unrestricted use, distribution, and reproduction in any medium, provided the original work is properly cited.




Chief Editor

Stefano Bellucci , Italy

















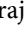
















Associate Editors

Ilaria Armentano, Italy
Stefano Bellucci , Italy
Paulo Cesar Morais , Brazil
William Yu , USA

Academic Editors

Buzuayehu Abebe, Ethiopia
Domenico Acierno , Italy
Sergio-Miguel Acuña-Nelson , Chile
Katerina Aifantis, USA
Omer Alawi , Malaysia
Nageh K. Allam , USA
Muhammad Wahab Amjad , USA
Martin Andersson, Sweden
Hassan Azzazy , Egypt
Ümit Ağbulut , Turkey
Vincenzo Baglio , Italy
Lavinia Balan , France
Nasser Barakat , Egypt
Thierry Baron , France
Carlos Gregorio Barreras-Urbina, Mexico
Andrew R. Barron , USA
Enrico Bergamaschi , Italy
Sergio Bietti , Italy
Raghvendra A. Bohara, India
Mohamed Bououdina , Saudi Arabia
Victor M. Castaño , Mexico
Albano Cavaleiro , Portugal
Kondareddy Cherukula , USA
Shafiul Chowdhury, USA
Yu-Lun Chueh , Taiwan
Elisabetta Comini , Italy
David Cornu, France
Miguel A. Correa-Duarte , Spain
P. Davide Cozzoli , Italy
Anuja Datta , India
Loretta L. Del Mercato, Italy
Yong Ding , USA
Kaliannan Durairaj , Republic of Korea
Ana Espinosa , France
Claude Estournès , France
Giuliana Faggio , Italy
Andrea Falqui , Saudi Arabia



Matteo Ferroni , Italy
Chong Leong Gan , Taiwan
Siddhartha Ghosh, Singapore
Filippo Giubileo , Italy
Iaroslav Gnilitzkiy, Ukraine
Hassanien Gomaa , Egypt
Fabien Grasset , Japan
Jean M. Greneche, France
Kimberly Hamad-Schifferli, USA
Simo-Pekka Hannula, Finland
Michael Harris , USA
Hadi Hashemi Gahruei , Iran
Yasuhiko Hayashi , Japan
Michael Z. Hu , USA
Zhengwei Huang , China
Zafar Iqbal, USA
Balachandran Jeyadevan , Japan
Xin Ju , China
Antonios Kelarakis , United Kingdom
Mohan Kumar Kesarla Kesarla , Mexico
Ali Khorsand Zak , Iran
Avvaru Praveen Kumar , Ethiopia
Prashant Kumar , United Kingdom
Jui-Yang Lai , Taiwan
Saravanan Lakshmanan, India
Meiyong Liao , Japan
Shijun Liao , China
Silvia Licoccia , Italy
Zainovia Lockman, Malaysia
Jim Low , Australia
Rajesh Kumar Manavalan , Russia
Yingji Mao , China
Ivan Marri , Italy
Laura Martinez Maestro , United Kingdom
Sanjay R. Mathur, Germany
Tony McNally, United Kingdom
Pier Gianni Medaglia , Italy
Paul Munroe, Australia
Jae-Min Myoung, Republic of Korea
Rajesh R. Naik, USA
Albert Nasibulin , Russia
Ngoc Thinh Nguyen , Vietnam
Hai Nguyen Tran , Vietnam
Hiromasa Nishikiori , Japan

Sherine Obare , USA
Abdelwahab Omri , Canada
Dillip K. Panda, USA
Sakthivel Pandurengan , India
Dr. Asisa Kumar Panigrahy, India
Mazeyar Parvinzadeh Gashti , Canada
Edward A. Payzant , USA
Alessandro Pegoretti , Italy
Oscar Perales-Pérez, Puerto Rico
Anand Babu Perumal , China
Suresh Perumal , India
Thathan Premkumar , Republic of Korea
Helena Prima-García, Spain
Alexander Pyatenko, Japan
Xiaoliang Qi , China
Haisheng Qian , China
Baskaran Rangasamy , Zambia
Soumyendu Roy , India
Fedlu Kedir Sabir , Ethiopia
Lucien Saviot , France
Shu Seki , Japan
Senthil Kumaran Selvaraj , India
Donglu Shi , USA
Muhammad Hussnain Siddique , Pakistan
Bhanu P. Singh , India
Jagpreet Singh , India
Jagpreet Singh, India
Surinder Singh, USA
Thangjam Ibomcha Singh , Republic of Korea
Korea
Vidya Nand Singh, India
Vladimir Sivakov, Germany
Tushar Sonar, Russia
Pingan Song , Australia
Adolfo Speghini , Italy
Kishore Sridharan , India
Marinella Striccoli , Italy
Andreas Stylianou , Cyprus
Fengqiang Sun , China
Ashok K. Sundramoorthy , India
Bo Tan, Canada
Leander Tapfer , Italy
Dr. T. Sathish Thanikodi , India
Arun Thirumurugan , Chile
Roshan Thotagamuge , Sri Lanka

Valeri P. Tolstoy , Russia
Muhammet S. Toprak , Sweden
Achim Trampert, Germany
Tamer Uyar , USA
Cristian Vacacela Gomez , Ecuador
Luca Valentini, Italy
Viet Van Pham , Vietnam
Antonio Vassallo , Italy
Ester Vazquez , Spain
Ajayan Vinu, Australia
Ruibing Wang , Macau
Magnus Willander , Sweden
Guosong Wu, China
Ping Xiao, United Kingdom
Zhi Li Xiao , USA
Yingchao Yang , USA
Hui Yao , China
Dong Kee Yi , Republic of Korea
Jianbo Yin , China
Hesham MH Zakaly , Russia
Michele Zappalorto , Italy
Mauro Zarrelli , Italy
Osman Ahmed Zeleke, Ethiopia
Wenhui Zeng , USA
Renyun Zhang , Sweden

Contents

Silica Nanoparticle Coating of $\text{NaYF}_4:(\text{Yb}^{3+}, \text{Er}^{3+})$ Upconversion Phosphor

Taehun Jang , MaengJun Kim , and Sang Ho Sohn 



Research Article (8 pages), Article ID 8961362, Volume 2022 (2022)

Effect of SC Parameters on Material Characteristics for Al 5083-Based Hybrid Matrix Composites Using Taguchi RSM Technique



A. U. Rao, K. Ramasamy, A. Pradeep, P. S. Satheesh Kumar, Srikanth Karumuri, and Bhiksha Gugulothu 

Research Article (7 pages), Article ID 7654128, Volume 2022 (2022)

Applications of Natural Violet Pigments from Halophilic *Chromobacterium violaceum* PDF23 for Textile Dyeing with Antimicrobial and Antioxidant Potentials




Antonyraj Matharasi Perianaika Anahas, Subramanian Kumaran , Mahmoud Kandeel ,

Gangatharan Muralitharan, Jenifer Silviya, Geja Lakshmi Adhimoolum, Mani Panagal, Sampath Renuka

Pugazhvendan , Gopal Suresh, A. Wilson Aruni, Senthil Rethinam, and Nainangu Prasannabalaji 



Research Article (13 pages), Article ID 3885396, Volume 2022 (2022)

Wear Behavior and FESEM Analysis of LM 25 Alloy MMHCs Reinforced with Fe_3O_4 and Gr by Utilizing Taguchi's Technique

G. Gokilakrishnan, R. Sathishkumar , N. S. Sivakumar , S. Kaliappan, S. Sekar, Pravin P. Patil, Ram Subbiah, K. P. Yuvaraj, and Feleke Worku Tadesse 


Research Article (10 pages), Article ID 3203057, Volume 2022 (2022)

Optimization of Tensile and Impact Strength for Injection Moulded Nylon 66/Sic/B₄C Composites

G. Boopathy, V. Vanitha, K. Karthiga, Bhiksha Gugulothu , A. Pradeep, Hari Prasadarao Pydi, and S. Vijayakumar 


Research Article (9 pages), Article ID 4920774, Volume 2022 (2022)

Influence of Methods of Nanomaterial Testing on Product Supply and an IoT-Based Solution for Making a Perfect Choice

D. K. Nagarathi , V. Ramya , Latha Parthiban, and Yalew Asres 



Research Article (10 pages), Article ID 9370008, Volume 2022 (2022)

Analysis and Experimental Investigation of A356 Aluminium Alloy Hybrid Composites Reinforced with Gr- Fe_3O_4 -B₄C Nanoparticles Synthesised by Selective Laser Melting (SLM)

J. Anoop, Vijay Ananth Suyamburajan, P. Sekhar Babu, and Sisay Addis Filketu 



Research Article (8 pages), Article ID 7510499, Volume 2022 (2022)

Microstructure and Mechanical Behaviour of Ti-6Al-4V Matrix Reinforced with WCp Developed by Squeeze Casting

R. Sivakumar, B. R. Senthil Kumar, G. Gopalarama Subramaniyan, M. Sivaraja, M. P. Natarajan, Pravin P. Patil, S. Kaliappan , K. P. Yuvaraj, and Kassie Jemberu Abebe 



Research Article (9 pages), Article ID 6381265, Volume 2022 (2022)

Bioinspired Crosslinked Nanocomposites of Polyvinyl Alcohol-Reinforced Cellulose Nanocrystals Extracted from Rice Straw with Ethanedioic Acid

Kwok-Mern Chin, Sung Ting Sam , Hui Lin Ong, Yee Shian Wong, Wai Kian Tan, and Vilay Vannaladsaysy 



Research Article (16 pages), Article ID 3225211, Volume 2022 (2022)

Fabrication of Silver Nanoparticles Using *Fimbristylis miliacea*: A Cheap and Effective Tool against Invasive Mosquito Vector, *Aedes albopictus*

Mathalaimuthu Baranitharan, Mahmoud Kandeel , Govindan Shanmugavel, Kumaravel Kaliyaperumal, Kumaran Subramanian , Kuppusamy Elumalai, Jayapal Gokulakrishnan, Hari Irrusappan, Senthil Rethinam, and S. Velmurugan 




Research Article (9 pages), Article ID 4083663, Volume 2022 (2022)

Effects of Thermal Barrier Coating Using Various Dosing Levels of Aluminium Oxide Nanoadditive Fuel on Diesel in Compressed Ignition Engine

V. S. Shaisundaram , S. Saravanakumar, V. Balambica, D. Sendil Kumar, M. Chandrasekaran, R. Muraliraja, A. Muniappan, and Yalew Asres 







Research Article (10 pages), Article ID 8355098, Volume 2022 (2022)

e-Modeling and Evolution of Nanolubricant Coupled Machining Parameters Using Statistical Tool

M. Sangeetha, Lilly Mercy, Dillipkumar Sahoo, P. Gunasekar, T. R. Praveenkumar , Habtamu Fekadu Gemedo , and Rajesh Madasamy 


Research Article (19 pages), Article ID 8946460, Volume 2022 (2022)

Experimental Analysis Using USRP for Novel Wavelet-Based Spectrum Sensing for 2.2 GHz Band Communication Using LabVIEW

Kalpana Devi Perumal , E. D. Kanmani Ruby , M. Dhivya , G. Aloy Anuja Mary , V. Kavitha , and Umamahesawari Kandasamy 

Research Article (8 pages), Article ID 4947224, Volume 2022 (2022)




Sustainability Improvement of Ethanol Blended Gasoline Fuelled Spark Ignition Engine by Nanoparticles

J. Thamilarasan, V. Ravikumar, S. Prasanna Raj Yadav , Jyothi Yarlagaadda, Ashok Kumar, S.

Ramasubramanian, P. Sambandam, Challa Parvathi Rudesh, and Yalew Asres 

Research Article (8 pages), Article ID 7793947, Volume 2022 (2022)

Hybrid Novel Additive Manufacturing for Sustainable Usage of Waste

Balaji Devarajan , V. Bhuvaneswari, B. Arulmurugan , A. V. N. S. L. Narayana, A. K. Priya, V. D. N. Kumar Abbaraju, K. S. Mukunthan, Amit Kumar Sharma, Sam Sung Ting, and Chandran Masi 

Research Article (12 pages), Article ID 2697036, Volume 2022 (2022)





Wear Behavioral Study of Hexagonal Boron Nitride and Cubic Boron Nitride-Reinforced Aluminum MMC with Sample Analysis

Vasudeva Rao, P. Periyaswamy, A. Bovas Herbert Bejaxhin , E. Naveen, N. Ramanan, and Aklilu Teklemariam 







Research Article (10 pages), Article ID 7816372, Volume 2022 (2022)

Contents


Additive Manufacturing for Aerospace from Inception to Certification

Devarajan Balaji , Jarabala Ranga, V. Bhuvaneswari, B. Arulmurugan , L. Rajeshkumar , Mohan Prasad Manimohan, G. Ramya Devi, G. Ramya, and Chandran Masi 
Review Article (18 pages), Article ID 7226852, Volume 2022 (2022)



Tribological Characteristics of GCI-EN31 Steel Surface Contact with Dry Sliding Condition

S. Ananth , P. Sivaprakasam , J. Udaya Prakash , B. Ravi , G. Kalusuraman , and R. Sundarakannan 
Research Article (11 pages), Article ID 6478781, Volume 2022 (2022)


Analysis of Physical, Ocular, and Aquaphobic Properties of Zirconium Oxide Nanofilms by Varying Sputtering Pressure

Sujit Kumar, Vikramaditya Dave, Muthamil Bala Krishnan, V. Amudha, S. Gomathi, Sanjay Soni, Syed Hamim Jeelani, Ram Subbiah, and Kassu Negash 
Research Article (10 pages), Article ID 8752664, Volume 2022 (2022)



Optimization of Cold Spray Process Inputs to Minimize Porosity and Maximize Hardness of Metal Matrix Composite Coatings on AZ31B Magnesium Alloy

Ashokkumar Mohankumar , Thirumalaikumarasamy Duraisamy, Deepak Sampathkumar, Sathiyamoorthy Ranganathan, Guruprasad Balachandran, Murugan Kaliyamoorthy, Mathanbabu Mariappan, and Lijalem Mulugeta 
Research Article (17 pages), Article ID 7900150, Volume 2022 (2022)







Surface Roughness Evaluation in Turning of Nimonic C263 Super Alloy Using 2D DWT Histogram Equalization

S. Lakshmana Kumar , M. Thenmozhi , R. M. Bommi , Chakaravarthy Ezilarasan , V. Sivaraman , and Sivaprakasam Palani 
Research Article (11 pages), Article ID 9378487, Volume 2022 (2022)



Multiparametric Optimization on Influence of Ethanol and Biodiesel Blends on Nanocoated Engine by Full Factorial Design

A. P. Venkatesh, T. P. Latchoumi, S. Chezhian Babu, K. Balamurugan, S. Ganesan, M. Ruban , and Lijalem Mulugeta 
Research Article (9 pages), Article ID 5350122, Volume 2022 (2022)

Adiabatic CMOS-Based Electrostatic MEMS Actuation for Reduced Dynamic Power and Switching Activity

P. Muthu , P. T. Vasanth Raj , R. M. Bommi , M. Baskar , S. Selvaganapathi , and P. Sivaprakasam 
Research Article (13 pages), Article ID 5416342, Volume 2022 (2022)

Analysis of Mechanical Properties for Al-MMC Fabricated through an Optimized Stir Casting Process




Bhiksha Gugulothu , N. Nagarajan, A. Pradeep, G. Saravanan, S. Vijayakumar , and Janardhana Rao
Research Article (7 pages), Article ID 2081189, Volume 2022 (2022)

Improvement Study on Blood Test Investigation by Nanoparticle-Coated Colour-Coded Sample Paper

P. Jayakumar , S. Padmanabhan , B. Sheela Rani, B. Balamugundan, and Lijalem Mulugeta 










Research Article (9 pages), Article ID 8277421, Volume 2022 (2022)

Estimation of Entropy for Log-Logistic Distribution under Progressive Type II Censoring

M. Shrahili , Ahmed R. El-Saeed, Amal S. Hassan, Ibrahim Elbatal , and Mohammed Elgarhy 

Research Article (10 pages), Article ID 2739606, Volume 2022 (2022)

Nanomaterials: A Promising Therapeutic Approach for Cardiovascular Diseases

Hitesh Chopra , Shabana Bibi, Awdhesh Kumar Mishra , Vineet Tirth, Sree Vandana Yerramsetty, Sree Varshini Murali, Syed Umair Ahmad , Yugal Kishore Mohanta , Mohamed S. Attia , Ali Algahtani , Fahadul Islam, Abdul Hayee , Saiful Islam, Atif Amin Baig , and Talha Bin Emran 

Review Article (25 pages), Article ID 4155729, Volume 2022 (2022)

Research Article

Silica Nanoparticle Coating of $\text{NaYF}_4:(\text{Yb}^{3+}, \text{Er}^{3+})$ Upconversion Phosphor

Taehun Jang , MaengJun Kim , and Sang Ho Sohn 

Department of Physics, Kyungpook National University, Daegu 41566, Republic of Korea

Correspondence should be addressed to Sang Ho Sohn; shsohn@knu.ac.kr

Received 25 March 2022; Revised 24 May 2022; Accepted 8 July 2022; Published 28 July 2022

Academic Editor: N Senthilkumar

Copyright © 2022 Taehun Jang et al. This is an open access article distributed under the Creative Commons Attribution License, which permits unrestricted use, distribution, and reproduction in any medium, provided the original work is properly cited.

To improve its light conversion efficiency, $\text{NaYF}_4:(\text{Yb}^{3+}, \text{Er}^{3+})$ upconversion (UC) phosphor, which generates one visible photon by absorbing two or more near-infrared photons, was coated with SiO_2 nanoparticles. The surface modification of phosphor was performed by using a modified sol-gel method as a function of the concentration of colloidal silica employed as the surface coating precursor. It was found that the PL intensities depend on the concentration of colloidal silica. When a 2.7 wt% concentration of colloidal silica was used, the $\text{NaYF}_4:(\text{Yb}^{3+}, \text{Er}^{3+})$ phosphor exhibited a homogeneous coating with silica and an approximately 9% increase in the PL intensity, as compared with that of the non-coated sample of $\text{NaYF}_4:(\text{Yb}^{3+}, \text{Er}^{3+})$ phosphor. This increase in the PL intensity can be explained by the suppression of the nonradiative recombination of electron-hole pairs via surface defects. The experimental results suggest that the surface modification of upconversion phosphors with a silica coating of the appropriate concentration is a simple and effective solution to improve the light conversion efficiency of upconversion phosphors used in optoelectronic devices.

1. Introduction

Thus far, hexagonal NaYF_4 nanocrystals with sizes in the 20–30 nm range have been the most efficient host materials for green and blue upconversion (UC) phosphors exhibiting visible emission by IR excitation [1]. In the host material, Y^{3+} can be replaced at any ratio by the rare earth ions Yb^{3+} and Er^{3+} for green UC phosphors. Meanwhile, significant research has been accomplished to improve the material properties of lanthanide-doped upconversion nanoparticles (UCNPs), particularly the quantum yield (QY) of solar cells and biochips. Among such research, studies on the influence of shelling with meso- and microporous silica on fluorescence characteristics are notable examples [1, 2].

Figure 1 depicts the UC processes of Er^{3+} and Yb^{3+} codoped NaYF_4 phosphors. The main absorption process of Yb^{3+} is the $2F_{7/2} \rightarrow 2F_{5/2}$ transition at 980 nm [3]. The most dominant excitation path in Er^{3+} is $4I_{15/2} \rightarrow 4I_{11/2} \rightarrow 4F_{7/2}$, which requires two energy transfers for the $2F_{7/2} \rightarrow 2F_{5/2}$ transition of Yb^{3+} . Subsequent multiphonon

relaxation populates the emitting $2H_{11/2}$ and $4S_{3/2}$ states. Through further excitation and cross-relaxation processes, the populations of the $2H_{9/2}$ and $4F_{5/2}$ states were also obtained [4, 5]. A previous study using a delicate photoluminescence measurement reported that the QY of UCNPs was lower than 0.3% for the green emission in $\text{NaYF}_4:(\text{Er}^{3+}, \text{Yb}^{3+})$ UCNP phosphors, whereas a QY of 3% was measured for an upconversion microparticle (UCMP) phosphor [6]. Despite extensive research [1, 2, 7–10], satisfactory QYs have seldom been obtained. Therefore, the QY of UCNPs should be improved using a specific method. UCNP phosphors exhibit a larger surface area/bulk volume ratio than UCMP phosphors. The surfaces of the phosphors exhibit inevitable surface defects that are formed when they are synthesized. Therefore, the surface defect density per unit volume of UCNP phosphors can be larger than that of UCMP phosphors. It is well known that nonradiative decay can occur via the surface defects of emissive materials. This could explain why the QY of the UCNP phosphors is significantly lower than that of the UCMP phosphors. It is of interest that research based on the energy transfer mechanism [3, 11] for

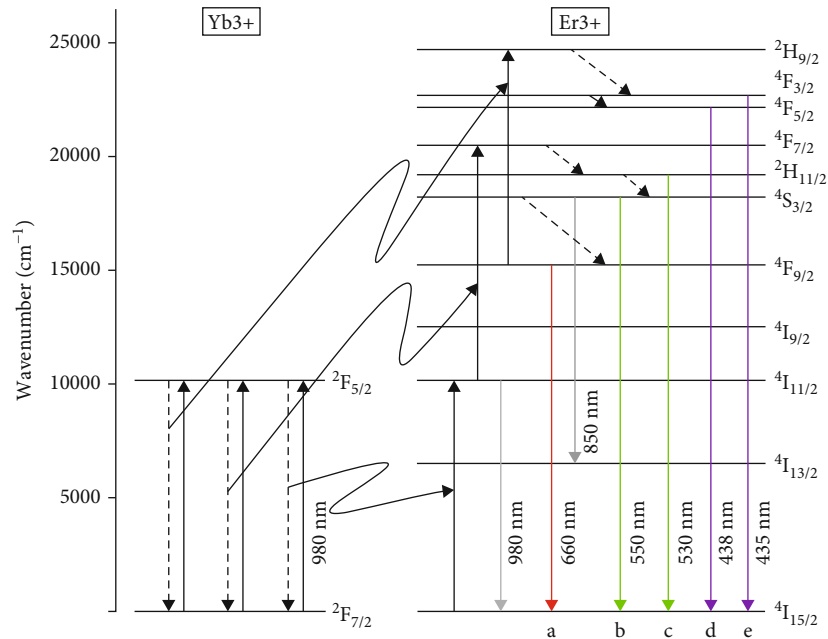


FIGURE 1: UC processes in Er^{3+} and Yb^{3+} codoped NaYF_4 phosphors.

the improvement of the QY of UCMP phosphors has been accomplished. From the viewpoint of the QY, UCMP phosphors are more promising than UCNP phosphors.

Earlier studies [12–14] related to the surface modification of microphosphors have suggested that surface coating with oxides is an important technique for improving phosphor characteristics, such as luminance. The present study is aimed at substantiating the same and suggests a silica nanoparticle coating on the surface of the UCMP phosphors. To obtain nanoparticle-coated UCMP phosphors with improved luminance performance, we prepared $\text{NaYF}_4:(\text{Yb}^{3+}, \text{Er}^{3+})$ microphosphors coated with SiO_2 nanoparticles using a modified sol–gel method and investigated their optical properties. The modified sol–gel method used for surface treatment in this work is a simple and low-temperature (below 100°C) process, as compared with other chemical methods [15].

2. Materials and Methods

Commercially available hexagonal $\text{NaYF}_4:(\text{Yb}^{3+}, \text{Er}^{3+})$ (18% and 2% doped, respectively) microphosphor (KPT 980 nm, Shanghai Keyan Phosphor Technology Co., Ltd.) was coated with SiO_2 using a modified sol–gel method in which colloidal silica (LUDOX-AM-30; Sigma-Aldrich Chemicals Pvt., Ltd.) with an average particle size of 12 nm was employed as a precursor. As reported in our earlier studies [12, 13], the SiO_2 -coated phosphors were obtained as follows: (1) Various concentrations of colloidal SiO_2 nanoparticles were prepared by dilution using deionized (DI) water. (2) 10 g of $\text{NaYF}_4:(\text{Yb}^{3+}, \text{Er}^{3+})$ was added to 100 ml of diluted colloidal SiO_2 with continuous stirring using a magnetic bar for 3 h. (3) The resulting phosphor suspensions were washed twice with DI water. (4) SiO_2 -coated phosphors were obtained by filtering and drying the washed phosphor suspension at

80°C for 12 h. The morphological properties of the coated and the noncoated UC phosphors were compared using a scanning electron microscope (SEM). To perform surface analysis, an X-ray photoelectron spectroscopy (XPS) system (ULVAC-PHI Quantera SXM) equipped with a monochromated Al $K\alpha$ source and a hemispherical analyzer was used. The energy resolution of the XPS system for high-resolution core-line scans was set to 0.1 eV. The spot size was set to 0.4 mm.

As shown in Figure 2, a PL measurement system was set up to determine the UC efficiencies of the phosphor samples. A simple IR laser diode with a wavelength of 980 nm was used for excitation. An equal amount of phosphor powder was placed in a quartz cuvette. The laser and quartz cuvettes were reproducibly positioned on an optical table. The optical spectrum was acquired by configuring instruments manufactured by EG&G Princeton Applied Research. All measurements were performed at room temperature. The emitted light was coupled into a fixed optical fiber and measured in the 384–716 nm range using a zodel 1237 dual-port optical modulation amplitude (OMA) spectrograph with a Model 1420 photodiode array (PDA). The metal pipe holder is used to fix the optical fiber. The electrical signal acquisition was performed using a Model 1461 detector interface.

3. Results and Discussion

Figure 3 presents the SEM images of the $\text{NaYF}_4:(\text{Yb}^{3+}, \text{Er}^{3+})$ phosphors coated with nanoparticles at several colloidal silica concentrations and the noncoated phosphors. The size of the non-coated UC phosphor was in the 1–10 μm range, as shown in Figure 3(a). As shown with dotted circles in Figures 3(b)–3(e), it can be easily observed that the surfaces of the $\text{NaYF}_4:(\text{Yb}^{3+}, \text{Er}^{3+})$ phosphors are covered with fine

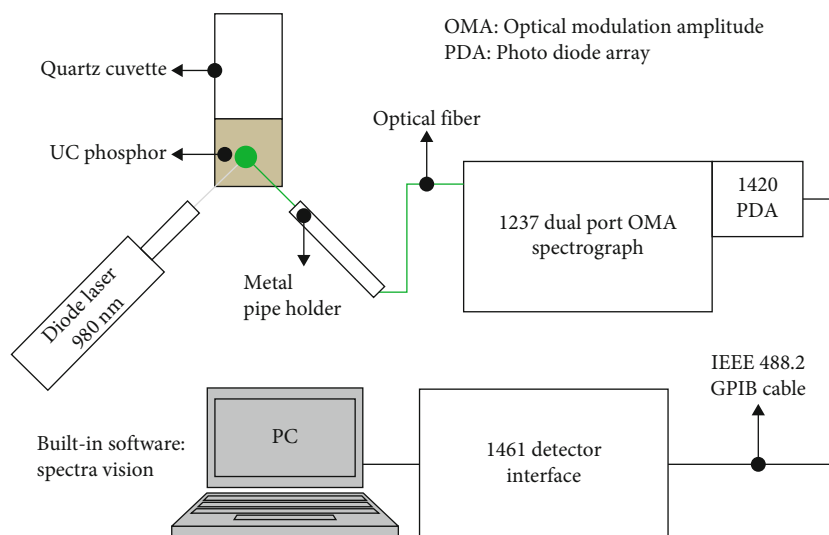


FIGURE 2: PL measurement system for the UC efficiencies of the phosphor samples.

nanoparticles featuring a size of ~ 100 nm. As expected, it was observed that the silica concentration significantly affected the surface morphology of the UC phosphors. For the 0.3 wt% and 1.5 wt% concentrations, the coverage of nanoparticles was insufficient to coat the UC phosphors homogeneously, as shown in Figures 3(b) and 3(c). For the 2.7 wt% condition, a homogeneous coating was obtained, as shown in Figure 3(d). For all higher mole concentrations such as 5.0 wt%, the uniformity of the coating on the UC phosphors was observed to deteriorate, exhibiting a type of cluster. As shown in Figure 3(e), the existence of large clusters of nanoparticles implies that, before adhesion to the surface of the UC phosphors, the nanoparticles aggregate and then couple with the UC phosphors. However, at this point, it was difficult to confirm whether the fine nanoparticles in the SEM images were SiO_2 nanoparticles. For this purpose, surface analysis, such as XPS, was required.

Figure 4 shows the XPS spectra of the respective elements of the $\text{NaYF}_4:(\text{Yb}^{3+}, \text{Er}^{3+})$ phosphor, with respect to the SiO_2 concentrations. Figures 4(a)–4(f) illustrate the survey scan, Si 2p, O 1s, Na 1s, Y 3d, and F 1s XPS spectra, respectively. In Figure 4(a), to compare between the relative XPS peak intensity, only peaks for silica concentration of 2.7 wt% are introduced because we could not draw all peaks for five silica concentrations in a graph without overlapping. The survey scan spectrum reveals the presence of Si, O, Na, Y, and F elements. As shown in Figure 4(b), Si peaks were observed only in the SiO_2 -coated phosphor, unlike the noncoated phosphor (0 wt%). From the NIST Standard Reference Database 20, it is found that Si 2p peak shown in Figure 4(b) originates from the convolution of the peaks related to the Si-O bonds. In addition, as exhibited in Figure 4(c), strong O peaks are observed in the SiO_2 -coated phosphor, compared to the noncoated phosphor (0 wt%). The weak O peaks observed in the non-coated phosphor are probably related to the presence of residual oxygen in the $\text{NaYF}_4:(\text{Yb}^{3+}, \text{Er}^{3+})$ phosphor, which is an intrinsic impurity. Thus, the presence of SiO_2 nanoparticles covering

the $\text{NaYF}_4:(\text{Yb}^{3+}, \text{Er}^{3+})$ phosphors can be confirmed by the Si 2p and O 1s spectra. Further, it can be confirmed that the nanosized particles observed in Figure 3 are composed of SiO_2 . In addition, as expected, it was observed that the Na- and F-related peaks decreased to a large extent after silica coating. It should be noted that, for all the samples coated with SiO_2 nanoparticles, the Na 1s, Y 3d, and F 1s peaks yield slight shifts (0.2–0.3 eV) to higher binding energies, as compared with those for the noncoated phosphor. This suggests that the residual NaF compound affects the chemical binding energy of the respective elements of the NaYF_4 host crystal, causing a small shift to lower binding energies in the case of the noncoated $\text{NaYF}_4:(\text{Yb}^{3+}, \text{Er}^{3+})$ phosphor. To the best of our knowledge, no references for any elements consisting of NaYF_4 have been registered in scientific databases. However, a similar stoichiometric compound such as sodium fluoroborate (NaBF_4) can provide a reasonable explanation. According to the NIST Standard Reference Database 20, version 3.5, for NaF, the Na 1s and F 1s reference peaks are observed at 1071.2 eV and 684.5 eV, respectively. However, for NaBF_4 , the Na 1s and F 1s reference peaks appear at 1072.7 eV and 687 eV, respectively. Thus, it is suggested that these shifts are due to the absence of NaF. These results are consistent with the XPS results described above. In addition, Y 3d peaks shown in Figure 4(e) have well-resolved spin-orbit components corresponding to the total angular momentum $J = 3/2$, and $J = 5/2$ states. The peak observed in the vicinity of 153 eV in Figure 4(e) is associated with Si 2s.

Figure 5(a) shows the PL spectra in the visible region for the $\text{NaYF}_4:(\text{Yb}^{3+}, \text{Er}^{3+})$ phosphors coated with silica at several concentrations. In Figure 5(a), the main emission wavelength regions labeled A, B, C, D, and E are associated with the emission transitions shown in the energy-level diagrams depicted in Figure 1. For clarity, enlarged figures of the specific wavelength ranges in Figure 5(a) are also shown in Figures 5(b)–5(e). For all the wavelengths in the emission spectrum shown in Figure 5(a), the integrated area was

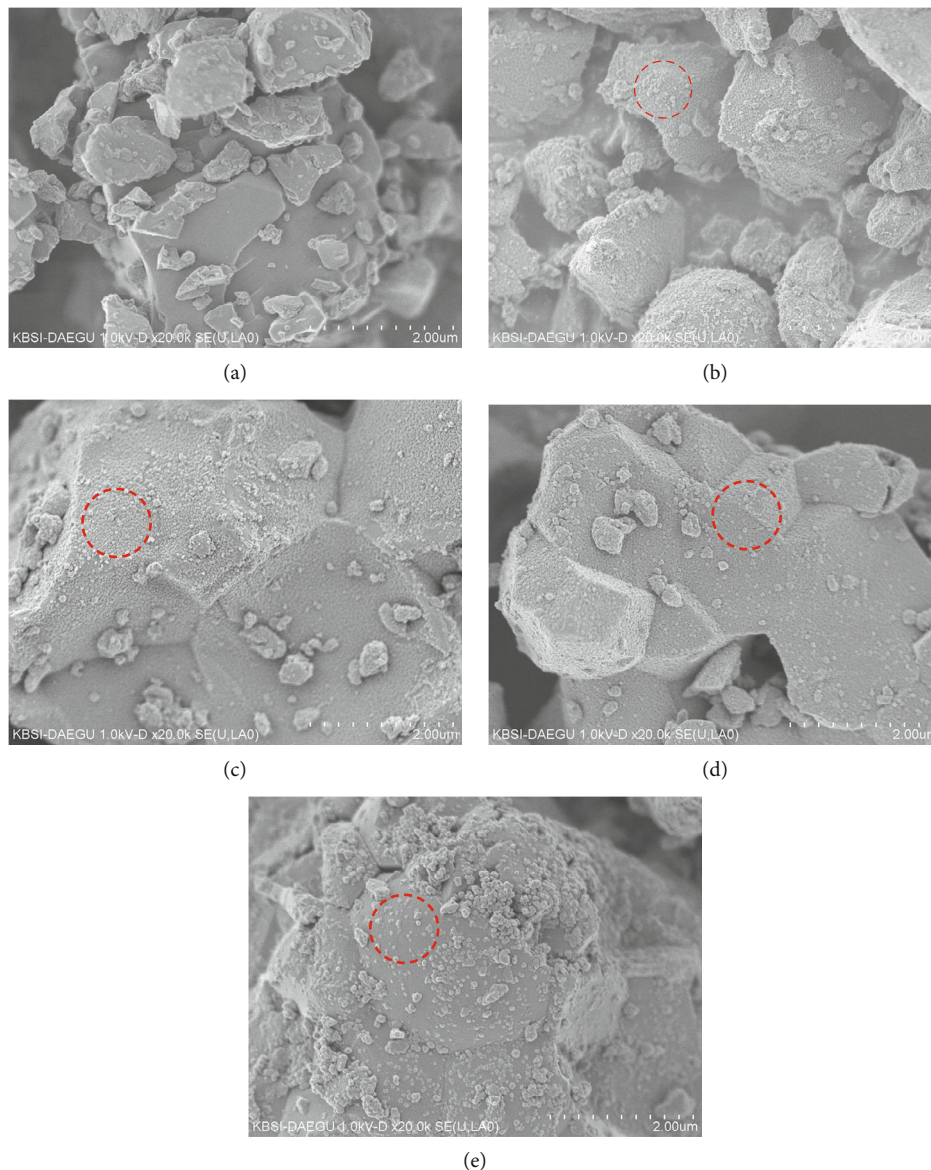


FIGURE 3: SEM images of $\text{NaYF}_4:(\text{Yb}^{3+}, \text{Er}^{3+})$ phosphors coated with nanoparticles at several colloidal silica concentrations and noncoated phosphor ((a) noncoated 0 wt%, (b) 0.3 wt%, (c) 1.4 wt%, (d) 2.7 wt%, and (e) 5.0 wt%). The dotted circles represent nanoparticles coated on the surface of $\text{NaYF}_4:(\text{Yb}^{3+}, \text{Er}^{3+})$ microphosphors.

calculated to enable a quantitative comparison. The estimated calculation demonstrated that the intensities of the silica-coated phosphors at the 0.3 wt%, 1.4 wt%, and 2.7 wt% conditions were higher than those of the noncoated samples (0 wt%), without exhibiting any wavelength shifts in the core-level transition regions, thereby indicating that the presence of SiO_2 particles on the surface of the UC phosphors affects the PL intensity. For the 0.3 wt% and 1.4 wt% conditions, an increase of approximately 2% in the PL intensity was observed. The maximum PL performance was observed for the concentration of 2.7 wt%, whereby a PL characteristic improvement of approximately 9% was detected, as compared with that of the noncoated UC phosphors. These results suggest that the increase in the PL intensity is strongly related to the uniformity of the surface

modification with oxides, as shown in Figures 3(b)–3(d). In contrast, for the 5 wt% condition, a decrease of almost 10% in the PL intensity of the coated phosphors was observed, as compared with that of the noncoated UC phosphors. These results can be easily analyzed based on the morphological properties acquired by the SEM measurements, as shown in Figure 4. As shown in Figure 3(e), a homogeneous nanoparticle coating is barely obtained. This was caused by the aggregation of SiO_2 nanoparticles, which hindered the impinging light from being absorbed by the phosphors and the emitted light from being transmitted. The influence of SiO_2 coating on the $\text{NaYF}_4:(\text{Yb}^{3+}, \text{Er}^{3+})$ UCNP has been reported in earlier research [1, 2, 15–18]. It is known that SiO_2 coating causes the $\text{NaYF}_4:(\text{Yb}^{3+}, \text{Er}^{3+})$ UCNP to protect UCNP from dissolution [1, 15], to improve the temperature

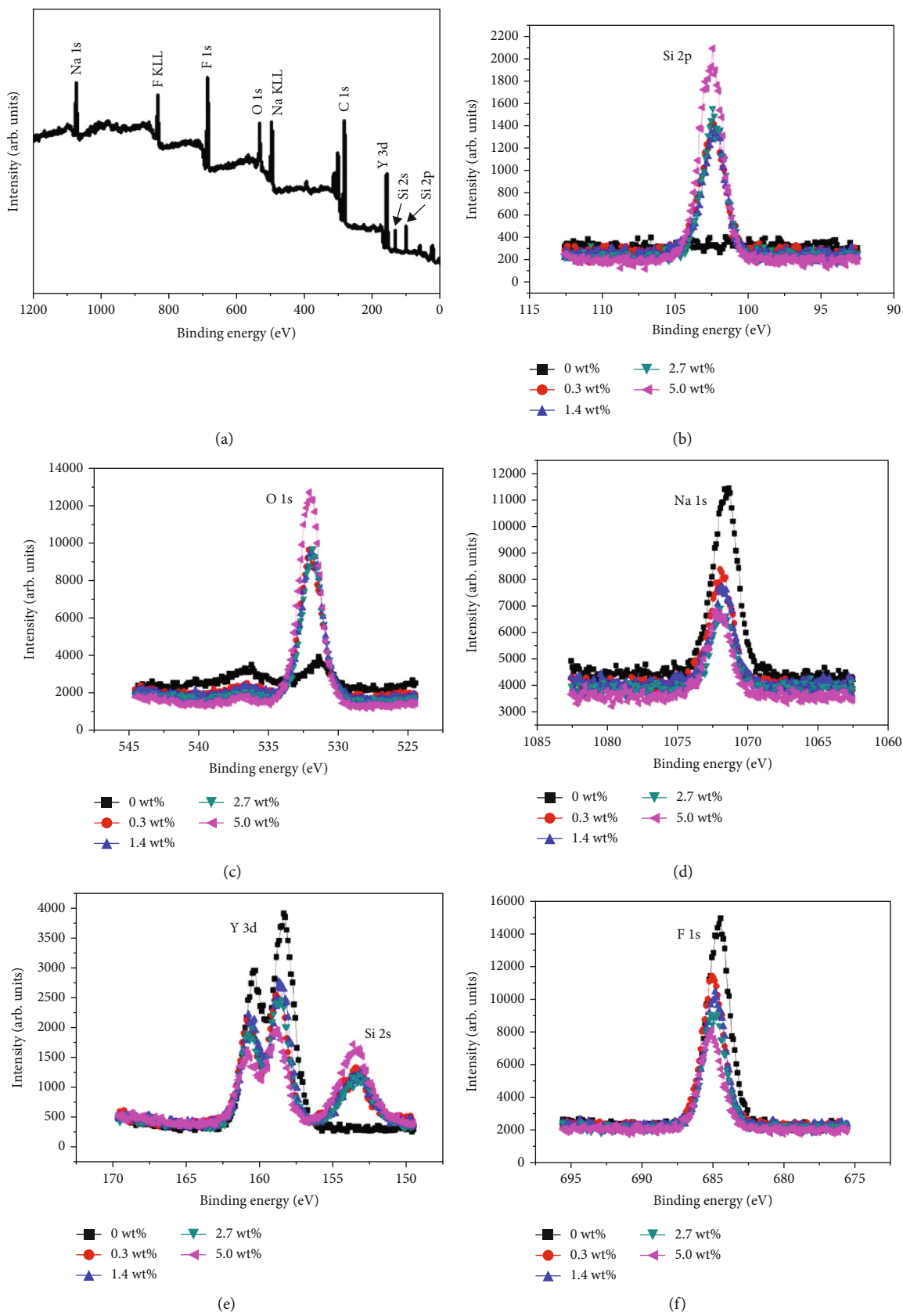


FIGURE 4: XPS spectra of the respective elements of $\text{NaYF}_4:(\text{Yb}^{3+}, \text{Er}^{3+})$ phosphor with respect to SiO_2 concentrations. (a) The survey scan, (b) Si 2p, (c) O 1s, (d) Na 1s, (e) Y 3d, and (f) F 1s XPS spectra.

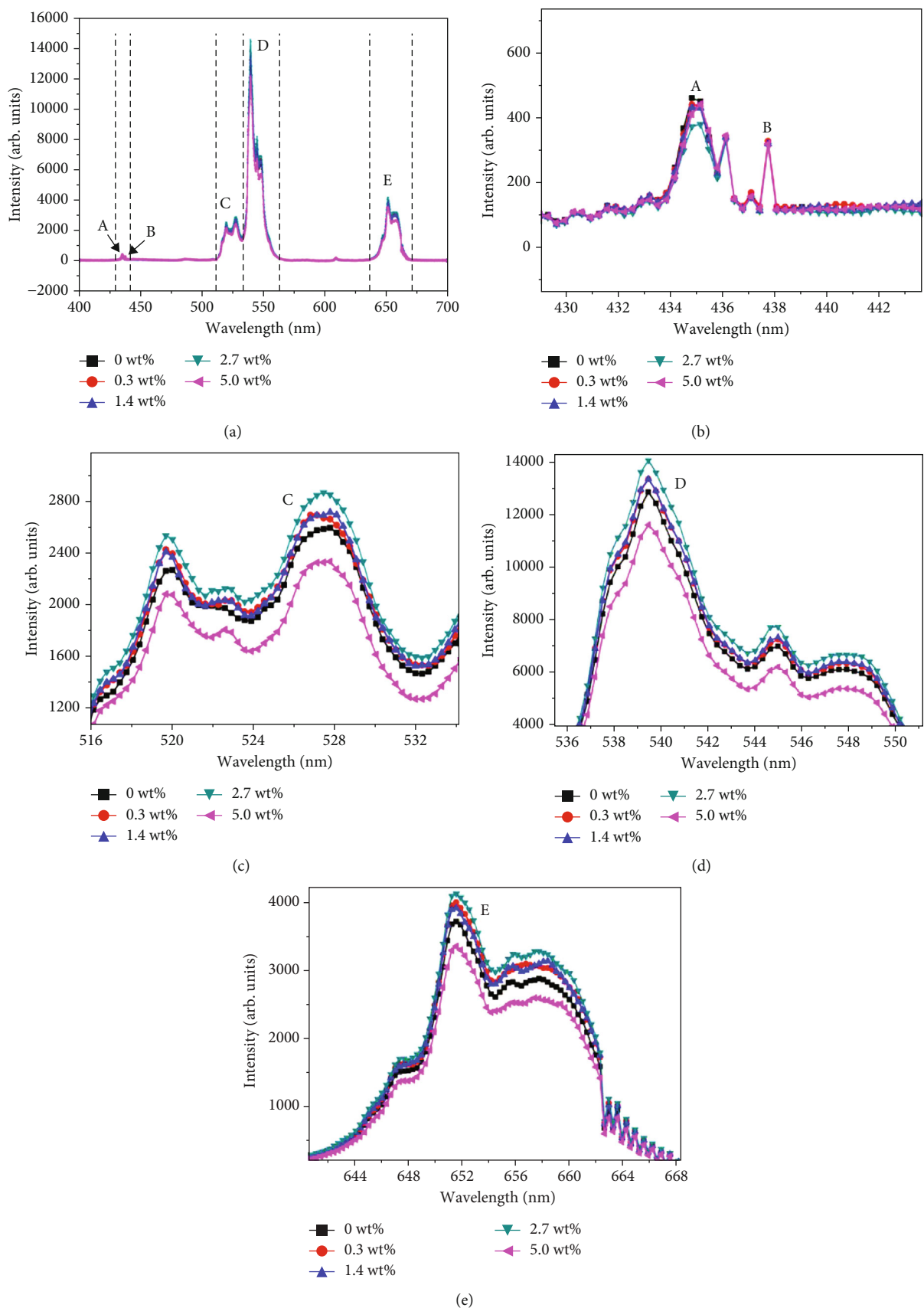


FIGURE 5: (a) PL spectra in the visible region for the NaYF₄:(Yb³⁺, Er³⁺) phosphors coated with SiO₂ at several concentrations. (b–e) Peaks denoted by A, B, C, D, and E in (a).

stability [2], to restore the chemical activity in aqueous media [16], to protect core from degradation in proteolytic solvents [17], and to enhance the adhesion of metal particles. But, as a whole, these studies report a decrease in PL intensities after SiO₂ coating on the NaYF₄:(Yb³⁺, Er³⁺) UCNP. The reason for it has not been argued in detail besides the light scattering effect on both emission and incident light by the SiO₂ layer. Meanwhile, it is known that SiO₂@metal coating on the NaYF₄:(Yb³⁺, Er³⁺) UCNP results in an increase in the PL intensity by means of exciton–plasmon coupling, resulting from the metal coating [18].

Our samples consist of SiO₂ nanoparticles coated on upconversion microsilica phosphors (UCMP), in contrast to those reported in earlier research [1, 2, 15–18]. Our NaYF₄:(Yb³⁺, Er³⁺) UCMP is not a nanoparticle but a bulky particle with lots of surface defects. Therefore, if SiO₂ coating reduces the surface defects, it is expected that the SiO₂ nanoparticles in our samples are a significant factor contributing toward the PL intensity, in contrast to the results reported in earlier studies [16]. Generally, radiation excites the bulky phosphor and generates free electron–hole pairs (e–h pairs). These e–h pairs diffuse into the surface defects and recombine nonradiatively, resulting in a decrease in the PL intensity [19]. SiO₂ nanoparticles coated on microsilica phosphors could reduce surface defects and suppress the nonradiative recombination of e–h pairs via the surface defects, thus resulting in a higher PL intensity. Thus, the increase in the PL intensity due to the surface coating of the phosphors with oxide nanoparticles can be explained on the basis of the suppression of nonradiative recombination via surface defects, among the several other mechanisms discussed in an earlier study [13]. However, there is still no direct tangible evidence in favor of this mechanism in SiO₂-coated NaYF₄:(Yb³⁺, Er³⁺) microsystems. To achieve this, a powerful tool for detecting the defects on phosphor surfaces, such as electron spin resonance (ESR) analysis, is required. Nevertheless, distinguishing between surface defects, bulk defects, and their entities in small phosphor grains using ESR signals [20] is considerably difficult. We expect that our results will be useful for the surface modification of other UC materials, such as KBaY(MoO₄)₃:Yb₃₊, Er₃₊ and NaYF₄:Yb,Er@SiO₂, which are promising candidates for use in optical sensors [21, 22].

4. Conclusion

In this study, to improve the light conversion efficiency of upconversion phosphor, silica nanoparticle-coated NaYF₄:(Yb³⁺, Er³⁺) microphosphors were prepared by a modified sol–gel method using colloidal silica as a function of concentration. The optimal concentration of colloidal silica was determined by comparing its morphological and optical properties. The NaYF₄:(Yb³⁺, Er³⁺) phosphor coated with colloidal silica (2.7 wt%) yielded an approximately 9% increase in the PL intensity, as compared with that of the noncoated phosphor, likely because of the suppression of nonradiative recombination via surface defects. The experimental results suggest that the surface coating of phosphors with an appropriate oxide is a simple and effective

solution to improve the light conversion efficiency of UCMP phosphors.

Data Availability

All the data used to support the findings of this study are available from the corresponding author upon request.

Conflicts of Interest

The authors declare that there are no conflicts of interest regarding the publication of this paper.

Acknowledgments

This research was supported by the Basic Science Research Program through the National Research Foundation of Korea (NRF), funded by the Ministry of Education (NRF-2019R11A1A3A01041101).


References

- [1] M. I. Saleh, B. Rühle, S. Wang, J. Radnik, Y. You, and U. Resch-Genger, “Assessing the protective effects of different surface coatings on NaYF₄:Yb³⁺, Er³⁺ upconverting nanoparticles in buffer and DMEM,” *Scientific Reports*, vol. 10, no. 1, pp. 1–11, 2020.
- [2] R. G. Geitenbeek, P. T. Prins, W. Albecht, A. van Blaaderen, B. M. Weckhuysen, and A. Meijerink, “NaYF₄:Er³⁺, Yb³⁺/SiO₂Core/Shell upconverting nanocrystals for luminescence thermometry up to 900 K,” *Journal of Physical Chemistry C*, vol. 121, no. 6, pp. 3503–3510, 2017.
- [3] H. Huang, H. Zhou, J. Zhou et al., “Enhanced anti-stocks luminescence in LaNbO₄:Ln³⁺ (Ln³⁺= Yb³⁺, Er³⁺/Ho³⁺/Tm³⁺) with abundant color,” *RSC Advances*, vol. 7, no. 27, pp. 16777–16786, 2017.
- [4] G. Gong, Y. Song, H. Tan et al., “Design of core/active-shell NaYF₄:Ln³⁺@NaYF₄:Yb³⁺ nanophosphors with enhanced red-green-blue upconversion luminescence for anti-counterfeiting printing,” *Composites Part B: Engineering*, vol. 179, p. 107504, 2019.
- [5] A. Dubey, A. K. Soni, A. Kumari, R. Dey, and V. K. Rai, “Enhanced green upconversion emission in NaYF₄:Er³⁺/Yb³⁺/Li⁺ phosphors for optical thermometry,” *Journal of Alloys and Compounds*, vol. 693, pp. 194–200, 2017.
- [6] J.-C. Boyer and F. C. J. M. van Veggel, “Absolute quantum yield measurements of colloidal NaYF₄:Er³⁺, Yb³⁺ upconverting nanoparticles,” *Nanoscale*, vol. 2, no. 8, pp. 1417–1419, 2010.
- [7] X. Zhou, X. Xia, B. E. Smith et al., “Interface-dependent radiative lifetimes of Yb³⁺, Er³⁺ co-doped single NaYF₄ upconversion nanowires,” *ACS Applied Materials & Interfaces*, vol. 11, no. 25, pp. 22817–22823, 2019.
- [8] C. Homann, L. Krukewitt, F. Frenzel et al., “NaYF₄:Yb,Er/NaYF₄ core/shell nanocrystals with high upconversion luminescence quantum yield,” *Angewandte Chemie International Edition*, vol. 57, no. 28, pp. 8765–8769, 2018.
- [9] H. Anwer, J. W. Park, and J.-W. Park, “Near-infrared to visible photon transition by upconverting NaYF₄:Yb³⁺, Gd³⁺, Tm³⁺@Bi₂WO₆ core@shell composite for bisphenol A degradation in solar light,” *Applied Catalysis B: Environmental*, vol. 243, pp. 438–447, 2019.

- [10] F. T. Rabouw, P. T. Prins, P. Villanueva-Delgado, M. Castelijns, R. G. Geitenbeek, and A. Meijerink, "Quenching pathways in $\text{NaYF}_4:\text{Er}^{3+},\text{Yb}^{3+}$ Upconversion Nanocrystals," *ACS Nano*, vol. 12, no. 5, pp. 4812–4823, 2018.
- [11] A. A. Vidyakina, I. E. Kolesnikov, N. A. Bogachev et al., "Gd³⁺ + -doping effect on upconversion emission of $\text{NaYF}_4:\text{Yb}^{3+},\text{Er}^{3+}/\text{Tm}^{3+}$ microparticles," *Materials*, vol. 13, no. 15, p. 3397, 2020.
- [12] I. Y. Jung, Y. Cho, S. G. Lee et al., "Optical properties of the $\text{BaMgAl}_{10}\text{O}_{17}:\text{Eu}^{2+}$ phosphor coated with SiO_2 for a plasma display panel," *Applied Physics Letters*, vol. 87, no. 19, p. 191908, 2005.
- [13] S. H. Sohn, J. H. Lee, and S. M. Lee, "Effects of the surface coating of $\text{BaMgAl}_{10}\text{O}_{17}:\text{Eu}^{2+}$ phosphor with SiO_2 nano-particles," *Journal of Luminescence*, vol. 129, no. 5, pp. 478–481, 2009.
- [14] J. H. Seo and S. H. Sohn, "Surface modification of the $(\text{Y,Gd})\text{BO}_3:\text{Eu}^{3+}$ phosphor by dual-coating of oxide nanoparticles," *Materials Letters*, vol. 64, no. 11, pp. 1264–1267, 2010.
- [15] W. Deng, L. Sudheendra, J. Zhao et al., "Upconversion in $\text{NaYF}_4:\text{Yb},\text{Er}$ nanoparticles amplified by metal nanostructures," *Nanotechnology*, vol. 22, no. 32, pp. 325604–325612, 2011.
- [16] K. L. Reddy, P. K. Sharma, A. Singh et al., "Amine-functionalized, porous silica-coated $\text{NaYF}_4:\text{Yb}/\text{Er}$ upconversion nanophosphors for efficient delivery of doxorubicin and curcumin," *Materials Science & Engineering, C*, vol. 96, pp. 86–95, 2019.
- [17] G. Arzumanyan, D. Linnik, K. Mamatkulov et al., "Synthesis of $\text{NaYF}_4:\text{Yb},\text{Er}@/\text{SiO}_2@\text{Ag}$ core-shell nanoparticles for plasmon-enhanced upconversion luminescence in bio-applications," *Annals of Biomedical Science and Engineering*, vol. 3, pp. 13–18, 2019.
- [18] J. Shen, Z. Q. Li, Y. R. Chen et al., "Influence of SiO_2 layer thickness on plasmon enhanced upconversion in hybrid $\text{Ag}/\text{SiO}_2/\text{NaYF}_4:\text{Yb},\text{Er},\text{Gd}$ structures," *Applied Surface Science*, vol. 270, pp. 712–717, 2013.
- [19] T. Jüstel and H. Nikol, "Optimization of luminescent materials for plasma display panels," *Advanced Materials*, vol. 12, no. 7, pp. 527–530, 2000.
- [20] B. S. Chakrabarty, K. V. R. Murthy, and T. R. Joshi, "TSL-EPR correlation study of $\text{LaPO}_4:\text{Ce},\text{Tb}$," *TŪBĪTAK Journal of Physics*, vol. 26, p. 193, 2002.
- [21] K. Li, D. Zhu, and H. Lian, "Up-conversion luminescence and optical temperature sensing properties in novel $\text{KBaY}(\text{MoO}_4)_3:\text{Yb}^{3+},\text{Er}^{3+}$ materials for temperature sensors," *Journal of Alloy and Compounds*, vol. 816, pp. 152554–152560, 2020.
- [22] Z. Li, L. Wang, Z. Wang, X. Liu, and Y. Xiong, "Modification of $\text{NaYF}_4:\text{Yb},\text{Er}@/\text{SiO}_2$ nanoparticles with gold nanocrystals for tunable green-to-red upconversion emissions," *Journal of Physical Chemistry C*, vol. 115, no. 8, pp. 3291–3296, 2011.

Research Article

Effect of SC Parameters on Material Characteristics for Al 5083-Based Hybrid Matrix Composites Using Taguchi RSM Technique

A. U. Rao,¹ K. Ramasamy,² A. Pradeep,³ P. S. Satheesh Kumar,⁴ Srikanth Karumuri,⁵ and Bhiksha Gugulothu ⁶

¹Department of Civil Engineering, Manipal Institute of Technology, Manipal Academy of Higher Education, Manipal, 576104 Karnataka, India

²Department of Electronics and Communication Engineering, KIT-KalaignarKarunanidhi Institute of Technology, Coimbatore, India

³Department of Mechanical Engineering, Saveetha School of Engineering, SIMATS, Chennai, India

⁴Department of Science and Humanities, NPR College of Engineering and Technology, Natham, Dindigul District, Tamil Nadu, India

⁵Department of Mechanical Engineering, Mizan-Tepi University, Ethiopia

⁶Department of Mechanical Engineering, Bule Hora University, Post Box No. 144, Ethiopia

Correspondence should be addressed to Bhiksha Gugulothu; bhikshamg@gmail.com

Received 23 March 2022; Accepted 14 July 2022; Published 25 July 2022

Academic Editor: Chang Chuan Lee

Copyright © 2022 A. U. Rao et al. This is an open access article distributed under the Creative Commons Attribution License, which permits unrestricted use, distribution, and reproduction in any medium, provided the original work is properly cited.

This research concentrated on material characteristics such as tensile property (TS) and hardness (HV) for AA-5083 manufactured using the stir casting (SC) process. The reinforcing elements silicon carbide (SiC-7.5%) and flyash (FA-5%) in the form of powders will be added to Al alloy to improve the characteristics of composites. Response surface methodology (RSM) was a scientific technique to make optimizing task at stir casting parameters. As per central composite design (CCD), 20 samples (L1-L20) were fabricated at a variation of factors such as stirrer speed (A) 350-550 rpm, stir time (B) 15-35 min, and stir temperature (C) 750-950°C. The result presented that best TS and HV exhibited at experiments L5 (A2-450 rpm, B1-15min, and C1-750°C) and L6 (A1-350 rpm, B1-15min, and C1-750°C). Design expert software (DES) is one of the optimization tools that employed to determine analysis of variance (ANOVA) and the best optimal parameter levels of SC. ANOVA helped to check contribution of SC factors on TS and HV, and it was noticed that mechanical properties were improved with increasing stir speed and stir time but it was reduced with rising of temperature.

1. Introduction

The chemical element like Al lacks sufficient strength when used to manufacture components in industrial business areas [1]. To address these challenges, particles or particulate reinforcements such as alumina, silicon-based carbides and oxides, TiB_2 , and TiO_2 are blended with Al to increase the strength of heavy items [2]. Al 5083 is made from many chemical elements including Mg, Mn, and Si. This kind of alloy is generally used in different application such as ship construction, automobile bodies, mine skip work [3], and pressure containers [4]. Stir SC routine is implemented in

cheap wise which was able to create difficult designed products among various fabrication techniques powder metallurgy, plasma sintering, etc. [5, 6]. Numerous researches suggested that using a single metal would not be able to produce the needed material properties [33, 34]. It is applied in several production enterprises [7]. B_2O_3 , B_6O , and BN_3O_6 are added to the primary matrix as reinforcements to improve material properties [8, 9]. TiC is to improve resistance [10] and wear property while adding on Al alloy [11]. SiC is one of the ceramic metal which had less density compare to titanium carbide [12]. Most of the researchers chose it to add up with different metals to develop properties

of material [13]. Nowadays, AMC products are made with light mass [14]; FA powder possesses light weight that avail due to burning waste items of steam boiler plants. Ravi Kumar et al. [15] prepared AA7075 composites by adding Al₂O₃ (2-6%) and SiC (3-9%) through stir casting route and found reduction of tensile strength at 180°C for Al₂O₃ (6%)-SiC 9% strengthened with 7075 Al which happened due to not properly mixing of particles in heat treatment process. SAESSI et al. [16] examined the wear performance and tribological behaviour of grained Al5083 alloy/boron carbide at room and prominent temperatures. Low wear rate was observed at 200°C during application of 80 N load. Christy et al. focused on properties, optimization of stir casted specimens of scrap Al alloy reinforced with Al₂O₃. Four factors were considered in the optimization progress such as squeeze-pressure, time, preheat-temperature, and speed of stirpart. It was detected that the highest UTS (433 MPa) was occurred at L5 sample of 100 MPa, 45S, 250°C, and 525 rpm from ANOVA outcome [17]. Karthik et al. [18] studied the optimization of squeeze cast processing factors of Al2219 alloy through Taguchi routine. Optimized factors for Al-2219 alloy was found at squeeze pressure of 650 MPa, temperature of 225°C, and melt temperature 700°C that make to improve metallographic arrangement and mechanical characteristics. Amra et al. [19] prepared samples via casting method and studied about structural analysis and wear rate of Al-5083 strengthen with CeO₂/SiC. All prepared composites possessed greater hardness and wear opposition compared to base metal 5083. Generally, 5083 alloys have been applied in variety of fields such as rail cars, vehicle bodies, tip truck bodies, mine skips, and cages. AA7068 with boron carbide samples were produced by SC method with variant of parameter levels and also studied about corrosion rate. The mixture of reinforcement and stir-time were chief influencing factors which is improving corrosion resistance [20]. Akhlaghi et al. [21] explained the influence of casting hotness on distribution particles and porosity for SiC-A356 composites. Zhang et al. examined the effect of stir speed, time of stirring, and temperature on Al-6.8Mg-SiC [22]. Li-na et al. [23] noticed that the tensile properties increased due to an increment of homogeneous reinforcement, reducing stirring temperature in AA6061/ABO + SiCp hybrid composites. AA-5083 and FA were effectively produced through FSP method with different speed and feed rate. The higher hardness value was measured at 1400 rpm and 25 mm/min [24]. A popular mathematical and statistical technique for simulating and examining a process in which the variables and the objective by many variables is called response surface methodology (RSM). This first of three in-depth instructions demonstrates how to utilise the Design-Expert® programme for RSM which is helping for optimization process. Taguchi-related RSM technique was utilized to conduct optimal process on AA 6061 alloy; effects of HV and UTS were analyzed by ANOVA test [25]. Pal et al. have investigated to determine the ultimate tensile strength and hardness of AA 5456 alloy particles produced with SiC/flyash powder using a stir casting device, and there was more improvement of hardness and UTS around 87 HV and 109 MPa due to

proper mixing of reinforced powders [27]. Metal matrix composites made by stir casting and made of aluminium, silicon carbide, and aluminum and boron nitride were studied by Reddy et al. When compared to pure aluminum, they discovered that the produced hybrid metal matrix composites had better mechanical and metallurgical characteristics [32]. Gugulothu et al. analysed wear behavior of Al5052 with addition of alumina/ZrSiO₄ with aid of Taguchi optimization techniques, in which load is the dominant characteristic that determines wear behavior of prepared samples by roughly 45%, followed by reinforcing weight percentage 29.5% and sliding speed 25.5 percent [28]. Outputs with the help of design expert software, optimizations of Ts-156 MPa, and 75 HV were measured from impacted optimal parameters (speed of stirrer A: 309 rpm, time B: 13 min, temperature C: 840°C on AMCs samples) [29]. A metal matrix composite made of Al 7075 and SiC was created by Suresh et al. They discovered that the composite material had a lower rate of wear than the basic metal. They noticed that when the silicon carbide content increased, the wear rate decreased [31]. The work presented that an increase of stirrer rotation, squeeze pressure, and time duration affect behavior of composites [26]. After understanding various literature reviews, we aim to fabricate 5083 material which added on FA/SiC for optimizational experimentations.

2. Experimental Arrangement and Testing

Generally, Al-5083 has higher yield strength and is used in a variety of sectors, including engine body fabrication. Table 1 has mentioned Al compositions. Silicon carbide particle is with a diameter of 25 microns and a density of 3.6 g/cm³. Initially, 7.5% SiC and 5% FA were heated separately around 400°C and heated 5083 plate around 650-700°C at 7-10 minutes before addition of molten particles to furnace. Stir them well with a stirrer at different speeds ranging from 350 to 550 RPM, at temperatures ranging from 750 to 950°C for 15 to 35 minutes. Inert gas-Ar was used as an oxidizing avoider throughout the entire experiment (Figure 1). Afterward, formulated mould metals transferred into preferred shape dies to create 20 sample according to central composite design (CCD). This procedure is to be continued for remaining casting influences of stir speed (450,550 rpm) and time duration (25.35 min) at temperature of (850,950°C) mentioned at Table 2. Hardness tester (UH-350 model) was utilized to determine specimens hardness with help of (1/16) ball indenter apply the load 150 kgf at 10 seconds dwell time. As per ASTM E3, samples have been prepared to find tensile strength using load of 10 KN by universal testing machine. The basic parameters which is frequently used in the investigation of wear processes are stirrer speed, time, and temperature. The so-called wear factor is also computed using these values.

3. RSM Technique

Response surface methodology (RSM) is an arithmetical tool to achieve superior process control so that manufacturing feature can be enhanced considerably. CCD method was

TABLE 1: Aluminum alloy 5083 compositions.

| Elements | Silicon | Iron | Copper | Manganese | Magnesium | Zinc | Titanium | Chromium | Aluminum |
|------------------|-----------|-----------|----------|-----------|-----------|----------|-----------|-----------|----------|
| Contribution (%) | 0.50-0.60 | 0.40-0.50 | 0.2-0.30 | 0.75-0.80 | 4-4.5 | 0.3-0.40 | 0.15-0.20 | 0.10-0.20 | Balance |

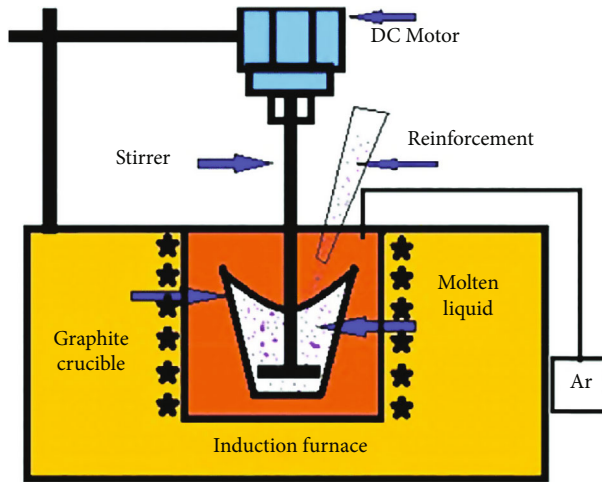


FIGURE 1: Stir casting process setup.

TABLE 2: SC input factor details.

| Factors | Level I | Level II | Level III |
|----------------------|---------|----------|-----------|
| Stir speed (A) | 350 | 450 | 550 |
| Stirring time (B) | 15 | 25 | 35 |
| Stir temperature (C) | 750 | 850 | 950 |

applied on casting process parameters of Al5083/SiC/FA. To determine best process parameter, DOE was constructed and produced for twenty samples at three variables. Process factors such as stirrer speed, stir time, and temperature were changed as per L20. Based on the experimental design, output responses (TS and HV) are acquired after exposing the samples to various mechanical property characterizations [30]. SN ratios (signal to noise) is log functions of output that aid for predicting the best process outcomes. The S/N ratio is calculated using the response variables received from the experimental studies. Depending on that whether the variable has to be maximized or reduced, Equation (1) is employed to transform the variables into S/N ratios.

$$\frac{S}{N} = 10 \log_{10} \left(\frac{P_s}{P_n} \right). \quad (1)$$

4. Result Discussion

Tensile strength is assessed with UTM. This is equipped with a load cell that measures tensile force. A tensile test is also frequently used to gauge tensile strength among other characteristics. Totally, 20 samples have been prepared for conducting the experiment to find out TS and BHN. From Table 3, it can be noticed that tensile strength (TS) for L8 and L5 were maximum, trailed by L16. In this study, interpreting the influence of a single process parameter was

TABLE 3: Tensile property and hardness observations.

| Runs | A (rpm) | B (min) | C (°C) | TS (MPa) | HV |
|------|---------|---------|--------|----------|------|
| L1 | 350 | 15 | 750 | 150.2 | 85.0 |
| L2 | 350 | 25 | 850 | 126.1 | 75.2 |
| L3 | 350 | 35 | 950 | 145.8 | 81.3 |
| L4 | 350 | 25 | 850 | 138.4 | 72.5 |
| L5 | 350 | 35 | 750 | 175.7 | 74.6 |
| L6 | 350 | 15 | 950 | 152.5 | 75.4 |
| L7 | 350 | 35 | 850 | 163.6 | 70.2 |
| L8 | 450 | 15 | 750 | 178.2 | 83.7 |
| L9 | 450 | 25 | 850 | 164.9 | 83.5 |
| L10 | 450 | 35 | 950 | 159.2 | 76.7 |
| L11 | 450 | 25 | 850 | 145.5 | 81.8 |
| L12 | 450 | 35 | 750 | 129.8 | 77.9 |
| L13 | 450 | 15 | 950 | 138.4 | 80.9 |
| L14 | 550 | 15 | 750 | 159.4 | 79.6 |
| L15 | 550 | 25 | 850 | 169.4 | 75.9 |
| L16 | 550 | 35 | 950 | 170.3 | 82.2 |
| L17 | 550 | 25 | 850 | 153.7 | 73.5 |
| L18 | 550 | 35 | 750 | 148.8 | 68.5 |
| L19 | 550 | 15 | 950 | 158.6 | 74.9 |
| L20 | 550 | 35 | 850 | 161.3 | 78.6 |

extremely difficult, because the process factors were altered consecutively using the CCD technique. For applications purpose, greater tensile strengths should be required, so L8 and L5 process parameters may be considered. TS values (126.1-178.2 MPa) were improved because of reinforcements distributed evenly in matrix and followed increase parameters of speed and time. The standard error have identified from 0.41 to 2.59 and average error -1.04 in whole experiments. TS_{\min} was obtained at L2 (350 rpm, 25 min at 850°C) due to the deficiency of reinforcement and more temperature, whereas maximum TS was identified at L8 (450 rpm, 15 minutes with 750°C). Figure 2 showed the effect of interaction of stirrer rotation vs. stir time vs. temperature on tensile strength and hardness for made Al5083 composite. From the graphical illustration, there was an increase in TS when the B and A were increased up to 5-10 min and 300-320 rpm. However, at speed more than 400 rpm, there was a substantial negative or reduction of TS; when interaction between speed and temperature is until 720-750°C and 380-400 rpm, there was an improvement of tensile strength obtained. At constant stirring speed of 400 rpm, the outcome of the interaction influence of B and C parameters in TS of generated composites 5083. Increasing temperature up to 800 and time 25 min enhanced tensile strength; however, there was a loss in TS when B and C were more than 25 minutes and 810°C. Similarly, the maximum hardness is

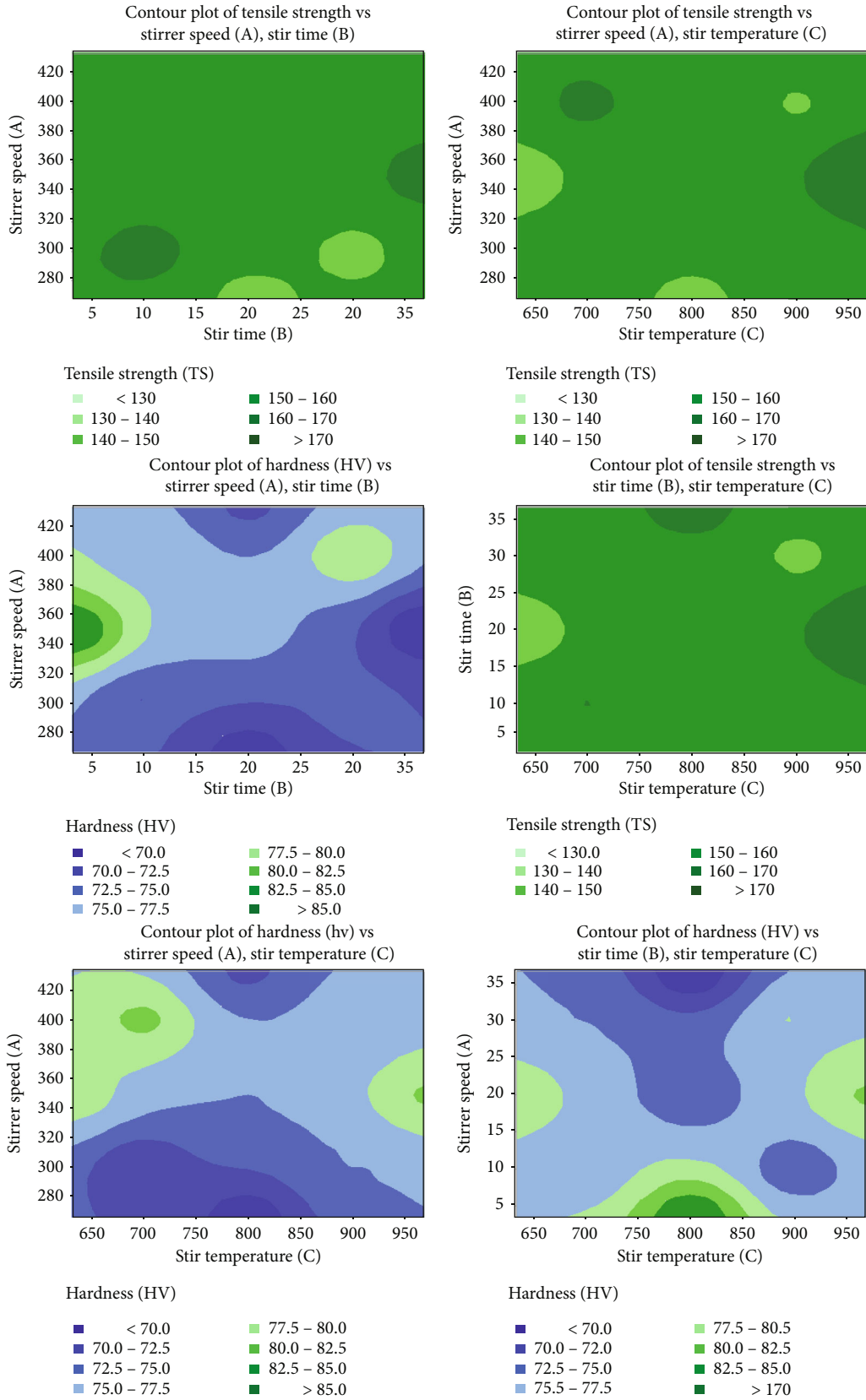


FIGURE 2: Contour plots of UTS and BHN with stir casting factors.

TABLE 4: ANOVA model-TS.

| Sources | SS | DF | MS | <i>F</i> ratio | <i>P</i> |
|-------------------|--------|----|-------|----------------|----------|
| Model | 582.97 | 13 | 52.5 | 2.278 | 1.212 |
| A | 19.08 | 1 | 16.1 | 0.047 | 0.044 |
| B | 0.3842 | 1 | 0.254 | 0.001 | 0.039 |
| C | 21.86 | 1 | 18.9 | 0.055 | 0.920 |
| A * B | 310.0 | 1 | 200.0 | 0.578 | 0.046 |
| A * C | 61.2 | 1 | 60.5 | 0.175 | 0.775 |
| B * C | 21.0 | 1 | 18.0 | 0.052 | 0.824 |
| A * A | 16.6 | 1 | 14.6 | 0.042 | 0.842 |
| B * B | 92.6 | 1 | 72.5 | 0.210 | 0.687 |
| C * C | 100.5 | 1 | 97.2 | 0.281 | 0.718 |
| Residual | 3755.8 | 14 | 346.1 | | |
| Fit | 1871.9 | 3 | 359.4 | 1.09 | 0.487 |
| P. error | 1859.0 | 3 | 332.8 | | |
| Aggregate (Total) | 3 | 19 | | | |

TABLE 5: ANOVA-hardness.

| Source | SS | DF | MS | <i>F</i> | <i>p</i> |
|-------------------|-------|----|-------|----------|----------|
| Model | 352.7 | 13 | 35.2 | 3.31 | 0.184 |
| A | 65.2 | 1 | 65.2 | 4.10 | 0.052 |
| B | 42.3 | 1 | 42.3 | 2.58 | 0.192 |
| C | 0.398 | 1 | 0.398 | 0.027 | 0.923 |
| A * B | 3.00 | 1 | 3.00 | 0.143 | 0.042 |
| A * C | 52.6 | 1 | 52.6 | 3.59 | 0.175 |
| B * C | 14.8 | 1 | 14.8 | 0.696 | 0.526 |
| A ² | 37.5 | 1 | 37.5 | 2.05 | 0.253 |
| B ² | 9.3 | 1 | 9.3 | 0.399 | 0.523 |
| C ² | 50.9 | 1 | 50.9 | 3.24 | 0.142 |
| Residual | 198.2 | 14 | 19.8 | | |
| Lack-fit | 148.7 | 3 | 48.2 | 4.41 | 0.402 |
| Error | 66.4 | 3 | 22.2 | | |
| Aggregate (Total) | 487.3 | 19 | | | |

attained at A of 340–380 rpm and B of 5–15 min when graph is plotted between A and B. HV was improved at B (330–420 rpm) and C (650–750°C) while interaction plot between parameters B and C.

The L1 sample had the highest hardness, followed by the L8 and L9 samples. Increasing the stir speed and time resulted in enhanced matrix density, dislocation containment, and increased hardness values. Furthermore, the inclusion of SiC particles inhibits plastic deformation of the composites during force applied by indenter on sample surface that improving hardness (HV). L7 sample exhibited the lowest HV due to more porosity or gaps in the matrix. Highest and least hardness (85 and 68.5) were observed at L1 (350 rpm, 15 min, 750°C) and L7 (350 rpm, 850°C at 35 min) correspondingly. From Table 4, two interactions (BC and AC) and squared interactions (A², B², C²) are not significant due to $p > 0.05$, whereas stir speed (A), stir time

(B), and interaction of AB are most significant parameters since $p < 0.05$ and the contribution of A and B variables are more comparing to stir temperature to improve TS property. In the case of hardness, A is the most influence factor that gives more contribution followed by B and C in Table 5, and also, the model is outstanding because Fisher ratio (*F*) was not higher than 5.

5. Conclusion

Al 5083 with two reinforcements (silicon carbide/fly ash) at different weight percent composites were produced through stir casting (SC) process. The central composite design at response surface approach were used to assess the impact of individual and combined interactions of three processing parameters of SC on the formation of Al 5083-SiC-FA composite. The modifications of SC input considerations that give effects on mechanical properties of tensile strength and hardness. The ANOVA findings revealed that the stirring parameters impact each attribute, with chosen two-way interactions (stir speed and time) having a significant effect at a 95% confidence level. Maximum amount of TS and HV was obtained on L8 and L1 specimens and lowest values identified at L2 and L3, respectively. According to the response surface technique. Temperature and speed values of less than 750°C and 390 rpm were shown to have a favorable influence at TS and HV responses, whereas values beyond that might have less mechanical properties, due to proper distribution of particles with base metal 5083 alloy tended to make changes in material characteristics and improving the mechanical behavior.

Data Availability

The data used to support the findings of this study are included in the article. Should further data or information be required, these are available from the corresponding author upon request.

Disclosure

This was performed as a part of the Employment Bule Hora University, Ethiopia.

Conflicts of Interest

The authors declare that there are no conflicts of interest regarding the publication of this paper.

Acknowledgments

The authors appreciate the technical assistance to complete this experimental work from the Department of Mechanical Engineering, Bule Hora University, Ethiopia. The author thanks Department of Civil Engineering, Manipal Institute of Technology, Manipal; Department of Electronics and Communication Engineering, Kalaingar Karunanidhi Institute of Technology, Coimbatore; Department of Mechanical Engineering, Saveetha School of Engineering, Chennai; Department of Science and Humanities, NPR College of

Engineering and Technology, Dindigul; and Department of Mechanical Engineering, Mizan-Tepi University, Ethiopia, India, for their support of draft writing.





References

- [1] C. Rajaganapathy, D. Vasudevan, A. D. Bruno, and T. Rajkumar, "Tribological and mechanical characteristics of AA6082/TiC/WC-based aluminium composites in dry and wet conditions," *Materials Today: Proceedings*, vol. 37, pp. 1133–1136, 2021.
- [2] P. Paramasivam and S. Vijayakumar, "Mechanical characterization of aluminium alloy 6063 using destructive and non-destructive testing," *Materials Today: Proceedings*, 2021.
- [3] A. P. Pasupulla, H. A. Agisho, S. Seetharaman, and S. Vijayakumar, "Characterization and analysis of TIG welded stainless steel 304 alloy plates using radiography and destructive testing techniques," *Materials Today: Proceedings*, vol. 51, pp. 935–938, 2022.
- [4] B. Gugulothu, P. S. Satheesh Kumar, B. Srinivas, A. Ramakrishna, and S. Vijayakumar, "Investigating the Material Removal Rate Parameters in ECM for Al 5086 Alloy- Reinforced Silicon Carbide/Flyash Hybrid Composites by Using Minitab-18," *Advances in Materials Science and Engineering*, vol. 2021, Article ID 2079811, 6 pages, 2021.
- [5] M. Ravichandran, M. Meignanamoorthy, G. P. Chellasivam, J. Vairamuthu, A. S. Kumar, and B. Stalin, "Effect of stir casting parameters on properties of cast metal matrix composite," *Materials Today: Proceedings*, vol. 22, pp. 2606–2613, 2020.
- [6] R. Ramamoorthi, J. J. M. Hillary, R. Sundaramoorthy, J. D. J. Joseph, K. Kalidas, and K. Manickaraj, "Influence of stir casting route process parameters in fabrication of aluminium matrix composites—a review," *Materials Today: Proceedings*, vol. 45, pp. 6660–6664, 2021.
- [7] J. Zhu, W. Jiang, G. Li, F. Guan, Y. Yu, and Z. Fan, "Microstructure and mechanical properties of SiCnp/Al6082 aluminium matrix composites prepared by squeeze casting combined with stir casting," *Journal of Materials Processing Technology*, vol. 283, p. 116699, 2020.
- [8] H. P. Pydi, A. Pradeep, S. Vijayakumar, and R. Srinivasan, "Examination of various weld process parameters in MIG welding of carbon steel on weld quality using radiography & magnetic particle testing," *Materials Today: Proceedings*, 2022.
- [9] R. M. Badizi, A. Parizad, M. Askari-Paykani, and H. R. Shahverdi, "Optimization of mechanical properties using D-optimal factorial design of experiment: Electromagnetic stir casting process of A357– SiC nanocomposite," *Transactions of Nonferrous Metals Society of China*, vol. 30, no. 5, pp. 1183–1194, 2020.
- [10] K. Ravikumar, K. Kiran, and V. S. Sreebalaji, "Characterization of mechanical properties of aluminium/tungsten carbide composites," *Measurement*, vol. 102, pp. 142–149, 2017.
- [11] H. P. Pydi, A. P. Pasupulla, S. Vijayakumar, and H. A. Agisho, "Study on microstructure, behavior and Al₂O₃ content flux A-TIG weldment of SS-316L steel," *Materials Today: Proceedings*, vol. 51, pp. 728–734, 2022.
- [12] A. A. Adediran, A. A. Akinwande, O. A. Balogun, and B. J. Olorunfemi, "Optimization studies of stir casting parameters and mechanical properties of TiO₂ reinforced Al 7075 composite using response surface methodology," *Scientific Reports*, vol. 11, no. 1, pp. 1–20, 2021.
- [13] P. Sathishkumar, V. Deepakaravind, P. Gopal, and P. Azhagiri, "2021. Analysis the mechanical properties and material characterization on magnesium metal matrix nano composites through stir casting process," *Materials Today: Proceedings*, vol. 46, pp. 7436–7441, 2021.
- [14] S. Rangrej, V. Mehta, V. Ayar, and M. Sutaria, "Effects of stir casting process parameters on dispersion of reinforcement particles during preparation of metal composites," *Materials Today: Proceedings*, vol. 43, pp. 471–475, 2021.
- [15] M. Ravi Kumar, H. N. Reddappa, R. Suresh, and M. Gangadharappa, "Effect of heat treatment on tensile strength of Al7075/Al₂O₃/SiCp hybrid composite by stir casting technique," *Materials Today: Proceedings*, vol. 5, no. 10, pp. 22460–22465, 2018.
- [16] M. Saessi, A. Alizadeh, and A. Abdollahi, "Wear behavior and dry sliding tribological properties of ultra-fine grained Al5083 alloy and boron carbide-reinforced Al5083-based composite at room and elevated temperatures," *Transactions of Nonferrous Metals Society of China*, vol. 31, no. 1, pp. 74–91, 2021.
- [17] J. V. Christy, R. Arunachalam, A. H. I. Mourad, P. K. Krishnan, S. Piya, and M. Al-Maharbi, "Processing, properties, and microstructure of recycled aluminum alloy composites produced through an optimized stir and squeeze casting processes," *Journal of Manufacturing Processes*, vol. 59, pp. 287–301, 2020.
- [18] A. Karthik, R. Karunanithi, S. A. Srinivasan, and M. Prashanth, "The optimization of squeeze casting process parameter for AA2129 alloy by using the Taguchi method," *Materials Today: Proceedings*, vol. 27, pp. 2556–2561, 2020.
- [19] M. Amra, K. Ranjbar, and S. A. Hosseini, "Microstructure and wear performance of Al5083/CeO₂/SiC mono and hybrid surface composites fabricated by friction stir processing," *Transactions of the Nonferrous Metals Society of China*, vol. 28, no. 5, pp. 866–878, 2018.
- [20] K. Gurusami, S. Shalini, and T. Sathish, "2020. Optimization of stir casting parameters for corrosion rate analysis of AA7068–Boron carbide composites," *Materials Today: Proceedings*, vol. 33, pp. 4650–4655, 2020.
- [21] F. Akhlaghi, A. Lajevardi, and H. M. Maghanaki, "2004. Effects of casting temperature on the microstructure and wear resistance of compocast A356/SiCp composites: a comparison between SS and SL routes," *Journal of Materials Processing Technology*, vol. 155, pp. 1874–1880, 2004.
- [22] H. Zhang, L. Geng, L. Guan, and L. Huang, "Effects of SiC particle pretreatment and stirring parameters on the microstructure and mechanical properties of SiCp/Al-6.8Mg composites fabricated by semi-solid stirring technique," *Materials Science and Engineering A*, vol. 528, no. 1, pp. 513–518, 2010.
- [23] L. N. Guan, L. Geng, H. W. Zhang, and L. J. Huang, "Effects of stirring parameters on microstructure and tensile properties of (ABOw+ SiCp)/6061Al composites fabricated by semi-solid stirring technique," *Transactions of Nonferrous Metals Society of China*, vol. 21, pp. s274–s279, 2011.
- [24] G. V. N. B. Prabhakar, N. R. Kumar, and B. R. Sunil, "Surface metal matrix composites of Al5083 - fly ash produced by friction stir processing," *Materials Today: Proceedings*, vol. 5, no. 2, pp. 8391–8397, 2018.
- [25] P. Lakshmikanthan and B. Prabu, "Optimization on stir casting process parameters of aluminium alloy (AL6061) nickel coated graphite (NCG) metal matrix composite using Taguchi based RSM," *Materials Science*, vol. 9, no. 6, pp. 260–269, 2016.

- [26] J. J. Moses, I. Dinaharan, and S. J. Sekhar, "Prediction of influence of process parameters on tensile strength of AA6061/TiC aluminum matrix composites produced using stir casting," *Transactions of Nonferrous Metals Society of China*, vol. 26, no. 6, pp. 1498–1511, 2016.
- [27] D. Pal, S. Vijayakumar, T. V. J. Rao, and R. S. R. Babu, "An examination of the tensile strength, hardness and SEM analysis of Al 5456 alloy by addition of different percentage of SiC/flyash," *Materials Today: Proceedings*, vol. 62, pp. 1995–1999, 2022.
- [28] B. Gugulothu, S. L. Sankar, S. Vijayakumar et al., "Analysis of wear behaviour of AA5052 alloy composites by addition alumina with zirconium dioxide using the Taguchi-grey relational method," *Advances in Materials Science and Engineering*, vol. 2022, 7 pages, 2022.
- [29] B. Gugulothu, S. Seetharaman, S. Vijayakumar, and D. J. Rani, "Process parameter optimization for tensile strength and Hardness of Al-MMC using RSM technique," *Materials Today: Proceedings*, vol. 62, pp. 2115–2118, 2022.
- [30] B. Gugulothu, N. Nagarajan, A. Pradeep, G. Saravanan, S. Vijayakumar, and J. Rao, "Analysis of Mechanical Properties for Al-MMC Fabricated through an Optimized Stir Casting Process," *Journal of Nanomaterials*, vol. 2022, 7 pages, 2022.
- [31] S. Suresh, G. H. Gowd, and M. L. S. Deva Kumar, "Tribological behavior of Al 7075/SiC metal matrix nano-composite by stir casting method," *Journal of The Institution of Engineers (India): Series D*, vol. 100, no. 1, pp. 97–103, 2019.
- [32] P. S. Reddy, R. Kesavan, and B. Vijaya Ramnath, "Investigation of mechanical properties of aluminium 6061-silicon carbide, boron carbide metal matrix composite," *Silicon*, vol. 10, no. 2, pp. 495–502, 2018.
- [33] M. Vigneshkumar, P. Ashoka Varthanan, and Y. Maria Ambrose Raj, "Finite element-based parametric studies of nugget diameter and temperature distribution in the resistance spot welding of AISI 304 and AISI 316L sheets," *Indian Institute of Metals*, vol. 72, no. 2, pp. 429–438, 2019.
- [34] M. Vigneshkumar and P. A. Varthanan, "Comparison of RSM and ANN model in the prediction of the tensile shear failure load of spot welded AISI 304/316 L dissimilar sheets," *International Journal of Computational Materials Science and Surface Engineering*, vol. 8, no. 2, pp. 114–130, 2019.

Research Article

Applications of Natural Violet Pigments from Halophilic *Chromobacterium violaceum* PDF23 for Textile Dyeing with Antimicrobial and Antioxidant Potentials

Antonyraj Matharasi Perianaika Anahas,¹ Subramanian Kumaran ²,
Mahmoud Kandeel ^{3,4}, Gangatharan Muralitharan,¹ Jenifer Silviya,⁵
Geja Lakshmi Adhimoolam,⁵ Mani Panagal,⁶ Sampath Renuka Pugazhvendan ⁷,
Gopal Suresh,⁸ A. Wilson Aruni,^{9,10} Senthil Rethinam,¹¹ and Nainangu Prasannabalaji ⁸

¹Department of Microbiology, Centre of Excellence in Life Sciences, Bharathidasan University, Palkalaiperur, Tiruchirappalli, 620 024 Tamil Nadu, India

²Centre for Drug Discovery and Development, Sathyabama Institute of Science and Technology, Chennai, 600119 Tamil Nadu, India

³Department of Biomedical Sciences, College of Veterinary Medicine, King Faisal University, Al-ahsa, Saudi Arabia

⁴Department of Pharmacology, Faculty of Veterinary Medicine, Kafrelshikh University, Kafrelshikh, Egypt

⁵Department of Microbiology, Jaya College of Arts and Science, Thiruninravur, Chennai, 602 024 Tamil Nadu, India

⁶Department of Biotechnology, Annai College of Arts and Science, Kumbakonam, 612503 Tamil Nadu, India

⁷Department of Zoology, Arignar Anna Government Arts College, Cheyyar, 604407 Tamil Nadu, India

⁸PG & Research Department of Microbiology, Sri Sankara Arts and Science College, Kanchipuram, 631561 Tamil Nadu, India

⁹School of Medicine, Loma Linda University, CA-92354, USA

¹⁰AMITY University, Mumbai, Maharashtra, India

¹¹Ege University, Turkey

Correspondence should be addressed to Subramanian Kumaran; kumarans.cddd@sathyabama.ac.in and Nainangu Prasannabalaji; applenpb@gmail.com

Received 25 April 2022; Accepted 28 June 2022; Published 23 July 2022

Academic Editor: V. Vijayan

Copyright © 2022 Antonyraj Matharasi Perianaika Anahas et al. This is an open access article distributed under the Creative Commons Attribution License, which permits unrestricted use, distribution, and reproduction in any medium, provided the original work is properly cited.

Natural colorants have emanated as a significant substitute to highly toxic synthetic dyes. The present study highlights the dyeing efficiency of violet pigment produced from *Chromobacterium violaceum* PDF23. A halophilic bacterium *C. violaceum* PDF23 produce violet pigments were isolated from the Great Salt Lake situated in Chennai, India. Based on morphology and 16S rRNA gene sequencing, a halophilic bacterium was identified as *C. violaceum* PDF23. The violet dye from *C. violaceum* PDF23 exhibited antimicrobial efficacy against *S. aureus*, *B. subtilis*, *E. coli*, *P. aeruginosa*, and *C. albicans*. The violet pigment exhibited radical scavenging potential with IC₅₀ value of 14.40 µg/mL. The dye ability of colorant was evaluated using mordants on two distinct fabrics, i.e., silk satin and cotton, and colorfastness measurements were recorded. The CIE L * a * b * qualities of the dyed fabrics were assessed, as well as their colorfastness quality. The current research findings suggest that violet pigment has potent antimicrobial and antioxidant activity and it could be used as alternative to synthetic dye in the textile industry.

1. Introduction

Anthropogenic activity-induced ecosystem toxicity is a complex and significant issue that society, scientists, and regulatory agencies are struggling around the world [1, 2]. Synthetic dyes have been used extensively in the industrial processes of food, fabrics, health supplements, and pharmaceutical products [3]. Synthetic dyes raise carcinogenic levels in the ecosystem, such as sulfur, phosphorus, nitrogen, and other heavy metal ions, which promote the growth of algae, fungi, and cyanobacteria [4]. The negative consequences of synthetic dye manufacture and application, such as mutagenicity and toxicity, have prompted health-conscious consumers to seek out more eco-friendly and greener colorants known as natural dyes [5–7]. Synthetic dyes have been prohibited worldwide by environmental organizations from the USA, Germany, and Italy due to their fatal and carcinogenic impacts, and natural dyes are being promoted to conserve the environment around the world [8].

To combat the drawbacks of synthetic dyes, natural dyes have attracted the interest of researchers and industrialists due to their non-hazardous, bio-degradable, sustainable, nonallergic, anticancer, and environment-friendly properties [9, 10]. Natural dyes have also performed a significant role in preventive medicine, including anti-inflammatory, antihemolytic, antipyretic, antifungal, antioxidant, and antibacterial activities [11]. Natural dyes are recognized to be safer for the environment and produce less harmful waste during textile dyeing than synthetic colorants [7, 12].

Natural dyes have a variety of advantages, including light stability, heat stability, and pH stability [13]. Similarly, the use of natural colorants as a textile fabric has gained much importance as a result of similar qualities. The production of natural colors in the food coloring industry has been increased to 10–15% per year, and growing perception of food colorants and the detrimental effects of synthetic colorants is the key reason behind the growing demand. There is a global prohibition on the manufacture and import of synthetic dye-based colors and clothing accessories in several nations throughout the world [12].

Natural colorants generated from microorganisms are commonly employed as dyeing agents because of their inexpensive production costs, ease of extraction, higher productivity through strain creation, and lack of temporal fluctuations [13]. Natural colorants produced by bacteria, fungi, algae, and cyanobacteria were used in textile industries [14]. Due to the high demand for natural dyes, industrial manufacturing of these products is rapidly rising. As a result, new varieties of natural colorants have been introduced, dramatically expanding the paradigm of hygiene and protection. The annual rate of the dye industry is predicted to increase about 7%, and the demand is expected to increase \$7.79 billion by 2020 [15].

For dyeing fabrics, microbial dyes have been used extensively. *C. violaceum* has been widely investigated in the production of violacein, while different bacterial species have been identified in diverse amounts and process parameters [13, 16]. Due to its therapeutic potential and mechanism of action, violacein pigment produced by *Chromobacterium*

has received extensive interest [17, 18]. Violacein has a wide range of therapeutic potential including broad-spectrum antimicrobial properties, potent bactericidal and anticancer properties, and antimalarial, antiulcerogenic, antiviral, antibiotic, antitumor, and antiparasite properties [19–21]. Many bacterial strains synthesize violacein, including *Chromobacter* [22, 23], *Pseudoalteromonas* [24, 25], *Janthinobacterium* [26, 27], and *Duganella* [28]. In addition, bacterial strains producing violacein have been isolated from various geographical regions.

Mordanting takes significant use of the materials, both color and severity, by combining three types of complexation [29]. In natural fibers, the use of mordants offers great color strength. The most often used mordants are alum, nickel, chromium, iron, copper, and tannic acid [30]. Bio-mordants are non-toxic to humans and the environment, are eco-friendly, and are less expensive for dyeing [12, 31].

Radiation technique is gaining prominence in the fabric industry, particularly in dyeing process, because of its technical and economical efficiency, as well as its acceptability [31, 32]. The low color intensity derived from natural dyes has led to the use of advanced approaches such as irradiation techniques in the fabric industries to overcome this constraint [12, 33]. These radiations not only improve the colorant extraction efficiency and improve the dyeing technique faster, but it is also significantly more efficient in terms of duration, expense, manpower, and energy [34]. The ultrasonic radiation process, as a green technique in natural dyeing, offers a lot of potential for isolating colorants from natural sources [35, 36].

In this study, we identified a new bacterial strain of halophilic *C. violaceum* PDF23 that produces a compound of violet pigment with a wide array of biomedical applications. The violet pigments showed wide range of antimicrobial properties, antioxidant capacity, and application in textile dyeing of fabrics. In future, researchers should aim to study whether these properties could be imparted to textiles to obtain fabrics for special applications.

2. Materials and Methods

2.1. Sampling Site. Soil sediments were collected from 12 different locations at Great Salt Lake located in Chennai, India (Lat. 12°43' 53.99" N Long. 80°13' 0.41" E) (Figure 1). All of these samples were obtained aseptically in sterile plastic containers, which were placed in the icebox and transported for processing to the laboratory.

2.2. Bacterial Strain Isolation and Purification. Serial dilution and plating methods were used to isolate bacteria, according to the method of Verma et al. [37]. The 10⁻¹ dilution was made by mixing 1 g of soil in 9 mL of 0.85% saline. An aliquot of 0.01 mL was taken from each dilution (10⁻² to 10⁻⁶) and plated on petri plates containing nutrient agar and incubated at 25°C. A total of 5 distinct morphological colonies are identified for 12 isolates (PDF11 to PDF23) as shown in Table 1. The violet-colored bacterial isolate was identified as PDF23 among the various bacterial isolates. The PDF23

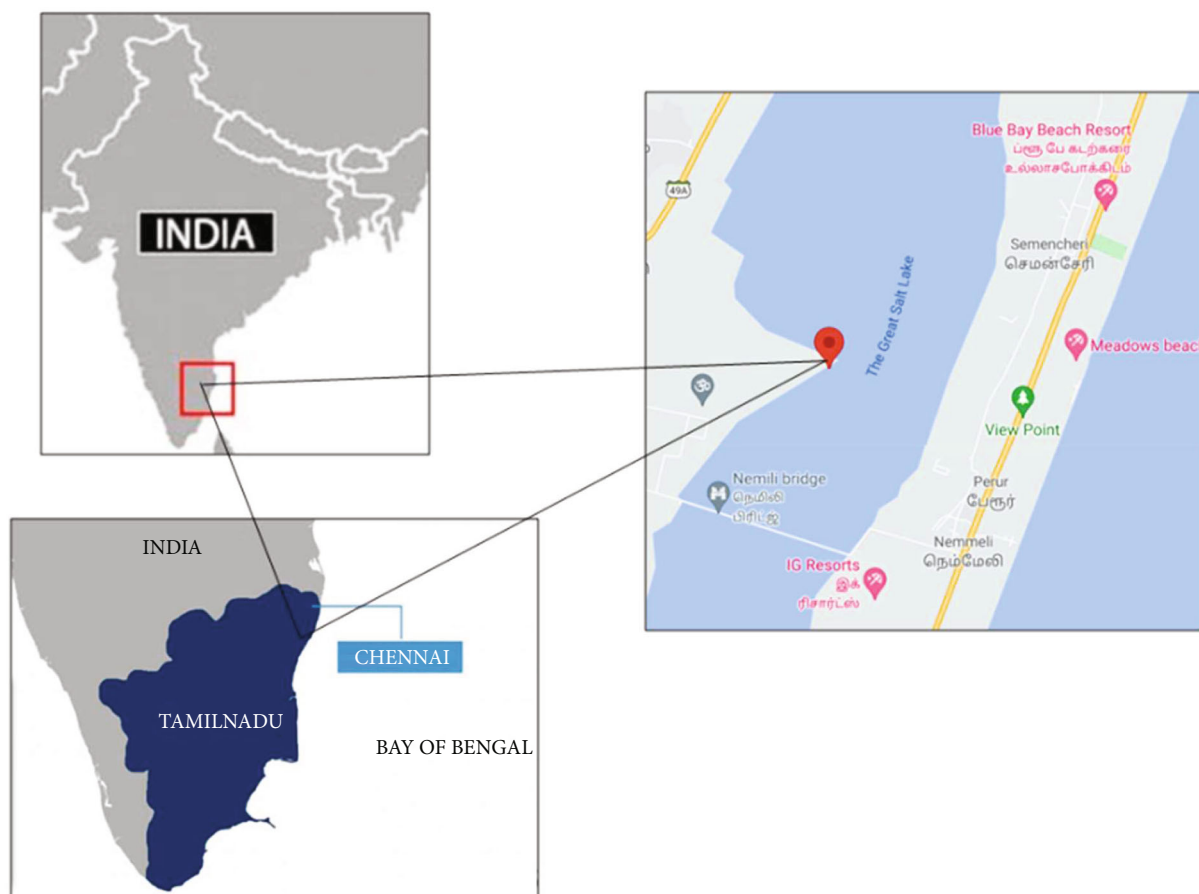


FIGURE 1: Map of India, Tamilnadu showing Chennai, Great Salt Lake ($10^{\circ} 50' N 78^{\circ} 46'E$), where the halophilic sediment samples were collected shown in red.

TABLE 1: Pigment-producing bacteria were isolated from various sites around Great Salt Lake in Chennai, India.

| S. No. | Organism | Pigment | Gram staining |
|--------|----------|-------------|---------------|
| PDF12 | | Yellow | (-ve) rod |
| PDF13 | | Yellow | (+ve) cocci |
| PDF14 | | Red | (-ve) rod |
| PDF15 | | Yellow | (+ve) cocci |
| PDF16 | | Red | (-ve) rod |
| PDF17 | | Orange | (-ve) rod |
| PDF18 | | Pale yellow | (+ve) cocci |
| PDF19 | | Red | (-ve) rod |
| PDF20 | | Yellow | (-ve) rod |
| PDF21 | | Pale yellow | (+ve) cocci |
| PDF22 | | Red | (-ve) rod |
| PDF23 | | Violet | (-ve) rod |

isolate was purified after three consecutive streaks on nutrient agar medium and stored at $-80^{\circ}C$.

2.3. Biochemical Analysis of Bacterial Isolate PDF23. Gram staining, cell morphology, and pigment synthesis were used to identify the violet-colored bacterial isolate PDF23.

Enzyme activity such as oxidase, catalase, urease, triple sugar iron agar test, citrate test, indole, MR-VP test [38, 39], and motility test were carried out according to method of Litchfield and Gillevet [40].

2.4. Molecular Analysis

2.4.1. DNA Extraction. The bacterial isolate PDF23 was grown to reach an A_{600} of 1.0. After growing, the cells were harvested by centrifugation at 10,000 rpm for 5 min at $4^{\circ}C$. As previously mentioned by [41], total genomic DNA was extracted from bacterial cell pellets. Genomic DNA was resolved on a 1% agarose gel with 1X TAE buffer, and DNA was imaged using a gel documentation unit (Bio-Rad, USA) [39].

2.4.2. Analysis of 16S rRNA Gene by PCR Amplification. Total genomic DNA was employed in PCR amplification of the 16S rRNA gene using primers 27 F ($5'-AGAGTTGGATCTGGCTCG-3'$) and 1492R ($5'-ACCTTGTTACGACTT-3'$) [42]. The PCR cycling conditions were set as initial denaturation at $94^{\circ}C$ for 2 min followed by 35 cycles of denaturation at $94^{\circ}C$ for 30 s, annealing at $52^{\circ}C$ for 30 s, and extension at $72^{\circ}C$, 2 min, with a final extension of

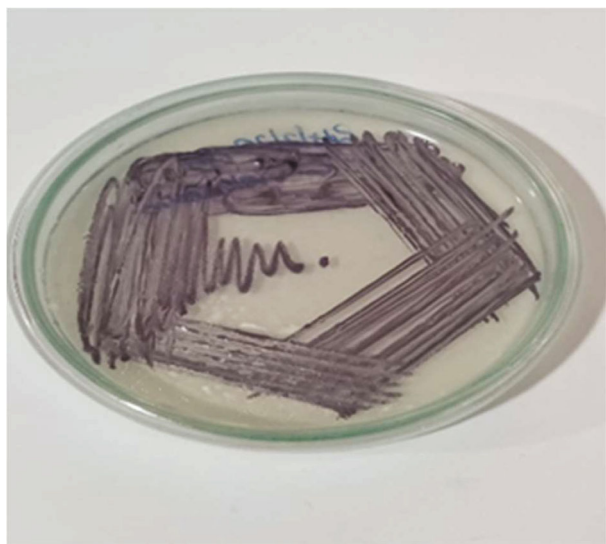


FIGURE 2: Isolated violet pigment producing bacterium *C. violaceum* PDF23.

TABLE 2: Biochemical characterization of selected violet pigment producing isolate PDF23.

| Characteristics | PDF23 |
|-----------------------------|-------|
| Catalase | + |
| Oxidase | + |
| Methyl red | — |
| Voges-Proskauer | — |
| Citrate | + |
| Urease | — |
| Gelatinase | + |
| Hydrogen sulfide production | — |
| Triple sugar iron agar test | A/A |
| Glucose | + |
| Mannitol | — |
| Sorbitol | — |
| Rhamnose | — |
| Sucrose | — |
| Arabinose | — |
| Lysine | — |
| Arginine | + |

+ denotes presence and – denotes absence; A/A indicates alkaline slant/acidic butt.

10 min at 72°C. The PCR product was separated on 1% agarose gel.

2.4.3. Sequencing and Phylogenetic Tree Construction. The 16S rRNA gene PCR product was purified and sequenced on both strands using 27 F and 1492R primers using the PCR cleanup kit (Qiagen, USA). MEGA X was used to generate a phylogenetic tree using the neighbor joining method [43]. The PDF23 bacterial isolate 16S rRNA nucleotide

TABLE 3: Partial 16S rRNA gene sequence of *C. violaceum* PDF23 submitted in NCBI database.

```

GTGCCAGCAGCCGCGTAATACGTAGGGTGCAGCGTTA
ATCGGAATTACTGGGCGTAA
AGCGTGCGCAGGCGGTTGTGCAAGTCTGATGTGAAAGCC
CCGGGCTTAACCTGGGAACG
GCATTGGAGACTGCACAGCTAGAGTGCAGTCAGAGGG
GGGTAGAATTCCACGTGTAGCAG
TGAAATGCGTAGAGATGTGGAGGAATACCGATGGCG
AAGGCAGCCCCCTGGGATGACAC
TGACGCTCATGCACGAAAGCGTGGGGAGCAAACAGG
ATTAGATACCCTGGTAGTCCACG
CCCTAAACGATGTCAACTAGCTGTTGGGGGTTTGAATCC
TTGGTAGCGTAGCTAACGCGT
GAAGTTGACCGCCTGGGGAGTACGGCCGCAAGGTTA
AAACTCAAAGGAATTGACGGGGA
CCCGCACAAGCGGTGGATGATGTGGATTAATTCGATGCA
ACGCGAAAAACCTTACCTGCT
CTTGACATGTACGGAACCTGCCAGAGATGGCTTGGTGCC
CGAAAGGGAGCCGTAACACA
GGTGCTGCATGGCTGTCGTCAGCTCGTGTGTCGTGAGATGT
TGGGTAAAGTCCCGCAACGAG
CGCAACCCT

```

sequences were submitted to the GenBank database, and accession numbers were received (MT176501).

2.5. Growth and Violacein Production. The growth and synthesis of violacein from PDF23 strain were evaluated in a modified nutrient broth with sodium chloride deprivation. An overnight culture dissolved in saline solution was used as the inoculum at a 5% (v/v) concentration. The experiment was carried out in a 250-mL Erlenmeyer flask and incubated at 25°C under agitation (180 rpm). To determine the increase in biomass and violacein, 1 mL of distilled ethanol was added to the pellet-pigment extract and homogenized to attain the ethanol-phase pigment and 1 mL of culture broth was extracted and separated by centrifugation at 10,000 rpm for 10 min. The filtrate was agitated again, and the pellet and supernatant were extracted. The absorbance of ethanolic supernatant was measured at 575 nm to assess the presence of violacein. For biomass quantification, the pellet was dissolved in 1 mL saline, and the absorbance was measured at 600 nm [44].

2.6. Extraction of Violacein Dye. The violet pigment was extracted from a 24-hr-old *C. violaceum* cell suspension using the following procedure. Bacteria cells were harvested after an incubation time of 24 hrs, and the cells were collected by centrifugation simultaneously at a speed of 7,000 rpm and 4°C. Pellets were obtained by the extraction methods, and three different solvents were applied to each separate pellet, methanol, acetone, and ethyl acetate, where the solution was also separated by centrifugation at 7,000 rpm for 4°C. The separation technique was replicated till the pellet turned colorless. Violet and blue dyes were extracted from *C. violaceum* using this extraction process. To remove methanol, acetone, and ethyl acetate from the pigments, the rotary evaporator was used to obtain the

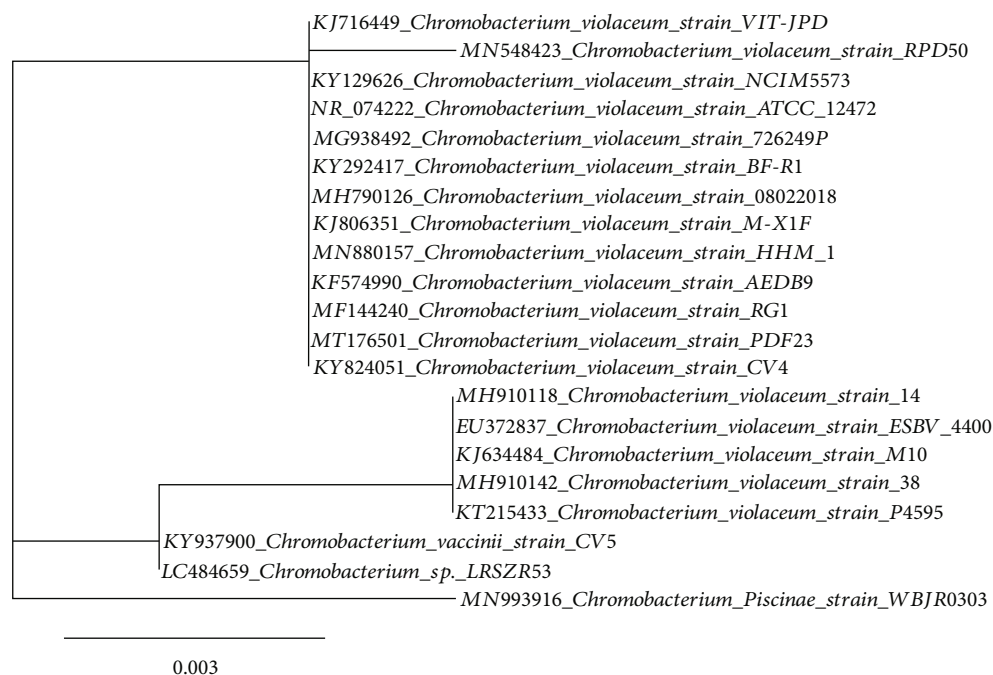


FIGURE 3: *C. violaceum* PDF23 (shown in red line) is closely linked to other violacein-producing *C. violaceum* species, according to a phylogenetic tree based on 16S rRNA gene sequences received from the NCBI. 0.003 substitutions per nucleotide position are indicated by the scale bar.

pigments in crude form. The time required for condensation at 45°C was 1 h per 250 mL. For 1 L of solution, crude extraction yielded around 0.2 g of pigments [45].

2.7. Characterization of Natural Dye

2.7.1. UV-Vis Spectral Analysis. The methanol extract of crude pigment was evaluated using the UV-vis spectrophotometer (Shimadzu UV-1601PC) between 800 and 200 nm for maximum wavelength [46].

2.7.2. Fourier Transform-Infrared Spectroscopy (FT-IR). FT-IR spectrophotometer (Shimadzu FTIR-8400S) was used to determine violet pigment derived from *C. violaceum* PDF23 in the wave number range from 400 to 4000 cm^{-1} . On the diamond glass of the spectrophotometer, approximately 2 μg of dyes were mounted [47]. Various functional groups found in the pigments were identified using the FTIR spectrum.

2.8. Applications of Violet Pigment in Textile Dyeing

2.8.1. Fabrics. Two types of fabrics, silk satin and cotton, were used to evaluate the dye-ability of pigments.

2.8.2. Dyeing of Fabric Samples. For all fabric samples of liquid *C. violaceum* PDF23 dye for both silk and cotton, staining was performed at boiling temperature (100°C). Silk fabric dyeing was performed at a dye concentration of 2%, with a fabric: liquid proportion (1 : 50) and varying mordant concentrations at 60°C and an interval of 60 min. After staining, the colored fabric was rinsed at 60°C for 15 min with 3 g/L of nonionic detergent, then washed with cold

TABLE 4: Extraction and production of natural pigment from *C. violaceum*.

| S.no. | Solvent extraction | Production of natural dye |
|-------|--------------------|---------------------------|
| 1. | Methanol | +++ (blue) |
| 2. | Acetone | ++ (violet) |
| 3. | Ethyl acetate | ++ (violet) |
| 4. | Water | + (colorless) |

Dye strength graded as follows: + - low, ++ - moderate, and +++ - extremely high.

water, and allowed to dry at 37°C. For staining of silk satin and cotton fabrics, four parameters affecting color efficiency and intensity were evaluated: mordants, mordant concentration, fabric pretreatment, and natural pigment strength characteristics [48].

2.8.3. Mordant. Ferrous sulfate, sodium silicate, alum, copper sulfate, and calcium hydroxide were used in the forms of mordants [49].

2.8.4. Pretreatment of Fabric. Before proceeding to the pretreatment process, about 1 g of fabric was soaked in alum and Na_2CO_3 . The solution was heated for 2 hrs along with the fabrics to ensure that the fabrics were processed efficiently. The fabric was rinsed and dried at 37°C. Silk was pretreated in a similar manner, except sodium carbonate. Pretreatment of the fabric was done to remove pectic compounds and cotton wax found in cotton weave fabrics, as well as particles on the surface of silk fabrics. The sample, which includes alum and Na_2CO_3 , was prepared for pretreatment of cotton fabrics by dissolving 0.2 g alum and

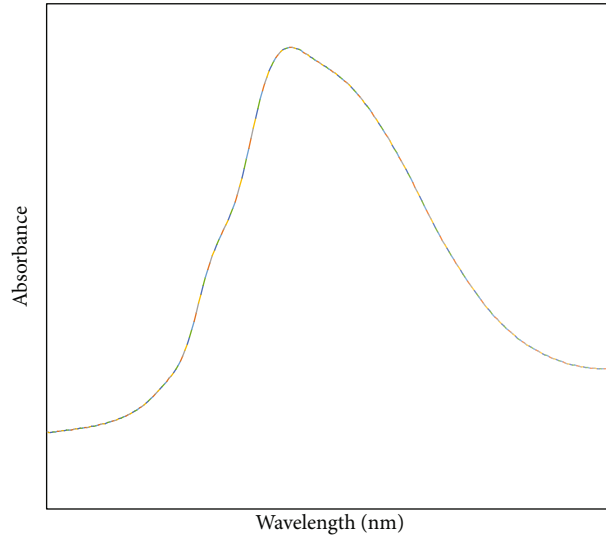


FIGURE 4: UV-visible spectrum of violacein pigment produced by *C. violaceum* PDF23.

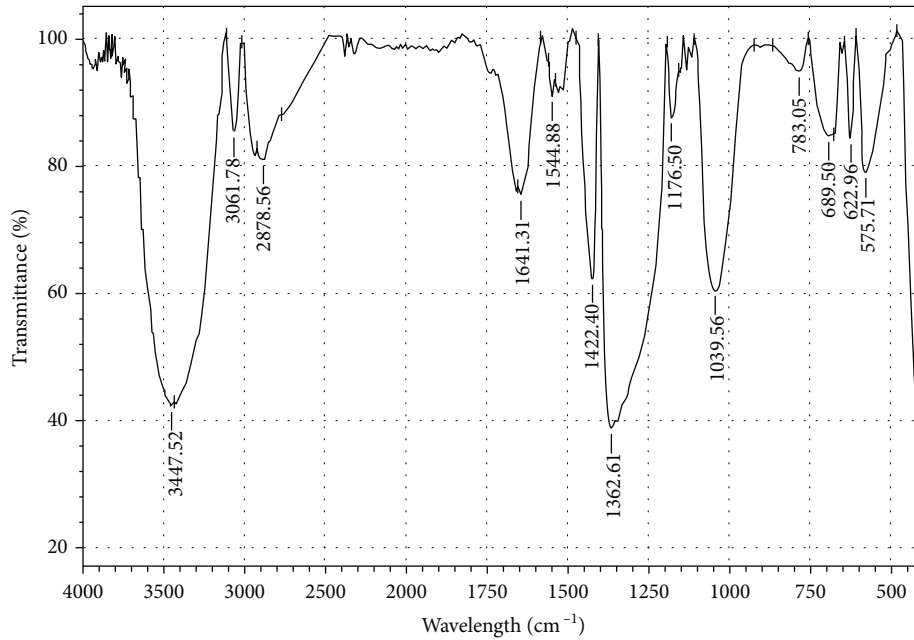


FIGURE 5: FT-IR spectra of violacein pigment produced by *C. violaceum* PDF23.

0.06 g Na_2CO_3 in 30 mL of distilled water, heating and thoroughly mixing by homogenization [50].

2.9. Assessment of Dyed Fabric

2.9.1. Color Strength and Colorfastness Standard Tests. The colored fabrics were analyzed in compliance with ISO standard techniques. The transmittance of the colored materials was measured using a UV-vis spectrophotometer (Premier Color Scan, Model: SS 5145A, India). The Kubelka-Munk equation was used to calculate absolute color characteristics (K/S values) [47].

$$\frac{K}{S} = \frac{(1-R)^2}{2R} - \frac{(1-R_0)^2}{2R_0} \quad (1)$$

where R is the decimal fraction of dyed fabric reflectance, R_0 is the decimal fraction of undyed fabric reflectance, K is the absorption coefficient, and S is the scattering coefficient.

2.10. Antimicrobial Activity by Minimum Inhibitory Concentration (MIC). The antimicrobial efficacy of violet pigments was used to evaluate the percentage of inhibition against human pathogens such as *S. aureus*, *B. subtilis*, *E. coli*, *P. aeruginosa*, and *C. albicans* [51]. The bacterial strains were seeded in Mueller Hinton broth incubated at 37°C for 24 hrs, while the yeast grown in Sabouraud dextrose broth incubated at 30°C for 24 hrs. All the test strains were adjusted to 10^6 CFU/mL (McFarland standard) and used for assay. Different concentrations of violet pigments (0.25,

TABLE 5: $L * a * b *$ value for *C. violaceum* violet pigment dyed with silk fabric.

| S. No. | Fabrics | Solvent | $L *$ | $a *$ | $b *$ |
|--------|------------|---------------|-------|-------|-------|
| 1. | Silk satin | Methanol | 81.23 | 12.82 | 30.94 |
| | | Acetone | 60.47 | 5.61 | 18.21 |
| | | Ethyl acetate | 63.89 | 8.93 | 22.85 |
| | | Water | 42.57 | 1.47 | 12.37 |
| | | Methanol | 72.14 | 10.53 | 24.71 |
| 2. | Cotton | Acetone | 51.10 | 4.65 | 8.49 |
| | | Ethyl acetate | 58.35 | 6.47 | 16.12 |
| | | Water | 31.85 | 0.98 | 7.95 |

0.50, 1.0, and 2.0 mg/mL) were loaded into the wells to obtain final volume of 200 μ L in microtiter plate. For bacterial strains, microtiter plates were incubated at 37°C and for yeast strains at 30°C. After incubation, the plates were recorded for bacterial and fungal growth inhibition using microtiter plate reader.

2.11. Antioxidant Efficacy of Violacein Pigments. The DPPH analysis was performed based on the decolorization efficiency of this molecule in the presence of antioxidants and robust technique for measuring the scavenging ability of free radicals [52]. Ascorbic acid was used as the standard control. In 1 mL of 3 mM DPPH solution, different concentrations of violet dye (5–100 μ g/mL) were added and incubated in the dark for 30 min at 30°C. The color transition from violet to yellow was measured at 517 nm. The IC_{50} value denotes the dye concentration required to scavenge 50% of the free radicals generated by DPPH.

Using the following equation, the percent inhibition was quantified:

$$\% \text{Inhibition} = (A_c - A_s / A_c) \times 100, \quad (2)$$

where A_c denotes control absorbance and A_s denotes pigment absorbance.

3. Result and Discussion

3.1. Isolation of Bacterial Isolates. Samples of soil sediment were obtained from 12 distinct locations at Great Salt Lake located in Chennai, India (Table 1). Different bacterial isolates were obtained from soil samples, including *C. violaceum*, which was rapidly identified due to its distinctive violet colonies (Figure 2). Bacterial strains were isolated using both enrichment and filtration methods, and they thrived at temperatures between 22°C and 37°C. On nutrient agar plates, the colonies were violet in color, oval, slightly elevated, with a whole margin, shiny, clear, and smooth surface. *C. violaceum* is a nonsporing, motile, gram-negative coccobacillus.

3.2. Biochemical and Physiological Characterization of Bacterial Isolate PDF23. The bacterial strain *C. violaceum* showed positive results for oxidase, methyl red test, and cit-

rate utilization test whereas negative for catalase, urease, indole production, and Voges-Proskauer test. The TSI test was positive for glucose and no production of sulfide. Casein and fat were hydrolyzed by our isolate of *C. violaceum*, but not starch. It has ability to oxidize and ferment glucose, but it has not capable to oxidize or ferment sucrose. It did not produce hydrogen sulfide or indole on SIM agar, but it did show motility. *C. violaceum* exhibited an alkaline slant and an acidic butt on TSI medium, with no hydrogen sulfide or gas production. Lactose and sucrose were not used, but proteolysis and glucose fermentation were identified. Table 2 summarizes the results of biochemical tests performed on *C. violaceum* PDF23 used in this study.

The bacterial species identification was influenced by characterization of the isolate through various physiological and biochemical studies. Further, molecular phylogenetic study and the comparison of different biochemical test results with those published from other countries have authenticated its identification [53–55]. *Chromobacterium* sp. has capability to metabolize various organic substrates and provides the bacterium the advantage of living in natural environments with minimal amounts of carbon or nutrients. *Chromobacterium* sp. showed uniform phenotypic and biochemical characteristics and were documented from different natural habitats, while diverse physiological characteristics are adapted to adverse environment [53, 54, 56].

3.3. Molecular Phylogenetic Analysis. The 16S rRNA gene was amplified by PCR, yielding an amplicon of around 1500 bp, which was used to identify the bacterial isolate PDF23. Following amplification, sequencing of the 16S rRNA gene produced a 602 bp amplicon, which was then submitted to Blast analysis (Table 3). The 16S rRNA gene sequence of PDF23 showed 99.67% identical to 16S rRNA gene sequence of *C. violaceum* strain RG1 (MF144240). *C. violaceum* PDF23 nucleotide sequence has been submitted to GenBank with the accession number MT176501.1. The 16S rRNA gene sequence analysis of our bacterial isolate showed 99% similarity with *C. violaceum*.

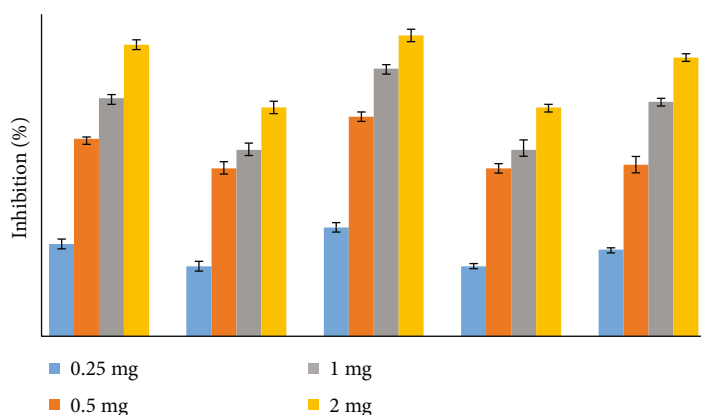
The first 20 16S rRNA gene sequences of *C. violaceum* PDF23 showed >99.67% similarity in BLASTN, indicating that the *C. violaceum* PDF23 isolate grouped together with other *C. violaceum* strains in a separate clade assisted by 99% bootstrap values. It belongs to a separate clade and also phylogenetically distinct from the three *Chromobacterium* species previously identified (*C. vaccinii* strain CV5, *C. piscinae* WBJR0303, and *Chromobacterium* sp. LRSZR53) (Figure 3).

C. violaceum, a gram-negative bacteria, present a wide range of tropical and subtropical environments in the atmosphere as a saprophyte, especially in water and soil [57]. It is a β -proteobacterium that has reignited biotechnological interest due to its wide economic, therapeutic, and ecological potential [58]. This free-living bacterium has a high degree of adaptability, allowing it to survive in extreme environmental conditions [59]. Similar to our study, a violet pigment producing bacteria *C. violaceum* UTM5 (HM132057) was isolated and characterized from soil samples taken from wastewater treatment system at oil refinery in Negeri

TABLE 6: Colorfastness qualities of natural dyed cotton fabric and silk satin in the presence of different mordants.

| Fabrics | Mordant | Colorfastness | | | | | | | | | |
|------------|---|---------------|---------|-----|----------------------|-----|--------------|-----|-------|-----|-----|
| | | Light | Washing | | Rubbing/ crocking | | Perspiration | | Water | | |
| | | | DC | S | Dry | Wet | CC | DC | CC | DC | |
| Silk satin | No | 1 | 2/3 | 3/4 | 5 | 4/5 | 4/5 | 4/5 | 4/5 | 4/5 | 4/5 |
| | Alum | 1/2 | 4/5 | 5 | 5 | 5 | 4/5 | 5 | 4/5 | 5 | |
| | Fe ₂ (SO ₄) ₃ | 1 | 3/4 | 4/5 | 4/5 | 4/5 | 4/5 | 5 | 4/5 | 5 | |
| | CuSO ₄ | 1 | 4/5 | 4/5 | 5 | 5 | 3/4 | 4/5 | 4/5 | 4/5 | |
| | Ca(OH) ₂ | 2 | 4/4 | 4/5 | 5 | 5 | 4/5 | 4/5 | 5 | 4/5 | |
| Cotton | No | 1 | 1/2 | 2 | 4/5 | 4 | 4/5 | 4/5 | 5 | 5 | |
| | Alum | 1 | 4/5 | 5 | 4 | 4/5 | 4/5 | 5 | 4/5 | 5 | |
| | Fe ₂ (SO ₄) ₃ | 2 | 4/5 | 4 | 4/5 | 4/5 | 3/4 | 4/5 | 5 | 5 | |
| | CuSO ₄ | 2/3 | 4 | 4/5 | 4 | 4/5 | 4/5 | 4/5 | 4/5 | 4/5 | |
| | Ca(OH) ₂ | 1 | 4/5 | 3/4 | 4 | 4/5 | 5 | 4/5 | 4/5 | 5 | |

S: staining on white fabric; DC: determining color; CC: color change; 1 denotes very poor; 2 denotes poor; 3 denotes fair; 4 denotes good; and 5 denotes excellence.

FIGURE 6: Antimicrobial activity of violacein pigment from *C. violaceum* PDF23 showing inhibition against selected human pathogens.

Sembilan, Malaysia [49]. This is the first evidence of the violet pigment-producing halophilic *C. violaceum* PDF23 being isolated from Great Salt Lake located in Chennai, India.

3.4. Production of Natural Dye from *C. violaceum*. Three different solvents include methanol, acetone, ethyl acetate, and water and were used to extract natural pigment from *C. violaceum*, whereas ethyl acetate extract from the broth medium was used effectively as a dye. Compared to ethyl acetate and acetone extract, methanol solvents have been shown to contain high concentrations of colorants. While extracted using methanol solvent, *C. violaceum* developed blue colorants, whereas acetone and ethyl extracts generated violet colorants (Table 4).

The natural dyes have been synthesized in the media intracellularly inside the cells. *C. violaceum* could therefore produce various types of pigments from various extraction techniques. Earlier studies have shown that dyes derived from different microbial sources, such as fungi, plants, and other bacterial species primarily extracted from intracellular

cells. Similarly, Hiroshi [60] stated that a bluish violet dye was extracted from *Janthinobacterium lividum* using various solvents at different concentrations.

3.5. Characterization of Natural Dye

3.5.1. UV-Vis Spectral Analysis. The strong absorption spectra were observed between 500 to 700 nm. For *C. violaceum*, the maximum wavelength at 575 nm is shown in Figure 4. Study by Lu [61] observed that the *C. violaceum* dye in methanol developed a greater absorption at 576 nm. Therefore, both the maximum absorbance wavelengths agree with existing studies to suggest that bacterial colorants are of the same genus.

The violet dye in methanol showed a sharp peak with absorption maximum at 575 nm and confirms the formation of chromophore groups including alkene and carbonyl, which are responsible for electronic absorption. While the carbon atom absorbs positively at a narrower UV-Vis wavelength, due to the presence of n-electrons, the intensity significantly reduces at longer wavelengths. Therefore, the

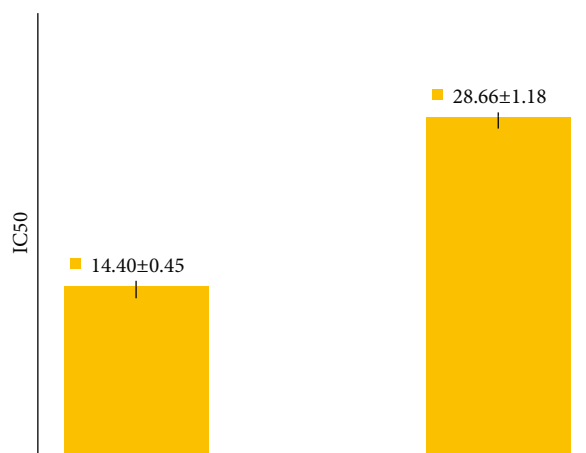


FIGURE 7: DPPH was used to assess the antioxidant activity of *C. violaceum* PDF23 violet pigments. Results are based on an average of three separate experiments and standard deviation is represented by the error bars.

significant characteristic of the alkene groups in relating to the cross-linking effect would be that the higher the influence of double conjugated bonds, the greater the wavelength of absorption (bathochromic shift) [62].

3.5.2. Fourier Transform-Infrared Spectroscopy (FT-IR). The structural detection of violacein was done using FT-IR spectroscopy (Figure 5). The crude methanolic extract results from the FTIR study are as follows: $3700\text{--}3000\text{ cm}^{-1}$ (OH), 3447 cm^{-1} (N-H), 3061 cm^{-1} amide, 2878 cm^{-1} (C=O amide), 1641 cm^{-1} (C=C), 1544 cm^{-1} (C-O phenol), and 1422 cm^{-1} and 1362 cm^{-1} (C-N). The low absorption wavelength for the carbonyl group could be formed due to the aromatic ring cross-linking effect, resulting in the π electrons of both unsaturated groups being delocalized. This decreases the double bonds formed between the carbon atoms, resulting in a decrease in the wavelength from 1176 cm^{-1} , i.e., typical carbonyl group absorption wavelength at 1039 cm^{-1} , and alkene stretching frequency from 783 cm^{-1} , i.e., typical alkene absorption wavelength at 689 cm^{-1} . The vibration function of the carbonyl group in the double bond structure was formed due to these conditions [62].

3.6. Dyeing of Fabric Samples

3.6.1. Color Measurement. The measurements of CIE $L^* a^* b^*$ for silk satin and cotton fabrics stained with *C. violaceum* dye are shown in Table 5. The properties of L^* reflect the lightness or darkness interpreted. The number 0 denotes black, while the number 100 denotes white. The scores of ($+a^*$) are red and ($-a^*$) are orange, whereas yellow are ($+b^*$) and blue are ($-b^*$). Cotton fabrics have lower L^* scores than silk satin in terms of dyes. The L^* score for methanol extract of both silk satin and cotton fabrics has the maximum values of 81.23 and 72.14, respectively, indicating that the dye is similar to the white colors. Ethyl acetate extract yielded the darkest colors as previously described; moreover, they showed higher L^* scores that were 63.89 and 58.35 for silk satin and cotton fabrics, respectively. The a^* and b^* scores of colored fabrics are provided in Table 5 and indicated that all the textile fabrics were

stained with *C. violaceum* extract and were found in the red–yellow region.

In contrast, Yusoff et al. [28] stated that the dye extracted from actinomycetes provided a low a^* score in the red region range ($+a$) as well as a lower L^* score indicating the closest to white color. Similar findings were reported from the extract of *C. violaceum* indicating the values ($+a$) and ($-b$) as colored on microfiber cloths and polyester fabrics suggesting the red-blue region even when these dyes were processed at different temperatures, although the value of a^* remains unchanged ($+a$) as in the red zone. Moreover, the L^* score for these dyes was more than 50, reflecting white color shades [49].

3.6.2. Colorfastness Properties. Natural dyes also need a metallic mordant to improve the adsorption capacity between the textile fabrics and the dye, and various mordants often significantly reduce the dye from fading or washing out after exposure to light. Colored cotton fabrics and silk satin were mordanted with alum, ferrous sulfate, copper sulfate, and slake lime in this analysis, while the control fabrics were not mordanted. The stained fabrics were tested for rubbing, washing, transpiration, and light colorfastness properties. The assessments were done based on MS ISO specifications with a rating scale of 1 to 5, where 1 indicates worst and 5 denotes the best. The data for the evaluation of transpiration, washing, rubbing, and light fastness are provided in Table 6. Wet and dry rubbing durability received a grade of 4 to 5, indicating fair to excellent performance. The fabrics colorfastness to light was assessed by comparing them to blue wool standards on a scale of 1 to 5, with 1 being the least and 5 being the highest.

In both cotton and silk satin, the use of slake lime mordant appears to result in darker color than the control fabrics. A golden colored fabric appeared in $\text{Fe}_2(\text{SO}_4)_3$, whereas CuSO_4 changed the colored fabric into shades of grey. Conversely, alum produced no substantial variation was observed between the color produced on the dyed fabrics and the control samples.

As shown in Table 6, $\text{Fe}_2(\text{SO}_4)_3$ and CuSO_4 improve the light fastness of cotton from 1 (control) to 2 and 2/3,

respectively, while alum and slaked lime improve the light fastness of silk satin from 1 (control) to 2 and 2/3, respectively. Similarly, Ahmad et al. [49] also stated that the light fastness ranking of silk satin stained with natural violacein dye along with mordant alum and slaked lime was observed to enhance from 1 (control) to 2. It could be attributed to interaction with transition metal ions, which decreases the chromophore valence electrons, resulting in increased resistance to photocatalytic degradation [63]. The findings indicated that in particular, the colored silk and cotton showed low light fastness, giving grades between 1 and 2/3. In general, it is well documented that the characteristics of light fastness were weak among natural colorants that generally offered low grades. For example, the grade of bluish-violet dye derived from *Janthinobacterium lividum* was as low as 1 [64], whereas dye extracted from the barks of *Ixonanthes icosandra* Jack offered a score of 2 for the characteristics of light fastness [65].

In this work, when alum is being used as the mordant, good colorfastness of the fabric was observed for washing. This is although Al^{3+} could act as an effective electron acceptor to form link bonds with the dye molecule, preceded by the development of an insoluble complex, thus improving the pigments binding interactions to the fibers [66]. Some colorfastness studies have proven that in the absence of mordant, cotton and silk satin have fair (4) to excellent (5) colorfastness characteristics for transpiration, rubbing/crocking, and water. The strong affinity of the dye to cellulose and protein could be attributed to this effect [49].

It has also been demonstrated that dyes would function as both direct pigment and mordant stain, because without the aid of certain other additives, the dyes would bind to the fabric molecules. It could also function to bind it to the fabric in the presence of a synthetic agent known as a mordant. Compared to un-mordanted fabric, the colorfastness result of dyed fabric mordanted with alum is good. A potential perspective for this finding is that the auxochrome groups present in the dye ($-OH$ and $-NH_2$) resulted in the effective production of metal compounds with the fabrics and the ability to form very strong bonds with the dye and fabrics.

The evaluation of colorfastness to perspiration is shown in Table 6. The result for colorfastness provided a good to excellent grade of 3/4-5 for color change, while the rating for color staining was fair to excellent ranged from 4 to 5. In contrast, the bluish-violet dye derived from *Janthino bacteriumlividum* provided a fair score of colorfastness characteristics [64]. The effect of colorfastness to washing provided a color change score between 1/2 and 5. It clearly demonstrates that the ranking is comparatively low to excellence.

For staining, the grade was high, from 4/5 to 5, for both silk and cotton. As a consequence, this could be attributed that the dye in soap and water faded quickly, and did not affect silk and cotton stains. However, a good ranking of 4 for red and violet dyes derived from *Serratia marcescens* and *C. violaceum* was demonstrated by Zulkifli et al. [67]. While the scores for colorfastness to light and washing were poor for both colorfastness measurements, the ranking

towards perspiration and rubbing was excellent providing grades between 4 and 5. Conversely, more advancement would make to enhance the quality of the pigments, particularly for light and washing to colorfastness.

3.7. Applications of Violet Pigment in Textile Dyeing Fabrics

3.7.1. Antimicrobial Efficacy of Violet Dye. In the initial screening, crude methanolic extract of *C. violaceum* culture was evaluated for the antimicrobial efficacy against two gram-positive (*S. aureus* and *B. subtilis*), two gram-negative (*E. coli* and *P. aeruginosa*), and one fungal strains (*C. albicans*). Violacein-containing culture extract was capable of inhibiting growth of all tested strains between 12 and 54% significantly at a high concentration of 2 mg L^{-1} compared with control. The growth of *S. aureus* was inhibited for 39% even at concentration of 0.5 mg L^{-1} , whereas the least affected strain was *P. aeruginosa*. *C. albicans* was the most susceptible fungal strain with 50 and 15% growth inhibition at 2 and 0.25 mg L^{-1} of the extract, respectively (Figure 6).

3.7.2. Antioxidant Activity of Violacein Pigments of *C. violaceum* PDF23. The radical scavenging assay evaluated the antioxidant activity of violet pigments. The IC_{50} value was $14.40\text{ }\mu\text{g/mL}$ and $28.66\text{ }\mu\text{g/mL}$ for violet pigments and ascorbic acid, respectively (Figure 7).

These findings suggest that the violet pigments of *C. violaceum* PDF23 is more potent in scavenging free radicals than ascorbic acid. The plausible reason for the absence of catalase activity in *C. violaceum* PDF23 could be the significant antioxidant potential of violet pigments. A crucial role in the advancement of a wide range of pathological chronic diseases such as diabetes and cancer has been proposed for the generation of free radicals [68]. Consequently, treatment with free radical scavenging antioxidants such as microbial dyes *C. violaceum* PDF23 has the ability to prevent, prolong, or alter many of these diseases.

4. Conclusion

Microbial pigments are a potential source of natural dyes, with a wide range of applications in the textile industry. The study highlights the natural dye production from microbes isolated from Great Salt Lake in Chennai, India. The PDF23 bacterial isolate was identified as *C. violaceum*, which differed from other members of the genus phylogenetically. Violet pigment was observed to be capable of dyeing both cotton and silk satin. Interestingly, fabrics dyed with violet pigment scored fair (3/4) to excellent (5) in all of the colorfastness properties (except light). Violet pigment was efficiently used in textile dyeing in this study, highlighting that it can be used as a substitute for synthetic dye. This is the first report of violet colored pigments isolated from *C. violaceum* PDF 23 (Great Salt Lake) with antimicrobial and antioxidant properties and textile dyeing applications.

Data Availability

The datasets used and/or investigated during the current study are available from the corresponding authors upon reasonable request.

Conflicts of Interest

The authors have declared no conflict of interest.

Acknowledgments

The authors are grateful to the management of Sathyabama Institute of Science and Technology, Chennai, for supporting the original article. Professor K. R. Venkatesan, Principal, Sri Sankara Arts and Science College, Kanchipuram, Tamilnadu, India, has provided us with invaluable assistance and encouragement. This work was supported by the Deanship of Scientific Research, Vice Presidency for Graduate Studies and Scientific Research, King Faisal University, Saudi Arabia [Project No. GRANT1079].

References

- [1] R. Naidu, B. Biswas, I. R. Willett et al., "Chemical pollution: a growing peril and potential catastrophic risk to humanity," *Environment International*, vol. 156, article 106616, 2021.
- [2] M. Shahid, M. Nadeem, and H. F. Bakhat, "Environmental toxicology and associated human health risks," *Environmental Science and Pollution Research*, vol. 27, no. 32, pp. 39671–39675, 2020.
- [3] H. B. Slama, A. Chenari Bouket, Z. Pourhassan et al., "Diversity of synthetic dyes from textile industries, discharge impacts and treatment methods," *Applied Sciences*, vol. 11, no. 14, p. 6255, 2021.
- [4] M. Yusuf, "Synthetic dyes: a threat to the environment and water ecosystem," *Textiles and Clothing*, vol. 19, pp. 11–26, 2019.
- [5] S. Adeel, F. U. Rehman, M. K. Khosa et al., "Eco-friendly isolation of colorant from arjun bark for dyeing of bio-mordanted cotton fabric," *Journal of Natural Fibers*, vol. 8, pp. 1–2, 2021.
- [6] A. Haji and M. Naebe, "Cleaner dyeing of textiles using plasma treatment and natural dyes: a review," *Journal of Cleaner Production*, vol. 265, article 121866, 2020.
- [7] K. Amutha and N. Sudhapriya, "Dyeing of textiles with natural dyes extracted from *Terminalia arjuna* and *Thespesia populnea* fruits," *Industrial Crops and Products*, vol. 148, article 112303, 2020.
- [8] K. Phan, E. Van Den Broeck, V. Van Speybroeck, K. De Clerck, K. Raes, and S. De Meester, "The potential of anthocyanins from blueberries as a natural dye for cotton: a combined experimental and theoretical study," *Dyes and Pigments*, vol. 176, article 108180, 2020.
- [9] F. Wang, J. Gong, X. Zhang, Y. Ren, and J. Zhang, "Preparation of biocolorant and eco-dyeing derived from polyphenols based on laccase-catalyzed oxidative polymerization," *Polymers*, vol. 10, no. 2, p. 196, 2018.
- [10] P. M. dos Santos Silva, T. R. Fiaschitello, R. S. de Queiroz et al., "Natural dye from *Croton urucurana* Baill. bark: extraction, physicochemical characterization, textile dyeing and color fastness properties," *Dyes and Pigments*, vol. 173, article 107953, 2020.
- [11] S. Rai, P. K. Dutta, and G. K. Mehrotra, "Natural antioxidant and antimicrobial agents from agrowastes: an emergent need to food packaging," *Waste and Biomass Valorization*, vol. 11, no. 5, pp. 1905–1916, 2020.
- [12] W. U. Arifeen, F. U. Rehman, S. Adeel, M. Zuber, M. N. Ahmad, and T. Ahmad, "Environmental friendly extraction of walnut bark-based juglone natural colorant for dyeing studies of wool fabric," *Environmental Science and Pollution Research*, vol. 28, no. 36, pp. 49958–49966, 2021.
- [13] I. Luzardo-Ocampo, A. K. Ramírez-Jiménez, J. Yañez, L. Mojica, and D. A. Luna-Vital, "Technological applications of natural colorants in food systems: a review," *Food*, vol. 10, no. 3, p. 634, 2021.
- [14] T. Sen, C. J. Barrow, and S. K. Deshmukh, "Microbial pigments in the food industry-challenges and the way forward," *Frontiers in Nutrition*, vol. 6, p. 7, 2019.
- [15] K. Malik, J. Tokkas, and S. Goyal, "Microbial pigments: a review," *International Journal of Microbial Resource Technology*, vol. 4, pp. 361–365, 2012.
- [16] L. Dufosse, "Microbial pigments from bacteria, yeasts, fungi, and microalgae for the food and feed industries," in *Natural and artificial flavoring agents and food dyes*, pp. 113–132, Academic Press, 2018.
- [17] R. Dikshit and P. Tallapragada, "Comparative study of natural and artificial flavoring agents and dyes," in *Natural and artificial flavoring agents and food dyes*, pp. 83–111, Academic Press, 2018.
- [18] S. Y. Choi, K. H. Yoon, J. I. Lee, and R. J. Mitchell, "Violacein: properties and production of a versatile bacterial pigment," *Bio Med Research International*, vol. 2015, pp. 1–8, 2015.
- [19] M. Kanelli, M. Mandic, M. Kalakona et al., "Microbial production of violacein and process optimization for dyeing polyamide fabrics with acquired antimicrobial properties," *Frontiers in Microbiology*, vol. 9, p. 1495, 2018.
- [20] T. S. Vishnu and M. Palaniswamy, "Isolation and identification of *Chromobacterium* sp. from different ecosystems," *Asian Journal of Pharmaceutical and Clinical Research*, vol. 9, no. 9, pp. 253–257, 2016.
- [21] C. A. Aruldass, S. R. Masalamany, C. K. Venil, and W. A. Ahmad, "Antibacterial mode of action of violacein from *Chromobacterium violaceum* UTM5 against *Staphylococcus aureus* and methicillin-resistant *Staphylococcus aureus* (MRSA)," *Environmental Science and Pollution Research*, vol. 25, no. 6, pp. 5164–5180, 2018.
- [22] M. Durán, A. N. Ponezi, A. Faljoni-Alario, M. F. Teixeira, G. Z. Justo, and N. Durán, "Potential applications of violacein: a microbial pigment," *Medicinal Chemistry Research*, vol. 21, no. 7, pp. 1524–1532, 2012.
- [23] S. C. Lopes, Y. C. Blanco, G. Z. Justo et al., "Violacein extracted from *Chromobacterium violaceum* inhibits plasmodium growth in vitro and in vivo," *Antimicrobial Agents and Chemotherapy*, vol. 53, no. 5, pp. 2149–2152, 2009.
- [24] M. O. Moss and C. Ryall, "Distribution of *Chromobacterium* in a Lowland River," *Microbial Ecology*, vol. 7, no. 2, pp. 139–149, 1981.
- [25] T. Hoshino, "Violacein and related tryptophan metabolites produced by *Chromobacterium violaceum*: biosynthetic mechanism and pathway for construction of violacein core," *Applied Microbiology and Biotechnology*, vol. 91, no. 6, pp. 1463–1475, 2011.

- [26] S. A. Mccarthy, R. M. Johnson, D. Kakimoto, and T. Sakata, "Effects of various agents on the pigment (Violacein) and antibiotic production of *Alteromonas luteoviolacea*," *Bulletin of the Japanese Society of Scientific Fisheries*, vol. 51, no. 7, pp. 1115–1121, 1985.
- [27] X. Zhang and K. Enomoto, "Characterization of a gene cluster and its putative promoter region for violacein biosynthesis in *Pseudoalteromonas* sp. 520P1," *Applied Microbiology and Biotechnology*, vol. 90, no. 6, pp. 1963–1971, 2011.
- [28] Y. Lu, L. Wang, Y. Xue et al., "Production of violet pigment by a newly isolated psychrotrophic bacterium from a glacier in Xinjiang, China," *Biochemical Engineering Journal*, vol. 43, no. 2, pp. 135–141, 2009.
- [29] F. Pantanella, F. Berlutti, C. Passariello, S. Sarli, C. Morea, and S. Schippa, "Violacein and biofilm production in *Janthinobacterium lividum*," *Journal of Applied Microbiology*, vol. 102, no. 4, pp. 992–999, 2007.
- [30] H. Wang, P. Jiang, Y. Lu et al., "Optimization of culture conditions for violacein production by a new strain of *Duganella* sp. B2," *Biochemical Engineering Journal*, vol. 44, no. 2-3, pp. 119–124, 2009.
- [31] M. Yusuf, F. Mohammad, M. Shabbir, and M. A. Khan, "Eco-dyeing of wool with *Rubia cordifolia* root extract: assessment of the effect of *Acacia catechu* as biomordant on color and fastness properties," *Textiles and Clothing Sustainability*, vol. 2, no. 1, pp. 1–9, 2017.
- [32] F. Shahmoradi Ghaheh, M. K. Moghaddam, and M. Tehrani, "Comparison of the effect of metal mordants and biomordants on the colorimetric and antibacterial properties of natural dyes on cotton fabric," *Coloration Technology*, vol. 137, no. 6, pp. 689–698, 2021.
- [33] S. Kiran, A. Hassan, S. H. Adeel et al., "Green dyeing of microwave treated silk using coconut coir based tannin natural dye," *Industria Textila*, vol. 71, no. 3, pp. 227–234, 2020.
- [34] S. Adeel, M. Zuber, and K. M. Zia, "Microwave-assisted extraction and dyeing of chemical and bio-mordanted cotton fabric using harmful seeds as a source of natural dye," *Environmental Science and Pollution Research*, vol. 25, no. 11, pp. 11100–11110, 2018.
- [35] F. U. Rehman, S. Adeel, T. Ahmad, A. Mateen, and N. Amin, "Statistical optimization of parameters for eco-friendly dyeing of cotton using direct red 31 dye," *Journal of Natural Fibers*, vol. 25, pp. 1–11, 2021.
- [36] X. Ma, Y. Wei, S. Wang, X. Zuo, and B. Shen, "Sustainable ultrasound-assisted ultralow liquor ratio dyeing of cotton fabric with natural turmeric dye," *Textile Research Journal*, vol. 90, no. 5-6, pp. 685–694, 2020.
- [37] K. M. Zia, S. Adeel, H. Aslam, M. K. Khosa, and M. Zuber, "Influence of ultrasonic radiation on extraction and green dyeing of mordanted cotton using neem bark extract," *Journal of Industrial and Engineering Chemistry*, vol. 77, pp. 317–322, 2019.
- [38] S. Adeel, M. Azeem, F. U. Rehman et al., "Sustainable utilization of ultrasonic radiation in extraction and dyeing of wool fabric using logwood (*Haematoxylum campechianum*) extracts," *Textile and Apparel*, vol. 29, pp. 181–185, 2019.
- [39] J. P. Verma, D. K. Jaiswal, and P. K. Maurya, "Screening of bacterial strains for developing effective pesticide-tolerant plant growth-promoting microbial consortia from rhizosphere soils of vegetable fields of eastern Uttar Pradesh, India," *Energy Ecology and Environment*, vol. 1, no. 6, pp. 408–418, 2016.
- [40] R. M. Smibert and N. R. Krieg, "Phenotypic characterization," *Methods for General and Molecular Bacteriology*, P. Gerhardt, R. G. Murray, W. A. Wood, and N. R. Krieg, Eds., pp. 611–654, 1994.
- [41] C. D. Litchfield and M. P. Gillevet, "Microbial diversity and complexity in hypersaline environments: a preliminary assessment," *Journal of Industrial Microbiology and Biotechnology*, vol. 28, no. 1, pp. 48–55, 2002.
- [42] V. Hemraj, S. Diksha, and G. Avneet, "A review on commonly used biochemical test for bacteria," *Innovare Journal of Life Sciences*, vol. 1, pp. 1–7, 2013.
- [43] J. Sambrook, E. F. Fritsch, and T. Maniatis, *Molecular Cloning: a Laboratory Manual*, N. Irwin, Ed., Cold Spring Harbor Laboratory Press, 2009.
- [44] S. Gupta, P. Sharma, K. Dev, M. Srivastava, and A. Sourirajan, "A diverse group of halophilic bacteria exist in Lunsu, a natural salt water body of Himachal Pradesh, India," *Springer Plus*, vol. 4, no. 1, pp. 1–9, 2015.
- [45] S. F. Altschul, W. Gish, W. Miller, E. W. Myers, and D. J. Lipman, "Basic local alignment search tool," *Journal of Molecular Biology*, vol. 215, no. 3, pp. 403–410, 1990.
- [46] A. Sasidharan, N. K. Sasidharan, D. B. Amma, R. K. Vasu, A. V. Nataraja, and K. Bhaskaran, "Antifungal activity of violacein purified from a novel strain of *Chromobacterium* sp. NIIST (MTCC 5522)," *Journal of Microbiology*, vol. 53, no. 10, pp. 694–701, 2015.
- [47] W. W. Ahmad, M. R. Ahmad, and M. I. Ab Kadir, "Dyeing of polyester and polyester microfibre with natural dye from bacteria source," *Proceedings of the International Colloquium in Textile Engineering, Fashion, Apparel and Design*, pp. 119–123, Springer, Singapore, 2014.
- [48] W. A. Ahmad, N. Z. Yusof, N. Nordin, Z. A. Zakaria, and M. F. Rezali, "Production and characterization of violacein by locally isolated *Chromobacterium violaceum* grown in agricultural wastes," *Applied Biochemistry and Biotechnology*, vol. 167, no. 5, pp. 1220–1234, 2012.
- [49] F. Li, F. Xue, and X. Yu, "GC-MS, FTIR and Raman analysis of antioxidant components of red pigments from *Stemphylium lycopersici*," *Current Microbiology*, vol. 74, no. 4, pp. 532–539, 2017.
- [50] C. K. Venil, N. Z. Yusof, C. A. Aruldass, and W. A. Ahmad, "Application of violet pigment from *Chromobacterium violaceum* UTM5 in textile dyeing," *Biologia*, vol. 71, no. 2, pp. 121–127, 2016.
- [51] W. A. Ahmad, W. Y. Ahmad, Z. A. Zakaria, and N. Z. Yusof, "Application of bacterial pigments as colorant," in *Application of Bacterial Pigments as Colorant*, pp. 57–74, Springer, Berlin, Heidelberg, 2012.
- [52] N. F. Ali and R. S. El-Mohamedy, "Eco-friendly and protective natural dye from red prickly pear (*Opuntia lasiacantha* Pfeiffer) plant," *Journal of Saudi Chemical Society*, vol. 15, no. 3, pp. 257–261, 2011.
- [53] N. Prasannabalaji, G. Muralitharan, R. N. Sivanandan, S. Kumaran, and S. R. Pugazhvendan, "Antibacterial activities of some Indian traditional plant extracts," *Asian Pacific Journal of Tropical Disease*, vol. 2, pp. S291–S295, 2012.
- [54] K. P. Renukadevi and M. Vineeth, "Antimicrobial, antioxidant and cytotoxicity activity of pigment produced from *Serratia marcescens*," *European Journal of Biomedical and Pharmaceutical Sciences*, vol. 4, pp. 265–269, 2017.
- [55] A. A. Antunes, M. L. R. B. Silva, C. A. A. Silva, and G. M. Campos-Takaki, "Characterization of *Chromobacterium violaceum*

- isolated from Paca River, Pernambuco, Brazil,” *Revista de Biologia e Ciências da Terra*, vol. 1, pp. 48–55, 2006.
- [56] C. Y. Chang, Y. T. Lee, K. S. Liu, Y. L. Wang, and S. M. Tsao, “*Chromobacterium violaceum* infection in Taiwan: a case report and literature review,” *Journal of Microbiology, Immunology, and Infection*, vol. 40, pp. 272–275, 2007.
- [57] A. Jitmuang, “Human *Chromobacterium violaceum* infection in Southeast Asia: case reports and literature review,” *Southeast Asian Journal of Tropical Medicine and Public Health*, vol. 39, no. 3, pp. 452–460, 2008.
- [58] M. Hungria, M. F. Nicolás, C. T. Guimarães, S. N. Jardim, E. P. Gomes, and A. T. R. Vasconcelos, “Tolerance to stress and environmental adaptability of *Chromobacterium violaceum*,” *Genetics and Molecular Research*, vol. 3, no. 1, pp. 102–116, 2004.
- [59] N. Durán and C. F. Menck, “*Chromobacterium violaceum*: a review of pharmacological and industrial perspectives,” *Critical Reviews in Microbiology*, vol. 27, no. 3, pp. 201–222, 2001.
- [60] S. Y. Choi, S. Lim, K. H. Yoon, J. I. Lee, and R. J. Mitchell, “Biotechnological activities and applications of bacterial pigments violacein and prodigiosin,” *Journal of Biological Engineering*, vol. 15, no. 1, pp. 1–6, 2021.
- [61] T. B. Creczynski-Pasa and R. V. Antônio, “Energetic metabolism of *Chromobacterium violaceum*,” *Genetics and Molecular Research*, vol. 3, no. 1, pp. 162–166, 2004.
- [62] K. A. Hiroshi, “Isolation of bacteria producing bluish-purple pigment and use for dyeing,” *Japan Agricultural Research Quarterly*, vol. 34, pp. 131–140, 2000.
- [63] J. Mohan, *Organic Spectroscopy: Principles and Applications*, Alpha Science International, UK, 2007.
- [64] W. W. Yusoff, S. S. Mohamad, and W. W. Ahmad, “Fastness Properties and Color Analysis of Natural Colorants from Actinomycetes Isolates on Silk Fabric,” *Proceedings of the International Colloquium in Textile Engineering, Fashion, ,* pp. 113–118, Apparel and Design Springer, Singapore, 2014.
- [65] R. Christie, “Colour chemistry,” *Royal Society of Chemistry, United Kingdom*, vol. 46, pp. 118–120, 2001.
- [66] C. K. Venil, Z. A. Zakaria, and W. A. Ahmad, “Bacterial pigments and their applications,” *Process Biochemistry*, vol. 48, no. 7, pp. 1065–1079, 2013.
- [67] J. Miyaura and C. Tatsumi, “Studies on the antibiotics from actinomycetes an antibiotics pigment from *Streptomyces* F-23b,” *Bulletin of Osaka Prefecture University Series B*, vol. 12, pp. 129–137, 1960.
- [68] Y. H. Lee and H. D. Kim, “Dyeing properties and colour fastness of cotton and silk fabrics dyed with *Cassia tora* L. extract,” *Fibers and Polymers*, vol. 5, no. 4, pp. 303–308, 2004.

Research Article

Wear Behavior and FESEM Analysis of LM 25 Alloy MMHCs Reinforced with Fe_3O_4 and Gr by Utilizing Taguchi's Technique

G. Gokilakrishnan,¹ R. Sathishkumar ,² N. S. Sivakumar ,³ S. Kaliappan,⁴ S. Sekar,⁵ Pravin P. Patil,⁶ Ram Subbiah,⁷ K. P. Yuvaraj,⁸ and Feleke Worku Tadesse ⁹

¹Department of Mechanical Engineering, Sri Eshwar College of Engineering, Coimbatore, Tamil Nadu, India

²Department of Electrical and Electronics Engineering, SRM TRP Engineering College, Trichy, Tamil Nadu, India

³Mechatronics Engineering, Tishk International University, Erbil, Kurdistan Region, Iraq

⁴Department of Mechanical Engineering, Velammal Institute of Technology, Chennai, Tamil Nadu, India

⁵Department of Mechanical Engineering, Rajalakshmi Engineering College, Rajalakshmi Nagar Thandalam, Chennai, 602 105 Tamil Nadu, India

⁶Department of Mechanical Engineering, Graphic Era Deemed to be University, Bell Road, Clement Town, Dehradun, Uttarakhand, India

⁷Department of Mechanical Engineering, Gokaraju Rangaraju Institute of Engineering and Technology, Hyderabad, Telangana, India

⁸Department of Mechanical Engineering, Sri Krishna College of Engineering and Technology, Coimbatore, Tamil Nadu, India

⁹School of Mechanical and Industrial Engineering, Institute of Technology, Debre Markos University, Debre Markos, Ethiopia

Correspondence should be addressed to Feleke Worku Tadesse; wwfeleke@gmail.com

Received 22 April 2022; Accepted 21 June 2022; Published 19 July 2022

Academic Editor: V. Vijayan

Copyright © 2022 G. Gokilakrishnan et al. This is an open access article distributed under the Creative Commons Attribution License, which permits unrestricted use, distribution, and reproduction in any medium, provided the original work is properly cited.

The current research is concerned with the production of an LM25- Fe_3O_4 -Gr metal matrix hybrid composites (MMHCs) and the analysis of its dry sliding wear conditions. The hybrid composites were made out of 3 wt% Fe_3O_4 and 4 wt% Gr particles with a mesh size of 200 meshes and were made using the stir casting method. Wear test on Taguchi's L9 orthogonal arrays employs three process parameters: load, sliding velocity, and distance, each changed for three levels on a pin-on-disc tester position. The wear behavior of hybrid composite was investigated using loads of 20 N, 40 N, and 60 N; velocities of 2 m/s, 4 m/s, and 6 m/s; and distances of 1,000 m, 2,000 m, and 3,000 m. The major parameters were developed utilizing the signal-to-noise ratio by selecting "smaller-is-better" wear rates and COF features. FESEM was used to look at the worn surfaces of the composite specimen in order to determine the wear mechanism. Wear properties are enhanced in materials having aluminium hybrid metal matrix composites. According to the ANOVA table, the load parameter has the greatest impact on wear resistance and coefficient of friction, with maximum load values of 35.64 N and 5.782 N, respectively.

1. Introduction

The applications in engineering and technology are increasingly using hybrid composite materials. Compared to natural composite materials, they provide a number of benefits including increased mechanical and physical properties [1]. Aluminium alloys are commonly used to manufacture aerospace, defense, medical equipment, and automotive spare parts due to their superior strength-to-weight ratio. With

adding suitable amount of metallic or nonmetallic reinforcements and manufactured them as MMCs, the properties of aluminium alloys can be improved. In the aerospace, defense, automobile, marine, medical instruments, and other mechanical industries, MMCs are increasingly being used to replace traditional metallic alloys. To meet the recent demands of advanced engineering applications, researchers have looked into aluminium alloy-based MMCs [2]. Electrical, food, chemical, and marine applications are just a few of

the many applications for the LM25. It is widely used in the automotive industry, where it is commonly used to cast cylinder blocks, wheels, heads, and other parts [3].

AMCs reinforced with iron oxide (Fe_3O_4) were recently developed utilizing a simple and inexpensive industrialized method [4, 5]. This composite's excellent physical and mechanical properties make it an exceptional multipurposeful, lightweight, and proficient material for engineering and technology intentions. This research is required to improve the composite's electrical conductivity due to the effect of Fe_3O_4 [6].

The hardness of the AMCs reinforced with Gr particles decreased with a linear increase in the Gr content, regardless of the manufacturing process used to create the composite materials [7–10]. Because the structure of a bony lubricating film by Gr particles barred straight contact of sliding surfaces and abridged ploughing effects of Al fragment, the wear resistance of AMCs toughened with Gr particles was superior to that of pure aluminium matrix, resulting in easier machining of these composite materials pretend by a variety of techniques [11–14].

With 5% wt of graphite reinforcement, composite compression strength increased by around 108 percent. With 15% graphite reinforcement in the copper matrix, however, there was a significant reduction in compression strength. The wear properties of composite materials have been improved by incorporating graphite into the copper matrix [15]. Suresh et al. manufactured LM25-B4C-Gr- Fe_3O_4 -based hybrid composites by stir casting route and mechanical behaviors. The consequences explained that LM25-B4C-Gr- Fe_3O_4 hybrid composites must be investigated as an outstanding material wherever high strength, ultimate tensile strength, and wear resistance are enhanced [16, 17]. Radhika et al. calculated mechanical properties and wear characteristics of LM25/SiC/ Al_2O_3 hybrid MMCs and fabricated by utilized liquid metallurgy route. The results of worn out surfaces of composites were investigated using SEM and it was found that the mechanical properties and wear resistance augmented as the weight percentage of reinforcement augmented [18]. Siddesh Matti et al. synthesized and evaluated the wear behavior Al7075 alloy composites reinforced with mica, fly ash, and red mud particles prepared by stir casting route. The findings of the hybrid composites were subjected to microstructural studies and wear properties testing is improved [19].

Nagarajan Lenin et al. investigated manufacturing and machining of LM25 reinforced with fly ash and boron carbide (B4C) hybrid composites by using stir casting and WEDM. The results showed the composite's mechanical and machining properties are improved and to be used in several engineering applications [20]. Radhika and Raghu developed LM25/TiC MMCs using liquid metallurgy process and the mechanical properties such as hardness and tensile strength were enhanced on the composite. The microstructural assessment divulges that uniform spreading was achieved in the composites [21]. Gowthamkumar et al. modelled the influence of solidification and flow rate of the molten alloy in a recycled aluminium LM-25 alloy with a high Fe concentration. Mechanical

TABLE 1: Chemical composition of LM25 aluminium alloy.

| Composition | % |
|-------------|---------|
| Si | 7.23 |
| Fe | 0.73 |
| Cu | 0.12 |
| Mn | 0.14 |
| Mg | 0.29 |
| Cr | 0.02 |
| Ni | 0.02 |
| Sn | 0.01 |
| Ti | 0.02 |
| Pb | 0.01 |
| Zn | 0.14 |
| Al | Balance |



FIGURE 1: Casted LM25- Fe_3O_4 -Gr MMHCs specimen.

and microstructural characterizations were used to assess the flow ability and mechanical behavior of cast aluminium scrap, which was compared to a FEA model through simulation [22]. Squeeze casting was used to study and investigate the sliding wear behavior of LM 25, Al/10 wt. percent fly ash composites, AA/10 wt. percent steel particles composites, and AA/5wt. percent FA/5 wt. percent SP hybrid composites. However, Al/FA/SP hybrid composites outperformed Al alloy, Al/FA, and Al/SP composites in terms of wear resistance [23]. Hiremath investigated LM25-borosilicate glass particle composites using the stir casting method, and the findings show that the hardness improves linearly as the reinforcement amount inside the matrix increases. It is also clear that the cold material's Volumetric Heat Capacities have a significant impact not only on the quality of the castings produced but also on the hardness of the AMCs [24]. Elango et al. [11] studied the wear properties of LM25 and composites supplemented with SiC and Titanium Dioxide (TiO_2). The strengthening enhanced the wear resistance of the LM 25 alloy, according to the findings [25].

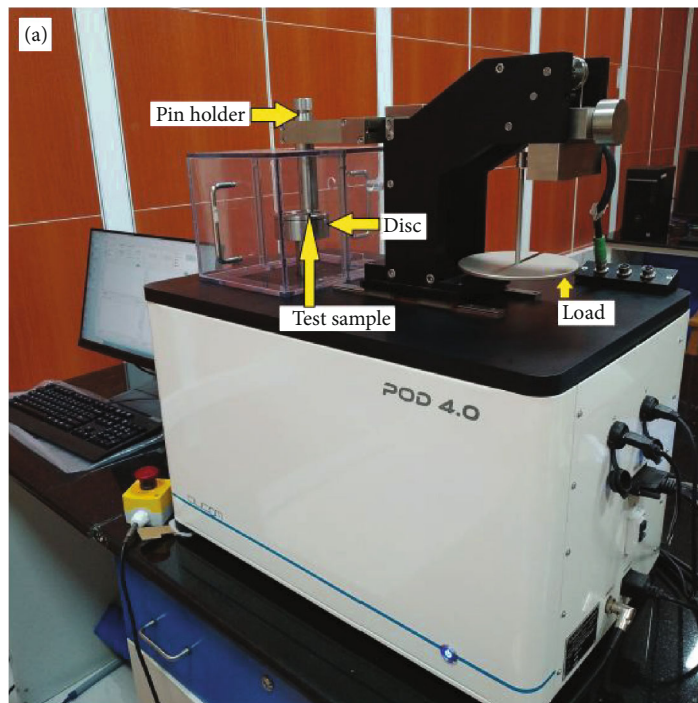


FIGURE 2: Wear testing machine.

In Technology and Science, the signal-to-noise ratio (SNR) is defined as a calculation that compares the level of a chosen signal to the level of background noise [26]. In this case, SNR is calculated by comparing the signal inside a material's imperfection region to the signal within the material's sound area. The SNR is defined as the ratio of the signal intensity recorded in the ROI, i.e., the inhomogeneous area of the specimen, to the standard deviation of the signal intensity in an area outside the ROI [26].

The SNR can be calculated in a variety of methods, according to scientific literature. A list of seven commonly used SNR equations in the scientific community is shown below [27].

$$\text{SNR} = \frac{\text{ALS}}{\text{SD}} \quad (1)$$

where

SNR = signal-to-noise ratio

ALS= the average level of the signal in the defect region

SD= the standard deviation of the noise in the reference or sound region

According to the literature, LM25 aluminium alloy hybrid metal matrix composite reinforced with 3 wt% Fe₃O₄ and 4 wt% Gr particles was produced by stir casting route to improve the wear properties for automotive, aerospace, and industrial tenders. The tribological behavior of the composite is still being investigated using Taguchi's method to estimate the wear rate and coefficient of friction.

TABLE 2: Process parameters and their levels.

| Levels | Load (N) | Sliding velocity (m/s) | Sliding distance (m) |
|--------|----------|------------------------|----------------------|
| 1 | 20 | 2 | 1000 |
| 2 | 40 | 4 | 2000 |
| 3 | 60 | 6 | 3000 |

2. Materials and Methods

2.1. Material Selection. The LM25 aluminium alloy, with a density of 2.68 gm/cm³ and properties such as weight, toughness, and temperature transfer, was chosen as the base medium due to its use in automotive pistons. The reinforcement of Fe₃O₄ particles with 200 mesh sizes was chosen to improve wear resistance. It has a density of 5.24 gm/cm³, a superior hardness than SiC, WC, and TiC, and exceptional substance and thermal permanence, making it an ideal reinforcement for improving the alloy's wear performance. The graphite, which has a density of 2.26 g/cm³, is also used as a reinforcement material, and the composite hardness diminishes as the adding percent of graphite (Gr) augments [28, 29]. The substance compositions of the LM25 aluminium alloy were determined using spectroscopy, as shown in Table 1.

2.2. Stir Casting Method. Owing to its outlay—value, the stir casting method was used to manufacture and fabricate the composite. The LM25 major matrix was liquefied in a stir casting setup furnace, encased in a crucible. The alloy was dissolved in a static gas ambiance, which barred substance reactions and resulted in a casting. The preheated

TABLE 3: L9 orthogonal array.

| S.No | Load (N) | Process parameters | | Wear rate (mm ³ /m) | S/N ratio (db) | COF | S/N ratio (db) |
|------|----------|--------------------|--------------|--------------------------------|----------------|-------|----------------|
| | | Velocity (m/s) | Distance (m) | | | | |
| 1 | 20 | 2 | 1000 | 0.017 | 35.38 | 0.527 | 5.56 |
| 2 | 20 | 4 | 2000 | 0.016 | 35.71 | 0.513 | 5.79 |
| 3 | 20 | 6 | 3000 | 0.016 | 35.82 | 0.502 | 5.98 |
| 4 | 40 | 2 | 1000 | 0.051 | 25.99 | 0.583 | 4.68 |
| 5 | 40 | 4 | 2000 | 0.049 | 26.04 | 0.564 | 4.97 |
| 6 | 40 | 6 | 3000 | 0.047 | 26.44 | 0.573 | 4.83 |
| 7 | 60 | 2 | 1000 | 0.098 | 20.11 | 0.543 | 5.30 |
| 8 | 60 | 4 | 2000 | 0.096 | 20.31 | 0.532 | 5.48 |
| 9 | 60 | 6 | 3000 | 0.093 | 20.61 | 0.521 | 5.66 |

reinforcements were added during the usual intermission behind liquefy and stirred for 8 minutes at 450 rpm to ensure uniform reinforcement particle distribution. The liquefied metal was then poured into preheated (400°C) moulds with dimensions of 100 x 14 mm and allowed to solidify at 840°C, as shown in Figure 1.

2.3. *Wear Test.* Figure 2 shows the results of wear tests using a pin-on-disc apparatus provided by DUCOM on a variety of work pieces.

The cast component was turned in a circular specimen with dimensions of 12 mm x 30 mm. The sample was subjected to dry sliding wear tests using a DUCOM pin-on-disc apparatus in accordance with L9 orthogonal arrays [30]. A rotating steel disc (EN-31) with a hardness of VH114 held test pins (12-30 mm) in place. Throughout the experiment, an 80 mm path diameter was maintained. The cantilever beam, which imparts an equivalent amount of energy to the sample that will come into contact with the opposing visage, remained loaded.

The pin is forced into contact with the disc by the applied load. As a result of surface wear, the pin's size adjusts slightly, allowing the lever arm to be transferred. The LVDT measures the separate wear by disarticulating the switch limb. Before and after the experiment, the specimen was dressed appropriately. The sample's mass loss was taken into account and rehabilitated as volume thrashing and, as a result, wear rates.

During standard intermissions, friction sensors were used to calculate the CoF between the pin and the revolving disc, which was then confirmed using the WINDUCOM software. The average coefficient of friction is stretched by taking the average of those values.

2.4. *Taguchi's Method.* The L9 orthogonal array and Taguchi's method were chosen to achieve the best results with the fewest trials possible, and the experimentation plan remained unchanged (Table 2). The S/N ratio and ANOVA were used to calculate the wear rates of the specimen and the average CoF by using Mini Tab software. The experiment was guided by the following parameters: applied load, sliding

TABLE 4: Response table for S/N ratios–wear rate.

| Level | Load (N) | Speed (m/s) | Distance (m) |
|-------|----------|-------------|--------------|
| 1 | 35.64 | 27.16 | 27.16 |
| 2 | 26.16 | 20.69 | 20.69 |
| 3 | 13.68 | 27.63 | 27.63 |
| Delta | 21.96 | 6.94 | 6.94 |
| Rank | 1 | 2 | 3 |

TABLE 5: Response means–wear rate.

| Level | Load (N) | Speed (m/s) | Distance (m) |
|-------|----------|-------------|--------------|
| 1 | 0.006918 | 0.007063 | 0.007783 |
| 2 | 0.009143 | 0.007167 | 0.008070 |
| 3 | 0.005987 | 0.007817 | 0.006203 |
| Delta | 0.002187 | 0.001650 | 0.001870 |
| Rank | 1 | 2 | 3 |

velocity, and sliding distance, all of which differed between levels (Table 2).

2.5. *Field Emission Scanning Electron Microscopy (FESEM).* In the microanalysis and failure analysis of solid inorganic materials, field emission scanning electron microscopy (FESEM) is widely used. High exaggerations, high-resolution imagery, and precise measurements of very small facial features and objects are all possible with scanning electron microscopy. FESEM presents absolute elevated declaration descriptions of the sample by focusing an electron beam transversely across the surface.

3. Results and Discussion

3.1. *Tribological Behavior.* The composite's tribological behavior was assessed, including wear rates and coefficients of friction. The results and their S/N ratios are shown in Table 3. The investigation's findings were assessed using ANOVA, which is used to investigate the stimulus of the considered wear strictures, namely, applied load, sliding

TABLE 6: ANOVA result.

| Sources | Degree of freedom (DF) | Squares sum (seq SS) | Mean square (adj MS) | F value | P value | Contribute level (%) | Error (%) |
|--------------|------------------------|----------------------|----------------------|---------|---------|----------------------|-----------|
| Load (N) | 2 | 12.191 | 6.575 | 0.88 | 0.641 | 35.46 | 2.8 |
| Speed (m/s) | 2 | 7.391 | 4.196 | 0.56 | 0.577 | 29.63 | 1.5 |
| Distance (m) | 2 | 8.356 | 4.628 | 0.63 | 0.743 | 25.85 | 1.7 |

speed, and sliding distance, all of which have a significant impact on routine measures. Using analysis of variance, it is possible to determine unambiguously which independent variable rules over the others, as well as the percentage contribution of those independent variables.

For the aluminium alloy LM25, 4% Gr, and 3% Fe₃O₄, the ANOVA results for wear rate and COF for three factors varied at three levels and interfaces for three levels and interfaces. The lower value of wear rates is 0.00355 at a velocity of 6 m/s and a load of 20 N. The higher value of wear rates is 0.01367 at a velocity of 2 m/s and a load of 60 N.

Table 3 shows that as the composites' velocity augmented, the wear rates of the composites decreased. The significance level for this analysis is =0.05, which corresponds to a 95 percent confidence level. Sources contributing to the performance measures with a *P*-value of less than 0.05 were considered statistically significant contributors.

3.2. Analysis of Signal-to-Noise Ratio. Taguchi's technique uses an S/N ratio to specify the position of structure based on their stimulus. Tables 4–6 show S/N ratios of wear rates. For this study, "smaller-is-better" characteristics were used. The delta value of conforming structure is determined by the variation among the peak values. The plunging mandate of the delta value retained its assigned position. In terms of wear rate, load remained the primary constraint, with distance and velocity as its stimuli. The conforming ranking of structure is specified in the last row of Tables 4–6. Finest wear behavior was observed at third levels of load (1st rank) and speed (2nd rank) and 2nd level in sliding distance (3rd rank).

The influence of each parameter on ANOVA results has been calculated, and the load is a major contributing factor that influenced wear performance by 35.46 percent; the next significant parameter is speed percentage, which influenced wear performance by 29.63 percent; and sliding speed, which influenced wear rate by 25.85 percent (Table 6).

The stimulus on the coefficient of friction was ranked first by distance, followed by load and sliding velocity (Tables 7–9). It is possible that the distance rank is due to the presence of tough reinforcements. As the distance between the sliding surfaces grows, the reinforcement particles that protrude from the surface become fissured, aggregating the contact area between the sliding surfaces and reducing friction. The best CoF was found at the third levels of load (1st rank), speed (2nd rank), and sliding distance (2nd level) (3rd rank).

The load is a major contributing factor that influenced wear performance by about 5.86 percent; the next significant parameter is speed percentage, which influenced wear performance by about 4.975 percent; and sliding speed is the

TABLE 7: Response table for S/N ratios–coefficient of friction.

| Level | Load (N) | Speed (m/s) | Distance (m) |
|-------|----------|-------------|--------------|
| 1 | 5.782 | 5.185 | 5.185 |
| 2 | 4.833 | 5.418 | 5.418 |
| 3 | 5.483 | 5.495 | 5.495 |
| Delta | 0.950 | 0.311 | 0.311 |
| Rank | 1 | 2 | 3 |

TABLE 8: Response means–CoF.

| Level | Load (N) | Speed (m/s) | Distance (m) |
|-------|----------|-------------|--------------|
| 1 | 0.005842 | 0.008496 | 0.006584 |
| 2 | 0.008456 | 0.006892 | 0.007965 |
| 3 | 0.006852 | 0.009512 | 0.005431 |
| Delta | 0.003258 | 0.002478 | 0.002974 |
| Rank | 1 | 2 | 3 |

last influencing factor that influenced CoF by about 3.569 percent (Table 9).

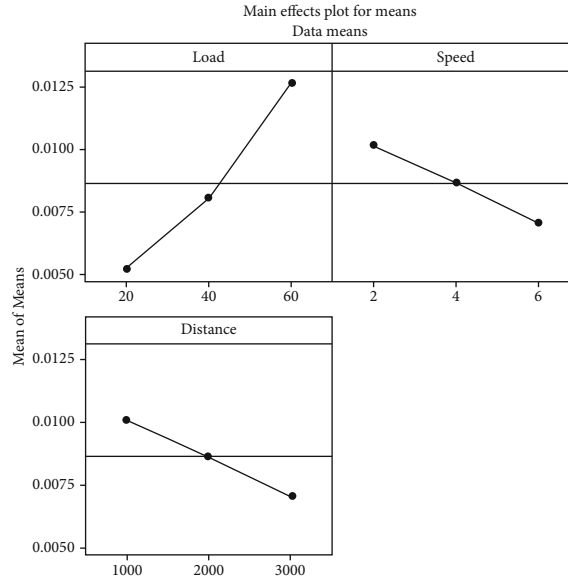
3.3. Influence of Wear Rate Parameters on the Responses. The effects of process variables on wear rates and friction coefficient were studied. As a mean plot, Figure 2(a) depicts the trend of the corresponding responses. Figure 2(b) shows the optimal level of parameters using S/N ratios. The following sections go over the effects of parameters on responses in detail.

3.3.1. Effect of Load. Wear rates increase as the applied load increases, as shown in Figures 3(a) and 3(b). The fringe surge of wear rate remained pragmatic from 20 N to 40 N, whereas the severe surge from 40 N to 60 N was severe. The material's elastic distortion is to blame for this drift. Temperature increases to the sliding surface had fewer effects on the elastic distortion at low loads (20 N and 40 N). Adding a load (60 N) to the specimen causes a temperature spike over the sliding surface, even at slow sliding velocities. The high temperature caused plastic deformation of the surface, resulting in the adhesion of pin surfaces to the disc. As a result of this adhesion, more material is removed, dramatically increasing wear rates [31].

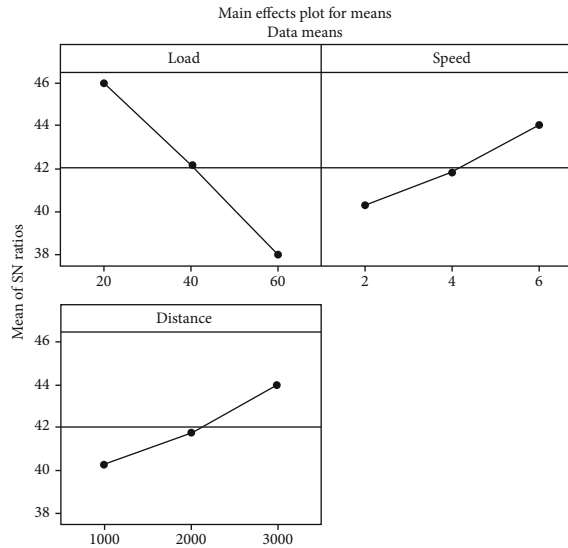
3.3.2. Effect of Distance. Wear rates were found to be decreasing as distance increased. The converse kin is construed by this diminishing to drift, as shown in Figures 2(a) and 2(b). When comparing the wear rate between 1,000 m and 2,000 m to the wear rate between

TABLE 9: ANOVA result.

| Sources | Degree of freedom (DF) | Squares sum (seq SS) | Mean square (adj MS) | F value | P value | Contribute level (%) | Error (%) |
|--------------|------------------------|----------------------|----------------------|---------|---------|----------------------|-----------|
| Load (N) | 2 | 10.782 | 5.658 | 0.75 | 0.598 | 5.86 | 2.5 |
| Speed (m/s) | 2 | 6.235 | 3.259 | 0.61 | 0.657 | 4.975 | 1.6 |
| Distance (m) | 2 | 9.456 | 4.980 | 0.54 | 0.862 | 3.569 | 1.4 |



(a)



Signal-to-noise: Smaller is better

(b)

FIGURE 3: (a) Main effect plot for means–wear rate. (b) Main effect plot for S/N ratios–wear rate.

2,000 m and 3,000 m, the wear rate between 1,000 m and 2,000 m decreased significantly. The behavior be capable of stabilized through the incidence of stiff reinforcements that appear as piercing brusqueness on the composite specimen’s surface. Reinforcement particles that protrude from the composite surface reduce the area among the

specimen and the disc at first, which augments the wear rate and CoF.

The distance among the sliding surfaces increases; these asperities become compacted and blunt, escalating the area among the sliding surfaces [32]. This possibly explains the improved wear behavior at long distances.

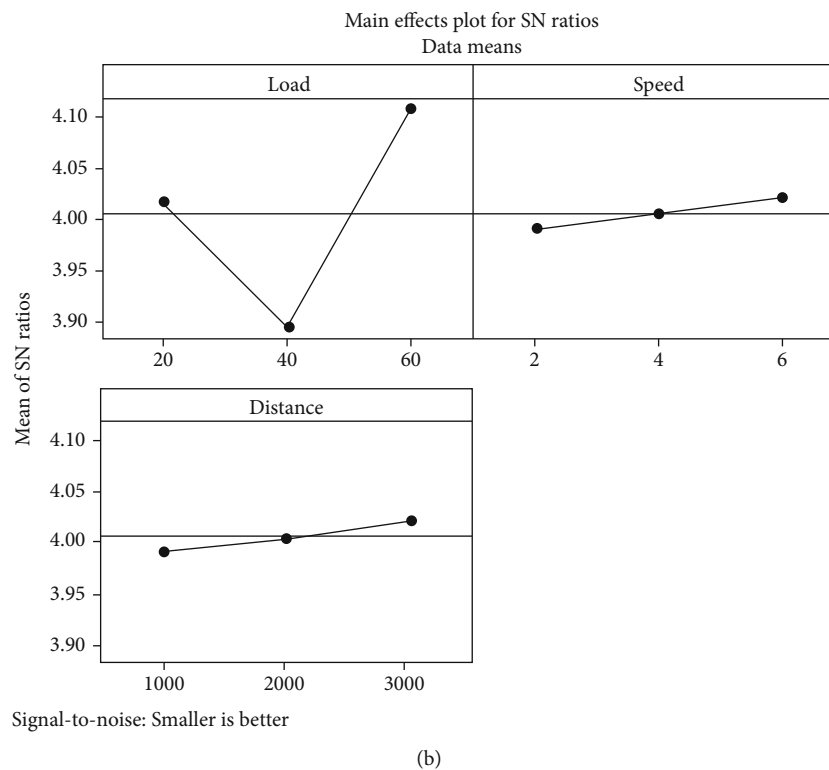
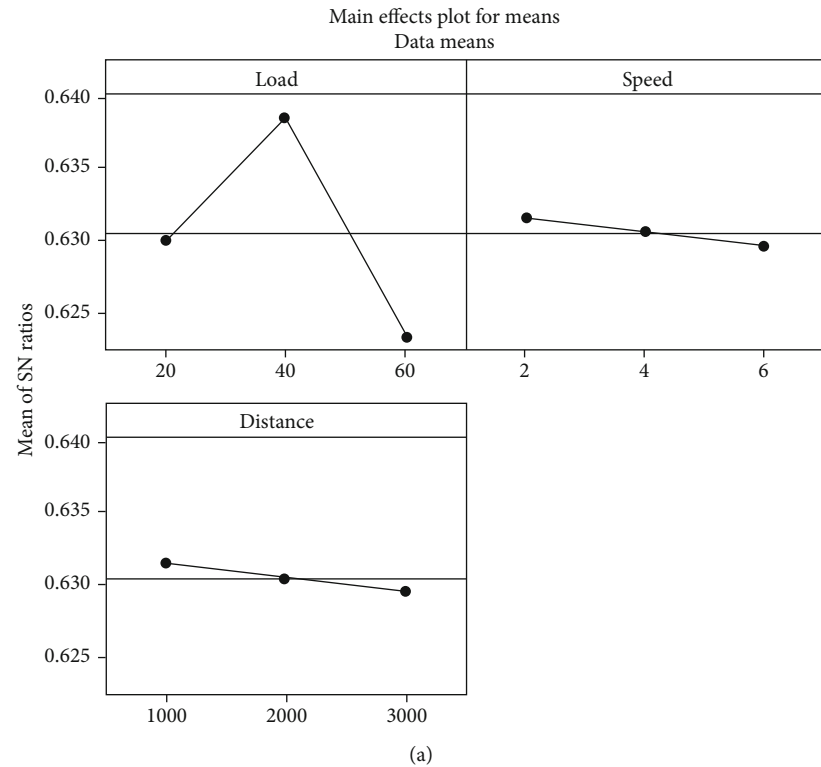


FIGURE 4: (a) Main effect plot for means–coefficient of friction. (b) Main effect plot for S/N ratios–coefficient of friction.

3.3.3. *Effect of Velocity.* With increasing velocity, the rejoiners were pragmatic to be diminishing (Figures 2(a) and 2(b)). The formation of a tribo-layer can help with this. The aluminium has the ability to form an oxide layer on its external fringe. The temperature of the contact surface

rises when sliding at high speeds, causing the material to corrode. This miracle refers to the transport of materials in the form of a mechanically mixed layer, also known as a tribo-layer. This film determination acted as a barricade or lubricant among the surfaces during velocity upsurges,

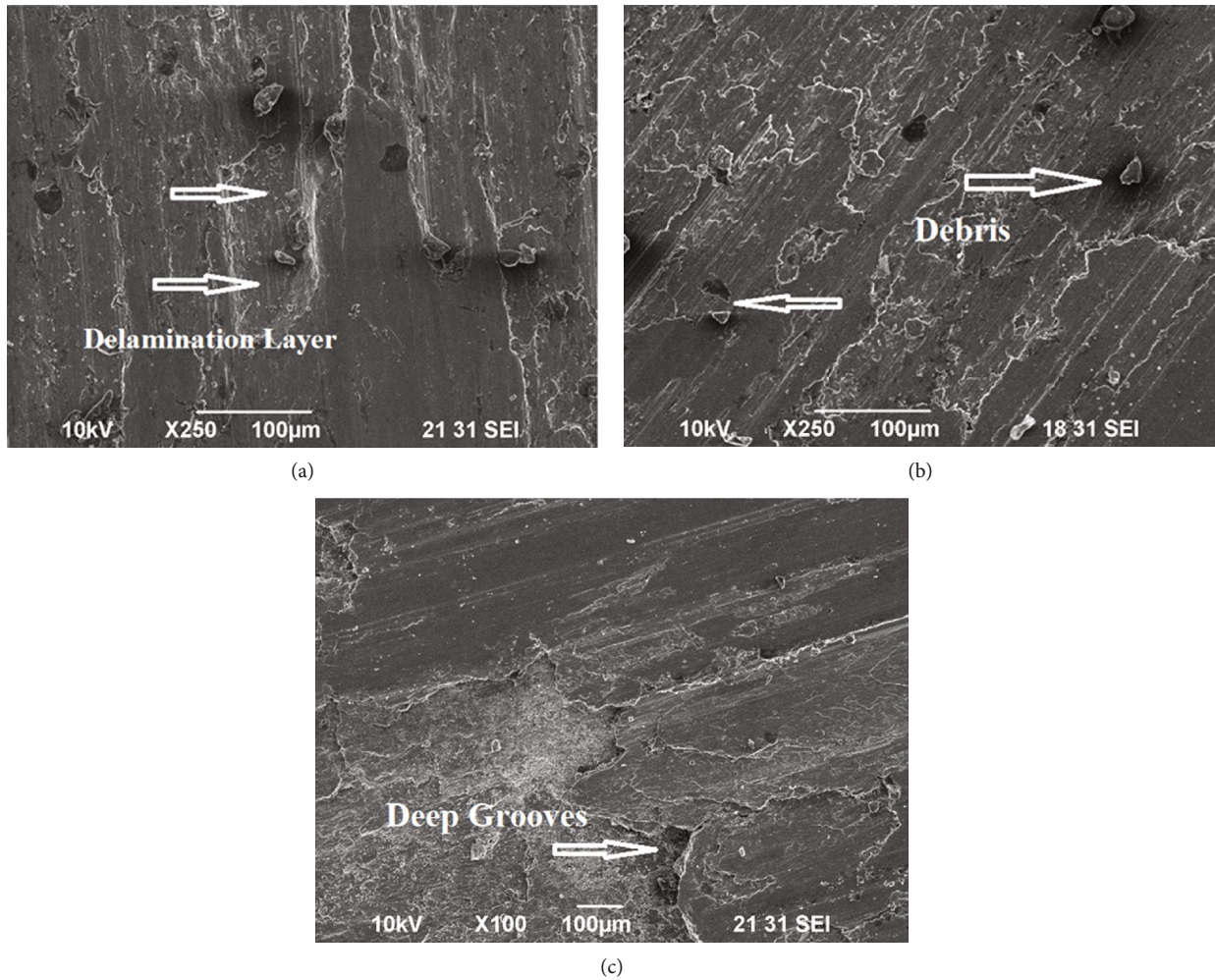


FIGURE 5: (a–c) Typical SEM micrographs of composites.

reducing wear rates [33]. The stumpy load (20 N), superior sliding velocity (6 m/s), and greatest distance were the best parameters for improving the composite's tribological behavior (3,000 m).

3.4. Influence of Coefficient of Friction Parameters on the Responses. The consequence of progression strictures on the CoF was still being assessed. Figure 4(a) depicts the drift of the agreeing reply angrily, while Figure 4(b) depicts the finer echelon of strictures utilizing S/N ratios. The effects of strictures on reply angrily were conversed in depth in the progressive segments.

3.4.1. Effect of Load. The coefficient of friction increases as the applied load increases, as shown in Figures 3(a) and 3(b). The fragmentation of the oxide layer can cause an increase in coefficient of friction. At stumpy loads, the particles that were hauling lacking throughout downhill react among the impression and structure of the film. The temperature over the contact surface had a big impact on this boron oxide film. The friction among the sliding surfaces is increased as a result [34].

3.4.2. Effect of Distance. As the distance between the two points grows, the CoF appears to be diminishing. The converse kin is construed by reducing to drift, as shown in Figures 4(a) and 4(b). When comparing the CoF between 1,000 m and 2,000 m to the COF between 2,000 m and 3,000 m, the CoF between 1,000 m and 2,000 m decreased significantly. The occurrence of stiff reinforcements that proceed as piercing brusqueness on the surface of the composite specimen can brace the behavior.

3.4.3. Effect of Velocity. As the velocity augments, these film acts as an obstruction or lubricant among the surfaces, diminishing the CoF (Figures 4(a) and 4(b)).

3.5. FESEM Analysis. The use of a FESEM to examine wear surfaces fashioned into dry sliding wear in a stable environment is an important tool for determining composite wear and tear behavior. Figure 5 shows composites with morphological decorations such as cavernous permanent undulations, micro pits, debris, and broken particles on their wear surfaces. The dilapidated façade of the Al-Fe₃O₄-Gr composite (Figure 5(a)) shows the presence of delaminated layers. The sliding surface depicted in this diagram has been

clearly stimulated by the stratum. The surfaces appear smooth as well, thanks to the graphite reinforcement. On the surface of the Al-Fe₃O₄-Gr composite, deep grooves can be seen (Figure 5(b)), which may have contributed to the increased wear loss.

The surface of the Al-Fe₃O₄-Gr composite (Figure 5(c)) clearly reveals fragments and kaput particles. Imprecise dances and fine scuff had formed on the worn surface. The wear mechanisms are defined by the structure of undulations, which are shaped by the humanizing exploit of stiff abruptness on the counteract disc and toughened dilapidated fragments. If the amount of boron carbide was increased, wear would be reduced. At high speeds, the temperature rises faster than the sliding surface, causing the material to oxidize and the material to transfer between the pin and counter face, resulting in the formation of MML. This layer contributes to good tribological properties at high speeds [35–37].

4. Conclusions

The following explanation was faded commencing this present investigative work:

- (i) The stir casting route was used to successfully fabricate an LM25 aluminium alloy hybrid metal matrix composite reinforced with 3 wt% Fe₃O₄ and 4 wt% Gr particles
- (ii) The wear rate and CoF have an unswerving relationship among the load, but are inversely related to the sliding speed and distance, according to tribological findings
- (iii) The wear and tear rate was determined primarily by load, pursued by distance and sliding velocity, whereas the CoF is influenced disproportionately by distance, pursued by load and sliding velocity
- (iv) Stumpy load (20 N), superior sliding velocity (6 m/s), and most distance were the best circumstances for attaining superior tribological characteristics (3,000 m).
- (v) At high velocities, SEM analysis exposed the wear mechanism. This research into tribological behavior can be put to good use in determining the supreme materials for use in the automotive industry, wherever sliding contact is predictable
- (vi) For a longer component life, conformist automotive elements such as pistons, piston liners, brake rotors, and cylinder heads can be replaced among these AMCs

Data Availability

The data used to support the findings of this study are included in the article. Should further data or information be required, these are available from the corresponding author and upon request.

Conflicts of Interest

The authors declare that they have no conflicts of interest.



References

- [1] N. Bouhfid, M. Raji, R. Boujmal et al., *Numerical modeling of hybrid composite materials*, Series in Composites Science and Engineering, Woodhead Publishing, 2019.
- [2] R. Pandiyarajan, P. Maran, S. Marimuthu, and K. C. Ganesh, “Mechanical and tribological behavior of the metal matrix composite AA6061/ZrO₂/C,” *Journal of Mechanical Science and Technology*, vol. 31, no. 10, pp. 4711–4717, 2017.
- [3] A. Mazahery and M. O. Shabani, “Influence of the hard coated B₄C particulates on wear resistance of Al-Cu alloys,” *Composites: Part B*, vol. 43, no. 3, pp. 1302–1308, 2012.
- [4] E. Bayraktar and D. Katundi, “Development of a new aluminium matrix composite reinforced with iron oxide (Fe₃O₄),” *Journal Of Achievements In Materials And Manufacturing Engineering*, vol. 38, no. 1, pp. 7–14, 2010.
- [5] D. Katundi, F. Ayari, E. Bayraktar, M.-J. Tan, and A. Tosun Bayraktar, “Design of aluminum matrix composites reinforced with nano iron oxide (Fe₃O₄),” in *In: AMPT, 15th international conference on “Advanced materials processing technologies”* no. 2012, pp. 1–12, Australia, 2012.
- [6] E. Bayraktar, M.-H. Robert, I. Miskioglu, and A. Tosun Bayraktar, “Mechanical and tribological performance of aluminium matrix composite reinforced with nano iron oxide (Fe₃O₄),” in *Composite, Hybrid, and Multifunctional Materials*, Conference Proceedings of the Society for Experimental Mechanics, G. Tandon, Ed., pp. 185–192, Springer, Cham, 2014.
- [7] A. M. Hassan, G. M. Tashtoush, and A. K. J. Ahmed, “Effect of graphite and/or silicon carbide particles addition on the hardness and surface roughness of Al-4 wt% Mg alloy,” *Journal of Composite Materials*, vol. 41, no. 4, pp. 453–465, 2007.
- [8] F. Akhlaghi and Z. A. Bidaki, “Influence of graphite content on the dry sliding and oil impregnated sliding wear behavior of Al 2024-graphite composites produced by in situ powder metallurgy method,” *Wear*, vol. 266, no. 1-2, pp. 37–45, 2009.
- [9] A. Baradeswaran and A. E. Perumal, “Wear and mechanical characteristics of Al 7075/graphite composites,” *Composites: Part B*, vol. 56, pp. 472–476, 2014.
- [10] S. N. Prashant, N. Madeva, and V. Auradi, “Preparation and Evaluation of Mechanical and Wear Properties of 6061Al Reinforced with Graphite Particulate Metal Matrix Composite,” *Int. J. Metall. Mater. Sci. Eng.*, vol. 2, no. 3, pp. 85–95, 2012.
- [11] Y. B. Liu, J. D. Hu, Z. Y. Cao, and P. K. Rohatgi, “Wear resistance of laser processed Al-Si-graphite composites,” *Wear*, vol. 206, no. 1-2, pp. 83–86, 1997.
- [12] C. B. Lin, R. J. Chang, and W. P. Weng, “A study on process and tribological behavior of Al alloy/Gr. (p) composite,” *Wear*, vol. 217, no. 2, pp. 167–174, 1998.
- [13] L. Krishnamurthy, B. K. Sridhara, and B. D. Abdul, “Comparative study on the machinability aspects of aluminium silicon carbide and aluminium graphite composites,” *Materials and Manufacturing Processes*, vol. 22, no. 7-8, pp. 903–908, 2007.
- [14] V. Suresh, A. D. Praneet, and J. Anoop, “Ingenious analysis on machining parameters of aluminium alloy (LM25)/graphite (Gr)/boron carbide (B₄C) hybrid composites using wire electrical discharge machining (WEDM),” *Materials Today Proceedings*, vol. 37, no. 2, pp. 3112–3117, 2021.

- [15] J. Kumar and S. Mondal, "Microstructure and properties of graphite-reinforced copper matrix composites," *Journal of the Brazilian Society of Mechanical Sciences and Engineering*, vol. 40, no. 4, p. 196, 2018.
- [16] S. Vellingiri, "An experimental and investigation on the microstructure hardness and tensile properties of Al-GrFe₃O₄ hybrid metal matrix composites," *FME Transactions*, vol. 47, no. 3, pp. 511–517, 2019.
- [17] V. Suresh, P. Vikram, R. Palanivel, and R. F. Laubscher, "Mechanical and wear behavior of LM25 Aluminium matrix hybrid composite reinforced with Boron carbide, Graphite and Iron oxide," *Materials Today: Proceedings*, vol. 5, pp. 27852–27860, 2018.
- [18] N. Radhika, T. V. Balaji, and S. Palaniappan, "Studies on mechanical properties and tribological behaviour of LM25/SiC/Al₂O₃ composites," *Journal of Engineering Science and Technology*, vol. 10, no. 2, pp. 134–144, 2019.
- [19] S. Matti, B. P. Shivakumar, S. Shashidhar, and M. Nagaral, "Dry sliding wear behavior of Mica, Fly Ash and Red Mud particles reinforced Al7075 alloy hybrid metal matrix composites," *Journal of Science and Technology*, vol. 14, no. 4, pp. 310–318, 2021.
- [20] N. Lenin, M. Sivakumar, G. Selvakumar et al., "Optimization of process control parameters for WEDM of Al-LM25/Fly Ash/B₄C hybrid composites using evolutionary algorithms: a comparative study," *Metals*, vol. 11, no. 7, p. 1105, 2021.
- [21] N. Radhika and R. Raghu, "Prediction of mechanical properties and modeling on sliding wear behaviour of LM25/TiC composite using response surface methodology," *Particulate Science and Technology*, vol. 36, no. 1, pp. 104–111, 2018.
- [22] K. Gowthamkumar, G. Sathiyaseelan, and C. Bhagyanathan, "Effect of strontium (Sr) and iron (Fe) on solidification process of recycled aluminum LM-25 alloy," *International Research Journal of Engineering and Technology*, vol. 6, no. 6, pp. 2792–2795, 2019.
- [23] P. Shanmughasundaram, D. P. Venkatesh, N. Ashok, and N. T. Demeke, "Influence of temperature on tribological behaviour of dual reinforced aluminium MMCs," *Journal Of Mines, Metals & Fuels*, vol. 68, no. 6, pp. 189–195, 2020.
- [24] A. Hiremath, A. Amar Murthy, S. V. Pranavathmaja, A. Jajodia, and R. Sreenath, "Effect of end chills, reinforcement content and carburization on the hardness of LM25-borosilicate glass particulate composite," *Journal of Mechanical Engineering and Sciences*, vol. 12, no. 4, pp. 4203–4215, 2018.
- [25] G. Elango, B. K. Raghunath, K. Palanikumar, and K. Tamizhmaran, "Sliding wear of LM25 aluminium alloy with 7.5% SiC+2.5% TiO₂ and 2.5% SiC+7.5% TiO₂ hybrid composites," *Journal of Composite Materials*, vol. 48, no. 18, pp. 2227–2236, 2014.
- [26] W. Marijke and Y. Rosseel, "On the definition of signal-to-noise ratio and contrast-to-noise ratio for fMRI data," *PLoS One*, vol. 8, no. 11, article e77089, 2013.
- [27] R. Usamentiaga, C. Ibarra-Castanedo, and X. Maldague, "More than fifty shades of grey: quantitative characterization of defects and interpretation using SNR and CNR," *Journal of Nondestructive Evaluation*, vol. 37, no. 2, p. 25, 2018.
- [28] P. Ravindran, K. Manisekar, P. Narayanasamy, N. Selvakumar, and R. Narayanasamy, "Application of factorial techniques to study the wear of Al hybrid composites with graphite addition," *Materials and Design*, vol. 39, pp. 42–54, 2012.
- [29] M. Nagaral, R. Pavan, P. S. Shilpa, and V. Auradi, "Tensile behavior of B₄C particulate reinforced Al2024 alloy metal matrix composites," *FME Transactions*, vol. 45, pp. 93–96, 2017.
- [30] P. Vijian and V. P. Arunachalam, "Optimization of squeeze cast parameters of LM6 aluminium alloy for surface roughness using Taguchi method," *Journal of Materials Processing Technology*, vol. 180, no. 1–3, pp. 161–166, 2006.
- [31] R. N. Rao and S. Das, "Wear coefficient and reliability of sliding wear test procedure for high strength aluminium alloy and composite," *Materials and Design*, vol. 31, no. 7, pp. 3227–3233, 2010.
- [32] L. Zhang, X. B. He, X. H. Qu, B. H. Duan, X. Lu, and M. L. Qin, "Dry sliding wear properties of high volume fraction SiCp/Cu composites produced by pressure less infiltration," *Wear*, vol. 265, no. 11–12, pp. 1848–1856, 2008.
- [33] F. Gul and A. Mehmet, "Effect of the reinforcement volume fraction on the dry sliding wear behaviour of Al-10Si/SiCp composites produced by vacuum infiltration technique," *Composite Science and Technology*, vol. 64, no. 13–14, pp. 1959–1966, 2004.
- [34] M. Uthayakumar, S. Aravindan, and K. Rajkumar, "Wear performance of Al-SiC-B₄C hybrid composites under dry sliding conditions," *Materials and Design*, vol. 47, p. 456, 2013.
- [35] S. Basavarajappa, G. Chandramohan, A. Mahadevan, M. Thangavelu, R. Subramanian, and P. Gopalakrishnan, "Influence of sliding speed on the dry sliding wear behaviour and the subsurface deformation on hybrid metal matrix composite," *Wear*, vol. 262, no. 7–8, pp. 1007–1012, 2007.
- [36] V. Suresh, N. Hariharan, S. Paramesh, M. Prasath Kumar, and P. Arun Prasath, "Tribological behaviour of aluminium/boron carbide (B₄C)/graphite (Gr) hybrid metal matrix composite under dry sliding motion by using ANOVA," *International Journal of Materials and Product Technology*, vol. 53, no. 3/4, pp. 204–217, 2016.
- [37] V. Suresh, N. Hariharan, and S. Vellingiri, "An investigation on the tensile properties and micro-structure of hybrid metal matrix composites," *International Journal of Materials and Product Technology*, vol. 56, no. 1/2, pp. 84–94, 2018.

Research Article

Optimization of Tensile and Impact Strength for Injection Moulded Nylon 66/SiC/B₄C Composites

G. Boopathy,¹ V. Vanitha,² K. Karthiga,³ Bhiksha Gugulothu ,⁴ A. Pradeep,⁵ Hari Prasadarao Pydi,⁴ and S. Vijayakumar ⁶

¹Department of Aeronautical Engineering, Vel Tech Rangarajan Dr. Sagunthala R&D Institute of Science and Technology, Chennai 600062, India

²Department of Mathematics, Tamil Nadu Government Polytechnic College, Madurai, Tamil Nadu, India

³Department of Mathematics, M. Kumarasamy College of Engineering, Karur, Tamil Nadu, India

⁴Department of Mechanical Engineering, Bule Hora University, Post Box No. 144, Ethiopia

⁵Department of Mechanical Engineering, Saveetha School of Engineering, SIMATS, Chennai, India

⁶Department of Mechanical Engineering, BVC Engineering College (Autonomous), Odalarevu, 533210 Andhra Pradesh, India

Correspondence should be addressed to Bhiksha Gugulothu; bhikshamg@gmail.com

Received 7 April 2022; Revised 19 June 2022; Accepted 30 June 2022; Published 18 July 2022

Academic Editor: Domenico Acierno

Copyright © 2022 G. Boopathy et al. This is an open access article distributed under the Creative Commons Attribution License, which permits unrestricted use, distribution, and reproduction in any medium, provided the original work is properly cited.

The mechanical properties of different polymer matrix composites are discussed in this research study. These composites are multiphase materials in which reinforcing elements and a polymer matrix are suitably combined. The mechanical properties of 18 PMCs, including nylon 66 reinforced with 5, 15, and 25% wt% silicon carbide (SiC) and nylon 66 reinforced with 5, 15, and 25% wt% boron carbide (B₄C), were evaluated using an injection moulding technique at three different injection pressures in this study. The optimization of process parameters like reinforcement material, reinforcement quantity, and injection pressure to maximize the tensile and impact strength of nylon 66 composites are the main focus of this study. It is observed that the specimens 25% SiC with an injection pressure of 90 MPa has optimised tensile strength, while the specimen 5% B₄C with an injection pressure of 90 MPa has optimised impact strength.

1. Introduction

Factors including wear, vibrations, and noise influence the strength and reliability of the materials used to make the gears. The gears can be made out of metal or nonmetallic materials. Gears are made up of both metallic and nonmetallic materials. The most common metal gears are cast iron, carbon steel, stainless steel, cast steel, and alloy steels. For lighter load applications, aluminium alloys, brass alloys, bronze alloys, magnesium alloys, nickel alloys, and other nonmetallic materials are employed. Nonmetallic materials including wood, jute, compressed paper, and synthetic polymers like nylon are used in gears to reduce noise, wear, and other concerns. Because of their light weight and desirable qualities required in particular applications, composite materials have recently found applications in gears. Nylons,

Teflon, and other composite materials are widely utilised in office equipment, textile machines, and other light-weight devices. Due to their superior mechanical qualities and light weight as compared to their base metal, many polymer and metal-based composites, such as Al-SiC composite, have lately found utility. Composite gears are a promising material for gear drive in the future, according to continuous research.

The importance of gearing in power transmission cannot be overstated, according to the author. Polymer gears are becoming more commonly used as a result of their advantages. When evaluating any gearbox that is used in a car, temperature is a crucial issue to consider. Nylon 66 gear's superior dampening and self-lubrication properties considerably reduce temperature. Experiments were undertaken to measure the temperature that occurs in the gear box of a moped when nylon 66 helical gear is used instead of metal

gear [1]. For over 50 years, thermoplastic resins have been used in dentistry. Their applications are becoming more popular, as is public interest in nylon-based materials. Thermoplastic resins will almost certainly find new applications in the future to help patients with damaged or missing teeth as new properties emerge. Dentists must meet the increasing demand for prosthetic rehabilitation as the population ages and quality-of-life expectations rise. In this paper, we will go over the properties of nylon-based materials in detail, as well as their numerous dental implications [2]. The effects of theoretical and numerical approaches to stress at the tooth base were compared. They discovered that the outcomes were strikingly similar. In addition, they predicted how the tooth would respond to dynamic loading in terms of stress and displacement [3]. However, there is a significant disadvantage of nanoparticles; increasing the amount of reinforcement increases the amount of porosity, which is an important factor in strength reduction [4].

For strong, exact, and calm power transmission equipments, a more precise examination of stuff attributes is required. The FEM helps analysts in foreseeing twisting and contact pressure and assists them with considering the pressure conveyance without playing out an actual test or testing. With the improvements in FEM innovation, it is currently conceivable to play out various tests by changing the stuff boundaries and materials significantly quicker and at a lower cost. On account of its accuracy in expectation, the FEM is regularly used to confirm test discoveries. Fatigue, crack, wear, and stress crack are the disappointment modes in diminishing request of recurrence [5]. Injection moulding is one of the most widely recognized polymer handling techniques, due to its high creation rate and capacity to make exceptionally perplexing calculations for a minimal price and surprisingly fast. Explore the impact of different infusion shaping boundaries on gear proficiency, including melt temperature, form temperature, pressing strain, pressing time, infusion time, and cooling time [6].

To improve the mechanical properties of nylon, which is widely used in science and engineering, various reinforcements were tried with pure nylon 6 and nylon 66. The ceramic microparticles have slightly increased the strength of these materials, which have reached a certain standard with the elements of the alloy. The most common of these ceramics are silicon carbide and boron carbide [7]. B_4C particles are suitable for use as strength enhancer materials due to their superior properties on a wide scale [8]. As a result, researchers set out to create high-strength composites by combining B_4C with aluminium alloys in order to achieve synergistic and complementary behaviours between nylon and ceramic particles [9].

The impact of manufacturing methods on machine cut and injection moulded polymer gears was studied, as well as the wear rate behaviour of polymer composites, principally acetal, nylon, and polycarbonate. The author discovered that the manufacturing process had no effect on acetal or nylon gears [10]. On a twin-screw extruder, researchers created a composite of nylon 66 with varying quantities of Al_2O_3 nanoparticles. The research revealed that alumina reinforcement improves tensile, flexural, and impact



FIGURE 1: Silicon carbide.



FIGURE 2: Boron carbide.

strength, and various new composite applications were proposed [11]. CNT-reinforced nylon 66 nanofibres electrically spun straight into normal Portland cement were used to create a cementitious material. Hardened cement's mechanical strength and microstructure were also greatly improved [12]. Electrospinning was used to make nylon 66 nanofibres, which were used to interleave mode II analysis of unidirectional glass and carbon fibre composites. The failure modes of nylon 66 spur gears of both unreinforced and fibre reinforced were investigated. Increased wear on the gear tooth surface, gear tooth deformation, and a skin crack at the tooth root part were all observed as major failures [13].

Using moulding simulation software, they discovered that gate styles and positions have a significant impact on the polymer flow front filling pattern inside the mould cavity. The melt temperature and packing time have a greater effect on the quality characteristics of the moulded gear observed using the grey-based Taguchi optimization approach than the other examined parameters [14]. Infusion embellishment was used by researchers to create an example made of normal fibre and glass half breed composites for gear applications. They calculated the elastic, flexural, and impact strength of an example built to ASTM specifications.

TABLE 1: Properties of silicon carbide and boron carbide.

| S. no. | Properties | Values | | |
|--------|---------------------------------|---|-----------------|------------------|
| | | Nylon 66 | Silicon carbide | Boron carbide |
| 1 | Chemical formula | (C ₁₂ H ₂₂ N ₂ O ₂) _n | SiC | B ₄ C |
| 2 | Density (kg/m ³) | 1140 kg/m ³ | 3210 | 2520 |
| 3 | Melting point (K) | 507 K | 3000 | 3036 |
| 4 | Young's modulus (GPa) | 1.6 to 23 | 476 | 450-472 |
| 5 | Flexural strength (MPa) | 80-260 | 324 | 375 |
| 6 | Ultimate tensile strength (MPa) | 60-240 | 310 | 261-569 |
| 7 | Thermal conductivity (W/km) | 0.24 | 41 | |

They discovered that woven fibre glass mixture composites exhibit a significant increase in rigidity. Composites made with banana glass banana (BGB) and glass banana glass (GBG) overlays had more grounded mechanical properties [13].

The value of gearing in power transmission cannot be overstated. Polymer gears are being more commonly used as a result of their advantages. Temperature is a vital parameter in performance testing for any gearbox that is used in a car. Nylon 66 gears excellent damping and self-lubrication properties greatly reduce temperature. Experimentation has been carried out in this regard to assess the temperature that occurs in the gear box of a moped when nylon 66 helical gear is used instead of metal gear [1]. Through the analysis in polymer composite gear with reinforcement of E-Glass GSM in various proportions, detailed analysis concluded that polymer composite gears have less wear rate related with conventional cast iron gears [15]. Composite was made using nylon 66 with various percentages of silica fume particulates through injection moulding machine to examine tensile, compression, flexural, impact, and heat distortion temperature (HDT). The improvements in tensile and HDT properties of nylon 66-silica fume composites were concluded [16]. This study introduces the fractional effort of fostering a polymer composite gear utilizing nylon 66 with silicon carbide and boron carbide as reinforcement materials.

2. Materials and Methods

2.1. Matrix Material—Nylon 66. The word “nylon” refers to a group of synthetic polymers. Polyamides that are aliphatic or semiaromatic are used. It is a thermoplastic substance that can be formed into fibers, films, or fibers. It is a synthetic fiber that comes in a number of grades, including nylon 6, nylon 66, nylon 11, and nylon 12. Nylon 66 is a common term for a group of synthetic polymers referred to as aliphatic polyamides. It is one of the most widely used plastics. The materials used to produce gears, sprocket wheels, chains, and other rotating spares are determined by their strength and service conditions such as wear, tear, and noise, among other factors [9]. In general, improved mechanical properties with weight reduction can be achieved primarily by introducing reinforcement materials in nylon polymer matrix, design optimization, and use of better manufacturing processes.

TABLE 2: Moulding machine parameters.

| Sl. no | Parameter | Value |
|--------|--|--------------|
| 1 | Oven preheating time | 1 hour |
| 2 | Oven preheating temperature | 40 to 60°C |
| 3 | Injection pressure machine maximum | 200 bar |
| 4 | Holding pressure | 70 bar |
| 5 | Clamping pressure | 110 bar |
| 6 | Injection pressure | 80bar |
| 7 | Holding time | 8 sec |
| 8 | Sample cooling time | 75 sec |
| 9 | Mould open time | 5 sec |
| 10 | Setting time | 40 sec |
| 11 | Moulding time | 20 sec |
| 12 | Bottom or nozzle zone temperature | 275 to 295°C |
| 13 | Top zone temperature (thermostat controller) | 80°C |

2.2. Reinforcement Materials—SiC and B₄C. SiC is a chemical compound made up of carbon and silicon. It is created through a high-temperature electrochemical reaction between sand and carbon. SiC is a fantastic abrasive material that has been used to make grinding wheels and other abrasive products for over a century. SiC has progressed to become one of the highest-quality professional ceramics with superior mechanical properties. In a range of high-performance applications, it is used as abrasives, refractory materials, and ceramics. Figure 1 depicts the SiC powder.

Boron carbide (B₄C) is a hard material that ranks third in terms of hardness after diamond and cubic boron nitride (CBN). Carbon is reacted with B₂O₃ in an electric arc furnace; carbo-thermal reduction or gas phase methods are used to produce B₄C powder. B₄C powders are frequently treated and filtered to remove metallic impurities before being utilised commercially. Figure 2 depicts B₄C in granular and powder form. Table 1 lists the properties of nylon 66, SiC, and B₄C.

2.3. Composite Fabrication. Because of its high crystalline nature, nylon has exceptional physical and mechanical qualities, according to the literature. It has a broader range of uses for gears used in office machines, textile machines,

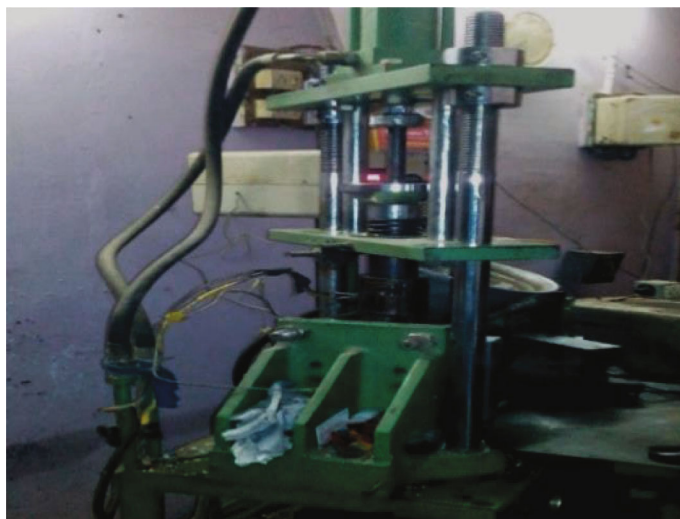


FIGURE 3: Semiautomatic moulding machine.

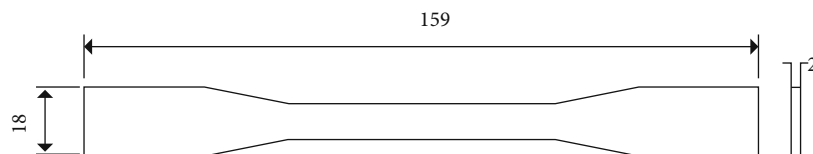


FIGURE 4: Schematic diagram of tensile test specimen.



FIGURE 5: Tensile test specimen.

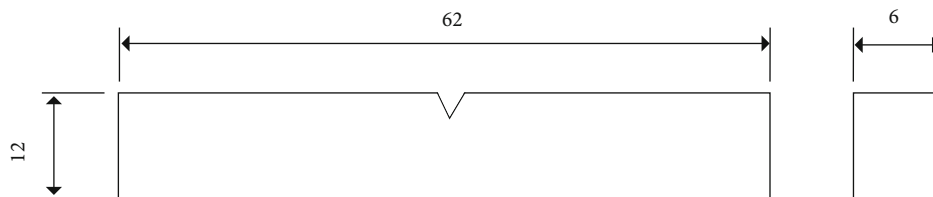


FIGURE 6: Schematic diagram of impact test specimen.



FIGURE 7: Impact test specimen.

TABLE 3: Process parameters and their levels.

| Terms | Factors/parameters | Level 1 | Level 2 | Level 3 |
|-------|--------------------------|---------|---------|---------|
| A | Type of RM | SiC | B4C | — |
| B | wt% of RM content (%) | 5 | 15 | 25 |
| C | Injection pressure (MPa) | 80 | 90 | 100 |

TABLE 4: Experimental results.

| Sl. no. | Type of RM | wt% of RM content (%) | Injection pressure (MPa) | Tensile strength (MPa) | Impact strength (J) | S/N ratio | |
|---------|------------|-----------------------|--------------------------|------------------------|---------------------|------------------|-----------------|
| | | | | | | Tensile strength | Impact strength |
| 1 | SiC | 5 | 80 | 54.66 | 1.96 | 34.75 | 31.73 |
| 2 | SiC | 5 | 90 | 50.66 | 1.97 | 34.09 | 32.59 |
| 3 | SiC | 5 | 100 | 48.45 | 2.00 | 33.71 | 33.40 |
| 4 | SiC | 15 | 80 | 45.33 | 1.88 | 33.13 | 33.56 |
| 5 | SiC | 15 | 90 | 46.33 | 1.82 | 33.32 | 32.79 |
| 6 | SiC | 15 | 100 | 46.33 | 1.85 | 33.32 | 32.80 |
| 7 | SiC | 25 | 80 | 53.85 | 1.87 | 34.62 | 33.17 |
| 8 | SiC | 25 | 90 | 55.85 | 1.96 | 34.94 | 34.58 |
| 9 | SiC | 25 | 100 | 49.85 | 1.96 | 33.95 | 34.58 |
| 10 | B4C | 5 | 80 | 45.65 | 4.0 | 33.19 | 30.53 |
| 11 | B4C | 5 | 90 | 44.65 | 4.0 | 33.00 | 31.03 |
| 12 | B4C | 5 | 100 | 43.65 | 4.1 | 32.80 | 31.55 |
| 13 | B4C | 15 | 80 | 41.33 | 3.2 | 32.33 | 31.28 |
| 14 | B4C | 15 | 90 | 43.33 | 3.33 | 32.74 | 31.73 |
| 15 | B4C | 15 | 100 | 42.33 | 3.0 | 32.53 | 32.80 |
| 16 | B4C | 25 | 80 | 46.85 | 2.2 | 33.41 | 32.78 |
| 17 | B4C | 25 | 90 | 47.85 | 2.1 | 33.60 | 32.82 |
| 18 | B4C | 25 | 100 | 41.85 | 2.0 | 32.43 | 32.58 |

and even large equipment for noise/vibration reduction, among other things. Particles are put to nylon polymers to improve their qualities and minimise the over cost of composite products. In general, reinforced nylon polymers outperform base nylon in terms of characteristics. In this study, nylon was utilised as the basis material for the composites preparation. As foundation ingredients, two grades of nylon are used: nylon 6 and nylon 66. The particles of SiC and B₄C are used as reinforcing materials. SiC and B₄C are thought to have good thermal conductivity, a stable crystal structure, low toxicity, high hardness, and a low price. The addition of reinforcement improves the mechanical properties of these nylon composites, making them excellent for gear applications.

Injection moulding is a widespread method of making products out of thermoplastic and thermosetting polymers. The materials are mixed in a heated barrel before being forced into a mould cavity, where they cool and harden to the shape of the mould cavity. Injection moulding is used to make a wide range of parts, from minor components to whole car body panels. The injection moulding process comprises four stages: clamping, injection, cooling, and ejection. It takes between 2 seconds and 2 minutes to complete.

TABLE 5: Response table for signal to noise ratios of tensile strength.

| Level | Type of RM | % of RM content | Inj. pressure |
|-------|------------|-----------------|---------------|
| 1 | 33.98 | 33.59 | 33.57 |
| 2 | 32.89 | 32.89 | 33.61 |
| 3 | | 33.83 | 33.12 |
| Delta | 1.09 | 0.93 | 0.49 |
| Rank | 1 | 2 | 3 |

After enough time has passed, the cooled component can be evacuated from the mould by the ejection mechanism, which is attached to the back half of the mould. When the mould is opened, a mechanism is employed to force the part out. After the component is removed, the mould can be clamped shut, allowing the next shot to be injected. After the injection moulding cycle, any postprocessing is usually required. Granules, pellets, or powders can be used to compute the initial raw materials required. The following parameters are set in the unit to get good quality components from injection moulding shown in Table 2. The semiautomatic injection moulding machine is shown in Figure 3.

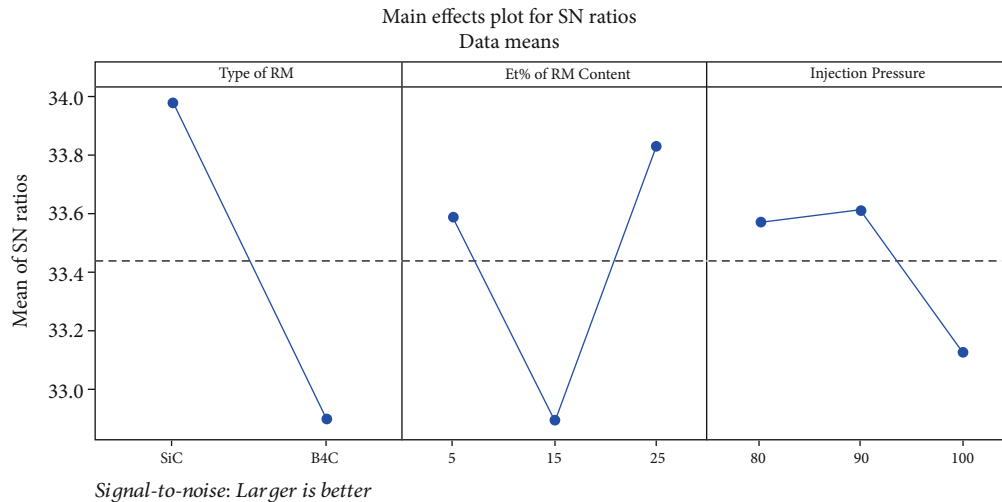


FIGURE 8: Effect of control factors on tensile strength of nylon 66 composites. Optimum levels: type of RM = SiC; wt% of RM content = 25%; Inj. pressure = 90 MPa.

TABLE 6: ANOVA table for tensile strength.

| Source | DF | Adj SS | Adj MS | F value | P value | % of contribution |
|-----------------|----|---------|--------|---------|---------|-------------------|
| Type of RM | 1 | 5.3438 | 5.3438 | 43.47 | 0 | 50.73 |
| % of RM content | 2 | 2.8308 | 1.4154 | 11.51 | 0.002 | 26.87 |
| Inj. pressure | 2 | 0.885 | 0.4425 | 3.6 | 0.06 | 8.40 |
| Error | 12 | 1.4753 | 0.1229 | | | 14.00 |
| Total | 17 | 10.5348 | | | | 100.00 |

2.4. Mechanical Testing

2.4.1. Tensile Strength. Young's modulus, elastic limit, elongation, proportional limit, yield point, yield strength, tensile strength, percentage of reduction in area, and other tensile parameters are all determined via tensile testing. Specimens are frequently subjected to the tensile test [10]. The most common specimen geometries are the dog-bone shape and straight side type with end tabs. All of the specimens in this investigation were injection moulded in the shape of a dog bone with a dimension of $159 \times 18 \times 2$ mm as per ASTM D638. Figures 4 and 5 depict the schematic diagram specimen and injection moulded tensile test specimen, respectively.

2.4.2. Impact Strength. Material properties at greater deformation speeds are assessed through impact testing. The impact testing is used to assess the toughness and notch sensitivity of engineered materials. It is used to assess the toughness of metals, but polymers, ceramics, and composites are also subjected to similar testing. The impact of a heavy pendulum or hammer, descending at a predetermined velocity through a fixed distance, breaks the notched test specimen [11]. The energy absorbed by the fragmented specimen is measured in this test. Figure 6 shows a schematic representation of an Izod impact test specimen. Figure 7 depicts the notched impact test specimen. A notch

TABLE 7: Response table for signal to noise ratios of impact strength.

| Level | Type of RM | % of RM content | Inj. pressure |
|-------|------------|-----------------|---------------|
| 1 | 5.657 | 9.016 | 7.639 |
| 2 | 9.536 | 7.687 | 7.645 |
| 3 | | 6.087 | 7.505 |
| Delta | 3.879 | 2.929 | 0.14 |
| Rank | 1 | 2 | 3 |

was cut into the specimen before it was placed on the impact testing equipment.

2.5. Optimization—Taguchi Method. The application of the Taguchi methodology is highly desirable because it gives phase and analysis phase. The quality of the gears produced is influenced by injection moulding process parameters, type of the RM, and the content of the RM. As a result, determining the optimal parameters is critical [12]. The reinforcement materials SiC, B4C, wt. percent of reinforce materials content, and injection moulding pressure are considered influencing characteristics for this research effort since they affect the mechanical strength of the composite specimens created. Appropriate parameter level with a small number of experiments. It is a method for performing experiments and analysing the effect of many parameters on the response

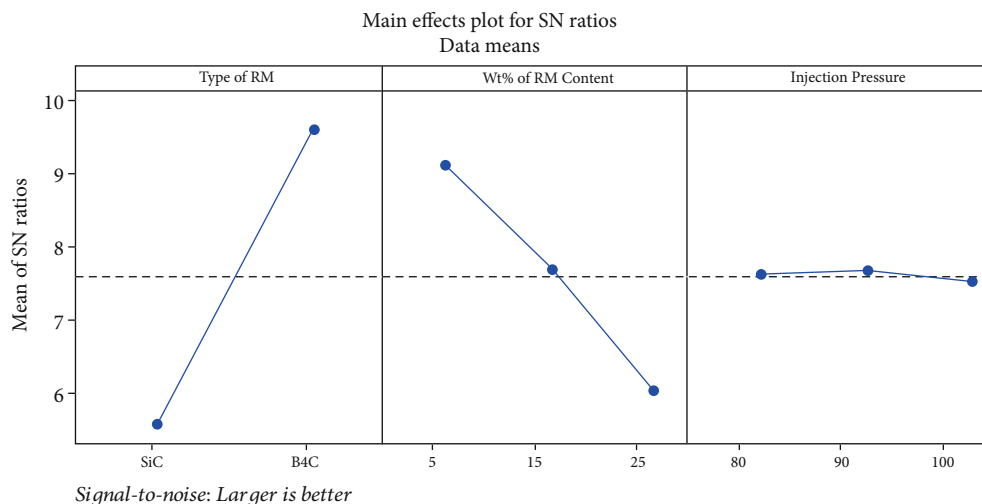


FIGURE 9: Effect of control factors on impact strength nylon 66 composites. Optimum levels: type of RM = B₄C; wt% of RM content = 5%; Inj. pressure = 90 MPa.

that is based on a systematic statistical approach [14]. The Taguchi approach is carried out in three stages in general. Planning, experimentation, and analysis are the three phases [13]. Composite specimens are constructed with two base materials, nylon 66 and nylon 6, as well as two RMs, SiC and B₄C, which are added in weight percents of 5%, 15%, and 25%, respectively. Injection moulding is used to create nylon composite specimens at a specific pressure and temperature.

2.5.1. Planning Phase. The main goal of this research is to develop controllable aspects in order to improve mechanical strength qualities. At three stages, the type of reinforcing materials, the weight percent of support content, and the injection moulding pressure are all monitored [15]. In light of the writing overview, the reaches for the cycle boundaries are set. Because the collaborations are of minor importance, it was decided in this focus on that the primary impacts are the most important [16]. Table 3 lists the variables and their levels for nylon 6 composites. Minitab 17 is used to create the experimental arrangement.

2.5.2. Experimental Phase. In this stage, the analyses are directed according to Taguchi's test plan involving L18 symmetrical cluster for nylon 66 composites [17].

2.5.3. Analysis Phase. The investigation is carried out using Minitab 17 programming at this level. The product calculates the normal value of the S/N ratio of each border at a given level. The S/N ratio is important for achieving a higher boundary level. The product plots the S/N ratio in accordance with the quality brand selected [18].

3. Results and Discussion

Table 4 shows the results of the experiment.

3.1. Tensile Strength of Nylon 66. Response Table 5 can be used to see how different characteristics affect tensile

strength. The response table shows the average response characteristics for each level of the individual element in the experimental design. Based on their delta values, the factors are ranked from most to least influential. Table 5 clearly indicates the importance and rank of the criteria studied, as seen in Figure 8.

Figure 8 shows the principle impact plot for S/N proportions obtained from the product. The figure reveals that the variables, reinforcement material (A), and wt% of reinforcement material content (B) largely affect S/N proportion relating to rigidity of nylon 66 composite.

The analysis of variance (ANOVA) is used to investigate the model association between the response variable tensile strength and the independent factors (A, B, and C). The ANOVA findings for tensile strength are shown in Table 5. The *P* value can be used to verify the relevance of the components. At a 95% confidence level, the elements that are statistically significant are validated. The parameter makes a significant influence to the performance if the *P* value is less than 0.05 [10]. This indicates that the parameter has a stronger influence on the mechanical strength of the nylon 66 composite material. The kind of RM has the largest impact on tensile strength, as shown in Table 6. It is followed by factors B and C. The ANOVA table also shows the percentage influence of each parameter on mechanical strength.

3.2. Impact Strength of Nylon 66. Response Table 7 can be used to determine the effect of various parameters on impact strength. It also demonstrates the relevance of parameters in ranking, as shown in Figure 9.

The ANOVA result for impact strength is shown in Table 8. The importance of the components can be validated using a *P* value at a 95% confidence level.

3.3. Confirmation Experiment. The final stage is to look at the best interaction parameters after acquiring the ideal collaboration parameters through exploratory data analysis. Confirmation tests are performed to check if the Taguchi

TABLE 8: ANOVA table for impact strength.

| Source | DF | Adj SS | Adj MS | F value | P value | % of contribution |
|---------------------|----|---------|---------|---------|---------|-------------------|
| Type of RM | 1 | 67.723 | 67.7227 | 33.01 | 0 | 57.28 |
| % of RM content | 2 | 25.811 | 12.9056 | 6.29 | 0.014 | 21.83 |
| Inj. pressure (MPa) | 2 | 0.076 | 0.0379 | 0.02 | 0.982 | 0.06 |
| Error | 12 | 24.616 | 2.0514 | | | 20.82 |
| Total | 17 | 118.226 | | | | 100.00 |

TABLE 9: Optimum factor levels for maximum properties of nylon 66 composites.

| Properties | Type of RM | Weight % of RM content | Injection pressure (MPa) |
|------------------------|------------------|------------------------|--------------------------|
| Tensile strength (MPa) | SiC | 25 | 90 |
| Impact strength (J) | B ₄ C | 5 | 90 |

upgrading process produces accurate finishes. According to the confirmatory study, the ideal level of boundaries derived will actually deliver closer quality features, with individual values being 15% closer to the certifiable ones. Table 9 demonstrates the improved properties of nylon 66 composites as a result of the response analysis.

4. Conclusion

The foremost goal of this research paper is to investigate the tensile and impact strength of polymer composites as a preliminary study for the development of polymer composite gears. In this study, the emphasis was solely on the optimization portion of analysing the role of RM type, RM content percentage, and injection pressure. In this study, 18 PMCs were made using nylon 66 reinforced with 5, 15, and 25% wt% SiC and B₄C using an injection moulding machine at 80, 90, and 100 MPa injection pressure in each case. The tensile and impact tests were carried out in accordance with ASTM guidelines. The Taguchi technique was used to establish the optimal value of tensile and impact strength with variations in wt% of RM content and injection pressure. It is believed that the load transfer mechanism and dislocations contribute the most positively, while porosity has the most negative effect, based on mechanical testing and morphological analysis. In mechanical strength analysis, the load transfer mechanism was shown to be the most important factor for both reinforcements. In addition, geometrically essential dislocations discovered in boron carbide particles significantly contributed to the increase in strength. As a result, the manufacturing process and volumetric content parameter for spur gear design can be claimed to be congruent with current studies and to be suggestions for future research.

Data Availability

The data used to support the findings of this study are included in the article. Should further data or information be required, these are available from the corresponding author upon request.

Disclosure

This study was performed as a part of the employment of Bule Hora University, Ethiopia.

Conflicts of Interest

The authors declare that there are no conflicts of interest regarding the publication of this paper.

Acknowledgments

The authors appreciate the technical assistance to complete this experimental work from the Department of Mechanical Engineering, Bule Hora University, Ethiopia. The author thanks the Department of Aeronautical Engineering, Vel Tech Rangarajan Dr. Sagunthala R&D Institute of Science and Technology, India, Department of Mathematics, Tamil Nadu Government Polytechnic College and M. Kumaramany College of Engineering, Department of Mechanical Engineering, Saveetha School of Engineering, Chennai, and Department of Mechanical Engineering, BVC Engineering College (Autonomous), Andhra Pradesh, for their support of draft writing.

References

- [1] A. N. Taywade and V. G. Arajpure, "Design and development of nylon 66 plastic helical gears in automobile application," *International Journal of Engineering Research & Technology*, vol. 3, no. 9, 2014.
- [2] K. Shivani and B. Shekhar, "Polyamides in dentistry," *International Journal of Scientific Study*, vol. 1, no. 1, pp. 20–25, 2013.
- [3] A. Shubham and N. Ajmera, "Static and dynamic analysis of spur gear," *International Journal of Mechanical Engineering and Technology*, vol. 7, no. 4, pp. 8–21, 2016.
- [4] H. Porwal, P. Tatarko, S. Grasso, J. Khaliq, I. Dlouhy, and M. J. Reece, "Graphene reinforced alumina nano-composites," *Carbon*, vol. 64, pp. 359–369, 2013.
- [5] A. Z. Ismail Ali, N. D. I. Daing Mohamad, and M. Wafuiddin, "Investigating bending strength of spur gear: a review," *MATEC Web of Conferences*, vol. 90, pp. 01037–01039, 2017.
- [6] S. K. Lal and H. Vasudevan, "Optimization of injection moulding process parameters in the moulding of low-density polyethylene (LDPE)," *International Journal of Engineering Research and Development*, vol. 7, no. 5, pp. 35–39, 2013.
- [7] T. Varol and A. Canakci, "Effect of particle size and ratio of B₄C reinforcement on properties and morphology of nanocrystalline Al₂O₃-B₄C composite powders," *Powder Technology*, vol. 246, pp. 462–472, 2013.

- [8] C. Wu, K. Ma, J. Wu et al., "Influence of particle size and spatial distribution of B₄C reinforcement on the microstructure and mechanical behavior of precipitation strengthened Al alloy matrix composites," *Materials Science and Engineering A*, vol. 675, pp. 421–430, 2016.
- [9] H. Yang, T. D. Topping, K. Wehage, L. Jiang, E. J. Lavernia, and J. M. Schoenung, "Tensile behavior and strengthening mechanisms in a submicron B₄C-reinforced Al trimodal composite," *Materials Science and Engineering A*, vol. 616, pp. 35–43, 2014.
- [10] K. A. Alharbi, "Wear and mechanical contact behavior of polymer gears," *Journal of Tribology*, vol. 141, no. 1, article 011101, 2019.
- [11] L. Guglani and T. C. Gupta, "Wear and mechanical properties of nylon 66–Al₂O₃ microcomposite," *Journal of Reinforced Plastics and Composites*, vol. 36, no. 17, pp. 1254–1262, 2017.
- [12] T. N. M. Nguyen, D. Y. Yoo, and J. J. Kim, "Cementitious material reinforced by carbon nanotube-nylon 66 hybrid nanofibers: mechanical strength and microstructure analysis," *Materials Today Communications*, vol. 23, p. 100845, 2020.
- [13] R. Sakthivel and D. Rajendran, "Experimental investigation and analysis a mechanical properties of hybrid polymer composite plates," *International Journal of Engineering Trends and Technology*, vol. 9, no. 8, pp. 407–414, 2014.
- [14] N. M. Mehat, K. Shahrul, and A. R. Othman, "Modeling and analysis of injection moulding process parameters for plastic gear industry application," *ISRN Industrial Engineering*, vol. 2013, Article ID 869736, 10 pages, 2013.
- [15] S. S. Abdelhady, S. H. Zoalfakar, M. A. Agwa, and A. A. Ali, "Treated basalt fibers reinforced nylon 6, 6/epoxy hybrid nanofibril composites," *Journal of Thermoplastic Composite Materials*, vol. 35, no. 4, pp. 555–569, 2022.
- [16] V. L. Raja and A. Kumaravel, "Studies on physical and mechanical properties of silica fume-filled nylon 66 polymer composites for mechanical components," *Polymers and Polymer Composites*, vol. 23, no. 6, pp. 427–434, 2015.
- [17] G. Boopathy, K. Gurusami, M. Chinnapandian, and K. R. Vijayakumar, "Optimization of process parameters for injection moulding of nylon 6/SiC and nylon 6/B₄C polymer matrix composites," *Fluid Dynamics & Materials Processing*, vol. 18, no. 2, pp. 223–232, 2022.
- [18] K. Karthik, D. Rajamani, A. Manimaran, and J. Udaya Prakash, "Evaluation of tensile properties on glass/carbon/Kevlar fiber reinforced hybrid composites," *Materials Today: Proceedings*, vol. 39, no. 4, pp. 1655–1660, 2021.

Research Article

Influence of Methods of Nanomaterial Testing on Product Supply and an IoT-Based Solution for Making a Perfect Choice

D. K. Nagarathi ^{1,2} **V. Ramya** ¹ **Latha Parthiban**,³ and **Yalew Asres** ⁴

¹Department of Computer Science and Engineering, Annamalai University, Annamalainagar, 608002, India

²Office of Registrar, Tamil Nadu Teachers Education University, Chennai, 600097 Tamil Nadu, India

³Department of Computer Science, Community College, Pondicherry University, Lawspet, 605008 Pondicherry, India

⁴Department of Mechanical Engineering, Faculty of Manufacturing, Institute of Technology, Hawassa University, Ethiopia

Correspondence should be addressed to D. K. Nagarathi; kaavya_naga@yahoo.com, V. Ramya; ramyshri@yahoo.com, and Yalew Asres; yalewa@hu.edu.et

Received 19 April 2022; Accepted 30 May 2022; Published 16 July 2022

Academic Editor: V. Vijayan

Copyright © 2022 D. K. Nagarathi et al. This is an open access article distributed under the Creative Commons Attribution License, which permits unrestricted use, distribution, and reproduction in any medium, provided the original work is properly cited.

Human ear is equivalent to nanomaterials as it has nonporous membrane which decides the hearing ability. The water content and its movements in that tectorial gel membrane are controlled by nanoscale pores. Apart from many disease threats and the age and other issue-related disabling hearing impairment, loss of sensitiveness of nanomaterial, namely, nanopored tectorial gel membrane, is a serious issue. Appropriate supplement must be provided to compensate age-related hearing loss by measuring some innovation methods. The test for hearing loss and cost of hearing aid are another threat. Many studies reported that people do not feel comfortable with their hearing aid and avoided to use it after purchase. The telephonic survey was conducted at Tamil Nadu, India region, which discloses that the hearing aid center is doing continuous motivation over the phone to wear hearing aid after purchase; many people do not turn back for even battery purchase. Very rare people report for free service too. This piece of research is aimed at analysing the root cause of not wearing hearing aid and addressing various possibilities to support them with IoT-based solution requirement to discard this issue. The two kinds of test were conducted for the same patient, and hearing aid was provided to give supplement to compensate sensitiveness loss of tectorial gel membrane. Their effectiveness was measured and analysed scientifically. The Taguchi method was incorporated to formulate the experiments with the natural cases like age, gender, and method of testing the nanomaterial, namely, nanopored tectorial gel membrane sensitiveness (hearing loss/or hearing ability) and existing nature of sensitiveness (severe loss and minor loss) at 2 levels. The observations were analysed with Taguchi analysis and discussed. An integrated solution of IOT-based measuring system was discussed to rid the issues.

1. Introduction

The ability of nanopore tectorial gel membrane (nanomaterial) or loss of hearing is accountable when it exceeds 35 decibels [1]. The World Health Organization (WHO) disclosed some facts that 2.5 billions will be the victims in this case by 2050 and at least 700 million may demand rehabilitation for hearing. Unsafe hearing practice is another issue which will affect 1 billion people (young adults). The statistics further extended that nearly 432 million youth and adults as well as 34 million children require support for their

disabling hearing impairment. The pathogenesis of hearing impairment is poorly understood, and no diagnostic tools to distinguish among subgroups are currently available. Patients are generally left with broad therapy alternatives like cochlear implantation, hearing aids, or steroids [2]. Magdy et al. explored localised delivery methods and effective distribution, at ear anatomy, ear obstacles. Also included are the applications of hydrogels and nanocapsules via localised distribution of medicine to the middle ear, as well as middle and inner ear illnesses [3]. Investigate the time necessary to attain equilibrium of kinetics of the adsorption

process or as the molecular sieving by Nano porous membrane, to investigate time of our of equilibrium processes [4]. Loss of hearing ability is a progressive happening in human life; it will become high at old age [5]. Such loss could be generally notable at 40+ age, and loss growth steep will linearly up with respect to age still 80 [6]. Globally, 30% of 60+ aged people are suffered by age-related hearing loss [7] and estimated that in 2030, age-related hearing loss can be among the top 15 leading burden diseases [8]. Apart from common gathering for any family or social occasion, this issue is severely influencing in quality of life especially answering doctors' queries, responding to sound horn at crowd, busy road work place, etc. [9]. Hence, the age-related hearing loss not only affects successful aging by birth [10] but also other aging of human body like productive and healthy aging [1, 10]. In smart cities, people have facility to check their hearing loss and adopt suitable hearing aid. As reported in earlier studies, 23% of hearing aid holders are not using their hearing aid due to behavioral intention [11, 12].

2. Need for This Research

Nanosensitive human ear test for hearing deficient could not complete with physical alone successfully, and it needs psychological aspect too. A sample survey released by WHO is that in the populated China, 65+ aged people population was 9.5% (123 million) at the year of 2000, at 2015, it was 16.5% (214 million), and based on the growth rate, such population will be 25.6% (332 million) in the year of 2050 [1]. Internet-based healthcare assistance must be improved to compensate healthcare of such aged people to ensure their life's quality [13]. Apart from other care, hearing loss affects their basic life and it is classified as one of the top prevalent age-related chronic diseases [14]. But it can be compensated by adopting appropriate hearing aid [15]. Hearing aid supports them to compensate the deficiency at acceptable level [16]. But after adopting hearing aid, the patient is not using that hearing aid due to his dissatisfaction. This investigation addresses the solution for complete test of ear material for making his appropriate choice of hearing aid to compensate by a hearing aid with complete satisfaction.

3. IoT Technology

IoT technological support extends to connect hearing device to the online healthcare services [17]. The IoT technology helps the hearing aid user to fix appointment with doctors, booking their periodical or special checkup. IoT devices are internet-based, and they are utilized for collecting the required data, monitoring specific thing, and also utilizing for control purpose too [18]. IoT is highly supported for developing the smart grids [19], smart cities [20, 21], smart weathers [22], smart transportation [23], smart healthcare [24], in particular E-Health [25], M-health [26, 27], and S-health [28]. IoT is a technology to help to people share and communicate at real time including audio, video, text, doc, files, and simulation with online signals [29]. Hence, IoT is a promising solution to many human-related disabili-

ty issues. The nanopore human ear gel membrane (nanomaterial) sensitiveness could be measured more accurately with IoT technological-based test setup.

4. Nonuse of Hearing Aid

Most of the hearing-deficient patients adopt hearing aid, and they did not use. The technological advancements improve the clarity of hearings but may not fulfil in test methodology which was used to measure hearing supplement needed. Psychological barriers for nonuse of hearing aid are demonstrated in Figure 1. People behaviors are some of the applicable behaviors which are discussed below.

- (i) Planned behavior is one of the highlighted reasons at this stage that human in the state of lack of control perceived feelings while interacting with new persons [30, 31]. This usually overcome by availing the facility to meet such situation [32] and manage such situation by self-efficacy [33]
- (ii) Lack of acceptance to adopt new hearing aid is another thing by which the people hesitate to it [34]. This can be overcome by perceived usefulness and attitude. The perceived usefulness means the human must have strong belief that new hearing aid will strongly help, useful, and supports at all situation to execute their doings [35]. And attitude is one by which human has intention to try new things to do or update himself periodically or adopt new hearing aid by considering fashion, etc. [35–38]
- (iii) According to first version of unified theory of acceptance, the people seeks facilitating conditions, effort, and performance expectancy as well as social influence [39]
- (iv) According to second version of unified theory, the people adapt and accept new hearing aid based on degree of playfulness, price factor [40], own habit, age, gender and experience [38], and intention [41]. They need people's rating, reviews, comments, advertisements, etc., about the usefulness particular hearing aid [19, 42–44]
- (v) As per the senior technology acceptance model, the elder people decide new thing or hearing aid based on the usefulness and usage of the same [45]
- (vi) Based on the self-determination theory, people adapt hearing aid by intrinsic (just for enjoyment or fun) or extrinsic (realizing its purpose) motivation [46]
- (vii) The theory of reasoned action said that the people adopt the hearing aid based on the subjective norms and attitude. The people adopt hearing aid with trust on results of audiology [47]

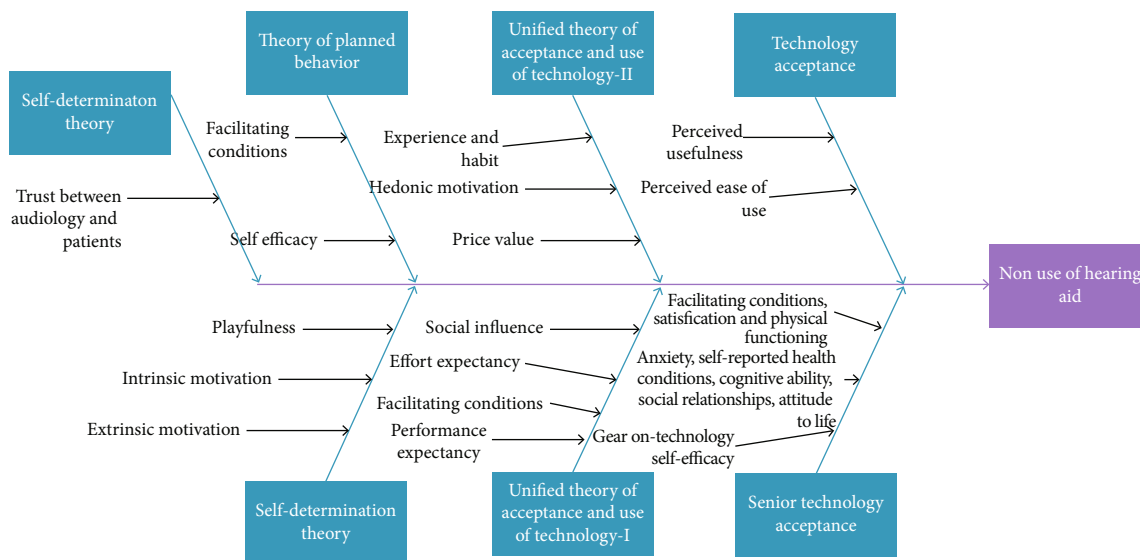


FIGURE 1: Behavioral theories behind the nonuse of hearing aid.

TABLE 1: General linear model: factors and their levels.

| Factors | Type of factor | Varying level | Level 1 | Level 2 |
|---------------------------------|----------------|---------------|------------------|--|
| Male patient (age in years) | Fixed | 2 | 42 | 64 |
| Test method (choice of testing) | Fixed | 2 | App (mobile app) | Audiometry (conventional testing method) |
| Female patient (age in years) | Fixed | 2 | 48 | 73 |
| Hearing loss (classification) | Fixed | 2 | Minor | Major |

Method of factor coding (-1, 0, +1).

TABLE 2: Taguchi experimental design summary.

| | |
|---------------|----------------------|
| Taguchi array | L8 (2 ⁴) |
| Factors | 4 |
| Runs | 8 |

5. The Experimental Setup

The experimental design is followed by Taguchi analysis. Age-related hearing loss is a common issue but managing such hearing loss by male and female is not common. The responding to new voice is difficult, and at the same time, female and male voice echoes to responder is common. Impact of selection of hearing aid based on free mobile app and paid audiometric app effects may influence in the selection hearing aid. People adopted reading glass majorly based on the shop level reading test [48–50]. Such trend now spreads on society to adopt hearing aid too. People adopted hearing aid by online market too. Hence, this paper analyses the influence of such practice in the response on human voice [51, 52]. All the samples considered are the self-fitting hearing aid users. The hearing loss category is carefully selected on the range; the 3 male and 3 female samples have almost equal loss 70% and 45% according to the respective class like major loss as well as minor loss patients as well as age group 2 (major and minor loss category) × 2 (

male and female) × 2 (age group) × 2 hearing aid; hence, total samples are 24. The test was conducted at test room with 3-feet distance. The hearing air fitted to them was based on two-category adoption of hearing aid by mobile app-based test performance and also hearing aid. According to the design, the variables considered are young female with major hearing loss in the age group 40-50 and 60 to 75 are preferred as a sample with two categories of major and hearing minor loss category; hence, there are 12 samples from female category. Similarly, samples were considered from male side from two age groups and affected by major and minor hearing loss. The consolidated sample details were utilized for creating the Taguchi design of L8 in the Minitab v.18. The general linear model was created to feed the input to the software for experimental designing and analysing responses shown in Table 1. The design summary is presented in Table 2. The numerical 42 and 48 are codes for 40+ age group of male and female samples, respectively, similar to 64 and 73 codes for 60+ age group of male and female samples, respectively. The hearing loss is almost the same for the respective category of male and female. Figure 2 demonstrates the sample selections for investigation.

The LED TV was connected to computer to feed the random questions to the patients. The deployed question is to be asked by one patient, and it must be answered to opponent patients. This was evaluated by the perforce by 50 marks, and then, the patients interchange their position;

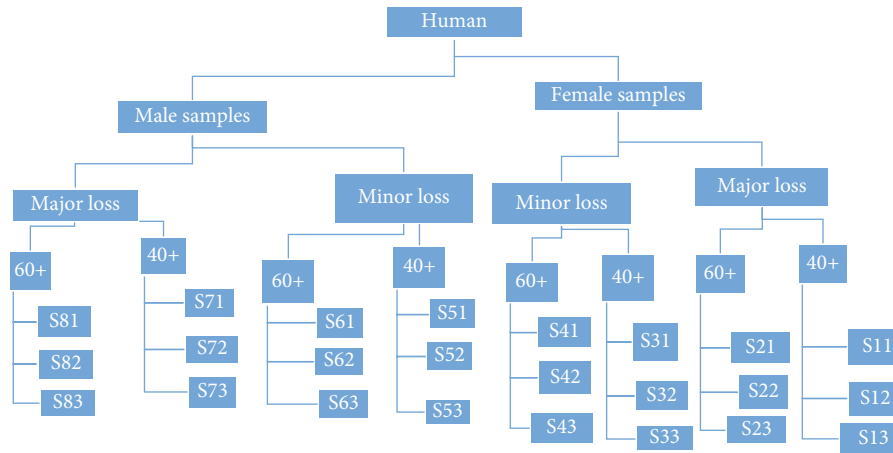


FIGURE 2: Samples from four different patient population.

TABLE 3: Taguchi L8 experimental design.

| Expt No. | Male patient | Test method | Female patient | Hearing loss |
|----------|--------------|-------------|----------------|--------------|
| 1 | 42 | App | 48 | Minor |
| 2 | 42 | App | 48 | Major |
| 3 | 42 | Audiometry | 73 | Minor |
| 4 | 42 | Audiometry | 73 | Major |
| 5 | 64 | App | 73 | Minor |
| 6 | 64 | App | 73 | Major |
| 7 | 64 | Audiometry | 48 | Minor |
| 8 | 64 | Audiometry | 48 | Major |

the next patient asks questions, and opponent patient is now responding for the question; this is also evaluated for 50 marks. The total response for the respective experiment is the sum of these two marks. Hence, the response measurement is based on the answer of male patient for female patient's queries which is displayed on the backside of responder vice versa. This experimental procedure followed for 8 different combinations of patients without repeating the questions for queries for any turn for both female to male patients. The five different observers evaluated the performance, and their round off average score is considered as experimental observations. Table 3 shows the L8 Taguchi experimental design and net responses observed on respective experiment.

6. Results and Discussions

The observations are analysed by Taguchi analysis. The Taguchi analysis results are presented in Table 4, in which the average outcomes of three different observers were considered for avoiding the observational error. The signal here mentioned is favourable response, and noise is unfavourable response. Table 5 shows the factor wise level signal to noise ratio for the response of net response. Usually when quality character set is larger and better, the values come as negative. But high signal to noise ratio is a matter on this (Table 5).

High value in that column indicates the level at which factor favours to the response. That is, the signals were observed for method of testing for adopting hearing aid, male category patients. Female category patients and loss category of them. The delta value indicates the nature of influence various factors on total response. The higher delta value indicates higher influence. Such a way that as the delta value is 2.067, the hearing nature of loss is a major influencing factor in attaining the response. The next higher influencing factor is method tested to adopt the hearing aid (delta = 1.90; refer to Table 5), the third influencing factor is male patients (delta = 1.90; refer to Table 5). The least influencing factor is female patients where delta value is 0.73.

Figure 3 shows that the nature of influence of four different factors was considered in this experiment as variable. The first plot shows the higher signal (Table 5, S/N ratio = -2.881 , level 2, first graph of Figure 3) for aged male patients (senior citizen). That is, the senior citizen responses found better than the young people. During the discussion, they disclosed that the young adults (age group 40-50) feel discomfort by mismatch of hearing aid for two different ranges. The adoption of new hearing aid degraded their ability as they are feeling about their inability. In the case of elder people, they said that as they feel something better than nothing, they can perform well but they could not understand some questions though they answered for the question of the same patient.

The second plot in Figure 3 resembles that high app-based hearing aid selection gave high signals than the audiometry-based selection hearing aid for the same patients (Table 5, S/N ratio = -3.373 , level 1, 2nd graph of Figure 3). The group response was much higher sound on hearing than another hearing aid (audiometry test-based selected). So, they can perform much better when compared to use of audiometry test-based selected. They added higher noise may shorter duration of wear for hearing by discomfort.

In Figure 3, third plot shows that signal is higher for young female adults (aged 40 to 50 years) than senior citizen category (Table 5, S/N ratio = -2.789 , level 1). Though that factor did not influence significantly in the overall response (Table 6, $P = 0.153$; $P > 0.05$). But discussion disclosed the

TABLE 4: Experimental observations and Taguchi output of signal to noise ratio.

| Expt. No. | Trail 1 | Trail 2 | Trail 3 | Average | Net response | SNRA1 | FITS |
|-----------|---------|---------|---------|---------|--------------|--------------|--------|
| 1 | 71 | 82 | 78 | 77.00 | 77.00% | -2.270185497 | 0.7675 |
| 2 | 64 | 59 | 61 | 61.33 | 61.00% | -4.2934033 | 0.6125 |
| 3 | 58 | 53 | 59 | 56.67 | 57.00% | -4.882502887 | 0.5875 |
| 4 | 47 | 43 | 46 | 45.33 | 45.00% | -6.935749724 | 0.4325 |
| 5 | 83 | 81 | 84 | 82.67 | 83.00% | -1.618438152 | 0.8475 |
| 6 | 69 | 73 | 70 | 70.67 | 71.00% | -2.974833026 | 0.6925 |
| 7 | 81 | 77 | 79 | 79.00 | 79.00% | -2.047458174 | 0.7575 |
| 8 | 59 | 57 | 54 | 56.67 | 57.00% | -4.882502887 | 0.6025 |

TABLE 5: Results of Taguchi analysis-signal to noise ratio and ranking of parameters.

| Level | Male patient | Test method | Female patient | Hearing loss |
|-------|--------------|-------------|----------------|--------------|
| 1 | -4.595 | -2.789 | -3.373 | -2.705 |
| 2 | -2.881 | -4.687 | -4.103 | -4.772 |
| Delta | 1.715 | 1.898 | 0.729 | 2.067 |
| Rank | 3 | 2 | 4 | 1 |

acceptance of the inability and lack of confidence on support of the hearing aid. The young adult group females had intention to prove themselves as they are not deaf so they paid over concentration on the examinations. There was controversy on senior citizen side that by habitual, they respond little and have doubt on the hearing. In Figure 3, the fourth plot resembles the nature of hearing loss influences on completing the conversation between patients (Table 5, S/N ratio = -2.705, level 1). The hearing loss is highly influencing factor (rank 1, delta = 2.07, Table 5) to complete the conversation cycle (response). The signal is high when the loss is less; that is, those samples under the minor loss responded well than the major loss persons.

The experimented statistics was further analysed by ANOVA by considering the general linear model. Figure 4 confirms that the observations are obeying the natural law that is statistical assumption well. The observations are closely appearing to the mean line.

Table 6 demonstrates statistics results for the experimental observations which were obtained from ANOVA output from the statistical model developed in Minitab v.18. The results of ANOVA confirm the contribution which was classified in the Taguchi analysis. The lower P value indicates the higher contribution in generating the response. According to value of P , if it is less than 0.05, the factor is significantly influencing on generating the response. If the P value is greater than 0.1, it is said to be insignificant in generating the response. Apart from 4 factors, only one factor is found insignificant so the model can be accepted. The P value is very low for hearing loss ($P = 0.007$; $P < 0.05$). It meant that hearing loss nature has low sensitiveness of nanoporous membrane. The next high influencing factor was test method as $P = 0.011$ and $P < 0.05$. Then, age is one of the influences but less than nature of loss and test method. The gender is either not influencing significantly or the influence of the gender factor is not significant in

the measurement of sensitiveness of nanoporous membrane. Figure 5 shows the percentage of contribution in the response generation was 40% by nature of hearing loss. Similarly, for method of testing employed in adaption of hearing aid, it was 30% and patient of male category found 26% and female found very little, that is, 4% only. Table 7 gives the validation of statistical model and observations recorded. In the model summary, the R^2 must be at least 95%. As the statistical model yielded 97.28%, the model is fit which did not violate the statistical assumptions.

Table 8 discloses the deep analysis results though the hearing loss highly influences on response generation as the low hearing loss patients ($P = 0.007$; $P < 0.05$) performed well in the experiments conducted. Similarly, in the male patients, particularly young adult performed well, and the young adult man contribution influences positively ($P = 0.013$; $P < 0.05$) in completing the conversation, and in selection of hearing aid with the test results, mobile app method influence ($P = 0.011$; $P < 0.05$) is better than audiometry in completing the conversation cycle. The response relationship is diagrammatically depicted in the 3D surface plot (Figure 6). The mathematical relation between variable on net outcome of response is presented in the following equation:

$$\begin{aligned}
 \text{Net response} = & 0.6625 - 0.0625 \text{ male patient}_{42} \\
 & + 0.0625 \text{ male Patient}_{64} + 0.0675 \\
 & * (\text{test method}_{\text{app}}) - 0.0675 \\
 & * (\text{test method}_{\text{audiometry}}) + 0.0225 \quad (1) \\
 & * (\text{female patient}_{48}) - 0.0225 \\
 & * (\text{female patient}_{73}) + 0.0775 \\
 & * (\text{hearing loss}_{\text{minor}}) - 0.0775 \\
 & * (\text{hearing loss}_{\text{major}})
 \end{aligned}$$

As Table 7 shows that $R^2 > 95$, the above mathematical prediction model exhibits good agreement with the tested results.

7. Experimented Model: Evaluating Hearing Attainment

In this experimented model, interacting the male and female completes conversation. Though the samples (patients)

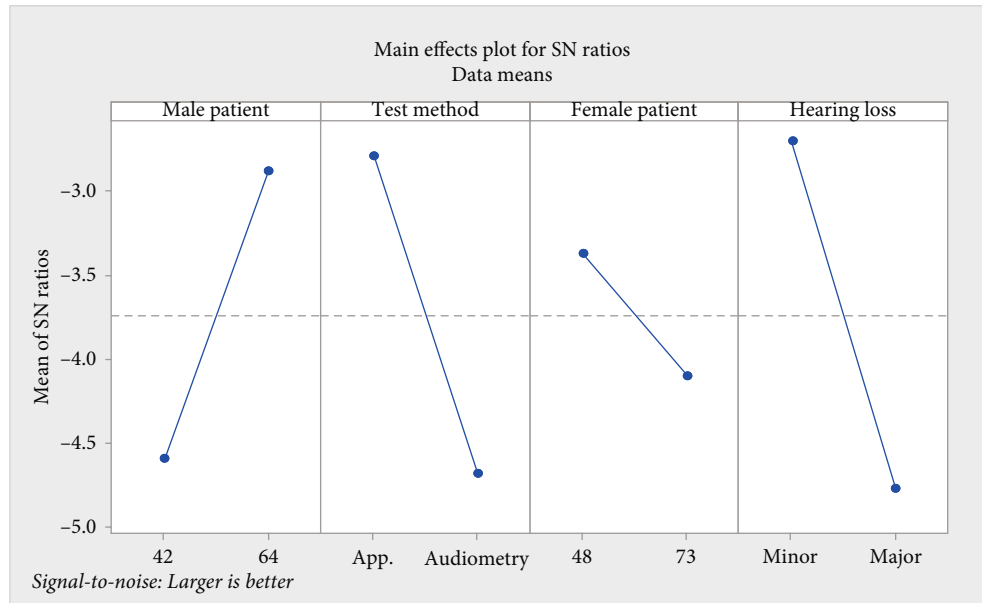


FIGURE 3: Results of Taguchi analysis nature of influence of factors for completing the conversation of two patients with respect to mean signal to noise ratio.

TABLE 6: ANOVA results on net response.

| Source | DF | Adj SS | Adj MS | F value | P value |
|---------------------------------|----|----------|----------|---------|---------|
| Male patient (age in years) | 1 | 0.031250 | 0.031250 | 22.99 | 0.013 |
| Test method (choice of testing) | 1 | 0.036450 | 0.036450 | 32.64 | 0.011 |
| Female patient (age in years) | 1 | 0.004050 | 0.004050 | 3.63 | 0.153 |
| Hearing loss (classification) | 1 | 0.048050 | 0.048050 | 43.03 | 0.007 |
| Error | 3 | 0.003350 | 0.00111 | | |
| Total | 7 | 0.123150 | | | |

possess similar as well as different hearing loss, all patients (samples) were compensated with their hearing loss by adapting 2 different hearing aids based on the test result of audiometry as well as mobile app test. The experimented results not only depend on the instrument supplied, test for hearing loss, male and female voice, etc., but something beyond according to the behavioral theories. So, the supply of hearing aid must increase the confident and really support for them when they use. Most of the patients do not know how to handle the situation when hearing aid is not supporting as per their expectation/need based on the situation and environmental condition, especially at interviews, some important meetings, etc.

8. Proposed Model

It is a magic model so this can be fulfilled by IoT technologies, which will increase the trust on hearing aid for new patient. The mismatch of requirements of hearing supplement which measured (at tested condition/environment/state of mind) with performance while using at real-world environment made him hurt and induces the nonuse of hearing aid. The allowances and ranges provided shall be insufficient for some occasions for many reasons. Based on

brainstorming with doctors and hearing aid center experts, it was found that trust on device supplied plays vital role. Such worthwhile trust cannot be completely made by simple sweet motivational words but his experience can do it easily. So, the proposed method is allowing the patients to validate the use of hearing aid many of his real-world situations. This allows him to adapt a suitable hearing aid to provide almost complete solution for his hearing deficiency.

This proposal measures exactly how much supplement the patient needs to compensate his hearing loss. In the proposed measuring system, a voice sensor or a mind sensor is coupled to self-fitting hearing aid through the IoT device. The IoT device extracts the data and stores in the cloud as well as supports for online monitoring and supports to the patient as and when he needs. Initially, self-fitting hearing aid for testing hearing supplement requirement for the patient is measured by means of audiometry test. The wireless connection will be provided between the IoT device and hearing aid. The voice sensor regulates the hearing aid. The voice sensor acts when the patient says “pardon” to augment the supplement (receiving capacity) until the patient says “okay.” If he feels loud, he must say “please” to reduce the hearing supplement. The patient must add “okay” if he understands conversation either from person or media or

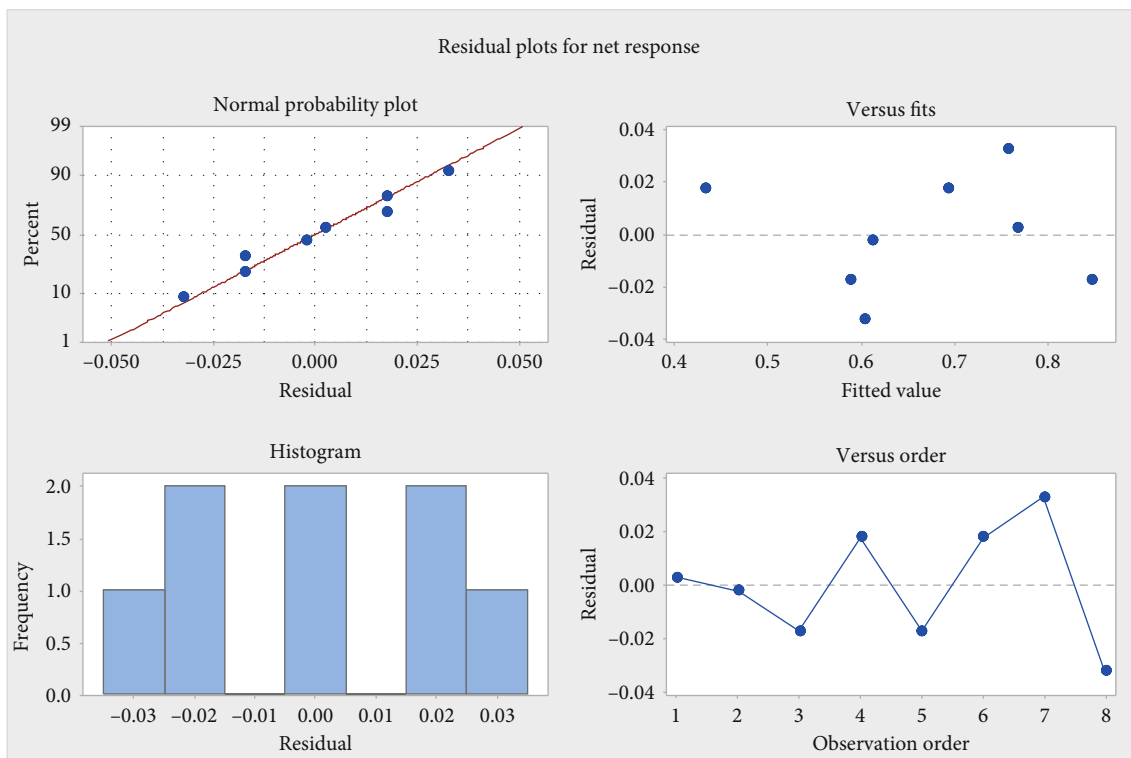


FIGURE 4: Statistical validation of observation with respect to mean line.

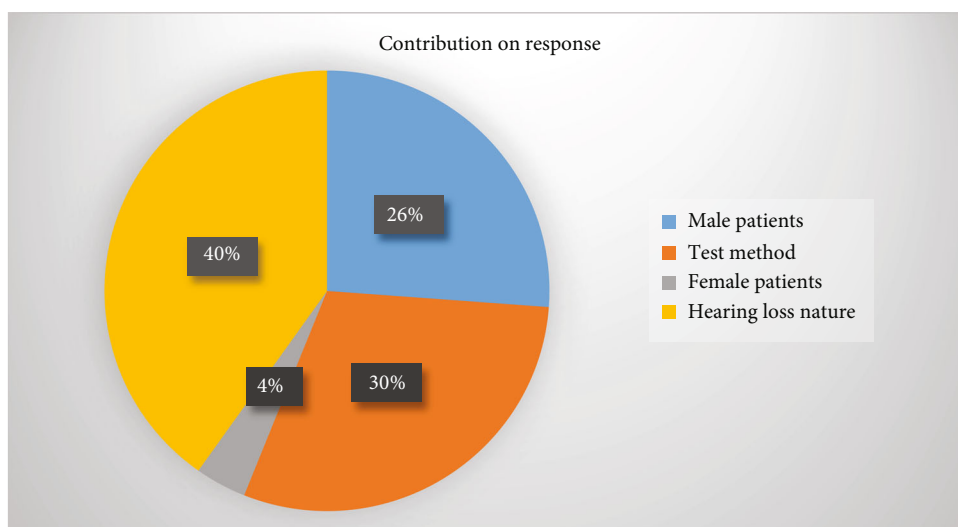


FIGURE 5: Percentage of contribution of factors in completing the conversations (response).

TABLE 7: Model summary—a result of model validation.

| S | R-sq | R-sq (Adj) | R-sq (pred) |
|-----------|--------|------------|-------------|
| 0.0334166 | 97.28% | 93.65% | 80.66% |

accepting the music or sounds from various nonverbal sources like birds and instrumental music, to maintain the level of supplement. The okay is the level which is to be measured and considered as sample observation of required supplement. From these observations, the real supplement requirements could be identified.

Limitation of this study may be stated as the hearing loss level of major and minor are considered but could not found the patient samples with the same hearing loss at the same age but age group considered as 40+ and 60+. But after experimented, it was coming to realize that it is sufficient to justify the deficiency on methods.

TABLE 8: The ANOVA results on level of individual factor.

| Term | Coef | SE Coef | T value | P value |
|----------------------|---------|---------|---------|---------|
| Constant | 0.6625 | 0.0118 | 56.07 | 0.000 |
| Male patient (42) | -0.0625 | 0.0118 | -5.29 | 0.013 |
| Test method (app) | 0.0675 | 0.0118 | 5.71 | 0.011 |
| Female patient (48) | 0.0225 | 0.0118 | 1.90 | 0.153 |
| Hearing loss (minor) | 0.0775 | 0.0118 | 6.56 | 0.007 |

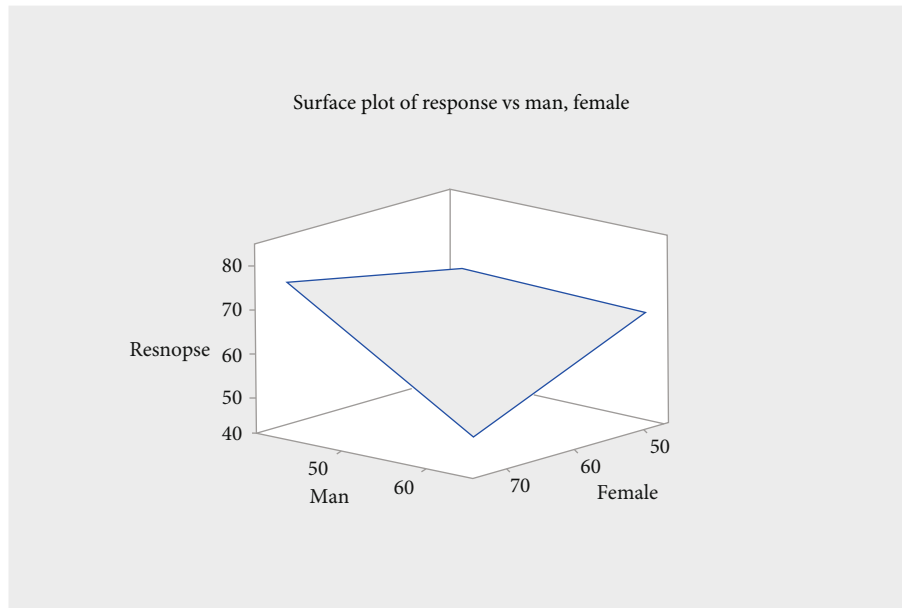


FIGURE 6: 3D surface plot response of male and female samples with respect to age.

9. Conclusion

Ability of nanopore tectorial gel membrane (nanomaterial) or loss of human ear testing is considered as sensitive material and measured its physical capabilities to measure the compensation/supplement need. This investigation addressed that measure of supplement requirements for understanding the nonverbal sounds/nonverbal vocalizations is not enough, and of measure supplement requirements for understanding the verbal sound is mandatory to supply appropriate hearing aid to compensate the deficient of the ear material. The following are the findings:

- (i) It was found that the nonuse of supplement instrument for compensating nanopore tectorial gel membrane not only depends on the instrument supplied, test for hearing loss, male and female voice, etc., but something beyond that according to the behavioral theories
- (ii) From the experimental results, it reveals that measure of supplement need for ear material is to listen well, not measure to hear well, because many patients repeated this reasons that they heard the sound but could not understand. From the behav-

ioral theory, it is suggested that understanding can be improved by enhancing the trust on device by the proposed testing method and based testing and supply of the hearing aid based on the IoT-based test outcomes

- (iii) Hence, the supplement for compensating nanopore tectorial gel membrane (hearing) is to be highly personalized and must take personalized care on observing supplement requirements. The patient himself believes that the supplement works for compensating well supplement instrument for compensating well the sensitiveness loss of his nanopore tectorial gel membranes on his respective ear. The conversion of patient requirements into technical data by the hearing aid center is through IoT. Hence, the supplied device will bring the entire satisfaction on hearing for complete day to day conversation through his best responses at his living environments

Data Availability

The data used to support the findings of this study are included in the article. Should further data or information

be required, they can be obtained from the corresponding author upon request.

Disclosure

This research was performed as a part of the employment of Hawassa University, Ethiopia.

Conflicts of Interest

The authors declare that there are no conflicts of interest regarding the publication of this article.

Acknowledgments

The authors thank Annamalai University and Tamil Nadu Teachers Education University for providing facilities and support to complete this research work.

References

- [1] World Health Organization, "Deafness and hearing loss," *Fact Sheet N.300*, 2015, <http://www.who.int/mediacentre/factsheets/fs300/en/>.
- [2] M. S. Peter, A. Warnecke, and H. Staecker, "A window of opportunity: perilymph sampling from the round window membrane can advance inner ear diagnostics and therapeutics," *Journal of Clinical Medicine*, vol. 11, no. 2, p. 316, 2022.
- [3] M. Magdy, E. Elmowafy, M. Elassal, and R. A. H. Ishak, "Localized drug delivery to the middle ear: recent advances and perspectives for the treatment of middle and inner ear diseases," *Journal of Drug Delivery Science and Technology*, vol. 69, article 103149, 2022.
- [4] E. Ren, P. Guilbaud, and F. X. Coudert, "High-throughput computational screening of nanoporous materials in targeted applications," 2022, <https://arxiv.org/abs/2202.09886>.
- [5] International Standards Organization (ISO), *Acoustics-Statistical Distribution of Hearing Thresholds as a Function of Age, ISO-7029*, ISO, Basel, Switzerland, 2000.
- [6] K. J. Cruickshanks, T. L. Wiley, T. S. Tweed et al., "Prevalence of hearing loss in older adults in Beaver Dam, Wisconsin: the epidemiology of hearing loss study," *American Journal of Epidemiology*, vol. 148, no. 9, pp. 879–886, 1998.
- [7] World Health Organization, *Prevention of blindness and deafness: estimates*, 2012, <http://www.who.int/pbd/deafness/estimates/en/>.
- [8] C. D. Mathers and D. Loncar, "Projections of global mortality and burden of disease from 2002 to 2030," *PLoS Medicine*, vol. 3, no. 11, article e442, 2006.
- [9] H.-W. Wahl, V. Heyl, P. M. Drapaniotis et al., "Severe vision and hearing impairment and successful aging: a multidimensional view," *The Gerontologist*, vol. 53, no. 6, pp. 950–962, 2013.
- [10] On aging, forum, and National Research Council, *Hearing loss and healthy aging: workshop summary*, 2014.
- [11] M. Tomita, W. C. Mann, and T. R. Welch, "Use of assistive devices to address hearing impairment by older persons with disabilities," *International Journal of Rehabilitation Research*, vol. 24, no. 4, pp. 279–290, 2001.
- [12] N. Cobelli, L. Gill, F. Cassia, and M. Ugolini, "Factors that influence intent to adopt a hearing aid among older people in Italy," *Health & Social Care in the Community*, vol. 22, no. 6, pp. 612–622, 2014.
- [13] A. Solanas, C. Patsakis, M. Conti et al., "Smart health: a context-aware health paradigm within smart cities," *IEEE Communications Magazine*, vol. 52, no. 8, pp. 74–81, 2014.
- [14] K. M. Kiely, B. Gopinath, P. Mitchell, C. J. Browning, and K. J. Anstey, "Evaluating a dichotomized measure of self-reported hearing loss against gold standard audiometry: prevalence estimates and age bias in a pooled national data set," *Journal of Aging and Health*, vol. 24, no. 3, pp. 439–458, 2012.
- [15] E. B. Mantello, C. Silva, E. Massuda, M. Hyppolito, and A. Reis, "Relationship between speech perception and level of satisfaction of hearing aid users," *International archives of otorhinolaryngology*, vol. 20, no. 4, pp. 315–320, 2016.
- [16] R. M. Cox and G. C. Alexander, "The International Outcome Inventory for Hearing Aids (IOI-HA): psychometric properties of the English version: El Inventario Internacional de Resultados para Auxiliares Auditivos (IOI-HA): propiedades psicometricas de la version en ingles," *International Journal of Audiology*, vol. 41, no. 1, pp. 30–35, 2002.
- [17] R. Wright and L. Keith, "Wearable technology: if the tech fits, wear it," *Journal of Electronic Resources in Medical Libraries*, vol. 11, no. 4, pp. 204–216, 2014.
- [18] T. Nam and T. A. Pardo, "Conceptualizing smart city with dimensions of technology, people, and institutions," in *Proceedings of the 12th annual international digital government research conference: digital government innovation in challenging times*, pp. 282–291, New York, 2011.
- [19] S. Chen, S. Song, L. Li, and J. Shen, "Survey on smart grid technology," *Power system technology*, vol. 33, no. 8, pp. 1–7, 2009.
- [20] I. A. Hashem, I. Yaqoob, N. B. Anuar, S. Mokhtar, A. Gani, and S. U. Khan, "'Big data' on cloud computing: review and open research issues," *Information Systems*, vol. 47, pp. 98–115, 2015.
- [21] M. Dohler, C. Ratti, J. Paraszczak, and G. Falconer, "smart cities [Guest Editorial]," *IEEE Communications Magazine*, vol. 51, no. 6, pp. 70–71, 2013.
- [22] W. Fan and A. Bifet, "Mining big data: current status, and forecast to the future," *ACM SIGKDD explorations newsletter*, vol. 14, no. 2, pp. 1–5, 2013.
- [23] H. Adeli and X. Jiang, *Intelligent Infrastructure: Neural Networks, Wavelets, and Chaos Theory for Intelligent Transportation Systems and Smart Structures*, CRC press, 2008.
- [24] H. Demirhan, "A smart healthcare systems framework," *It Professional*, vol. 15, no. 5, pp. 38–45, 2013.
- [25] G. Eysenbach and A. R. Jadad, "Evidence-based patient choice and consumer health informatics in the internet age," *Journal of Medical Internet Research*, vol. 3, no. 2, article e841, 2001.
- [26] R. Istepanian, S. Laxminarayan, and C. S. Pattichis, Eds., *M-Health: Emerging Mobile Health Systems*, Springer Science & Business Media, 2006.
- [27] T. Sathish, K. Palani, L. Natrayan, A. Merneedi, M. V. De Poures, and D. K. Singaravelu, Eds., "Synthesis and Characterization of Polypropylene/Ramie Fiber with Hemp Fiber and Coir Fiber Natural Biopolymer Composite for Biomedical Application," *International Journal of Polymer Science*, vol. 2021.
- [28] A. Solanas, C. Patsakis, M. Conti et al., "Constantinos Patsakis, Mauro Conti, Ioannis S. Vlachos, Victoria Ramos, Francisco Falcone, Octavian Postolache et al. "Smart health: a context-

- aware health paradigm within smart cities.”, *IEEE Communications Magazine*, vol. 52, no. 8, pp. 74–81, 2014.
- [29] M. Mital, V. Chang, P. Choudhary, A. Papa, and A. K. Pani, “Adoption of internet of things in India: a test of competing models using a structured equation modeling approach,” *Technological Forecasting and Social Change*, vol. 136, pp. 339–346, 2018.
- [30] I. Ajzen, “From intentions to actions: a theory of planned behavior,” in *Action Control*, pp. 11–39, Springer, Berlin, Heidelberg, 1985.
- [31] I. Ajzen, “The theory of planned behavior,” *Organizational behavior and human decision processes*, vol. 50, no. 2, pp. 179–211, 1991.
- [32] H. C. Triandis, “Values, attitudes, and interpersonal behavior,” in *Nebraska Symposium on Motivation*, University of Nebraska Press, 1979.
- [33] A. Bandura, “Self-efficacy mechanism in human agency,” *American Psychologist*, vol. 37, no. 2, pp. 122–147, 1982.
- [34] F. D. Davis, “Perceived usefulness, perceived ease of use, and user acceptance of information technology,” *MIS Quarterly*, vol. 13, no. 3, pp. 319–340, 1989.
- [35] L. Hasher and R. T. Zacks, “Automatic and effortful processes in memory,” *Journal of Experimental Psychology: General*, vol. 108, no. 3, pp. 356–388, 1979.
- [36] J. M. Jennings and L. L. Jacoby, “Automatic versus intentional uses of memory: aging, attention, and control,” *Psychology and Aging*, vol. 8, no. 2, pp. 283–293, 1993.
- [37] S. Taylor and P. Todd, “Assessing IT usage: the role of prior experience,” *MIS Quarterly*, vol. 19, no. 4, pp. 561–570, 1995.
- [38] S. Taylor and P. A. Todd, “Understanding information technology usage: a test of competing models,” *Information Systems Research*, vol. 6, no. 2, pp. 144–176, 1995.
- [39] V. Venkatesh, M. G. Morris, G. B. Davis, and F. D. Davis, “User acceptance of information technology: toward a unified view,” *MIS Quarterly*, vol. 27, no. 3, pp. 425–478, 2003.
- [40] D. Bakan, *The Duality of Human Existence: An Essay on Psychology and Religion*, 1966.
- [41] H. J. Lee, H. J. Cho, W. Xu, and A. Fairhurst, “The influence of consumer traits and demographics on intention to use retail self service checkouts,” *Marketing Intelligence & Planning*, vol. 28, no. 1, pp. 46–58, 2010.
- [42] V. Venkatesh, J. Y. L. Thong, and X. Xin, “Consumer acceptance and use of information technology: extending the unified theory of acceptance and use of technology,” *MIS Quarterly*, vol. 36, no. 1, pp. 157–178, 2012.
- [43] S. S. Kim and N. K. Malhotra, “A longitudinal model of continued IS use: an integrative view of four mechanisms underlying postadoption phenomena,” *Management Science*, vol. 51, no. 5, pp. 741–755, 2005.
- [44] S. S. Kim, N. K. Malhotra, and S. Narasimhan, “Research note—two competing perspectives on automatic use: a theoretical and empirical comparison,” *Information Systems Research*, vol. 16, no. 4, pp. 418–432, 2005.
- [45] K. Chen and A. H. S. Chan, “The ageing population of China and a review of gerontechnology,” *Geron*, vol. 10, no. 2, pp. 63–71, 2011.
- [46] R. M. Ryan and E. L. Deci, “Self-determination theory and the facilitation of intrinsic motivation, social development, and well-being,” *American Psychologist*, vol. 55, no. 1, pp. 68–78, 2000.
- [47] L. Natrayan, S. Prasad Jones Christydass, S. Sivananthan, R. Kamalakannan, V. Vijayan, and P. Paramasivam, “Experimental Investigation on Tribological Behaviour of AA6066: HSS-Cu Hybrid Composite in Dry Sliding Condition,” *Advances in Materials Science and Engineering*, vol. 2022, pp. 1–7, 2014.
- [48] T. Sathish, P. Jagadeesh, S. M. Rangappa, and S. Siengchin, “Mechanical and thermal analysis of coir fiber reinforced jute/bamboo hybrid epoxy composites,” *Polymer Composites*, vol. 1, 2022.
- [49] S. Perumal, D. Sundaresan, R. Sivanraju, N. Tesfie, K. Ramalingam, and S. Thanikodi, “Heat transfer analysis in counter flow shell and tube heat exchanger using of design of experiments,” *Thermal Science*, vol. 26, no. 2 Part A, pp. 843–848, 2022.
- [50] S. Perumal, V. Venkatraman, R. Sivanraju, A. Mekonnen, S. Thanikodi, and R. Chinnappan, “Effects of nanofluids on heat transfer characteristics in shell and tube heat exchanger,” *Thermal Science*, vol. 26, no. 2 Part A, pp. 835–841, 2022.
- [51] P. Jagadeesh, S. M. Rangappa, and S. Siengchin, “Studies on mechanical and thermal properties of cellulosic fiber fillers reinforced epoxy composites,” *Polymer Composites*, vol. 1, 2022.
- [52] T. Sathish, N. Sabarirajan, S. P. J. Christydass et al., “Synthesis and optimization of deesterified acacia-alginate nanohydrogel for amethopterin delivery,” *Bioinorganic Chemistry and Applications*, vol. 2022, Article ID 7192919, 10 pages, 2022.

Research Article

Analysis and Experimental Investigation of A356 Aluminium Alloy Hybrid Composites Reinforced with Gr-Fe₃O₄-B₄C Nanoparticles Synthesised by Selective Laser Melting (SLM)

J. Anoop,¹ Vijay Ananth Suyamburajan,¹ P. Sekhar Babu,² and Sisay Addis Filketu ³

¹Department of Mechanical Engineering, Vels Institute of Science, Technology & Advanced Studies (VISTAS), Chennai, Tamilnadu, India

²Department of Mechanical Engineering, Narsimha Reddy Engineering College, Hyderabad, India

³School of Mechanical and Industrial Engineering, Institute of Technology, Debre Markos University, Debre Markos, Ethiopia 269

Correspondence should be addressed to Sisay Addis Filketu; sisayaddis123@gmail.com

Received 27 April 2022; Accepted 22 June 2022; Published 9 July 2022

Academic Editor: V. Vijayan

Copyright © 2022 J. Anoop et al. This is an open access article distributed under the Creative Commons Attribution License, which permits unrestricted use, distribution, and reproduction in any medium, provided the original work is properly cited.

Additive manufacturing techniques (AMTs) evolved quickly from simple prototype options to promising additive manufacturing techniques. The additive technologies, which include point-by-point material merging, full melting, and solidification of powder particles, provide potential unique braves and advantages with nanometal powders. In the fabrication of A356 aluminium alloy-based hybrid metal matrix nanocomposites, graphite (Gr), iron oxide (Fe₃O₄), and boron carbide (B₄C) are used as nanoreinforcement. Famous AMTs like selective laser melting have created A356 hybrid nanocomposites (SLM). The ingot was made out of a cylindrical slot measuring 14 × 100 mm. The percentages 2%, 4%, and 6% are added to the reinforcements Gr, Fe₃O₄, and B₄C. Microtensile and microhardness tests were used to determine the outcome of the reinforcement. Microtensile and microhardness parameters are assessed using microtensile test equipment and a Vickers hardness tester, with the specimen prepared in accordance with ASTM standards. A356 with 2, 4, and 6% reinforcing has a Vickers Hardness Number (VHN) of 144, 163, and 188, respectively. As the boron carbide reinforcement is increased, the load value of graphite and iron oxide (2, 4, and 6%) rises. The greatest ultimate tensile strengths are 260.10, 290.06, and 325.43 N/mm², respectively. The bonding structure of nanocomposites is assessed using an OM, and then, microtensile specimens are assessed using a SEM. As a result of the superior effect of the diverse reinforcements Gr, Fe₃O₄, and B₄C, more increased tensile and hardness qualities have been attained.

1. Introduction

Nowaday's rapid developments in engineering and technology have a huge demand for lightweight and high-strength materials with good tensile, wear, and hardness properties for particular use in aeronautical, automobile, medical, marine, and defence departments. Aluminium and their alloys are espoused in enormous applications, in particular aeronautical, automobile, medical, sports, defence, petrochemical engineering, and marine, outstanding to their superb properties like high strength, good thermal conductivity, high wear, and corrosion resistance [1–3]. Most of the researchers used casting [4, 5], powder metallurgy

[6–8], and heat treatment techniques [9–11] to improve the mechanical properties of aluminium alloys. These traditional techniques are inadequate to meet technological demand. The application of modern advancement to the manufacturing of products and parts with high mechanical properties is the major intention of material processing.

Metal matrix composites (MMCs) are an essential role in lightweight and high-strength materials that venture to coalesce the high solidness, stiffness, and sturdiness provided by a metal matrix [12–14]. Research shows that the formation of metal matrix composites with the addition of the different reinforcements into the matrix can improve the mechanical properties appreciably. Generally

used reinforcements include particle, whisker, and fiber. When comparing whisker and fiber, particle reinforcement has more benefits produced in the matrix such as processing, uniform microstructure, and cost [15]. Consequently, particle reinforcement MMCs have been used in aeronautical industries, automotive industries, and medical and defence departments. Nanoparticles by adding a metal matrix improve the strength of MMCs extensively due to disarticulation and dispersal strengthening. Nanoparticles assist to enhance mechanical properties such as strength, wear resistance, and hardness of MMCs [16].

When high strength is required, A356 aluminium casting alloys are employed in the manufacture of aviation components. The need for lightweight, high-strength components is expanding all the time. Aluminium matrix composites are being touted as a new generation of possible materials for a wide range of technical applications. For Aluminium Metal Matrix Composites (AMMCs), generally used nanoparticle reinforcement contains B_4C , SiC, Gr, TiB_2 , Al_2O_3 , and TiC [17–19].

B_4C is an elegant reinforcement material because of its superb strength, microhardness, wear resistance, high specific stiffness, good damping capacity, excellent thermal conductivity, chemical and thermal stability, high melting point, high wettability, low density, and good interfacial bonding property with aluminium comparable to Al_2O_3 , TiB_2 , TiC, and SiC [20–22].

Dirisenapu et al. [23] reported that the tensile strength of the nanocomposites increased with an increase in B_4C nanoparticles and percentage of elongation; density is decreased.

Chandrasekaran et al. [24] investigated Al- B_4C cermet fabricated by additive manufacturing; the hardness of the composite reached as high as 80 Ra with an increase of 59.3 Vol% B_4C particle.

Poovazhagan et al. [25] studied the added Nanob $4c$ in AMCs and enhanced its hardness, tensile strength, wear resistance, and good ductility, and impact resistance of the Al alloy was retained.

Graphite is another important secondary reinforcement material because of its constructive dry sliding wear condition for AMCs. In the current research, graphite favoured in AMCs improved both wear resistance and machinability. The incorporation of graphite diminishes the surface porosity and enhances mechanical and tribological properties continuously [26–28].

Saini et al. [29] observed that hardness of the hybrid composite had increased significantly to added nanosilica particles and graphite flake as reinforcements. These new hybrid composites can be used for various applications including engine piston, automobile components, and microelectronic devices.

Zhang et al. [30] prepared two variety composites Al-SiC-graphite and Al-SiC-graphene and observed reinforcement and microstructure by using SEM, TEM, XRD, and Raman spectroscopy. The added graphite flake reinforcement is partly desquamated into thinner ones, and the clusters of graphite with a size as large as $10\ \mu m$ can still be observed in the Al-graphite sample.

Alaneme et al. [31] developed Al-Mg-Si alloy with steel and graphite particle composites prepared by stir casting.

All the mechanical properties are reduced slightly with an augment in graphite content and trailed the composite reinforced with 8 wt.% steel.

Fe_3O_4 is a third reinforcement, and it plays an important role in the aerospace industry. The addition of Fe_3O_4 nanoparticle reinforcements in the AMCs enhanced the magnetic permeability of composites and thermal properties lacking mechanical degradation [32]. Fereiduni et al. [33] used Fe_3O_4 nanoparticles in the welding process to Al-Fe intermetallics due to their small size and heat generated.

AMCs produced with selective laser melting (SLM) have attracted all embracing attention in the lightweight application fields [34]. AMCs manufactured by SLM efficiently can accomplish greater mechanical properties compared to conventional manufacturing. Martin et al. [35] reported crack-free AA7075 elements achieved by mixing nano-ZrH₂ particles with 7075 powder before SLM. All through solidification, the recently shaped Al_3Zr phase obviously assisted granule modification, because of which the mechanical properties are enhanced. Gu et al. [36] discussed that the effect of nanoparticle reinforcement on the strength and ductility of materials is enhanced simultaneously as manufactured by SLM. Zhang et al. [37] fabricated SiC/AlSi₁₀Mg composites by SLM technique, and the microstructure and mechanical properties of composites are investigated. The AMCs show the highest yield strength and modulus among values of 408 MPa and 90 GPa, respectively. In the current research work, the AMCs- B_4C -Gr- Fe_3O_4 hybrid composite is fabricated by selective laser melting (SLM) and investigated tensile, hardness, and microstructure.

2. Experimental Details

2.1. Powder Preparation. The experiment's matrix materials were A356 alloy powder (60 m, $=2.662\ g/cc$) acquired from Bhoomi Metal & Alloys in Maharashtra. B_4C powder (30 m, $2.25\ g/cc$), Gr powder (100 m, $2.26\ g/cc$), and Fe_3O_4 powder (60 m, $4.9\ g/cc$) were acquired from Intelligent Materials Private Limited in Punjab and Saveer Biotech Limited in Uttar Pradesh, respectively. In a planetary ball mill, three samples (2, 4, and 6) of the A356- B_4C -Gr- Fe_3O_4 hybrid composite powder were prepared. The details of the sample powder are mentioned in Table 1.

2.2. SLM Process. The A356- B_4C -Gr- Fe_3O_4 specimens were created on an SLM machine designed by ARCI in Hyderabad, India, as shown in Figure 1. An SLM machine is fitted with a fiber laser with a wavelength of 1076 nm. The entire experiment was carried out with a continuous-wave laser with a power of 400 W and a spot size of 110 m. To prevent the specimens from oxidising, the SLM procedure was carried out in a vacuum, as described in earlier literature reviews [25–27]. The pressure in the chamber was fixed at 6×10^{-3} Pa. In addition, an argon gas flow was incorporated into the experimental setting in order to evaluate the impact of atmospheric conditions on the make superiority. The chamber was emptied to the abovementioned pressure. During laser irradiation, the chamber pressure was adjusted to $1.5 \cdot 10^3$ Pa by using argon gas to produce flow. Table 2 and

TABLE 1: Sample powder details.

| Sample no. | Composite powder | A356 | B ₄ C | Gr | FE ₃ O ₄ |
|------------|---|------|------------------|----|--------------------------------|
| 1 | | 94 | 2 | 2 | 2 |
| 2 | A356-B ₄ C-Gr-FE ₃ O ₄ | 88 | 4 | 4 | 4 |
| 3 | | 82 | 6 | 6 | 6 |



FIGURE 1: The SLM experimental setup.

TABLE 2: The list of SLM process machine specifications and laser process parameters.

| | |
|-----------------------|----------------------------------|
| Fiber laser | 400 W |
| Spot sizes | 80-115 μ m |
| Scan processing speed | 10 m/s |
| Build area | 280 \times 280 \times 365 mm |
| Layer thickness | 20-100 μ m |
| Platform heating | 200 $^{\circ}$ C |

Figure 2 show the process parameters and SLM procedure. The experiment was carried out with each combination of process parameters to construct single-layer samples with a dimension of 14 mm \times 100 mm.

3. Testing of Composite

3.1. Microstructural Investigation. The optical microscope was used to examine the SLM specimens, as illustrated in Figure 3. To produce a better disparity, the samples were ground with 220, 400, 600, and 1000 grades of emery paper, then refined with diamond suspensions of 6, 4, and 2 mm diameters, and etched using Kroll's reagent (15 mL of HF, 40 mL of HNO₃, and 60 mL of water, ASTM E407) for 30 seconds. Optical microscopy was used to investigate the microstructure (1000x magnifications, GX51, Olympus).

3.2. Microhardness. When test samples are very small or thin in a composite sample, microhardness testing is a technique for estimating a material's hardness on a microscopic scale. Microhardness was assessed on this specimen using UHL VMHT digital microhardness equipment, as illustrated in Figure 4. Ranges of indents may be completed on the sample with the aid of computer control, and the hardness can be computed (load range from 0.3 to 30 kgf) for the purpose of detachment from an orientation point. This microhard-

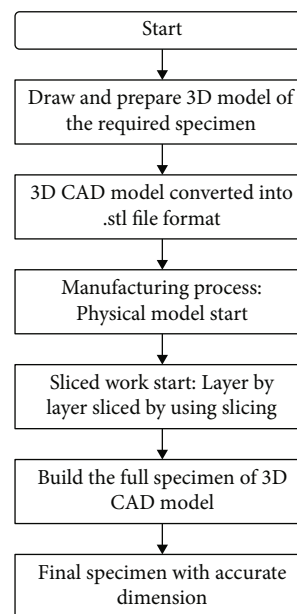


FIGURE 2: Flow chart of SLM process.



FIGURE 3: Optical microscope.



FIGURE 4: Microhardness tester (UHL VMHT digital).

ness apparatus is very well suited to create fractures on the sample surface, allowing the rupture robustness to be assessed.

3.3. Tensile Test. Microtension tests are used to measure the strength and ductility of nanocomposites under uniaxial tensile stresses in the development of novel alloys for quality control, commercial shipment acceptance testing, and structural design assistance. It was validated in accordance

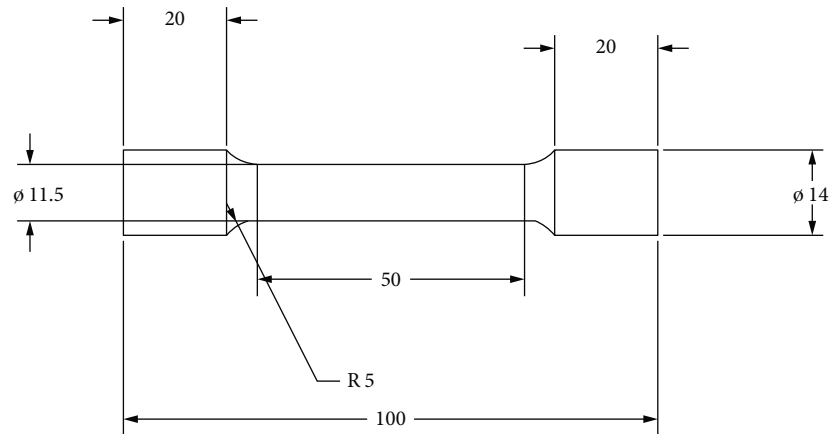


FIGURE 5: Microtensile test specimen.



FIGURE 6: Multipurpose microtensile testing machine.

with ASTM B-557M standards using three specimens, each measuring 100 mm in length and 14 mm in diameter, as illustrated in Figure 5 for each AMC family. The microtension was customary in any form at room temperature specifically the methods of determination of yield strength, yield point, elongation, tensile strength, and reduction of area. The multipurpose microtensile testing machine type (Max. static load ± 3000 N and Max. dynamic load ± 2500 N) among dutiful seize is used to hold the tensile specimen as shown in Figure 6.

3.4. SEM. In the microanalysis and failure analysis of nanocomposites, scanning electron microscopy (SEM) is used very professionally. It is done at high exaggerations, produces high-resolution pictures, and precisely measures very small facial features and objects. By rastering a focused electron beam across the surface and distinguishing between generated and backscattered electron signals, SEM offers comprehensive high-resolution images of the material. Figure 7 shows the SEM.



FIGURE 7: Scanning electron microscopy (SEM).

4. Result and Discussion

4.1. Microstructure. Figure 8 shows the fascia microstructures of A356 with 2, 4, and 6% B4C-Gr-Fe₃O₄ at magnifications of 100. The nanocomposite specimen remained sophisticated in terms of removing particles from the surface. Optical microscopes are expected to support particle distribution vestiges. The additive manufacturing process was inspected under an optical microscope to determine the specimen reinforcement pattern. The homogeneous dispersion of nanoparticles in the matrix material of the A356 alloy was clearly visible. The presence of nanoparticles leads to the formation of cracks, which leads to elastic deformation with increases in load. Composite rupture is represented by dimples, voids, clusters, and cracks. Fragile composite fracture in the form of cracks and rupture is due to the strong interfacial bonding between the reinforcements and the A356 matrix.

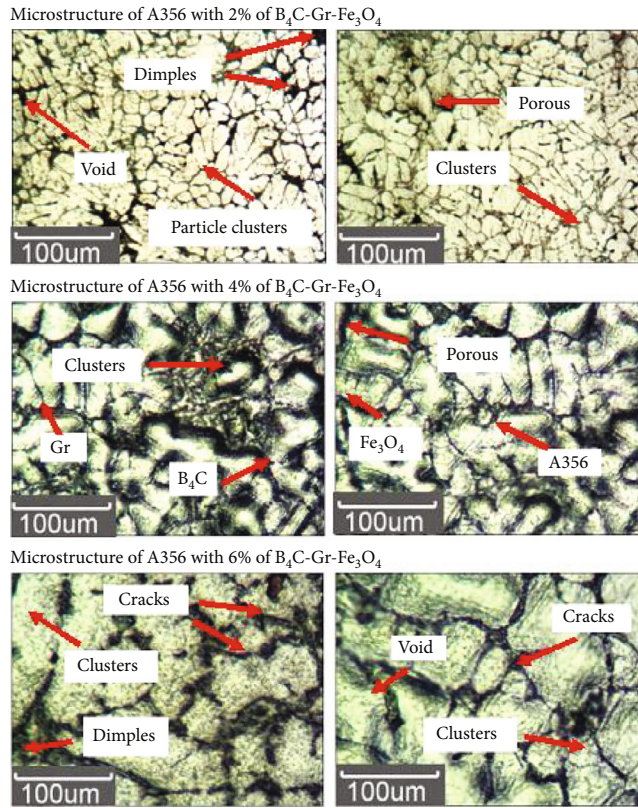


FIGURE 8: Microstructure of A356 with reinforcement B_4C -Gr- Fe_3O_4 .

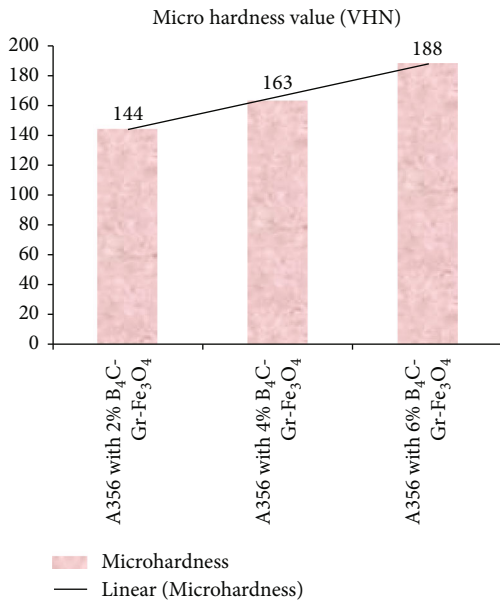


FIGURE 9: The microhardness values.

4.2. *Microhardness.* The specimen for the microhardness test was prearranged with a length and diameter of 10 mm × 12 mm. The surface to be examined should have a metallographic finish; hence, emery sheets of various grit sizes (100-1000) were used to finish the surface.

TABLE 3: Microhardness value of A356 with B_4C -Gr- Fe_3O_4 hybrid composites.

| Microhardness value (VHN) | |
|------------------------------------|-----|
| A356 with 2% B_4C -Gr- Fe_3O_4 | 144 |
| A356 with 4% B_4C -Gr- Fe_3O_4 | 163 |
| A356 with 6% B_4C -Gr- Fe_3O_4 | 188 |

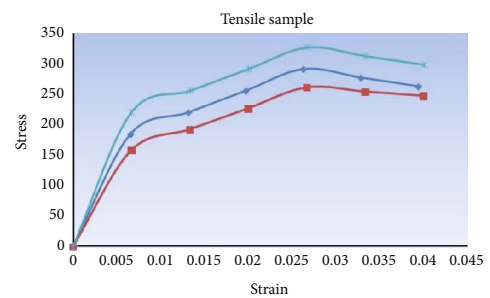


FIGURE 10: Stress vs. strain (UTS value in N/mm^2).

TABLE 4: Ultimate strength value of A356 with B_4C -Gr- Fe_3O_4 hybrid composites.

| Ultimate strength value (N/mm^2) | |
|--------------------------------------|--------|
| A356 with 2% B_4C -Gr- Fe_3O_4 | 260.10 |
| A356 with 4% B_4C -Gr- Fe_3O_4 | 290.06 |
| A356 with 6% B_4C -Gr- Fe_3O_4 | 325.43 |

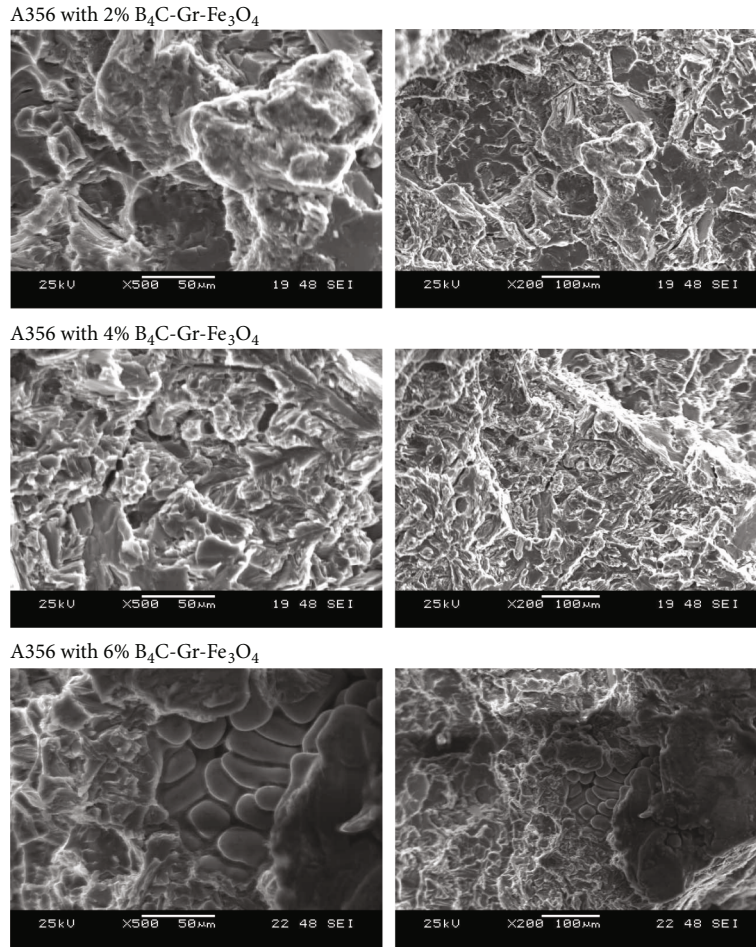


FIGURE 11: FESEM of tensile specimen (fracture analysis).

Equation (1) calculates the microhardness:

$$MH = \frac{MAL}{AI}, \quad (1)$$

where,

MH is microhardness

MAL is maximum applied load, and

AI is the area of indentation.

The Vickers Hardness Number (VHN) for A356 with 2, 4, and 6% reinforcement is 144, 163, and 188, respectively. With the reinforcement of 4% graphite and 3% ferrous oxide, the microhardness value of LM25 was 112. As the percentage of graphite (Gr) in the composites increases, the hardness of the normal particles falls [38]. When compared to matrix A356 alloy, the combined BHN value of A356/Gr/B₄C is 63.1 and the hardness value of the hybrid composite increased by roughly 56.1 percent. The harder B₄C ceramic particles are responsible for the increased hardness [39–41]. The research used A356 nanoparticles and reinforcements to achieve the better improvement in microhardness demonstrated in Figure 9 and Table 3.

4.3. Tensile Test. The ultimate tensile strength and stress-strain of the composites are improved with increased rein-

forcement, as shown in Figure 10. The variance in ultimate tensile strength with the AMMCs is shown in Table 4. The load value of graphite and iron oxide (2, 4, and 6 percent) increases as the boron carbide reinforcement is increased. 260.10, 290.06, and 325.43 N/mm² are the maximum ultimate tensile strengths, respectively [40, 41].

4.4. FESEM. When the manufactured composite material was subjected to fracture analysis, the results were as indicated in Figure 11. The FESEM image of the broken surface shows the mixing behaviour of ductile fracture, brittle fracture, and ploughing of reinforced material. Ductile fracture behaviour is caused by plastic deformation of the material prior to fracture, which results in the creation of a hollow. The quick and sudden fracture under stress causes brittle fracture behaviour. Transverse ruptures cause the ploughing fracture, which results in a deep hole-like cavity. All of these point to the fracture mixing behaviour [41].

5. Conclusion

SLM successfully created hybrid nanocomposites of B₄C-GFe₃O₄ with varied reinforcements (2, 4, and 6). The microstructural analysis demonstrated that particles were distributed uniformly throughout the matrix material.

Fractographic analysis was used to examine the tensile characteristics of the produced MMCs. The following are the results and conclusions of the hardness and tensile test:

- (i) The microhardness of nanocomposite A356 with 2, 4, and 6% reinforcement is 144, 163, and 188 VHN, according to the findings of a microhardness test
- (ii) Tensile testing of nanocomposite A356 with 2, 4, and 6% reinforcement yielded 260.10, 290.06, and 325.43 N/mm², respectively
- (iii) The fractographic images reveal a combination of ductile and brittle fracture behaviours, as well as ploughing of reinforced material
- (iv) Ductile fracture behaviour is caused by plastic deformation of the material prior to fracture, which results in the creation of a hollow. The quick and sudden fracture under stress causes brittle fracture behaviour. Transverse ruptures cause the ploughing fracture, which results in a deep hole-like cavity

Data Availability

The data used to support the findings of this study are included in the article. Should further data or information be required, these are available from the corresponding author and upon request.

Conflicts of Interest

The authors declare that they have no conflicts of interest.

References

- [1] S. Dadbakhsh, R. Mertens, L. Hao, J. Van Humbeeck, and J.-P. Kruth, "Selective laser melting to manufacture "in situ" metal matrix composites: a review," *Advanced Engineering Materials*, vol. 21, no. 3, article 1801244, 2019.
- [2] T. B. Sercombe and X. Li, "Selective laser melting of aluminium and aluminium metal matrix composites: review," *Materials Technology*, vol. 1–9, 2015.
- [3] B. Jiang, L. Zhenglong, C. Xi, L. Peng, L. Nannan, and C. Yanbin, "Microstructure and mechanical properties of TiB₂-reinforced 7075 aluminum matrix composites fabricated by laser melting deposition," *Ceramics International*, vol. 45, no. 5, pp. 5680–5692, 2019.
- [4] N. Verma and S. C. Vettivel, "Characterization and experimental analysis of boron carbide and rice husk ash reinforced AA7075 aluminium alloy hybrid composite," *Journal of Alloys and Compounds*, vol. 741, pp. 981–998, 2018.
- [5] D. Bandhu, A. Thakur, R. Purohit, R. K. Verma, and K. Abhishek, "Characterization & evaluation of Al₇₀₇₅ MMCs reinforced with ceramic particulates and influence of age hardening on their tensile behavior," *Journal of Mechanical Science and Technology*, vol. 32, no. 7, pp. 3123–3128, 2018.
- [6] M. Ravichandran, A. Naveen Sait, and V. Anandkrishnan, "Al-TiO₂-Gr powder metallurgy hybrid composites with cold upset forging," *Rare Metals*, vol. 36, pp. 686–696, 2014.
- [7] H. S. Kumaraswamy, V. Bharath, and T. Krishna Rao, "Microstructure and mechanical properties of sintered Al₂₀₂₄ hybrid MMCs," *Journal of Physics: Conference Series*, vol. 1455, no. 1, article 012024, 2020.
- [8] A. Alizadeh, M. Maleki, and A. Abdollahi, "Preparation of super-high strength nanostructured B₄C reinforced Al-2Cu aluminum alloy matrix composites by mechanical milling and hot press method: microstructural, mechanical and tribological characterization," *Advanced Powder Technology*, vol. 28, no. 12, pp. 3274–3287, 2017.
- [9] J. Mohamadigangaraj, S. Nourouzi, and H. Jamshidi Aval, "The effect of heat treatment and cooling conditions on friction stir processing of A390-10 wt% SiC aluminium matrix composite," *Materials Chemistry and Physics*, vol. 263, article 124423, 2021.
- [10] M. M. Moradi, H. J. Aval, and R. Jamaati, "Effect of pre and post welding heat treatment in SiC-fortified dissimilar AA6061-AA2024 FSW butt joint," *Journal of Manufacturing Processes*, vol. 30, pp. 97–105, 2017.
- [11] A. Mohamed and F. Samuel, "A review on the heat treatment of Al-Si-Cu/Mg casting alloys," *Heat Treatment-Conventional and Novel Applications*, vol. 1, pp. 55–72, 2012.
- [12] V. Suresh, N. Hariharan, and S. Vellingiri, "An investigation on the tensile properties and micro-structure of hybrid metal matrix composites," *International Journal of Materials and Product Technology*, vol. 56, no. 1/2, pp. 84–94, 2018.
- [13] M. Jawaid and M. Thariq, *Handbook Sustainable Composites for Aerospace Applications*, Woodhead Publishing, Cambridge, 2018.
- [14] J. Anoop and S. Vijay Ananth, "Fabrication process and characterization of A356 aluminium alloy reinforced with Gr-Fe₃O₄-B₄C hybrid nanoparticles manufactured by selective laser melting (SLM)," in *4th International Conference on Advances in Mechanical Engineering*, p. 238, Chennai, 2022.
- [15] N. K. Bhoi, H. Singh, and S. Pratap, "Developments in the aluminum metal matrix composites reinforced by micro/nano particles – a review," *Journal of Composite Materials*, vol. 54, no. 6, pp. 813–833, 2020.
- [16] S. Saravanan, A. Godwin Antony, V. Vijayan, M. Loganathan, and S. Baskar, "Synthesis of SiO₂ nano particles by using sol-gel route," *International Journal of Mechanical Engineering and Technology*, vol. 1, pp. 785–790, 2019.
- [17] M. Cabeza, I. Feijoo, P. Merino et al., "Effect of high energy ball milling on the morphology, microstructure and properties of nano-sized TiC particle-reinforced 6005A aluminium alloy matrix composite," *Powder Technology*, vol. 321, pp. 31–43, 2017.
- [18] S. J. S. Chelladurai, R. Arthanari, K. Krishnamoorthy, K. S. Selvaraj, and P. Govindan, "Effect of copper coating and reinforcement orientation on mechanical properties of LM6 aluminium alloy composites reinforced with steel mesh by squeeze casting," *Transactions of the Indian Institute of Metals*, vol. 71, no. 5, pp. 1041–1048, 2018.
- [19] M. Senthil Kumar, M. Vanmathi, and G. Sakthivel, "SiC reinforcement in the synthesis and characterization of A356/Al₂O₃/SiC/Gr reinforced composite-paving a way for the next generation of aircraft applications," *Silicon*, vol. 13, no. 8, pp. 2737–2744, 2021.
- [20] S. Das, M. Chandrasekaran, S. Samanta, P. Kayarogam, and P. Davim, "Fabrication and tribological study of AA6061 hybrid metal matrix composites reinforced with SiC/B₄C nanoparticles," *Industrial Lubrication and Tribology*, vol. 71, no. 1, pp. 83–93, 2019.

- [21] M. J. Nasr Isfahani, F. Payami, M. A. Asadabad, and A. A. Shokri, "Investigation of the effect of boron carbide nanoparticles on the structural, electrical and mechanical properties of Al-B₄C nanocomposites," *Journal of Alloys and Compounds*, vol. 797, pp. 1348–1358, 2019.
- [22] L. Poovazhgan, S. Vijayananth, and S. Sivaganesan, "Optimizing ultrasonic power on fabricating aluminum nanocomposites reinforced with boron carbide nanoparticles," *Materials Science Forum*, vol. 979, pp. 28–33, 2020.
- [23] G. Dirisenapu, L. Dumpala, and S. P. Reddy, "The influence of B₄C and BN nanoparticles on Al 7010 hybrid metal matrix nanocomposites," *Emerging Materials Research*, vol. 9, no. 3, pp. 558–563, 2020.
- [24] S. Chandrasekaran, R. Lu, R. Landingham et al., "Additive manufacturing of graded B₄C-Al cermets with complex shapes," *Materials & Design*, vol. 188, article 108516, 2020.
- [25] L. Poovazhagan, K. Kalaichelvan, and T. Sornakumar, "Processing and performance characteristics of aluminum-nano boron carbide metal matrix nanocomposites," *Materials and Manufacturing Processes*, vol. 31, no. 10, pp. 1275–1285, 2016.
- [26] S. Arif, B. Jamil, M. B. N. Shaikh, T. Aziz, A. H. Ansari, and M. Khan, "Characterization of surface morphology, wear performance and modelling of graphite reinforced aluminium hybrid composites," *Engineering Science and Technology, an International Journal*, vol. 23, no. 3, pp. 674–690, 2019.
- [27] B. Guntreddi and A. Ghosh, "Anti-frictional role of diamond and graphite suspended bio-oil based nano- aerosols at sliding interface of Al-SiC_p and WC-6Co," *Tribology International*, vol. 153, article 106596, 2021.
- [28] S. Mohamad, S. Liza, and Y. Yaakob, "Strengthening of the mechanical and tribological properties of composite oxide film formed on aluminum alloy with the addition of graphite," *Surface and Coatings Technology*, vol. 403, article 126435, 2020.
- [29] S. Saini, A. Gupta, A. J. Mehta, and S. Pramanik, "Rice husk-extracted silica reinforced graphite/aluminium matrix hybrid composite," *Journal of Thermal Analysis and Calorimetry*, vol. 147, pp. 1157–1166, 2022.
- [30] J. Zhang, Q. Liu, S. Yang, Z. Chen, Q. Liu, and Z. Jiang, "Microstructural evolution of hybrid aluminum matrix composites reinforced with SiC nanoparticles and graphene/graphite prepared by powder metallurgy," *Progress in Natural Science: Materials International*, vol. 30, no. 2, pp. 192–199, 2020.
- [31] K. K. Alaneme, A. V. Fajemisin, and N. B. Maledi, "Development of aluminium-based composites reinforced with steel and graphite particles: structural, mechanical and wear characterization," *Journal of Materials Research and Technology*, vol. 8, no. 1, pp. 670–682, 2019.
- [32] N. Ashrafi, A. H. M. Ariff, M. Sarraf, S. Sulaiman, and T. S. Hong, "Microstructural, thermal, electrical, and magnetic properties of optimized Fe₃O₄-SiC hybrid nano filler reinforced aluminium matrix composite," *Materials Chemistry and Physics*, vol. 258, p. 123895, 2021.
- [33] E. Fereiduni, M. Movahedi, and A. Baghdadchi, "Ultrahigh-strength friction stir spot welds of aluminium alloy obtained by Fe₃O₄ nanoparticles," *Science and Technology of Welding and Joining*, vol. 23, no. 1, pp. 63–70, 2017.
- [34] M. P. Behera, T. Dougherty, and S. Singamneni, "Conventional and additive manufacturing with metal matrix composites: a perspective," *Procedia Manufacturing*, vol. 30, pp. 159–166, 2019.
- [35] J. H. Martin, B. D. Yahata, J. M. Hundley, J. A. Mayer, T. A. Schaedler, and T. M. Pollock, "3D printing of high-strength aluminium alloys," *Nature*, vol. 549, no. 7672, pp. 365–369, 2017.
- [36] D. Gu, H. Wang, D. Dai, P. Yuan, W. Meiners, and R. Poprawe, "Rapid fabrication of Al-based bulk-form nanocomposites with novel reinforcement and enhanced performance by selective laser melting," *Scripta Materialia*, vol. 96, pp. 25–28, 2015.
- [37] Y. Zhang, J. Sun, and R. Vilar, "Characterization of (TiB + TiC)/TC₄ in situ titanium matrix composites prepared by laser direct deposition," *Journal of Materials Processing Technology*, vol. 211, no. 4, pp. 597–601, 2011.
- [38] P. Ravindran, K. Manisekar, P. Narayanasamy, N. Selvakumar, and R. Narayanasamy, "Application of factorial techniques to study the wear of Al hybrid composites with graphite addition," *Materials and Design*, vol. 39, pp. 42–54, 2012.
- [39] P. R. Jadhav, B. R. Sridhar, M. Nagaral, and J. I. Harti, "Mechanical behavior and fractography of graphite and boron carbide particulates reinforced A356 alloy hybrid metal matrix composites," *Advanced Composites and Hybrid Materials*, vol. 3, no. 1, pp. 114–119, 2020.
- [40] S. Vellingiri, "An experimental and investigation on the micro-structure hardness and tensile properties of Al-GrFe₃O₄ hybrid metal matrix composites," *FME Transactions*, vol. 47, no. 3, pp. 511–517, 2019.
- [41] V. Suresh, P. Vikram, R. Palanivel, and R. F. Laubscher, "Mechanical and wear behavior of LM25 aluminium matrix hybrid composite reinforced with boron carbide, graphite and iron oxide," *Materials Today: Proceedings*, vol. 5, pp. 27852–27860, 2018.

Research Article

Microstructure and Mechanical Behaviour of Ti-6Al-4V Matrix Reinforced with WCp Developed by Squeeze Casting

R. Sivakumar,¹ B. R. Senthil Kumar,² G. Gopalarama Subramaniyan,³ M. Sivaraja,⁴
M. P. Natarajan,⁵ Pravin P. Patil,⁶ S. Kaliappan ,⁷ K. P. Yuvaraj,⁸
and Kassie Jemberu Abebe ⁹

¹Department of Civil Engineering, E.G.S. Pillay Engineering College, Nagapattinam, Tamil Nadu, India

²Department of Aeronautical Engineering, Nehru Institute of Engineering and Technology, Coimbatore, India

³Department of Mechanical Engineering, Saveetha Engineering College, Chennai, India

⁴Centre for Materials Research, Nehru Institute of Technology, Coimbatore, India

⁵Department of Mechanical Engineering, Bharath Institute of Higher Education and Research, Chennai, India

⁶Department of Mechanical Engineering, Graphic Era Deemed to Be University, Bell Road, Clement Town, Dehradun, Uttarakhand, India

⁷Department of Mechanical Engineering, Velammal Institute of Technology, Chennai, Tamil Nadu, India

⁸Department of Mechanical Engineering, Sri Krishna College of Engineering and Technology, Coimbatore, Tamil Nadu, India

⁹School of Mechanical and Industrial Engineering, Institute of Technology, Debre Markos University, Debre Markos, Ethiopia

Correspondence should be addressed to Kassie Jemberu Abebe; kassiejemberu@gmail.com

Received 27 April 2022; Revised 13 June 2022; Accepted 17 June 2022; Published 8 July 2022

Academic Editor: V. Vijayan

Copyright © 2022 R. Sivakumar et al. This is an open access article distributed under the Creative Commons Attribution License, which permits unrestricted use, distribution, and reproduction in any medium, provided the original work is properly cited.

The aim of this study is to evaluate the wear and micro hardness of a Ti-6Al-4V matrix reinforced with 10% and 15% tungsten carbide particle (WCp) composite manufactured using the squeeze casting process. Optical microscopy is used to determine the microstructures of the composite. A pin-on-disc wear test equipment and Vickers hardness at atmospheric temperature were used to examine the wear behaviour wear rate, CoF, and micro hardness qualities of primed samples. Loads of 10 N to 80 N, velocities of 4 m/s, and distances of 1000 m to 2000 m are considered for analyzing the wear behaviour of Ti-6Al-4V composites. The wear rate values are 25.683 for 10% WCp, 30.957 for 15% WCp, and 37.683 and 30.957 for 20% WCp. A scanning electron microscope (SEM) is utilized to examine the worn surface of the composites. For 10% WCp, the CoF values are 0.82 and 0.87, and for 15% WC, 0.88 and 0.956. The micro hardness values are 692 VHN for 10% WCp and 835 VHN for 15% WCp. The wear rate, microstructure, SEM images, coefficient of friction, and hardness of TMCs for totaling reinforcing tungsten carbide particle (WCp) possessions were discovered to be improved.

1. Introduction

Importance in the development of innovative materials with elegant properties is growing on a regular basis, and composite materials, which are primarily developed of composite materials, are marketed as a simple and improved method of obtaining materials with exceptional properties [1–3]. Metal matrix composites (MMCs) are a form of manufacturing and technology material that incorporates a strong rein-

forcement addicted to a metal matrix to increase qualities with particular stiffness, specific strength, wear resistance, good corrosion resistance, hardness, and high elastic modulus [4, 5]. Titanium and titanium alloys have a number of unique characteristics, such as high specific strength and lightweight, which support the use of titanium and titanium alloys as a matrix material in future structures [6–8]. TMCs have a wide range of applications in the automotive, aerospace, and marine industries [6, 9].

In recent years, a growing number of studies have been carried out to improve metal matrix composites by utilizing reinforcement [4–6, 10]. As a result, if researchers can discover a suitable reinforcement to improve the mechanical characteristics of Ti–6Al–4V matrix composites, the Ti–6Al–4V will be able to overcome some shortcomings, such as reduced hardness and Young’s modulus [11, 12], and find new uses. Because of its high hardness, high thermal stability, high modulus, approximate thermal expansion coefficient, and Poisson’s ratio to Ti–6Al–4V matrix, tungsten carbide (WCp) is a preferred choice for reinforcement [13–15]. As a result, WCp is likely to be a good reinforcing material for Ti–6Al–4V matrix composites, which should have outstanding mechanical characteristics.

Particle-reinforced TMCs exhibited considerable routine increase in terms of strength, creep resistance, wear resistance, low density, high toughness, corrosive resistance, thermal stability, and erosion [10, 16]. Particularly, squeeze casting possessed the strong interfacial rapport strength to accomplish the superior intensification effect, further than the conventional augmentation method.

Titanium dioxide, silicon carbide, titanium carbide, boron carbide, aluminium oxide, titanium nitrate, zirconium carbide, graphite, tungsten carbide, titanium diboride, aluminium nitride, and carbon nanotube are often used in TMCs. The physical, chemical, and mechanical properties of this reinforcement were excellent [11–16].

Chen et al. [17] applied WC/W₂C eutectic reinforcement in TMCs owed to the subordinate interfacial reactivity amid W₂C and Ti. Such W solid solution interface is additional effectual to relocate anxiety from the matrix to the WC/W₂C than to facilitate of the TiC layer.

Sivakumar et al. [18] fabricated Ti–6Al–4V (Ti64)/SiCp with improved hardness and compressive strength. The ideal density was attained at a compaction pressure of 6.035 MPa, and microstructure annotations indicated that TMCs exhibited improved wettability and bonding structure.

Li et al. [19] produced novel combination composites TMC/CNT that show potential in industry due to their higher-quality features such as high elastic modulus and low density. Fabrication procedures have an impact on the characteristics of TMCs, which has a considerable impact on their machinability, according to the findings.

Ren et al. [20] used powder metallurgy to fabricate titanium matrix composites with 20% Wp. Due to the charisma of many strengthening mechanisms, such as tungsten segment strengthening and firm elucidation strengthening, 20WP/Ti reveals outstanding perfunctory properties. The addition of Wp reinforcing phases masks the composite’s adiabatic shear sensitivity. Kellen and Amit [21] created titanium-boron carbide-boron nitride composites, with overall results of crack-free titanium-matrix composites with superior hardness of 700 HV and 99.1 percent density, as well as a staggering 33% reduction in corrosion bunch growth in the air when compared to commercially pure titanium.

Yang et al. [22] investigated Ti/CaTiO₃ particles, finding that the CaTiO₃ particles effectively increased Ti strength

TABLE 1: The compositions of titanium Ti-6Al-4V alloy (grade 5).

| Alloying elements | Chemical composition (wt%) |
|-------------------|----------------------------|
| Al | 7.83 |
| Fe | 0.36 |
| C | 0.06 |
| N | 0.04 |
| O | 0.3 |
| H | 0.0236 |
| V | 6.35 |
| Ti | 85.04 |

TABLE 2: The chemical composition of WC.

| WC elements | Fe | Cr | Ni | C | W |
|-------------------------------|-----|-----|-----|-----|-----------|
| WC chemical composition (wt%) | 0.6 | 5.7 | 8.8 | 4.4 | Remaining |



FIGURE 1: Squeeze casted specimen: (a) Ti-6Al-4V with 10 wt% WC composites; (b) Ti-6Al-4V with 15 wt% WC composites.



FIGURE 2: Pin-on-disc wear test machine.

TABLE 3: Wear test parameters.

| | |
|-----------------------------|--------------|
| Load (N) | 10 to 80 |
| Sliding velocity (m/s) | 4 |
| Sliding distance (m) | 1000 to 2000 |
| Dimension (dia × length mm) | 30 × 100 |

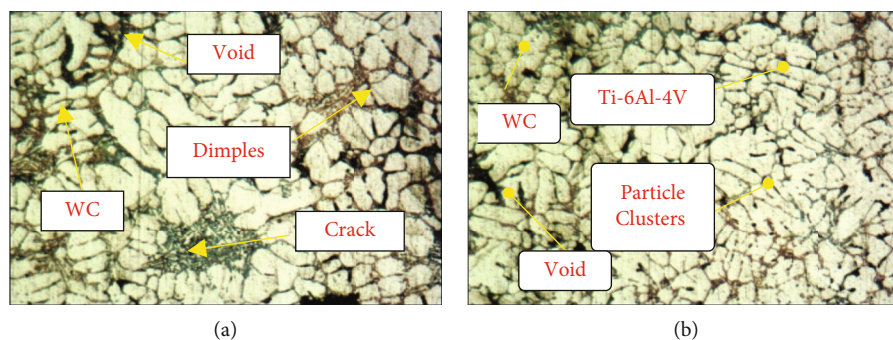


FIGURE 3: Squeeze casting microstructure of (a) Ti-6Al-4V with 5 wt% of WC and (b) Ti-6Al-4V with 10 wt% of WC.

without sacrificing elongation to malfunction. It is situated with the goal of increasing yield strength from 450 MPa for pure Ti to more than 850 MPa for TMCs with only a 2.5 wt% addition of CaTiO_3 , while maintaining a 30 percent elongation to failure.

Sun et al. [23] looked into how Ti/TiB composites were made using vacuum induction melting and multidirectional forging techniques. A spheroidized-phase, uniformly distributed TiB and dual-scale silicides were visible in the micrograph of the consequential composite. Its agility was greatly improved, with an elongation of up to 120 percent. The easy instigation of fractures at grain boundaries and the deterioration were the main reasons for the decrease in strength. Cast WCp/Ti was fabricated by laser injection process, according to Liu et al. [24]. WCp has the advantage of delivering fewer carbon atoms. The coating reveals superior ductility and conceals the retort invention TiC. Under an external load, the retort layers are effective at load transfer.

Stir casting, powder metallurgy, and squeeze casting are some of the most commonly used invention techniques in TMCs [25–27]. Squeeze casting advantage is cast machine parts manufactured in a solitary stride route with stumpy squeeze pressure. As a result, squeeze casting is a good method for making machine components when combined with cheap initial materials [28–31].

Dmitruk et al. [32] developed Ti-Al-C/Al-Si MMCs using the squeeze casting method, which allows for the efficient production of pore-free MAX phase-based MMCs with significantly higher wear resistance and hardness than commonly available Al-Si alloys.

The primary goal of this study is to look into the capabilities of various aspects, such as

- (i) introducing new materials: squeeze casting was used to create tungsten carbide particles (WCp) reinforced with titanium alloy Ti-6Al-4V alloys
- (ii) hardness and wear resistance are improved by Ti-6Al-4V alloys/WCp composites
- (iii) the bonding of the composites is examined using an optical microscope (OM) and a scanning electron microscope (SEM)

2. Materials and Methods

2.1. Matrix and Reinforcement. The primary matrix in this investigation was Ti-6Al-4V alloys (grade 5), and the density is 4.53 g/cc. Ti-6Al-4V alloys combine strength, density, great corrosion resistance, good ductility, heat treatability, and toughness in an astonishing way. Grade 5 titanium alloys have excellent welding and fabrication properties, as indicated in Table 1 [16, 33–36].

Tungsten carbide (WC) is an attractive reinforcement for matrix alloys [16, 37, 38] because of its extreme hardness, high modulus of elasticity, high melting temperature, and excellent wettability. Because of the significant density gradient, it is very important to make WC particles reinforced composites with a harmonised distribution of WCp using squeezing techniques [39, 40]. As a result, WCp was chosen as a reinforcement particle in the current study. In Table 2, the WCp substance concertos are presented. 5 and 10 wt% WCp with a typical particle size of 40 m were tested in addition to reinforcement.

2.2. Preparation of Composite: Squeeze Casting Techniques.

In general, squeeze casting is defined as a secondary process in composites stir casting techniques [41]. Due to rousing, the metal congealed under force to reduce porosity in squeeze casting. The force unit's main components were a punch and a special cylindrical steel die. There was a 0.05 to 0.1 mm agreement between the punch and the die to keep the force contained by the die and avoid melt seepage during pressing. The TMCs created by stir casting were melted again and accurately cast into a 300°C preheated die mould. After that, the punch was instantly subordinated to the fluid metal's surface. After maintaining a 150 MPa applied force for 4 minutes, the congeal casting was used to prepare the specimen 100 × 30 mm as shown in Figure 1.

2.3. Microstructure Tests, Wear Test, and Hardness Test. The overall work piece remained academic in nature, removing any garbage that was there on a surface level. Molecule transport is still monitored using a visual magnifying lens. The projection approach was examined using an optical magnifying tool to identify the support example of a cast structure. A section of the castings remained uncut. They were grained to produce 100 coarseness silicon carbide

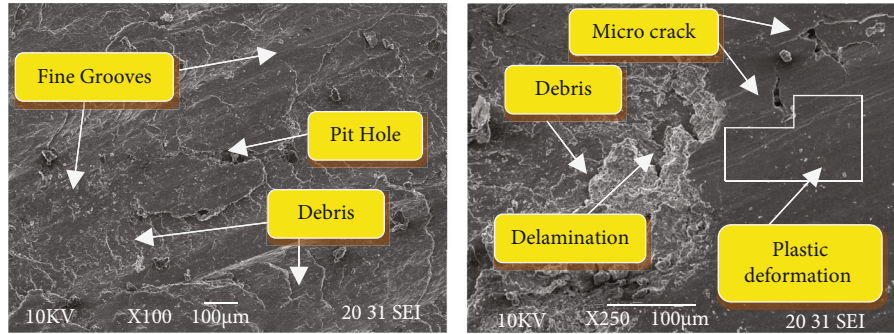


FIGURE 4: Worn surface analysis of squeeze casting wear specimen.

TABLE 4: Wear rate values of Ti-6Al-4V matrix with 10% WCp (sliding distance 1000 m).

| Applied load | Ti-6Al-4V matrix with 10% of WCp | Ti-6Al-4V matrix with 15% of WCp |
|--------------|----------------------------------|----------------------------------|
| 10 | 11.848 | 16.848 |
| 20 | 13.156 | 18.156 |
| 30 | 15.9735 | 20.9735 |
| 40 | 17.099 | 22.099 |
| 50 | 19.407 | 24.407 |
| 60 | 21.042 | 26.042 |
| 70 | 23.331 | 28.331 |
| 80 | 25.683 | 30.957 |

TABLE 5: Wear rate values of Ti-6Al-4V matrix with 15% WCp (sliding distance 1000 m).

| Applied load | Ti-6Al-4V matrix with 10% of WCp | Ti-6Al-4V matrix with 15% of WCp |
|--------------|----------------------------------|----------------------------------|
| 10 | 22.848 | 28.848 |
| 20 | 24.156 | 31.156 |
| 30 | 26.9735 | 33.9735 |
| 40 | 27.099 | 36.099 |
| 50 | 29.407 | 39.407 |
| 60 | 32.042 | 42.042 |
| 70 | 34.331 | 45.331 |
| 80 | 37.683 | 47.957 |

paper before optical reconnaissance, followed by 200 to 1000 emery paper assessments. To obtain a superior difference, Keller’s reagent was employed to clean and carve the samples. The samples were visualised at various magnifications to demonstrate the occurrence of fortifications and the conveyance of the metal lattice diverse components/mixes that were accessible in graphite and boron carbide, which are difficult to distinguish by optical micrographs.

Microanalyses of strong inorganic materials are both aided by SEM microscopy. Filtering electron microscopy allows for high misrepresentations, high-goal symbolism, and exact quantification of extremely minute face features and objects. SEM gives finished high-goal symbolism of the tester by rastering an engaged electron pillar across the surface and recognising determined or backscattered electron signals. A vitality dispersive X-beam analyzer is also used to invest with basic location and quantitative compositional data.

An additional sample was tested for dry sliding wear using a pin-on-disc equipment provided by DUCOM, as illustrated in Figure 2. The specimen was positioned next to the neutralising face of a revolving disc circular with a 60 mm wide wear route. Using a deadweight stacking structure, the specimen was put next to the circular disc. Wear tests were performed on several specimens with typical loads of up to 80 N and a sliding speed of 4 m/s. Under the same environmental circumstances as those mentioned below, wear experiments were done for a total sliding separation

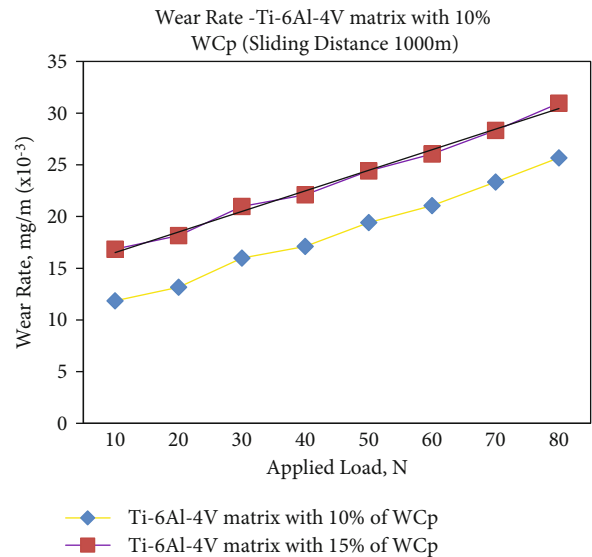


FIGURE 5: Wear rate of Ti-6Al-4V matrix with 10% WCp (sliding distance 1000 m).

of 1000 to 2000 m. Table 3 shows the complexities of the wear test limits.

Micro hardness testing is a technique for determining the micro hardness of a material using an infinitesimal scale as a reference. The MVH-II advanced miniaturised scale hardness instrument was used to calculate micro hardness

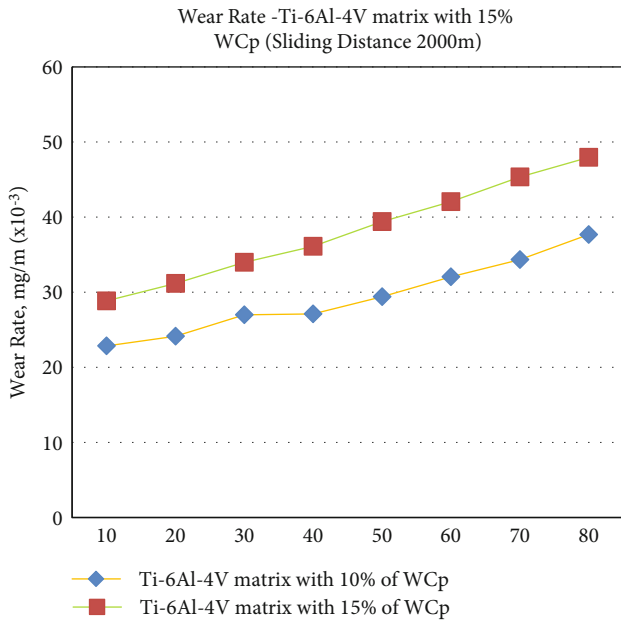


FIGURE 6: Wear rate of Ti-6Al-4V matrix with 10% WCp (sliding distance 1000 m).

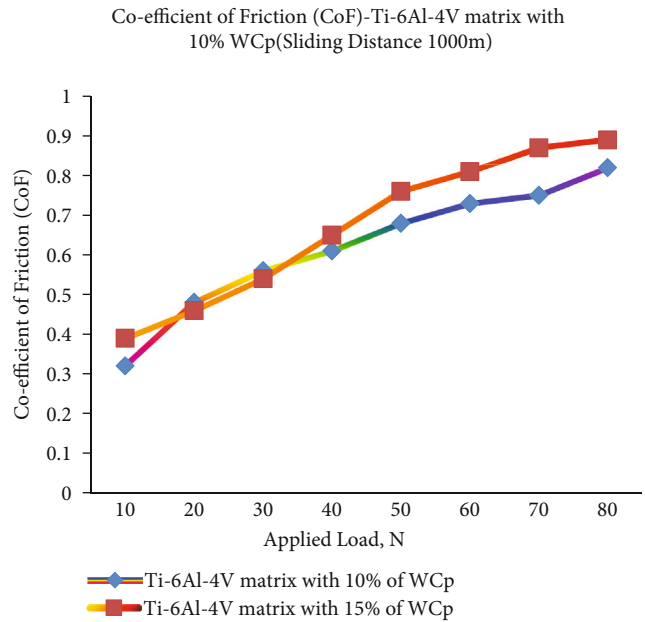


FIGURE 7: μ -Ti-6Al-4V matrix with 10%WCp (sliding distance 1000 m).

TABLE 6: μ values of Ti-6Al-4V matrix with 10% WCp (sliding distance 1000 m).

| Applied load | Ti-6Al-4V matrix with 10% of WCp | Ti-6Al-4V matrix with 15% of WCp |
|--------------|----------------------------------|----------------------------------|
| 10 | 0.32 | 0.39 |
| 20 | 0.48 | 0.46 |
| 30 | 0.56 | 0.54 |
| 40 | 0.61 | 0.65 |
| 50 | 0.68 | 0.76 |
| 60 | 0.73 | 0.81 |
| 70 | 0.75 | 0.87 |
| 80 | 0.82 | 0.89 |

TABLE 7: μ values of Ti-6Al-4V matrix with 15% WCp (sliding distance 2000 m).

| Applied load | Ti-6Al-4V matrix with 10% of WCp | Ti-6Al-4V matrix with 15% of WCp |
|--------------|----------------------------------|----------------------------------|
| 10 | 0.468 | 0.52 |
| 20 | 0.568 | 0.578 |
| 30 | 0.596 | 0.635 |
| 40 | 0.628 | 0.72 |
| 50 | 0.695 | 0.785 |
| 60 | 0.778 | 0.8469 |
| 70 | 0.84 | 0.924 |
| 80 | 0.88 | 0.9556 |

for this study. A diamond stone indenter is placed on the material to be tested, which can range in weight from a few grammes to one kilogramme. The length of the impres-

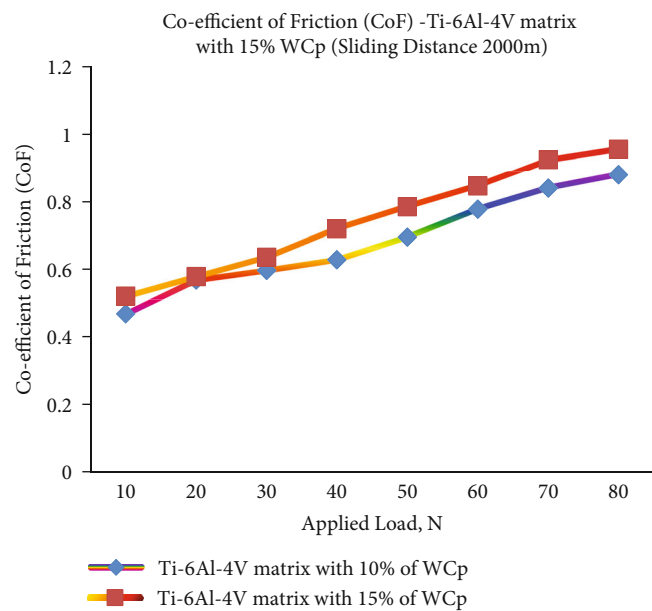


FIGURE 8: μ -Ti-6Al-4V matrix with 15%WCp (sliding distance 2000 m).

sion is defined by the size of a magnifying lens, and the applied force is used to estimate the assessment of micro hardness. A square-formed indenter is utilized in most micro hardness testing. They picked a load that is applied to the material using the analyzer’s dead loads [16].

3. Result and Discussion

3.1. *Optical Microscope and SEM Analysis.* Figures 3(a) and 3(b) show TMCs formed by squeeze casting and their

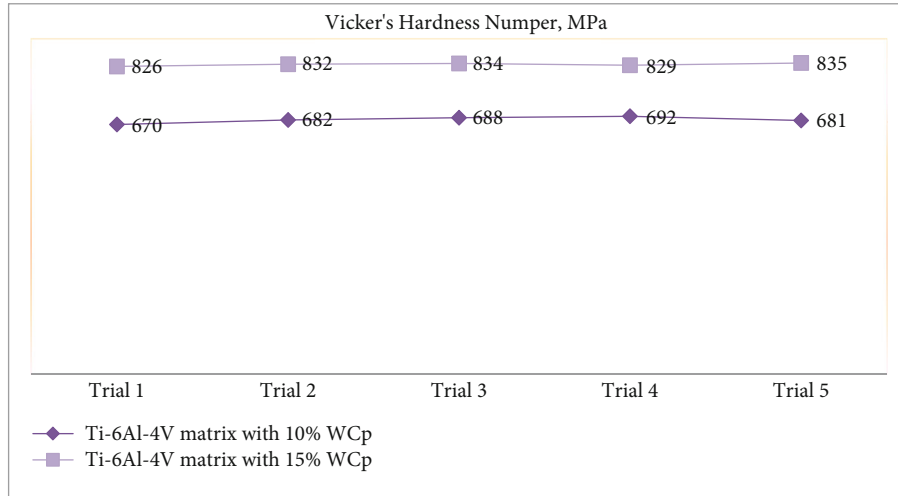


FIGURE 9: Micro hardness of the Ti-6Al-4V alloy matrix reinforced with WCp.

microstructure (b). When compared to stir casting, the superior uniform distribution of WCp in the titanium alloy matrix material was clearly perceived. The presence of WCp has a proclivity for the formation of cracks, and the resulting bonding leads to resilient warp with increased conignment. The exceptionally strong interfacial connection between the tungsten carbide particle and the titanium matrix causes rapid fracture of composites in the form of fractures and shatter, which is assessed by dimples, voids, clusters, and cracks [41–46].

Figure 4 demonstrates the worn surface of squeeze casting Ti-6Al-4V with 10% WCp and 15% WCp composites at up to 80 N load. As a result of the heavy force at the make contact with surface, the result displays the arrangement of plastic deformation, fine grooves, debris, delamination, micro fractures, and pit holes, as well as the path to further amount of material subtraction from the samples. Furthermore, it was well known that void, delamination, and particle supplement deficiencies were not found on worn surfaces. As a result of luminosity plastic deformation at the contact surface due to squeezing, our findings point to a moderate delamination with fewer damages and tiny grooves [42–45].

3.2. Wear Rate Analysis and Coefficient of Friction (CoF).

Wear regularly arises while multipart facades living being contacted mutually owing to relative motion; accordingly, material defeat arises. Therefore, the amount of wear is supposed to be moderated in practical applications automotive, aircraft, spacecraft, medical equipment, and defense, particularly for decisive works. The figure shows the wear rate of different WCp reinforcements and sliding distance various from 1000 m to 2000 m. The wear rate values are listed in Tables 4 and 5.

Figures 5 and 6 show how the wear rates of Ti-6Al-4V alloys reduce as the WCp augments virtually. The wear rate values are 25.683 for 10% WCp, 30.957 for 15% WCp, and 37.683 and 30.957 for 20% WCp. The Ti-6Al-4V/WCp com-

posite materials accurately confirm a cryptogram of superior wear rate, in which the influence of applied load ranges from 10 N to 80 N on wear rate and is only evident beginning the fracture amid the wear rate curve connives for varied wt percent of reinforcements. The WCp is important for the wear rate of urbanised TMCs, and the majority of researches have noticed the same residue [16, 42].

CoF is computed as

$$\mu = \frac{FF}{P}, \quad (1)$$

where μ is the coefficient of friction, FF is the frictional force, and P is the applied load.

When the sliding speed and distance were increased from 1000 to 2000 m, the WCp and applied load revealed a reduction in μ . With a virtual increase in the WCp, μ of Ti alloys decreases. It is easy to imagine that low CoF values for TMCs were reached at sliding speeds. The μ values for 10% WCp are 0.82, 0.87, and 0.88 and 0.956 for 15% WCp, respectively, as shown in Tables 6 and 7. When compared to Figures 7 and 8, it is clear that the TMCs substantiate a pattern of increased μ . Nearby, the collision of WCp and applied stress up to 80 N on μ has widened, as seen by the crack between the μ camber conspiring for 10% and 15% of reinforcements. The μ values grow continuously as WCp overhangs from the matrix [43]. The current research enfolds up for μ growth for all TMC samples as the applied load rises, with the goal of additionally expanding at sliding speed.

3.3. *Micro Hardness.* Figure 9 illustrates the micro hardness of Ti-6Al-4V alloys reinforced with 10% and 15% WCp. The micro hardness of the composite samples primarily depends on the circulation of WCp. Enhanced micro hardness can be attained in nearly every one of the TMC samples by inserting the tungsten particles and glowing spreading in the matrix. The micro hardness values are listed in Table 8.

TABLE 8: Micro hardness values of the Ti-6Al-4V alloy matrix reinforced with WCp.

| Trial | Ti-6Al-4V matrix with 10% WCp | Ti-6Al-4V matrix with 15% WCp |
|-------|-------------------------------|-------------------------------|
| 1 | 670 | 826 |
| 2 | 682 | 832 |
| 3 | 688 | 834 |
| 4 | 692 | 829 |
| 5 | 681 | 835 |

The micro hardness values are 692 VHN for 10% WCp and 835 VHN for 15% WCp. The consequences illustrated to advance the superior micro hardness of the composite by using a squeeze casting route to prepare the composites. The Ti-6Al-4V alloy matrix material reinforced with TiC, TiB, B4C, BN, and (Ti,Mo)C/C particles achieved hardness of 766 HV, 19.6 GPa, 971 HV, 1168 HV, and 15 GPa, respectively, and compared with the current investigation, using WCp particles improved superior hardness of the composites [44–49].

4. Conclusion

The subsequent interpretation was haggard commencing this present investigative work:

- (i) Squeeze castings were produced efficiently using two distinct TMCs, including Ti-6Al-4V alloys strengthened with 10% and 15% WCp
- (ii) When compared to stir casting, the superior uniform distribution of WCp in the Ti-6Al-4V alloy matrix material was perceptibly assumed
- (iii) The significance indicated the preparation of plastic deformation, superior grooves, debris, delaminating, micro fractures, and pit holes due to deep force at the contact surface, verifying the approach to supplemental quantity of material deletion from the samples
- (iv) The wear rate values are 25.683 for 10% WCp, 30.957 for 15% WCp, and 37.683 and 30.957 for 20% WCp. It is established that Ti-6Al-4V/WCp composites authenticate a higher wear rate cypher, that the conflict of applied load up to 80 N on wear rate is extremely large, and that the rupture between the wear rate connives for different wt percent of reinforcements which purely manifest beginning the rupture between the wear rate connives for different wt percent of reinforcements. For 10% WCp, the CoF values are 0.82 and 0.87, and for 15% WCp, 0.88 and 0.956
- (v) The micro hardness values are 692 VHN for 10% WCp and 835 VHN for 15% WCp. The fine showed to precede the higher micro hardness of the TMCs by using a squeeze casting route to practice the composites

Data Availability

The data used to support the findings of this study are included in the article. Should further data or information be required, these are available from the corresponding author and upon request.

Conflicts of Interest

The authors declare that they have no conflicts of interest.

References

- [1] R. Arunachalam, P. K. Krishnan, and R. A. Muraliraja, "Review on the production of metal matrix composites through stir casting–furnace design, properties, challenges, and research opportunities," *Journal of Manufacturing Processes*, vol. 42, pp. 213–245, 2019.
- [2] H. Attar, S. Ehtemam-Haghighi, D. Kent, and M. S. Dargusch, "Recent developments and opportunities in additive manufacturing of titanium-based matrix composites: a review," *International Journal of Machine Tools and Manufacture*, vol. 133, pp. 85–102, 2018.
- [3] V. Suresh, N. Hariharan, S. Paramesh, M. Prasath Kumar, and P. Arun Prasath, "Tribological behaviour of aluminium/boron carbide (B<SUB align="right">4C)/graphite (Gr) hybrid metal matrix composite under dry sliding motion by using ANOVA," *International Journal of Materials and Product Technology*, vol. 53, no. 3/4, pp. 204–217, 2016.
- [4] G. Huang, W. Hou, and Y. Shen, "Evaluation of the microstructure and mechanical properties of WC particle reinforced aluminum matrix composites fabricated by friction stir processing," *Materials Characterization*, vol. 138, pp. 26–37, 2018.
- [5] X. Zeng, W. Liu, B. Xu, G. Shu, and Q. Li, "Microstructure and mechanical properties of Al–SiC nanocomposites synthesized by surface-modified aluminium powder," *Metals*, vol. 8, no. 4, p. 253, 2018.
- [6] M. D. Hayat, H. Singh, Z. He, and P. Cao, "Titanium metal matrix composites: an overview," *Composite Part: A*, vol. 121, pp. 418–438, 2019.
- [7] G. Singh and U. Ramamurty, "Boron modified titanium alloys," *Progress in Materials Science*, vol. 111, article 100653, 2020.
- [8] S. Sun, E. Zhao, C. Hu et al., "Deformation behavior and softening mechanism of TiB reinforced near- α titanium matrix composite during hot compression," *Journal of Materials Research and Technology*, vol. 9, no. 6, pp. 13250–13263, 2020.
- [9] X. N. Mu, H. M. Zhang, H. N. Cai et al., "Microstructure evolution and superior tensile properties of low content graphene nanoplatelets reinforced pure Ti matrix composites," *Materials Science and Engineering: A*, vol. 687, pp. 164–174, 2017.
- [10] L. Wang, Q. Fan, X. Zhu et al., "Effect of tungsten micro-scale dispersed particles on the microstructure and mechanical properties of Ti-6Al-4V alloy," *Journal of Alloys and Compounds*, vol. 851, article 156847, 2021.
- [11] M. Meignanamoorthy, M. Ravichandran, S. V. Alagarsamy, C. Chanakyan, S. Dinesh Kumar, and S. Sakthivelu, "Effect of various reinforcements on properties of metal matrix composites: a review," *Materials Today Proceedings*, vol. 27, pp. 1118–1121, 2020.
- [12] V. Suresh, N. Hariharan, and S. Vellingiri, "An investigation on the tensile properties and micro-structure of hybrid metal

- matrix composites," *Int. J. Materials and Product Technology*, vol. 56, no. 1/2, pp. 84–94, 2018.
- [13] K. Kondoh, "Titanium metal matrix composites by powder metallurgy (PM) routes," *Titanium Powder Metallurgy: Science, Technology and Applications*, vol. 34, pp. 277–297, 2015.
- [14] I. N. Maliutina, H. Si-Mohand, R. Piolet et al., "Laser cladding of γ -TiAl intermetallic alloy on titanium alloy substrates," *Metallurgical and Materials Transactions A*, vol. 47, no. 1, pp. 378–387, 2016.
- [15] L. Geng, D. R. Ni, J. Zhang, and Z. Z. Zheng, "Hybrid effect of TiBw and TiCp on tensile properties of *in situ* titanium matrix composites," *Journal of Alloys and Compounds*, vol. 463, no. 1-2, pp. 488–492, 2008.
- [16] R. Venkatesan Govindarajan, P. P. Sivakumar, S. Patil et al., "Effect of tungsten carbide addition on the microstructure and mechanical behavior of titanium matrix developed by powder metallurgy route," *Advances in Materials Science and Engineering*, vol. 2022, 7 pages, 2022.
- [17] H. Chen, Z. Gui, X. Wang, X. Gao, and D. Liu, "A novel nano interface for particulate-reinforced titanium matrix composites," *Journal of the American Ceramic Society*, vol. 105, no. 1, pp. 67–75, 2022.
- [18] G. Sivakumar, V. Ananthi, and S. Ramanathan, "Production and mechanical properties of nano SiC particle reinforced Ti-6Al-4V matrix composite," *Transactions of Nonferrous Metals Society of China*, vol. 27, no. 1, pp. 82–90, 2017.
- [19] G. Li, K. Munir, W. Cuie, Y. Li, and S. Ding, "Machinability of titanium matrix composites (TMC) reinforced with multi-walled carbon nanotubes," *Journal of Manufacturing Processes*, vol. 56, pp. 131–146, 2020.
- [20] Y. Ren, P. Chen, Z. Li, Z. Zhang, Y. Lv, and C. Zhang, "Effect of strain rate on the mechanical properties of a tungsten particle reinforced titanium matrix composite," *Journal of Materials Research and Technology*, vol. 15, pp. 984–995, 2021.
- [21] K. D. Traxel and A. Bandyopadhyay, "Designing high-temperature oxidation-resistant titanium matrix composites via directed energy deposition-based additive manufacturing," *Materials and Design*, vol. 212, article 110205, 2021.
- [22] J. Yang, J. Shen, Y. Liang et al., "Advanced tensile properties and strain rate sensitivity of titanium matrix composites reinforced with CaTiO_3 particles," *Journal of Alloys and Compounds*, vol. 897, article 163229, 2022.
- [23] S. Sun, E. Zhao, C. Hu, Y. An, and W. Chen, "Precipitation behavior of silicide and synergetic strengthening mechanisms in TiB-reinforced high-temperature titanium matrix composites during multi-directional forging," *Journal of Alloys and Compounds*, vol. 867, article 159051, 2021.
- [24] D. Liu, P. Hu, and G. Min, "Interfacial reaction in cast WC particulate reinforced titanium metal matrix composites coating produced by laser processing," *Optics and Laser Technology*, vol. 69, pp. 180–186, 2015.
- [25] S. K. Thandalam, S. Ramanathan, and S. Sundarrajan, "Synthesis, microstructural and mechanical properties of *ex situ* zircon particles (ZrSiO_4) reinforced metal matrix composites (MMCs): a review," *Journal of Materials Research and Technology*, vol. 4, no. 3, pp. 333–347, 2015.
- [26] J. Khosravi, M. K. B. Givi, M. Barmouz, and A. Rahi, "Microstructural, mechanical, and thermophysical characterization of Cu/WC composite layers fabricated via friction stir processing," *International Journal of Advanced Manufacturing Technology*, vol. 74, no. 5-8, pp. 1087–1096, 2014.
- [27] W. A. Waleed, A. Chathriyan, and R. S. S. Vimal, "Experimental investigation on the influence of process parameters in thermal drilling of metal matrix composites," *FME Transactions*, vol. 46, no. 3, pp. 171–176, 2018.
- [28] S. Chatterjee, S. Ghosh Sur, S. Bandyopadhyay, and A. Basumallick, "Effect of microstructure and residual stresses on nano-tribological and tensile properties of Al_2O_3 - and SiC-reinforced 6061-Al metal matrix composites," *Journal of Composite Materials*, vol. 50, no. 19, pp. 2687–2698, 2016.
- [29] S. Vellingiri, V. Senthil, and Z. Basha, "Modelling and multi objective optimization of LM13 aluminium alloy squeeze cast process parameters using Taguchi and genetic algorithm," *Meta*, vol. 57, no. 1-2, pp. 55–55, 2018.
- [30] R. Soundararajan, A. Ramesh, S. Sivasankaran, and A. Sathishkumar, "Modeling and analysis of mechanical properties of aluminium alloy (A413) processed through squeeze casting route using artificial neural network model and statistical technique," *Advances in Materials Science and Engineering*, vol. 2015, 16 pages, 2015.
- [31] A. B. Elshalakany, T. A. Osman, A. Khattab, B. Azzam, and M. Zaki, "Microstructure and mechanical properties of MWCNTs reinforced A356 aluminum alloys cast nanocomposites fabricated by using a combination of rheocasting and squeeze casting techniques," *Journal of Nanomaterials*, vol. 2014, 14 pages, 2014.
- [32] A. Dmitruk, A. Żak, K. Naplocha, W. Dudziński, and J. Morgiel, "Development of pore-free Ti-Al-C MAX/Al-Si MMC composite materials manufactured by squeeze casting infiltration," *Materials Characterization*, vol. 146, pp. 182–188, 2018.
- [33] R. Choudhary, A. Kumar, G. Yadav, R. Yadav, V. Kumar, and J. Akhtar, "Analysis of cryogenic tool wear during electrical discharge machining of titanium alloy grade 5," *Materials Today: Proceedings*, vol. 26, pp. 864–870, 2020.
- [34] M. Swapna Sai, V. Dhinakaran, K. P. Manoj Kumar, V. Rajkumar, B. Stalin, and T. Sathish, "A systematic review of effect of different welding process on mechanical properties of grade 5 titanium alloy," *Materials Today: Proceedings*, vol. 21, pp. 948–953, 2020.
- [35] D.-f. Mo, T.-f. Song, Y.-j. Fang et al., "A review on diffusion bonding between titanium alloys and stainless steels," *Advances in Materials Science and Engineering*, vol. 2018, 15 pages, 2018.
- [36] G. Deepak Kumar, S. Uday Kumar, S. Chattopadhyaya, and S. Mandal, "Investigation into the TIG welded joint of titanium G-5 alloy sheet," *IOP Conference Series: Materials Science and Engineering*, vol. 377, pp. 1–8, 2018.
- [37] Q. Ma, Y. Li, and J. Wang, "Effects of Ti addition on microstructure homogenization and wear resistance of wide-band laser clad Ni60/WC composite coatings," *International Journal of Refractory Metals and Hard Materials*, vol. 64, pp. 225–233, 2017.
- [38] Y. Wu, X. Liu, G. Ma, C. Li, and J. Zhang, "High energy milling method to prepare Al/WC composite coatings in Al-Si alloys," *Journal of Alloys and Compounds*, vol. 497, no. 1-2, pp. 139–141, 2010.
- [39] A. Lekatou, A. E. Karantzalis, A. Evangelou et al., "Aluminium reinforced by WC and TiC nanoparticles (*ex-situ*) and aluminate particles (*in-situ*): microstructure, wear and corrosion behaviour," *Materials & Design*, vol. 65, pp. 1121–1135, 2015.
- [40] S. Amirkhanlou, M. Ketabchi, N. Parvin, S. Khorsand, and F. Carreno, "Effect of processing cycles on aluminum/tungsten

- carbide composites prepared by continual annealing and press bonding process,” *IOP Conference Series: Materials Science and Engineering*, vol. 63, pp. 12002–12004, 2014.
- [41] A. V. Pozdniakov, A. Lotfy, A. Qadir et al., “Development of Al-5Cu/B₄C composites with low coefficient of thermal expansion for automotive application,” *Materials Science & Engineering A*, vol. 688, pp. 1–8, 2017.
- [42] N. Radhika and R. Raghu, “Investigation on mechanical properties and analysis of dry sliding wear behavior of Al LM13/AlN metal matrix composite based on Taguchi’s technique,” *Journal of Tribology*, vol. 139, no. 4, pp. 1–18, 2016.
- [43] N. Selvakumar and P. Narayanasamy, “Optimization and effect of weight fraction of MoS₂ on the tribological behavior of Mg-TiC-MoS₂ hybrid composites,” *Tribology Transactions*, vol. 59, no. 4, pp. 733–747, 2016.
- [44] L. Li, D. Wang, W. Song, J. Gong, Q. Hu, and X. Zeng, “Microstructures and mechanical properties of WCP/Ti-6Al-4V composite coatings by laser melt injection and laser-induction hybrid melt injection,” *Surface and Coatings Technology*, vol. 385, article 125371, 2020.
- [45] J. A. Vreeling, V. Ocelík, and J. T. M. De Hosson, “Ti-6Al-4V strengthened by laser melt injection of WCp particles,” *Acta Materialia*, vol. 50, no. 19, pp. 4913–4924, 2002.
- [46] O. F. Ochonogor, E. T. Akinlabi, K. D. Nyembwe, S. Pityana, and M. B. Shongwe, “Particle variations and effect on the microstructure and microhardness of Ti6Al4V hybrid metal matrix system,” *Procedia Manufacturing*, vol. 7, pp. 616–621, 2017.
- [47] W.-H. Wei, Z.-N. Shao, J. Shen, and X.-M. Duan, “Microstructure and mechanical properties of in situ formed TiC-reinforced Ti-6Al-4V matrix composites,” *Materials Science and Technology*, vol. 34, no. 2, pp. 1–8, 2018.
- [48] Y. Wen, T. Guo, Y. Zhou, H. Bai, and Z. Wang, “Nanoindentation characterization on microhardness of micron-level TiC and TiB reinforcements in in-situ synthesized (TiC+TiB)/Ti-6Al-4V composite,” *Frontiers in Materials*, vol. 6, p. 205, 2019.
- [49] A. Biedunkiewicz, P. Figiel, D. Garbiec et al., “Influence of elemental carbon (EC) coating covering nc-(Ti,Mo)C particles on the microstructure and properties of titanium matrix composites prepared by reactive spark plasma sintering,” *Materials*, vol. 14, no. 1, p. 231.

Research Article

Bioinspired Crosslinked Nanocomposites of Polyvinyl Alcohol-Reinforced Cellulose Nanocrystals Extracted from Rice Straw with Ethanedioic Acid

Kwok-Mern Chin,¹ Sung Ting Sam ^{1,2}, Hui Lin Ong,^{1,3,4} Yee Shian Wong,⁵ Wai Kian Tan,⁶ and Vilay Vannaladsaysy ⁷

¹Faculty of Chemical Engineering Technology, Universiti Malaysia Perlis (UniMAP), 02600 Arau, Perlis, Malaysia

²Centre of Excellence Geopolymer and Green Technology (CEGeoGTech), Universiti Malaysia Perlis, Kompleks Pusat Pengajian Jejawi 2, Taman Muhibbah, 02600 Arau, Perlis, Malaysia

³Centre of Excellence for Biomass Utilization, Universiti Malaysia Perlis, Lot 17, Kompleks Pusat Pengajian Jejawi 2, 02600 Arau, Perlis, Malaysia

⁴Taiwan-Malaysia Innovation Center for Clean Water and Sustainable Energy (WISE Center), Lot 17, Kompleks Pusat Pengajian Jejawi 2, 02600 Arau, Perlis, Malaysia

⁵Faculty of Civil Engineering Technology, Universiti Malaysia Perlis (UniMAP), 02600 Arau, Perlis, Malaysia

⁶Institute of Liberal Arts and Science, Toyohashi University of Technology, Toyohashi, Aichi 441-8580, Japan

⁷Department of Mechanical Engineering, Faculty of Engineering, National University of Laos (NUOL), P.O. Box 3166, Sokpaluang Campus, 01005 Lao-Thai Friendship Rd, Vientiane Capital City, Laos

Correspondence should be addressed to Sung Ting Sam; stsam@unimap.edu.my and Vilay Vannaladsaysy; vilay_me@fe-nuol.edu.la

Received 16 March 2022; Accepted 11 June 2022; Published 4 July 2022

Academic Editor: V. Vijayan

Copyright © 2022 Kwok-Mern Chin et al. This is an open access article distributed under the Creative Commons Attribution License, which permits unrestricted use, distribution, and reproduction in any medium, provided the original work is properly cited.

In this study, cellulose nanocrystals (CNC) were extracted from rice straw and incorporated into polyvinyl alcohol (PVOH) as reinforcement nanofillers. Multiple nanocomposites with different CNC contents were prepared. Extracted CNC appear as long, well-defined rodlike crystals with a high aspect ratio (41). Nanocomposites with 3 wt% of CNC significantly exhibit improved tensile strength (60.4%) and maximum degradation temperature (287°C). Moreover, they demonstrate a decrease in water vapor permeability rate and in the swelling and solubility indices of PVOH/CNC. Significant improvements were observed when nanocomposites were crosslinked specifically in terms of tensile strength (104.8%) and maximum degradation temperature (364°C). They also demonstrate greatly reduced water vapor permeability rate, swelling, and solubility indices. The optimum CNC amount for both nanocomposites is 3 wt%.

1. Introduction

Plastic is a synthetic polymer that is versatile and durable and has a low production cost; it is also the material of choice for numerous applications worldwide. However, plastics are non-degradable. The significant increase in the use of and dependence on plastics has also increased the waste stream, and this is an issue for the ecosystem and the environment [1–4]. The common nondegradable polymers, such as polyethylene,

polypropylene, polyvinyl chloride, and polystyrene, are consumer market dominators that constitute the vast majority of the products that end up in landfills; moreover, they are extremely resistant to degradation [5–10]. In response to this, researchers must design environmentally friendly substitutes (e.g., polymers that are biodegradable when exposed to the environment). One of the most perfect examples of biodegradable synthetic polymers is polyvinyl alcohol (PVOH). PVOH is a conventional water-soluble polymer with a substantial

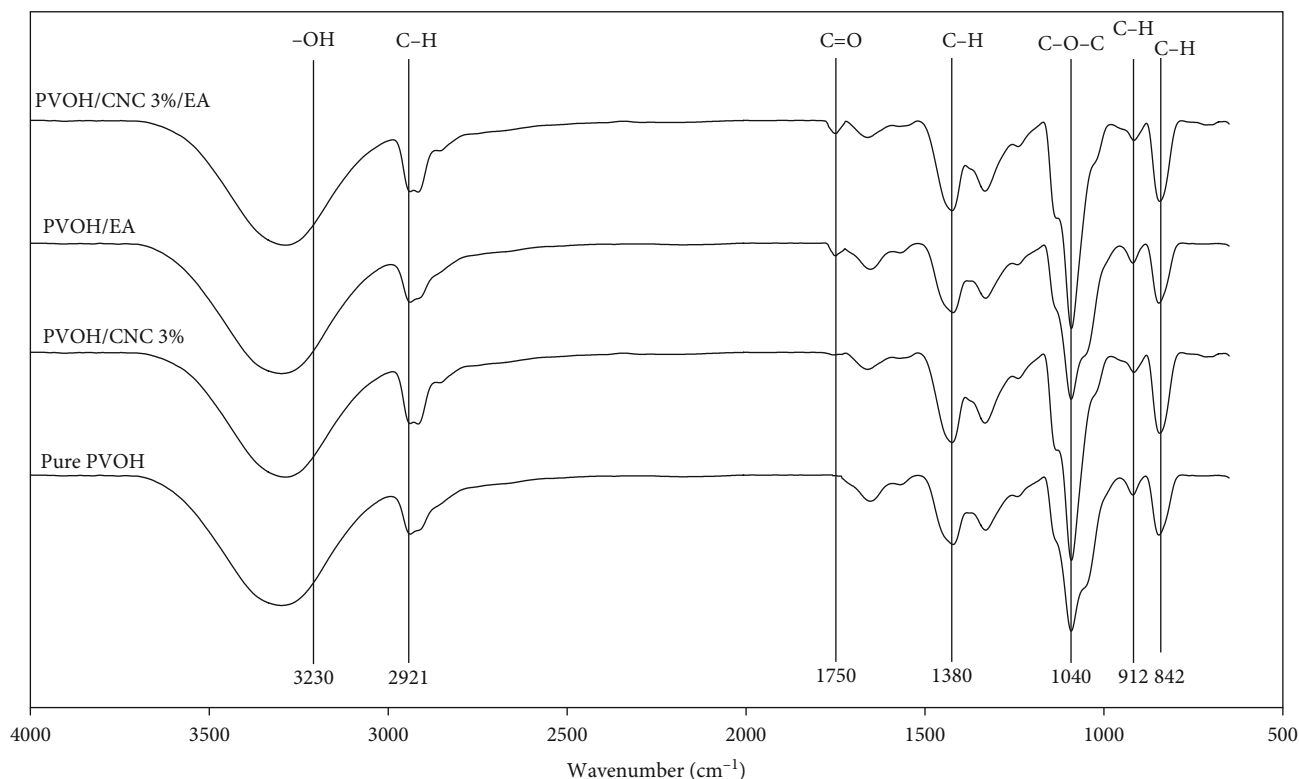


FIGURE 1: FTIR spectra of pure PVOH, crosslinked PVOH, and crosslinked and non-crosslinked nanocomposites with 3 wt% CNC.

value to the manufacturing industry as it is nontoxic and fully biodegradable and has exceptional biocompatibility [11–13]. PVOH can be adaptively manufactured to suit multiple applications by varying its degree of hydrolysis and its average molecular weight. In addition, PVOH is used in packaging industries owing to its excellent film-forming capability (but only in niche applications due to its water sensitivity).

Researchers are currently focusing on the enhancement and improvement of the properties of neat polymers through the addition of small amounts of inexpensive and environmentally friendly fillers. The conversion of “waste to wealth” is a common interest among the scientific and global communities; thus, agricultural wastes, such as rice straw, sugarcane bagasse, and soy hulls, are the main materials used in the current research. Nanotechnology has warranted exciting opportunities within the realm of material science, especially in the use of nanocellulose derived from renewable sources to improve the properties of polymers as reinforcement filler materials. Nanocellulose exists in multiple forms, namely, cellulose nanocrystals (CNC) and cellulose nanofibers (CNF), depending on the extraction method [14]. CNF are mainly obtained through mechanical fibrillation (a process that requires a huge amount of energy), whereas the production of CNC depends on strong chemical treatment, such as acid hydrolysis [15–18]. Compared with CNF, CNC retain only the crystalline regions of cellulose and are thus preferred [19–23]. However, the inherent hydrophilic nature of CNC with $-OH$ side groups limits their widespread use as reinforcement fillers. The mechanical strength of hydrophobic polymer-reinforced CNC is unfavorable due to the incompat-

ibility between the two counterparts, leading to weak dispersion and serious agglomeration of the CNC [24–26]. To solve these compatibility issues, surface functionalization of nanocellulose, such as TEMPO oxidation, acetylation, acylation, silylation, and polymer grafting, is performed to promote dispersibility of the CNC in hydrophobic polymers by changing the hydrophilic nature of CNC. However, these methods require tedious processing routes and may disrupt the structural integrity of the CNC [27]. Hence, CNC are best utilized in a natural state.

Despite its limitation in widespread applications, neat PVOH can be modified to suit the needs for its end-use application. PVOH crosslinking is one of the best solutions as this method is capable of inducing a tight three-dimensional structured network of molecules that demonstrate hydrophobicity and enhanced properties [28–32]. The hydroxyl groups present in PVOH are the target of reactions, most commonly with chemical compounds, such as dialdehydes, anhydrides, and carboxylic acids [33–38]. Research on crosslinkers such as glutaraldehyde [39–41], epichlorohydrin [42, 43], formaldehyde [44, 45], hexamethoxymethylmelamine [46], and sodium trimetaphosphate [47, 48] indicates that they are not preferable owing to their toxicity. Therefore, the focus of this study is the crosslinking reaction between a natural dicarboxylic acid and ethanedioic acid (EA) on PVOH with different CNC ratios as it is the simplest crosslinking reaction and is environmentally friendly. The tensile properties, degree of crystallinity, and water and thermal stability of non-crosslinked and crosslinked nanocomposites are investigated.

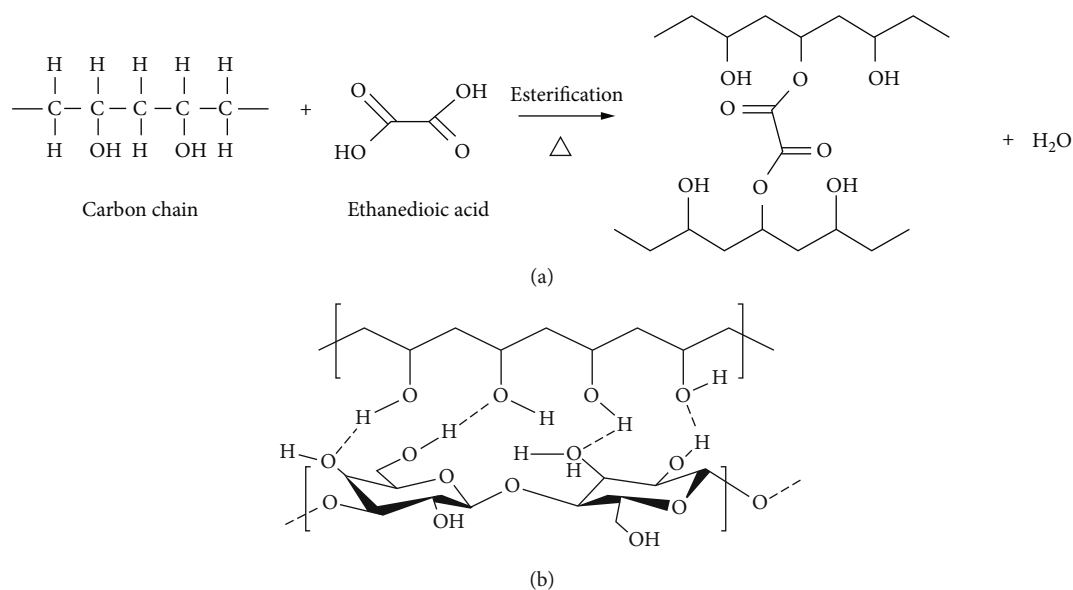


FIGURE 2: (a) Crosslinking mechanism between PVOH carbon chains with EA. (b) Schematic representation of the interaction between PVOH carbon chains and CNC.

2. Methods

2.1. Materials. Dried rice straw was obtained from a paddy field located in Arau, Perlis, Malaysia ($6^{\circ}25'58.0''N + 100^{\circ}13'56.8''E$). PVOH (98% hydrolyzed) with an Mw of 89,000–98,000 was purchased from Sigma-Aldrich (Malaysia). Sodium hydroxide (NaOH), sodium chlorite ($NaClO_2$), and acetic acid glacial (CH_3COOH) was purchased from Merck (Malaysia), Acros Organics (Malaysia), and HmbG (Malaysia), respectively. The sulfuric acid (95%–97%) used for the CNC extraction was purchased from Merck (Malaysia). EA was purchased from Sigma-Aldrich (Malaysia). Deionized water was used consistently throughout the experiment.

2.2. Microcrystalline Cellulose and CNC Extraction. Dried rice straw was washed with water to remove dirt and other impurities before drying in an enclosed environment for 48 h. The rice straw was then converted to a powder form by using a mill grinder prior to separation through a $150\ \mu m$ mesh screen. Microcrystalline cellulose (MCC) and CNC from rice straw were extracted through alkaline treatment, bleaching, and acid hydrolysis with slight modification to the process described by Chan and coworkers [49]. Next, the separated rice straw powder was treated with a 4% aqueous solution of NaOH (w/w) for a total of 2 h at $80^{\circ}C$ under mechanical stirring. Then, the rice straw fiber was washed several times with deionized water until the pH reached 7. Subsequently, the rice straw fiber was bleached with a solution comprising equal parts ($v : v$) acetate buffer (40 g NaOH, 75 mL glacial acetic acid, diluted to 1 L with distilled water) and sodium hypochlorite (1.7 wt% $NaClO_2$). This treatment was performed at $80^{\circ}C$ for 2 h under mechanical stirring. The fiber was washed with deionized water until the pH reached 7 again. A total of four cycles of alkaline and bleaching treatment were completed to

obtain a milky white MCC pulp. Acid hydrolysis was performed with 64 wt% H_2SO_4 at the optimal temperature of $45^{\circ}C$ for 45 min. This process is important to eliminate the amorphous regions of cellulose to achieve the desired highly crystalline CNC. Immediately after 45 min, tenfold of cold deionized water was added to halt the hydrolysis reaction. The suspension was then washed with a copious amount of deionized water and centrifuged at 10,000 rpm. This process was repeated until a CNC suspension with a pH of 6–7 was achieved. Gravimetric method which consist of convection oven drying of CNC at $105^{\circ}C$ was adopted to determine the final concentration of CNC in the final suspension after sonication [50].

2.3. Preparation of PVOH/CNC Nanocomposites. PVOH/CNC-film nanocomposites were produced using the solution casting method. PVOH powder was dissolved in water at $90^{\circ}C$ with mechanical stirring for 2 h in order to obtain a 2 wt% solution. CNC of known weight percentages (1, 3, 5, and 7 wt%) were added concurrently. For nanocomposite films with EA, 5 wt% of EA was added during the final 30 min to prevent acidolysis. The final solution was poured into a glass mold and oven-dried at $40^{\circ}C$ for 24 h. Thermally crosslinked films were obtained via thermal curing of the films with EA in a convection oven at $130^{\circ}C$ for 30 min. All the films were stored in a desiccator for 72 h before the measurements were performed.

2.4. Fourier Transform Infrared Spectroscopy. Fourier transform infrared spectroscopy (FTIR) spectra were obtained through a small cut of PVOH/CNC and PVOH/CNC/EA nanocomposite films in the range of $4,000$ to $650\ cm^{-1}$ wavenumbers with 32 scans using a PerkinElmer Spectrum 10 spectrophotometer. Beforehand, the samples were washed thoroughly with water and acetone to remove the unreacted excess EA on the surface of the samples. The samples were

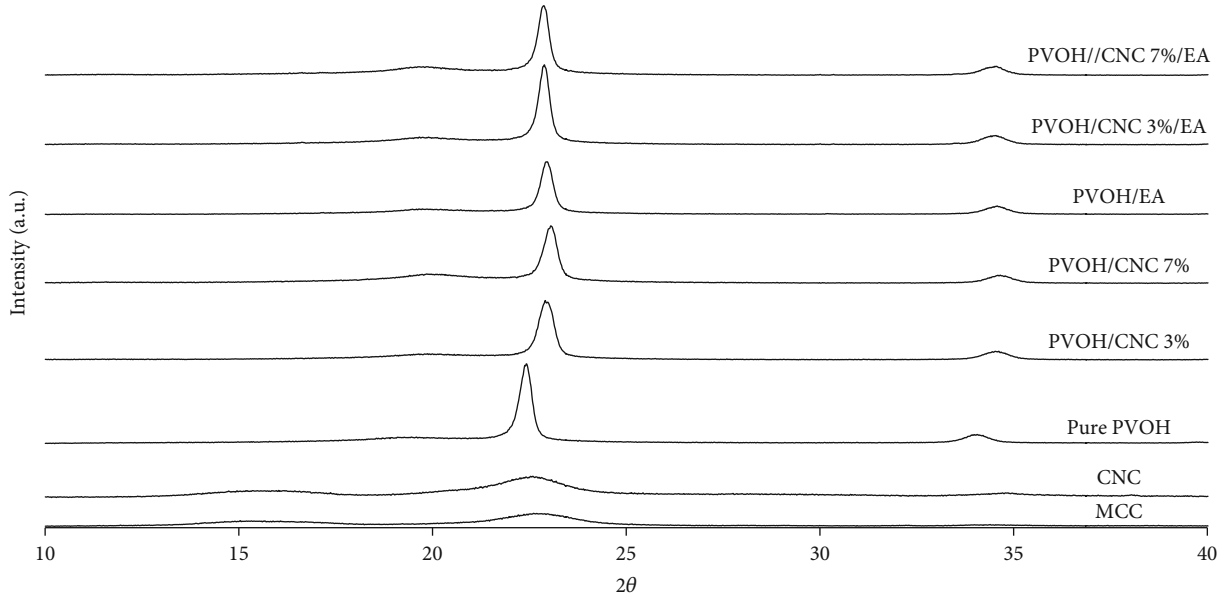


FIGURE 3: XRD diffractogram of nanocomposites of varying CNC contents with and without the addition of EA.

TABLE 1: CrI of MCC, CNC, pure PVOH, crosslinked PVOH, and crosslinked and non-crosslinked nanocomposite with 3 wt% and 7 wt% CNC.

| Sample | Crystallinity index (CrI) |
|----------------|---------------------------|
| Pure PVOH | 66.1% |
| PVOH/CNC 3% | 70.4% |
| PVOH/CNC 7% | 67.5% |
| PVOH/EA | 65.0% |
| PVOH/CNC 3%/EA | 69.1% |
| PVOH/CNC 7%/EA | 65.5% |
| MCC | 60.8% |
| CNC | 74.3% |

then oven-dried to remove moisture before analysis was conducted.

2.5. X-Ray Diffraction. A Bruker D2 Phaser X-ray diffractometer with a monochromatic Cu-K α radiation source was used to obtain the X-ray diffraction (XRD) patterns of the CNC and the PVOH nanocomposites. The measurement parameters were 0.02° step size in the range of 10° to 40° of a 2 θ angle. The crystallinity index (CrI) was determined by calculating the peak area from the diffraction peaks using the Segal method. The formula of the calculation is as follows:

$$\text{Crystallinity index (CrI)} = \frac{(I_{002} - I_{AM})}{I_{002}} \times 100, \quad (1)$$

where CrI denotes the degree of crystallinity (%), I_{002} is the maximum intensity of 0 0 2 lattice diffraction, and I_{AM} is the diffraction intensity at 2 θ = 18°.

2.6. Tensile Properties. The tensile properties of the nanocomposite films were examined on a universal testing machine (Instron 5567) in accordance with the ASTM D-882 standard procedure. A total of five 100 × 10 mm rectangular samples were cut precisely from the nanocomposite films, and the test was conducted at a crosshead speed of 20 mm/min. The tensile strength, elongation at break, and Young's modulus were obtained.

2.7. Field Emission Scanning Electron Microscopy. The surface morphology of the tensile-fractured surfaces of the nanocomposite films was observed using a field emission scanning electron microscope (FESEM, Carl Zeiss Leo Supra 50 VP Field Emission). A small cut of the fractured surface from each of the nanocomposites was adhered onto the specimen stage with carbon tape. All the samples were sputter-coated with platinum before they were examined at an accelerated voltage of 5 kV under a high-vacuum condition.

2.8. Transmission Electron Microscopy. To determine the morphology of the CNC, 10 μ L of 0.005 wt% CNC suspension was placed on a transmission electron microscopy (TEM) grid for 2 min. Excess liquid was removed with filter paper, followed by negative staining with uranyl acetate solution for another 2 min. Excess uranyl acetate solution was blotted with filter paper before letting the CNC dry at an ambient temperature. The CNC were observed under a transmission electron microscope (LIBRA 120) at 100 keV. The average length and diameter of the CNC were determined from 50 representative CNC using the ImageJ and Origin software. Gaussian distribution curves were obtained using the Origin software.

2.9. Thermogravimetric Analysis. Thermogravimetric analysis (TGA) and derivative thermogravimetry (DTG) curves were obtained through the thermal behavior analysis of the

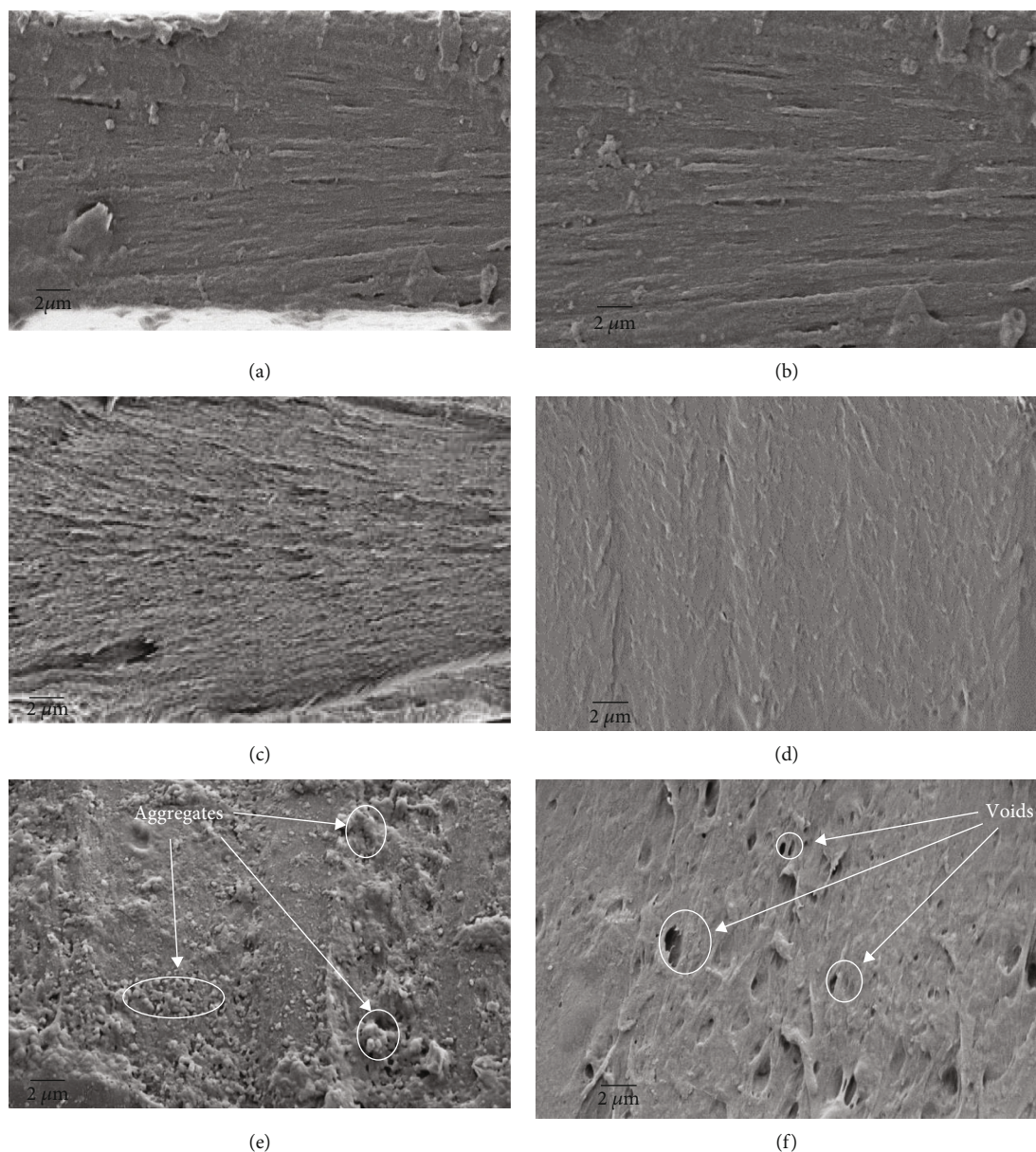


FIGURE 4: FESEM micrographs of (a) pure PVOH, (b) crosslinked PVOH, (c) 3 wt% PVOH/CNC, (d) crosslinked 3 wt% PVOH/CNC, (e) 7 wt% PVOH/CNC, and (f) crosslinked 7 wt% PVOH/CNC. Magnification: $\times 3,000$.

nanocomposites using a thermogravimetric analyzer (TGA Q50 V20.13 Build 39). A nanocomposite film (estimated weight: 5 mg) was cut and placed on the heating pan before heating from room temperature to 650°C at a rate of $10^{\circ}\text{C}/\text{min}$. Nitrogen gas purging was performed before the start of the measurement. The temperature values obtained when the weight loss of the sample reached 10% and 30% of the original weight are denoted as $T_{10\%}$ and $T_{30\%}$. T_{MAX} is the temperature at maximum weight loss of the sample.

2.10. Moisture Vapor Permeation Rate. The moisture vapor permeation (MVP) rate was determined in accordance with the wet-cup method (ASTM E96). Glass bottles with a mouth opening of 1 cm^2 were filled with deionized water and sealed with adhesive to prevent the escape of water vapor. The film samples were placed on top of these bottles

and in a humidity chamber that was set to maintain an ambient temperature of 25°C with a relative humidity of 40%. The weight of the bottle was determined every 24 h for 7 days. The MVP was calculated using

$$\text{MVP} = \frac{W_{\text{before}}}{A \times t} \quad (2)$$

W_{before} is the initial weight of the bottle filled with water and nanocomposite film. A is the mouth area of the bottle. t is the time (hours).

2.11. Swelling and Solubility Indices. Nanocomposite films ($5 \times 5\text{ cm}$) were prepared and immersed in 100 mL deionized water for 24 h at room temperature. After 24 h, the nanocomposite films were removed and dried using filter paper

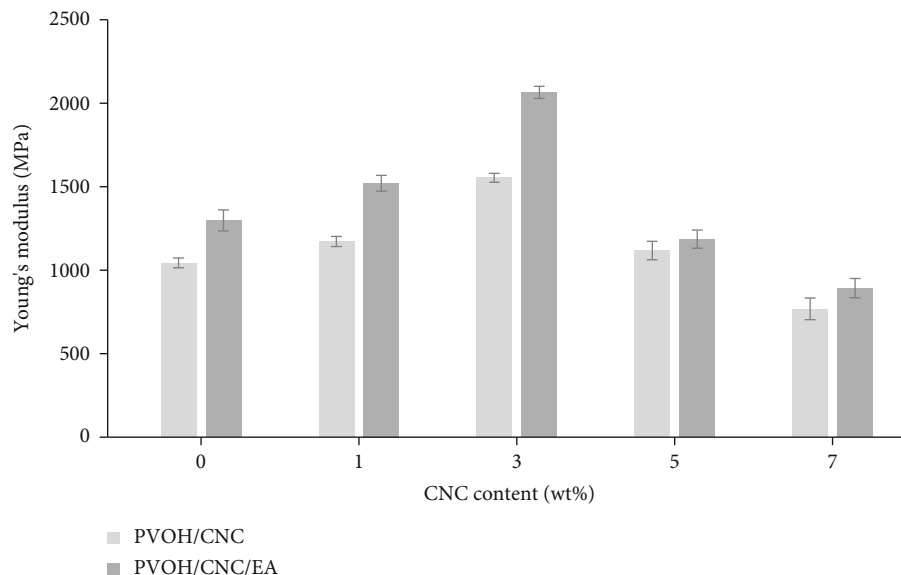


FIGURE 5: Young's modulus of the nanocomposites with varying CNC contents with and without the addition of EA.

before the weight gain and swelling were measured. The swelling index (SwI) was calculated using Equation (3). Due to the difficulty of the dissolution of fully hydrolyzed PVOH in water at room temperature, the solubility index (SoI) was determined through film immersion in heated deionized water (90°C) for 15 min. SoI was calculated using Equation (4).

$$\text{SwI} = \frac{W_{\text{gain}} - W_{\text{initial}}}{W_{\text{initial}}}, \quad (3)$$

$$\text{SoI} = \frac{W_{\text{initial}} - W_{\text{remain}}}{W_{\text{initial}}}. \quad (4)$$

W_{initial} is the initial weight of the sample. W_{gain} is the weight gain of the sample. W_{remain} is the remaining weight of the sample.

3. Results and Discussion

3.1. FTIR. Figure 1 presents the FTIR spectra of pure PVOH, crosslinked PVOH, and crosslinked and non-crosslinked nanocomposites with 3 wt% CNC. There are minor differences in the spectrum curves between the parallel compositions of nanocomposites. The broad peak at $3,230 \text{ cm}^{-1}$ of all the nanocomposites indicates the availability of the -OH groups in the intermolecular and intramolecular hydrogen bonding between PVOH and CNC [51]. The peak at $2,921 \text{ cm}^{-1}$ for all the nanocomposites indicates the vibration of the aliphatic C-H alkyl groups. The bands appearing at wavenumbers of 912 and 842 cm^{-1} show the presence of the stretching vibrations of the C-H bond in PVOH [52]. For the crosslinked nanocomposites, the appearance of a small peak at $1,750 \text{ cm}^{-1}$ proves the success of the crosslinking reaction due to the formation of ester C=O bonds [53]. The peak at the wavenumber of $1,680 \text{ cm}^{-1}$ for all nanocomposites is due to the presence of adsorbed water, whereas the

peak at $1,380 \text{ cm}^{-1}$ indicates the presence of the C-H vibration band. The peak intensity increased for the nanocomposites with CNC at $1,040 \text{ cm}^{-1}$ (but it did not for pure PVOH) due to the C-O-C vibration from the pyranose ring present in the cellulose [32].

3.2. Interactions between Polyvinyl Alcohol, Cellulose Nanocrystals, and Ethanedioic Acid. As presented in Figure 2(a), the crosslinking mechanism is attributed to the esterification reaction between PVOH and EA. Intermolecular diester bonds are formed as a result of the linkage between the carboxyl groups of EA with the hydroxyl groups of PVOH in high-temperature environments (as was proven in Section 3.1). Either one or both carboxylic acid end groups of EA will react with the hydroxyl end group of PVOH, resulting in the formation of strong crosslink bridges that improve the SwI, SoI, and tensile properties of the nanocomposites. Conversely, Figure 2(b) presents the interaction between the hydroxyl groups of PVOH and CNC through the formation of hydrogen bonds.

3.3. X-Ray Diffraction. Figure 3 presents the XRD diffraction patterns of MCC, CNC, pure PVOH, crosslinked PVOH, and crosslinked and non-crosslinked nanocomposites (3 and 7 wt%). The well-defined characteristic peaks of the cellulose type I lattice structures, occurring around 16.1° and 22.4° , are observed for CNC [54]. The unaltered diffraction peaks of the CNC in comparison with MCC confirm that the acid hydrolysis treatment employed to extract CNC through the removal of unwanted amorphous regions did not affect the crystalline nature of the cellulose. The narrower and sharper peak demonstrated by CNC at 22.4° indicates that it exhibits a better crystal lattice structure and a higher cellulose index than MCC [55, 56]. This translates to a greater reinforcing ability on the tensile properties of PVOH (discussed in Section 3.6). As presented in Table 1, the CrI of CNC increased to 74% due to the release of

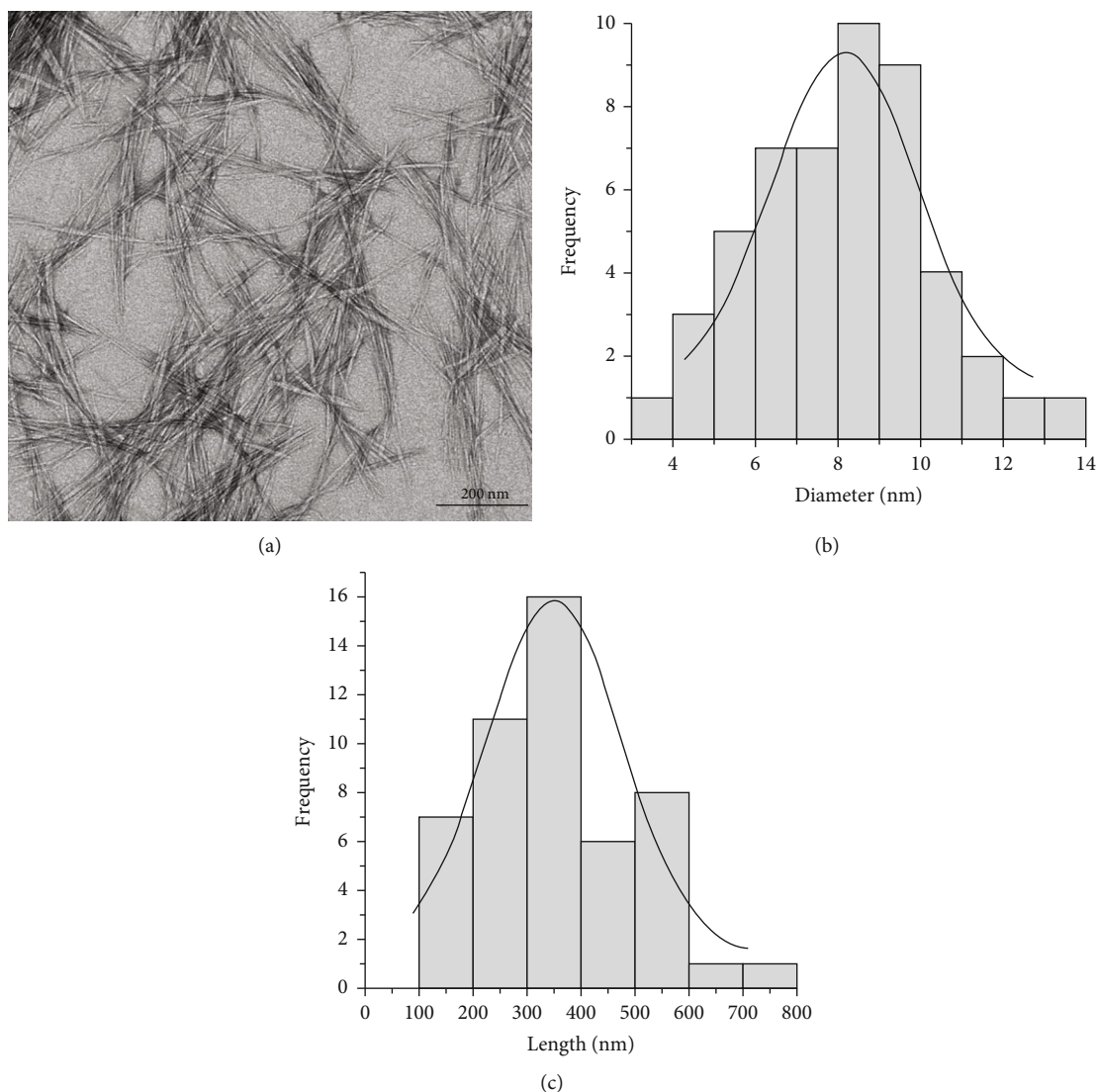


FIGURE 6: TEM image of (a) CNC extracted from rice straw with their (b) diameter and (c) length distributions. Magnification: $\times 25,000$.

individual crystallites from the hydrolytic cleavage of the glycosidic bonds in the amorphous regions. For both the non-crosslinked and crosslinked nanocomposites, the CrI improved with the addition of CNC due to the increase in the amount of crystalline material in the system [57]. At a higher filler content of CNC (7 wt%), the CrI decreased. This is mostly due to the effect that the steric hindrance of CNC, which is the retardation of chemical reactions that disrupts the formation of intermolecular bonds between molecules, has on the organized structure of the carbon-carbon polymer chains in PVOH. A similar occurrence was reported by Hoseini et al. [58] when the CrI dropped during high carbon nanotube loading in a polyamide-6 polymer. The addition of EA as the crosslinker decreased the CrI of the nanocomposites. This occurred because after crosslinking, the interactions between the PVOH chains limited the mobility of the molecular chain motion, hampering the crystallization process and negatively affecting the crystallinity of the crosslinked films. A similar decrease in crystallinity findings was observed by Nataraj et al. [59] when chitosan films

were crosslinked with citric acid. Wu et al. [60] also reported a decrease in peak intensity (indicating a drop in the percentage of crystallinity) after crosslinking starch films with citric acid.

3.4. Tensile Fracture Surface. Figures 4(a)–4(f) present the FESEM micrographs of the tensile-fractured surfaces of non-crosslinked and crosslinked nanocomposites exhibiting different morphologies. From Figures 4(a) and 4(b), it can be observed that the crosslinking of pure PVOH resulted in a much smoother fracture surface when compared with pure PVOH. Similar findings were reported by Jain et al. [61] on crosslinked PVOH with hydrochloric acid. Figure 4(c) presents a rougher, bristly cross-sectional fracture due to the existence of strong interactions between the CNC and PVOH matrix. These findings indicate that the non-crosslinked 3% nanocomposite suffered from a brittle fracture. This is also supported by the results presented in Figure 5, in which the incorporation of CNC increased Young's modulus, thereby increasing the brittleness of the

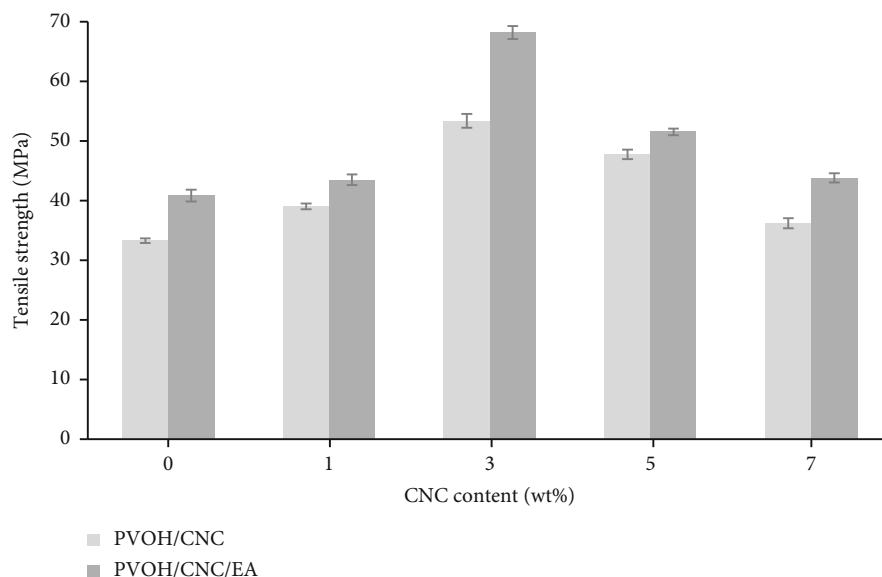


FIGURE 7: Tensile strength of the nanocomposites with varying CNC contents with and without the addition of EA.

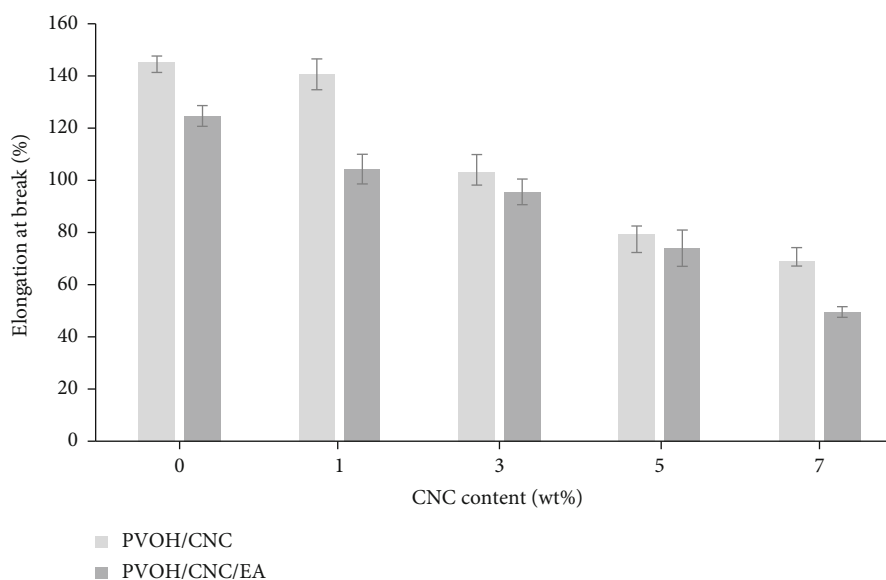


FIGURE 8: Elongation at break of the nanocomposites with varying CNC contents with and without the addition of EA.

nanocomposite. As can be seen from Figure 4(d), the cross-linked 3% nanocomposite exhibited a smoother, wavelike fracture surface structure, suggesting a relative homogeneous dispersion of CNC within the nanocomposite. Similar findings were also obtained in PVOH/functionalized CNC composite films by Chen et al. [62]. There are also no observable internal cracks or phase separations attributed to the greater tensile strength of crosslinked nanocomposites when compared with non-crosslinked nanocomposites [62]. In Figures 4(e) and 4(f), the voids, aggregates, and coarser surfaces shown throughout the fracture surfaces led to a weaker transfer of strength. This directly translated to a decrease in tensile strength and Young's modulus.

3.5. Morphology. As can be seen from Figure 6(a), the CNC extracted from rice straw appeared as long, well-defined rod-like crystals. The Gaussian distribution for the CNC diameter presented in Figure 6(b) confirmed that it was in the range of 3–14 nm. The standard deviation, reduced chi-squared, and *R*-squared values obtained were 2.1 nm, 1.3, and 0.88, respectively. As can be seen from Figure 6(c), the length of the CNC obtained was in the range of 100–800 nm. The standard deviation, reduced chi-squared, and *R*-squared values obtained were 139.0 nm, 9.74, and 0.68, respectively. The average length was 331.97 nm, and the average diameter was 8.11 nm. The aspect ratio of the CNC, calculated from the ratio of the length over the

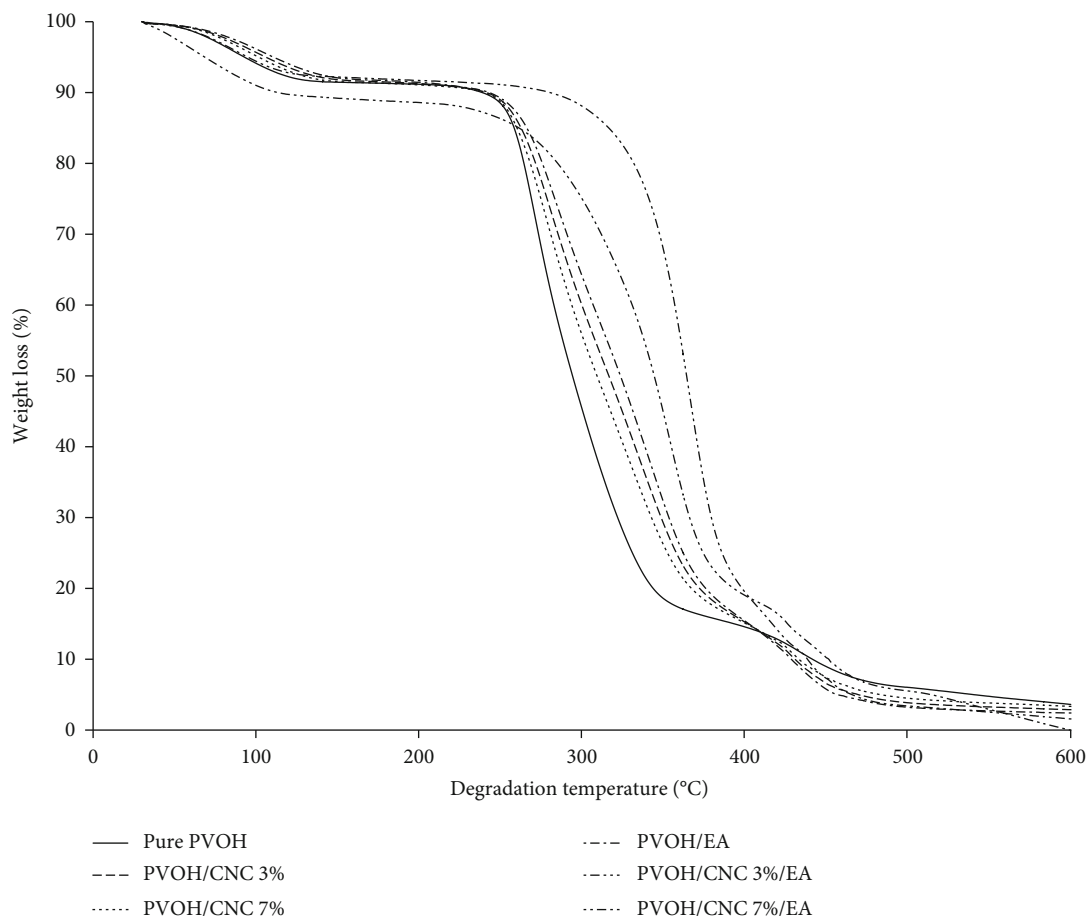


FIGURE 9: Thermogram of the nanocomposites with varying CNC contents with and without the addition of EA.

TABLE 2: TGA data from the thermal decomposition of nanocomposites with varying CNC contents with and without the addition of EA.

| Sample | $T_{10\%}$ (°C) | $T_{30\%}$ (°C) | T_{MAX} (°C) |
|----------------|-----------------|-----------------|----------------|
| Pure PVOH | 239 | 273 | 275 |
| PVOH/CNC 3% | 241 | 285 | 287 |
| PVOH/CNC 7% | 240 | 281 | 282 |
| PVOH/EA | 243 | 291 | 342 |
| PVOH/CNC 3%/EA | 280 | 348 | 364 |
| PVOH/CNC 7%/EA | 213 | 312 | 356 |

diameter, was 41. This value was higher than the aspect ratio of the rice straw CNC extracted by Lu and Hsieh [63]. This result demonstrated that the preliminary cyclic treatment performed on the CNC, prior to extraction, was effective. Moreover, the aspect ratio reported in this study was higher than that of the CNC extracted from other reported cellulosic sources, such as commercial MCC (16.8), corncob (37), switchgrass (38), cotton (13), and onion skin (10.1) [64–67].

3.6. Tensile Properties. Figure 7 presents the comparison of the tensile strengths of the crosslinked and non-crosslinked

nanocomposites with varying CNC contents. The tensile strength of non-crosslinked nanocomposites improved (increasing in value to 60.4%) as the CNC content increased up until 3 wt%. The crosslinked nanocomposites also demonstrated an upward trend, but the increase was much more pronounced (up to 104.8%) due to additional factors, such as the improved transfer of strength from the crosslinking network to the nanocomposite. The excellent compatibility of PVOH with CNC facilitated the homogeneous distribution of the CNC throughout the PVOH, as is shown in Figure 4(c). This, coupled with the success of hydrogen intermolecular and intramolecular bond formation, led to the positive enhancement in tensile strength. The nature of CNC, which is widely known to be strong and possess large interfacial surface area, also contributed to such an enhancement [68]. In CNC above 3 wt% for both the crosslinked and non-crosslinked nanocomposites, factors such as reaching the filler-saturation point and agglomeration start to exert detrimental effects on the tensile strength of the nanocomposites [69]. In the case of the crosslinked nanocomposites, the improvement in tensile strength is attributed to the formation of the crosslink bridges through the intermolecular ester bonding between the PVOH chains (as is illustrated in Figure 2(b)). This interaction within the matrix contributed to the development of a more compact structure than the non-crosslinked nanocomposites. The drop in strength

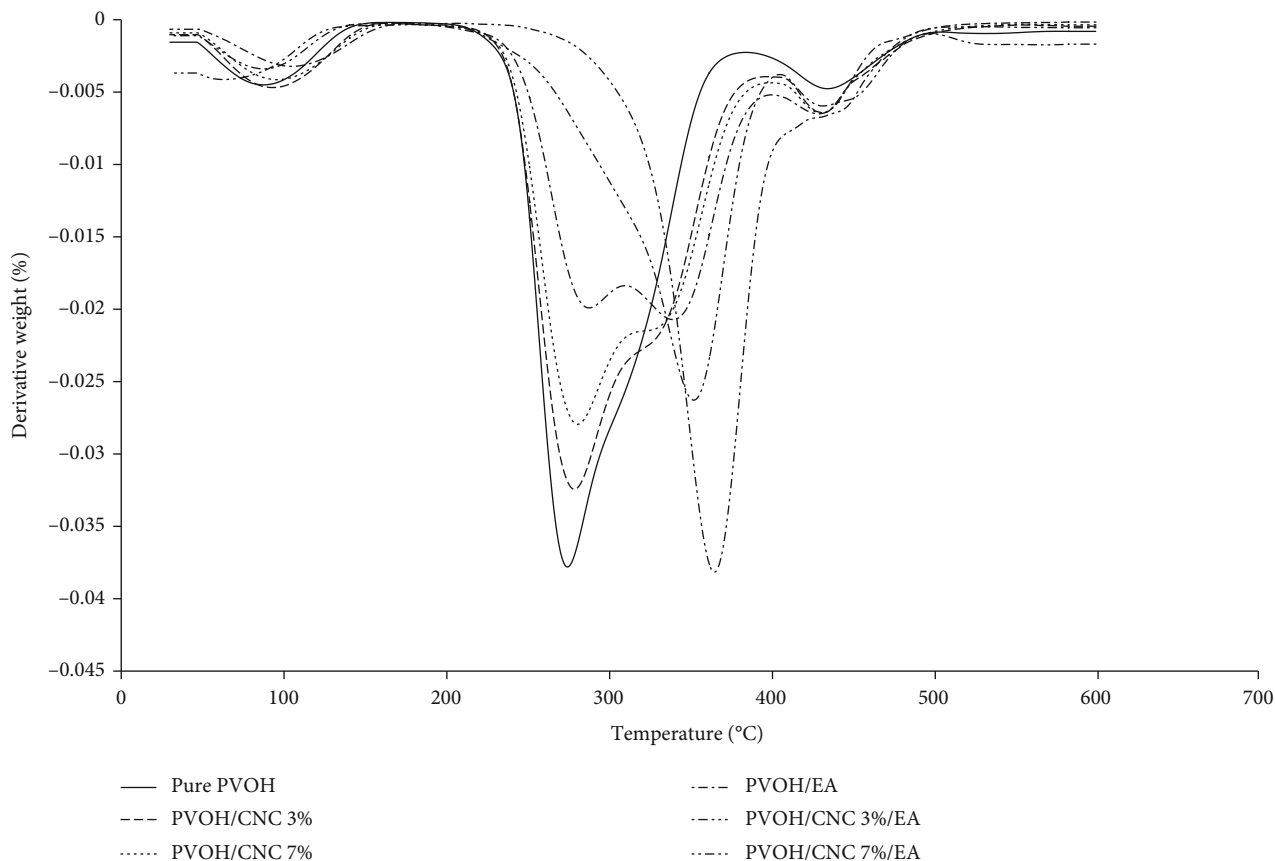


FIGURE 10: Differential thermogravimetry (dTG) curve of the nanocomposites with varying CNC contents with and without the addition of EA.

beyond 3 wt% may be due to the reduced availability of the hydroxyl groups as they were already used to form the crosslinks. A reduced number of hydroxyl groups prevents excess CNC from forming hydrogen bonds with PVOH, leading to unreacted CNC. This unreacted CNC agglomerates, forming random localized weak points on the nanocomposite.

Figure 8 presents the comparison of elongation at break values between crosslinked and non-crosslinked nanocomposites with varying CNC contents. In all cases, the increase in the amount of CNC slightly reduced the elongation of break in nanocomposites due to the addition of CNC with known stiff and rigid structures as reinforcement filler materials [68]. Consequently, the ductility of the nanocomposites was reduced (due to the diminishing content of PVOH) when the CNC content increased. A similar trend was observed in crosslinked nanocomposites in which the elongation of break was found to be much lower than that of non-crosslinked nanocomposites. Such a reduction in elasticity after crosslinking indicates that the nanocomposites lost their ductile nature as their polymer chain mobility was reduced by the formation of crosslinked networks. Jose reported similar findings when citric acid was used as the crosslinker for PVA/starch/graphene nanocomposites [70]. The elongation at break values was also found to decrease when glutaraldehyde was used a crosslinking agent in polyvinyl alcohol/chitosan composites [71]. There is even a phenomenon demonstrating that crosslinkers exert a plasticizing effect, but this is at the expense of

tensile strength. Wu et al. [60] demonstrated that when a higher citric acid content was used for crosslinking, the elongation at break was favored, but it significantly reduced the tensile strength. The unreacted excess citric acid content acted as the plasticizer, reducing the interactions between the PVOH carbon chains. Therefore, the incorporation of crosslinking agents in optimum amounts can improve the properties of the nanocomposites. However, any excess crosslinking agent will act as a plasticizer and cause a negative impact.

The significant increase in Young's modulus for both crosslinked and non-crosslinked nanocomposites up until 3 wt% is presented in Figure 5. With 1 wt% CNC content in non-crosslinked and crosslinked nanocomposites, the increase in Young's modulus was 12% and 17%, respectively. With 3 wt% CNC in non-crosslinked and crosslinked nanocomposites, the highest increase in Young's modulus was approximately 49% and 59%, respectively. The addition of stiff CNC to the polymer matrix led to the formation of rigid CNC networks that translated to the stiffness and improved strength of the nanocomposites. The 3 wt% CNC non-crosslinked nanocomposites exhibited a greater increase in Young's modulus than PLLA-grafted CNC with a similar CNC weight percentage [72]. Young's modulus also significantly increased after crosslinking. Ben Shalom et al. [73] reported that crosslinking of PVOH/CNC with 1,2,3,4-butanetetracarboxylic acid further improved the stiffness and strength of the composites. These findings are in agreement with the results presented in Figure 5.

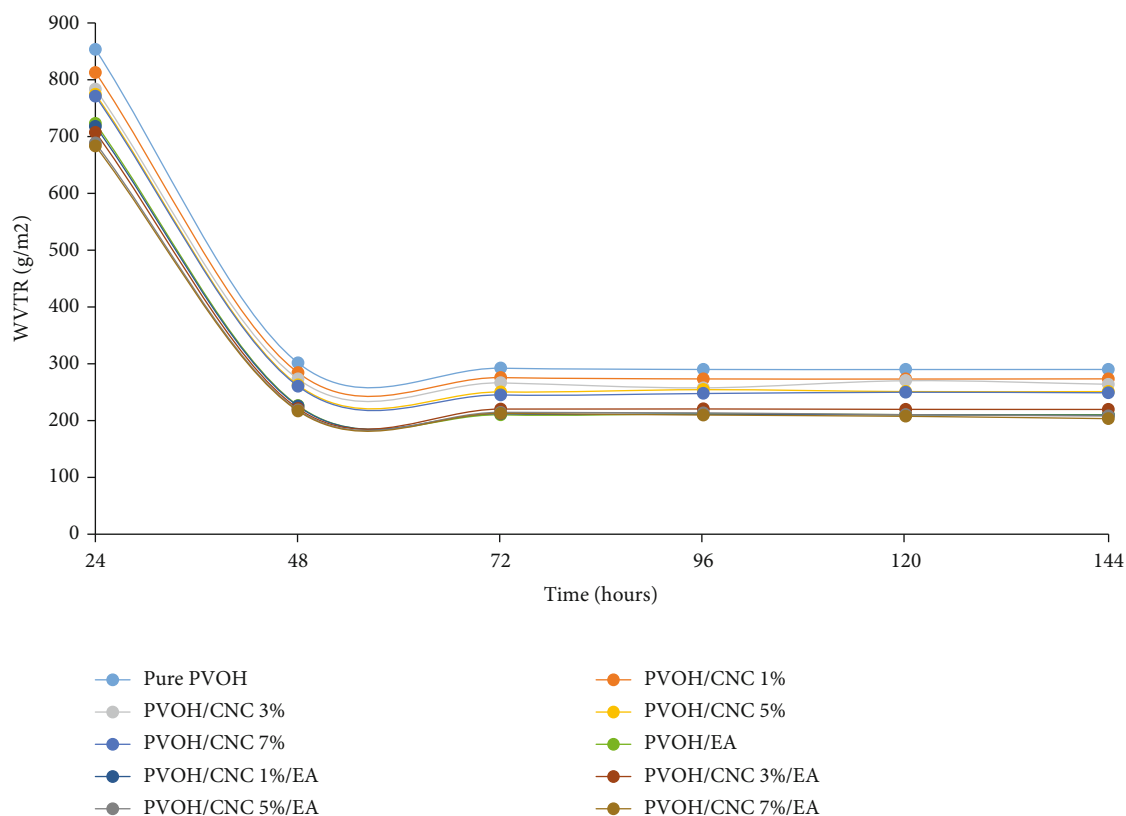


FIGURE 11: The MVP of nanocomposites with varying CNC contents with and without the addition of EA.

3.7. Thermogravimetric Analysis. TGA was conducted to analyze the thermal behavior of crosslinked and non-crosslinked nanocomposites of varying CNC contents. The three important regions of weight loss are disclosed in the thermogravimetric curve presented in Figure 9. The initial weight loss occurred at approximately 40°C–100°C and is observed for all nanocomposites. This event is attributed to the loss of water through evaporation, mostly of free bound water molecules that are loosely attached to the surface of the nanocomposites [44]. The next weight loss event occurred at around 210°C–400°C and is attributed to the degradation of the nanocomposites. The nanocomposites lost approximately 70% of their total weight, and this region is the most important for indicating their thermal stability. Weight loss is mainly attributed to the degradation of volatile products such as intrinsic water content and unsaturated compounds.

The last weight loss event occurred at greater than 400°C (at approximately 440°C) and is attributed to the degradation of polyene, hydrocarbons, and chain scission of the nanocomposites [74]. As presented in Table 2, crosslinked nanocomposites were found to exhibit greater $T_{10\%}$, $T_{30\%}$, and T_{MAX} values. After the occurrence of crosslinking, the $T_{10\%}$, $T_{30\%}$, and T_{MAX} values of pure PVOH increased from 239°C, 273°C, and 275°C to 243°C, 291°C, and 342°C, respectively. A similar increase was observed for the $T_{10\%}$, $T_{30\%}$, and T_{MAX} values of crosslinked PVOH with the addition of CNC, from 241°C, 285°C, and 287°C to 280°C, 348°C, and 364°C, respectively. The increase in the thermal decomposition temperature

indicated the occurrence of crosslinking. These results are in agreement with the findings of Stelescu et al. [75] in which the occurrence of crosslinking of ethylene propylene diene monomers with butyl rubber composites was proven by the resulting improvement in the $T_{10\%}$, $T_{30\%}$, and T_{MAX} values. This improvement is highly beneficial as the crosslinked nanocomposites are more thermally stable and more resistant to thermal degradation.

Figure 10 presents the derivative weight loss curve of the nanocomposites. Crosslinked PVOH had four degradation steps, whereas pure PVOH and the other nanocomposites had only three degradation steps. Sonker et al. [76] reported similar findings on crosslinked PVOH with suberic acid and terephthalic acid. For the crosslinked nanocomposites with 3 and 7 wt% of CNC, the addition of CNC caused the second and third steps to coalesce, forming only one strong derivative weight peak. Song et al. [77] presented similar findings on the thermal degradation steps for the Fenton free radical crosslinking of PVOH with the addition of CNC. It is also evident in Figure 10 that the addition of CNC increased the maximum degradation temperature of the nanocomposite with 3 wt% CNC but reduced it when 7 wt% CNC was added. At higher filler content, factors such as CNC agglomeration dominated, and the thermal stability of the nanocomposites was reduced. A comparable occurrence on the thermal behavior of PVOH/CNC extracted from commercial cellulose at higher filler loading was also demonstrated in the report by Song et al. [77]. The degradation peak from

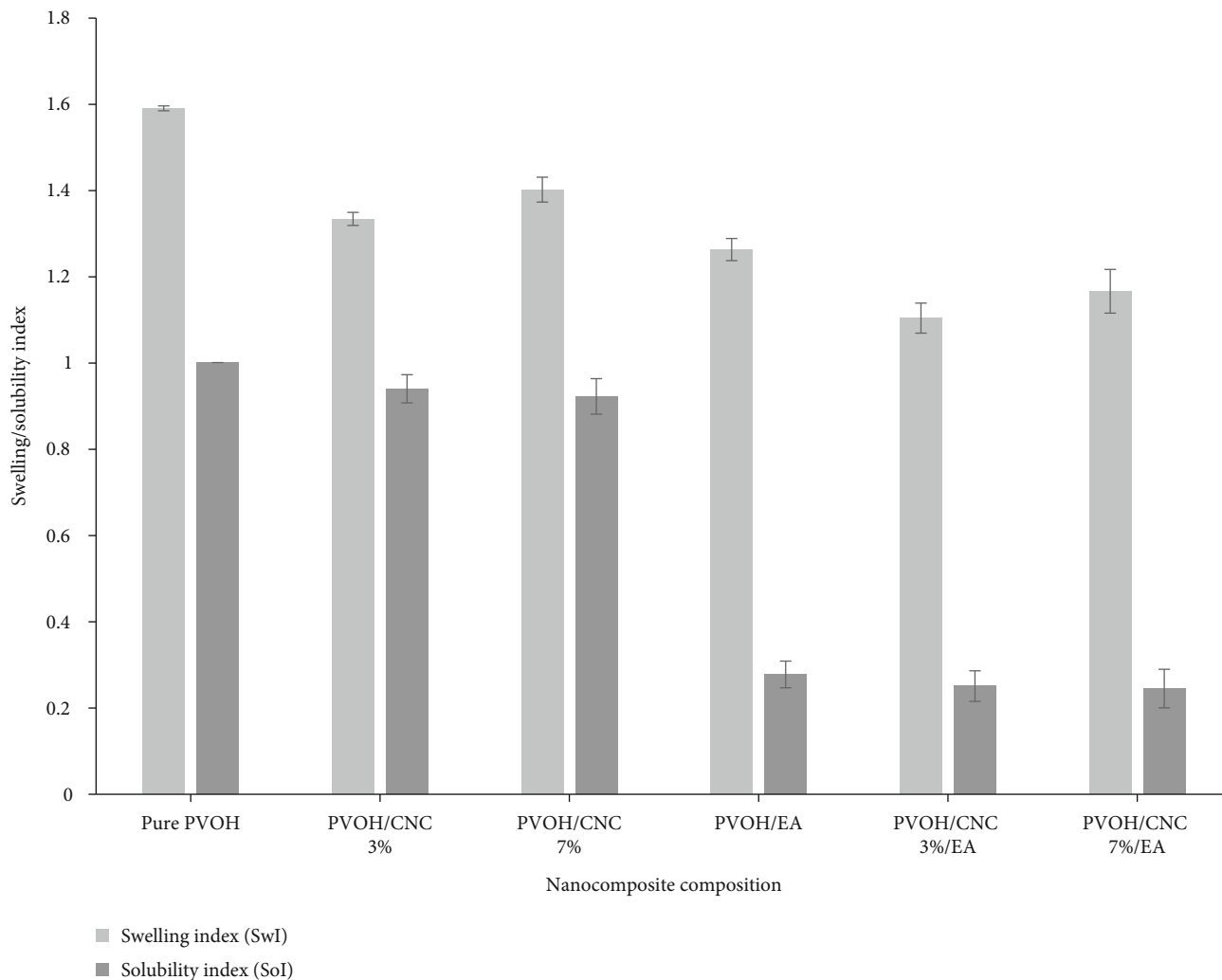


FIGURE 12: SoI and SwI of the nanocomposites with varying CNC contents with and without the addition of EA.

the DTG curve indicates an increased thermal stability of the nanocomposites with 3 and 7 wt% CNC when compared with pure PVOH. As presented in Table 2, the T_{MAX} value significantly increased after crosslinking, most prominently for the nanocomposites with 3 wt% (from 287°C to 364°C). The obvious shift of the peak of the crosslinked nanocomposites to the right indicated that there is a great improvement in thermal stability.

3.8. Water Vapor Permeation Rate. The MVPs of crosslinked and non-crosslinked nanocomposites with varying CNC contents are presented in Figure 11. Moisture vapor transmission through films (especially hydrophilic films) independently varies with its degree of hydrophilicity. Moisture tends to interact with the polymeric matrix of the film, increasing its moisture permeability. Non-crosslinked nanocomposites are more inclined to have a higher MVP value compared with crosslinked nanocomposites owing to their higher hydrophilic behavior. During the initial exposure of nanocomposite films to moisture, swelling slowly occurs, causing distortions in the polymer chain conformation within the films [78, 79]. At 48 h, the MVP value starts to

taper and remains at a steady state. Water, acting as a plasticizer, loosens the polymer chains, which leads to an increase in the MVP [80]. Pure PVOH most clearly demonstrates this effect. The addition of CNC substantially reduced the MVP value for all the nanocomposites. At higher CNC concentrations, most of the water molecules are blocked from passing through the polymer matrix, as the increase in CNC disrupts the water molecule pathways. CNC significantly reduces the diffusibility of moisture vapor owing to its size and swelling constraints, as well as its strong network formation in nanocomposite films. Nair et al. [81] obtained similar findings on the reduction in the MVP of nanocellulose films. The reduction in the MVP is more pronounced with crosslinked nanocomposites with increased CNC content. This is due to the synergistic effect from the crosslinked bridges with CNC, thereby favoring their application as thin packaging films for moisture-sensitive materials, such as food and beverage products [82].

3.9. Solubility and Swelling Index. The SoI and SwI are presented in Figure 12. The results indicate that the SoI of the crosslinked nanocomposites significantly decreased when

compared with that of the non-crosslinked nanocomposites, from an estimated index of 1 to 0.25. This result proves that the proposed crosslinking reaction with EA (as was discussed in Section 3.2) was successful as it increased the hydrophobicity of the nanocomposites to water. However, the addition of CNC only minimally affected the SoI index. This is likely due to CNC's similar hydrophilic nature to the polymer matrix. The SwI was at its lowest in the 3 wt% of PVOH/CNC nanocomposite when compared with pure PVOH and the nanocomposite with 7 wt% of CNC. A similar trend was observed for the crosslinked nanocomposites. PVOH is a hydrophilic material that tends to easily attract water molecules owing to its free hydroxyl groups. The difference in the swelling behavior is attributed to its crystallinity, where the non-crosslinked nanocomposite films with higher CrI values augmented the difficulty of the water to penetrate the PVOH network [83]. The formation of dense, three-dimensional network structures as a result of crosslinking additionally reduced the intermolecular spaces. This favorably affected the SwI value (even at a lower CrI value) for the non-crosslinked nanocomposites [84, 85]. According to Alessandra Bersanetti et al. [84], the reduction in the SwI after crosslinking was due to the diminished availability of excess hydroxyl groups to form hydrogen bonds with water molecules. In the case of PVOH with 7 wt% CNC, for both crosslinked and non-crosslinked nanocomposites, agglomerated and unreacted CNC imparted voids and imperfections throughout the film, which are presented in Figures 4(e) and 4(f), respectively. These findings consequently resulted in an increase in the SwI.

4. Conclusion

This study successfully extracted cellulose nanocrystal (CNC) from rice straw and used it as a reinforcement filler on polyvinyl alcohol. The utilization of EA as a crosslinker proved successful and produced very favorable results. A distinctive improvement in the tensile strength and Young's modulus of non-crosslinked nanocomposites and an even greater improvement in crosslinked nanocomposites were observed. The XRD data indicated that there was an increase in the degree of crystallinity of the nanocomposites when CNC was added. After crosslinking, the nanocomposites exhibited a decrease in the degree of crystallinity. The extracted CNC had a high aspect ratio of 41 and appeared as long, well-defined rodlike crystals. The maximum degradation temperature of the nanocomposites increased at the optimum content of 3 wt% CNC. An additional increase was observed after crosslinking. Crosslinking reduced the values of MVP, solubility index, and swelling index, favoring its application in thin-film packaging for moisture-sensitive materials. Although the addition of CNC is promising and this study revealed its benefits by improving on certain niche properties of PVOH, it does not favor widespread use. Crosslinking of the nanocomposite to drastically reduce its hydrophilicity and significantly improve its tensile and thermal properties must be performed before it can be widely used. In conclusion, the optimum CNC content was 3 wt% for both crosslinked and non-crosslinked nanocomposites.

Data Availability

The experimental data used to support the findings discussed in this study are included within the article.

Conflicts of Interest

The authors declare no conflict of interest.

Acknowledgments

The authors are thankful to Universiti Malaysia Perlis for providing the facilities necessary to perform this research. This research was performed as a part of the employment of Universiti Malaysia Perlis.

References

- [1] C. A. Bernardo, C. L. Simões, and L. M. C. Pinto, "Environmental and economic life cycle analysis of plastic waste management options. A review," in *AIP Conference Proceedings*, vol. 1779, Graz, Austria, 2016.
- [2] L. C. M. Lebreton, J. Van Der Zwet, J. W. Damsteeg, B. Slat, A. Andrady, and J. Reisser, "River plastic emissions to the world's oceans," *Nature Communications*, vol. 8, no. 1, pp. 1–10, 2017.
- [3] J. Vince and B. D. Hardesty, "Plastic pollution challenges in marine and coastal environments: from local to global governance," *Restoration Ecology*, vol. 25, no. 1, pp. 123–128, 2017.
- [4] S. L. Wong, N. Ngadi, T. A. T. Abdullah, and I. M. Inuwa, "Current state and future prospects of plastic waste as source of fuel: a review," *Renewable and Sustainable Energy Reviews*, vol. 50, pp. 1167–1180, 2015.
- [5] N. Chaukura, W. Gwenzi, T. Bunhu, D. T. Ruziwa, and I. Pumure, "Potential uses and value-added products derived from waste polystyrene in developing countries: a review," *Resources, Conservation and Recycling*, vol. 107, pp. 157–165, 2016.
- [6] T. P. Haider, C. Völker, J. Kramm, K. Landfester, and F. R. Wurm, "Kunststoffe der zukunft? Der einfluss von bioabbaubaren polymeren auf umwelt und gesellschaft," *Angewandte Chemie*, vol. 131, no. 1, pp. 50–63, 2019.
- [7] S. Huysman, J. De Schaepe-meester, K. Ragaert, J. Dewulf, and S. De Meester, "Performance indicators for a circular economy: a case study on post-industrial plastic waste," *Resources, Conservation and Recycling*, vol. 120, pp. 46–54, 2017.
- [8] T. Leejarkpai, T. Mungcharoen, and U. Suwanmanee, "Comparative assessment of global warming impact and eco-efficiency of PS (polystyrene), PET (polyethylene terephthalate) and PLA (polylactic acid) boxes," *Journal of Cleaner Production*, vol. 125, pp. 95–107, 2016.
- [9] E. J. North and R. U. Halden, "Plastics and environmental health: the road ahead," *Reviews on Environmental Health*, vol. 28, no. 1, pp. 1–8, 2013.
- [10] J. E. Weinstein, B. K. Crocker, and A. D. Gray, "From macroplastic to microplastic: degradation of high-density polyethylene, polypropylene, and polystyrene in a salt marsh habitat," *Environmental Toxicology and Chemistry*, vol. 35, no. 7, pp. 1632–1640, 2016.
- [11] B. M. Dominguez-Martinez, H. E. Martínez-Flores, J. D. J. Berrios, C. G. Otoni, D. F. Wood, and G. Velazquez, "Physical characterization of biodegradable films based on chitosan,




- polyvinyl alcohol and *Opuntia mucilage*,” *Journal of Polymers and the Environment*, vol. 25, no. 3, pp. 683–691, 2017.
- [12] M. C. Lin, C. W. Lou, J. Y. Lin, T. A. Lin, Y. S. Chen, and J. H. Lin, “Biodegradable polyvinyl alcohol vascular stents: structural model and mechanical and biological property evaluation,” *Materials Science and Engineering: C*, vol. 91, pp. 404–413, 2018.
- [13] J. Jalvandi, M. White, Y. Gao, Y. B. Truong, R. Padhye, and I. L. Kyratzis, “Polyvinyl alcohol composite nanofibres containing conjugated levofloxacin-chitosan for controlled drug release,” *Materials Science and Engineering: C*, vol. 73, pp. 440–446, 2017.
- [14] K. P. Y. Shak, Y. L. Pang, and S. K. Mah, “Nanocellulose: recent advances and its prospects in environmental remediation,” *Beilstein Journal of Nanotechnology*, vol. 9, no. 1, pp. 2479–2498, 2018.
- [15] Y. H. Feng, T. Y. Cheng, W. G. Yang et al., “Characteristics and environmentally friendly extraction of cellulose nanofibrils from sugarcane bagasse,” *Industrial Crops and Products*, vol. 111, pp. 285–291, 2018.
- [16] A. L. M. P. Leite, C. D. Zanon, and F. C. Menegalli, “Isolation and characterization of cellulose nanofibers from cassava root bagasse and peelings,” *Carbohydrate Polymers*, vol. 157, pp. 962–970, 2017.
- [17] S. Nie, K. Zhang, X. Lin et al., “Enzymatic pretreatment for the improvement of dispersion and film properties of cellulose nanofibrils,” *Carbohydrate Polymers*, vol. 181, pp. 1136–1142, 2018.
- [18] D. Yue and X. Qian, “Isolation and rheological characterization of cellulose nanofibrils (CNFs) from coir fibers in comparison to wood and cotton,” *Polymers (Basel)*, vol. 10, no. 3, p. 320, 2018.
- [19] C. C. S. Coelho, M. Michelin, M. A. Cerqueira et al., “Cellulose nanocrystals from grape pomace: production, properties and cytotoxicity assessment,” *Carbohydrate Polymers*, vol. 192, pp. 327–336, 2018.
- [20] S. Collazo-Bigliardi, R. Ortega-Toro, and A. Chiralt Boix, “Isolation and characterisation of microcrystalline cellulose and cellulose nanocrystals from coffee husk and comparative study with rice husk,” *Carbohydrate Polymers*, vol. 191, pp. 205–215, 2018.
- [21] J. Lamaming, R. Hashim, C. P. Leh, and O. Sulaiman, “Properties of cellulose nanocrystals from oil palm trunk isolated by total chlorine free method,” *Carbohydrate Polymers*, vol. 156, pp. 409–416, 2017.
- [22] R. A. Ilyas, S. M. Sapuan, and M. R. Ishak, “Isolation and characterization of nanocrystalline cellulose from sugar palm fibres (*Arenga pinnata*),” *Carbohydrate Polymers*, vol. 181, pp. 1038–1051, 2018.
- [23] S. Naduparambath, T. V. Jiniitha, V. Shaniba, M. P. Sreejith, A. K. Balan, and E. Purushothaman, “Isolation and characterisation of cellulose nanocrystals from sago seed shells,” *Carbohydrate Polymers*, vol. 180, pp. 13–20, 2018.
- [24] J. P. De Mesquita, C. L. Donnici, I. F. Teixeira, and F. V. Pereira, “Bio-based nanocomposites obtained through covalent linkage between chitosan and cellulose nanocrystals,” *Carbohydrate Polymers*, vol. 90, no. 1, pp. 210–217, 2012.
- [25] A. Dufresne, “Processing of polymer nanocomposites reinforced with polysaccharide nanocrystals,” *Molecules*, vol. 15, no. 6, pp. 4111–4128, 2010.
- [26] E. Fortunati, I. Armentano, Q. Zhou et al., “Multifunctional bionanocomposite films of poly(lactic acid), cellulose nanocrystals and silver nanoparticles,” *Carbohydrate Polymers*, vol. 87, no. 2, pp. 1596–1605, 2012.
- [27] K. M. Chin, S. Sung Ting, H. L. Ong, and M. Omar, “Surface functionalized nanocellulose as a veritable inclusionary material in contemporary bioinspired applications: a review,” *Journal of Applied Polymer Science*, vol. 135, no. 13, p. 46065, 2018.
- [28] J. A. Sirviö, S. Honkaniemi, M. Visanko, and H. Liimatainen, “Composite films of poly(vinyl alcohol) and bifunctional cross-linking cellulose nanocrystals,” *ACS Applied Materials & Interfaces*, vol. 7, no. 35, pp. 19691–19699, 2015.
- [29] T. Song, S. Tanpichai, and K. Oksman, “Cross-linked polyvinyl alcohol (PVA) foams reinforced with cellulose nanocrystals (CNCs),” *Cellulose*, vol. 23, no. 3, pp. 1925–1938, 2016.
- [30] A. K. Sonker, N. Tiwari, R. K. Nagarale, and V. Verma, “Synergistic effect of cellulose nanowhiskers reinforcement and dicarboxylic acids crosslinking towards polyvinyl alcohol properties,” *J. Polym. Sci. Part A Polym. Chem.*, vol. 54, no. 16, pp. 2515–2525, 2016.
- [31] S. A. Stone, P. Gosavi, T. J. Athauda, and R. R. Ozer, “In situ citric acid crosslinking of alginate/polyvinyl alcohol electrospun nanofibers,” *Materials Letters*, vol. 112, pp. 32–35, 2013.
- [32] S. Wang, J. Ren, W. Li, R. Sun, and S. Liu, “Properties of polyvinyl alcohol/xylan composite films with citric acid,” *Carbohydrate Polymers*, vol. 103, no. 1, pp. 94–99, 2014.
- [33] Y. Dou, B. Zhang, M. He, G. Yin, Y. Cui, and I. N. Savina, “Keratin/polyvinyl alcohol blend films cross-linked by dialdehyde starch and their potential application for drug release,” *Polymers (Basel)*, vol. 7, no. 3, pp. 580–591, 2015.
- [34] J. Li, Y. Li, Y. Song, S. Niu, and N. Li, “Ultrasonic-assisted synthesis of polyvinyl alcohol/phytic acid polymer film and its thermal stability, mechanical properties and surface resistivity,” *Ultrasonics Sonochemistry*, vol. 39, no. May, pp. 853–862, 2017.
- [35] M. Lim, H. Kwon, D. Kim, J. Seo, H. Han, and S. B. Khan, “Highly-enhanced water resistant and oxygen barrier properties of cross-linked poly(vinyl alcohol) hybrid films for packaging applications,” *Progress in Organic Coatings*, vol. 85, pp. 68–75, 2015.
- [36] P. Maji, A. Gandhi, S. Jana, and N. Maji, “Preparation and characterization of maleic anhydride cross-linked chitosan-polyvinyl alcohol hydrogel matrix transdermal patch,” *Journal of PharmaSciTech*, vol. 2, no. 2, pp. 62–67, 2013.
- [37] A. K. Sonker, H. D. Wagner, R. Bajpai, R. Tenne, and X. M. Sui, “Effects of tungsten disulphide nanotubes and glutaric acid on the thermal and mechanical properties of polyvinyl alcohol,” *Composites Science and Technology*, vol. 127, pp. 47–53, 2016.
- [38] Z. Wu, J. Wu, T. Peng et al., “Preparation and application of starch/polyvinyl alcohol/citric acid ternary blend antimicrobial functional food packaging films,” *Polymers (Basel)*, vol. 9, no. 12, pp. 102–119, 2017.
- [39] Y. An, T. Koyama, K. Hanabusa et al., “Preparation and properties of highly phosphorylated poly(vinyl alcohol) hydrogels chemically crosslinked by glutaraldehyde,” *Polymer (Guildf)*, vol. 36, no. 11, pp. 2297–2301, 1995.
- [40] X. Qin, G. Dou, G. Jiang, and S. Zhang, “Characterization of poly(vinyl alcohol) nanofiber mats cross-linked with glutaraldehyde,” *Journal of Industrial Textiles*, vol. 43, no. 1, pp. 34–44, 2013.
- [41] R. Rudra, V. Kumar, and P. P. Kundu, “Acid catalysed cross-linking of poly vinyl alcohol (PVA) by glutaraldehyde: effect of crosslink density on the characteristics of PVA membranes used in single chambered microbial fuel cells,” *RSC Advances*, vol. 5, no. 101, pp. 83436–83447, 2015.

- [42] K. Das, D. Ray, N. R. Bandyopadhyay et al., "Preparation and characterization of cross-linked starch/poly(vinylalcohol) green films with low moisture absorption," *Industrial and Engineering Chemistry Research*, vol. 49, no. 5, pp. 1520–5045, 2010.
- [43] B. Sreedhar, D. K. Chattopadhyay, M. S. H. Karunakar, and A. R. K. Sastry, "Thermal and surface characterization of plasticized starch polyvinyl alcohol blends crosslinked with epichlorohydrin," *Journal of Applied Polymer Science*, vol. 101, no. 1, pp. 25–34, 2006.
- [44] A. N. Frone, C. A. Nicolae, R. A. Gabor, and D. M. Panaitescu, "Thermal properties of water-resistant starch - polyvinyl alcohol films modified with cellulose nanofibers," *Polymer Degradation and Stability*, vol. 121, pp. 385–397, 2015.
- [45] S. Liu, L. Wang, B. Zhang, B. Liu, J. Wang, and Y. Song, "Novel sulfonated polyimide/polyvinyl alcohol blend membranes for vanadium redox flow battery applications," *Journal of Materials Chemistry A*, vol. 3, no. 5, pp. 2072–2081, 2015.
- [46] L. Chen, S. H. Imam, S. H. Gordon, and R. V. Greene, "Starch-polyvinyl alcohol crosslinked film— performance and biodegradation," *Journal of Environmental Polymer Degradation*, vol. 5, no. 2, pp. 111–117, 1997.
- [47] M. Chaouat, C. le Visage, W. E. Baillet et al., "A novel cross-linked poly(vinyl alcohol) (PVA) for vascular grafts," *Advanced Functional Materials*, vol. 18, no. 19, pp. 2855–2861, 2008.
- [48] A. D. A. Morandim-Giannetti, R. C. Silva, O. Magalhães, P. Schor, and P. A. Bersanetti, "Conditions for obtaining polyvinyl alcohol/trisodium trimetaphosphate hydrogels as vitreous humor substitute," *Journal of Biomedical Materials Research Part B: Applied Biomaterials*, vol. 104, no. 7, pp. 1386–1395, 2016.
- [49] C. H. Chan, C. H. Chia, S. Zakaria, I. Ahmad, and A. Dufresne, "Production and characterisation of cellulose and Nano-Crystalline cellulose from kenaf core wood," *BioResources*, vol. 8, no. 1, pp. 785–794, 2012.
- [50] N. Amiralian, P. K. Annamalai, C. J. Garvey, E. Jiang, P. Memmott, and D. J. Martin, "High aspect ratio nanocellulose from an extremophile spinifex grass by controlled acid hydrolysis," *Cellulose*, vol. 24, no. 9, pp. 3753–3766, 2017.
- [51] D. Liu, Y. Dong, D. Bhattacharyya, and G. Sui, "Novel sandwiched structures in starch/cellulose nanowhiskers (CNWs) composite films," *Composites Communications*, vol. 4, pp. 5–9, 2017.
- [52] S. Mathew, J. Mathew, and E. K. Radhakrishnan, "Polyvinyl alcohol/silver nanocomposite films fabricated under the influence of solar radiation as effective antimicrobial food packaging material," *Journal of Polymer Research*, vol. 26, no. 9, pp. 1–10, 2019.
- [53] K. M. Chin, S. T. Sam, H. L. Ong, Y. S. Wong, and W. K. Tan, "Biodegradation improvement of bioinspired crosslinked and noncrosslinked polyvinyl alcohol nanocomposites with cellulose nanocrystals extracted from rice straw through natural soil burial exposure," *Polymer Composites*, pp. 1–11, 2022.
- [54] W. P. Flauzino Neto, H. A. Silvério, N. O. Dantas, and D. Pasquini, "Extraction and characterization of cellulose nanocrystals from agro-industrial residue - soy hulls," *Industrial Crops and Products*, vol. 42, pp. 480–488, 2013.
- [55] A. Kumar, Y. Singh Negi, V. Choudhary, and N. K. Bhardwaj, "Characterization of cellulose nanocrystals produced by acid-hydrolysis from sugarcane bagasse as agro-waste "Characterization of cellulose nanocrystals produced by acid-hydrolysis from sugarcane bagasse as agro-waste," *Journal of Materials Physics and Chemistry*, vol. 2, no. 1, pp. 1–8, 2014.
- [56] M. R. K. Sofla, R. J. Brown, T. Tsuzuki, and T. J. Rainey, "A comparison of cellulose nanocrystals and cellulose nanofibres extracted from bagasse using acid and ball milling methods," *Advances in Natural Sciences: Nanoscience and Nanotechnology*, vol. 7, no. 3, p. 035004, 2016.
- [57] A. Saxena, M. Foston, M. Kassae, T. J. Elder, and A. J. Ragauskas, "Biopolymer nanocomposite films reinforced with nanocellulose whiskers," *Journal of Nanoscience and Nanotechnology*, vol. 12, no. 1, pp. 218–226, 2012.
- [58] A. H. A. Hoseini, M. Arjmand, U. Sundararaj, and M. Trifkovic, "Significance of interfacial interaction and agglomerates on electrical properties of polymer-carbon nanotube nanocomposites," *Materials and Design*, vol. 125, no. - April, pp. 126–134, 2017.
- [59] D. Nataraj, S. Sakkara, M. Meghwal, and N. Reddy, "Cross-linked chitosan films with controllable properties for commercial applications," *International Journal of Biological Macromolecules*, vol. 120, pp. 1256–1264, 2018.
- [60] H. Wu, Y. Lei, J. Lu et al., "Effect of citric acid induced crosslinking on the structure and properties of potato starch/chitosan composite films," *Food Hydrocolloids*, vol. 97, p. 105208, 2019.
- [61] N. Jain, A. Verma, and V. K. Singh, "Dynamic mechanical analysis and creep-recovery behaviour of polyvinyl alcohol based cross-linked biocomposite reinforced with basalt fiber," *Materials Research Express*, vol. 6, no. 10, p. 105373, 2019.
- [62] Y. Chen, J. Zhu, H. Y. Yu, and Y. Li, "Fabricating robust soft-hard network of self-healable polyvinyl alcohol composite films with functionalized cellulose nanocrystals," *Composites Science and Technology*, vol. 194, p. 108165, 2020.
- [63] P. Lu and Y. Lo Hsieh, "Preparation and characterization of cellulose nanocrystals from rice straw," *Carbohydrate Polymers*, vol. 87, no. 1, pp. 564–573, 2012.
- [64] H. Yu, H. Zhang, M. Song, Y. Zhou, J. Yao, and Q. Ni, "From cellulose nanospheres, nanorods to nanofibers: various aspect ratio induced nucleation/reinforcing effects on polylactic acid for robust-barrier food packaging," *ACS Applied Materials & Interfaces*, vol. 9, no. 50, pp. 43920–43938, 2017.
- [65] J. Rhim, J. P. Reddy, and X. Luo, "Isolation of cellulose nanocrystals from onion skin and their utilization for the preparation of agar-based bio-nanocomposites films and their utilization for the preparation of agar-based bio-nanocomposites films," *Cellulose*, vol. 22, no. 1, pp. 407–420, 2015.
- [66] Q. Wu, Y. Meng, K. Concha et al., "Influence of temperature and humidity on nano-mechanical properties of cellulose nanocrystal films made from switchgrass and cotton," *Industrial Crops and Products*, vol. 48, pp. 28–35, 2013.
- [67] C. Liu, B. Li, H. du et al., "Properties of nanocellulose isolated from corncob residue using sulfuric acid, formic acid, oxidative and mechanical methods," *Carbohydrate Polymers*, vol. 151, pp. 716–724, 2016.
- [68] P. Phanthong, P. Reubroycharoen, X. Hao, G. Xu, A. Abudula, and G. Guan, "Nanocellulose: extraction and application," *Carbon Resources Conversion*, vol. 1, no. 1, pp. 32–43, 2018.
- [69] K. Choo, Y. C. Ching, C. H. Chuah, S. Julai, and N. S. Liou, "Preparation and characterization of polyvinyl alcohol-chitosan composite films reinforced with cellulose nanofiber," *Materials (Basel)*, vol. 9, no. 8, p. 644, 2016.
- [70] J. Jose and M. A. Al-Harathi, "Citric acid crosslinking of poly(vinyl alcohol)/starch/graphene nanocomposites for superior properties," *Iranian Polymer Journal*, vol. 26, no. 8, pp. 579–587, 2017.

- [71] Z. Cui, Z. Zheng, L. Lin et al., "Electrospinning and crosslinking of polyvinyl alcohol/chitosan composite nanofiber for transdermal drug delivery," *Advances in Polymer Technology*, vol. 37, no. 6, p. 1928, 2018.
- [72] E. Lizundia, E. Fortunati, F. Dominici et al., "PLLA-grafted cellulose nanocrystals: role of the CNC content and grafting on the PLA bionanocomposite film properties," *Carbohydrate Polymers*, vol. 142, pp. 105–113, 2016.
- [73] T. Ben Shalom, Y. Nevo, D. Leibler et al., "Cellulose nanocrystals (CNCs) induced crystallization of polyvinyl alcohol (PVA) super performing nanocomposite films," *Macromolecular Bioscience*, vol. 19, no. 3, p. 1800347, 2019.
- [74] P. A. Sreekumar, M. A. Al-Harathi, and S. K. De, "Reinforcement of starch/polyvinyl alcohol blend using nano-titanium dioxide," *Journal of Composite Materials*, vol. 46, no. 25, pp. 3181–3187, 2012.
- [75] M. D. Stelescu, A. Airinei, E. Manaila et al., "Effects of electron beam irradiation on the mechanical, thermal, and surface properties of some EPDM/butyl rubber composites," *Polymers (Basel)*, vol. 10, no. 11, pp. 1206–1221, 2018.
- [76] A. K. Sonker, K. Rathore, R. K. Nagarale, and V. Verma, "Crosslinking of polyvinyl alcohol (PVA) and effect of crosslinker shape (aliphatic and aromatic) thereof," *Journal of Polymers and the Environment*, vol. 26, no. 5, pp. 1782–1794, 2018.
- [77] M. Song, H. Yu, J. Gu, S. Ye, and Y. Zhou, "Chemical crosslinked polyvinyl alcohol/cellulose nanocrystal composite films with high structural stability by spraying Fenton reagent as initiator," *International Journal of Biological Macromolecules*, vol. 113, no. 2017, pp. 171–178, 2018.
- [78] M. P. Weir, D. W. Johnson, S. C. Boothroyd et al., "Distortion of chain conformation and reduced entanglement in polymer-graphene oxide nanocomposites," *ACS Macro Letters*, vol. 5, no. 4, pp. 430–434, 2016.
- [79] R. Maria and H. Poetes, *Dynamic and Static Conformations at the Water-Solid Interface*, University of Cambridge, 2009.
- [80] C. Rieu, L. Bertinetti, R. Schuetz et al., "The role of water on the structure and mechanical properties of a thermoplastic natural block co-polymer from squid sucker ring teeth," *Bioinspiration & Biomimetics*, vol. 11, no. 5, pp. 1–10, 2016.
- [81] S. S. Nair, J. Zhu, Y. Deng, and A. J. Ragauskas, "High performance green barriers based on nanocellulose," *Sustainable Chemical Processes*, vol. 2, no. 1, pp. 1–7, 2014.
- [82] J. Wang, D. J. Gardner, N. M. Stark, D. W. Bousfield, M. Tajvidi, and Z. Cai, "Moisture and oxygen barrier properties of cellulose nanomaterial-based films," *ACS Sustainable Chemistry & Engineering*, vol. 6, no. 1, pp. 49–70, 2018.
- [83] W. Ma, P. Zhang, B. Zhao et al., "Swelling resistance and mechanical performance of physical crosslink-based poly(vinyl alcohol) hydrogel film with various molecular weight," *Journal of Polymer Science Part B: Polymer Physics*, vol. 57, no. 24, pp. 1673–1683, 2019.
- [84] P. A. Bersanetti, V. H. Escobar, R. F. Nogueira, F. dos Santos Ortega, P. Schor, and A. de Araújo Morandim-Giannetti, "Enzymatically obtaining hydrogels of PVA crosslinked with ferulic acid in the presence of laccase for biomedical applications," *European Polymer Journal*, vol. 112, pp. 610–618, 2019.
- [85] B. Singh and A. Kumar, "Graft and crosslinked polymerization of polysaccharide gum to form hydrogel wound dressings for drug delivery applications," *Carbohydrate Research*, vol. 489, p. 107949, 2020.

Research Article

Fabrication of Silver Nanoparticles Using *Fimbristylis miliacea*: A Cheap and Effective Tool against Invasive Mosquito Vector, *Aedes albopictus*

Mathalaimuthu Baranitharan,¹ Mahmoud Kandeel ,^{2,3} Govindan Shanmugavel,⁴ Kumaravel Kaliyaperumal,⁵ Kumaran Subramanian ,⁶ Kuppusamy Elumalai,⁷ Jayapal Gokulakrishnan,⁸ Hari Irrusappan,⁹ Senthil Rethinam,¹⁰ and S. Velmurugan ¹¹

¹Unit of Vector Control, Phytochemistry and Nanotechnology, Department of Zoology, Annamalai University, Annamalai Nagar, 608 002 Tamil Nadu, India

²Department of Biomedical Sciences, College of Veterinary Medicine, King Faisal University, Al-Ahsa, Saudi Arabia

³Department of Pharmacology, Faculty of Veterinary Medicine, Kafr El Sheikh University, Kafr El Sheikh, Egypt

⁴Department of HSS, Puducherry Technological University, Puducherry, India

⁵National Navel Orange Engineering Research Centre, Gannan Normal University, Ganzhou, Jiangxi, China

⁶Centre for Drug Discovery and Development, Sathyabama Institute of Science and Technology, Chennai, Tamil Nadu 600119, India

⁷Department of Advanced Zoology & Biotechnology, Government Arts College for men (Autonomous), Chennai, 600035 Tamil Nadu, India

⁸Department of Zoology, Poomphar College (Autonomous), Melaiyur, 609107 Tamil Nadu, India

⁹Center Health Research and Innovation, National Center for Vector Borne Disease Control, New Delhi, India

¹⁰Ege University, Turkey

¹¹Department of Biology, School of Natural Science, Madawalabu University, Oromiya Region, Ethiopia

Correspondence should be addressed to S. Velmurugan; velkas.cas@gmail.com

Received 1 April 2022; Accepted 1 June 2022; Published 30 June 2022

Academic Editor: V. Vijayan

Copyright © 2022 Mathalaimuthu Baranitharan et al. This is an open access article distributed under the Creative Commons Attribution License, which permits unrestricted use, distribution, and reproduction in any medium, provided the original work is properly cited.

Mosquitoes are the most critical group of insects in the context of public health, since they transmit key parasites and pathogens, causing millions of deaths annually. *Aedes albopictus* is an important invasive mosquito vector of dengue fever across urban and semiurban areas of India. In this study, we biofabricated silver nanoparticles (AgNPs) using the *Fimbristylis miliacea* aqueous leaf extract (*Fm*-ALE) as reducing and stabilizing agent. The synthesis of *Fm*-AgNPs was confirmed by the excitation of surface plasmon resonance and orange-brown color using ultraviolet-visible (UV-vis) spectrophotometry. High-resolution scanning electron microscopic (HR-SEM) and transmission electron microscopic (TEM) showed the clustered (size 0.5 μm) and quasi-spherical structures of *Fm*-AgNPs. The formation of AgNPs has been characterized by X-ray diffraction (XRD) spectroscopy. Fourier transform infrared (FTIR) spectroscopy investigated the identity of secondary metabolites, which may act as *Fm*-AgNP capping agents. These results propose that AgNPs synthesized provided from those *Fm*-ALE have the high sources to be improved into the most suitable materials useful for protecting and killing the invasive mosquito vector, *Ae. albopictus* populations. The acute toxicity of *Fm*-ALE synthesized Ag NPs, and a combined treatment testing blends of mosquito vector was evaluated against I, II, III, and IV instar larva's (ILs) of *Ae. albopictus*. The LC_{50} values of *Fm*-ALE (174.39 ppm I-ILs, 214.40 ppm II-ILs, 232.38 ppm III-ILs, and 251.62 ppm IV-ILs) and *Fm*-AgNPs synthesized were 23.78 ppm I-ILs; 27.88 ppm II-ILs; 31.47 ppm III-ILs; 36.68 ppm IV-ILs, respectively. Likewise, *Fm*-AgNP synthesis was more toxic than ALE in the invasive mosquito vector and recorded from UV-vis spectrum, FTIR, TEM, and XRD analysis. These results propose that AgNPs synthesized provided from those *Fm*-ALE have the high sources to be improved into the most suitable materials useful for protecting and killing the invasive mosquito vector, *Ae. albopictus* populations.

1. Introduction

Mosquito and mosquito-borne diseases (MBDs) are successfully spreading throughout the entire world, with an inordinate impact on adolescents and children, which are more important responsible for significant global morbidity and mortality [1]. The insect-borne disease is at risk of developing worldwide following globalization and the enlargement of travel and trade from areas colonized by vectors. *Aedes albopictus* (*Ae. albopictus* and tiger mosquito) is a belligerent, and aggressive, is arising entirely global as a population health danger following its basic process in current Chikungunya virus (CHIKV) and dengue virus (DENV) outbreaks, and is one of the most invasive animal species for one hundred in the world, and in less than 30 years, it has developed across the five continents, colonizing abundant lands [2–4]. Hence, the very quick enlargement of species was caused by the worldwide profession of tires and the ability to release maximum eggs that diapauses and resists almost cold winters of temperate areas [5–8]. Commonly, public alertness and general knowledge of *Aedes*-transmitted diseases may improve the likelihood of patients being discussed with a doctor. Its symptoms are agreeable to an arboviral disease improved soon after coming again from a country, where the disease is endemic [9, 10].

In the current year, bioactivity-way for a fabrication process of metal-NPs has been recommended as sources of natural, ecological-friendly replacement to classic physiochemical methods [11]. Specifically, AgNP synthesis is developing as multiple intention agents, because the reason to their biosynthesis is very easy and inexpensive, protection permanent over time, and most effective on arboviruses and human pathogenic bacteria [12, 13]. Population entering into any region mostly dengue, yellow fever, and disadvantages exist may control utilizing medicinal plant-derived repellents role [14–16].

Fimbristylis miliacea (*Fm* and medicinal herbs) sanctified with differential medicinal components are a potential of myriad compounds advantages for plant biologists, zoologist researchers, and human being population around the world, working in pursuit to detect source lead compounds from natural medicinal plant sources. It is all important, cell processes are activated by the potential composed by the metabolism of foods mainly by oxidation reactive, and essential energy with radicals like peroxid (ROS), superoxide and hydroxyl (OH), and imparts oxidative stress on the cells (IOSC). The signification research and recognition of benign phytochemicals from the *Fm*-medicinal plant thus become very significant in current years, and its species of variety plant has been pharmaceutical sources like antioxidant, anti-nociceptive, anti-inflammatory, antipyretic, antimicrobial, cytotoxic, hepatoprotective, and antidiabetic effects [17]. Since *Fimbristylis miliacea* is an easily available grass type with abundant phytoconstituent in this exploration, we stated a pattern to AgNP synthesis using the *Fm*-ALE, and it is a cheap and eco-friendly fabric process as a highly reducing and stabilizing agent. Here, we demonstrate a convenient eco-friendly green synthesis route for preparing AgNPs using *Fm*-ALE, and they are subjected to subsequent

analytical and biological characterization for investigating antibacterial and larvicidal abilities for controlling human disease-transmitting invasive mosquito vector, *Ae. albopictus* as shown in Figure 1.

2. Materials and Methods

2.1. Collection and Preparation. Silver nitrate (Ag^+) was procured from Lakshmi Scientific Chemicals Ltd., Pondicherry in India. *Fm*-fresh leaf was gathered from the Western Ghats Forest (WGF) ($10^{\circ}36'N$ to $10^{\circ}14'N$ latitude and $76^{\circ}49'E$ to $76^{\circ}77'E$ longitude), Erode District, India. After, the glassware was cleaned thoroughly in acid and washed off with triple-distilled water. The new identification was proved at the Department of Botany, Annamalai University, and specimens were numbered (Authentication Number SVC/BOT/131). Leaves were retained in our department laboratory and ready for use upon request. *Fm*-fresh leaves were dried in the shade, and ALE was produced by blending 30 g of air-dried leaves with 300 mL of water, with stable stirring on a magnetic stirrer. Then, air-dried ALE was left for 3 h and separated by Whatman No. 1 filter paper. It was saved in an amber-colored airtight bottle at 10°C temperature until research.

2.2. Target Medical Pest. Larvae stage, such as I, II, III, and IV-ILs of medical important pest *Ae. albopictus*, was taken from stagnant fresh water at around from side by side from Poompuhar College to Sirkazhi down ($11^{\circ}14'N$ to $11^{\circ}23'N$ latitude and $79^{\circ}81'E$ to $79^{\circ}73'E$ longitude), Nagapattinam District in India. *Ae. albopictus* is identified by ICMR, Madurai in India, and carried to the laboratory for continuous rearing. Dog biscuits+yeast powder mixed feed was (3 : 1 ratio) utilized to culture the mosquito under ($27 \pm 2^{\circ}\text{C}$, $75 \pm 5\%$ relative humidity, with a photoperiod of 12L:12D) possible environment.

2.3. Larval Bioassay. The protocol was accepted for larval bioassay and concentration range from 10 to $250 \mu\text{g/mL}$. The necessary *Fm*-ALE and AgNPs were mixed (249 mL) in triple-distilled water. After, each research was assayed against 3rd instars of twenty-five larvae, repeated 5 times. The lethal concentration (50/90) and other statistical data were calculated by using Probit analysis [19].

2.4. Primary Chemical Analysis. The PCA is followed by the methods [20, 21]. We screened the bioactive chemical constituents (CCs) detecting the presence of secondary metabolites such as alkaloids, flavonoids, saponins, steroids, tannins, terpenoids, tri-terpenoids, anthraquinones, amino acid, phenol, glycosides, carbohydrate, protein, and phytochemicals in the *Fm*-ALE.

2.5. Silver Nanoparticle (AgNP) Synthesis. AgNO_3 90 mL Mm added with *Fm*-ALE 10 mL was made in 250 mL conical flasks for decreases into Ag^+ ions. After that, the mixture was kept for 1 h at $27 \pm 3^{\circ}\text{C}$ in the laboratory conditions. Wherein, the first initial stage was detection of *Fm*-AgNPs containing dark brown color change in the mixture (ALE

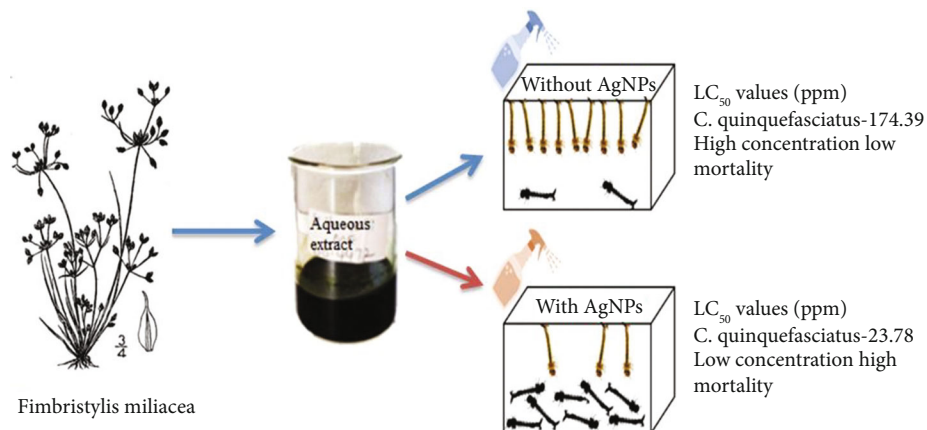


FIGURE 1: Schematic illustration of green synthesis of AgNPs using *Fm*-ALE for effective invasive vector mosquito control applications.

TABLE 1: Larvicidal activity of *Fm*-aqueous extract against *Ae. albopictus*.

| Stages | LC ₅₀ (mg/L) | 95% confidence limits | | LC ₉₀ (mg/L) | Slope | Regression | χ^2 |
|-------------------------|-------------------------|-----------------------|--------|-------------------------|----------|---------------------------|----------|
| | | LCL | UCL | | | | |
| Instars 1 st | 174.39 | 164.66 | 184.78 | 271.29 | 3.642772 | $y = 3.642 \times -2.669$ | 4.721 |
| Instars 2 nd | 214.40 | 201.40 | 230.41 | 332.01 | 2.728162 | $y = 2.728 \times -1.352$ | 3.516 |
| Instars 3 rd | 232.38 | 217.07 | 252.56 | 357.69 | 2.448937 | $y = 2.448 \times -1.084$ | 2.508 |
| Instars 4 th | 251.62 | 234.66 | 275.24 | 371.21 | 1.648359 | $y = 1.648 \times -1.467$ | 1.911 |

Values represent the mean of five replications. Mortality of the after 24 h of exposure period LC₅₀ = lethal concentration brings out 50% mortality and LC₉₀ = lethal concentration brings out 90% mortality. LCL = lower confidence limit; UCL = upper confidence limit; χ^2 = chi-square. ^aSignificant at $p < 0.05$.

TABLE 2: Larvicidal activity of *Fm*-AgNPs synthesized against *Ae. albopictus*.

| Stages | LC ₅₀ (mg/L) | 95% confidence limits | | LC ₉₀ (mg/L) | Slope | Regression | χ^2 |
|-------------------------|-------------------------|-----------------------|-------|-------------------------|----------|---------------------------|----------|
| | | LCL | UCL | | | | |
| Instars 1 st | 23.78 | 21.56 | 25.83 | 44.40 | 4.628878 | $y = 4.628 \times -0.048$ | 4.048 |
| Instars 2 nd | 27.88 | 25.48 | 30.20 | 52.35 | 3.134263 | $y = 3.134 \times +0.989$ | 0.490 |
| Instars 3 rd | 31.47 | 29.10 | 33.91 | 56.61 | 2.447822 | $y = 2.447 \times +0.935$ | 0.422 |
| Instars 4 th | 36.68 | 34.32 | 39.32 | 60.95 | 1.462074 | $y = 1.462 \times +0.659$ | 0.326 |

Values represent the mean of five replications. Mortality of the after 24 h of exposure period LC₅₀ = lethal concentration brings out 50% mortality and LC₉₀ = lethal concentration brings out 90% mortality. LCL = lower confidence limit; UCL = upper confidence limit; χ^2 = chi-square. ^aSignificant at $p < 0.05$.

+AgNO₃). The entire reaction is granted in a dark place to avoid photoactivation. For the purification activity, acquired *Fm*-AgNPs allowed to ultracentrifugation above 6,000 rpm for 20 min. After the centrifugation, the supernatant was rejected, and the pellet was cautiously diluted with triple-distilled H₂O [22]. Further, mixed material was placed in the laboratory, labeled, and stocked for further analysis.

2.6. Characterization of AgNPs. After the Ag⁺ ion solution was intently watched carefully by using UV-vis spectroscopy, purified *Fm*-AgNPs (biomolecules) in the FTIR spectroscopy, and obtained to dry at 60°C, the air-dried powder was inflicted to XRD spectroscopy to identify their exact structure and material [23]. *Fm*-ALE mediated synthesis of AgNP process such as UV, FT-IR, TEM, and XRD analyses.

2.7. Data Analysis. The larvicidal activity (%) data of invasion mosquito, *Ae. albopictus* larvae, were subjected to different statistical baggage, LC₅₀/LC₉₀, LCL, UCL, regression, chi-square, slope, etc. All the values were calculated by (IBM) SPSS statistical new version 20.0 version.

3. Results and Discussion

3.1. Larvae Bioassay of *Fm*-ALE Extract and AgNP Synthesis. The larval bioassay of *Fm*-ALE treatment was tested against I, II, III, and IV-ILs of important invasive mosquitoes and is shown in Table 1. The LC₅₀/LC₉₀ values of *Fm*-ALE appeared to be effective against I-ILs (174.39/271.29 µg/mL), II-ILs (214.40/332.01 µg/mL), III-ILs (232.38/357.69 µg/mL), and IV-ILs (251.62/371.21 µg/mL) invasive



FIGURE 2: Phytochemical test present in the *Fm*-ALE.

mosquito larvae, *Ae. albopictus*. Table 2 shows the treatment of *Fm*-AgNPs synthesized and had the following LC_{50} and LC_{90} values; ILs had LC_{50}/LC_{90} values of 23.78/44.40 $\mu\text{g}/\text{mL}$; II-ILs had values of 27.88/52.35 $\mu\text{g}/\text{mL}$; III-ILs had values of 31.47/56.61 $\mu\text{g}/\text{mL}$; IV-ILs had values of 36.68/60.95 $\mu\text{g}/\text{mL}$. A control contained nil mortality in the same time assay, and the χ^2 value was significant at $p < 0.05$ level.

3.2. Preliminary Analysis. *Fm*-ALE was screened for the presence of major phytochemicals (MPCs) such as alkaloids (Figure 2(a)), flavonoids (Figure 2(b)), saponins (Figure 2(c)), steroids (Figure 2(d)), tannins (Figure 2(e)), terpenoids (Figure 2(f)), tri-terpenoids (Figure 2(g)), phenol (Figure 2(h)), carbohydrate (Figure 2(i)), protein

(Figure 2(j)), phytosterols (Figure 2(k)), and all for test tube (Figure 2(l)) except anthraquinones, amino acid, and glycosides responsible of mosquitocidal activity (Table 3).

3.3. UV, XRD, SEM, and TEM Analysis of *Fm*-AgNPs. The *Fm*-ALE of AgNP (AgNO_3 +ALE) composite was indicated and confirmed via the orange-brown color change (Figure 3). Figure 4 shows the AgNO_3 solution turned brown within 2 min with the addition of *Fm*-ALE and the control AgNO_3 solution (without ALE) showed no change of any color. There was no absorption peak in the UV-vis spectrum, which can reduce Ag^+ ions and produce AgNPs of incubation at the highest pH (Figures 5 and 6). The preparation of the AgNPs synthesized from *Fm*-ALE was

TABLE 3: Phytochemical screening of *Fm*-ALE.

| S. no. | Phytoconstituents | Aqueous |
|--------|-------------------|---------|
| 1 | Alkaloids | +++ |
| 2 | Flavonoids | + |
| 3 | Saponins | ++ |
| 4 | Steroids | — |
| 5 | Tannins | + |
| 6 | Terpenoids | +++ |
| 7 | Tri-terpenoids | ++ |
| 8 | Anthraquinones | — |
| 9 | Amino acid | — |
| 10 | Phenol | + |
| 11 | Glycosides | — |
| 12 | Carbohydrate | ++ |
| 13 | Protein | + |
| 14 | Phytosteroids | ++ |

+++ : strongly positive phytochemical group; ++ : positive phytochemical group; + : trace phytochemical group; — : absence of phytochemical group.



FIGURE 3: *Fm*-ALE-mediated synthesis of AgNPs process.

evaluated through a spectrophotometer in a range of wavelengths from 200 to 1200 nm.

Figure 7 shows the high-resolution scanning electron microscopic (HR-SEM) and transmission electron microscopic (TEM) analysis supplies the information about the sizes, and morphology of AgNPs was obtained ranging from 41 to 60 nm. The morphology of the AgNPs is quasispherical as seen in the SEM image. There was cluster formation of an average size of 0.5 μm due to evaporation of suspended liquid causing the particles to cluster around the outer edge to form quasispherical structures. Figure 5 displays the formation of *Fm*-AgNPs characterized using XRD analysis. The six well defined characteristic diffraction peaks at 27.8°, 32.2°, 46.1°, 54.8°, 57.5°, and 76.7° correspond to the

face-centered cubic crystal-shaped structure of metallic silver. The interplanar spacing (d) values were obtained as 3.196, 2.769, 1.963, 1.671, 1.600, and 1.240 Å using Bragg's formula from the XRD pattern and were further corroborated crystalline nature of *Fm*-AgNPs. The lattice constant was calculated was 3.196 Å which was well-matching with standard data (JCPDS PDF04-0783). The peak broadening was observed due to the formation of nanoparticles. The peak intensity of the (corresponding 111 to 311) plane indicated the purity of AgNPs. It is significant to record that the intensity ratio between 36° and 53° peaks is lesser than the value of the standard (0.48 versus 0.5).

3.4. FT-IR Analysis. Figure 6 shows the that FTIR spectrum showed major peaks at 3571.77, 3423.39, 1986.17, 1055.96, 1038.12, 981.81, 726.78, 600.26, 567.83, 495.03, 454.77, and 428.76 cm^{-1} . Above the peak value, they correspond to functional groups like the alcohol group in lower (C=O band stretch, alkoxy, 3571.77 cm^{-1}), alcohol and phenol group in strong and broad (O-H stretch, H-bonded, 3423.39 cm^{-1}), aromatic group in strong (C-H bend stretch, 1986.17 cm^{-1}), aliphatic amines group in medium (C-N stretch, 1055.96, 1038.12 cm^{-1}), alkenes group in strong (C-H rock, 981.81, 726.78 cm^{-1}), and alkyl halides group in medium (C-Br stretch, 600.26, 567.83 cm^{-1}).

4. Discussion

According to the latest World malaria report, there were 241 million cases of malaria in 2020 compared to 227 million cases in 2019. The estimated number of malaria deaths stood at 627 000 in 2020—an increase of 69 000 deaths over the previous year [22]. Mosquitocidal resistance requires the growth of approaches for prolonging the use of more effective vector control compounds. The use of mixed differential insecticides and phytochemicals is one such approach that may be acceptable for mosquito control [23, 24]. Phytochemical compounds (PCMs) may act as the most suitable alternative to synthetic insect-killing activity in the future and are readily obtained in many research areas in the global because are comparably safe and inexpensive. Medicinal plants not only contain some AgNPs but are proven to be nonlethal for aquatic life stages of the mosquito vector, *Ae. albopictus*, and are easily biodegradable in the environment. In the current research, *Fm*-AgNPs synthesized were more toxic than ALE in the invasive mosquito vector and resulted from UV-vis spectrum, FTIR, TEM, and XRD analyses. Similarly, UV-vis spectrum, FTIR, TEM, and EDX analyses from *Helitropium indicum*-AgNPs and were highly larval killing activity ($\text{LC}_{50}/\text{LC}_{90}$ values of 72.72/126.86 $\mu\text{g}/\text{mL}$) [25]. Almost, spherical and cubic NPs are the very most general materials of AgNP synthesis green potentials [26]. Also, previously researched, the *Sargassum muticum*-derived synthesized AgNPs signify that they were very strong scattered, with AgNPs a size range of 43-79 nm [27]. This research is in agreement with a previous result; SEM focused that the *Hygrophila auriculata*-AgNPs synthesized were an almost spherical or cubic shape, with a mean size ranging from 9.0 to 30 nm and XRD acute peaks at 2θ values of 38.13 (111),

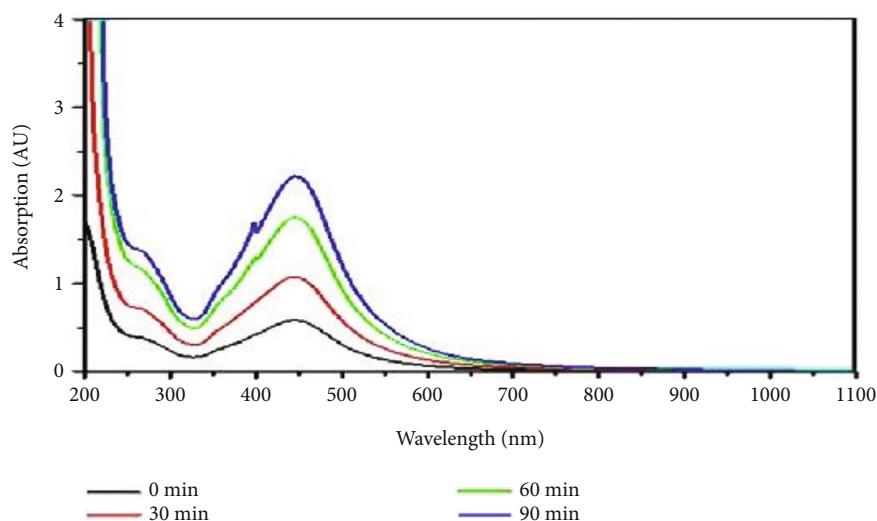


FIGURE 4: UV-vis spectral of AgNO_3 with *Fm*-ALE.

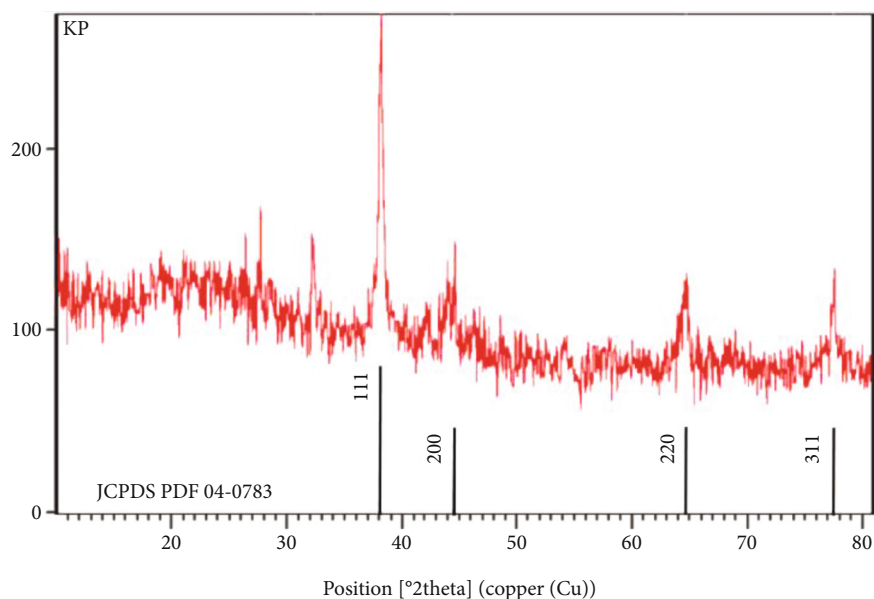
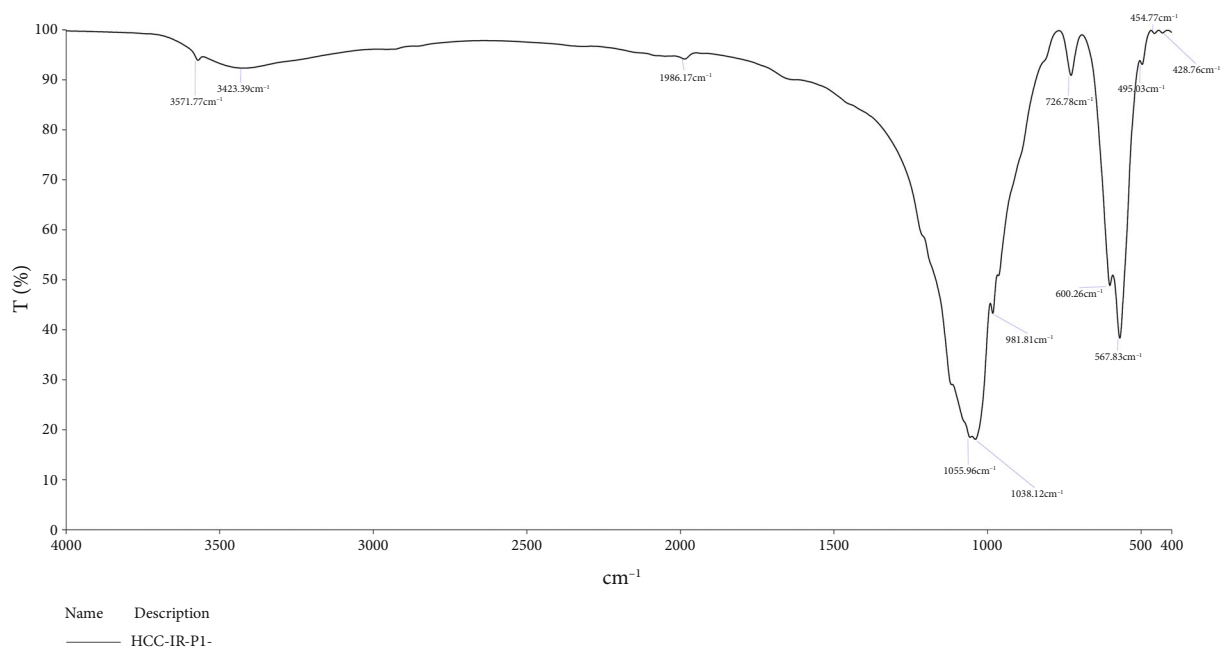
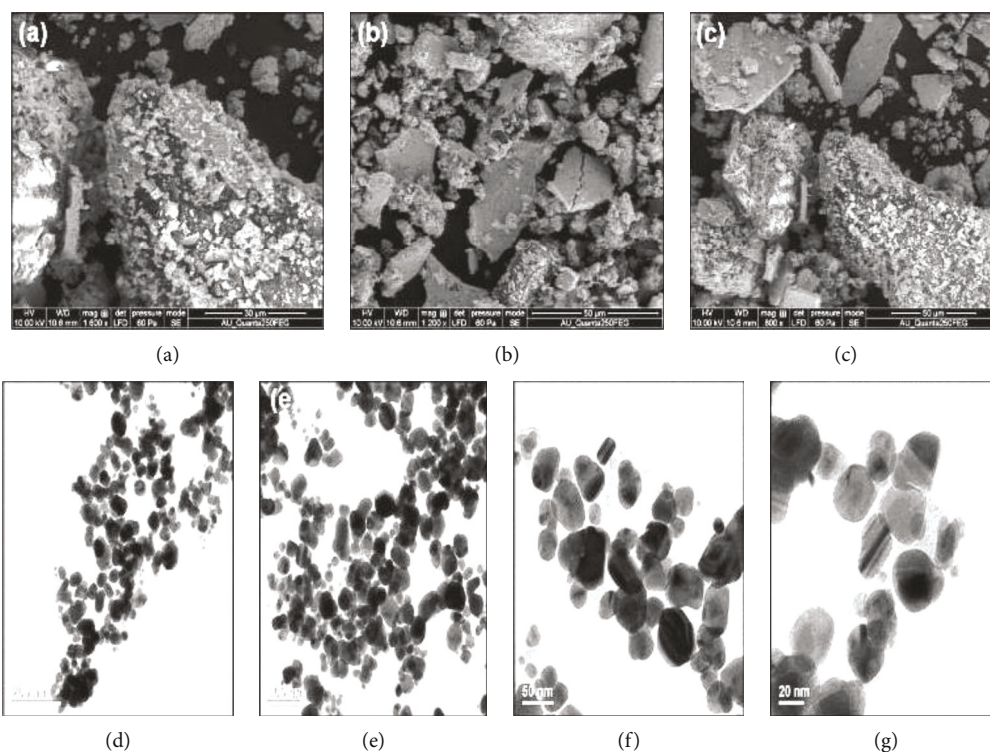


FIGURE 5: X-ray diffraction (XRD) analysis of AgNPs synthesized using *Fm*-ALE.

44.31 (200), 64.44 (220), 77.37 (311) planes of the cubic face-centered Ag [28]. FTIR analysis of the purified *Chomeliaasiatica*-AgNPs, and the bands due to hydrogen-bonded (O-H stretch, 3222.44 cm^{-1}), alkenes (C-H stretch, 2922.23 cm^{-1} and 2853.35 cm^{-1}), nitriles ($\text{C}\equiv\text{N}$ (triple bond) stretch, 2209.12 cm^{-1}), aromatics (C-C stretch, 1593.43 cm^{-1}), aliphatic amines (C-N stretch, 1240.74 cm^{-1}), alkyl halides (C-H stretch, 1167.81 cm^{-1}), alcohol (C-O stretch, 1102.98 cm^{-1}), and alkyl halides (C-C1 stretch, 833.39 cm^{-1}) [24].

The present investigation shows that the $\text{LC}_{50}/\text{LC}_{90}$ values of *Fm*-ALE appeared to be effective against 1st instars ($174.39/271.29\text{ }\mu\text{g/mL}$), 2nd instars ($214.40/332.01\text{ }\mu\text{g/mL}$), 3rd instars ($232.38/357.69\text{ }\mu\text{g/mL}$), and 4th instars ($251.62/371.21\text{ }\mu\text{g/mL}$) invasive mosquito larvae, *Ae. albopictus*. The detection of the current investigation corresponds with

some of the next other previous research, the $\text{LC}_{50}/\text{LC}_{90}$ values of *Polygonum hydropiper*-oil were $194.63/199.65\text{ ppm}$, and confertifolin was $2.02/3.16\text{ ppm}$ against the 2nd and 4th instars larvae of tiger mosquito [29]. *Fm*-AgNPs synthesized had the following: 1st instars larvae had $\text{LC}_{50}/\text{LC}_{90}$ values of $23.78/44.40\text{ }\mu\text{g/mL}$; 2nd instars larvae had values of $27.88/52.35\text{ }\mu\text{g/mL}$; 3rd instars larvae had values of $31.47/56.61\text{ }\mu\text{g/mL}$; and 4th instars larvae had values of $36.68/60.95\text{ }\mu\text{g/mL}$. Similarly, several previous reports supported the mosquito-killing activity (larval, eggs, and adults) potential of different indigenous medicinal plant-aqueous extract and AgNPs against important vector mosquitoes (IVMs) [26, 30–34]. Particularly, a biochemical method has been used to constant AgNPs synthesized that was researched opposite to *Ae. aegypti* larval killing activity

FIGURE 6: FTIR spectrum of *Fm*-AgNP synthesis.FIGURE 7: SEM (a–c) and TEM (d–g) images of spherical AgNPs synthesized using *Fm*-ALE.

[35]. Ginger was more effective with the lowest LC_{50} values of 1st instar 7 ppm, 2nd instar 23 ppm, 3rd instar 33 ppm, and 4th instar 35 ppm, after 8 and 16 h against dengue vector, *Ae. albopictus* [36].

The *Bryopsis pennata*-chloroform extract exhibited strong larval killing activity (LC_{50} value was 250.5 $\mu\text{g}/\text{mL}$) against the tiger mosquito vector, *Ae. albopictus* [37].

Cochliobolus lunatus-AgNP synthesis of larval killing activity was tested and LC_{50}/LC_{90} values of *Ae. aegypti* 2nd instars 1.29/3.08 ppm, 3rd 1.48/3.33 ppm, and 4th instars 1.58/3.41 ppm [38]. Similarly, larval death rates were recorded from *Jussiaea repens*-LEE, and MPC has larvicidal activity with an LC_{50}/LC_{90} value of *Ae. albopictus* that was 118.3/229.9 $\mu\text{g}/\text{mL}$ [39]. *Eucalyptus camaldulensis*- and *Eucalyptus*

urophylla-EO noticed 60/100% larval death rates at 100 µg/mL tested against invasive mosquito, *Ae. Albopictus* [7, 40].

5. Conclusion

In conclusion, the green plants showed that the environmentally benign and revived source of *Fm*-ALE is utilized as an effective lowering agent AgNP synthesis. *Fimbristylis miliacea* is an easily available grass plant with immense medical value utilized for its insect repellent activity. Following this, our reports recommend that *Fm*-plant can be used for the development of insect repellent pesticides in the future prospect. This research was aimed at defining key aspects, such as the nature of the specific molecules responsible for the insecticidal effect observed. Further, the promising effects showed these chemicals in the environment and population health and the field logistics required for utilize of such a local insecticide. The instability in the bioefficacy of medicinal plants tested against mosquito vectors is generally known by variations in the quality and quantity of active compounds and AgNPs. We convey advice that these *Fm*-ALE and AgNPs should be studied in the field for the confirmed potential control of invasive mosquito, *Ae. albopictus*.

Data Availability

The data used to support the findings of this study are included in the article.

Conflicts of Interest

The authors declare that they have no conflicts of interest.

Acknowledgments

This work was supported by the Deanship of Scientific Research, Vice Presidency for Graduate Studies and Scientific Research, King Faisal University, Saudi Arabia (Project No. GRANT834).

References

- [1] M. Baranitharan, B. Sawicka, J. Gokulakrishnan, and J. Gokulakrishnan, "Phytochemical profiling and larval control of *Erythrina variegata* methanol fraction against malarial and filarial vector," *Advances in Preventive Medicine*, vol. 2019, Article ID 2641959, 9 pages, 2019.
- [2] G. Rezza, L. Nicoletti, R. Angelini et al., "Infection with chikungunya virus in Italy: an outbreak in a temperate region," *Lancet*, vol. 370, no. 9602, pp. 1840–1846, 2007.
- [3] F. Schaffner, J. M. Medlock, and W. Bortelvan, "Public health significance of invasive mosquitoes in Europe," *Clinical Microbiology and Infection*, vol. 19, no. 8, pp. 685–692, 2013.
- [4] M. U. G. Kraemer, M. E. Sinka, K. A. Duda et al., "The global distribution of the arbovirus vectors *Aedes aegypti* and *Ae. Albopictus*," *eLife*, vol. 4, article e08347, 2015.
- [5] M. Q. Benedict, R. S. Levine, W. A. Hawley, and L. P. Lounibos, "Spread of the tiger: global risk of invasion by the mosquito *Aedes albopictus*," *Vector Borne and Zoonotic Diseases*, vol. 7, no. 1, pp. 76–85, 2007.
- [6] X. Huang, M. F. Poelchau, and P. A. Armbruster, "Global Transcriptional Dynamics of Diapause Induction in Non-Blood-Fed and Blood-Fed *Aedes albopictus*," *PLoS Neglected Tropical Diseases*, vol. 9, no. 4, article e0003724, 2015.
- [7] K. Krishnappa, M. Baranitharan, K. Elumalai, and J. Pandiyan, "Larvicidal and repellent effects of *Jussiaea repens* (L.) leaf ethanol extract and its major phyto-constituent against important human vector mosquitoes (Diptera: Culicidae)," *Environmental Science and Pollution Research*, vol. 27, no. 18, pp. 23054–23061, 2020.
- [8] M. Baranitharan, K. Krishnappa, K. Elumalai et al., "*Citrus limetta* (Risso) - borne compound as novel mosquitocides: effectiveness against medical pest and acute toxicity on non-target fauna," *South African Journal of Botany*, vol. 128, pp. 218–224, 2020.
- [9] B. Caputo, M. Manica, and G. Russo, "Knowledge, attitude and practices towards the tiger mosquito *Aedes albopictus*. A questionnaire based survey in Lazio region (Italy) before the 2020 chikungunya outbreak," *International Journal of Environmental Research and Public Health*, vol. 17, no. 11, p. 3960, 2020.
- [10] M. Baranitharan, J. Gokulakrishnan, and N. Sridhar, *Introduction of vector mosquitoes*, LAB Lambert Academic Publishing, 2018.
- [11] R. Rajan, K. Chandran, S. L. Harper, S. I. Yun, and P. T. Kalichelvan, "Plant extract synthesized nanoparticles: an ongoing source of novel biocompatible materials," *Industrial Crops and Products*, vol. 70, pp. 356–373, 2015.
- [12] D. Dinesh, K. Murugan, P. Madhiyazhagan et al., "Mosquitocidal and antibacterial activity of green-synthesized silver nanoparticles from *Aloe vera* extracts: towards an effective tool against the malaria vector *Anopheles stephensi*," *Parasitology Research*, vol. 114, no. 4, pp. 1519–1529, 2015.
- [13] V. Sujitha, K. Murugan, M. Paulpandi et al., "Green-synthesized silver nanoparticles as a novel control tool against dengue virus (DEN-2) and its primary vector *Aedes aegypti*," *Parasitology Research*, vol. 114, no. 9, pp. 3315–3325, 2015.
- [14] P. Mahesh Kumar, K. Murugan, K. Kovendan, J. Subramaniam, and D. Amaresan, "Mosquito larvicidal and pupicidal efficacy of *Solanum xanthocarpum* (family: Solanaceae) leaf extract and bacterial insecticide, *Bacillus thuringiensis*, against *Culex quinquefasciatus* say (Diptera: Culicidae)," *Parasitology Research*, vol. 110, no. 6, pp. 2541–2550, 2012.
- [15] M. Baranitharan, S. Dhanasekaran, J. Gokulakrishnan, K. Krishnappa, and J. Deepa, "Mosquito larvicidal properties of *Sesamum indicum* L. against *Aedes aegypti* (Linn.), *Anopheles stephensi* (Liston), *Culex quinquefasciatus* (Say) (Diptera: Culicidae)," *Life Science Archives*, vol. 3, pp. 130–136, 2015.
- [16] G. Benelli, "Research in mosquito control: current challenges for a brighter future," *Parasitology Research*, vol. 114, no. 8, pp. 2801–2805, 2015.
- [17] H. M. Ummah, R. Roni, F. Mahmuda et al., "Phytochemical analysis, antioxidant and anti-diarrhoeal activities of methanol extract of *Fimbristylis miliacea* (L.) Vahl," *Journal of Pharmacognosy and Phytotherapy*, vol. 12, no. 1, pp. 10–18, 2020.
- [18] World Health Organization, "Guidelines for laboratory and field testing of mosquito larvicides," in *Communicable disease control, prevention and eradication, WHO pesticide evaluation scheme*, WHO, Geneva, 2005, WHO/CDS/WHOPES/GCDPP/1.3.
- [19] D. J. Finney, "A statistical treatment of the sigmoid response curve," in *Probit analysis*, Cambridge University Press London 633, 1971.

- [20] M. Sathish Kumar, S. Selvakumar, M. R. K. Rao, and S. Anbuselvi, "Preliminary phytochemical analysis of *Dodonaeaviscosaleaves*," *Asian Journal of Plant Science and Research*, vol. 3, pp. 43–46, 2013.
- [21] B. Mathalaimuthu, D. Shanmugam, K. Kovendan, M. Kadarkarai, G. Jayapal, and G. Benelli, "Coleus aromaticus leaf extract fractions: A source of novelovicides, larvicides and repellents against Anopheles, Aedes and Culex mosquito vectors?," *Process Safety and Environ Protect*, vol. 106, pp. 23–33, 2017.
- [22] "Vector borne diseases," WHO, March 2020 (<https://www.who.int/news-room/fact-sheets/detail/vector-borne-diseases>).
- [23] G. Suresh, P. H. Gunasekar, D. Kokila et al., "Green synthesis of silver nanoparticles using Delphinium denudatum root extract exhibits antibacterial and mosquito larvicidal activities," *Spectrochimica Acta Part A: Molecular and Biomolecular Spectroscopy*, vol. 127, pp. 61–66, 2014.
- [24] M. Baranitharan, S. Alarifi, S. Alkahtani et al., "Phytochemical analysis and fabrication of silver nanoparticles using *Acacia catechu*: an efficacious and ecofriendly control tool against selected polyphagous insect pests," *Saudi Journal of Biological Sciences*, vol. 28, no. 1, pp. 148–156, 2021.
- [25] U. Muthukumar, M. Govindarajan, and M. Rajeswary, "Mosquito larvicidal potential of silver nanoparticles synthesized using *Chomelia asiatica* (Rubiaceae) against *Anopheles stephensi*, *Aedes aegypti*, and *Culex quinquefasciatus* (Diptera: Culicidae)," *Parasitology Research*, vol. 114, no. 3, pp. 989–999, 2015.
- [26] K. Veerakumar, M. Govindarajan, and U. Muthukumar, "Retracted article: mosquito larvicidal properties of silver nanoparticles synthesized using *Heliotropium indicum* (Boraginaceae) against *Aedes aegypti*, *Anopheles stephensi*, and *Culex quinquefasciatus* (Diptera: Culicidae)," *Parasitology Research*, vol. 113, no. 6, pp. 2363–2373, 2014.
- [27] G. Benelli, C. M. Lukehart, and C. M. Lukehart, "Special issue: applications of green synthesized nanoparticles in pharmacology, parasitology and entomology," *SJournal of Cluster Science*, vol. 28, no. 1, pp. 3–10, 2017.
- [28] P. Madhiyazhagan, K. Murugan, A. N. Kumar et al., "Sargassum muticum-synthesized silver nanoparticles: an effective control tool against mosquito vectors and bacterial pathogens," *Parasitology Research*, vol. 114, no. 11, pp. 4305–4317, 2015.
- [29] B. Subash, P. Vijayan, and M. Baranitharan, "Biosynthesis of silver nanoparticles using *Hygrophila auriculata*: a novel route of malarial fever vector mosquito control," *International Journal of Scientific & Technology Research*, vol. 8, pp. 4010–4018, 2019.
- [30] R. Maheswaran and S. Ignacimuthu, "Effect of *Polygonum hydropiper* L. against dengue vector mosquito *Aedes albopictus* L.," *Parasitology Research*, vol. 113, no. 9, pp. 3143–3150, 2014.
- [31] M. Govindarajan, S. L. Hoti, and G. Benelli, "Facile fabrication of eco-friendly nano-mosquitocides: biophysical characterization and effectiveness on neglected tropical mosquito vectors," *Enzyme and Microbial Technology*, vol. 95, pp. 155–163, 2016.
- [32] K. Elumalai, S. Dhanasekaran, and K. Krishnappa, "Larvicidal activity of saponin isolated from *Gymnema sylvestre* R. Br. (Asclepiadaceae) against Japanese encephalitis vector, *Culex tritaeniorhynchus* Giles (Diptera: Culicidae)," *European Review for Medical and Pharmacological Sciences*, vol. 17, no. 10, pp. 1404–1410, 2013.
- [33] J. Gokulakrishnan, M. Baranitharan, S. Dhanasekaran et al., "Mosquito larvicidal properties of *Ocimum sanctum* Linn. (Lamiaceae) against *Aedes aegypti* (Linn.), *Anopheles stephensi* (Liston), *Culex quinquefasciatus* (say)," *Life Science Archives*, vol. 1, pp. 46–52, 2015.
- [34] K. Kovendan, B. Chandramohan, D. Dinesh et al., "Green-synthesized silver nanoparticles using *Psychotria nilgiriensis*: toxicity against the dengue vector *Aedes aegypti* (Diptera: Culicidae) and impact on the predatory efficiency of the non-target organism *Poecilia sphenops* (Cyprinodontiformes: Poeciliidae)," *Journal of Asia-Pacific Entomology*, vol. 19, no. 4, pp. 1001–1007, 2016.
- [35] A. Jebanesan, M. Baranitharan, K. Kovendan, and P. B. Avery, "Impact of *Punica granatum*-based green larvicide on the predation rate of *Polypedates cruciger* for the control of mosquito vectors, *Anopheles stephensi* and *Culex quinquefasciatus* (Diptera: Culicidae)," *International Journal of Tropical Insect Science*, vol. 41, no. 2, pp. 1075–1085, 2021.
- [36] N. K. Arjunan, K. Murugan, C. Rejeeth, P. Madhiyazhagan, and D. R. Barnard, "Green synthesis of silver nanoparticles for the control of mosquito vectors of malaria, filariasis, and dengue," *Vector-Borne and Zoonotic Diseases*, vol. 12, no. 3, pp. 262–268, 2012.
- [37] S. Nasir, I. Nasir, M. Asrar, and M. Debboun, "Larvicidal and pupicidal action of medicinal plant extracts against dengue mosquito *Aedes albopictus* (Skuse)," *Indian Journal of Animal Research*, vol. 51, no. 1, pp. 155–158, 2017.
- [38] K. X. Yu, C. L. Wong, R. Ahmad, and I. Jantan, "Mosquitocidal and oviposition repellent activities of the extracts of seaweed *Bryopsis pennata* on *Aedes aegypti* and *Aedes albopictus*," *Molecules*, vol. 20, no. 8, pp. 14082–14102, 2015.
- [39] R. B. Salunkhe, S. V. Patil, C. D. Patil, and B. K. Salunke, "Larvicidal potential of silver nanoparticles synthesized using fungus *Cochliobolus lunatus* against *Aedes aegypti* (Linnaeus, 1762) and *Anopheles stephensi* Liston (Diptera; Culicidae)," *Parasitology Research*, vol. 109, no. 3, pp. 823–831, 2011.
- [40] S. S. Cheng, C. G. Huang, Y. J. Chen, J. J. Yu, W. J. Chen, and S. T. Chang, "Chemical compositions and larvicidal activities of leaf essential oils from two eucalyptus species," *Bioresource Technology*, vol. 100, no. 1, pp. 452–456, 2009.

Research Article

Effects of Thermal Barrier Coating Using Various Dosing Levels of Aluminium Oxide Nanoadditive Fuel on Diesel in Compressed Ignition Engine

V. S. Shaisundaram¹, S. Saravanakumar,² V. Balambica,³ D. Sendil Kumar,⁴ M. Chandrasekaran,⁵ R. Muraliraja,⁵ A. Muniappan,⁶ and Yalew Asres⁷

¹Department of Automobile Engineering, Vels Institute of Science Technology and Advanced Studies (VISTAS), Chennai, India

²Department of Automobile Engineering, Easwari Engineering College, Chennai, India

³Department of Mechatronics Engineering, Bharath Institute of Higher Education & Research, Chennai, India

⁴Department of Mechanical Engineering, Sri Ganesh College of Engineering & Technology, Puducherry, India

⁵Department of Mechanical Engineering, Vels Institute of Science Technology and Advanced Studies (VISTAS), Chennai, India

⁶Institute of Mechanical Engineering, Saveetha School of Engineering, Saveetha Institute of Medical and Technical Science, Chennai, India

⁷Department of Mechanical Engineering, Faculty of Manufacturing, Institute of Technology, Hawassa University, Hawassa, Ethiopia

Correspondence should be addressed to V. S. Shaisundaram; shaisundaram@gmail.com

Received 25 March 2022; Accepted 10 May 2022; Published 21 June 2022

Academic Editor: V. Vijayan

Copyright © 2022 V. S. Shaisundaram et al. This is an open access article distributed under the Creative Commons Attribution License, which permits unrestricted use, distribution, and reproduction in any medium, provided the original work is properly cited.

Environmental effects of vehicle exhausts from internal combustion engines which accounts for about 90% of vehicles on the roads is posing a major threat to environmental safety, and it only continues to surge at an alarming rate now than ever. With diesel engines being the most cost-effective prime mover readily available, their contribution to environmental pollution problems is humongous. The harmful contaminants from diesel exhausts are particulate matter (PM) and hydrocarbon and nitrogen oxides (NO_x). So, efforts to curb environmental pollution are the need of the hour by making necessary improvements to reduce their local and global environmental impact. In this study, examine the effects of yttria- and alumina-stabilised zirconia coating on the piston head and cylinder lining of a single-cylinder diesel engine, as well as its performance and emissions. Various dosing amounts of nanoparticles of aluminium oxide were utilised as additives to diesel fuel in this study, on both coated and uncoated internal combustion engines. Many coated engine metrics improved significantly as a result of the research. The brake thermal efficiency has increased by 2.1 percent as compared to a conventional uncoated diesel engine, while brake-specific consumption has dropped by 3%, resulting in a reduction in dangerous chemicals.

1. Introduction

The prime reason for ecological issues, global warming, climate changes, etc. are because of human's ambitious need for material sophistication. With transportation being the major contributor among all, rapid industrial growth and urbanization have also surged the demand for electricity which in turn is majorly derived from noneco-friendly practise like coal, oil, natural gas, and nuclear energy. Additionally,

because of the competitive market practise, big industries compromise on environment-friendly approaches to produce the product at a faster rate. At present, because of the lack of stringent environmental policies and regulations, all these have aggravated and have already started to haunt life on earth. The most critical issue among all is air pollution is major because of automobile emission. Particularly, the internal combustion engine has a hard effect on the environment than anything else among automobile emissions, and it is more

commonly used over gasoline engines because of its better fuel economy. According to Navigant Consulting, the worldwide stock of motor vehicles will exceed 2 billion units in 2035.

In an internal combustion engine, the chemical energy of the fuel is converted to thermal energy, which is then used to perform mechanical work in the form of piston movement. In this process, toxic compounds are released from the engine exhaust. A number of researchers have proposed a variety of approaches to reduce this harmful emission by in-cylinder treatment; however, only a significant portion of proposals have proved to be effective practically. Further, catalytic prereaction treatment reduces the minimum threshold ignition energy required while also amplifying the flame velocity. This approach also seemingly formulates the catalytic surface temperature along with the contact between gas-phase reactants and the catalyst. Aluminium oxides, copper oxides, cobalt oxides, and iron oxides have also been used as fuel additives to change the composition of diesel fuel in order to minimise emissions.

Researchers were able to minimise engine emissions and improve the performance of a diesel particle filter in the lab by using an aluminium diesel fuel borne catalyst and bimetallic platinum [1–4]. One of the findings of the study reveals that there is a substantial difference in particle density, light-off temperature, and oxidation kinetics in accumulation mode. Despite the fact that the rate of oxidation increased following the addition of aluminium to the fuel, the amount of dosage had no effect [5–8]. Kamo et al. evaluated the impact of introducing aluminium oxide into biodiesel and discovered that it improved performance while also lowering NO_x and HC emissions [9, 10].

Currently, researchers around the globe are relentlessly working on discovering an automobile engine which does not emit toxic compounds in its exhaust fume while also not compromising on its performance. One of these breakthroughs is the application of thermal barrier coating (TBC) within the combustion chamber to improve thermal resistance and stability when working at many leap temperatures. It is important to keep in mind that the barrier coating material should have a greater thermal coefficient of expansion than the metal substrate in order to withstand more thermal shock [11]. Similar coating approaches with ceramic materials like TiO_2 , CeO_2 , mullite, CaO/MgO-ZrO_2 , and YSZ were also employed for practical purposes for engine applications [12, 13].

Thermal barrier coating materials like partially stabilised zirconia (PSZ) and nearly stabilised zirconia with 6–9 per cent yttria (YSZ) are commonly utilised. Even under harsh circumstances absorbed in gas turbines, diesel engines, and other engines, these materials have been shown to function better [14]. The efficiency of a diesel engine covered with 0.1 mm thickness and 0.5 mm breadth of YSZ was enhanced by 6% in Ramalingam et al.'s experiment at all speeds and loads. The heat barrier coating is applied to the piston crown, piston, and cylinder head to fully use the finding [15–17] Because of its wide variety of physical qualities, such as a high coefficient of thermal expansion, a high Poisson's ratio, low thermal conductivity, and structural stability at high temperatures, YSZ was chosen as a feasible material for TBC I [18–21].

In this discussion, the performance and combustion of a diesel engine, as well as the emission difficulties develop when yttria- and aluminium-stabilised zirconia coatings are applied to the cylinder liner and piston head and when aluminium oxide additive is added at various amounts (35 ppm, 45 ppm, and 55 ppm). The goal of this experiment is to reflect the engine's changes in performance and emission characteristics [22–25]. This research's findings are analysed, examined, reviewed, and presented in a systemic manner. At first, the diesel engine coated with aluminium oxide nanoparticle is subjected to varying level of dosage (35 ppm, 45 ppm, and 55 ppm, respectively). Then, on the second phase, the same engine is modified and experimented with thermal barrier coating to compare the outcome from both the methods.

2. Experimental Methods and Specification

2.1. Test Engine. The test was conducted in a single-cylinder, water-cooled, 4-stroke diesel engine (Tv1 type Kirloskar, India) that produced 5.2 kW at 1500 rpm. An eddy current dynamometer was used for the loading. The engine's drive shaft is attached to the dynamometer. To determine the mass of airflow rate, an orifice metre and a manometer with a 1% error are employed. The engine's specifications are summarised in Table 1(a). In addition, Figure 1 and Table 1(b) shows the experimental setup and component description of the tested engine. By manual calibration, a glass tube is utilised to calculate the amount of fuel consumed. The calculation was done by comparing the time necessary for a normal diesel engine to consume 10 cc of fuel.

Engine parameters:

A piezoelectric pressure transducer (AVL INDIMICRA 602-T10602A) was used to monitor cylinder pressure, while a magnetic pickup was used to assess crank angle. An AVL 365C Angle Encoder Indi Advanced was fitted at the front-end of the engine crank to measure the engine speed. After 50 repetitions of cylinder pressure at steady-state, an average value is determined. Heat dissipation at different cylinder pressure was determined carefully and loaded into the system. The data were then compared to a graph of a conventional diesel engine. A five-gas analyser was used to measure CO, HC, NO_x , CO_2 , and O₂ emissions (AVL Digas 444). A K-type chromyl alumini thermocouple was used to measure the temperature of the exhaust gas, while an AVL437 smoke metre was used to detect smoke.

The entire process was done at a steady speed of 1500 rpm in a nominal functioning state. To arrive at an average result, the tests were repeated three times. After allowing the engine to attain its ideal operating state, all emission characteristics were recorded. The data was personally checked and placed into the system to be analysed further.

2.2. Thermal Barrier Coating Synthesis by Plasma Spraying. Physical vapour deposition, atmospheric plasma, and other forms of thermal spraying techniques were used to grind the top facet of the cylinder liner and piston, respectively. Spray,

TABLE 1

(a) Engine specification

| Parameters | Values |
|---------------------|---|
| Type | Kirloskar TV-1 |
| General arrangement | Diesel engine test setup, vertical cylinder, water cooled |
| Power | 5.2 KW @ 1500 rpm |
| Speed | 1500 rpm |
| Number of cylinder | 1 |
| Number of strokes | Four |
| Compression ratio | 17.5 : 1 |
| Cylinder diameter | 87.5 mm |
| Stroke length | 110 mm |
| Type of ignition | C.I |

(b) Engine component description

| Temperature (°C) | Water flow liter/hour |
|----------------------------------|--------------------------------------|
| T1 - engine cooling water inlet | F1 - fuel line |
| T2 - engine cooling water outlet | F2 - air inlet |
| T3 - calorimeter water inlet | F3 - engine cooling water (200 L/hr) |
| T4 - calorimeter water outlet | F4 - calorimeter water (100 L/hr) |
| T5 - calorimeter exhaust gas in | PT - pressure transmitter |
| T6 - calorimeter exhaust gas out | N - crank angle encoder |

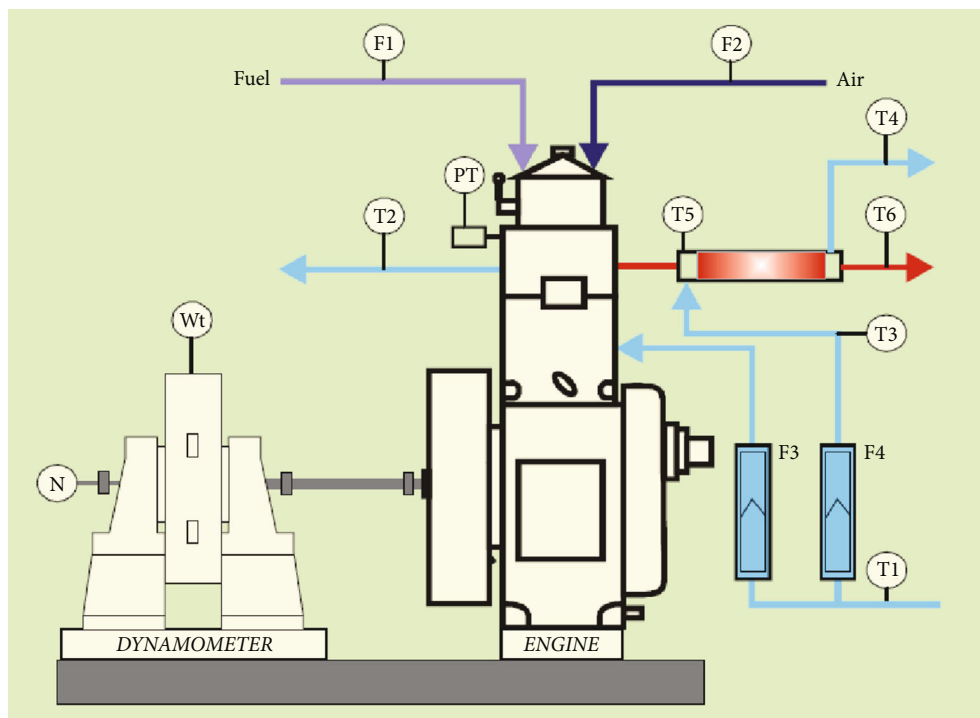


FIGURE 1: Experimental setup.

chemical deposition, and plasma arc methods were used in this technique. In this exploratory trial, the plasma spray technique is being used. The compression ratio in the cylinder

liner and coated piston is maintained by a surface layer with a thickness of 0.30 mm and 0.15 mm. The sprayed powders and bulk were mechanically bonded by sandblasting the

TABLE 2: Parameters of plasma spray coating.

| Parameter | Value |
|------------------------------------|-------|
| Plasma spray gun | 3 MB |
| Arc voltage (V) | 65-70 |
| Arc current (I) | 500 |
| Spray distance (mm) | 80 |
| Primary gas flow-argon (L/min) | 80 |
| Secondary gas flow-hydrogen(L/min) | 15 |
| Deposition rate, kg/h | 1.1 |

engine cylinder with alumina grits and piston. YSZ makes up 94% of the coating powder, with alumina making up 2% and ceria making up 4%. Table 2 shows the spray details for the piston and cylinder liner coatings of the engine, and Figure 2 depicts a plasma spray coating method.

2.3. Preparation of Test Fuel. Diesel is the primary fuel used in this research. Using a standard instrument, the calorific value and density of biodiesel were determined to be 850 kg/m³ and 34.5 MJ/kg, respectively. This method used aluminium oxide nanoparticles with a size of 10 to 20 nanometers and a density of 7.13 g/mL as fuel additives. The volume levels of aluminium oxide nanoparticles in the base fuel were changed between 35 ppm, 45 ppm, and 55 ppm. The volume levels of the nanoparticle sample were then calculated using an electronic balance. With the aid of an ultrasonic shaker, the sample was blended with the fuel. To get a homogeneous suspension, agitation is conducted for 30 minutes. To avoid sedimentation, the produced fuel was used as soon as possible.

2.4. Determination of Fuel Properties. Flash and fire points, as well as pour and cloud points, were used to determine the viscosity of gasoline. The flashpoint was measured with the Cleveland open flash and fire point equipment (ASTM 2007), and the viscosity was determined with the Redwood viscometer (British Standard Section 2000). The characteristics of the fuel sample utilised are shown in Table 3.

Fuel properties:

2.5. Procedure for Testing. Readings were observed three times after attaining the engine steady state, and mean value was determined. Enhanced combustion was witnessed when air intake is provided while using aluminium oxide as an additive in diesel. As a result, full oxidation of hydrocarbons occurred. In addition, the additive aluminium oxide was miscible with fuel. Different volume levels of 35 ppm, 45 ppm, and 55 ppm were added with diesel, following which the mixture is agitated for 30 minutes with help of ultrasonic shaker. Following that, the engine was started with varied amounts of aluminium oxide-containing diesel. The readings were removed. The coated piston and cylinder liner were reinstalled, and the process was repeated after the baseline piston and cylinder liner operation was completed. The combustion, emission, and performance metrics of coated and uncoated engines were compared between additive-containing diesel and regular diesel. The coated engine was removed after roughly 100 hours of operation to look for any changes in the coated piston crown and cylinder liner. Before starting the engine, the coated piston

crown and cylinder liner are shown in Figure 3. Figure 4 shows the coated piston crown and cylinder liner after the engine has been operating. The images also show that the coating used had small cracks around the margins of the piston crown. The outstanding sections, on the other hand, showed almost no fractures or abnormalities, indicating that the thermal barrier coating was stable under all loading conditions of engine running.

3. Results and Discussion

In terms of pollution, performance, and combustion, the coating's effects on the cylinder liner and piston head were investigated. The operation was carried out in a water-cooled single-cylinder, four-stroke engine using diesel fuel containing aluminium oxide additions at volume levels of 35 ppm, 45 ppm, and 55 ppm. Several performance parameters were observed and analysed for discrepancies under engine loading conditions, including BTE, BSFC, NO_x, CO, CO₂, and HC emissions and smoke.

3.1. Engine Performances

3.1.1. BSFC. Figure 5(a) shows the difference in TBC BSFC in uncoated and coated engines with different load and volume levels of aluminium oxide. When compared to regular diesel, aluminium oxide diesel has a lower BSFC (Kannan, Karvembu, and Anand 2011). The BSFC for diesel and diesel with aluminium oxide additions drops even more for engines with TBC. This is due to a greater combustion temperature, which results in a faster energy conversion rate during combustion. This ultimately leads to better combustion and better conservation of fuel [19]. A significant 3% lesser BSFC has been observed for coated engines with diesel containing various volumes of aluminium oxide than diesel-employed coated engines at part load conditions. From the preceding condition, it clearly illustrates that the presence of aluminium oxide improves the performance of the engine at part load conditions. In addition, an increased temperature is observed because of TBC. The BSFC of the coated engine is increased by 1% and 2% when diesel is added with aluminium oxide of 45 ppm and 55 ppm, respectively, in comparison to diesel operated engine at 75% load. At 75% load, 3% lesser BSFC is noticed for diesel-operated coated engine than standard diesel operation.

3.1.2. BTE. Figure 5(b) illustrates the difference in BTE of TBC coated and untreated engines with load for all tested fuels. When aluminium oxide is introduced, the BTE value rises. The addition of aluminium oxide nanoparticles to the fuel promotes complete combustion, as opposed to typical aluminium oxide fuel, which acts as an oxygen barrier, releasing or keeping oxygen depending on partial pressure. Finally, the BTE is increased when the aluminium oxide is used as a fuel additive. The coated diesel engine with aluminium oxide has a higher thermal efficiency than the base diesel. This happens because the piston crown has thermal resistance, which inhibits heat from being transported to the coolant or other media. As a result, the combustion is more uniform. At 85 percent load, the TBC engine with diesel improves BTE by 2.1 percent over conventional diesel performance.

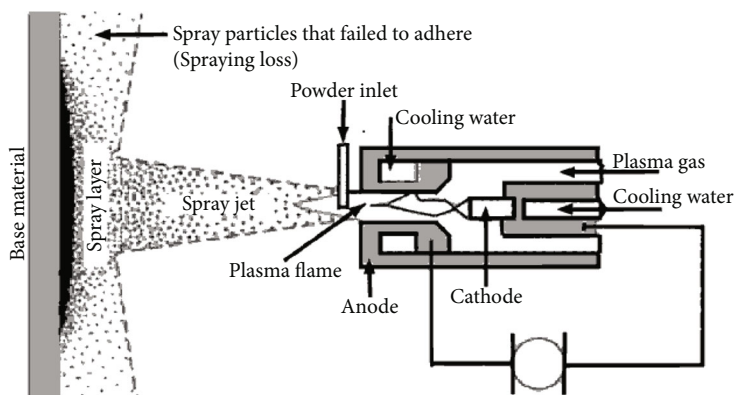


FIGURE 2: Plasma spray technique.

TABLE 3: Properties of fuel.

| Property | Normal diesel | Diesel +45 ppm Al ₂ O ₃ |
|---|---------------|---|
| Density of test fuel | 849 | 843 |
| Calorific value MJ/kg (ASTM D240) | 42.2 | 41.584 |
| Flash point °C | 50 | 53 |
| Fire point °C | 58 | 61 |
| Kinematic viscosity @40°C (centistokes) (ASTM D445) | 2.41 | 2.59 |

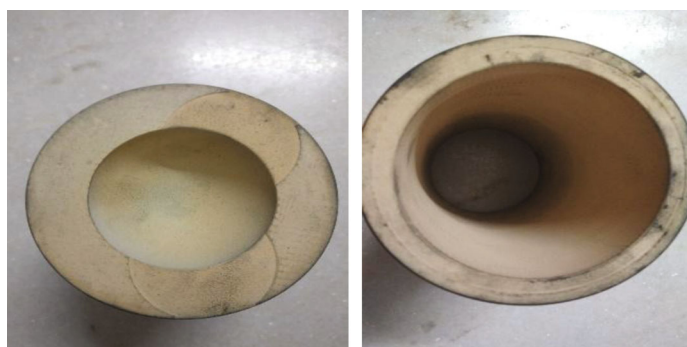
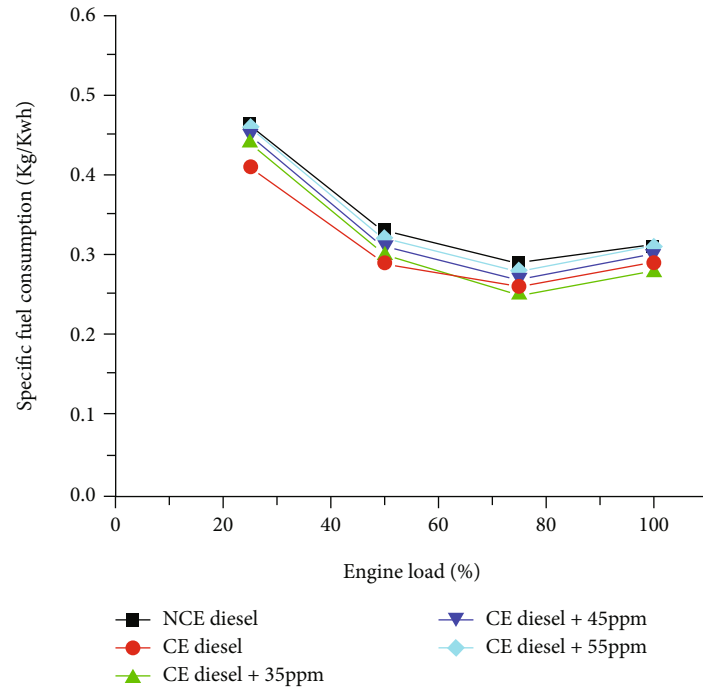


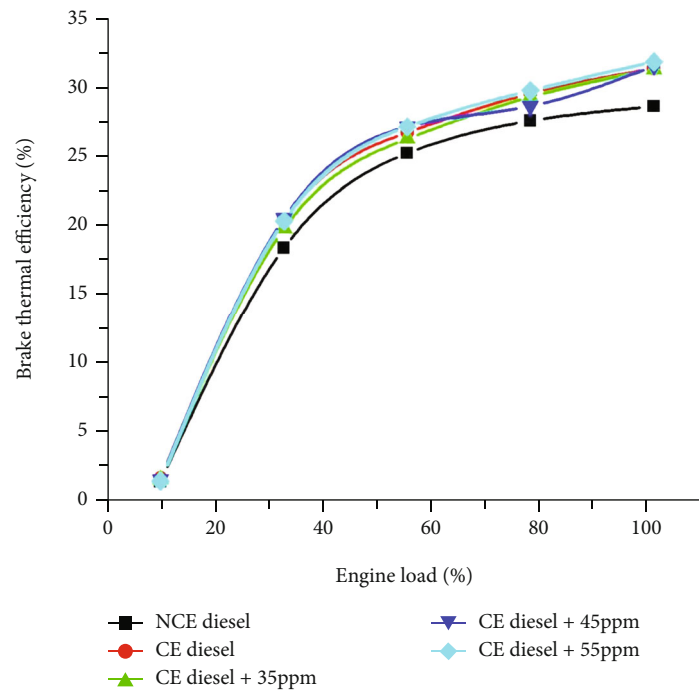
FIGURE 3: Coated engine for piston and cylinder liner.



FIGURE 4: After 100 hours of operation, the piston and cylinder liner are coated.



(a)



(b)

FIGURE 5: (a) BSFC vs. engine load. (b) Brake thermal efficiency vs. load on engine.

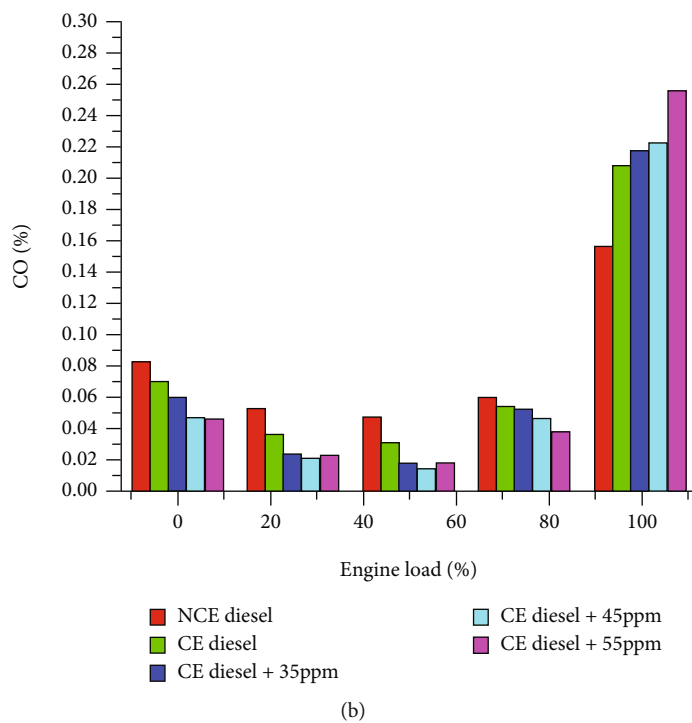
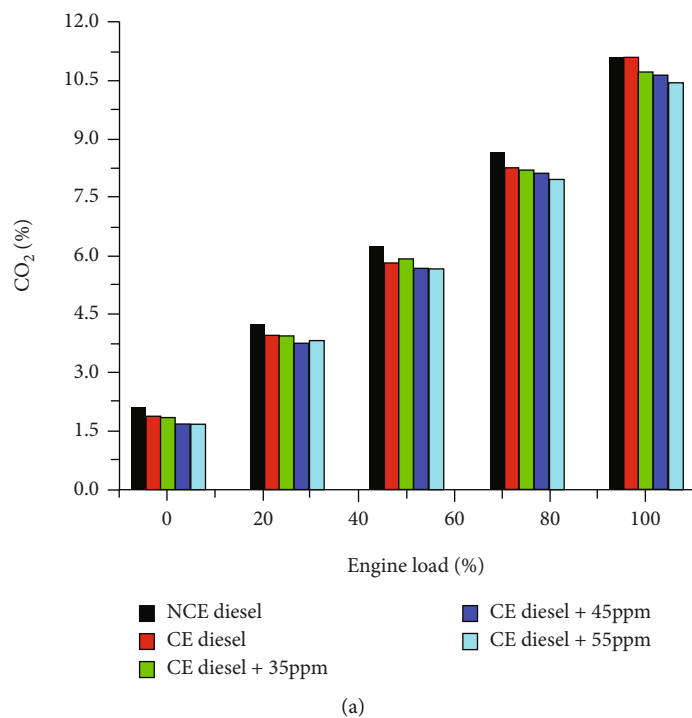
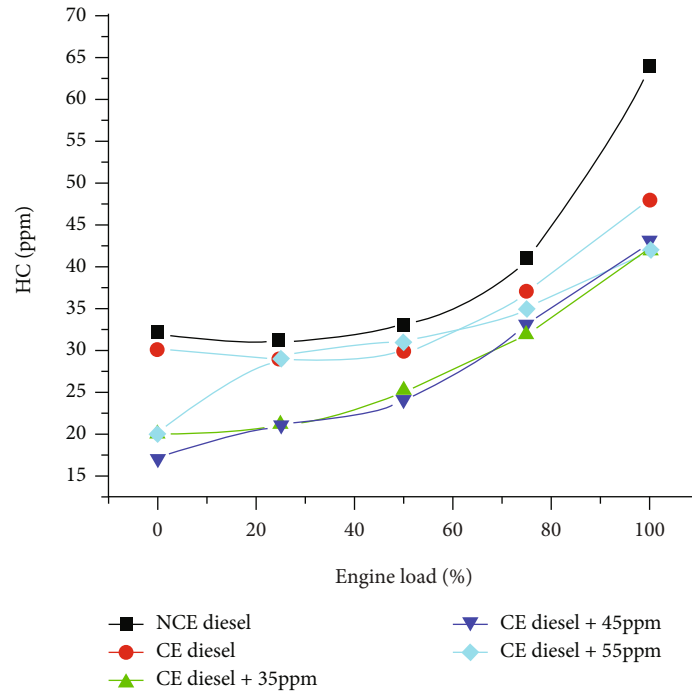
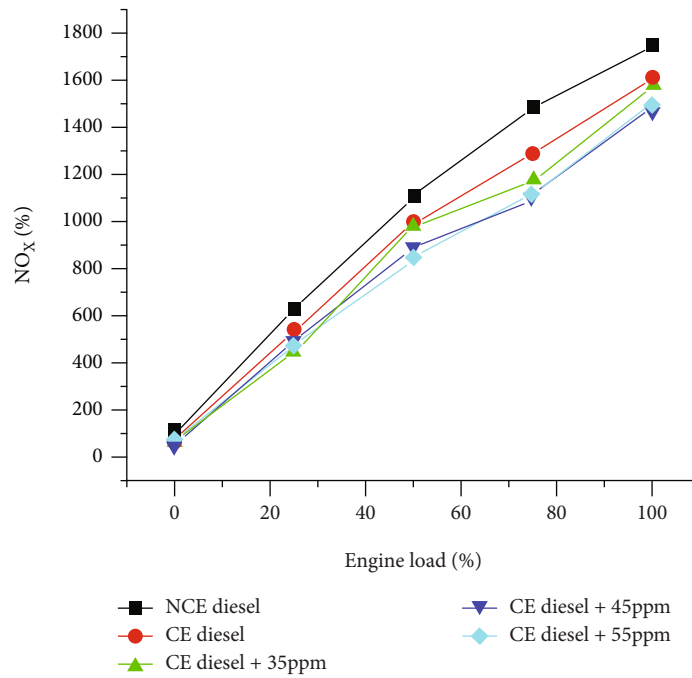


FIGURE 6: Continued.



(c)



(d)

FIGURE 6: (a) CO₂ vs. load on engine. (b) CO vs. engine load. (c) HC vs. load on engine. (d) NO_x vs. engine load.

3.2. Emission Parameters

3.2.1. CO₂ Emission. Figure 6(a) presents the change in CO₂ discharge with engine load. When the amount of aluminium oxide in diesel is changed, the CO₂ emissions rise when compared to regular diesel. As a result, enhanced combustion results from the use of all oxygen in the combustion chamber. This results in increased generation of CO₂ from CO [22], thereby reducing the levels of CO. CO₂ emission is increased for TBC engines. The combustion in the cylinder is improved by different dosages of aluminium oxide and high cylinder temperature. As a result, there is an increased CO₂ emission. At 75% of engine load with dosages of 35 ppm, 45 ppm, and 55 ppm of aluminium oxide, CO₂ emission is more than about 5.7%, 7%, and 8.9% for coated engines, respectively, when compared to that of the base diesel.

3.2.2. CO Emission. Figure 6(b) depicts a decrease in CO emissions as the engine load increases. This reduced CO emission is because of increased higher temperature in a cylinder with an increase in the load of the engine. Due to the aluminium oxide effect in the diesel, there is improved combustion, as a result of which CO emission is reduced. The additive aluminium oxide increases the oxidation of CO into CO₂. A further reduction in the emission of CO is noticed in engines with TBC. The coating generates high temperature which stimulates the conversion of CO into CO₂. Hence, TBC engines provide improved combustion [22]. CO emissions are reduced by roughly 0.8 percent, 1.4 percent, and 0.7 percent for coated engines at 75 percent of engine load with doses of 35 ppm, 45 ppm, and 55 ppm of aluminium oxide in diesel, respectively, when compared to basic diesel.

3.2.3. HC Emission. When there is incomplete combustion, there is an increased HC emission. Figure 6(c) gives the difference of HC emission with respect to engine load. When compared to base fuel operation, the addition of aluminium oxide to diesel results in lesser HC emission of about 7% at 75% load. This is due to the role of aluminium oxide in effecting the improved combustion. The coated engine has lesser HC emission compared to the uncoated one. This may be the result of high combustion temperatures after the burning phase by hindering the heat loss in coated engines. Eventually, effective use of air intake and increased oxidation of fuel [5] was carried out by improved combustion. Aluminium oxide dosages of 35 ppm, 45 ppm, and 55 ppm provide a 9%, 8%, and 6% reduction in HC emission, respectively, for coated engines associated with standard diesel-operated uncoated engines.

3.2.4. NO_x Emission. Figure 6(d) depicts the increase in NO_x emissions as engine load increases. The oxygen content and combustion temperature are determined by NO_x emissions. As aluminium oxide is added to diesel, it causes an increase in NO_x emissions when compared to base diesel. This increased emission is because of oxidation of nitrogen into its oxides by aluminium oxide while combustion. NO_x emission is higher comparatively in uncoated engine. This is due to high temperature that stimulates an early beginning of combustion. This changes the peak temperature and pres-

sure to TDC proximity. Thus, increase in NO emission is due to burning of fuel in premixed state [11]. Aluminium oxide dosages of 35 ppm, 45 ppm, and 55 ppm provide a 21%, 26%, and 25.5% in NO emission, respectively, for coated engines associated to standard diesel-operated uncoated engine at 75% load.

4. Conclusion

Following conclusions are arrived through the experimental study and investigation.

- (i) Ceria- and yttrium-stabilized zirconia-coated engine with different dosages of aluminium oxide and diesel provides an increase of 2.7% BTE and reduction of 3% BSFC at 75% load. Coated engines show a finer performance characteristics with test fuels at part load conditions
- (ii) When 35 ppm, 45 ppm, and 55 ppm of aluminium oxide are added to diesel, CO, HC, and Knox emissions are reduced for both coated and uncoated engines when running on regular diesel
- (iii) Influence of parameters like size of nanoparticle, dosing level, and preparation time has significant role in the fuel performance with fuel added with aluminium oxide nanoparticles as thermal barrier coating. For best performances of engine and emission reductions, Consistent effort has been put to get optimum combination of parameters. In parallel, a further research is being carried out on visualization techniques for analysing the characteristics of combination of additive fuels

Data Availability

The data used to support the findings of this study are included in the article. Should further data or information be required, these are available from the corresponding author upon request.

Disclosure

This study was performed as a part of the Employment Hawassa University, Ethiopia.

Conflicts of Interest

The authors declare that they have no conflicts of interest.

References

- [1] M. J. Abedin, H. H. Masjuki, M. A. Kalam, A. Sanjid, and A. M. Ashraful, "Combustion, performance, and emission characteristics of low heat rejection engine operating on various biodiesels and vegetable oils," *Energy Conversion and Management*, vol. 85, pp. 173–189, 2014.
- [2] M. J. Abedin, H. H. Masjuki, M. A. Kalam, A. Sanjid, S. A. Rahman, and B. M. Masum, "Energy balance of internal combustion engines using alternative fuels," *Renewable and Sustainable Energy Reviews*, vol. 26, pp. 20–33, 2013.

- [3] P. Bengtsson, T. Ericsson, and J. Wigren, "Coated with a thick thermal barrier coating thermal shock testing of burner cans," *Journal of Thermal Spray Technology*, vol. 7, no. 3, pp. 340–348, 1998.
- [4] S. W. Beyerlein and S. Wojcicki, "A lean-burn catalytic engine," *SAE Transactions*, vol. 97, no. 1, pp. 1040–1051, 1988.
- [5] S. H. Chan and K. A. Khor, "The effect of thermal barrier coated piston crown on engine characteristics," *Journal of Materials Engineering and Performance*, vol. 9, no. 1, pp. 103–109, 2000.
- [6] T. Hejwowski, "Comparative study of thermal barrier coatings for internal combustion engine," *Vacuum*, vol. 85, no. 5, pp. 610–616, 2010.
- [7] S. S. Hoseini, G. Najafi, B. Ghobadian, R. Mamat, N. A. C. Sidik, and W. H. Azmi, "The effect of combustion management on diesel engine emissions fueled with biodiesel-diesel blends," *Renewable and Sustainable Energy Reviews*, vol. 73, pp. 307–331, 2017.
- [8] H. Jung, D. B. Kittelson, and M. R. Zachariah, "The influence of a cerium additive on ultrafine diesel particle emissions and kinetics of oxidation," *Combustion and Flame*, vol. 142, no. 3, pp. 276–288, 2005.
- [9] R. Kamo, N. S. Mavinahally, L. Kamo, W. Bryzik, and E. E. Schwartz, "Injection characteristics that improve performance of ceramic coated diesel engines," *SAE Transactions*, vol. 108, no. 3, pp. 1476–1482, 1999.
- [10] S. Krishnamani, V. Harish, V. Harishankar, and T. M. Raj, "The experimental investigation on performance and emission characteristics of ceramic coated diesel engine using diesel and biodiesel," *Materials Today: Proceedings*, vol. 5, no. 8, pp. 16327–16337, 2018.
- [11] G. R. Kannan, R. Karvembu, and R. J. A. E. Anand, "Effect of metal based additive on performance emission and combustion characteristics of diesel engine fuelled with biodiesel," *Applied Energy*, vol. 88, no. 11, pp. 3694–3703, 2011.
- [12] C. R. C. Lima and J. M. Guilemany, "Adhesion improvements of thermal barrier coatings with HVOF thermally sprayed bond coats," *Surface and Coatings Technology*, vol. 201, no. 8, pp. 4694–4701, 2007.
- [13] M. Mohamed Musthafa, S. P. Sivapirakasam, and M. Udayakumar, "Comparative studies on fly ash coated low heat rejection diesel engine on performance and emission characteristics fueled by rice bran and pongamia methyl ester and their blend with diesel," *Energy*, vol. 36, no. 5, pp. 2343–2351, 2011.
- [14] A. K. Franta, T. R. Lenters, D. Mounce, B. Neradilek, and F. A. Matsen III, "The complex characteristics of 282 unsatisfactory shoulder arthroplasties," *Journal of Shoulder and Elbow Surgery*, vol. 16, no. 5, pp. 555–562, 2007.
- [15] S. Ramalingam, S. Rajendran, and P. Ganesan, "Performance improvement and emission control in a direct injection diesel engine using nano catalyst coated pistons," *Biofuels*, vol. 7, no. 5, pp. 529–535, 2016.
- [16] V. Sajith, C. B. Sobhan, and G. P. Peterson, "Experimental investigations on the effects of cerium oxide nanoparticle fuel additives on biodiesel," *Advances in Mechanical Engineering*, vol. 2, Article ID 581407, 2010.
- [17] N. Sunderland, T. Catalano, E. Kendall, D. McAuliffe, and L. Chenoweth, "Exploring the concept of moral distress with community-based researchers: an Australian study," *Journal of Social Service Research*, vol. 37, no. 1, pp. 73–85, 2011.
- [18] G. Sivakumar and S. S. Kumar, "Investigation on effect of yttria stabilized zirconia coated piston crown on performance and emission characteristics of a diesel engine," *Alexandria Engineering Journal*, vol. 53, no. 4, pp. 787–794, 2014.
- [19] J. Kumaraswamy, V. Kumar, and G. Purushotham, "Evaluation of the microstructure and thermal properties of (ASTM A 494 M grade) nickel alloy hybrid metal matrix composites processed by sand mold casting," *International Journal of Ambient Energy*, pp. 1–10, 2021.
- [20] G. Skillas, Z. Qian, U. Baltensperger, U. Matter, and H. Burtscher, "The influence of additives on the size distribution and composition of particles produced by diesel engines," *Combustion Science and Technology*, vol. 154, no. 1, pp. 259–273, 2000.
- [21] K. Logesh, M. Karthick, S. Baskar, and A. Sharma, "Performance and emissions characteristics of diesel engine run on Citrullus colocynthis biodiesel with zinc oxide additive," in *Advancement in Materials, Manufacturing and Energy Engineering*, I. I. Vol, Ed., pp. 513–520, Springer, Singapore, 2022.
- [22] K. Jayappa, V. Kumar, and G. G. Purushotham, "Effect of reinforcements on mechanical properties of nickel alloy hybrid metal matrix composites processed by sand mold technique," *Applied Science and Engineering Progress*, vol. 14, no. 1, pp. 44–51, 2021.
- [23] V. Balambica, S. Baskar, S. Padmanabhan et al., "Study on tribological characteristics of bio-lubricant formed from Brassica napus oil," *Materials Today: Proceedings*, 2022.
- [24] J. M. Valentine, J. D. Peter-Hoblyn, and G. K. Acres, *Emissions reduction and improved fuel economy performance from a bimetallic platinum/cerium diesel fuel additive at ultra-low dose rates (no. 2000-01-1934)*, SAE Technical Paper, 2000.
- [25] M. Selvamuthukumar, S. Baskar, and N. Joy, "Investigation on the lubricating behavior of cashew nut shell liquid oil as a renewable and reliable petrochemical product," *Materials Today: Proceedings*, vol. 44, pp. 3583–3588, 2021.

Research Article

e-Modeling and Evolution of Nanolubricant Coupled Machining Parameters Using Statistical Tool

M. Sangeetha,¹ Lilly Mercy,¹ Dillipkumar Sahoo,¹ P. Gunasekar,¹ T. R. Praveenkumar^{ID},² Habtamu Fekadu Gemedo^{ID},³ and Rajesh Madasamy^{ID}²

¹*School of Mechanical Engineering, Sathyabama Institute of Science and Technology, India*

²*Department of Construction Technology and Management, Wollega University, P.O. Box 395, Nekemte, Ethiopia*

³*Department of Food Technology and Process Engineering, Wollega University, P.O. Box 395, Nekemte, Ethiopia*

Correspondence should be addressed to T. R. Praveenkumar; pravirami@gmail.com

Received 29 March 2022; Revised 28 April 2022; Accepted 5 May 2022; Published 13 June 2022

Academic Editor: V. Vijayan

Copyright © 2022 M. Sangeetha et al. This is an open access article distributed under the Creative Commons Attribution License, which permits unrestricted use, distribution, and reproduction in any medium, provided the original work is properly cited.

Optimization is an essential action to select the effective input parameters for the responses obtained from machining. In this work, the combination of six sigma techniques and grey relational optimization are used for the corresponding input parameters, namely, spindle speed, feed rate, and drill diameter. The responses recorded are torque, thrust force, surface roughness, temperature, and ovality. Smaller the better response is preferred for all the output responses. Taguchi design of L27 array is preferred, and based on 27 combinations of input parameters, output responses are recorded. The thrust force and torque values are obtained in the graphical form during drilling process by the vertical machining center. After the drilling process the surface roughness of the hole is measured using profilometer. The probe in the profilometer is moved along the surface of the hole and the corresponding surface roughness values are noted for twenty-seven holes. The roundness of the hole is measured using a profile projector. The roundness of the hole is expanding due to the heat generated during the machining process. The expanded diameter of the hole is measured along the vertical and horizontal axes using the projector. Six sigma techniques are used to analyze the input parameters such as spindle speed, feed rate, and drill diameter. The optimization technique is used to determine the optimized parameters.

1. Introduction

Composites have the high specific strength and so the automobile and airplanes move at high speed with better fuel efficiency. Hybrid metal matrix composite is more advantageous compared to metal matrix composites since it is having the combined effect of improved mechanical properties, high wear resistance, and less wear of the tool while machining. Aluminium–Silicon-based metal matrix composites have major applications in automobile brakes and clutches. The orthogonal array, analysis of variance, and signal-to-noise ratio analyzed the machining parameters, and it also derived the optimal combination of input

parameters. It is also proved that the Taguchi method derived the solution with minimum number of trials compared to the full factorial design [1]. Giasin and Ayvar-Soberanis measured the ovality error and burr height as the output responses in the drilling process. It was proved that the burr height at the exit is maximum than at the entry of the work piece. The ovality error and burr height is reduced at the minimum feed rate [2]. Fernandez-Perez et al. analyzed the output responses such as hole quality and tool wear. The influence of input parameters in drilling the output responses tool wear and hole quality was analyzed. The analytical study revealed that the input parameters, speed and feed, greatly influenced the output

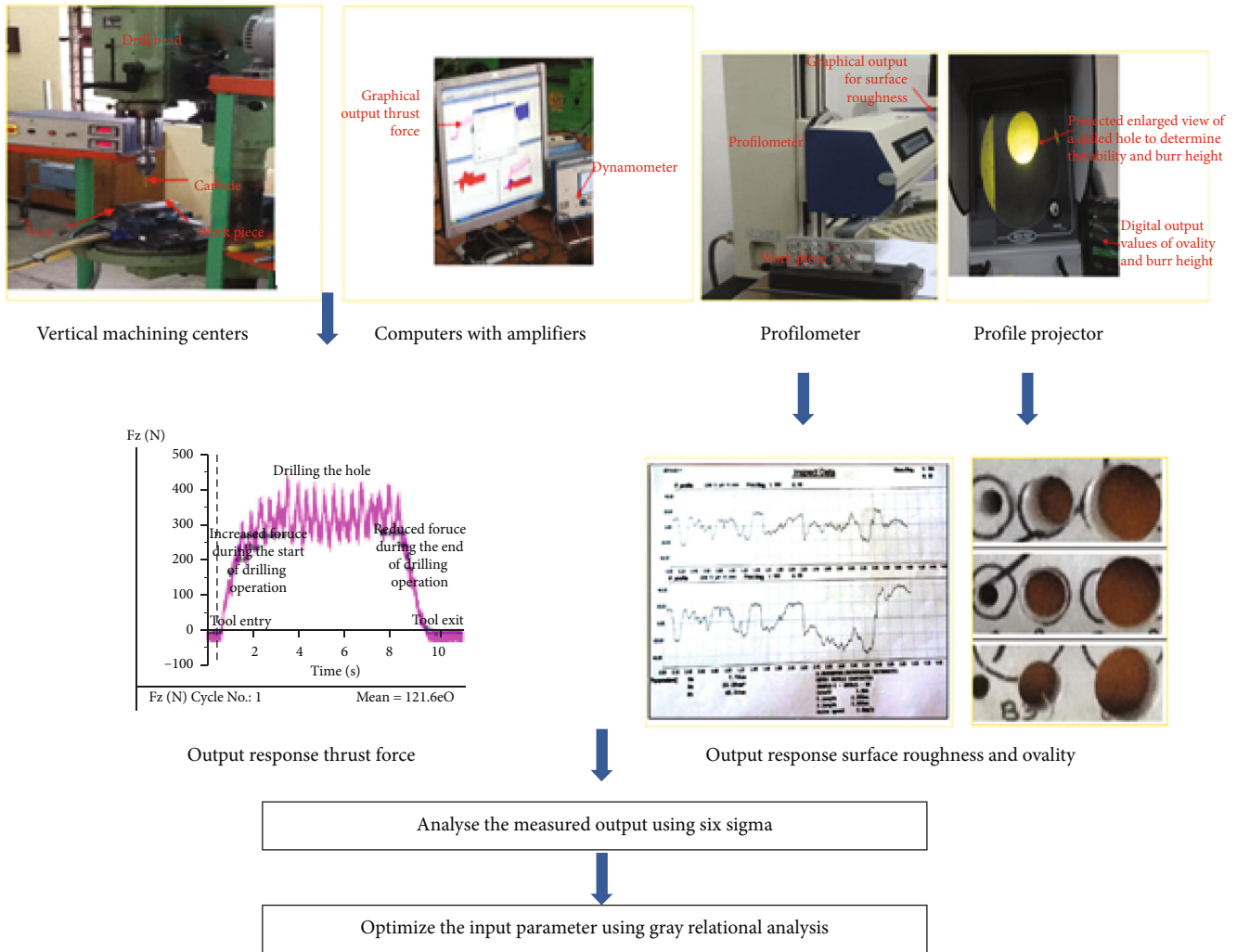


FIGURE 1: Experimental setup to record the output responses while drilling the metal matrix composites.

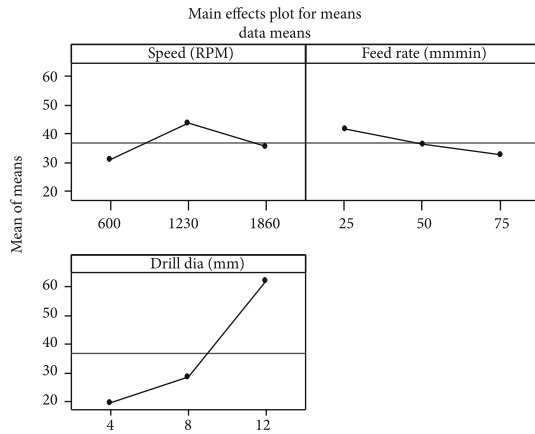
responses. The higher values of speed and feed resulted in less tool wear [3].

1.1. Literature on Machining of Metal Matrix Composites.

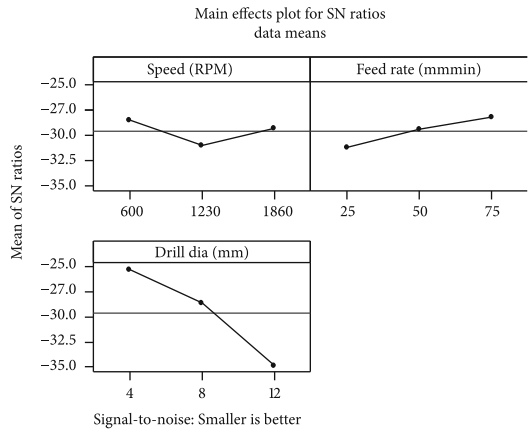
Ekici et al. proved the reinforcement of solid lubricant graphite as a third element to the aluminum and boron carbide composites reduced the thrust force value to 25% compared to aluminum-boron carbide. The surface roughness value is greatly influenced by the percentage of graphite added with the aluminum-boron carbide composites [4]. The percentage of error between the predicted and validated values is 4.5 for the aluminum alloy reinforced with aluminum nitride so the optimization prediction is liable. The optimum condition for minimum surface roughness is uncoated carbide drills 320 m/min cutting speed, 0.4 mm/tooth feed rate, axial depth 0.4 mm, and 10% of reinforcement [5]. The optimal machining parameters while machining hybrid metal matrix composites LM 6/fly ash/silicon carbide particle is 175 m/min cutting speed, 0.25 mm depth of cut, and 0.1 mm/rev feed [6]. A review was made on

machining hybrid metal matrix composites and concluded that the addition of third reinforcement with SiCp reduced the cutting force and improved the tool life and surface texture. In optimizing multiple responses, grey relational analysis is termed by the preferable technique by the researcher due to its simplicity [7]. Better hole quality and minimum surface roughness are achieved at maximum grey relational code value (GRC). The maximum value of GRC indicates the optimum input parameters and the maximum spindle speed; the minimum feed is termed as optimized values [8].

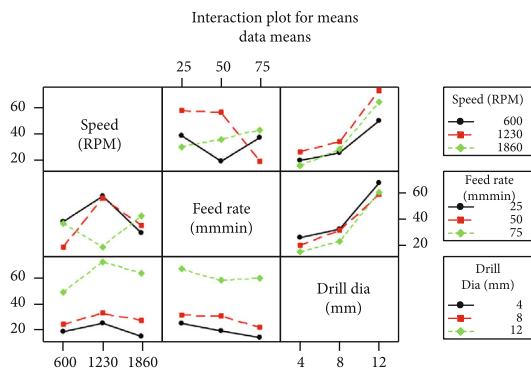
Priyadarshi and Sharma proved the reinforcement of nanosized silicon carbide particle in an aluminum alloy requires large cutting force (43 N) than hybrid reinforcement of nanosized silicon carbide particle and graphite requires less force (38 N). The optimization revealed that the hybrid reinforcement is better than individual reinforcement, and the confirmation test is within the acceptable limit of 5% [9]. The cutting speed influenced the surface roughness at the greater rate followed by feed and depth of cut. The error obtained is less than 5% between the modeled



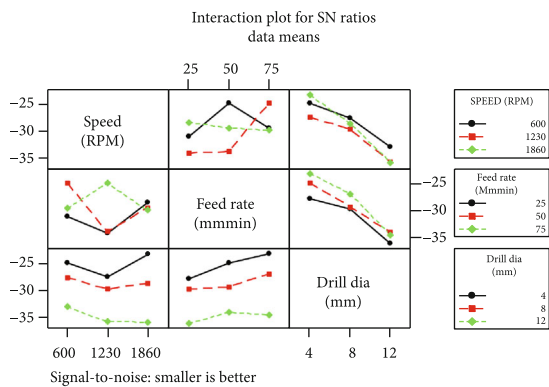
(a) Main effect plot for means



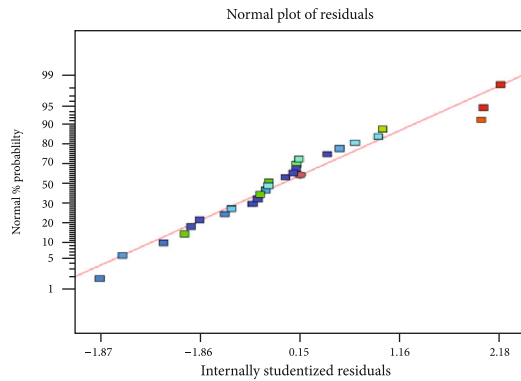
(b) Main effect plot for signal-to-noise ratio



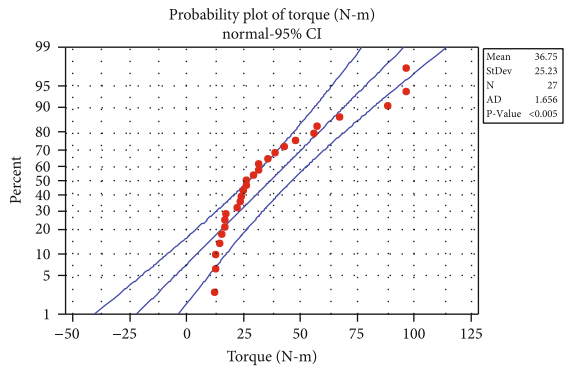
(c) Interaction plot for means



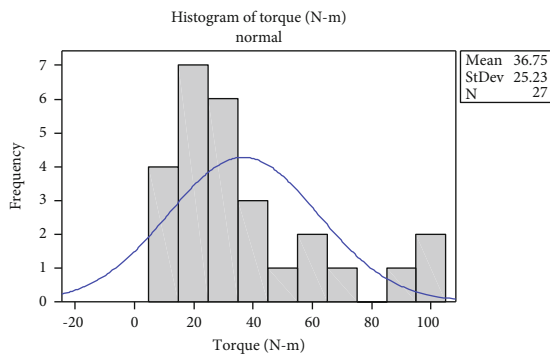
(d) Interaction plot for signal-to-noise ratio



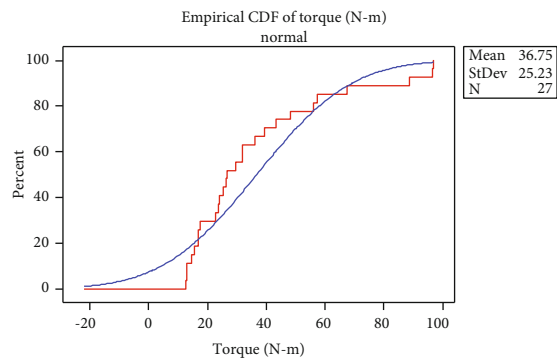
(e) Normal plot of residuals



(f) Probability plot of torque



(g) Histogram of torque with respect to frequency



(h) Empirical CDF of torque

FIGURE 2: Continued.

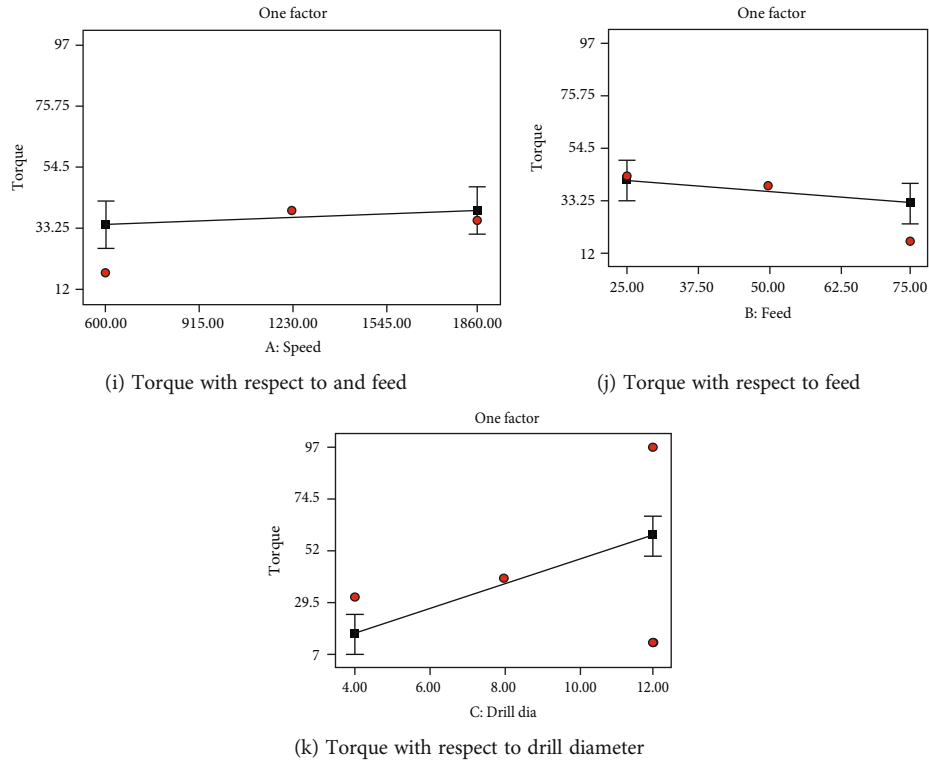


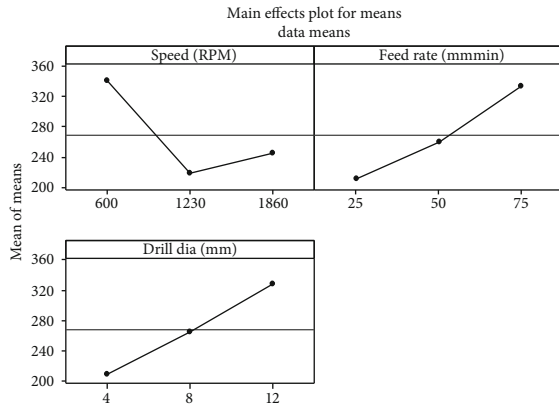
FIGURE 2: Analysis of torque using graphical output. *R*-square = 64.56% (obtained from response surface methodology).

TABLE 1: Response table for means (torque).

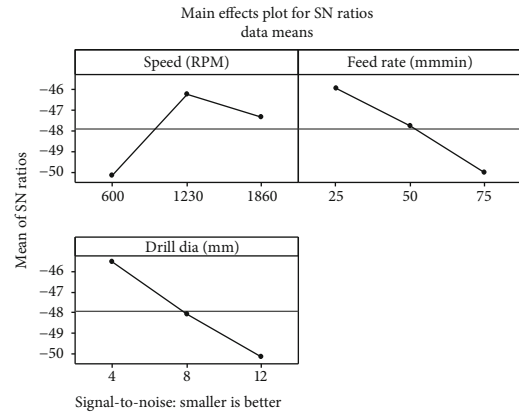
| Level | Speed (rpm) | Feed rate (mm/min) | Drill diameter (mm) |
|-------|-------------|--------------------|---------------------|
| 1 | 30.82 | 41.49 | 19.61 |
| 2 | 43.87 | 36.34 | 28.42 |
| 3 | 35.55 | 32.42 | 62.21 |
| Delta | 13.05 | 9.07 | 42.59 |
| Rank | 2 | 3 | 1 |

TABLE 2: ANOVA table for torque.

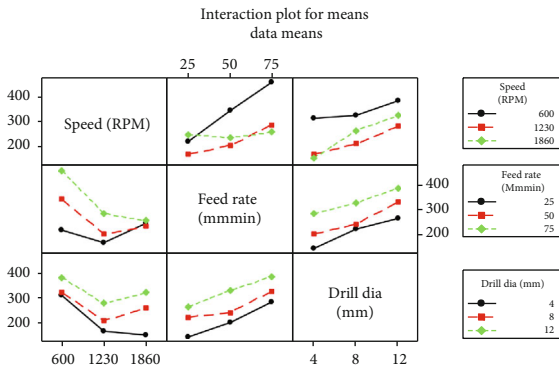
| Source | DF | Seq SS | Adj SS | Adj MS | <i>F</i> | <i>P</i> |
|--|----|---------|---------|---------|----------|----------|
| Regression | 9 | 10684.6 | 10684.6 | 1187.17 | 3.44 | 0.014 |
| Linear | 3 | 8635.3 | 837.8 | 279.25 | 0.81 | 0.506 |
| Speed (rpm) | 1 | 100.9 | 232.6 | 232.59 | 0.67 | 0.423 |
| Feed (mm/min) | 1 | 370.2 | 77.1 | 77.11 | 0.22 | 0.642 |
| Drill diameter (mm) | 1 | 8164.3 | 464.8 | 464.82 | 1.35 | 0.262 |
| Square | 3 | 1623.1 | 1623.1 | 541.05 | 1.7 | 0.234 |
| Speed (rpm)*speed (rpm) | 1 | 684.4 | 684.4 | 684.4 | 1.98 | 0.177 |
| Feed rate (mm/min)* feed rate (mm/min) | 1 | 2.3 | 2.3 | 2.28 | 0.01 | 0.936 |
| Drill diameter (mm)* drill diameter (mm) | 1 | 936.4 | 936.4 | 936.4 | 2.71 | 0.118 |
| Interaction | 3 | 426.1 | 426.1 | 142.02 | 0.41 | 0.747 |
| Speed (rpm)* feed rate (mm/min) | 1 | 161.7 | 161.7 | 161.7 | 0.47 | 0.503 |
| Speed (rpm) * drill diameter (mm) | 1 | 252.8 | 252.8 | 252.8 | 0.73 | 0.404 |
| Drill diameter (mm) * feed rate (mm/min) | 1 | 11.5 | 11.5 | 1.54 | 0.73 | 0.404 |
| Residual error | 17 | 5865.2 | 5862.2 | 345.01 | | |
| Total | 26 | 16549.7 | | | | |



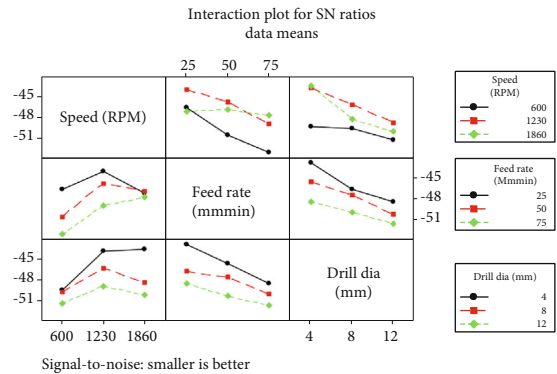
(a) Main effect plot for means



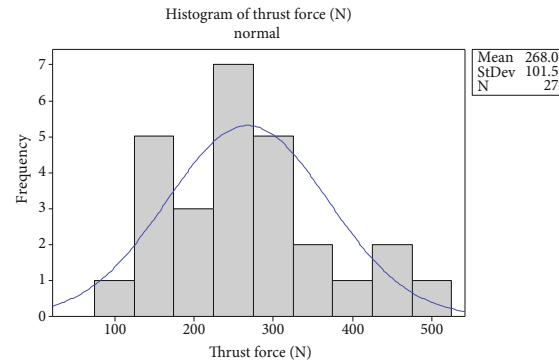
(b) Main effect plot for signal-to-noise ratio



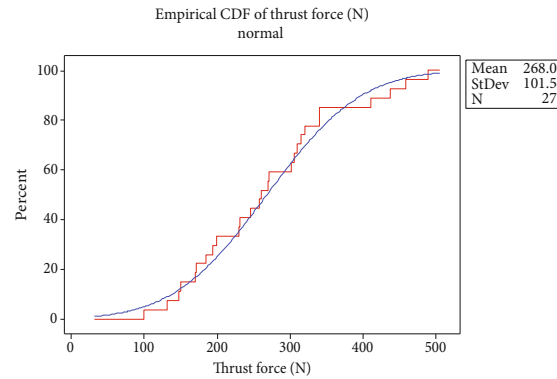
(c) Interaction plot for means



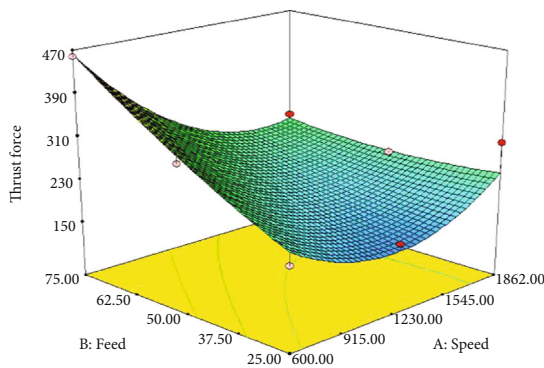
(d) Interaction plot for signal-to-noise ratio



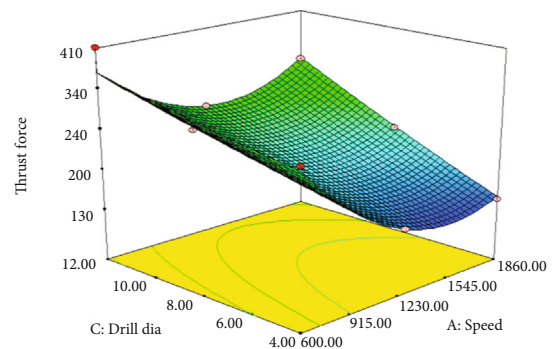
(e) Histogram of thrust force with respect to frequency



(f) Empirical CDF of thrust force

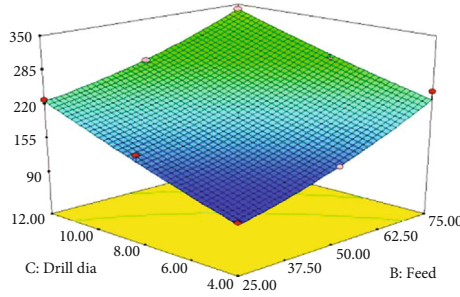


(g) 3D surface plot of thrust force with the combination of feed and speed



(h) 3D surface plot of thrust force with the combination of drill diameter and speed

FIGURE 3: CONTINUED.



(i) 3D surface plot of thrust force with the combination of drill diameter and feed

FIGURE 3: Analysis of torque using graphical output. *R*-square = 96.78% (obtained from response surface methodology).

TABLE 3: Response table for means (thrust force).

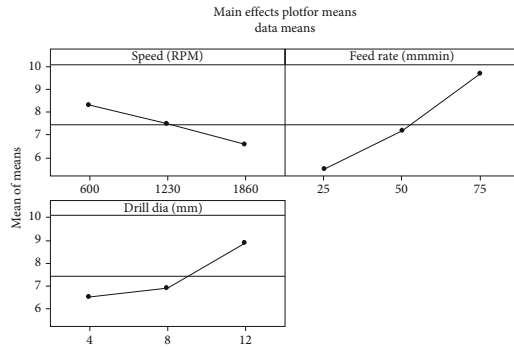
| Level | Speed (rpm) | Feed rate (mm/min) | Drill diameter (mm) |
|-------|-------------|--------------------|---------------------|
| 1 | 340.7 | 210.6 | 209.0 |
| 2 | 217.8 | 259.2 | 265.2 |
| 3 | 245.4 | 334.2 | 329.8 |
| Delta | 122.8 | 123.6 | 120.8 |
| Rank | 2 | 1 | 3 |

TABLE 4: ANOVA table for thrust force.

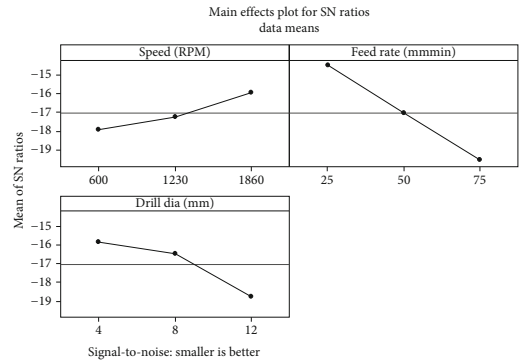
| Source | DF | Seq SS | Adj SS | Adj MS | <i>F</i> | <i>P</i> |
|--|----|--------|--------|---------|----------|----------|
| Regression | 9 | 259359 | 259359 | 28817.6 | 56.86 | 0.001 |
| Linear | 3 | 175261 | 30792 | 10264.1 | 20.25 | 0.001 |
| Speed (rpm) | 1 | 40860 | 22955 | 22954.9 | 45.29 | 0.001 |
| Feed (mm/min) | 1 | 68734 | 5285 | 5284.9 | 10.43 | 0.005 |
| Drill diameter (mm) | 1 | 65667 | 8 | 7.8 | 0.02 | 0.903 |
| Square | 3 | 35084 | 35084 | 11694.7 | 23.08 | 0.001 |
| Speed (rpm)*speed (rpm) | 1 | 33930 | 33930 | 33930.2 | 66.95 | 0.001 |
| Feed rate (mm/min)* feed rate (mm/min) | 1 | 1048 | 1048 | 1048.1 | 2.07 | 0.169 |
| Drill diameter (mm)* drill diameter (mm) | 1 | 106 | 106 | 105.8 | 0.21 | 0.653 |
| Interaction | 3 | 49014 | 49014 | 16337.9 | 32.24 | 0.001 |
| Speed (rpm)* feed rate (mm/min) | 1 | 41290 | 41290 | 41289.6 | 81.47 | 0.001 |
| Speed (rpm) * drill diameter (mm) | 1 | 7420 | 7420 | 7420 | 14.64 | 0.001 |
| Drill diameter (mm) * feed rate (mm/min) | 1 | 304 | 304 | 304.0 | 0.60 | 0.449 |
| Residual error | 17 | 8616 | 8616 | 506.8 | | |
| Total | 26 | 267974 | | | | |

and experimental values [10]. Aluminum composites reinforced with silicon carbide particle with different mesh size reinforcements such as 220 and 600 using the machining process. The output response cutting force is greatly influenced by the feed and the depth of cut whereas surface roughness is influenced by feed and preheating temperature. Minimum cutting force is obtained at 80°C and 100°C, and a good surface finish is obtained at 60°C [11]. With the addition of the third element in metal matrix composites, it increased the wear and friction resistance. The optimum input parameters to obtain the minimum friction and wear are 15 N load and 3.25 m/sec sliding speed [12]. The grey relational code is maximum at 0.2 mm the depth of cut,

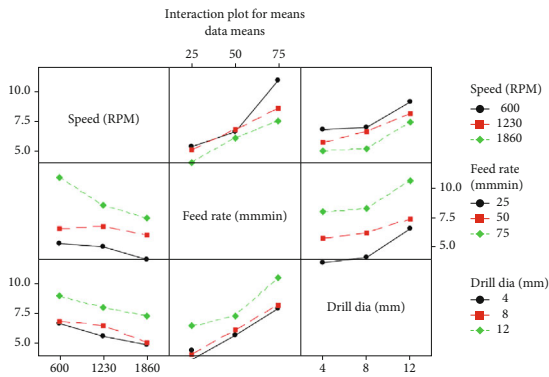
0.4 mm/rev feed, and 930 rpm speed. These optimal inputs reduced the surface roughness and tool temperature and maximize the material removal rate [13]. The material structure is the most significant factor for surface roughness, and the feed rate is the dominant factor that influences the thrust force in machining the aluminum alloy reinforced with alumina. The surface texture is increased by the addition of milled alumina with the aluminum alloy [14]. The optimized input parameters for better surface finish are cutting speed 900 rpm, feed rate 0.25 mm/rev, and depth of cut 0.5 mm. The feed has the major contribution of 82.6% followed by the depth of 6.8% and then cutting speed 6.43% [15]. The feed rate greatly influenced the thrust force and burr height



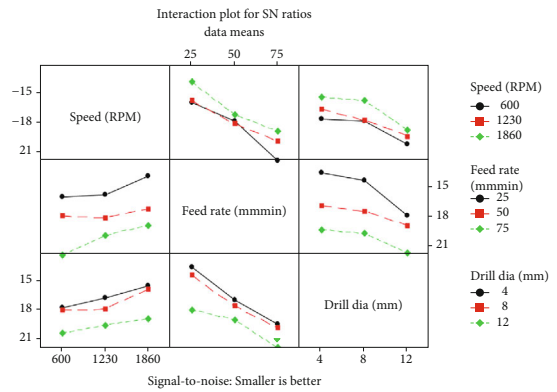
(a) Main effect plot for means



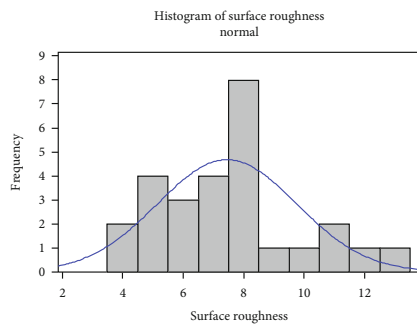
(b) Main effect plot for signal-to-noise ratio



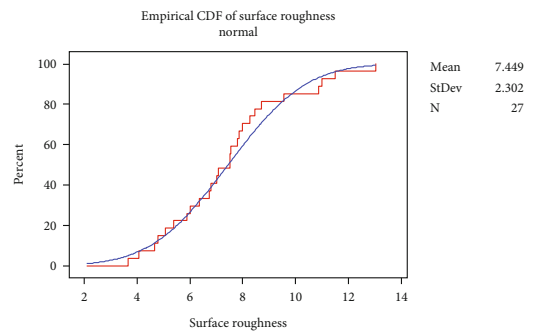
(c) Interaction plot for means



(d) Interaction plot for signal-to-noise ratio

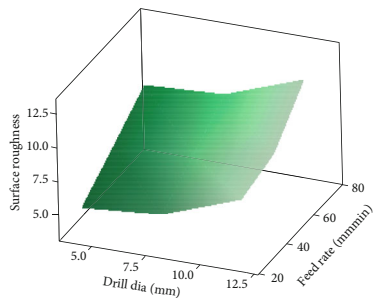


(e) Histogram of surface plot with respect to frequency



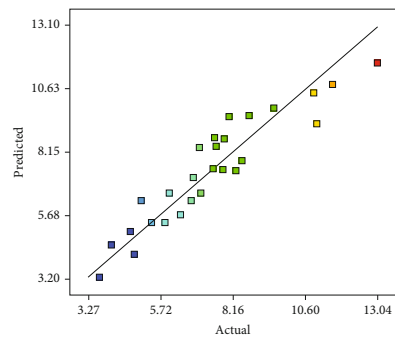
(f) Empirical CDF of surface roughness

Surface plot of surface roughness vs feed rate (mmmin), drill dia (mm)



(g) 3D surface plot of surface roughness with respect drill diameter and feed rate

Predicted vs. actual



(h) Predicted value vs. actual value

FIGURE 4: Analysis of surface roughness using graphical output. R -square = 92.41% (obtained from response surface methodology).

TABLE 5: Response table for means (surface roughness).

| Level | Speed (rpm) | Feed rate (mm/min) | Drill diameter (mm) |
|-------|-------------|--------------------|---------------------|
| 1 | 8.300 | 5.484 | 6.510 |
| 2 | 7.494 | 7.170 | 6.934 |
| 3 | 6.552 | 9.692 | 8.902 |
| Delta | 1.748 | 4.208 | 2.392 |
| Rank | 3 | 1 | 2 |

TABLE 6: ANOVA table for surface roughness.

| Source (surface roughness) | DF | Seq SS | Adj SS | Adj MS | F | P |
|--|----|---------|---------|---------|-------|-------|
| Regression | 9 | 127.308 | 127.308 | 14.1453 | 22.98 | 0.001 |
| Linear | 3 | 119.173 | 2.020 | 0.6733 | 1.09 | 0.379 |
| Speed (rpm) | 1 | 13.746 | 0.044 | 0.0438 | 0.07 | 0.793 |
| Feed (mm/min) | 1 | 79.674 | 0.732 | 0.7324 | 1.19 | 0.291 |
| Drill diameter (mm) | 1 | 25.752 | 1.044 | 1.0443 | 1.70 | 0.210 |
| Square | 3 | 4.651 | 4.651 | 1.5503 | 2.52 | 0.093 |
| Speed (rpm)*speed (rpm) | 1 | 0.028 | 0.028 | 0.0280 | 0.05 | 0.834 |
| Feed rate (mm/min)* feed rate (mm/min) | 1 | 1.050 | 1.050 | 1.0500 | 1.71 | 0.210 |
| Drill diameter (mm)* drill diameter (mm) | 1 | 3.573 | 3.573 | 3.5728 | 5.81 | 0.028 |
| Interaction | 3 | 3.484 | 3.484 | 1.1615 | 1.89 | 0.170 |
| Speed (rpm)* feed rate (mm/min) | 1 | 3.435 | 3.435 | 3.4347 | 5.58 | 0.030 |
| Speed (rpm) * drill diameter (mm) | 1 | 0.022 | 0.022 | 0.217 | 0.04 | 0.853 |
| Drill diameter (mm) * feed rate (mm/min) | 1 | 0.028 | 0.028 | 0.05 | 0.834 | |
| Residual error | 17 | 10.463 | 10.463 | | | |
| Total | 26 | 137.771 | | | | |

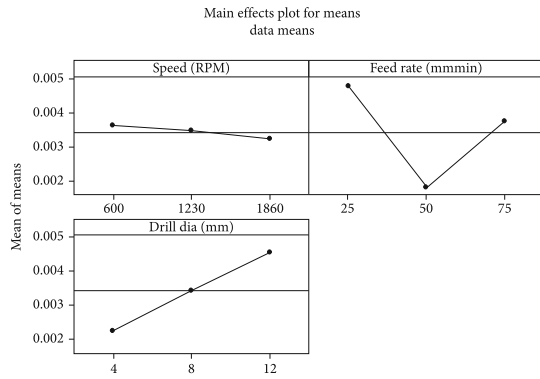
in drilling hybrid metal matrix composites (Al/15%SiC/4%graphite). The spindle speed is less influenced compared to the feed rate. At the lowest spindle speed of 1000 rpm and at a maximum feed rate of 1.5 mm/rev, the thrust force is 220 N [16].

Chaudhary et al. optimized aluminum silicate composite with spindle speed, feed rate, and drill diameter and output responses such as cylindricity, circularity, and surface finish, and various conclusions are made. The dimensional deviation is reduced with minimum drill bit diameter (6 mm). Circularity deviation is avoided at a minimum cutting speed (360 rpm) and minimum feed rate (0.095 mm/rev). Good surface finish is obtained by high cutting speed (680 rpm) and low feed rate (0.095 mm/rev). Cylindricity deviation is avoided with low spindle speed (680 rpm) and high feed rate (0.285 mm/rev) [17]. Confirmation test in optimizing A 356 reinforced with silicon carbide and boron carbide during machining operation revealed that the thrust force and surface roughness has 95% of the confidence interval. The analysis of variance deals with the influence of depth of cut and feed rate influence more with the cutting force and the surface roughness [18]. The best performance is obtained using uncoated carbide tool, the lower cutting speed of 119.2 m/min, and medium depth of cut 0.15 mm, and the corresponding grey relational grade value is 0.8084 [19]. The increased surface roughness (0.988 microns) is observed at

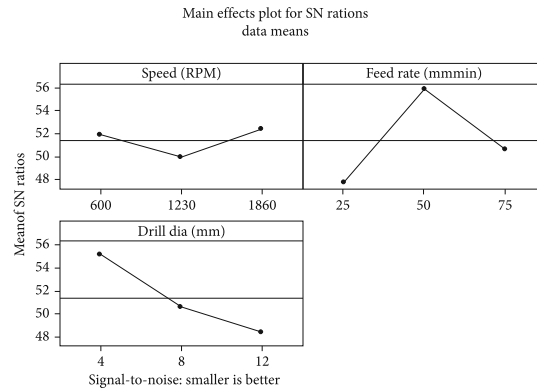
high cutting speed (m/min) and high feed rate (mm/rev) at the higher percentage of reinforcement (15%) [20]. The feed greatly influenced the uncut fiber factor followed by drill diameter and spindle speed. The uncut fiber factor is reduced by increasing the drill diameter [21]. The addition of graphite in the mixture of aluminum and silicon carbide particle improved the machinability and increased the tribological properties. The confirmation test during optimization showed improvement from 0.619 to 0.891 percentage [22]. Ganesh and Chandrasekaran proved in their experiment that the thrust force values increased to a maximum of 200 N at a higher feed rate and at low speed of 500 rpm. When the speed rose to 1000 rpm, the thrust force decreased [23, 24].

The literature reviewed above explain the fabrication of composites and machining of the prepared specimen. It also includes the influence of input parameters with the output response using various analyzing tools. These research results in the greater influenced by feed and drill diameter on the output responses. In this paper, HMMCs (LM25/treated SiCp with MWCNT) are subjected to drilling process and the influence of input parameters are analyzed using mathematical modeling technique.

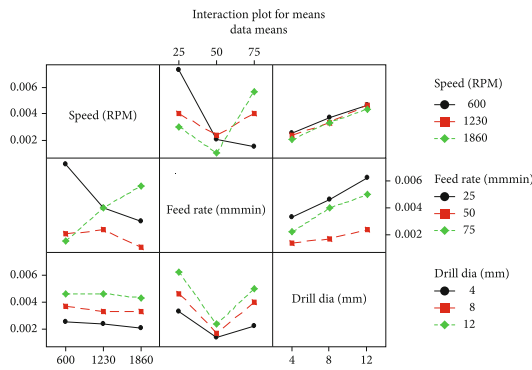
1.2. Scope and Objective. To perform the drilling operation on the specimen using the L_{27} orthogonal array. The drilling



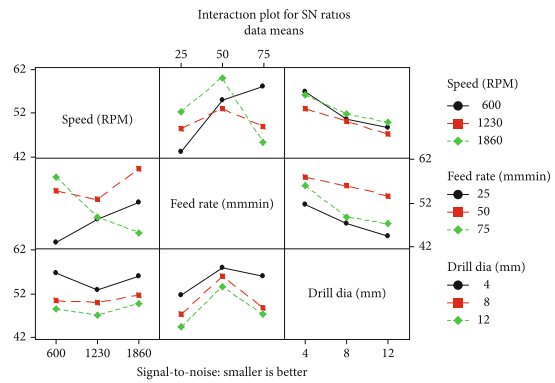
(a) Main effect plot for means



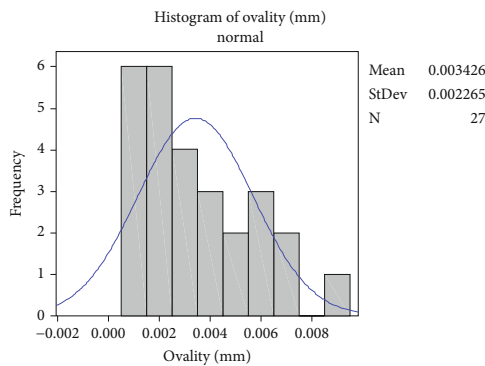
(b) Main effect plot for signal-to-noise ratio



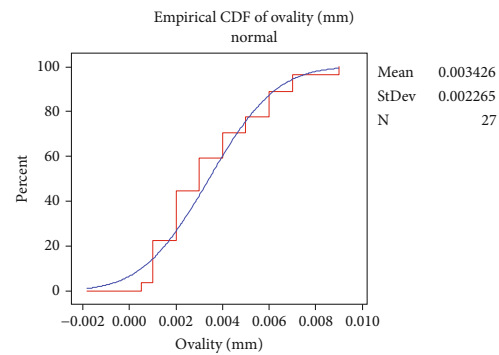
(c) Interaction plot for means



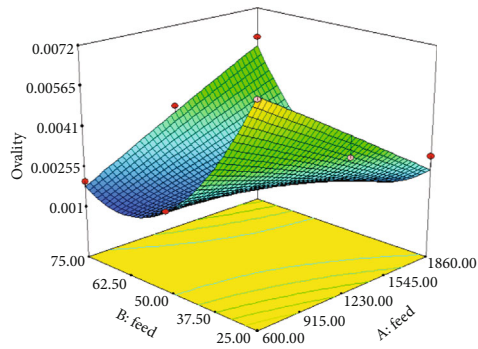
(d) Interaction plot for signal-to-noise ratio



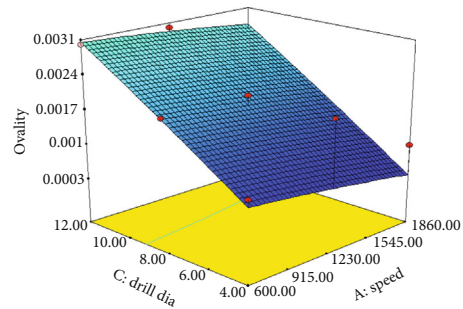
(e) Histogram of ovality with respect to frequency



(f) Empirical CDF of ovality



(g) 3D surface plot of ovality with respect to feed and speed



(h) 3D surface plot of ovality with respect to drill diameter and speed

FIGURE 5: Continued.

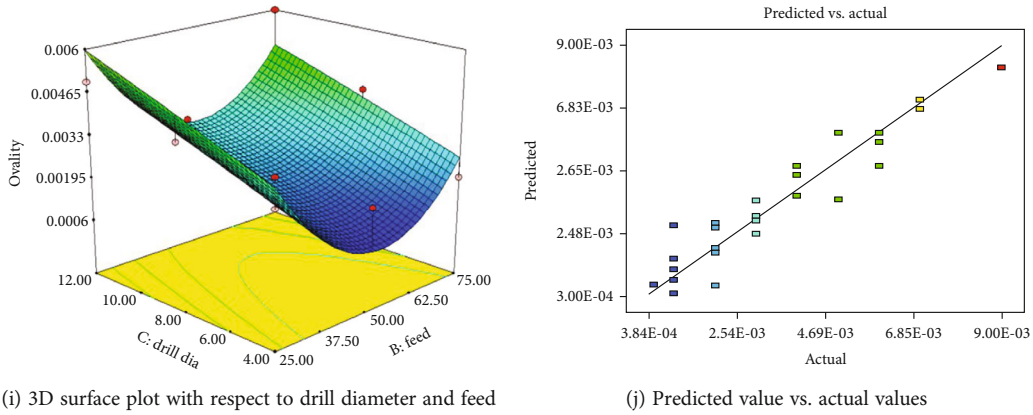


FIGURE 5: Analysis of ovality using graphical output. R -square = 89.95% (obtained from response surface methodology).

TABLE 7: Response table for means (ovality).

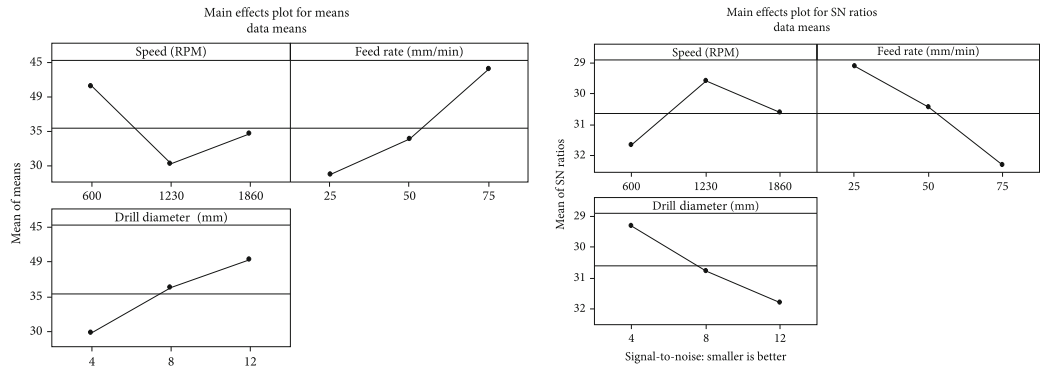
| Level | Speed (rpm) | Feed rate (mm/min) | Drill diameter (mm) |
|-------|-------------|--------------------|---------------------|
| 1 | 0.003611 | 0.004778 | 0.002278 |
| 2 | 0.003444 | 0.001778 | 0.003444 |
| 3 | 0.003222 | 0.003722 | 0.004556 |
| Delta | 0.000389 | 0.003000 | 0.002278 |
| Rank | 3 | 1 | 2 |

TABLE 8: ANOVA table for ovality.

| Source (ovality) | DF | Seq SS | Adj SS | Adj MS | F | P |
|--|----|----------|----------|----------|-------|-------|
| Regression | 9 | 0.000120 | 0.000120 | 0.000013 | 16.91 | 0.001 |
| Linear | 3 | 0.000029 | 0.000068 | 0.000023 | 28.6 | 0.001 |
| Speed (rpm) | 1 | 0.000001 | 0.000006 | 0.000006 | 7.59 | 0.014 |
| Feed (mm/min) | 1 | 0.000005 | 0.000062 | 0.000062 | 78.88 | 0.001 |
| Drill diameter (mm) | 1 | 0.000023 | 0.000 | 0.000 | 0.59 | 0.453 |
| Square | 3 | 0.000037 | 0.000037 | 0.000012 | 15.51 | 0.001 |
| Speed (rpm)*speed (rpm) | 1 | 0.000 | 0.000 | 0.000 | 0.01 | 0.940 |
| Feed rate (mm/min)* feed rate (mm/min) | 1 | 0.000037 | 0.000037 | 0.000037 | 46.52 | 0.001 |
| Drill diameter (mm)* drill diameter (mm) | 1 | 0.000 | 0.0000 | 0.0000 | 0.01 | 0.940 |
| Interaction | 3 | 0.000054 | 0.000054 | 0.000018 | 22.93 | 0.001 |
| Speed (rpm)* feed rate (mm/min) | 1 | 0.000054 | 0.000054 | 0.000054 | 68.74 | 0.001 |
| Speed (rpm) * drill diameter (mm) | 1 | 0.000 | 0.000 | 0.000 | 0.03 | 0.873 |
| Drill diameter (mm) * feed rate (mm/min) | 1 | 0.000 | 0.000 | 0.000 | 0.03 | 0.873 |
| Residual error | 17 | 0.000013 | 0.000013 | 0.000001 | | |
| Total | 26 | 0.000133 | | | | |

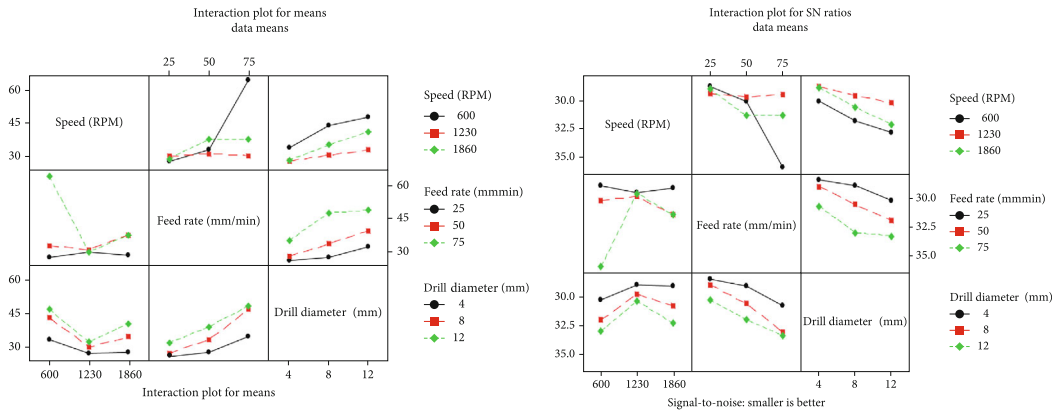
operation is done by considering the spindle speed, feed rate, and drill diameter as input parameter, and the output responses observed are thrust force, surface roughness, and ovality, to conduct wear test using the pin on disc device with inputs load, velocity, and percentage of reinforcement, to analyze the outputs responses using the statistical tool, and to optimize the input parameters using grey relational grade (GRG).

1.3. Methodology. The drilling process performed in the product with improved mechanical properties. The input parameters in drilling process are spindle speed, feed rate, and drill diameters of three different ranges, and the output responses recorded during machining process are torque, thrust force, surface roughness, ovality, and temperature. The effect of input parameters on the output responses is analyzed using response surface methodology and six sigma



(a) Main effect plot for means

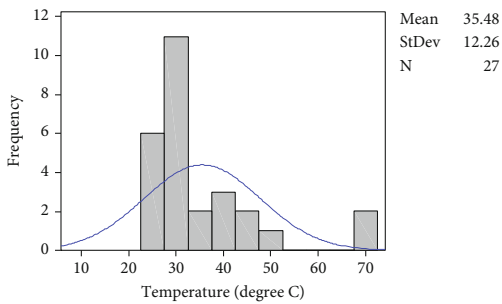
(b) Main effect plot for signal-to-noise ratio



(c) Interaction plot for means

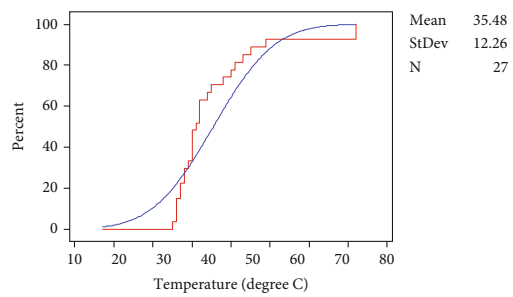
(d) Interaction plot for signal-to-noise ratio

Histogram of temperature (degree C) normal

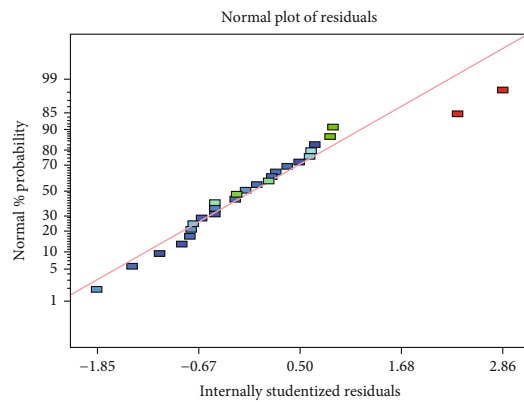


(e) Histogram of temperature with respect to frequency

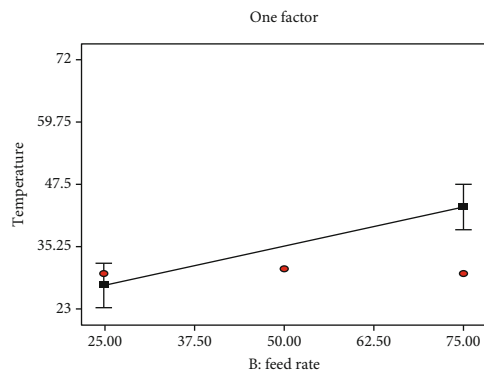
Empirical CDF of temperature (degree C) normal normal



(f) Empirical CDF of temperature



(g) Normal plot of residuals



(h) Temperature plot with respect to speed

FIGURE 6: Continued.

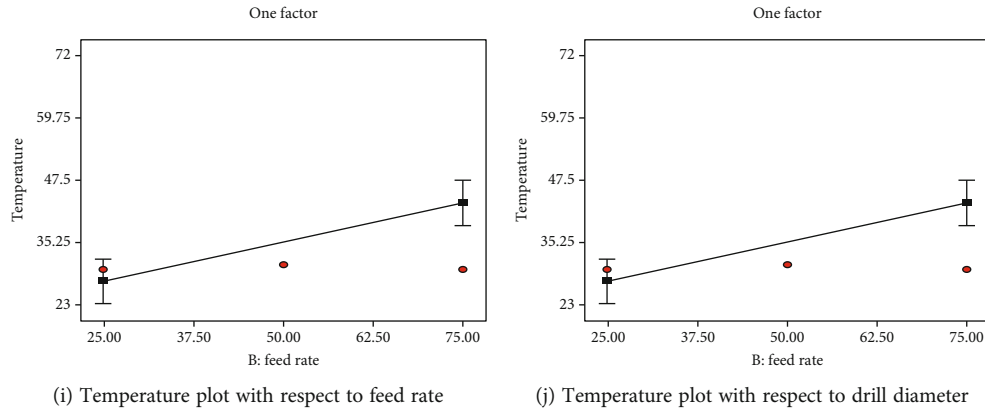


FIGURE 6: Analysis of temperature using graphical output. R – square = 71.86%.

TABLE 9

(a) Response table for means (temperature)

| Level | Speed (rpm) | Feed rate (mm/min) | Drill diameter (mm) |
|-------|-------------|--------------------|---------------------|
| 1 | 41.56 | 28.67 | 29.78 |
| 2 | 30.22 | 33.78 | 36.33 |
| 3 | 34.67 | 44 | 40.33 |
| Delta | 11.33 | 15.33 | 10.56 |
| Rank | 2 | 1 | 3 |

(b) ANOVA table for temperature

| Source (temp) | DF | Seq SS | Adj SS | Adj MS | F | P |
|--|----|---------|---------|---------|------|-------|
| Regression | 9 | 2810.08 | 2810.08 | 312.231 | 4.82 | 0.003 |
| Linear | 3 | 1772.94 | 169.74 | 56.580 | 0.87 | 0.474 |
| Speed (rpm) | 1 | 213.56 | 123.58 | 123.578 | 1.91 | 0.185 |
| Feed (mm/min) | 1 | 1058.00 | 15.72 | 15.719 | 0.24 | 0.629 |
| Drill diameter (mm) | 1 | 501.39 | 14.72 | 14.725 | 0.23 | 0.640 |
| Square | 3 | 422.39 | 422.39 | 140.796 | 2.17 | 0.128 |
| Speed (rpm)*speed (rpm) | 1 | 373.40 | 373.41 | 373.407 | 5.77 | 0.028 |
| Feed rate (mm/min)* feed rate (mm/min) | 1 | 39.19 | 39.19 | 39.185 | 0.61 | 0.447 |
| Drill diameter (mm)* drill diameter (mm) | 1 | 9.80 | 9.80 | 9.796 | 0.15 | 0.702 |
| Interaction | 3 | 614.75 | 614.75 | 204.917 | 3.17 | 0.051 |
| Speed (rpm)* feed rate (mm/min) | 1 | 574.08 | 574.08 | 574.083 | 8.87 | 0.008 |
| Speed (rpm) * drill diameter (mm) | 1 | 0.33 | 0.33 | 0.333 | 0.01 | 0.944 |
| Drill diameter (mm) * feed rate (mm/min) | 1 | 40.33 | 40.33 | 40.333 | 0.62 | 0.441 |
| Residual error | 17 | 1100.66 | 1100.66 | 64.745 | | |
| Total | 26 | 3910.74 | | | | |

techniques. The results are analyzed using analysis of variance. The input parameters are optimized. The optimized values of output responses are obtained using grey relational analysis (GRA). The wear test conducted on the fabricated product with input parameters load, sliding speed, and percentage of reinforcement. The wear rate of the tool observed before and after drilling to study the wear rate of the tool

after machining the hybrid metal matrix composite, and it is compared with the wear rate of the tool after machining the metal matrix composites. Figure 1 explains the experimental set up from machining of hybrid metal matrix composites and measurement of output responses such as torque, thrust forces, ovality, surface roughness, and temperature, the analysis of output responses using six sigma

TABLE 10: Output responses of machining operation.

| Ex no. | Speed (rpm) | Feed (mm/min) | Drill Dia (mm) | Torque (N-m) | Thrust force (N) | Surface roughness (μm) | Ovality (mm) | Temp ($^{\circ}\text{C}$) |
|--------|-------------|---------------|----------------|--------------|------------------|-------------------------------------|--------------|-----------------------------|
| 1 | 600 | 25 | 4 | 26.7 | 194 | 4.67 | 0.006 | 26 |
| 2 | 600 | 25 | 8 | 29.6 | 199 | 5.06 | 0.007 | 27 |
| 3 | 600 | 25 | 12 | 57.45 | 260 | 8.27 | 0.009 | 30 |
| 4 | 600 | 50 | 4 | 13.1 | 305 | 6.8 | 0.001 | 26 |
| 5 | 600 | 50 | 8 | 17.5 | 315.2 | 7 | 0.002 | 32 |
| 6 | 600 | 50 | 12 | 23.6 | 410 | 8 | 0.003 | 40 |
| 7 | 600 | 75 | 4 | 15.5 | 437 | 11 | 0.0005 | 49 |
| 8 | 600 | 75 | 8 | 26.5 | 458 | 10.86 | 0.002 | 72 |
| 9 | 600 | 75 | 12 | 67.43 | 488 | 13.04 | 0.002 | 72 |
| 10 | 1230 | 25 | 4 | 32 | 100.1 | 4.8 | 0.003 | 27 |
| 11 | 1230 | 25 | 8 | 43.26 | 170.3 | 5.4 | 0.004 | 30 |
| 12 | 1230 | 25 | 12 | 96.8 | 230 | 7.08 | 0.005 | 32 |
| 13 | 1230 | 50 | 4 | 32 | 149.5 | 6.74 | 0.002 | 28 |
| 14 | 1230 | 50 | 8 | 39.23 | 184.1 | 7.8 | 0.002 | 31 |
| 15 | 1230 | 50 | 12 | 96.5 | 270 | 7.86 | 0.003 | 34 |
| 16 | 1230 | 75 | 4 | 12.75 | 245.6 | 7.56 | 0.002 | 28 |
| 17 | 1230 | 75 | 8 | 16.91 | 271 | 8.71 | 0.004 | 30 |
| 18 | 1230 | 75 | 12 | 25.36 | 340 | 11.5 | 0.006 | 32 |
| 19 | 1860 | 25 | 4 | 16.88 | 131 | 3.65 | 0.001 | 25 |
| 20 | 1860 | 25 | 8 | 22.6 | 300.9 | 4.06 | 0.003 | 26 |
| 21 | 1860 | 25 | 12 | 48.1 | 310 | 6.37 | 0.005 | 35 |
| 22 | 1860 | 50 | 4 | 13 | 147.7 | 5.87 | 0.001 | 30 |
| 23 | 1860 | 50 | 8 | 36.06 | 231 | 6 | 0.001 | 38 |
| 24 | 1860 | 50 | 12 | 56.04 | 320 | 8.46 | 0.001 | 45 |
| 25 | 1860 | 75 | 4 | 14.6 | 170.9 | 7.5 | 0.004 | 29 |
| 26 | 1860 | 75 | 8 | 24.11 | 257.1 | 7.52 | 0.006 | 41 |
| 27 | 1860 | 75 | 12 | 88.6 | 340 | 9.54 | 0.007 | 43 |

techniques, and optimization of input parameters using grey relational analysis.

2. Analyze the Output Response Using Six Sigma Techniques and Response Surface Methodology

2.1. Analysis of Torque. Torque is measured using dynamometer connected to the vertical machining center. Torque is measured using a graphical form. The measured torque is analyzed using six sigma technique. Figures 2(a) and 2(b) show the main effect plot for means and signal-to-noise ratio.

In mean plot, the input parameter speed increased to a maximum value, and then, it reduced and in signal-to-noise ratio, the minimum speed is obtained at 1230 rpm, and then, it increased. The feed rate is maximum at 25 mm/min for mean plot whereas for signal-to-noise ratio, the feed rate is minimum at 25 mm/min. In mean plot, the drill diameter is maximum at 12 mm drill diameter, and in signal-to-noise plot, the minimum value is obtained at 12 mm drill diameter. Figures 2(c) and 2(d) explain the

interaction plot of means and signal-to-noise ratio in which each parameter is plotted in two different ways for better understanding. Figures 2(e) and 2(f) show the normal probability plot. Residuals are closer to diagonal line which represents ideal normal distribution, and the data is normally distributed. Figure 2(g) represents the histogram of torque with respect to frequency. The data values are in same interval size; at 10 Nm, the frequency level is 4; for 20 Nm, the graph shows the highest frequency of 7. The addition of all frequency values gives the normal frequency value of 27. Figure 2(h) shows empirical cumulative distribution function (CDF). CDF is the integral of probability distribution function. Figures 2(f), 2(i), and 2(j) explained the variation of output response torque with respect to speed, feed, and drill diameter. The R -square value in the table represent the percentage of data closer to the regression line.

The response of torque is listed in Table 1. This table displays the three levels of input parameters, and it influenced output response. Torque values are influenced by drill diameter with rank 1, and it is followed by speed with rank 2 and finally feed rate with rank 3. Analysis of variance (ANOVA) is the group of statistical models, and it is used to analyze the difference between the groups and among the groups. Mean

TABLE 11: S/N ratio and normalization values of output responses.

| Torque (N-m) | Thrust force (N) | S/N ratio | | | Normalization | | | | |
|-----------------|---------------------|--|-----------------|--------------------------------|-----------------|---------------------|--|-----------------|--------------------------------|
| | | Surface roughness (μm) | Ovality (mm) | Temp ($^{\circ}\text{C}$) | Torque (N-m) | Thrust force (N) | Surface roughness (μm) | Ovality (mm) | Temp ($^{\circ}\text{C}$) |
| -14.22 | -31.44 | 0.927 | 58.7 | -13.98 | 0.3651 | 0.8510 | 0.1938 | 0.2138 | 0.0000 |
| -15.11 | -31.66 | 0.23 | 57.41 | -14.31 | 0.4157 | 0.8551 | 0.2568 | 0.2265 | 0.0359 |
| -20.87 | -33.98 | -4.04 | 55.23 | -18.75 | 0.7428 | 0.8982 | 0.6429 | 0.2481 | 0.5196 |
| -8.03 | -36.46 | -2.34 | 74.31 | -13.98 | 0.0136 | 0.9444 | 0.4892 | 0.0595 | 0.0000 |
| -10.55 | -35.65 | -2.59 | 68.29 | -15.79 | 0.1567 | 0.9293 | 0.5118 | 0.1190 | 0.1972 |
| -13.14 | -37.94 | -3.75 | 64.77 | -17.73 | 0.3038 | 0.9719 | 0.6166 | 0.1538 | 0.4085 |
| -9.46 | -38.49 | -6.5 | 80.33 | -19.49 | 0.0948 | 0.9821 | 0.8653 | 0.0000 | 0.6002 |
| -14.15 | -38.9 | -6.4 | -20.8414 | -22.83 | 0.3612 | 0.9898 | 0.8562 | 1.0000 | 0.9641 |
| -22.26 | -39.45 | -7.99 | -20.3908 | -22.83 | 0.8217 | 1.0000 | 1.0000 | 0.9956 | 0.9641 |
| -15.7 | -25.69 | 0.69 | 64.77 | -14.31 | 0.4492 | 0.7440 | 0.2152 | 0.1538 | 0.0359 |
| -18.4 | -10.45 | 0.33 | 62.27 | -15.23 | 0.6025 | 0.4605 | 0.2477 | 0.1785 | 0.1362 |
| -25.4 | -32.92 | -2.69 | 60.33 | -15.79 | 1.0000 | 0.8785 | 0.5208 | 0.1977 | 0.1972 |
| -15.78 | -29.18 | -2.26 | 68.29 | -14.63 | 0.4537 | 0.8089 | 0.4819 | 0.1190 | 0.0708 |
| -17.56 | -30.98 | -3.53 | 68.29 | -15.51 | 0.5548 | 0.8424 | 0.5967 | 0.1190 | 0.1667 |
| -25.37 | 14.3 | -3.59 | 64.77 | -16.31 | 0.9983 | 0.0000 | 0.6022 | 0.1538 | 0.2538 |
| -7.79 | -33.49 | -3.26 | 68.29 | -14.63 | 0.0000 | 0.8891 | 0.5723 | 0.1190 | 0.0708 |
| -10.24 | -34.35 | -4.49 | 62.27 | -15.23 | 0.1391 | 0.9051 | 0.6835 | 0.1785 | 0.1362 |
| -13.77 | -36.32 | -6.9 | 58.75 | -15.79 | 0.3396 | 0.9418 | 0.9014 | 0.2133 | 0.1972 |
| -10.233 | -28 | 3.07 | 74.31 | -13.65 | 0.1387 | 0.7870 | 0.0000 | 0.0595 | -0.0359 |
| -12.77 | -35.25 | 2.14 | 64.77 | -13.98 | 0.2828 | 0.9219 | 0.0841 | 0.1538 | 0.0000 |
| -19.33 | -35.51 | -1.77 | 60.33 | -16.56 | 0.6553 | 0.9267 | 0.4376 | 0.1977 | 0.2810 |
| -7.96 | -29.07 | -1.06 | 74.31 | -15.23 | 0.0097 | 0.8069 | 0.3734 | 0.0595 | 0.1362 |
| -16.83 | -32.96 | -1.25 | 74.31 | -17.28 | 0.5133 | 0.8793 | 0.3906 | 0.0595 | 0.3595 |
| -20.71 | -35.79 | -4.23 | 74.31 | -18.75 | 0.7337 | 0.9319 | 0.6600 | 0.0595 | 0.5196 |
| -8.97 | -30.34 | -3.18 | 42.27 | -14.93 | 0.0670 | 0.8305 | 0.5651 | 0.3762 | 0.1035 |
| -13.33 | -33.89 | -3.21 | 58.75 | -17.94 | 0.3146 | 0.8966 | 0.5678 | 0.2133 | 0.4314 |
| -24.64 | -36.32 | -5.28 | 57.41 | -18.35 | 0.9568 | 0.9418 | 0.7550 | 0.2265 | 0.4760 |

square value in ANOVA is obtained by dividing sum of squares (SS) by degrees of freedom (DF). The F value is the ratio between the variance of group means and mean of within group variances. The P value is used to determine the smallest level of significance by avoiding the null hypothesis (Table 2).

2.2. Analysis of Thrust Force. Thrust force on a surface is normal and perpendicular to the normal reaction on the surface. Thrust force is measured using dynamometer in a vertical machining center in a graphical form. It is revealed that the thrust force is minimum at the entry and exit of tool, and it is maximum during the drilling process [25]. Figures 3(a) and 3(b) show the mean and signal-to-noise ratio, and they are opposite to each other. Main effect plot for means shows the peak point at 600 rpm, 75 mm/min of feed rate, and at 12 mm drill diameter and the corresponding speed, feed rate, and drill diameter are least in signal-to-noise ratio. Figures 3(c) and 3(d) explained the interaction plot for both means and signal-to-noise ratio, and it explained that each factor is plotted in two different ways. Figure 3(e) shows the histogram plot of thrust force in equal intervals with

respect to frequency. Figure 3(f) shows the empirical CDF of thrust force in terms of percentage. Figures 3(e)–3(g) explain the 3D surface plot of thrust force with respect to the combination of two input parameters. Thrust force increased to the largest with feed compared to the speed. Similarly, thrust force increased to the largest with drill diameter compared to speed. The percentage of thrust force closer to the regression line is about 96.78%. Tables 3 and 4 describe response table and ANOVA table for thrust force.

2.3. Analysis of Surface Roughness. Surface roughness of the drilled hole is measured using a profilometer by moving the probe of the profilometer along the drilled surface, and the corresponding values are obtained in the graphical form. Figures 4(a) and 4(b) represent main effect plot for means and signal-to-noise ratio, and the minimum surface roughness is obtained at 1860 rpm, 25 mm/min of feed rate, and 4 mm drill diameter for means, and the values are entirely conflicted with the signal-to-noise ratio. Figures 4(c) and 4(d) represent the interaction plot for means and signal-to-noise ratio, and it displayed the two different models in which each parameter is plotted. Figure 4(e) shows the

TABLE 12: Grey relational coefficient and grey relational code values of output responses.

| Torque (N-m) | Grey relational coefficient (GRC) | | | | GRG |
|--------------|-----------------------------------|-------------------------------------|--------------|-----------------------------|--------|
| | Thrust force (N) | Surface roughness (μm) | Ovality (mm) | Temp ($^{\circ}\text{C}$) | |
| 0.4406 | 0.7704 | 0.3828 | 0.3887 | 0.3333 | 0.4632 |
| 0.4611 | 0.7753 | 0.4022 | 0.3926 | 0.3415 | 0.4745 |
| 0.6603 | 0.8309 | 0.5833 | 0.3994 | 0.5100 | 0.5968 |
| 0.3364 | 0.8999 | 0.4946 | 0.3471 | 0.3333 | 0.4823 |
| 0.3722 | 0.8761 | 0.5059 | 0.3621 | 0.3838 | 0.5000 |
| 0.4180 | 0.9468 | 0.5660 | 0.3714 | 0.4581 | 0.5521 |
| 0.3558 | 0.9655 | 0.7877 | 0.3333 | 0.5557 | 0.5996 |
| 0.4390 | 0.9799 | 0.7767 | 1.0000 | 0.9329 | 0.8257 |
| 0.7371 | 1.0000 | 1.0000 | 0.9912 | 0.9329 | 0.9323 |
| 0.4758 | 0.6614 | 0.3892 | 0.3714 | 0.3415 | 0.4479 |
| 0.5571 | 0.4810 | 0.3993 | 0.3784 | 0.3666 | 0.4365 |
| 1.0000 | 0.8045 | 0.5106 | 0.3839 | 0.3838 | 0.6166 |
| 0.4779 | 0.7235 | 0.4911 | 0.3621 | 0.3498 | 0.4809 |
| 0.5290 | 0.7604 | 0.5536 | 0.3621 | 0.3750 | 0.5160 |
| 0.9966 | 0.3333 | 0.5569 | 0.3714 | 0.4012 | 0.5319 |
| 0.3333 | 0.8185 | 0.5390 | 0.3621 | 0.3498 | 0.4805 |
| 0.3674 | 0.8405 | 0.6124 | 0.3784 | 0.3666 | 0.5131 |
| 0.4309 | 0.8957 | 0.8353 | 0.3886 | 0.3838 | 0.5869 |
| 0.3673 | 0.7012 | 0.3333 | 0.3471 | 0.3255 | 0.4149 |
| 0.4108 | 0.8648 | 0.3531 | 0.3714 | 0.3333 | 0.4667 |
| 0.5919 | 0.8721 | 0.4706 | 0.3839 | 0.4102 | 0.5458 |
| 0.3355 | 0.7214 | 0.4438 | 0.3471 | 0.3666 | 0.4429 |
| 0.5068 | 0.8055 | 0.4507 | 0.3471 | 0.4384 | 0.5097 |
| 0.6525 | 0.8801 | 0.5953 | 0.3471 | 0.5100 | 0.5970 |
| 0.3489 | 0.7468 | 0.5348 | 0.4449 | 0.3580 | 0.4867 |
| 0.4218 | 0.8286 | 0.5364 | 0.3886 | 0.4679 | 0.5286 |
| 0.9205 | 0.8957 | 0.6711 | 0.3926 | 0.4883 | 0.6737 |

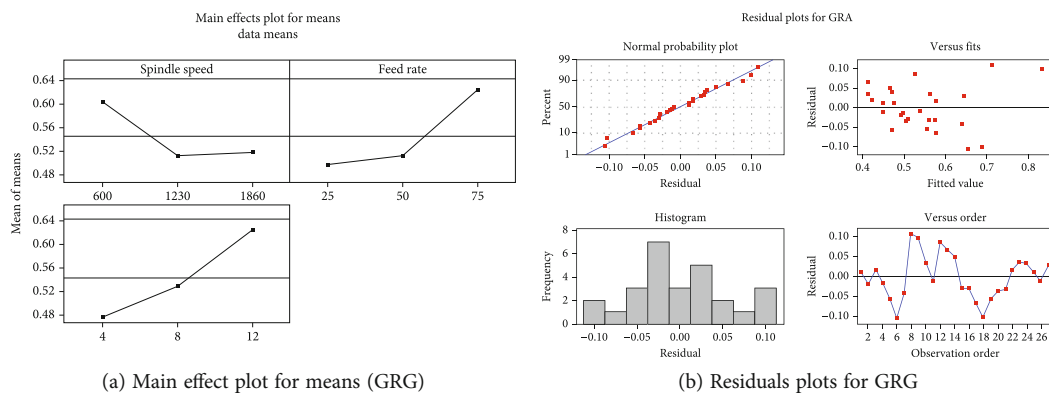


FIGURE 7: Detail plot of GRG.

histogram of surface plot, and it is used to derive normal residual plot as well as probability plot. Figure 4(f) displays the empirical cumulative distribution, and it represents the integral of probability distribution function. Figure 4(g) represents 3D surface plot in which surface roughness increased with the increased combination of feed and drill diameter. Figure 4(h) proved the closeness of predicted value with

the actual values. 92.4% of surface roughness values are accumulated closer to regression line, and it is represented as the *R*-square value. Response table of surface roughness indicates the influence of each input parameters on the output response surface roughness. The three levels of input parameters are listed in Table 5. Feed rate is influenced more on surface roughness with rank 1, and then drill diameter

TABLE 13: Response table for grey relational grade (GRG).

| Level | Spindle speed (rpm) | Feed rate (mm/min) | Drill diameter (mm) |
|-------|---------------------|--------------------|---------------------|
| 1 | 0.6029 | 0.4959 | 0.4776 |
| 2 | 0.5122 | 0.5125 | 0.5301 |
| 3 | 0.5184 | 0.6252 | 0.6259 |
| Delta | 0.0907 | 0.1294 | 0.1482 |
| Rank | 3 | 2 | 1 |

TABLE 14: ANOVA table for GRG.

| Source | DF | SEQ SS | ADJ SS | ADJ MS | <i>F</i> | <i>P</i> |
|----------------|----|----------|----------|----------|----------|----------|
| Regression | 9 | 0.266755 | 0.266755 | 0.029639 | 6.19 | 0.001 |
| Linear | 3 | 0.206308 | 0.206308 | 0.029639 | 6.19 | 0.001 |
| Spindle speed | 1 | 0.032132 | 0.032132 | 0.032132 | 6.71 | 0.019 |
| Feed rate | 1 | 0.075312 | 0.075312 | 0.075312 | 15.73 | 0.001 |
| Drill diameter | 1 | 0.098864 | 0.098864 | 0.098864 | 20.65 | 0.001 |
| Residual error | 17 | 0.081385 | 0.081385 | 0.004787 | | |
| Total | 26 | 0.34814 | | | | |

TABLE 15: Confirmation test to optimize the input parameters.

| Drilling parameters | Initial design | Optimal parameters | |
|-----------------------|----------------|----------------------|----------------------|
| | A1B3C3 | Prediction A3B2C1 | Experiment A3B2C1 |
| Torque | 67.43 | | 13 |
| Thrust force | 488 | | 147.7 |
| Surface roughness | 13.04 | | 5.87 |
| Ovality | 0.002 | | 0.001 |
| Temperature | 72 | | 30 |
| Grey relational grade | 0.9323 | 0.5445 | 0.4429 |

placed the next rank followed by spindle speed. ANOVA table for surface roughness is shown in Table 6. It explained the sum of square and mean square of linear form of input parameters, square values of input parameters, and interaction values of input parameters and their corresponding *P* and *F* values.

2.4. Analysis of Ovality. Ovality is the dimensional change along its diameter, horizontally and vertically. Ovality is measured by the profile projector. The drilled hole is projected on the screen with cross wires; then, the readings are noted using micrometers in the projector. Ovality occurred due to the heat generated during drilling operation. Figures 5(a) and 5(b) show the main effects plot for means and signal-to-noise ratio, and it describes variation of input parameters speed, feed rate, and drill diameter. Figures 5(c) and 5(d) display the interaction plot for means and signal-to-noise ratio. Figure 5(e) elaborates the histogram plot of ovality in terms of frequency in equal intervals; this histogram graph is related to normal probability distribution plot. Figure 5(f) represents empirical CDF of ovality in percentage. Figures 5(g)–5(i) describe the 3D surface plot of ovality in the combination of speed, feed rate, and drill diameter.

This graph explains there is a drastic increase in ovality with the increasing range of feed rate and drill diameter. Figure 5(j) shows the graph plotted between the actual value and predicted value, and the actual values are accumulated along the regression line. 89.95% of data gradually gathered along the regression line and it is denoted as *R* square.

Table 7 shows the response table for means (ovality) listed the three different levels of input parameters. The influence of feed rate on ovality is more since it is assigned to rank 1 followed by drill diameter which holds the second rank and with lower influence on ovality is spindle speed and it is assigned with the rank 3. ANOVA (Table 8) shows the analysis of variance such as speed, feed rate, and the drill diameter.

2.5. Analysis of Temperature. The temperature for each hole is determined by pointing the infrared temperature indicator in a position while the tool performs the drilling operation, and it indicates the specific temperature. Figures 6(a) and 6(b) represent the main effects plot for means as well as signal-to-noise ratio. In means plot, the maximum value is obtained at 600 rpm and minimum value is obtained at 1230 rpm, and it reverses in the signal-to-noise ratio. Figures 6(c) and 6(d) show the interaction plot for means and signal-to-noise ratio, and it explains the input parameters are plotted in two different ways. Figures 6(e)–6(g) are related to each other; the normalization plot is obtained from histogram of temperature in terms of frequency. The empirical CDF is obtained from the integral of probability distribution function. This normal residual plot shows the closest distribution of temperature data towards the regression line. Figures 6(h)–6(j) explain that, as the diameter increase the temperature increased, similarly when the feed rate increases the temperature increased and the value of temperature decreased as the speed increased. *R*-square value represent the accumulation of temperature data along

the regression line of about 71.86%. Response table for temperature represents that the influence of feed rate is more on temperature which is assigned to be rank 1; then, the percentage of influence of speed on temperature plays the second role and then the spindle speed (Table 9 (a)). Table 9(b) displays the analysis of variance table for temperature which listed the sum of squares; mean squares; F value and P value for linear form of input parameters of input parameters speed, feed rate, and drill diameter; square form of speed, feed rate, and drill diameters; and the interaction between the input parameters.

3. Optimize the Input Parameters Using Grey Relational Analysis (GRA) Techniques

GRA is one of the measurements in a grey system which briefs the correlation between the main factor and all other factors. It is an effective tool for multiresponse optimization. GRA used to evaluate and describe the relation of two or more things to the others when their direction of development is either varied or similar. Optimization is an essential action to select the effective input parameters for the responses obtained from machining. In this work, grey relational optimization is used. In this case, the output responses are listed in Table 10. For the corresponding input parameters, namely, spindle speed, feed rate, and drill diameter, the responses recorded are torque, thrust force, surface roughness, ovality and temperature, and smaller the better response is preferred for all the output responses.

3.1. Calculation of Signal-to-Noise Ratio and Normalization. The data obtained from the experiments are converted into signal-to-noise (S/N) ratio, and normalization values by the formula are listed in Table 11. The value obtained is negative since smaller the better concept is chosen, and the analysis is done to reduce the output response. Normalized the output responses as Z_{ij} using the formula: $Z_{ij} = \max(y_{ij}) - y_{ij} / \max(y_{ij}) - \min(y_{ij})$, where i is the number of experiments and j is the number of responses.

3.2. Calculation of Grey Relational Code. Grey relational coefficient (GRC) for the responses are calculated using the formula $G_{ij} = (\Delta \min + \epsilon \Delta \max) / (\Delta_{ij} + \epsilon \Delta \max)$, where $\Delta \min$ is the minimum value, $\Delta \max$ is the maximum value, and ϵ ranges from 0 to 1; then, the corresponding data are listed in Table 12. Grey relation grade (GRG) is calculated using the formula $GRG = (1/M) \cdot \sum G_{ij}$ and M is the number of responses. The optimized input parameters are obtained from the response table for GRC. The highest value is termed as rank 1, and its corresponding parameters are optimized inputs. Spindle speed of 600 rpm in level 1, 75 mm/min of feed rate in level 3, and 12 mm of diameter in level 3 are the optimized input values. Figure 7(a) shows the main effect plot of grey relational grade (GRG). The maximum value of speed is obtained at 600 rpm, 75 mm/min, and 12 mm of drill diameter. A1B3C3 is the initial design where A represents spindle speed, B feed rate, and C drill diameter.

Figure 7(b) displays the normal probability plot, fits, and histogram; all the four graphs are related to each other. In normal plot, the accumulation of data towards the regression lines indicate the less deviation, and this normal probability plot is derived from the histogram of residuals or GRG in terms of frequency. Response table for grey relational grade is displayed in Table 13. The input process parameters is listed in three levels in which the optimized value is chosen to be maximum. According to the spindle speed, level 3 is maximum compared to level 2 and 1. Feed rate and drill diameter level 3 are the maximum value compared to the other levels, so the predicted value is termed as A3B2C1, which is the predicted design, where A represents spindle speed, B represents feed rate, and C represents drill diameter. Table 14 is the analysis of variance which listed sequential sum of squares, mean sum of squares, F value, and P value. The optimal condition is set, and the selected experiments are carried out. The confirmation test is the final step to analyze the result obtained from the experiment. The average results obtained from the experiment is compared with the predicted average values. The optimal condition is set, and the selected experiments are carried out. The confirmation test is displayed in Table 15, and it shows the percentage is approximately equal.

4. Conclusion

Response surface methodology is used to generate the R -square value of the output responses which reveals the percentage of data accumulated along the regression line. Six sigma techniques are used to analyze the output responses using nominal probability plot, histogram plot, and main effect plot for means and noise-to-signal ratio while drilling hybrid metal matrix composites. The input parameter of feed rate and drill diameter greatly influenced the thrust force than the spindle speed.

4.1. The Data Are Analyzed Using Six Sigma and Response Surface Methodology

- (a) Drill diameter and speed values greatly influenced the torque compared to spindle speed during drilling process
- (b) Among the input parameters, the feed rate value is greatly influenced the thrust force and the corresponding R -square value is 96.78%
- (c) The surface roughness is raising along with the feed rate, and it declines as the spindle speed increased and the corresponding R -square value is 92.4%
- (d) In the output response, ovality is obtained using the optical projector and analyzed and the response is highly affected by feed rate and drill diameter. As the feed rate increases, the ovality increased and it decreased as the spindle speed increased and the accumulation of data along the regression line is 89.95%.

- (e) The output response, temperature, is mainly dependent on federate and spindle speed compared to drill diameter, and the *R*-square value is 71.86%.

4.2. *The Optimized Input Parameters Are Obtained Using Grey Relational Analysis.* The optimized input parameters are obtained using grey coefficient grade. The level of optimized input parameters is A1B3C3. The corresponding optimized values of input parameters are spindle speed of 600 rpm (A1), feed rate value of 75 mm/min (B3), and drill diameter of 12 mm (C3), and the confirmation test reveals that the predicted and experimental values are approximately equal, and hence, the design is significant.

Data Availability

The data used for the study is used in the manuscript itself.

Conflicts of Interest

On behalf of all authors, the corresponding author states that there is no conflict of interest.

References

- [1] J. A. Ghani, A. Choudhury, and H. H. Hassan, "Application of Taguchi method in the optimization of end milling parameters," *Journal of Materials Processing Technology*, vol. 145, no. 1, pp. 84–92, 2004.
- [2] K. Giasin and S. Ayvar-Soberanis, "An investigation of burrs, chip formation, hole size, circularity and delamination during drilling operation of GLARE using ANOVA," *Composite Structures*, vol. 159, pp. 745–760, 2017.
- [3] J. Fernandez-Perez, J. L. Cantero, J. Diaz-Alvarez, and M. H. Miguelez, "Influence of cutting parameters on tool wear and hole quality in composite aerospace components drilling," *Composite Structures*, vol. 178, pp. 157–161, 2017.
- [4] E. Ekici, A. R. Motorcu, and G. Uzun, "An investigation of the effects of cutting parameters and graphite reinforcement on quality characteristics during the drilling of Al/10B₄C composites," *Measurement*, vol. 95, pp. 395–404, 2017.
- [5] S. H. Tomadi, J. A. Ghani, C. H. Che Haron, H. Mas Ayu, and R. Daud, "Effect of cutting parameters on surface roughness in end milling of AlSi/AlN metal matrix composite," *Procedia Engineering*, vol. 184, pp. 58–69, 2017.
- [6] M. Nataraj and K. Balasubramanian, "Parametric optimization of CNC turning process for hybrid metal matrix composite," *International Journal of manufacturing Technology*, vol. 93, no. 1–4, pp. 215–224, 2017.
- [7] S. K. Lalmuan, S. Das, M. Chandrasekaran, and S. K. Tamang, "Machining investigation on hybrid metal matrix composites—a review," *Materials Today Proceedings*, vol. 4, no. 8, pp. 8167–8175, 2017.
- [8] D. E. Patil and V. A. Kamble, "Optimization of drilling parameters for material removal rate, hole accuracy and surface roughness by using grey relational analysis," *International Journal for Innovative Research in Science & Technology*, vol. 2, pp. 2349–6010, 2016.
- [9] D. Priyadarshi and R. K. Sharma, "Effect of type and percentage of reinforcement for optimization of the cutting force in turning of aluminium matrix nanocomposites using response surface methodologies," *Journal of Mechanical Science and Technology*, vol. 30, no. 3, pp. 1095–1101, 2016.
- [10] E. Baburaj, K. M. Sundaram, and P. Senthil, "Effect of high speed turning operation on surface roughness of hybrid metal matrix (Al-SiCp-fly ash) composite," *Journal of Mechanical Science and Technology*, vol. 30, no. 1, pp. 89–95, 2016.
- [11] U. A. Dabade and M. R. Jadhav, "Experimental study of surface integrity of Al/SiC particulate metal-matrix composites in hot machining," *Procedia CIRP*, vol. 41, pp. 914–919, 2016.
- [12] G. Pichayyapillai, P. Seenikannan, K. Raja, and K. Chandrasekaran, "Al6061 hybrid metal matrix composite reinforced with alumina and molybdenum disulphide," *Advances in Materials Science and Engineering*, vol. 2016, 9 pages, 2016.
- [13] P. C. Mishra, D. K. Das, M. Ukamanal, B. C. Routara, and A. K. Sahoo, "Multi-response optimization of process parameters using Taguchi method and grey relational analysis during turning AA 7075/SiC composite in dry and spray cooling environments," *International Journal of Industrial Engineering Computations*, vol. 6, no. 4, pp. 445–456, 2015.
- [14] S. Karabulut, "Optimization of surface roughness and cutting force during AA7039/Al₂O₃ metal matrix composites milling using neural networks and Taguchi method," *Measurement*, vol. 66, pp. 139–149, 2015.
- [15] C. Shoba, N. Ramanaiah, and D. N. Rao, "Optimizing the machining parameters for minimum surface roughness in turning Al/6% SiC/6%RHA hybrid composites," *Science*, vol. 10, pp. 220–229, 2015.
- [16] K. Palanikumar and A. Muniaraj, "Experimental investigation and analysis of thrust force in drilling cast hybrid metal matrix (Al-15%SiC-4%graphite) composites," *Measurement*, vol. 53, pp. 240–250, 2014.
- [17] G. Chaudhary, M. Kumar, S. Verma, and A. Srivastav, "Optimization of drilling parameters of hybrid metal matrix composites using response surface methodology," *Procedia Materials Science*, vol. 6, pp. 229–237, 2014.
- [18] G. M. Umesh Gowda, H. V. Ravindra, H. R. Gurupavan, G. Ugrasen, and G. V. Naveen Prakash, "Optimization of process parameters in drilling Al- Si₃N₄ metal matrix composites material using Taguchi technique," *Procedia Materials Science*, vol. 5, pp. 2207–2214, 2014.
- [19] K. Venkatesan, R. Ramanujam, J. Joel et al., "Study of cutting force and surface roughness in machining of Al alloy hybrid composite and optimized using response surface methodology," *Procedia Engineering*, vol. 97, pp. 677–686, 2014.
- [20] P. Jayaraman and K. L. Mahesh, "Multi-response optimization of machining parameters of turning AA6063 T6 aluminium alloy using grey relational analysis in Taguchi method," *Procedia Engineering*, vol. 97, pp. 197–204, 2014.
- [21] C. R. Prakash Rao and M. S. Bhagyashekar, "Effect of machining parameters on the surface roughness while turning particulate composites," *Procedia Engineering*, vol. 97, pp. 421–431, 2014.
- [22] P. Ghabezi and M. Khoran, "Optimisation of drilling parameters in composite sandwich structures (PVC core)," *Indian Journal of Science Research*, vol. 2, pp. 173–179, 2014.
- [23] P. Suresh, K. Marimuthu, S. Ranganathan, and T. Rajmohan, "Optimization of machining parameters in turning of Al-SiC-Gr hybrid metal matrix composites using grey-fuzzy algorithm," *Transactions of Nonferrous Metals Society of China*, vol. 24, no. 9, pp. 2805–2814, 2014.

- [24] R. Ramanujam, N. Muthukrishnan, and R. Raju, "Optimization of cutting parameters for turning Al-SiC (10p) MMC using ANOVA and grey relational analysis," *International Journal of Precision Engineering and Manufacturing*, vol. 12, no. 4, pp. 651–656, 2011.
- [25] M. Sangeetha and S. Prakash, "Experimental investigation of process parameters in drilling LM25 composites coated with multi wall carbon nano tubes using sonication process," *Achieves of Metallurgy and Materials*, vol. 62, no. 3, pp. 1761–1770, 2017.

Research Article

Experimental Analysis Using USRP for Novel Wavelet-Based Spectrum Sensing for 2.2 GHz Band Communication Using LabVIEW

Kalpana Devi Perumal ¹, E. D. Kanmani Ruby ¹, M. Dhivya ², G. Aloy Anuja Mary ¹,
V. Kavitha ³ and Umamaheswari Kandasamy ⁴

¹Department of ECE, Vel Tech Rangarajan Dr. Sagunthala R&D Institute of Science and Technology, Chennai, Tamil Nadu, India

²Department of ECE, New Horizon College of Engineering, Bengaluru, India

³Institute of ECE, Saveetha School of Engineering, SIMATS, Chennai, India

⁴Kebridehar University, Kebridehar, Ethiopia

Correspondence should be addressed to Umamaheswari Kandasamy; umasashwini@gmail.com

Received 21 April 2022; Accepted 19 May 2022; Published 4 June 2022

Academic Editor: V. Vijayan

Copyright © 2022 Kalpana Devi Perumal et al. This is an open access article distributed under the Creative Commons Attribution License, which permits unrestricted use, distribution, and reproduction in any medium, provided the original work is properly cited.

Spectrum sensing allows cognitive radio systems to detect relevant signals even in the presence of interference for reliable communication. Most of the existing spectrum sensing techniques use a particular signal-to-noise ratio model with assumptions and provide certain detection performance. Dynamic spectrum management techniques enabled the efficient allocation of channels to increasing number of users. In cognitive radio system, the dynamic spectrum management is efficient for sensing the channel occupancy and mobilizing the secondary user towards the unused primary user channel. For spectrum sensing, wavelet-based spectrum sensing method is analyzed and effectively made spectrum decision. The performance analysis is made for various SNR values with enhanced false alarm and throughput in spectrum management cognitive radio system in 2.2 GHz band communication.

1. Introduction

The wireless communication technology has rapid advancement in 5G and increases high scarce in spectrum resources [1]. The overall spectrum usage is calculated with a variation of 7-34%, which clearly explains that the spectrum is utilized very minimum of availability [2]. The reusing of temporarily unoccupied spectrum holes provided that the licensed user is not affected with any interference [3]. Every band of spectrum has different characteristics for a number of users and frequency range. The unused spectrum is detected by the spectrum sensing method by which the secondary user has the ability to select based on availability and data security as required. The parameters such as path loss, interference, wireless link, and delays are all determined. Efficient spectrum utilization is a significant challenge in managing a multifaceted communication system. With multiple users

with conflicting objectives sharing a common spectrum, some of whom may be hostile, prudent resource allocation is critical for effective frequency utilization [4]. The Federal Communications Commission (FCC) recently approved the use of an unlicensed device in the licensed band to address spectrum scarcity and inefficiency [5], which has sparked a lot of interest in this field of study. Cognitive radio, a software-defined radio (SDR) that can be reconfigured and reprogrammed, is one of the key enabling technologies to achieve this goal. The use of software processing to implement the radio system's operations is referred to as software-defined [6].

As part of the cognitive radio network (CRN), users must not only identify opportunities in the primary network but also ensure that those opportunities do not adversely affect the licensed network's users. It is necessary to have additional spectrum handover or mobility functionality in

this case because the primary user appears on the channel currently being used by the CRN user. Spectrum handover has been accomplished using a wide variety of methods, including bioinspired [7], Markov [8], and supervised machine learning [9] techniques. CR is one of the most effective techniques for ensuring fair and flexible frequency allocation in various wireless communication technologies [10, 11]. There has been an increase in the use of wireless communication learning techniques [12, 13]. Due to the rapid advancements in technology, SS must be continuously improved. Several issues arise in this context, such as the need for large amounts of frequency resources, spatial availability sensing, spectrum intelligence sensing, and energy-efficient protocol design. There is improved spectrum efficiency in wavelet-based spectrum sensing where the SUs use the spectrum without interfering with the PUs. Molina-Tenorio et al. [14] tried to come up with a new way to sense the multiband spectrum. This method is used in cognitive radios. Multiresolution analysis (wavelets), machine learning, and the Higuchi fractal dimension are the foundations of this method. Using this method, it is planned to connect several inexpensive software-defined radios so that they can sense a wide band of the radio electric spectrum. This work showed that the impulse noise elimination module did a good job of getting rid of high-frequency noise and sudden changes in the signal. The MBSS technique that was put into place worked well, with the same results as the simulations (0.98 of PS and two (mean) wrong samples when trying to find the PU transmission). Still, this device's performance could be better if it had a higher-gain antenna and if the SDR deployment was done in parallel, which would cut down on execution time and make better use of computing resources. The effective implementation of CR on GNU radio using an energy-based spectrum sensing method for real-time video transmission as a primary user was performed by Patil et al. [15]. The proposed system can indicate the frequency band occupancy by setting the detection output, according to the evaluation results. With the start of video transmission, the detection output changes to one. The goal of this project is to develop a spectrum sensing method that is best suited for detecting white spaces in video transmission as a primary user on the SDR platform [15]. The SDR is a wireless communications emerging technology that can be used with USRP and the GNU radio platform to implement cognitive radio detection. The results obtained in real time are proof-of-concept for the test bed that was constructed. Furthermore, the disparity in performance between the energy sensor simulations and test bed results highlights the hardware limitations [16]. Brodersen et al. [17] studied novel filter bank-based cooperative spectrum sensing. The study demonstrates that AFB-based CSS with FBMC waveform can significantly enhance performance. The second case study examines a novel CSS based on a maximum–minimum energy detector (Max–Min ED). It is anticipated that the proposed method will effectively address the issue of noise uncertainty (NU) with significantly less implementation complexity than existing methods. The developed algorithm with reduced complexity, improved detection performance, and improved reliability is

presented as an attractive solution to counteract the practical effects of a wireless channel with low SNR. Probability expressions in closed form are derived for the threshold, false alarm, and detection probabilities when frequency selective scenarios are considered under NU. The validity of the novel expressions is demonstrated by comparing them to respective simulation results.

2. Cognitive Radio

Spectrum management consists of allocating the specific frequency band to a specific secondary user shown in Figure 1. This allocation of spectrum depends on primary user activity and spectrum availability. If primary user behavior cannot be predicted for a certain band over a particular time period, then the cognitive radio system switches the secondary user to another band where the primary user behavior is fixed partially. The most suitable frequency band selection is the main criteria in spectrum management. Spectrum sharing needs other users coordination in the spectrum range except for malicious user if present in the system. It represents that the spectrum is an unoccupied band and is trying to collect the secondary user data. Spectrum mobility and its effective handover provides the uninterrupted communication for dynamic spectrum access. The spectrum holes are the unused spaces of the spectrum. If primary user becomes active, then the spectrum mobility is interrupted with the communication. The spectrum holes are the unused or underutilized spaces present in the spectrum. This system provides high data rate, long range, coverage, and less interference and operated in licensed and unlicensed band.

3. Spectrum Sensing Detection Method

Spectrum sensing is one of the most required detection processes implemented in cognitive radio systems. Cognitive radio systems allow the secondary users to learn the radio environment for detecting the primary user signal's presence by applying several methods and take decision for further transmission in the specified band. Figure 2 represents the spectrum sensing model.

The seamless spectrum sensing for a wide spectrum band provides the flexibility with respect to configurations as in [19] executing the parallel processing based on processing time. After detection of the available spectrum holes, the transmission terms of cognitive radio system are spectrum holes and power levels. To provide the dynamic spectrum management, the secondary users of the empty bands are required to align with primary users and interference temperature at the receiver should not exceed the limit [20]. The radio spectrum is periodically monitored by cognitive radio system and detected the presence of spectrum holes. When primary users (PUs) are active, then the secondary users in the same frequency band are not active. When the communication among SUs is active, then primary users want to transmit in the same frequency band. Hence, the secondary user is required to leave the band for specified time period in order to avoid interference. The transmitter power control needs to be adaptive as in [21].

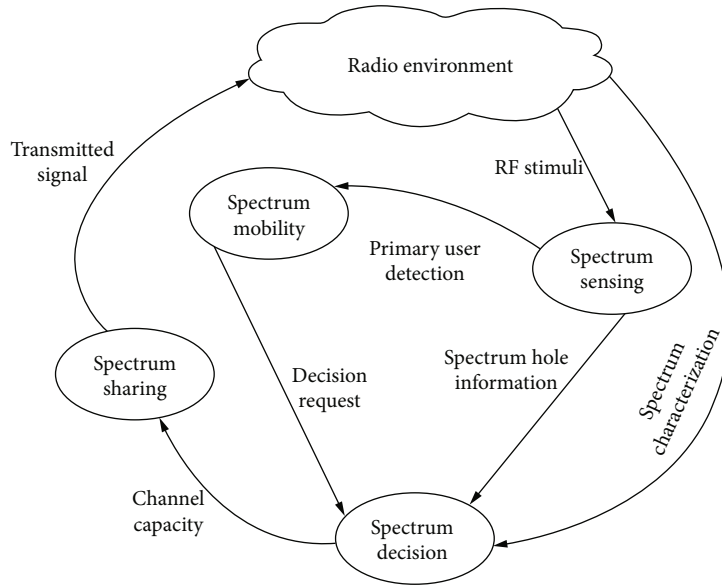


FIGURE 1: Spectrum management [18].

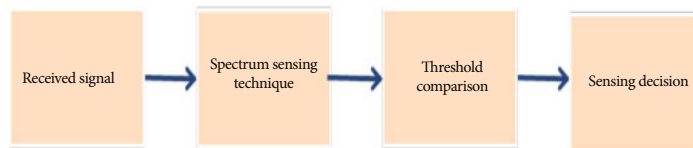


FIGURE 2: Spectrum sensing model.

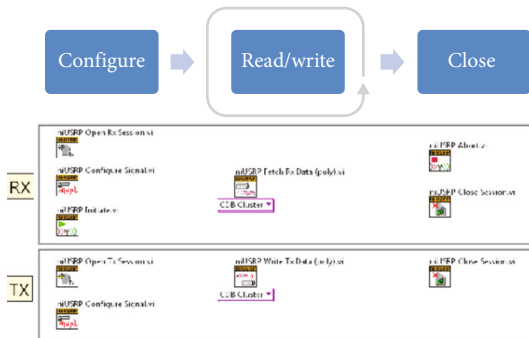


FIGURE 3: USRP transmit and receive functions.

4. Universal Software Radio Peripheral (USRP)

In comparison to current technologies that use radar to detect movement, programmable USRP radios are lighter and less expensive, and they can be programmed to send a signal through a wall and receive the reflection as it bounces off an object on the other side. Furthermore, USRP devices have the advantage of being programmable and operating in the license-free Industry, Scientific, and Medical (ISM) bands of 2.4–2.5 GHz and 4.9–5.85 GHz [22]. I/Q data is modulated and successfully handled by the USRP transmit and receive functions. The transmitter and receiver is configured to transmit and receive the I/Q data. Transmit functions include open, configure, write, and close the session.

Receive functions include open, configure, initiate, fetch the data, and close the session. Figure 3 shows the transmit and receive functions. The transmitter and receivers specifications of USRP are given in Table 1 and Table 2, respectively.

5. Proposed Wavelet-Based Spectrum Sensing Approach

The wavelet-based detection technique differs from other techniques in that it works in both the frequency and time domains, whereas other techniques only work in the frequency domain [23]. Because of its time-frequency characteristics, a wavelet is unique in that it can localize a signal in terms of frequency and time using its scaling and wavelet functions. For spectrum sensing, wavelets are implemented using filter banks with highly desirable properties [24]. The frequency bands of interest are commonly decomposed into a sequence of consecutive frequency subbands by applying wavelet-based spectrum sensing method. Wavelet-based detection method provides advantage in spectrum detection with simplicity and methods in terms of both simplicity and flexibility. This approach can be used to identify the spectrum holes in the radio resources for dynamic spectrum access. Consider the spectrum as the sequence of frequency subbands. Every subband has smooth power characteristics within the subband range but varies abruptly on the edge of the successive subband. With the use of the wavelet

TABLE 1: USRP2920 transmitter specifications.

| Specifications | Range |
|------------------------------------|--|
| Frequency range | 50 MHz to 2.2 GHz |
| Maximum output power (P_{out}) | 50 MHz to 1.2 GHz -50 mW to 100 mW 1.2 GHz to 2.2 GHz -30 mW to 70 mW |
| Gain range | 0 dB to 31 dB |

TABLE 2: USRP 2920 receiver specifications.

| Specifications | Range |
|-----------------|-------------------|
| Frequency range | 50 MHz to 2.2 GHz |
| Frequency step | <1 kHz |
| Gain range | 0 dB to 31 dB |

detection technique, the spectrum spaces may be observed in a given time instant by finding the obtained result. The energy of the reception signal is calculated to detect the presence of the primary user. From the detected spectrum, the primary user is present when a calculated energy level is greater than the threshold energy level. It also compares the output of the energy detector with a threshold that depends on the noise level and the signal is detected. Energy detection technique does not require prior knowledge of the primary user. But the details are required by matched filter, so it has relatively less complexity than other spectrum detection techniques [25]. $y(n)$ is equal to the sampled signal to be analyzed and $x(n)$ is equal to the input signal.

Primary user presence is confirmed when the energy of the signal is greater than the threshold.

Primary user absence is confirmed when the energy of the signal is lesser than the threshold.

Letybe considered the signal received which is represented in Figure 4.

If the spectrum energy level is found to be free which is detected by the secondary users, then communication will continue between secondary users. Spectrum monitoring is done periodically. After, certain iterations in the loop structure given in the following diagram provide the spectrum monitoring operation.

The power spectral density values for wavelet transformed signal are used to calculate edge. The block diagram of transmitter and receiver implemented in LabVIEW is shown in Figures 5(a) and 5(b). The edge is compared with sensing threshold λ . The sensing decision is expressed as follows:

- (i) If $e \geq \lambda$, PU signal absent
- (ii) If $e < \lambda$, PU signal present

The wavelet edge is considered for sensing decisions since one spike of the signal represents the power density of a given signal frequency, while multiple spikes represent the addition of noise. The power density function of noiseless signal and noisy signal is shown in Figures 6(a) and 6(b).

Spectrum sensing technique is arrived with edge detection in turn represents spectrum whole detection. The performance analysis is simulated for the wavelet transform energy detection and the conventional energy detection while the evaluation of the system was performed using the signal-to-noise ratio (SNR).

6. Simulation Results and Analysis

The simulation is done for transmitter section and receiver section. The transmitter section consists of generating the signal frequency and wavelet transformation of the samples is further calculated for power spectral density. The energy values calculated are used to determine the spectrum detection. The received signal is a complex signal; power spectral density is calculated on a linear scale of the frequency. The power spectra are calculated, estimating the periodogram. The IQ samples rate is considered 200k and gain of value 10. The front panel design of transmitter with specifications is depicted in Figures 7(a) and 7(b). The coerced gain frequency is considered 500MHz, USRP 2920 IP address is mentioned as 192.168.10.3

If no channel is selected by a secondary user within the band, then no common channel will be opted. Figure 8 represents the front panel of the USRP test bed. The detection of the signal for the carrier frequency of 1.4GHz is detected and PSD will be calculated periodically. The detection of the signal for the carrier frequency of 1.4GHz. False alarm probability is 0.01 kept for analysis. Smoothing factor is considered L with value 10, and then, probability of false alarm is represented by P_{fa} as 0.01. It gets compared with upper and lower thresholds. Table 3 shows the wavelet detection for trail 1 and trail 2. It exceeds the threshold. Hence, green light represents the primary user presence when primary user transmits the signal in the given frequency ranges. The experimental setup for USRP transmitter and receiver is shown in Figure 9.

Radio spectrum comprises of electromagnetic frequencies ranging lower than 30 GHz or having wavelength larger than 1 millimeter (mm). Various parts of the radio spectrum are allocated for different kinds of communication application varying from microphones to satellite communication. The IP address for USRP is 192.168.10.3, which makes the host to work as Host PC which is assigned an IP address in the same subnet. GUI application developed produces the FFT of the received signal. The designed application works as a broad band receiver; it fetches the signal from the external source environment and output as I and Q data into the appended file. After passing through USRP, the raw data bit streams are converted to arrays. FFT is performed

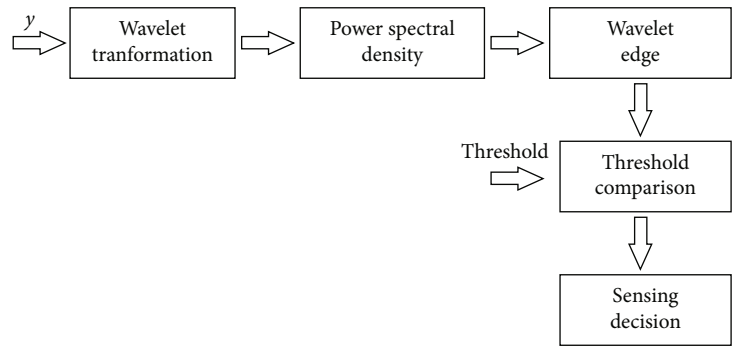
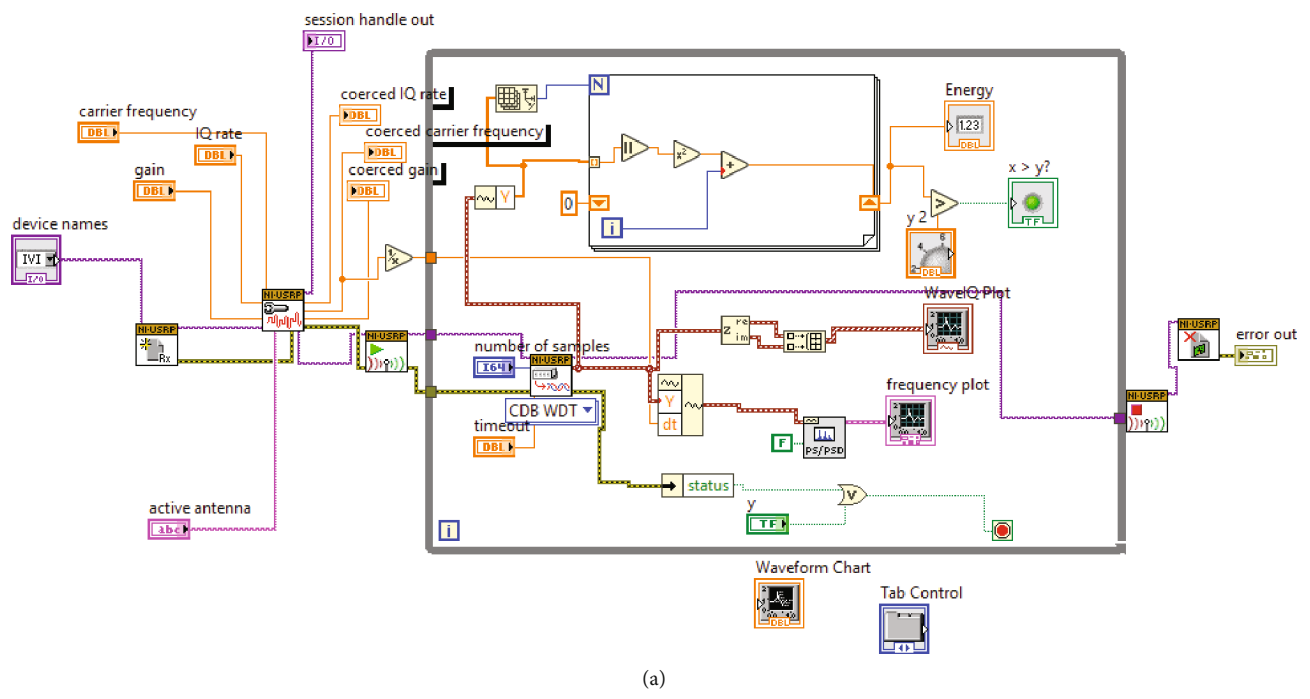
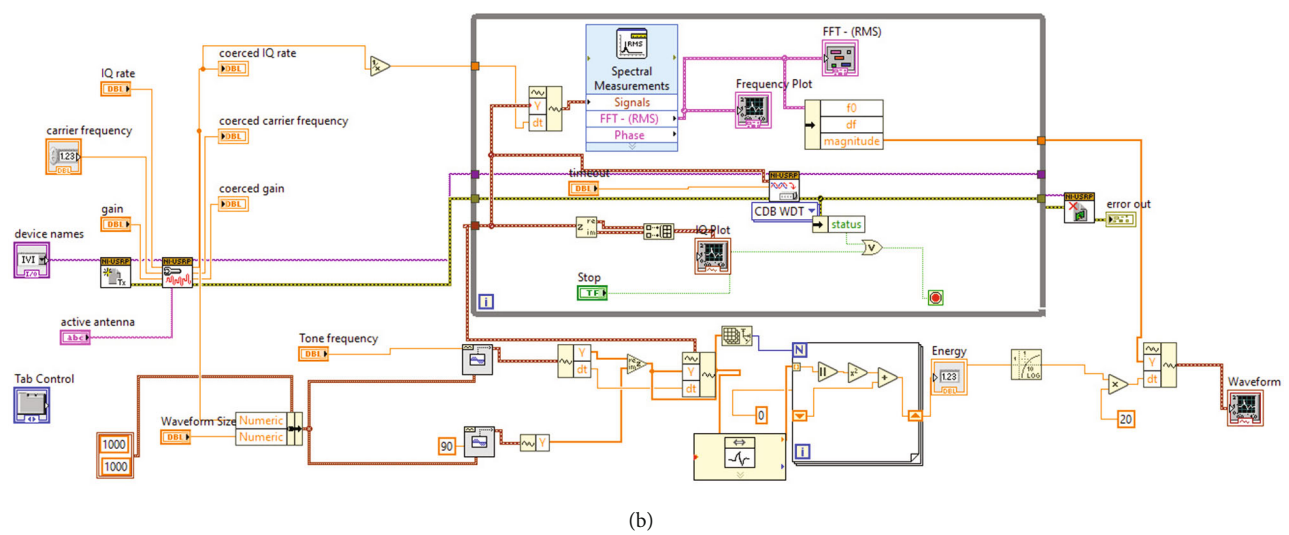


FIGURE 4: Wavelet-based sensing system model.



(a)



(b)

FIGURE 5: (a) Block diagram of baseband receiver. (b) Block diagram of baseband transmitter.

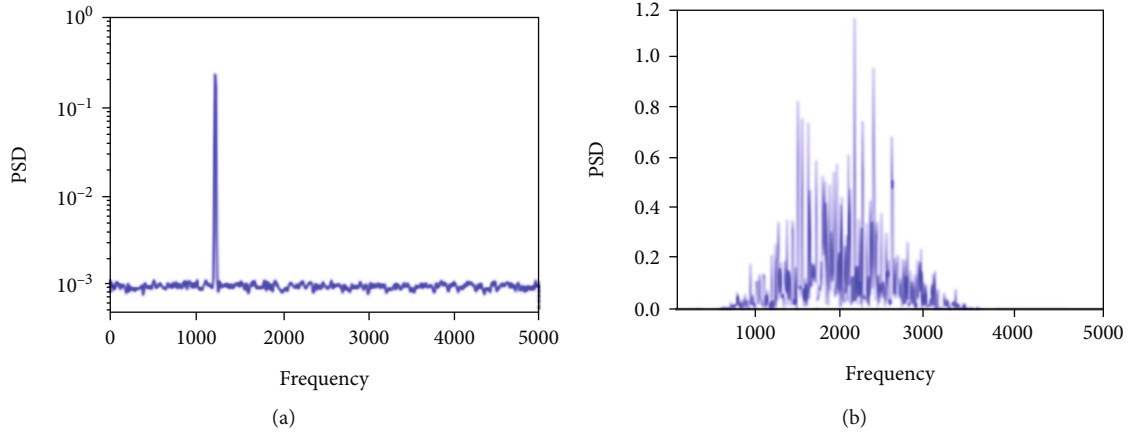


FIGURE 6: Power density function of (a) noiseless signal and (b) noisy signal.

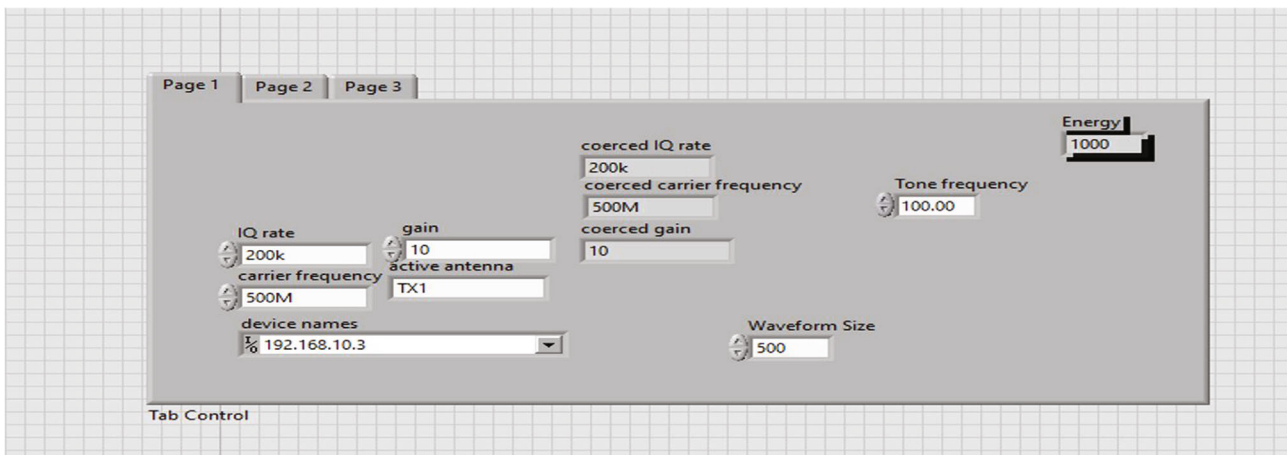
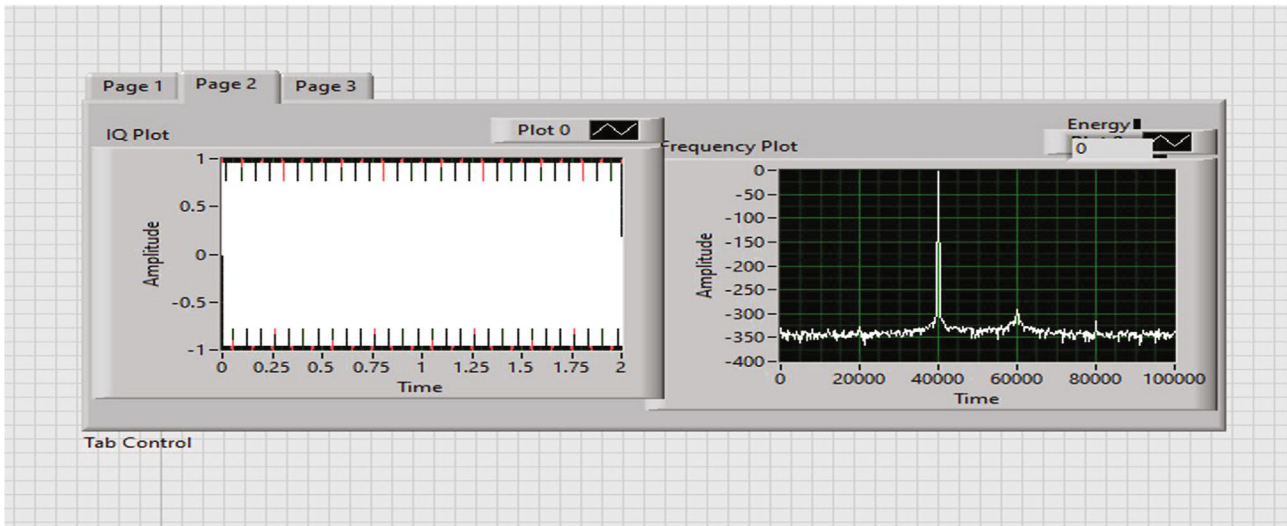


FIGURE 7: (a and b) Front panel design of transmitter with specifications.

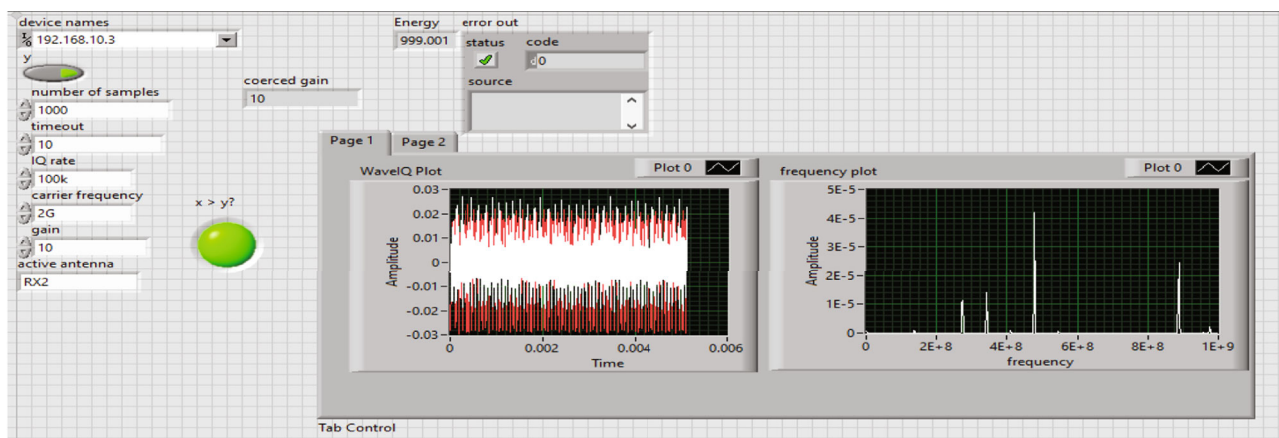


FIGURE 8: Front panel design for spectrum sensing by secondary users.

TABLE 3: Wavelet detection.

| Trail | Energy | Threshold for $P_{fa} = 0.01$ | Decision |
|-------|--------|-------------------------------|-----------------------|
| 1 | 10.225 | 4.0526 | Signal exist |
| 2 | 3.263 | 4.0526 | Signal does not exist |

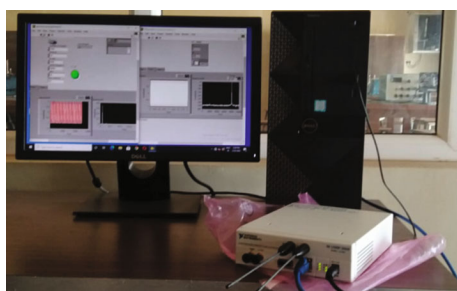


FIGURE 9: Experimental setup for USRP transmitter and receiver for spectrum detection.

with the help of signal processing blocks and it is passed through the Blackman-Harris window to overcome the spectral leakage effect.

7. Implementation

USRP 2920 can communicate the signal within the range of 50 MHz to 2.2 GHz, hence implanting the test bed under this frequency. The IQ samples are transmitted with the sampling rate of 200k and carrier frequency considered 2 GHz with gain values as 10 and waveform sizes are taken as 300. The data values are fetched from the USRP fetch block in receive mode. The energy values are calculated and the energy detection procedure is applied to the data values.

The test bed is implemented for and verified the energy detection as shown in Figure 9.

$$\text{No. of FFT Frames} = \frac{(\text{Decimation Rate} * \text{Time delay})}{\text{FFT window size}} \quad (1)$$

8. Conclusion

The sensing technique is proposed to implement a spectrum management system for the process of spectrum sensing at 50 MHz to 2.2 GHz frequencies using USRP. The peak power is observed around the frequency ranges. The spectrum detection method was identified in AWGN noise environment and does not depend on the channel and transmitter characteristics. The proposed cognitive radio method is used for efficient spectrum utilization even in low SNR regions. The dynamic spectrum management used to detect the spectrum enabled the efficient allocation of channels to increasing number of users. The performance analysis is proved for various SNR values with enhanced false alarm and throughput in spectrum management cognitive radio system in the given operated frequency band communication.

Data Availability

The data used to support the findings of this study are included within the article.

Conflicts of Interest

The authors declare that they have no conflicts of interest regarding the publication.

References

- [1] J. Lunden, V. Koivunen, and H. V. Poor, "Spectrum exploration and exploitation for cognitive radio: recent advances," *IEEE Signal Processing Magazine*, vol. 32, no. 3, pp. 123–140, 2015.
- [2] M. Wellens and P. Mähönen, "Lessons learned from an extensive spectrum occupancy measurement campaign and a stochastic duty cycle model," *Mobile Networks And Applications*, vol. 15, no. 3, pp. 461–474, 2010.
- [3] J. Mitola and G. Q. Maguire, "Cognitive radio: making software radios more personal," *IEEE Pers. Commun*, vol. 6, no. 4, pp. 13–18, 1999.
- [4] Z. Q. Luo, "Dynamic spectrum management: optimization and game theoretic formulations," in *Internet and Network Economics. WINE 2008. Lecture notes in computer science, C.*

- Papadimitriou and S. Zhang, Eds., Springer, Berlin, Heidelberg, 2008.
- [5] M. Marcus, J. Burtle, B. Franca, A. Lahjouji, and N. McNeil, "Federal communications commission spectrum policy task force," *Report of the unlicensed devices and experimental licenses working group*, 2002.
 - [6] M. B. Sajjan and M. N. Deshmukh, "Spectrum sensing and mobility management for cognitive radio," *Int J Sci Res and Development*, vol. 3, pp. 709–712, 2015.
 - [7] H. Anandakumar and K. Umamaheswari, "A bio-inspired swarm intelligence technique for social aware cognitive radio handovers," *Computers & Electrical Engineering*, vol. 71, pp. 925–937, 2018.
 - [8] A. Shakeel, R. Hussain, A. Iqbal, I. L. Khan, Q. U. Hasan, and S. A. Malik, "Analysis of efficient spectrum handoff in a multi-class hybrid spectrum access cognitive radio network using Markov modelling," *Sensors*, vol. 19, no. 19, p. 4120, 2019.
 - [9] H. Anandakumar and K. Umamaheswari, "Supervised machine learning techniques in cognitive radio networks during cooperative spectrum handovers," *Cluster Computing*, vol. 20, no. 2, pp. 1505–1515, 2017.
 - [10] W. S. H. M. W. Ahmad, N. A. M. Radzi, F. Samidi et al., "5G technology: towards dynamic spectrum sharing using cognitive radio networks," *IEEE Access*, vol. 8, pp. 14460–14488, 2020.
 - [11] M. Hirzallah, M. Krunz, B. Kecicioglu, and B. Hamzeh, "5g new radio unlicensed: challenges and evaluation," *IEEE Transactions on Cognitive Communications and Networking*, vol. 7, no. 3, pp. 689–701, 2021.
 - [12] Z. Shi, W. Gao, S. Zhang, J. Liu, and N. Kato, "Machine learning-enabled cooperative spectrum sensing for non-orthogonal multiple access," *IEEE Transactions on Wireless Communications*, vol. 19, no. 9, pp. 5692–5702, 2020.
 - [13] B. Shang and L. Liu, "Machine learning meets point process: spatial spectrum sensing in user-centric networks," *IEEE Wireless Communications Letters*, vol. 9, pp. 34–37, 2019.
 - [14] Y. Molina-Tenorio, A. Prieto-Guerrero, and R. Aguilar-Gonzalez, "Real-time implementation of multiband spectrum sensing using SDR technology," *Sensors*, vol. 21, no. 10, p. 3506, 2021.
 - [15] B. Rupali, K. D. K. Patil, and A. S. Gandhi, "SDR based energy detection spectrum sensing in cognitive radio for real time video transmission," *Modelling and Simulation in Engineering*, vol. 2018, Article ID 2424305, 2018.
 - [16] M. J. Rwodzi, *Energy-detection based spectrum sensing for cognitive radio on a real-time SDR platform [Master's thesis]*, University of Cape Town, 2016.
 - [17] R. W. Brodersen, A. Wolisz, D. Cabric, S. M. Mishra, and D. Willkomm, *CORVUS: a cognitive radio approach for usage of virtual unlicensed spectrum*, White paper, 2004.
 - [18] S. Dikmese, K. Lamichhane, and M. Renfors, "Novel filter bank-based cooperative spectrum sensing under practical challenges for beyond 5G cognitive radios," *EURASIP Journal on Wireless Communications and Networking*, vol. 2021, no. 1, 2021.
 - [19] W. Liu, D. Pareit, E. D. Poorter, and I. Moerman, "Advanced spectrum sensing with parallel processing based on software-defined radio," *EURASIP Journal on Wireless Communications and Networking*, vol. 2013, no. 1, 2013.
 - [20] S. Srinivasa and S. A. Jafar, "The throughput potential of cognitive radio: a theoretical perspective," *IEEE Communications Magazine*, vol. 45, no. 5, pp. 73–79, 2007.
 - [21] F. Ian, W. Y. Lee, M. C. Vuran, and S. Mohanty, "NeXt generation/dynamic spectrum access/cognitive radio wireless networks: a survey," *Elsevier Comput Networks*, vol. 50, no. 13, pp. 2127–2159, 2006.
 - [22] I. Cushman, D. B. Rawat, A. Bhimraj, and M. Fraser, "Experimental approach for seeing through walls using Wi-Fi enabled software defined radio technology," *Digital Communications and Networks*, vol. 2, no. 4, pp. 245–255, 2016.
 - [23] L. Fugal, *Conceptual wavelets in digital signal processing: an in-depth, practical approach for the non-mathematician*, Space & Signals Technical Pub., 2009.
 - [24] P. Y. Dibal, E. N. Onwuka, J. Agajo, and C. O. Alenoghena, "Application of wavelet transform in spectrum sensing for cognitive radio: a survey," *Physical Communication*, vol. 28, pp. 45–57, 2018.
 - [25] P. K. Devi and R. S. Bhuvaneshwaran, "Flexible reconfigurable architecture for SDR receiver," in *IEEE Malaysia international conference on Communications (MICC)*, pp. 265–270, Kuala Lumpur, Malaysia, 2013.

Research Article

Sustainability Improvement of Ethanol Blended Gasoline Fuelled Spark Ignition Engine by Nanoparticles

J. Thamilarasan,¹ V. Ravikumar,² S. Prasanna Raj Yadav³,³ Jyothi Yarlagadda,⁴ Ashok Kumar,⁵ S. Ramasubramanian,⁶ P. Sambandam,⁷ Challa Parvathi Rudesh,⁸ and Yalew Asres⁹

¹Department of Mechanical Engineering, Vel Tech Rangarajan Dr.Sagunthala R&D Institute of Science and Technology, Chennai, India

²Department of Mechanical Engineering, Sona College of Technology, Salem 636005, India

³Department of Mechanical Engineering, Easwari Engineering College, Chennai 600089, India

⁴Department of Mechanical Engineering, Vignan's Foundation for Science, Technology and Research, Guntur 522213, India

⁵Department of Mechanical Engineering, New Horizon College of Engineering, Marathahalli, Bangalore 560103, India

⁶Department of Automobile Engineering, Vels Institute of Science, Technology & Advanced Studies (VISTAS), Chennai, India

⁷Department of Automobile Engineering, Vel Tech Rangarajan Dr.Sagunthala R&D Institute of Science and Technology, Chennai, India

⁸Department of Aeronautical Engineering, Mangalore Institute of Technology and Engineering, Mangaluru, Karnataka 574225, India

⁹Department of Mechanical Engineering, Faculty of Manufacturing Institute of Technology, Hawassa University, Ethiopia

Correspondence should be addressed to S. Prasanna Raj Yadav; sprasannarajyadav@gmail.com and Yalew Asres; yalewa@hu.edu.et

Received 9 April 2022; Accepted 19 May 2022; Published 3 June 2022

Academic Editor: V. Vijayan

Copyright © 2022 J. Thamilarasan et al. This is an open access article distributed under the Creative Commons Attribution License, which permits unrestricted use, distribution, and reproduction in any medium, provided the original work is properly cited.

The sophisticated technology being used in automotive technology, as well as the increased use of vehicles, enables the engine to operate on a variety of alternative fuels. Natural or synthetic carbon-based connections are responsible for the formation of ethanol. They may be produced from a variety of sources, including agricultural feedstock, local crops, and even agricultural trash and waste products. Because they are in the form of a renewable resource, they may be employed in a variety of applications, including IC engines, where they can be used as fuel or as an addition, depending on their composition. It is possible to dramatically improve the performance of gasoline engines using a novel mix of nanoadditives, ethanol, and gasoline while simultaneously reducing the negative environmental impact. An ethanol-gasoline combination was used to power the engine in this work, which examined the effects of the alumina nanoaddition. Results reveal that thermal efficiency can be improved by up to 17% while fuel consumption can be reduced by up to 16% on a volume basis, indicating a considerable improvement over the basic engine. Also validated was a decrease in dangerous carbon monoxide emissions of as much as 14%, a reduction in unburned hydrocarbon emissions of 18.5%, and a significant reduction in oxygen of as much as 18%.

1. Introduction

As of right now, the vehicle industry is experiencing a boom in both demand and growth potential. The ever-increasing

demand for automobiles increases our reliance on a wide range of fossil fuels. Fossil fuels' nonrenewability and growing pollution have sparked a hunt for an alternate source of energy. The growing population density of automobiles

necessitates increased gasoline usage, which in turn reduces the supply and increases the price of the commodity. Therefore, it is vital to look for an alternative fuel that can efficiently replace the conventional gasoline without significant impact on the engine design and operation of the vehicle [1].

The inclusion of additional carbon group elements or the introduction of new alcohols is not a fresh concept. Alcohols are characterised by the polymerization of hydroxyl groups to carbon atoms. To put it another way, the C-H chain of conventional fuels may be changed as a consequence of the inclusion of these additives, leading in the formation of new polymer chains. Methanol and ethanol are the two most often used alcoholic fluids in internal combustion engines [2]. Finished additives and performance additives are the two types of fuel additives that may be used with gasoline. All petroleum refineries utilise finished fuel additives to satisfy and maintain finished fuel quality guidelines and regulations. Gasoline is often supplemented with performance additives in order to improve specific characteristics of the fuel or to provide new characteristics that are not already there [3]. The SI engine's combustion efficiency is improved and increased by adding the performance additive to the fuel. It also reduces the emissions from the cylinders. Among performance additives, oxygenated additives are mostly derived from biomass, a sustainable source of energy. Oxygenated compound performance additives are now being added to gasoline in order to minimise emissions and increase SI engine performance [4].

SI engine performance and emissions utilising ethanol-gasoline mixtures are affected by the air-fuel ratio. Using ethanol-gasoline mixes resulted in an increase in torque output, according to engine performance testing. In terms of heat use, however, there is little difference. With the addition of ethanol, CO and HC emissions were lowered. Emissions may be effectively decreased by utilising gasoline containing 10% ethanol, as shown in this research [5]. Nanoparticles have gained prominence in recent years as a result of their unique inherent properties, which have resulted in a decrease in emissions and an improvement in engine efficiency in the vast majority of applications. The density, viscosity, heat of vaporisation, volatility, flashpoint, and other characteristics of fuel may be changed by adding nanoadditives to it. Metallic nanocatalysts were used in base diesel or gasoline fuels in the early trials of the technology [6, 7].

Because of the oxygen present, ethanol burns cleanly and efficiently. Aside from its impact resistance and high latent heat of evaporation, ethanol is one of the alcohols that have lately been added to hydrocarbon fuels as an additive. The higher octane number of ethanol enables greater compression ratios in alcohol-powered engines, which improves thermal efficiency [8]. The impact of an alcohol catalyst in a spark-ignition engine was investigated, and it was discovered that the energy density of the mixed fuel decreased as the octane number increased. In addition to improving brake thermal efficiency, the use of ethanol may assist to minimise environmental pollution as well as save money on gasoline [9]. Various kinds of alcohol fuels have been studied in the literature for their impact on engine perfor-

mance and emissions of harmful pollutants, according to what has been found. When utilised as fuel in internal combustion engines, alcohols with a higher octane number than gasoline emit lower quantities of pollutants than gasoline does [2].

In order to outperform standard gasoline in terms of performance and emission characteristics, it has been explored if an auxiliary addition of alumina nanoparticle to an ethanol mixed fuelled engine would be beneficial. One of the key goals of this study is to increase thermal efficiency while also reducing fuel consumption while also reducing dangerous emissions and increasing the ability of the air/fuel to burn when nanoinflated. The light-power gasoline engine was subjected to an experimental research. The concentration of alumina nanoadditives is controlled at two different flow rates of 10 ppm and 20 ppm on a constant 20% ethanol-blended gasoline (E20) fuel. The essential test runs were carried out under a variety of load settings ranging from zero to full load in order to assure the best possible performance and the lowest possible pollutant emissions.

2. Materials and Method

Flex-fuel has different minimum and maximum vapor pressure requirements. These requirements change depending on year of evolution [10]. "Alcohol" refers to any organic compound that has the hydroxyl functional group (-OH) attached to the carbon atom of the molecule. As a result of oxygen being present in the hydroxyl functional group, alcohols burn evenly and create a significant amount of smaller pollutants and fine particulate matter. Reduced emissions are made possible by lower molecular mass alcohols like ethanol and methanol, as well as their greater flame speed and the absence of the elements phosphorus and sulphur [11]. In addition, the stoichiometric ratio of ethanol and gasoline is smaller than that of gasoline and diesel. Many researchers [12–16] achieved better performance on the blends of E20. The same quantity of air may burn a greater volume of fuel using this method, while compared to gasoline use, a larger reduction in fuel consumption was seen when using 20% ethanol, according to testing results. This resulted in an increase in flame thrust and calorific value, as well as a mixing of the air and fuel, which led to better combustion than could be achieved with gasoline alone.

When compared to pure gasoline, methanol and ethanol have greater oxygen concentration (49.93% vs. 34.7%), which encourages a more thorough burning of the fuel and minimises hazardous exhaust emissions. To avoid engine knocking, the Research Octane Number of the mixtures of ethanol and methanol is greater. Fuel consumption is projected to be greater for both ethanol and methanol since their lower heating value is lower than that of pure gasoline. The volumetric fuel efficiency of both alcohol fuels is improved by the increased densities. Due to the greater flow resistance of methanol and ethanol at low temperatures, this may have an impact on automotive fuel injection systems [17].

As the concentration of nanoparticles increases, they are being driven to the liquid surface in order to become more

TABLE 1: Properties of gasoline and ethanol blend.

| Sl No. | Property | Gasoline | Ethanol | E20 | ASTM testing methods |
|--------|---------------------------------------|----------|---------|------|----------------------|
| 1 | Lower heating value (MJ/kg) | 44.0 | 26.9 | 41.8 | ASTM D240 |
| 2 | Kinematic viscosity, at 20°C (cSt) | 0.5 | 1.5 | 0.67 | ASTM D445 |
| 3 | Density, at 15°C (kg/m ³) | 737 | 785 | 746 | ASTM D4052 |
| 4 | Flash point, (°C) | -40 | 14 | 29 | ASTM D93 |
| 5 | Research Octane Number, RON | 90 | 115 | 96 | ASTM D2699 |
| 6 | Motor Octane Number, MON | 82 | 100 | 83 | ASTM D2700 |
| 7 | Oxygen (%) | 0 | 35 | 7 | ASTM E385 |
| 8 | Stoichiometric air/fuel ratio | 14.5 | 8.9 | 13.3 | ASTM D5291 |

closely associated. Because of the strong cohesive force between the molecules in nanoparticles, they have a higher surface tension than larger particles. The average distance between the nanoparticles and the fuel molecules is decreasing. It is possible to increase the surface tension of nanoparticles by using the Van der Waals force rather than electrostatic repulsion [18]. The surface tension of nanoparticles fluctuates depending on the size and quantity of nanoparticles present. In response to variations in the bulk density of nanoparticles, variations in the attraction force between the nanoparticles and the surface tension of the fuel are seen. Surface tension in nanoparticles increases in proportion to the size of the nanoparticles being studied. The presence of smaller nanoparticles increases the surface charge density of larger nanoparticles, and the reverse is true [19]. Because of their strong heat conductivity and mechanical properties, alumina nanoparticles may have an impact on the combustion of biodiesel. Alumina is toxicologically volatile and irritating to the respiratory system, making it a poor choice for industrial applications. It reacts fast with water, forming hydrogen as a result. Because of the differences in size and shape of alumina nanoparticles, the combustion of mixed nanoparticle fuels is affected. It is possible to separate water molecules into hydrogen and oxygen in this manner [20]. Table 1 presents the properties of gasoline-ethanol blended fuel.

2.1. Experimental Details. The performance and emission characteristics of an ethanol mix and an alumina blend were investigated using a single-cylinder, four-stroke, air-cooled, spark-ignition engine operating under incremental load in this research. The engine that was used in the test was manufactured in accordance with the specifications listed in Table 2. To perform this investigation, it was chosen to use a single-cylinder, four-stroke, air-cooled spark-ignition engine with a compression ratio of 5:1 and a peak output of 3 kW at an engine speed of 3600 rpm, as well as a single-cylinder, four-stroke air-cooled engine. The incremental load was altered as a result of the mechanical loading. Figure 1 depicts a schematic illustration of the use of a light-duty gasoline engine for transportation. It was first necessary to start the engine with gasoline, after which it was subjected to a series of tests until steady-state working conditions were established. The brake thermal efficiency, specific fuel consumption, hydrocarbon, carbon monoxide, and oxygen emissions were all tested. All of the test runs

TABLE 2: Experimental engine specification.

| Parameter | Description |
|-------------------|------------------------------|
| Engine type | Four-stroke, single-cylinder |
| Rate power | 3.0 kW @ 3600 rpm |
| Displacement | 197 cc |
| Bore and stroke | 67 × 56 mm |
| Compression ratio | 5 : 1 |
| Cooling system | Air-cooled engine |

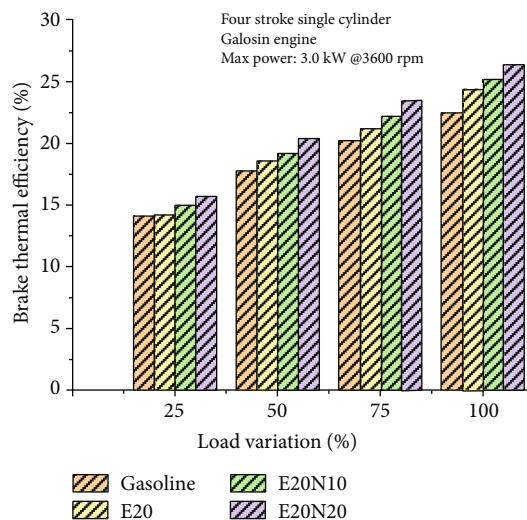


FIGURE 1: Impact of alumina on brake thermal efficiency on ethanol-gasoline engine.

were done using weights that were proportional to the weight of the load. When utilising ethanol-blended gasoline with alumina enrichment, the techniques are quite similar to those described above. The nanoparticles were examined for two distinct levels of contribution of 10 ppm and 20 ppm.

The Crypton CGP-700 Analyzer was utilised to conduct the analysis of the emission measurement for this investigation. NDIR (Nondispersive Infrared) techniques are used in this completely microprocessor-controlled exhaust gas analyzer. CO, CO₂, and hydrocarbons are all measured by this instrument. A second channel is supplied, which makes use of electrochemical oxygen measurement as well as a chemical sensor for nitrogen oxide detection. There is an

11-second reaction time to 95% of the final measurement while operating at operating pressures ranging from 750 to 1100 bar. It runs at a minimum flow rate of 5 litres/min. to ensure proper operation. During the experiments, the Crypton CGP-700 Analyzer was attached to the exhaust system, and the emission values were measured for a variety of fuel mixes under a variety of load circumstances [21–23]. The percentage of variance for each parameter may be calculated by comparing the results to those obtained from base fuel measurements.

The light-power gasoline engine was subjected to an experimental research with two concentration of alumina nanoadditives of 10 ppm and 20 ppm on a constant 20% ethanol-blended gasoline (E20) fuel. The fuel blend is prepared along with nanoadditives of alumina with 10 ppm and 20 ppm are represented at E20N10 and E20N20, respectively [24–26]. The essential test runs were carried out under a variety of load settings ranging from zero to full load in order to assure the best possible performance and the lowest possible harmful emissions.

3. Results and Discussion

3.1. Brake Thermal efficiency. Brake thermal efficiency (BTE) of E20N10 and E20N20 was found to be 12% and 17% higher than gasoline when tested under maximum load as shown in Figure 1. At maximum load, 25.2% and 26.4% efficiency recorded for above blends. With the addition of oxygen, one may improve thermal conductivity by increasing the alumina concentration. When compared to the single fuel, all of the samples had greater brake thermal efficiency. Ethanol and gasoline mixtures containing cerium oxide nanoparticle additions are responsible for this. The fuel contains nanoparticles, which extend the combustion process and provide a more thorough burn. An oxygen supply from the nanoparticles increases efficiency. In addition, it has been shown that the improvement in efficiency typically rises with the nanoparticle dose level [5].

E20N20 blend recorded 8.2% of BTE, which is greater than E20 because of the enhanced oxygen and improved combustion rate caused by the high alumina component. A more thorough combustion is enabled by the increased oxygen concentration in both methanol and ethanol. As a result, heat loss in the combustion chamber is minimised, resulting in an increase in thermal efficiency from the use of fuel mixes containing ethanol. These enhancements will eventually lead to an increase in the thermal efficiency of the engine's braking system. As a result, it ensures that the H/C ratio of ethanol is higher than that of gasoline fuel, which is excellent for enhancing engine thermal efficiency. When fuel consumption and air ratios are raised, this results in a higher rate of combustion, which increases engine performance [27].

3.2. Specific Fuel Consumption. When comparing all test settings, ethanol-gasoline showed the lowest specific fuel consumption (SFC). Blend ratios increase with engine load, and as seen in Figure 2, the SFC drops as a result. Compared to gasoline, E20N10 and E20N20 blends achieved 13.6% and

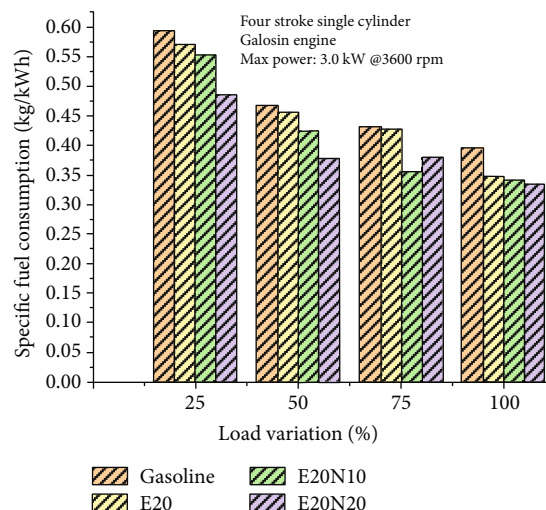


FIGURE 2: Impact of alumina on fuel consumption on ethanol-gasoline engine.

15.4% lower fuel consumption, respectively, and E20 blends achieved 12% lower fuel consumption, respectively, when compared with gasoline. Ethanol has a lower calorific value per mass and volume than pure gasoline, which accounts for the little rise. So, in order to get the same braking performance as gasoline, the engine needs more methanol fuel. Other than that, methanol-gasoline fuel has a greater BSFC because methanol has a higher density; hence, more mass is injected into the engine per volume at the same injection pressure [17].

The characteristics of fuel mixing must be considered in order to understand this behaviour. Compared to pure gasoline, mixing fuel raises the engine's operating temperature when utilised in a spark-ignition engine. The increased speed of the flame is a result of improved combustion owing to higher octane and the effects of a higher flame burning rate and a shorter combustion duration generated by blending fuels. As the amount of mixed fuel increases, less fuel is used during the combustion process, while heat transfer losses are decreasing at the same time.

3.3. Exhaust Gas Temperature. At the maximum load, blends of ethanol E20, E20N10, and E20N20 show 3%, 7.3%, and 11.6% increase of exhaust temperature as shown in Figure 3. As a result, EGT values have decreased as a result of increased combustion reaction and increased concentration of ethanol within the binary mix, which has led to a decrease in EGT values. Because of its higher LHV feature, ethanol had a substantial cooling effect on the combustion chamber temperature of the gasoline engine that was being evaluated, particularly near the end of the induction process. Accordingly, as a last point of reference, it is feasible that a significant decrease in the EGT may be attributable to the causes that were mentioned above. Because of its natural oxygen atoms in its molecular structure, ethanol exhibits more advanced physicochemical properties than typical gasoline fuel, even if it takes longer to ignite than other alcohol-based fuel options. Higher-order alcohol/gasoline mixes may

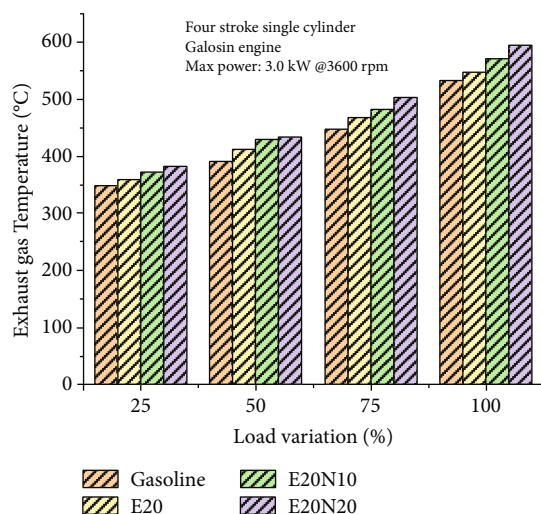


FIGURE 3: Impact of alumina on exhaust gas temperature on ethanol-gasoline engine.

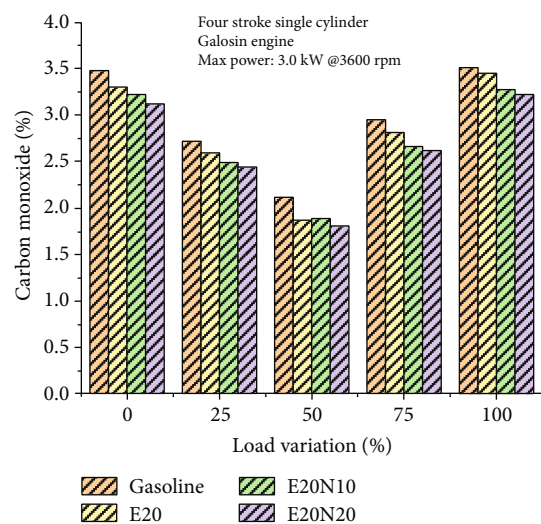


FIGURE 4: Impact of alumina on carbon monoxide emission in ethanol-gasoline engine.

thus reduce exhaust heat more effectively than straight gasoline in the SI engine being tested [28].

3.4. Emission Characteristics

3.4.1. Carbon Monoxide Emission. At the maximum load, blends of ethanol E20, E20N10, and E20N20 show 2%, 6.5%, and 8.2% reduction of carbon monoxide compared to gasoline as shown in Figure 4. Compared to gasoline, E20N10 and E20N20 blends achieved 10.8% and 14.5% lower CO, respectively, and E20 blends achieved 11.5% lower carbon emission when compared with gasoline. The usage of ethanol has resulted in a significant reduction in CO content, which is attributed to the presence of more oxygen molecules in the ethanol structure. The nanocomposite particles, on the other hand, may both boost the air-fuel homogeneity as a result of the lower viscosity of a mix and improve the burning rate and oxidation process. The effec-

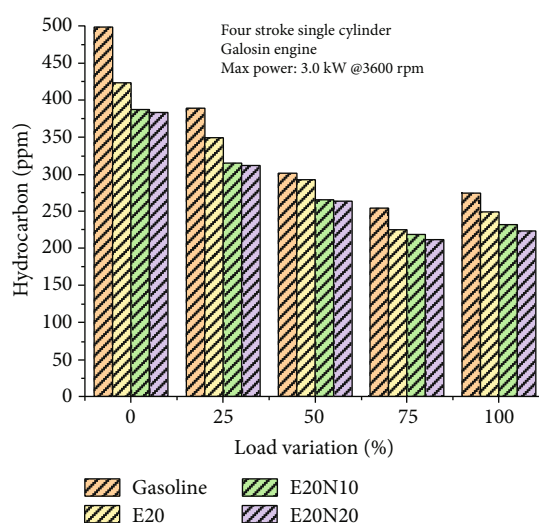


FIGURE 5: Impact of alumina on hydrocarbon emission on ethanol-gasoline engine.

tive combustion of the uniform charge of the nanoinvolved mix results in more and more oxidation of CO to CO₂, resulting in a decrease in the quantity of CO released into the atmosphere [6].

It is easier to ignite the stratified blending fuel ratio because it is closer to the cold cylinder wall and the sparking plug, which leads the flame propagation to quench closer to the plug and ignites the blend more quickly. On the other hand, having a wide lean burn limit both raises the temperature of the combustion process and accelerates the spread of the flame. This results in lower CO emissions due to the fact that the subsequent phase of the combustion process may release heat more quickly and for shorter amounts of time [14]. Using blended fuels, it may be seen that the concentration of carbon dioxide is decreased. As a result of having a low carbon to hydrogen ratio when mixing fuel, it also burns more effectively when the mixture is more homogeneous, resulting in a reduction in CO₂ emissions [27].

3.5. Hydrocarbon Emission. When loaded to their full capacity, ethanol blends E20, E20N10, and E20N20 exhibit reductions in hydrocarbon emissions of 9.1%, 15.6%, and 18.5% when compared to gasoline as shown in Figure 5. When compared to gasoline, E20N10 and E20N20 blends produced 19% and 20% fewer hydrocarbon emissions, respectively, while E20 blends produced 11.5% lower carbon emissions. The absence of oxygen, the low temperature, and the heterogeneity of the mixture are the primary reasons of full combustion failure and the creation of HC [12]. The quantity of hydrocarbons released is proportional to the amount of ethanol that is consumed. The higher the ethanol percentage, the more homogeneous the mixture becomes, which in turn leads to lower HC emissions and improved combustion. Combining various kinds of fuel not only enhances the effectiveness of the combustion process but also speeds up the process of wall quenching. As the speed of the engine increases, an enrichment of the mixture takes place, which results in increased HC emissions [15]. When

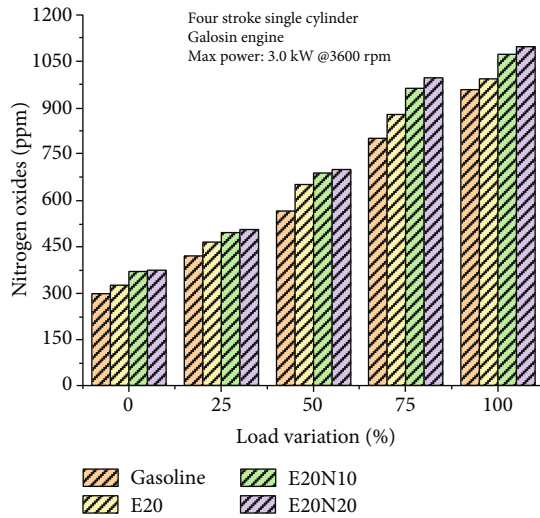


FIGURE 6: Impact of alumina on nitrogen oxide emission on ethanol-gasoline engine.

the engine speed increases, the HC concentration decreases because of the longer valve overlap duration at low speed and this drop becomes more pronounced at higher speeds. The difference in hydrocarbon emissions is related to the operation of the brake meaning effective pressure, which increases the cylinder temperature and hence improves combustion, resulting in a drop in hydrocarbon emissions [13].

3.5.1. Nitrogen Oxide Emission. Nanotechnology plays a key part in the release of oxygen from ethanol, which results in an increase in NO_x emissions in the exhaust. Reversing the equilibrium in favour of the retrograde reaction is achieved by the nanoparticle's gradual breakdown of the created NO_x bonds. It has been reported that the usage of metal additives, which are nanoparticles, may enhance combustion temperatures and, as a result, NO_x emissions [6]. Figure 6 indicates that when the maximum load is applied, the ethanol mixes E20, E20N10, and E20N20 result in a 3.5%, 11.9%, and 14.4% rise in nitrogen oxide, respectively. E20N20 mix has also been shown to have peak emissions of 24% at half load condition.

Additionally, when engine speed increases, so does the concentration of nitrogen oxides (NO_x). As opposed to blending fuel, NO_x emissions were found to be greater at all engine speeds when using gasoline fuel. As the load grows, there is a corresponding increase in the consumption of fuel, which causes the temperature of combustion to rise. As a result, there is an increase in the quantity of NO_x that is emitted into the atmosphere [13]. In addition, the increased cooling energy flow impact of mixed fuel, which slightly decreases cylinder gas pressure and the combustion time, is linked to this. In addition, delayed ignition timing may support lower NO_x emissions to a higher extent without reducing the increased thermal efficiency, since hydrogen flame propagation is fast and permits stable combustion to take place continuously [29].

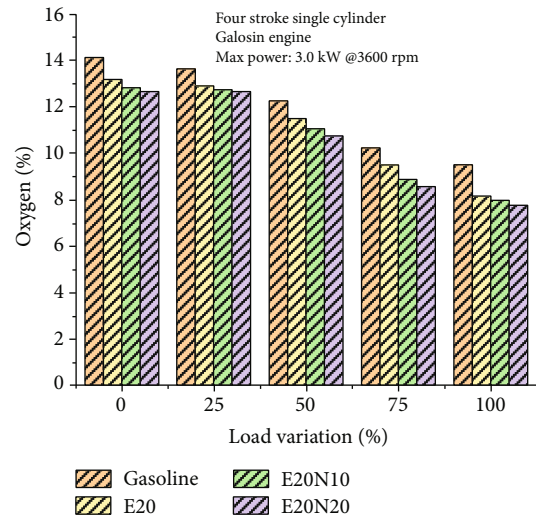


FIGURE 7: Impact of alumina on oxygen emission on ethanol-gasoline engine.

3.6. Oxygen Emission. The presence of oxygen is reduced by 14%, 16%, and 18.2% when the maximum load is applied to blends of ethanol E20, E20N10, and E20N20 compared to pure gasoline at the highest load as shown in Figure 7. E20N20 blends produced 9.5% fewer oxygen emissions as compared to E20 blends, owing to improved combustion characteristics. There is a possibility that enhanced oxygen emission was caused by the addition of alcohol to gasoline. This may be attributed, at least in part, to the naturally high oxygen concentration of the alcohol. As a consequence of this, a greater quantity of oxygen is discharged into the environment as a result of the higher alcohol blend ratio in the blend. This is due to the fact that the blend contains more alcohol [16]. Since oxygenated additives and ethanol accounted for a greater proportion in this mix than gasoline, O₂ emissions were noted to be higher than those of gasoline operation [28].

4. Conclusion

The negative impacts of conventional engine fuels on climate change and global warming have created a situation in which there is intense competition to develop an alternative fuel that is more environmentally friendly and non-harmful to the environment. It was discovered that mixing alcohol fuel with engine-designed gasoline was quite practical. The light-power gasoline engine was subjected to an experimental research. The concentration of alumina nanoadditives is controlled at two different flow rates of 10 ppm and 20 ppm on a constant 20% ethanol-blended gasoline (E20) fuel. Brake thermal efficiency of E20N10 and E20N20 was found to be 12% and 17% higher than gasoline when tested under maximum load. Compared to gasoline, E20N10 and E20N20 blends achieved 13.6% and 15.4% lower fuel consumption, respectively. On the emission, E20N10 and E20N20 blends achieved 10.8% and 14.5% lower CO, respectively, and 19% and 20% fewer hydrocarbon emissions, respectively, while E20 blends produced

11.5% lower carbon emissions when compared with pure gasoline. The presence of oxygen is reduced by 14%, 16%, and 18.2% when the maximum load is applied to blends of ethanol E20, E20N10, and E20N20 compared to pure gasoline at the highest load. As a result of this, researchers must find a way to lower the cost of producing ethanol from renewable feedstock's so that it may be used in IC engines at a lower cost than gasoline. Rather of relying on imported pure gasoline, nations will be able to produce an alternative fuel additive and reduce their need on it. Ethanol is a renewable, domestically produced fuel that can outperform gasoline due to its higher octane rating. The creation of ethanol in rural areas provides desperately needed jobs. In transportation, ethanol can be used instead of fossil fuels. It holds great promise for reducing carbon emissions from transportation and improving the environment.

Data Availability

The data used to support the findings of this study are included in the article. Should further data or information be required, these are available from the corresponding author upon request.

Disclosure

This study was performed as a part of the Employment Hawassa University, Ethiopia.

Conflicts of Interest

The authors declare that there are no conflicts of interest regarding the publication of this paper.

Acknowledgments

The authors would like to thank the Vel Tech Rangarajan Dr.Sagunthala R&D Institute of Science and Technology, Chennai, India, for their excellent support for the submission of their papers.

References

- [1] T. S. Kumar and B. Ashok, "Critical review on combustion phenomena of low carbon alcohols in SI engine with its challenges and future directions," *Renewable and Sustainable Energy Reviews*, vol. 152, article 111702, 2021.
- [2] M. B. Mobin Siddique, N. Khairuddin, N. A. Ali et al., "A comprehensive review on the application of bioethanol/biodiesel in direct injection engines and consequential environmental impact. Clean," *Engineering and Technology*, vol. 3, p. 100092, 2021.
- [3] M. Amine and Y. Barakat, "Properties of gasoline-ethanol-methanol ternary fuel blend compared with ethanol-gasoline and methanol-gasoline fuel blends," *Egyptian Journal of Petroleum*, vol. 28, no. 4, pp. 371–376, 2019.
- [4] M. Göktaş, M. Kemal Balki, C. Sayin, and M. Canakci, "An evaluation of the use of alcohol fuels in SI engines in terms of performance, emission and combustion characteristics: a review," *Fuel*, vol. 286, article 119425, 2021.
- [5] C. Ananda Srinivasan, C. G. Saravanan, and M. Gopalakrishnan, "Emission reduction on ethanol-gasoline blend using cerium oxide nanoparticles as fuel additive," *Particulate Science and Technology*, vol. 36, no. 5, pp. 628–635, 2018.
- [6] H. Taghavifar, B. K. Kaleji, and J. Kheyrollahi, "Application of composite TNA nanoparticle with bio-ethanol blend on gasoline fueled SI engine at different lambda ratios," *Fuel*, vol. 277, article 118218, 2020.
- [7] M. R. Saxena and R. K. Maurya, "Influence of fuel injection pressure and injection timing on nanoparticle emission in light-duty gasoline/diesel RCCI engine," *Particulate Science and Technology*, vol. 39, no. 5, pp. 641–650, 2021.
- [8] A. Yakın and R. Behçet, "Effect of different types of fuels tested in a gasoline engine on engine performance and emissions," *International Journal of Hydrogen Energy*, vol. 46, no. 66, pp. 33325–33338, 2021.
- [9] V. K. Kareddula and R. K. Puli, "Influence of plastic oil with ethanol gasoline blending on multi cylinder spark ignition engine," *Alexandria Engineering Journal*, vol. 57, no. 4, pp. 2585–2589, 2018.
- [10] T. L. Alleman, R. L. McCormick, and J. Yanowitz, "Properties of ethanol fuel blends made with natural gasoline," *Energy & Fuels*, vol. 29, no. 8, pp. 5095–5102, 2015.
- [11] M. Mourad and K. Mahmoud, "Investigation into SI engine performance characteristics and emissions fuelled with ethanol/butanol-gasoline blends," *Renewable Energy*, vol. 143, pp. 762–771, 2019.
- [12] M. I. Shajahan, S. Padmanabhan, J. J. Michael, and H. M. A. Hussein, "Environmental impact of oxyhydrogen addition on high-speed gasoline engine characteristics," *Energy Sources, Part A: Recovery, Utilization, and Environmental Effects*, pp. 1–14, 2020.
- [13] S. Padmanabhan, K. Giridharan, B. Stalin et al., "Sustainability and environmental impact of ethanol and oxyhydrogen addition on nanocoated gasoline engine," *Bioinorganic Chemistry and Applications*, vol. 2022, 1936412 pages, 2022.
- [14] W. Y. Lin, Y. Y. Chang, and Y. R. Hsieh, "Effect of ethanol-gasoline blends on small engine generator energy efficiency and exhaust emission," *Journal of the Air & Waste Management Association*, vol. 60, no. 2, pp. 142–148, 2010.
- [15] R. N. Rao, A. S. Silitonga, A. H. Shamsuddin et al., "Effect of ethanol and gasoline blending on the performance of a stationary small single cylinder engine," *Arabian Journal for Science and Engineering*, vol. 45, no. 7, pp. 5793–5802, 2020.
- [16] S. Uslu, H. Yaman, and M. K. Yesilyurt, "Optimization of parameters affecting the performance and emissions of a spark ignition engine fueled with n-pentanol/gasoline blends using taguchi method," *Arabian Journal for Science and Engineering*, vol. 46, no. 12, pp. 11711–11724, 2021.
- [17] M. Q. M. Tamam, N. R. Abdullah, W. J. Yahya, H. A. Kadir, Y. Putrasari, and M. A. Ahmad, "Effects of ethanol blending with methanol-gasoline fuel on spark ignition engine performance and emissions," *Journal of Advanced Research in Fluid Mechanics and Thermal Sciences*, vol. 83, no. 2, pp. 54–72, 2021.
- [18] M. Ghanbari, L. Mozafari-Vanani, M. Dehghani-Soufi, and A. Jahanbakhshi, "Effect of alumina nanoparticles as additive with diesel-biodiesel blends on performance and emission characteristic of a six-cylinder diesel engine using response surface methodology (RSM)," *Energy Conversion and Management: X*, vol. 11, article 100091, 2021.

- [19] M. S. Gad and S. Jayaraj, "A comparative study on the effect of nano-additives on the performance and emissions of a diesel engine run on Jatropha biodiesel," *Fuel*, vol. 267, article 117168, 2020.
- [20] M. S. Gad, S. M. Abdel Razek, P. V. Manu, and S. Jayaraj, "Experimental investigations on diesel engine using alumina nanoparticle fuel additive," *Advances in Mechanical Engineering*, vol. 13, no. 2, 2021.
- [21] S. Baskar, D. Sendil Kumar, R. Dhinakaran, A. Prabhakaran, B. Arun, and M. Shanmugam, "Experimental studies on mechanical and morphological properties of the natural and SBR/BR hybrid rubber," *Materials Today: Proceedings*, vol. 37, pp. 1503–1506, 2021.
- [22] K. Logesh, S. Baskar, B. Yuvan Siddarth, K. Arun Sherwin, and P. Naresh, "Multi-walled carbon nanotube mixed with isopropyl alcohol nanofluid for heat transfer applications," *Materials Today: Proceedings*, vol. 18, pp. 4690–4694, 2019.
- [23] J. Kumaraswamy, V. Kumar, and G. Purushotham, "A review on mechanical and wear properties of ASTM a 494 M grade nickel-based alloy metal matrix composites," *Materials Today: Proceedings*, vol. 37, pp. 2027–2032, 2021.
- [24] K. Jayappa, V. Kumar, and G. G. Purushotham, "Effect of reinforcements on mechanical properties of nickel alloy hybrid metal matrix composites processed by sand mold technique," *Applied Science and Engineering Progress*, vol. 14, no. 1, pp. 44–51, 2020.
- [25] V. K. Kumaraswamy and G. Purushotham, "Thermal analysis of nickel alloy/Al₂O₃/TiO₂ hybrid metal matrix composite in automotive engine exhaust valve using FEA method," *Journal of Thermal Engineering*, vol. 7, no. 3, pp. 415–428, 2021.
- [26] L. Karikalalan, M. Chandrasekaran, S. Venugopal, S. Jacob, and S. Baskar, "Investigations on diesel engine characteristics with Pongamia biodiesel at dissimilar compression ratios," *International Journal of Ambient Energy*, vol. 42, no. 9, pp. 1005–1008, 2021.
- [27] M. K. Mohammed, H. H. Balla, Z. M. H. Al-Dulaimi, Z. S. Kar-eem, and M. S. Al-Zuhairy, "Effect of ethanol-gasoline blends on SI engine performance and emissions," *Case Studies in Thermal Engineering*, vol. 25, article 100891, 2021.
- [28] H. Yaman and M. K. Yesilyurt, "The influence of n-pentanol blending with gasoline on performance, combustion, and emission behaviors of an SI engine," *Engineering Science and Technology, an International Journal*, vol. 24, no. 6, pp. 1329–1346, 2021.
- [29] D. Y. Dhande, N. Sinaga, and K. B. Dahe, "Study on combustion, performance and exhaust emissions of bioethanol-gasoline blended spark ignition engine," *Heliyon*, vol. 7, no. 3, article e06380, 2021.

Research Article

Hybrid Novel Additive Manufacturing for Sustainable Usage of Waste

Balaji Devarajan¹, **V. Bhuvanewari**¹, **B. Arulmurugan**¹, **A. V. N. S. L. Narayana**²,
A. K. Priya³, **V. D. N. Kumar Abbaraju**⁴, **K. S. Mukunthan**⁵, **Amit Kumar Sharma**⁶,
Sam Sung Ting⁷ and **Chandran Masi**⁸

¹Department of Mechanical Engineering, KPR Institute of Engineering and Technology, Tamilnadu, India

²Research Scholar, Ramachandra College of Engineering, India

³Department of Civil Engineering, KPR Institute of Engineering and Technology, Tamilnadu, India

⁴Department of Environmental Sciences, GITAM Institute of Science, Visakhapatnam, Andhra Pradesh 530045, India

⁵Department of Biotechnology, Manipal Institute of Technology, Manipal, Karnataka 576104, India

⁶Department of Physics, D.A.V. Post Graduate College, Dehradun, Uttarakhand 248001, India

⁷Faculty of Chemical Engineering Technology, Universiti Malaysia Perlis (UniMAP), Kompleks Pusat Pengajian Jejawi 3, 02600 Arau, Perlis, Malaysia

⁸Department of Biotechnology, College of Biological & Chemical Engineering, Addis Ababa Science & Technology University, Addis Ababa, Ethiopia

Correspondence should be addressed to Chandran Masi; chandran.chandran@aastu.edu.et

Received 8 March 2022; Accepted 11 April 2022; Published 31 May 2022

Academic Editor: N Senthilkumar

Copyright © 2022 Balaji Devarajan et al. This is an open access article distributed under the Creative Commons Attribution License, which permits unrestricted use, distribution, and reproduction in any medium, provided the original work is properly cited.

Additive manufacturing (AM) encompasses many forms of technologies and materials as 3D printing is being used in almost all industries. The variety of materials used includes but is not limited to plastics, ceramics, resins, metals, sand, textiles, biomaterials, glass, and food. Currently, in 3D printing technology, the printing mode of direct writing forming is widely applied. The raw material used is ceramic powder, and the direct writing forming of the ceramic could be applied to various fields of materials, chemistry, chemical engineering, and the like. This work is aimed at printing the nanopowder of nonsegregated waste into conventional components. The work is related to a system for converting nonsegregated waste material into the synthesized dough, comprising of a chamber, an ultraviolet (UV) disinfectant unit, a shedder, and a storage unit. The nonsegregated waste material is stored inside the chamber which dispenses the nonsegregated waste material into the UV disinfectant unit; said UV disinfectant unit removes the harmful germs and water content in the nonsegregated waste material to form solid waste. The disinfected solid waste enters the shedder which powders the solid waste. The powdered solid waste is stored in the storage unit. The powdered solid waste is mixed with components in a mixer to form a synthesized dough. The synthesized dough as the printable source is sent to a 3D printer which prints desired final component. The hardness value obtained for the printed component is 70 Brinell hardness units.

1. Introduction

The major problem faced by today's world is the reuse of waste material as such (without segregating it). So, this proposed work focuses on collecting and disinfecting the waste

material, making it a 3D printer's resource material without any waste material being left out (complete conversion—zero waste). The proposed work comprises of continuous conveyor system wherein it is the stage by stage processing of materials that leads to the complete conversion of waste into

useful products. The core objective is the complete conversion of waste into useful products without polluting the vicinity by any means.

Acrylonitrile butadiene styrene (ABS) is among the most common 3D printing filaments as well as another very common E-waste plastic. ABS is still not usually handled by governmental programs. Thereby, ABS might be a strong contender in the distributed recycling for AM (DRAM) approach, which could boost recyclability by giving clients a financial reason to recycle more frequently. In order to manufacture 3D printing filament as well as printed parts in both North America along with Australia using ABS E-waste, this research is aimed at investigating the importance of such ABS E-waste sources as well as methodologies. E-waste has been converted into 3D printer filament using two open-source extruder systems. The quality of this filament was evaluated using standard tensile as well as compression testing. Findings show the potential of E-waste ABS recycling for consumer and industrial applications, with a small reduction in mechanical properties. Researchers also showed that DRAM can considerably lower the price of 3D printer filament, but the carbon emissions from transformation highlighted the necessity of improving technological effectiveness in electricity generation between countries. As a result of the varying characteristics of ABS E-waste, appropriate labeling of materials is needed to advance recycling [1].

3D printing had already become increasingly popular in a variety of industrial sectors as the technology continues to advance. There are increasing amounts of consumables, waste as well as pollution being produced by 3D printing, which seems to have a negative impact on the environment. The fuzzy PID methodology is used to melt, shape, and wire different kinds of 3D printing essential items at various temperatures using this framework, which is premised on a monomicrocomputer. Waste from 3D printing can be recycled as well as print replacement parts effectively, reducing pollution as well as printing costs [2].

With the advancement of emerging technologies, 3-dimensional printers presently hold a significant position in a plethora of fields. The filament is one of the raw resources used by 3D printers which provide layered manufacturing. These printers have various raw material requisites. In comparison to other raw materials, filament is the favored raw material for a 3-dimensional printing machine. It is possible that the additive manufacturing process device will print incorrectly or will print something other than what was intended. It is critical that the printed materials can be recycled. Reusable filament for layered fabrication is at the heart of this project. Mechanical, electronic, and software methods have been used to establish a device that produced filaments with said appropriate size using a structure that included crushers, extrusion equipment, and water cooling units, as well as air cooling units [3]. Many university library maker areas are now offering 3D printing solutions. Waste can always be generated by both failed prints as well as the printing method itself. The viability of recycling and disposal 3D plastic as well as repurposing it as a new 3D printer filament has been investigated and eval-

uated thanks to a grant out of a regional academic library conglomerate. Others on campus have inquired about recycling or donating their 3D printers' waste filaments. In such an attempt to promote 3D printing as more environmentally friendly, we will examine the process, advantages, and drawbacks of reusing 3D printing filament [4].

For a broad spectrum of application domains, plastics' chemical and mechanical properties make them an excellent choice. Sadly, the nondegradability of plastic waste poses a major threat to the ecological environment [5–7]. On a global scale, recycling rates for plastic packaging are still low (around 14 percent) [8]. There is only a 32.5 wt percent recycling rate in Europe, where environmental stewardship is more prevalent. Although such figures are based on accumulated plastic waste, they do not represent the cumulative percentage of plastic garbage in circulation [9]. The European Plastics there in circular economy (CE) strategy is gaining traction in the policy as well as business discussions surrounding the viable progress of industrial manufacturing in order to combat this waste accumulation problem [10, 11]. The current concept of “take, make, dispose of” (linear economy) and its harmful impacts on depletion of natural resources, generation of waste, species extinction, contamination (soil, air, and water), and nonsustainable economic history seem to be the focus of CE [12]. CE is aimed at addressing this issue head-on. One of the most important aspects of incorporating CE into the plastics value chain is the verification of waste plastics as secondary raw materials (technical, economic, and legal) [13]. Open as well as closed recycling methodologies and also functional strategies to upcycling as well as downcycling can provide avenues for validating secondary raw materials [14].

Additive manufacturing (AM), as well known as 3D printing, has become increasingly important in the transformation from the sequential to the circular economy because of its direct production capacities. As a result of their capabilities to modify a mathematical method into points, lines, or areas of material to create a three-dimensional part, AM technologies are likely to revolutionize the manufacturing process [15–17]. Increased customer value, as well as the potential for disruption, has been generated by the expiration of its first patents [18, 19]. There will be a USD 23.33 billion global market for additive manufacturing in 2026 [20]. Traditional methods of production, on the other hand, have a hard time figuring out when as well as how to take benefit of the advantages. Product development could shift from conventional stage modeling techniques to iterative, agile methodologies by 2030, according to Jiang et al. [16].

AM can already be used to make a huge number of products, which has implications for global value chains in terms of geographic spread and density [21]. Since multimaterial and integrated functionality (e.g., electronics) can be produced to a large extent with AM printable products, it is anticipated that their reach would be somewhat significantly larger in the years ahead. Furthermore, on-site manufacturing of spare parts can change suppliers' roles in production lines [22]. Decentralized production types range from dispersed functionality to cloud manufacturing, according to Matt et al. Due to AM's ability to decentralize production

to locations near customers or, in the greatest extreme dispersed scenario, at the customer's premises [23–25], there is a need for transport that will be much more cautiously considered. AM technology also reduces market entry barriers, reduces capital requirements, and achieves an efficient minimal level production level to publicize dispersed, flexible production [26]; owing to this, the products can be tailored to meet the needs of specific niches or even individuals, rather than relying on economies of scale or scope [27, 28]. Because of these explanations, AM technique might lead to a transition in production from worldwide to local infrastructure. The industry and academia, as well as academic institutions, are working hard to move AM techniques away from rapid prototyping as well as tooling and toward direct digital manufacturing (DDM) [29, 30], which will have positive effects on the environment and society in general. It was found that the deployment of AM techniques in various industries was not primarily influenced by their environmental or social benefits, as demonstrated by Niaki et al. [31]. When it comes to AM implementation, only the financial aspect is relevant, with expense and time savings being the most important factors to keep in mind.

AM's potential on CE is still being explored. Understanding the contributions and obstacles to integrating AM progress with CE requirements is critical. For the purposes of this discussion, we will focus on the potential of AM for plastic garbage concerns [32]. The sustainable development of AM requires to be taken into consideration at an early stage, as the technology's spread is expected to continue there in years ahead. If AM can be used to promote in situ recycling in conjunction with widely dispersed consumer waste, it could reduce transport services [33] as well as the ecological consequences of strenuous resource exploitation while also making it possible for using regional raw material distribution networks [9]. AM can thus have been seen as a reuse method to recycle thermoplastic wastages as well as impact the framework of material delivery to optimize resource utilization efficiency. Although the open-source technique would be a crucial factor there in the regional recycling method [33, 34], it is not the only factor. However, for additive manufacturing to progress, a deeper knowledge of the reuse chain is required. When it comes to dispersed reprocessing or through DRAM, there are a number of questions to be answered. There are a number of steps that must be taken to turn plastic waste into supplementary raw substances for additive manufacturing (AM). As a result, the research presented here is a comprehensive review of the existing literature. Which additive production methods for thermoplastic recycling have made progress and which have been hindered? This paper's first contribution is a proposal for an AM-specific closed global recycling chain. Foremost, the published research maps out the progress made at every phase of the recycling sequence so that prospects, as well as obstacles, can be seen. CE's guiding fundamentals are often referred to as the "R framework procedures" [35–37]. Local specialties of such R framework might be implemented at the local level using AM as a driving advanced technology.

Numerous engineering implementations utilize carbon fiber-reinforced polymer (CFRP), which would be a slightly

elevated composite material made of carbon fiber and polymer [38]. Examples include wind turbine blades, airframes, and automotive components. However, the widespread use of one such substance has contributed to considerable energy as well as material usage during the manufacturing process, which also generates substantial waste. The worldwide annual demand for carbon fiber composites can be expected to approach 199 kilotons by 2022, up from the 2018 usage of 128 kilotons [39]. By 2030, Japan's CFRP recycling market is expected to be worth roughly 100 billion yen [40].

CFRP effluent is presently being discarded in landfills or burned. Carbon fibers are lost as well as carbon pollution is released as a result of their discretion, that is, environmental concerns. According to some countries, the quantities of garbage that is deposited in landfills are reduced by charging landfill taxes and encouraging material recycling, particularly for CFRP waste. In addition to reducing greenhouse gas emissions, recycling as well as reprocessing reclaimed carbon fibers (rCFs) provides a cost-effective and resource-efficient method for producing high-value carbon fibers. In most cases, the use of recycled carbon fiber (rCF) in the fabrication of new composite materials is not restricted to reclaiming carbon fiber. Both the recovery of carbon fibers from CFRP waste (i.e., the extraction of rCF from CFRP waste) as well as the manufacturing of rCF-reinforced polymer (rCFRP) (i.e., CFRP fabrication using rCF) are required to recycle CFRP [41, 42]. Carbon fiber extraction from CFRP is difficult because of the material's high corrosion resistance and inertness. Degradation of the resin and fiber extraction are just two of many methods used to recover and obtain high-performance carbon fibers from CFRP waste. It is possible to categorize these technologies into mechanical, thermolytic, and solvolytic methods. Carbon fibers have been successfully reclaimed from CFRP waste, proving the viability of many reclamation technologies [43]. In order to reuse CFRP waste, Palmer et al. used an 8 mm classification model screen as well as a movable hammer mill granulator [44].

The carbon fiber recyclization has been then divided into four grades. RCF was synthesized by heating carbon fiber-reinforced epoxy resin (CF/EP) to an elevated temperature of 800 degrees Celsius for 30 minutes, which left some left-over pyrolytic carbons upon that surface of the resin. The tensile strength deterioration of rCF was 18–36 percent [45] when Kim et al. used supercritical fluids at 405°C as well as 28 MPa to obtain rCF from CFRP. Carbon fiber has been derived from CFRP waste, but rCFs produced by such recycling techniques seem to be discontinuous, filamented, randomly and oriented and have low densities. This presents a new challenge for the industry. During CFRP production, continuous virgin carbon fibers (vCFs) are cut to the desired shape before they are recycled [46]. For continuous vCF fabrication, the current fabrication techniques are still not suitable [42]. With an efficient recycling method, carbon fibers can be restored with negligible mechanical characteristics as well as remanufactured into elevated engineering components. Wei et al. developed a method to incorporate nylon fibers into the amorphous rCF that also enhances its usefulness [47]. RCF was coated with polydopamine to improve its

dispersion in suspension, as well as a nonwoven mat has been created utilizing this technique [48]. In order to align discontinuous carbon fibers in a narrow gap between 2 parallel plates, the University of Bristol established the HiPerDiF (High-Performance Discontinuous Fiber) method. As nothing more than a result, 67% of short fibers were connected mechanical means in the dry preforms, with either a 3% range [49]. Remanufacturing mechanisms customized from conventional production mechanisms of fabric composite materials have been complicated as well as labor-intensive to manufacture rCFRP parts.

AM allows for fully automated significant forming of energy and material-efficient products and provides end-of-life remedies, as well as the selection of resource-efficient materials. Design liberty, digitization, production speed, and the reduction of waste are some of the reasons for the enhanced use of additive manufacturing [50, 51]. Although the 3D-printed thermoplastic components may possess complex geometries, their reduced mechanical properties, as well as the inability to function, are major concerns. As a result, the use of a carbon-fiber composite can help to resolve these issues [52]. To test the CFRP composite's flexural strength, modulus, and toughness, Ning et al. were using an FDM 3D printer to manufacture the component. The CFRP composite sample with 5 wt% carbon fiber content outperformed the genuine plastic sample by 11.82%, 16.82%, and 21.86%, respectively [53]. The printable composites had good electrical conductivity along with the oriented alignment of carbon fiber, as well as with volume internal resistance in the oriented alignment 6.8 times smaller than which in the direction perpendicular [54]. Huang et al. used an extrusion 3D printer to manufacture carbon fiber-filled resistive silicon rubbers. Carbon fiber has recently been shown to be an effective way to improve the effectiveness of 3D-printed components. As an outcome, the massive prices of 3D-printed elevated composite components seem to be large due to the use of carbon fiber in the AM process. The recent trend in the direct writing of the technique adapted in this work is printing of food stuffs like egg and meat, the printing of egg is successfully achieved [55], and similarly, more than 80% of conventional food is getting printed nowadays.

2. Comparison of Dough-Making Technique with Related Techniques

Table 1 shows the consolidation of existing work in dough-making process in AM which are collected from patents and other articles. From this, very few articles are selected and explained further to enable the novelty of the dough-making process. The 3D printing industry is experiencing rapid expansion. Many thermoplastic materials, which include recycled ones, can be used to make printable filaments. As a potential substitute to the current method of centrally collecting recyclable plastics, this article conducts a systematic review on the manufacturing of filaments for additive manufacturing processes using recycled polymers. The influence of processing mostly on physicochemical as well as mechanical characteristics of common thermoplastics was investigated. Widely viable filaments made from recycled

materials as well as devices that allow users to make their own filaments for 3D printing have been also examined in the study [56]. Table 2 lists and compares the existing dough-making techniques from waste plastic recycling.

Ramachandraiah reviewed and stated that in the article, they transform waste material into the dough as a printable source of 3D printing. In the extrusion process, fibrous meat food items have been deposited through a nozzle to create 3D structures of meat products. Extruders, which use a threaded conveyor or syringe structure and could still regulate temperature, hold an excellent guarantee for said 3D printing of meat food items also with required specification, despite the fact that other methodologies are still being developed. An extruder is used to create geometric 3D structures by extruding materials one layer at a time. The extrusion process, on the other hand, typically entails the utilization of semisolid mixtures, including such dough as well as chocolate. 3D-printed edibles such as dough, chocolate, and puree are now available for printing [57, 58]. Table 3 lists and compares the dough-making techniques from sustainable 3D-printed meat analogs.

In this article, they convert food waste into foodstuff. The food waste can be probably reduced in the case of 3D food printing technologies. It can be used in restaurants, buffets, hospitals, and even in houses. Where else, the instant work discloses about synthesized dough prepared from non-segregated waste material as source material for 3D printing. The nonsegregated waste material includes food, plastics, and E-waste. In D3, the food waste synthesis is preprocessed; where else in the instant work, the waste material synthesis is an in-built process and only on the specific blending improves the strength of the final product. More specifically, the system of the instant work converts entire waste material without leaving the toxic elements out [59, 60].

In this patent, they disclose an electronic waste-plastic waste recovery resource regeneration system and a method wherein electronic waste and plastic waste are alone segregated and converted into source material for 3D printers. It also discloses about recycling of plastic and E-waste using pulverizing and conveyor units, even though the 3D printing terminal of the material is not converted to source material for 3D printers. Recycling is a simple breaking down process, which is automated, but the instant work converts entire nonspecific waste material into the synthesized dough without toxicity leaving out and printing it into the final product. The system synthesizes the nonspecific waste material into useful products without any human intervention and without polluting the atmosphere [61].

This patent article discloses a paste metallic composite material for 3D printing, wherein metal paste and silicone are made into paste form and have the binding ability. It relates to paste metallic composite for 3D printing comprising of metal dust 80-90 part, silicone 5-10 part, tackifier 1-3 part, dispersant 1-2 part, and curing catalysts 0.1-0.5 part, wherein described metal dust is metallic tin powder and copper powder, at least one in metallic aluminum powder, metal iron powder, stainless steel powder, metal nickel powder, metallic titanium powder, and metal zinc forms so that weight ratio 1-3:10 is composite. Where else, the instant

TABLE 1: Consolidation of related works from patents and other articles.

| S. No. | Date of filing or publishing | Title | Article/patent application number |
|--------|------------------------------|---|-----------------------------------|
| 1 | 2020-08-26 | 3d printing filament as a second life of waste plastics—a review | Journal |
| 2 | 2020-06-30 | Preparation method and application of slurry for ceramic 3d printing | CN111777405A |
| 3 | 2019-18-12 | A juice bar transforms orange peels into 3D Printed cups – Source - https://www.3dnatives.com/en/orange-peels-3d-printed-cups | Web article |
| 4 | 2018-01-07 | Wood paste and objects made therefrom | WO2019135245 |
| 5 | 2017-09-05 | A kind of 3d printing environmental protection consumptive material | CN107556769A |
| 6 | 2016-11-16 | 3d printing process with increased strength of the manufactured object | DE102016222558A1 |
| 7 | 2016-08-29 | A kind of 3D printing discarded object cam-type processing equipment for pulverizing | CN106111243B |
| 8 | 2016-07-11 | A kind of green construction material printed for 3d and method of printing thereof | CN106186974A |
| 9 | 2016-05-29 | Additive manufacturing of rubber-like materials | US20190224914 |
| 10 | 2016-02-05 | 3d prints high-definition ecological plate | CN205395331U |
| 11 | 2015-08-04 | Paste metallic composite material for 3d printing and manufacturing method of paste metallic composite material for 3d printing | CN105108134A |
| 12 | 2015-02-16 | Method for preparing 3d printing material by use of recycled waste high-density polyethylene plastics | CN104629152A |
| 13 | 2015-02-16 | With reclaiming the method that 3d printed material prepared by the discarded raw material containing plant fiber | CN104711887B |
| 14 | 2015 | 3d printing with biomaterials towards a sustainable and circular economy – doi:10.3233/978-1-61499-486-2-i | Book |
| 15 | 2014-10-29 | A kind of biomass wood plastic composite for 3d printing and preparation method thereof | CN104356618B |
| 16 | 2014-09-02 | A kind of 3d prints compositions and its production and use | CN104230289B |
| 17 | 2014-08-10 | Methods and devices for three-dimensional printing or additive manufacturing of bioactive medical devices | WO2016025388 |
| 18 | 2014-07-07 | Sewage treatment device based on 3d printing biological stuffing | CN104045170A |
| 19 | 2014-04-03 | Electronic waste-plastic waste recovery resource-regeneration system and method | CN104191541A |

work discloses synthesized dough prepared from nonsegregated waste material as source material for 3D printing. The nonsegregated waste material includes food, plastics, and E-waste [62]. Table 4 lists and compares the dough making with a metallic paste composite manufacturing using 3D printing.

3. Printer Modification

The aim is to convert the waste into useful products is being proposed which includes the 3D printer being a part of it. The methodology adapted in the proposed work is shown in Figure 1 as process flowchart.

All the existing prior art explains specifically recycling the same kind of waste (for example, porcelain and orange peel) into useful products. In the proposed work, the system is developed for the nonsegregated waste comprised of food waste, plastic bags, E-waste, metal, and other materials, which is the value-added over the existing prior arts. This process started in the year 2017, initially planned to develop the 3D printer to print the light denser material as waste leaves as in par with light denser applications, for which patent filed in the year 2017, but the methodology adopted was different in our patent and then the material synthesized as per the printer modified by us. Therein, our product gives

similar strength. The core hurdle faced in this work is converting the waste leaf into machine printable form. The next phase started in the year 2018, wherein the material chosen was with higher density, that is, waste foundry sand. Processing of sand gave challenges like identifying the nontoxic binder and synthesizing it. Finally, after trying out several binders, we chose an organic and an inorganic binder which provided the better binding ability. Therein, the print is made and tested it is on par with the existing paste metallic composite printer as well as the ceramic slurry or paste printers, which are filed for a patent since 2015; this work uses waste foundry sand which also gave better strength. The proof of concept developed over 3 years, 2018, 2019, and 2020, is highlighted below.

4. Novel AM Method

Referring to Figure 2, the system comprises a chamber, an ultraviolet (UV) disinfectant unit, a shedder, a storage unit, a mixer, and a 3D printer. The nonsegregated waste material is collected and stored inside the chamber. It is Said nonsegregated waste material includes but is not limited to food, plastics, and E-waste. The chamber dispenses the nonsegregated waste material as per requirement into the UV disinfectant unit via a conveyor; said UV disinfectant

TABLE 2: Comparison of dough making with a review article on waste plastic recycling [59].

| S. No. | Reference document | Dough-making technique |
|--------|--|--|
| 1. | As an alternative to the current method of plastic recycling, filaments for 3D printers can be made from recycled polymers. Only plastic-based recycling is disclosed. | The instant work deals with nonsegregated waste recycling. |
| 2. | One specific waste recycling. | <p>The instant work discloses synthesized dough prepared from nonsegregated waste material as source material for 3D printing. The nonsegregated waste material includes food, plastics, and E-waste.</p> <p>The technical advancement lies in the making of synthesized dough from nonsegregated waste material, wherein versatile materials are collected and processed mixed with components in the right quantity at the right stage to form the dough state to achieve 3D printing.</p> <p>The system converts the nonsegregated waste material into the synthesized dough without human intervention.</p> |
| 3. | <p>Firstly, the material is separated as well as washed, and then, ground plastic is extracted.</p> <p>Extrusion at high temperatures is the next step in the process of preparing the ground material for use (the temperature should be set based on type of the polymer).</p> <p>With the extrusion method, granulated or polymer powder is fed into an extruder where it is heated and transformed into a homogeneous filament with precisely defined parameters for use in 3D printing (adapted to the size of the printer element and standardized diameter).</p> <p>The 3D printer accepts the freshly prepared filament.</p> <p>Analyses are conducted on the printed material (mechanical, structural, and rheological characteristics).</p> <p>Milling of the tested specimen is carried out for the second time.</p> <p>When it comes to modifying a material, an additional step is required: First, the mixture is mixed with an additional component as well as a binder (such as silicone oil), and then, it is extruded.</p> <p>By contrast, the second method calls for dissolving the ground element in an organic solvent along with a reinforcing component and then evaporating the solvent to obtain the ground material itself.</p> | <p>Nonsegregated waste material that includes food, plastics, and E-waste was collected and stored inside the chamber.</p> <p>The chamber dispenses nonsegregated waste material into the UV disinfectant unit via a conveyor; said UV disinfectant unit removes the harmful germs and water content in the nonsegregated waste material to form solid waste.</p> <p>The disinfected solid waste then enters the shedder which powders the solid waste.</p> <p>The powdered solid waste is then stored in the storage unit.</p> <p>The powdered solid waste is mixed with components one by one in the mixer to form the dough. Said components include waste foundry sand 5%, waste stone powder 5%, and binder 30%. The powdered solid waste is mixed with waste foundry sand and mixed well in the mixer to form a first mixture. The waste stone powder is then added to the first mixture and mixed well in the mixer to form a second mixture. Araldite is then added to the second mixture and mixed well in the mixer to form the synthesized dough.</p> <p>The synthesized dough which is used as a printable source is then sent to the 3D printer which prints the final component as per the requirement.</p> <p>The 3D printer includes UV lamp units fixed to the printing head on either side which disinfects the dough and as well as dries the dough. Drying the dough leads to the achievement of good binding of materials.</p> <p>The dough hardness is around 70 Brinell hardness units.</p> |

unit removes the harmful germs and water content in the nonsegregated waste material to form solid waste. The disinfected solid waste then enters the shedder which powders the solid waste. The powdered solid waste is then stored in the storage unit. The powdered solid waste is mixed with components in a mixer to form the synthesized dough. Said components consist of waste foundry sand, waste stone powder, and binder. The synthesized dough is then sent to the 3D printer which prints the final component as per the requirement. The synthesized dough is used as a printable source for 3D printing. The 3D printer includes UV lamp units fixed to the printing head on either side which disinfects the dough and as well as dries the dough. Drying the dough leads to the achievement of good binding of materials. In an aspect, the binder is Araldite.

5. Testing

Figure 3 shows the proof of concept developed for the novel additive manufacturing. Testing phase is initiated with varying by the proportionate of the materials selected. The materials are nonsegregated waste material, waste foundry sand, waste stone powder, and Araldite binder. It is to iterate and figured the best possible combination for higher strength of the composite material. Specifically, the hardness test is only performed.

5.1. Processing Method 1. About 55% of collected nonsegregated waste material is stored inside the chamber. The chamber dispenses nonsegregated waste material into the UV disinfectant unit via a conveyor; said UV disinfectant

TABLE 3: Comparison of dough making with a review article on sustainable 3D-printed meat analogs [59].

| S. No. | Referenced document | Dough-making technique |
|--------|--|--|
| 1 | <p>They transformed waste material into the dough as a printable source of 3D printing. Materials obtained from somewhere in vitro cell culture, insects, and meat byproducts/waste, as well as plants, have been proposed as potential sources for long-term 3DP meat alternatives.</p> <p>In the extrusion process, fibrous meat materials have been deposited via a nozzle to create 3D structures in meat food items.</p> | <p>The instant work deals with nonsegregated waste recycling.</p> |
| 2 | Only meat analogs recycling. | <p>The instant work discloses synthesized dough prepared from nonsegregated waste material as source material for 3D printing. The nonsegregated waste material includes food, plastics, and E-waste.</p> <p>The system converts the nonsegregated waste material into synthesized dough, wherein versatile materials are collected, assessed, and processed to form the dough state to achieve 3D printing.</p> |
| 3 | Waste recycling using meat material into scaffold | <p>Making synthesized dough with nonsegregated waste material into 3D printable form with better strength requires appropriate input at various stages.</p> <p>Complete blending and combining can be accomplished only therein, proper specific proportionate.</p> <p>Nonsegregated waste material that includes food, plastics, and E-waste was collected and stored inside the chamber.</p> <p>The chamber dispenses nonsegregated waste material into the UV disinfectant unit via a conveyor; said UV disinfectant unit removes the harmful germs and water content in the nonsegregated waste material to form solid waste.</p> <p>The disinfected solid waste then enters the shedder which powders the solid waste.</p> |
| 4 | <p>By straightforwardly exploiting freeze-dried cells because of both active biocatalysts and fillers, Qian and his colleagues developed a high-performance bioink with significantly increased cell loading density while also supplying favorable rheological properties for AM. Baker's yeast (<i>Saccharomyces cerevisiae</i>) loading density had been enhanced to 750 g/l cell dry weight as the first bioink prototype (orders of magnitudes higher than that in liquid culture). In the ink, the cells were crammed so closely together that they were almost touching. This study also found that by adding nanocellulose as just a selectable secondary filler, the researchers were able to control ink rheology (such as a critical parameter characterizing the elasticity of polymeric liquids and plateau modulus) as well as cell density (0–8.6109 cells/ml) over a diverse variety for tailored implementations.</p> | <p>The powdered solid waste is then stored in the storage unit.</p> <p>The powdered solid waste is mixed with components one by one in the mixer to form the dough. Said components include waste foundry sand 5%, waste stone powder 5%, and binder 30%. The powdered solid waste is mixed with waste foundry sand and mixed well in the mixer to form a first mixture. The waste stone powder is then added to the first mixture and mixed well in the mixer to form a second mixture. Araldite is then added to the second mixture and mixed well in the mixer to form the synthesized dough.</p> <p>The synthesized dough which is used as a printable source is then sent to the 3D printer which prints the final component as per the requirement.</p> <p>The 3D printer includes UV lamp units fixed to the printing head on either side which disinfects the dough and as well as dries the dough. Drying the dough leads to the achievement of good binding of materials.</p> <p>The dough hardness is around 70 Brinell hardness units.</p> |
| 5 | <p>Extruders, which use a threaded conveyor or syringe structure and can also regulate temperature, represent a promising for the 3D printing of meat food items with the desired design, despite the fact that other methods have been still being developed. A nozzle is used to extrude materials in a layer-over-layer fashion to create geometric 3D structures. In addition, semisolid pastes like dough, chocolate, and meat purees are commonly used in extrusion. Dough, chocolate, and puree are among the 3D-printed edibles.</p> | <p>This work discussed not simply printing it, synthesizing dough is novel, and thereby it is getting the print to provide better hardness. It cannot print dough of any nature to gain the required strength.</p> |

TABLE 4: Comparison of dough making with a metallic paste composite manufacturing using 3D printing [63].

| Referenced document | Dough-making technique |
|---|--|
| <p>The method for the paste metallic composite comprising of</p> <ol style="list-style-type: none"> 1) Dispersant of the metal dust of 80-90 weight portion and 1-2 weight portion is uniformly dispersed in high-speed disperser, for subsequent use 2) Metal dust of step1 dispersion treatment, the silicone of 5-10 weight portion, and the tackifier of 1-3 weight portion are added airtight stirred tank, setting stirred tank temperature is 60-65 DEG C; by the rotating speed mixing 20-30 min of 200-400 rpm, obtain metal powder and silicone is the body of paste of key component 3) Curing catalyts of 0.1-0.5 weight portion being added step-2 metal powder that obtains and silicone be the body of paste of key component, open the vacuum of the airtight stirred tank, vacuum pressure 0.1-0.3 MPa, and mix with the rotating speed of 50-100 rpm; curing catalyts are dispersed in metal powder completely, and silicone is in the body of paste of key component 4) By the material discharge that airtight for step-3 stirred tank obtains and seal and preservation, be a kind of paste metallic composite printed for 3D. | <p>Nonsegregated waste material that includes food, plastics, and E-waste was collected and stored inside the chamber. The chamber dispenses nonsegregated waste material into the UV disinfectant unit via a conveyor; said UV disinfectant unit removes the harmful germs and water content in the nonsegregated waste material to form solid waste.</p> <p>The disinfected solid waste then enters the shedder which powders the solid waste.</p> <p>The powdered solid waste is then stored in the storage unit.</p> <p>The powdered solid waste is mixed with components one by one in the mixer to form a dough. Said components include waste foundry sand 5%, waste stone powder 5%, and binder 30%. The powdered solid waste is mixed with waste foundry sand and mixed well in the mixer to form a first mixture. The waste stone powder is then added to the first mixture and mixed well in the mixer to form a second mixture. Araldite is then added to the second mixture and mixed well in the mixer to form the synthesized dough.</p> <p>The synthesized dough which is used as a printable source is then sent to the 3D printer which prints the final component as per the requirement.</p> <p>The 3D printer includes UV lamp units fixed to the printing head on either side which disinfects the dough and as well as dries the dough.</p> <p>Drying the dough leads to the achievement of good binding of materials.</p> <p>The dough hardness is around 70 Brinell hardness units.</p> |

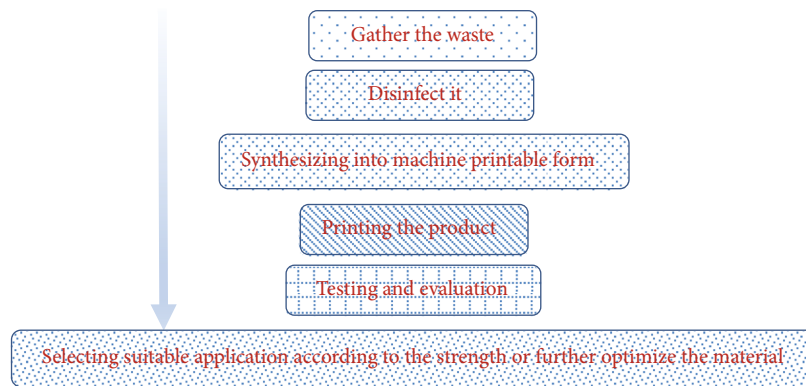


FIGURE 1: Process flowchart for the proposed work.

unit removes the harmful germs and water content in the nonsegregated waste material to form solid waste. The disinfected solid waste then enters the shedder which powders the solid waste. The shedder includes two stages of metal blades, first stage of metal blades sheds the solid waste into bigger granules, and the next stage of metal blades sheds the bigger granules into fine powder. The powdered solid waste is then stored in the storage unit. The powdered solid waste is mixed with components one by one in the mixer to form a dough. Said components consist of waste foundry sand 5%, waste stone powder 5%, and binder 30%. The powdered solid waste is mixed with about 5% of waste foundry sand and mixed well in the mixer to form a first mixture. About 5% of waste stone powder is then added to the first mixture

and mixed well in the mixer to form a second mixture. About 30% of Araldite is then added to the second mixture and mixed well in the mixer to form the synthesized dough. The synthesized dough is then sent to the 3D printer which prints the final component as per the requirement. The dough is used as the printable source for 3D printing. The 3D printer includes UV lamp units fixed to printing head on either side which disinfects the dough and as well as dries the dough. Drying the dough leads to the achievement of good binding of materials. The dough hardness is around 59 Brinell hardness units.

5.2. *Processing Method 2.* About 60% of collected nonsegregated waste material is stored inside the chamber. The

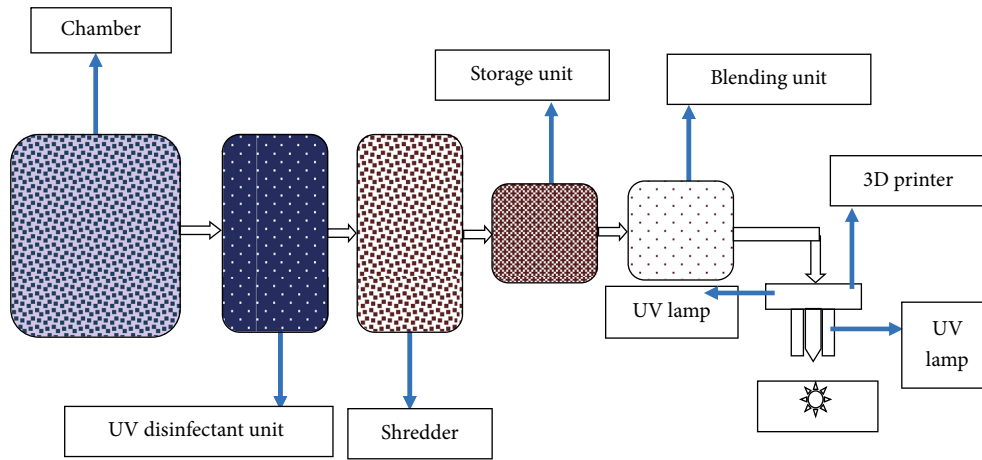


FIGURE 2: Novel AM system [64].

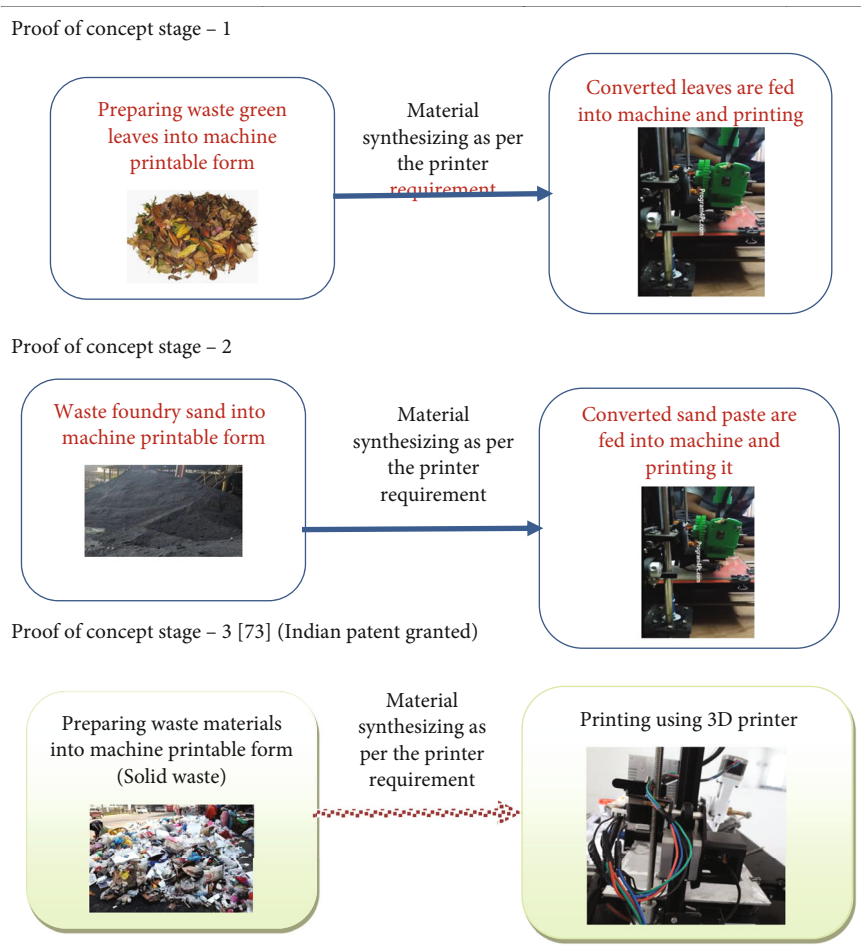


FIGURE 3: Proof of concept developed for the novel AM.

chamber dispenses nonsegregated waste material into the UV disinfectant unit via a conveyor; said UV disinfectant unit removes the harmful germs and water content in the nonsegregated waste material to form solid waste. The disinfected solid waste then enters the shredder which powders the solid waste. The powdered solid waste is then stored in the

storage unit. The powdered solid waste is mixed with components one by one in the mixer to form a dough. Said components include waste foundry sand 5%, waste stone powder 5%, and binder 30%. The powdered solid waste is mixed with about 5% of waste foundry sand and mixed well in the mixer to form a first mixture. About 5% of waste stone

powder is then added to the first mixture and mixed well in the mixer to form a second mixture. About 30% of Araldite is then added to the second mixture and mixed well in the mixer to form the synthesized dough. The synthesized dough is then sent to the 3D printer which prints the final component as per the requirement. The dough is used as the printable source for 3D printing. The 3D printer includes UV lamp units fixed to the printing head on either side which disinfects the dough and as well as dries the dough. Drying the dough leads to the achievement of good binding of materials. The dough hardness is around 70 Brinell hardness units.

5.3. Processing Method 3. About 65% of collected nonsegregated waste material is stored inside the chamber. The chamber dispenses nonsegregated waste material into the UV disinfectant unit via a conveyor; said UV disinfectant unit removes the harmful germs and water content in the nonsegregated waste material to form solid waste. The disinfected solid waste then enters the shredder which powders the solid waste. The powdered solid waste is then stored in the storage unit. The powdered solid waste is mixed with components one by one in the mixer to form the dough. Said components include waste foundry sand 5%, waste stone powder 5%, and binder 30%. The powdered solid waste is mixed with about 5% of waste foundry sand and mixed well in the mixer to form a first mixture. About 5% of waste stone powder is then added to the first mixture and mixed well in the mixer to form a second mixture. About 30% of Araldite is then added to the second mixture and mixed well in the mixer to form the synthesized dough. The synthesized dough is then sent to the 3D printer which prints the final component as per the requirement. The dough is used as the printable source for 3D printing. The 3D printer includes UV lamp units fixed to the printing head on either side which disinfects the dough and as well as dries the dough. Drying the dough leads to the achievement of good binding of materials. The dough hardness is around 54 Brinell hardness units.

From the above synthesis, it is clear that dough composition with waste material: 60%, waste foundry sand: 5%, waste stone powder: 5%, and binder: 30% achieves hardness around 70 Brinell hardness units.

The nonsegregated waste material is stored inside the chamber, said chamber dispenses the nonsegregated waste material into the UV disinfectant unit via a conveyor, and said UV disinfectant unit removes the harmful germs and water content in the nonsegregated waste material to form solid waste. The disinfected solid waste enters the shredder which powders the solid waste. The powdered solid waste is stored in the storage unit, the powdered solid waste is mixed with components in a mixer to form synthesized dough, and the synthesized dough as the printable source is sent to the 3D printer which prints desired final component. The shredder includes two stages of metal blades, the first stage of metal blades sheds the solid waste into bigger granules, and the next stage of metal blades sheds the bigger granules into fine powder. The UV lamp units are fixed to the printing head of the 3D printer on either side, and said

UV lamp units disinfect the dough and dry the dough. The components consist of waste foundry sand and waste stone powder, and binder is Araldite. The synthesized dough composition consists of the following components in weight percent, waste material: 60%, waste foundry sand: 5% waste stone powder: 5%, and binder: 30%.

6. Conclusion

Process of making dough and 3D print of it is explained in detail in this article. Initially, we gathered the related works, narrowed down it to most related articles, and then compared with this process. Thereby it shows the novelty of this process. Next, this process is explained in detail along with the various stages of developing proof of concept for this process. It provides path and tests the material printed for strength wherein the highest strength achieved is 70 Brinell hardness units. It is proposed as the best strength can be obtained in this technique.

Data Availability

The data used to support the findings of this study are included in the article. Should further data or information be required, these are available from the corresponding author upon request.

Conflicts of Interest

The authors declare that they have no conflicts of interest.

References

- [1] M. Mohammed, D. Wilson, E. Gomez-Kervin, A. Petsiuk, R. Dick, and J. M. Pearce, "Sustainability and feasibility assessment of distributed E-waste recycling using additive manufacturing in a bi-continental context," *Additive Manufacturing*, vol. 50, article 102548, 2022.
- [2] R. Huang, Q. Yao, and Y. Liu, "Waste recycling 3D printing and silk-making system," *Journal of Physics: Conference Series*, vol. 1550, no. 3, p. 032153, 2020.
- [3] E. Cirik, D. Açikgöz, C. Yalçinkaya, U. C. Topçu, I. Ertuna, and G. O. D. E. Ceren, "Design and manufacturing of the prototype system for recycling waste generated in 3 dimensional production to filaments by fused deposition modeling method," *Celal Bayar University Journal of Science*, vol. 17, no. 3, pp. 261–266, 2021.
- [4] J. L. Bossart, S. R. Gonzalez, and Z. Greenberg, "3D printing filament recycling for a more sustainable library makerspace," *College & Undergraduate Libraries*, vol. 27, pp. 1–16, 2020.
- [5] J. Hopewell, R. Dvorak, and E. Kosior, "Plastics recycling: challenges and opportunities," *Philosophical Transactions of the Royal Society B: Biological Sciences*, vol. 364, no. 1526, pp. 2115–2126, 2009.
- [6] M. W. Ryberg, M. Z. Hauschild, F. Wang, S. Averous-Monnery, and A. Laurent, "Global environmental losses of plastics across their value chains," *Resources, Conservation and Recycling*, vol. 151, article 104459, 2019.
- [7] R. C. Thompson, C. J. Moore, F. S. Vom Saal, and S. H. Swan, "Plastics, the environment and human health: current consensus and future trends," *Philosophical transactions of the royal*

- society B: biological sciences*, vol. 364, no. 1526, pp. 2153–2166, 2009.
- [8] J. N. Hahladakis and E. Iacovidou, “Closing the loop on plastic packaging materials: what is quality and how does it affect their circularity?,” *Science of the Total Environment*, vol. 630, pp. 1394–1400, 2018.
- [9] L. Kranzinger, R. Pomberger, D. Schwabl et al., “Output-oriented analysis of the wet mechanical processing of polyolefin-rich waste for feedstock recycling,” *Waste Management & Research*, vol. 36, no. 5, pp. 445–453, 2018.
- [10] European Commission, “A European strategy for plastics in a circular economy,” vol. 28, pp. 1–18, 2018.
- [11] M. Geissdoerfer, P. Savaget, N. M. Bocken, and E. J. Hultink, “The circular economy—a new sustainability paradigm?,” *Journal of Cleaner Production*, vol. 143, pp. 757–768, 2017.
- [12] N. Van Buren, M. Demmers, R. Van der Heijden, and F. Witlox, “Towards a circular economy: the role of Dutch logistics industries and governments,” *Sustainability*, vol. 8, no. 7, p. 647, 2016.
- [13] B. Simon, “What are the most significant aspects of supporting the circular economy in the plastic industry?,” *Resources, Conservation and Recycling*, vol. 141, pp. 299–300, 2019.
- [14] C. Zhuo and Y. A. Levendis, “Upcycling waste plastics into carbon nanomaterials: a review,” *Journal of Applied Polymer Science*, vol. 131, no. 4, 2014.
- [15] L. Chen, Y. He, Y. Yang, S. Niu, and H. Ren, “The research status and development trend of additive manufacturing technology,” *The International Journal of Advanced Manufacturing Technology*, vol. 89, no. 9–12, pp. 3651–3660, 2017.
- [16] R. Jiang, R. Kleer, and F. T. Piller, “Predicting the future of additive manufacturing: a Delphi study on economic and societal implications of 3D printing for 2030,” *Technological Forecasting and Social Change*, vol. 117, pp. 84–97, 2017.
- [17] Z. Rahman, S. F. B. Ali, T. Ozkan, N. A. Charoo, I. K. Reddy, and M. A. Khan, “Additive manufacturing with 3D printing: progress from bench to bedside,” *The AAPS Journal*, vol. 20, no. 6, pp. 1–14, 2018.
- [18] A. Beltagui, A. Rosli, and M. Candi, “Exaptation in a digital innovation ecosystem: the disruptive impacts of 3D printing,” *Research Policy*, vol. 49, no. 1, article 103833, 2020.
- [19] J. West and G. Kuk, “The complementarity of openness: how MakerBot leveraged Thingiverse in 3D printing,” *Technological Forecasting and Social Change*, vol. 102, pp. 169–181, 2016.
- [20] Augut 2019 <http://www.globenewswire.com/news-release/2019/03/18/1756526/0/en/Additive-Manufacturing-Market-To-Reach-USD-23-33-Billion-By-2026.html>.
- [21] A. O. Laplume, B. Petersen, and J. M. Pearce, “Global value chains from a 3D printing perspective,” *Journal of International Business Studies*, vol. 47, no. 5, pp. 595–609, 2016.
- [22] S. Zaroni, M. Ashourpour, A. Bacchetti, M. Zanardini, and M. Perona, “Supply chain implications of additive manufacturing: a holistic synopsis through a collection of case studies,” *The International Journal of Advanced Manufacturing Technology*, vol. 102, no. 9–12, pp. 3325–3340, 2019.
- [23] J. B. Roca, P. Vaishnav, R. E. Laureijs, J. Mendonça, and E. R. Fuchs, “Technology cost drivers for a potential transition to decentralized manufacturing,” *Additive Manufacturing*, vol. 28, pp. 136–151, 2019.
- [24] E. E. Petersen and J. Pearce, “Emergence of home manufacturing in the developed world: return on investment for open-source 3-D printers,” *Technologies*, vol. 5, no. 1, p. 7, 2017.
- [25] B. T. Wittbrodt, A. G. Glover, J. Laureto et al., “Life-cycle economic analysis of distributed manufacturing with open-source 3-D printers,” *Mechatronics*, vol. 23, no. 6, pp. 713–726, 2013.
- [26] M. Despeisse, M. Baumers, P. Brown et al., “Unlocking value for a circular economy through 3D printing: a research agenda,” *Technological Forecasting and Social Change*, vol. 115, pp. 75–84, 2017.
- [27] C. Hienerth, E. Von Hippel, and M. B. Jensen, “User community vs. producer innovation development efficiency: a first empirical study,” *Research Policy*, vol. 43, no. 1, pp. 190–201, 2014.
- [28] I. J. Petrick and T. W. Simpson, “3D printing disrupts manufacturing: how economies of one create new rules of competition,” *Research-Technology Management*, vol. 56, no. 6, pp. 12–16, 2013.
- [29] I. Gibson, D. W. Rosen, B. Stucker, and M. Khorasani, *Additive Manufacturing Technologies*, vol. 17, Springer, Cham, Switzerland, 2021.
- [30] J. Holmström, M. Holweg, S. H. Khajavi, and J. Partanen, “The direct digital manufacturing (r) evolution: definition of a research agenda,” *Operations Management Research*, vol. 9, no. 1–2, pp. 1–10, 2016.
- [31] M. K. Niaki, S. A. Torabi, and F. Nonino, “Why manufacturers adopt additive manufacturing technologies: the role of sustainability,” *Journal of Cleaner Production*, vol. 222, pp. 381–392, 2019.
- [32] A. Garmulewicz, M. Holweg, H. Veldhuis, and A. Yang, “Disruptive technology as an enabler of the circular economy: what potential does 3D printing hold?,” *California Management Review*, vol. 60, no. 3, pp. 112–132, 2018.
- [33] M. G. M. A. Kreiger, G. C. Anzalone, M. L. Mulder, A. Glover, and J. M. Pearce, “Distributed recycling of post-consumer plastic waste in rural areas,” *MRS Online Proceedings Library (OPL)*, vol. 1492, pp. 91–96, 2013.
- [34] P. Santander, F. A. C. Sanchez, H. Boudaoud, and M. Camargo, “Closed loop supply chain network for local and distributed plastic recycling for 3D printing: a MILP-based optimization approach,” *Resources, Conservation and Recycling*, vol. 154, article 104531, 2020.
- [35] L. Milios, “Advancing to a circular economy: three essential ingredients for a comprehensive policy mix,” *Sustainability Science*, vol. 13, no. 3, pp. 861–878, 2018.
- [36] P. Morseletto, “Targets for a circular economy,” *Resources, Conservation and Recycling*, vol. 153, article 104553, 2020.
- [37] P. Rosa, C. Sassanelli, and S. Terzi, “Towards circular business models: a systematic literature review on classification frameworks and archetypes,” *Journal of Cleaner Production*, vol. 236, article 117696, 2019.
- [38] J. Zhang, V. S. Chevali, H. Wang, and C. H. Wang, “Current status of carbon fibre and carbon fibre composites recycling,” *Composites Part B: Engineering*, vol. 193, article 108053, 2020.
- [39] W. Liu, H. Huang, H. Cheng, and Z. Liu, “CFRP reclamation and remanufacturing based on a closed-loop recycling process for carbon fibers using supercritical N-butanol,” *Fibers and Polymers*, vol. 21, no. 3, pp. 604–618, 2020.
- [40] H. Ueda, A. Moriyama, H. Iwahashi, and H. Moritomi, “Organizational issues for disseminating recycling technologies of carbon fiber-reinforced plastics in the Japanese industrial landscape,” *Journal of Material Cycles and Waste Management*, vol. 23, pp. 1–11, 2021.

- [41] S. Pimenta and S. T. Pinho, "Recycling carbon fibre reinforced polymers for structural applications: technology review and market outlook," *Waste Management*, vol. 31, no. 2, pp. 378–392, 2011.
- [42] G. Oliveux, L. O. Dandy, and G. A. Leeke, "Current status of recycling of fibre reinforced polymers: review of technologies, reuse and resulting properties," *Progress in Materials Science*, vol. 72, pp. 61–99, 2015.
- [43] K. Wong, C. Rudd, S. Pickering, and X. Liu, "Composites recycling solutions for the aviation industry," *SCIENCE CHINA Technological Sciences*, vol. 60, no. 9, pp. 1291–1300, 2017.
- [44] J. Palmer, L. Savage, O. R. Ghita, and K. E. Evans, "Sheet moulding compound (SMC) from carbon fibre recycle," *Composites Part A: Applied Science and Manufacturing*, vol. 41, no. 9, pp. 1232–1237, 2010.
- [45] Y. N. Kim, Y. O. Kim, S. Y. Kim et al., "Application of supercritical water for green recycling of epoxy-based carbon fiber reinforced plastic," *Composites Science and Technology*, vol. 173, pp. 66–72, 2019.
- [46] R. J. Tapper, M. L. Longana, H. Yu, I. Hamerton, and K. D. Potter, "Development of a closed-loop recycling process for discontinuous carbon fibre polypropylene composites," *Composites Part B: Engineering*, vol. 146, pp. 222–231, 2018.
- [47] H. Wei, W. Nagatsuka, H. Lee et al., "Mechanical properties of carbon fiber paper reinforced thermoplastics using mixed discontinuous recycled carbon fibers," *Advanced Composite Materials*, vol. 27, no. 1, pp. 19–34, 2018.
- [48] X. Huan, K. Shi, J. Yan et al., "High performance epoxy composites prepared using recycled short carbon fiber with enhanced dispersibility and interfacial bonding through polydopamine surface-modification," *Composites Part B: Engineering*, vol. 193, article 107987, 2020.
- [49] H. Yu, K. D. Potter, and M. R. Wisnom, "A novel manufacturing method for aligned discontinuous fibre composites (high performance-discontinuous fibre method)," *Composites Part A: Applied Science and Manufacturing*, vol. 65, pp. 175–185, 2014.
- [50] Y. Huang, M. C. Leu, J. Mazumder, and A. Donmez, "Additive manufacturing: current state, future potential, gaps and needs, and recommendations," *Journal of Manufacturing Science and Engineering*, vol. 137, no. 1, 2015.
- [51] S. H. Huang, P. Liu, A. Mokasdar, and L. Hou, "Additive manufacturing and its societal impact: a literature review," *The International Journal of Advanced Manufacturing Technology*, vol. 67, no. 5-8, pp. 1191–1203, 2013.
- [52] X. Wang, M. Jiang, Z. Zhou, J. Gou, and D. Hui, "3D printing of polymer matrix composites: a review and prospective," *Composites Part B: Engineering*, vol. 110, pp. 442–458, 2017.
- [53] F. Ning, W. Cong, J. Qiu, J. Wei, and S. Wang, "Additive manufacturing of carbon fiber reinforced thermoplastic composites using fused deposition modeling," *Composites Part B: Engineering*, vol. 80, pp. 369–378, 2015.
- [54] P. Huang, Z. Xia, and S. Cui, "3D printing of carbon fiber-filled conductive silicon rubber," *Materials & Design*, vol. 142, pp. 11–21, 2018.
- [55] L. Guo, X. Niu, X. Chen, F. Lu, J. Gao, and Q. Chang, "3D direct writing egg white hydrogel promotes diabetic chronic wound healing via self-relied bioactive property," *Biomaterials*, vol. 282, article 121406, 2022.
- [56] K. Mikula, D. Skrzypczak, G. Izydorczyk et al., "3D printing filament as a second life of waste plastics—a review," *Environmental Science and Pollution Research*, vol. 28, pp. 1–13, 2021.
- [57] K. R. Hart, J. B. Frketic, and J. R. Brown, "Recycling meal-ready-to-eat (MRE) pouches into polymer filament for material extrusion additive manufacturing," *Additive Manufacturing*, vol. 21, pp. 536–543, 2018.
- [58] K. Ramachandraiah, "Potential development of sustainable 3D-printed meat analogues: a review," *Sustainability*, vol. 13, no. 2, p. 938, 2021.
- [59] A. Akbar and K. M. Liew, "Assessing recycling potential of carbon fiber reinforced plastic waste in production of eco-efficient cement-based materials," *Journal of Cleaner Production*, vol. 274, article 123001, 2020.
- [60] December 2021 <https://foodyaari.com/reduction-of-food-waste-using-3-d-printing-technique/>.
- [61] P. Yu, *CN104191541A - Electronic Waste-Plastic Waste Recovery Resource-Regeneration System and Method*, 2014.
- [62] C. Qing and Z. Juntang, "CN105108134A paste metallic composite material for 3D printing and manufacturing method of paste metallic composite material for 3D printing," 2015.
- [63] X. Li, R. Bai, and J. McKechnie, "Environmental and financial performance of mechanical recycling of carbon fibre reinforced polymers and comparison with conventional disposal routes," *Journal of Cleaner Production*, vol. 127, pp. 451–460, 2016.
- [64] W. Guo, S. Bai, Y. Ye, and L. A. Zhu, "Recycling carbon fiber-reinforced polymers by pyrolysis and reused to prepare short-cut fiber C/C composite," *Journal of Reinforced Plastics and Composites*, vol. 38, no. 7, pp. 340–348, 2019.

Research Article

Wear Behavioral Study of Hexagonal Boron Nitride and Cubic Boron Nitride-Reinforced Aluminum MMC with Sample Analysis

Vasudeva Rao,¹ P. Periyaswamy,¹ A. Bovas Herbert Bejaxhin ,² E. Naveen,³ N. Ramanan,⁴ and Aklilu Teklemariam ⁵

¹Department of Mechanical Engineering, St. Peter's Institute of Higher Education and Research, Avadi, Chennai, India

²Institute of Mechanical Engineering, Saveetha School of Engineering, SIMATS, Thandalam, Chennai, India

³Department of Mechanical Engineering, Sri Sairam Engineering College, Chennai, India

⁴Department of Research & Development, Sync Engineering, Ambattur I.E. Ambattur, Chennai, India

⁵Department of Mechanical Engineering, Faculty of Manufacturing, Institute of Technology, Hawassa University, Ethiopia

Correspondence should be addressed to A. Bovas Herbert Bejaxhin; herbert.mech2007@gmail.com and Aklilu Teklemariam; akliluteklemariam@hu.edu.et

Received 8 February 2022; Accepted 12 April 2022; Published 24 May 2022

Academic Editor: Chang Chuan Lee

Copyright © 2022 Vasudeva Rao et al. This is an open access article distributed under the Creative Commons Attribution License, which permits unrestricted use, distribution, and reproduction in any medium, provided the original work is properly cited.

During the stir casting process, different percent weights of hexagonal boron nitride (HBN) and cubic boron nitride (CBN) were mixed with aluminum alloy 6061. The test specimens are then machined from the cast aluminum metal matrix composites. The tests are carried out utilizing an ASTM G99-compliant pin-on-plate tribometer on a pivoting EN32 circle. Minitab 16 is used to plan the dry sliding wear trials, which are set up in an orthogonal array. The input parameters are percent HBN addition and CBN addition, sliding speed, and load, and the wear rate was considered to be the output parameter. The actual density of the cast specimens was found to be greater than 90% of their theoretical density. The accumulation of HBN and CBN greatly enhances the wear resistance of aluminum metal matrix composites, according to research. The technique of regression analysis is utilized to establish genuine links between the wear rate and input parameters. The morphology of the worn out surfaces was examined using a scanning electron microscope (SEM). After numerous iterations, the simulation source of DEFORM 3D forecasts the stress and velocity component of the frictional surface contact area.

1. Introduction

The current requirement of automotive industries to improve the fuel efficiency with improved properties like friction and wear resistance that led to the development of low-cost and lightweight materials such as cylinder blocks, liners, piston, cam shafts, lifters, and brake drum materials. Selection of the right material for an engineering application depends on properties such as strength, density, light weight, melting point, conductivity, and cost. The density of aluminum being one-third of the steel makes it still a better choice for high-strength and low-weight requirements. Though aluminum and its alloys represent better mechanical properties, it shows degradation of wear resistance, which limits its application in engineering. In order to overcome these limi-

tations, addition of hard material (reinforcement) into soft (matrix) material improves the mechanical and tribological properties, termed as metal matrix composites (MMC).

In reference [1], AZ31B is selected as Mg matrix material and hard tungsten carbide (WC) particles as reinforcement material. Mg/WC composites reinforced with different weight proportions (0, 5, 10, and 15 wt.%) were made through the stir casting method. The wear test results denoted that the AZ31B/15 wt% WC composites have excellent tribological behavior when compared to the base magnesium matrix AZ31B alloy.

Natarajan et al. [1] evaluated the metal matrix composites (MMCs) reinforced with SiC particles that combine the matrix properties with those of the ceramic reinforcement, leading to higher stiffness and superior thermal stability with respect to the corresponding unreinforced alloys. However,

The SEM analysis of the weld zone shows evidence of a substantial grain refinement of the aluminium matrix and fracturing of reinforcement particles due to uniform distribution and dynamic recrystallization induced by the plastic deformation and frictional heating during welding.

The light-weight matrix materials used are aluminum, magnesium, and titanium. Among them, aluminum and magnesium draw the attention as preferred matrix materials due to their several attractive properties. Aluminum metal matrix composites (AMMCs) have demonstrated higher strength at high temperatures, a low coefficient of friction, thermal expansion, superior wear resistance, and stiffness. The hardness of the AMC increases with decreasing density with increasing wt percent of reinforcements. AMMCs have found its application in aircraft, aerospace, automobiles, and various other fields. The commercial application for Toyota engineering in the diesel engine piston, which offers higher wear resistance and strength at high temperatures than Cast Iron.

Wear is a property of an engineering system that is influenced by factors such as load, speed, temperature, hardness, foreign material presence, and the surrounding environment. Wearing situations may produce material wear in a variety of ways. Surface damage or material removal from one or both solid surfaces in a sliding, rolling, or impact action relative to one another might be the cause. Surface interactions at asperities are the most common source of wear. The material on the contacting surface may be removed, transferred to the mating surface, or broken apart as a wear particle during relative motion. Because a material's wear resistance is linked to its microstructure, which may change throughout the wear process, the microstructure seems to be highlighted in wear research. Wear research programmes must be thoroughly structured since metal wear is impacted by a number of elements.

As a result, some of the data has been standardized to make it more helpful. In a vehicle application, Natarajan et al. [1] evaluated traditional grey cast iron and aluminum metal matrix composite for friction material. They put the disc through a wear test, using pin as the brake shoe lining material. The disc is made of A356/25SiCp, while the pins are made of grey cast iron. Optical micrographs were used to examine the worn surfaces of Al-MMC, brake discs, and cast iron, and they concluded that Al-MMC had a higher wear resistance than cast iron. Singh [2] produced aluminum hybrid composites for tribological applications using Al/SiC/Gr. According to their findings, the hybrid composite outperforms the Al alloy in terms of wear resistance. They looked at the tribological layer, which was linked to wear patterns. The tribological properties of Al-MMC were studied by Mistry and Gohli [3]. They found that as the fraction of reinforcement in the matrix was raised, tribological property performance rose proportionately. They also discovered that reinforcing particles at the micro- and nanoscales improve wear qualities. Baradeswaran and Perumal [4] investigated the effects of B4C on Al7075 composites reinforced with K₂TiF₆ as a flux to prevent wetness. They discovered that increasing the volume of particles increased the composite's toughness. They also discovered that adding B4C boosted ultimate tensile, flexural, and wear strength. In addition, in the microstructure, a mechanically mixed layer of iron

and oxygen was discovered. With increasing B4C, the coefficient of friction dropped and was determined to be 0.32 at 10% B4C. Padmavathi and Ramakrishnan [5] used stir casting to investigate the wear and friction behavior of Al6061 with varying percentages of the multiwall carbon nanotube (MWCNT) and SiC. When comparing severe wear circumstances to mild wear conditions, it was discovered that the composite had a low wear rate and friction coefficient. There was a threshold load over which MWCNT had a negative impact on Al alloy wear resistance. The Al reinforced with SiC and MWCNT had improved dry abrasive wear resistance, according to the findings. As the percentage of MWCNT rose, the hardness increased and the specific wear rate dropped. Sidhartha et al. [6] stir cast aluminum-boron carbide MMC with a 5 wt% B4C content and an average size of 33 m. Wear tests were carried out on Taguchi's L₂₇ orthogonal array using three parameters and three levels of condition. The input parameters were the applied load, sliding velocity, and distance. Low load (10 N), high sliding velocity (3 m/s), and distance (2000 m/s) were determined to be the best conditions for good tribological properties. The mix projecting technique was used by Siddesh et al. [7] to make AMC of Al2219 alloy supported with B4C and MoS₂ particles. The density grew as the percent weight of B4C and MoS₂ increased, according to the findings. In the matrix, the microstructural analysis revealed a fine dispersion of reinforcing particles. With increasing percentages of B4C and MoS₂, the yield strength, yield stress, and ductility all reduced due to the formation of voids and nucleation. The composites outperformed the unreinforced Al2219 alloy in terms of wear resistance. Sharma et al. [8] used a stir casting technique to make AA6082 MMCs enhanced with graphite particles. The reinforcement was gradually increased from 0% to 12% in 3 percent increments. The micro- and macrotoughness of the composite reduced as the number of Gr particles increased.

The composite had a lower wear rate than unreinforced composites, and an ANOVA test revealed that the sliding distance was the most important element in composite wear. Riahi and Alpas [9] investigated the wear properties of hybrid A356-10% SiC-4% graphite and A356-5% Al₂O₃-3% graphite manufactured using stir casting processes. The creation of a tribo layer as well as an oxidized surface on both composites' contact surfaces regulated the wear rate, resulting in a mild wear regime for both composites throughout a wide range of loads and sliding speeds. Bindumadhavan et al. [10] studied the wear impact of A356/SiC dual-particle (DPS) composites (47 m and 120 m) and single-particle-sized composites (47 m). The DPS composites demonstrated increased wear resistance because the bigger SiC particles were identified to shelter the smaller ones from abrasive action by guiding the smaller particles to fulfill the wear resistant role. Hexagonal boron nitride and cubic boron nitride reinforced aluminum wear behavior were not reported in the literature survey. Praveenkumar et al. [11] have discussed that the increased WC content improves the yield strength, flexural strength, tensile strength, and microhardness of produced composites. The homogenous dispersion of WC particles throughout the Mg matrix may be seen in SEM pictures. Periyasamy et al. [12-13] have explained that due to dynamic recrystallization

generated by plastic deformation and frictional heating during welding, the microstructure analysis of the weld zone reveals significant grain refinement of the aluminium matrix and breaking of reinforcement particles. Also, determine the mechanical properties of Mg/WC composites prepared by the stir casting method. In [14, 15, 16], AA2024/Al₂O₃/SiC/Gr- and AA6061-reinforced SiC with different leaf ashes using advanced stir casting technique were discussed by Natrayan et al. on tribological behavior improvements of AA2024/Al₂O₃/SiC/Gr- and AA6061-reinforced SiC with different leaf ashes using an advanced stir casting method.

A new attempt was made to investigate the wear behavior of such composites including various percent weights of HBN and CBN. When aluminum slides across steel without any external lubrication, it adheres to the steel, resulting in a low-shear strength contact. As a result of the soft aluminum surface being ploughed by the asperities of steel and flaking of particle flakes from the transfer coating, wear debris may occur. The addition of ceramic reinforcement to the aluminum matrix decreases friction and wear. In addition, the simulation platform DEFORM 3D can be used to analyze wear behavior by providing stress and velocity components for the frictional contact region between the disc and the pin.

2. Materials and Methods

Despite the different casting fabrication methods available, stir casting is a popular fabrication and processing method because it is reasonably inexpensive and allows for the selection of materials and processing conditions. It can sustain high efficiency rates and allow for the production of exceedingly large parts. The cost of producing parts using the mix projecting approach is around one-third to one-half of the cost of producing parts using other major procedures. Costs are expected to drop to one-tenth for high-volume production as well. The distribution of the reinforcing material in the matrix alloy must be homogeneous, and the bonding strength between these two substances must be good, in order to attain optimal metal matrix composites MMC characteristics. The age of acceptable connection between molecular fortifications and fluid aluminum metal lattice during the casting process is dependent on good wetting. Acceptable wetting necessitates strong interface connections. The particles and metal matrix may establish these connections through mutual dissolution or reactivity. The design and features of the support metal interface govern the mechanical properties of MMCs in general. The movement and distribution of stress from the lattice to the support are enabled by a more solid contact, resulting in enhanced adaptability and strength. Particle dispersion in the lattice material during the soften phase of the projection cycle is influenced by mixing speed, warming temperature, mixing duration, slurry consistency, molecule wetting, mixing adequacy, and limiting gas entrapment. The stir casting procedures with the feeding arrangements of reinforcements and molten slag deposition into the mould cavity is shown in Figures 1(a)–1(c).

2.1. SEM Characterization. The form is round, and the essential characteristic of circular powder is that it has a high wear resistance and ductile property. As a result, the powder

is easily spread and quickly mixed with other materials in this circular section. The nanostructure of the size is 10 microns, so the powder material is highly ductile. Figures 2 (a) and 2(b) clearly show the size and shape of the powder. The same characterization is achieved but with different magnifications.

3. Experimental Procedure

3.1. Wear Testing. Using a pin-on-disc device, the dry sliding wear behavior of aluminum/HBN/CBN was examined (DUCOMTM brand). The game plan for pin-on-plate mechanical assembly is shown in Figure 3. The steel with the category of emergency number 32 steel can be used to make the disc, and the hardness has been recorded as 65 HRC. Procedures for an arm and linked loads, in general, press the pin against the plate at a certain load. The dry sliding wear tests were performed in accordance with the ASTM G 99 standard under dry sliding conditions of temperature (300°C, RH 55 percent and 5%). Milling and polishing cylindrical pins with a diameter of 10 mm and a length of 25 mm were done using the metallographic method. The specimens were thoroughly washed with acetone before testing to remove any dirt or foreign particles. The initial and end weights of the specimen were determined with an accuracy of 0.0001 grams using the Mitutoyo electronic weighing equipment. Wear measurement is done after a wear test to quantify the quantity of materials lost (or deteriorated) (and truly after a section in help for a while). Be contingent on the cause for the experiment, the category of wear, and the number and test size instances, and the material can be degraded as loss of weight and volume or variations in straight measurement. The disc was meant to revolve beneath the pin after the example was attached in the arm. The quantity of the workpiece is measured previously, and subsequently, the test with an alphanumeric balance and the loss of weight is calculatedly aimed at each combination of contribution limitations. The maximum wear was calculated using wear track photographs and SEM images.

4. Results and Discussions

Taguchi's three-level four factors of L₂₇ orthogonal array formation were used here for this research. Table 1 shows the input constraints and their levels. Table 2 shows the observations of the wear test. Minitab 16 programming was utilized to do more research.

The wear rate must be minimized when calculating the signal-to-noise ratio; the smaller the number, the better the quality features. As a result, the following equation is used to calculate the signal-to-noise ratio for mass loss: the less you have, the better. Figure 4 shows the main effect graphs of S/N ratios on the wear rate of composites.

$$\eta = -10 \times \log_{10} \left(\frac{1}{n} \sum y_i^2 \right). \quad (1)$$

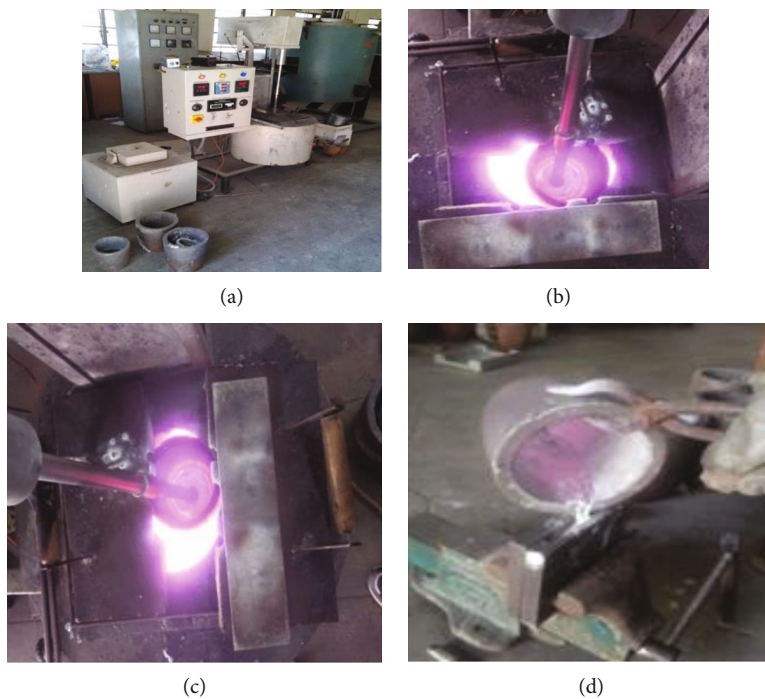


FIGURE 1: (a) Stir casting setup, (b) feeding of reinforcements, (c) stirring of composite slurry, and (d) pouring of the cast composite into dies.

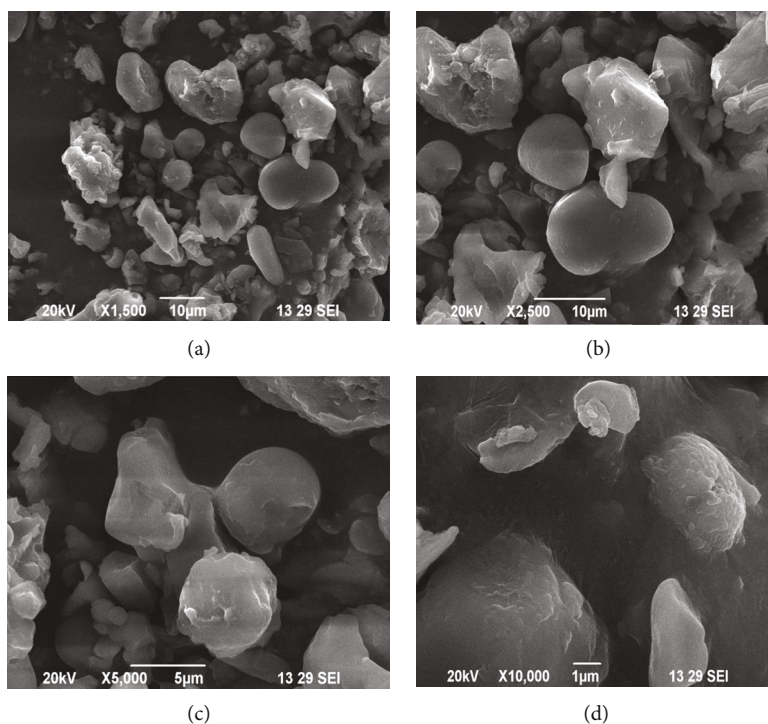


FIGURE 2: Microstructure illustration of (a)&(b) HBN and (c)&(d) CBN composites. The HBN particle size is $\times 1500$ and $\times 2500$ in $10 \mu\text{m}$, and the CBN size is $\times 5000$ in $5 \mu\text{m}$ and $\times 10000$ in $1 \mu\text{m}$ as shown in Figures 2(a) and (d).



FIGURE 3: Wear testing arrangements in the pin-on-disc apparatus.

TABLE 1: Input parameters of wear testing and its additions..

| Contribution factor | Level 1 | Level 2 | Level 3 |
|-------------------------|---------|---------|---------|
| HBN (%) | 0.5 | 1.0 | 1.5 |
| CBN (%) | 1.0 | 2.0 | 3.0 |
| Load (N) | 10 | 30 | 50 |
| Speed of sliding (m/s) | 1 | 2 | 3 |
| Distance of sliding (m) | 2000 | | |

The regression equation for this MMC's wear rate is provided by

$$\begin{aligned}
 \text{Wear rate} = & 0.63631 - (0.328127 * \% \text{HBN}) \\
 & - (0.0451929 * \% \text{CBN}) + (0.00144872 * \text{load}) \\
 & - (0.00146963 * \text{SS}) + (0.124477 * \% \text{HBN} * \% \text{HBN}) \\
 & - (0.0018006 * \% \text{CBN} * \% \text{CBN}) - (1.68475 e - 006 * \text{load} * \text{load}) \\
 & + (0.00661419 * \text{SS} * \text{SS}) + (0.0172865 * \% \text{HBN} * \% \text{CBN}) \\
 & - (0.000837525 * \% \text{HBN} * \text{load}) - (0.0151258 * \% \text{HBN} * \text{SS}) \\
 & - (0.000211329 * \% \text{CBN} * \text{load}) - (0.00844244 * \% \text{CBN} * \text{SS}) \\
 & + (0.000395297 * \text{load} * \text{SS}),
 \end{aligned}$$

$$S = 0.0109344 \quad R - Sq = 99.23\% \quad R - Sq(\text{adj}) = 98.29\% \quad (2)$$

Table 3 shows the percent contribution of input parameters for the wear rate using an analysis of variance (ANOVA) table.

4.1. Influence of Reinforcement Addition. The use of hexagonal boron nitride (self-lubricating) and cubic boron nitride in a soft and ductile matrix increases the hardness and hence reduces the wear rate of the matrix alloy, lowering the wear rate of composites. The dislocation density rises due to a thermal mismatch (difference in thermal expansion coefficient) among the matrix alloy and the reinforcements. Increased dislocation density improves the materials' resistance to plastic deformation and minimizes friction during sliding motion, minimizing crack propagation during wear. The Aluminum 94%, HBN 3%, and CBN 3% were used in reinforcement in this work. In the use of wt %, the wear resistance is verified by pin-on-disc.

TABLE 2: Observations of the wear test.

| Expt. no | % HBN | % CBN | Load (N) | Slidingspeed (m/s) | Wear rate (mm ³ /m) |
|----------|-------|-------|----------|--------------------|--------------------------------|
| 1 | 0.5 | 1 | 10 | 1 | 0.4515 |
| 2 | 0.5 | 1 | 30 | 2 | 0.4966 |
| 3 | 0.5 | 1 | 50 | 3 | 0.5546 |
| 4 | 0.5 | 2 | 10 | 2 | 0.3936 |
| 5 | 0.5 | 2 | 30 | 3 | 0.4369 |
| 6 | 0.5 | 2 | 50 | 1 | 0.4416 |
| 7 | 0.5 | 3 | 10 | 3 | 0.3397 |
| 8 | 0.5 | 3 | 30 | 1 | 0.3445 |
| 9 | 0.5 | 3 | 50 | 2 | 0.3691 |
| 10 | 1 | 1 | 10 | 2 | 0.3437 |
| 11 | 1 | 1 | 30 | 3 | 0.3846 |
| 12 | 1 | 1 | 50 | 1 | 0.3798 |
| 13 | 1 | 2 | 10 | 3 | 0.2965 |
| 14 | 1 | 2 | 30 | 1 | 0.3161 |
| 15 | 1 | 2 | 50 | 2 | 0.3264 |
| 16 | 1 | 3 | 10 | 1 | 0.2699 |
| 17 | 1 | 3 | 30 | 2 | 0.2727 |
| 18 | 1 | 3 | 50 | 3 | 0.2833 |
| 19 | 1.5 | 1 | 10 | 3 | 0.3212 |
| 20 | 1.5 | 1 | 30 | 1 | 0.3223 |
| 21 | 1.5 | 1 | 50 | 2 | 0.3268 |
| 22 | 1.5 | 2 | 10 | 1 | 0.2773 |
| 23 | 1.5 | 2 | 30 | 2 | 0.2842 |
| 24 | 1.5 | 2 | 50 | 3 | 0.2979 |
| 25 | 1.5 | 3 | 10 | 2 | 0.2070 |
| 26 | 1.5 | 3 | 30 | 3 | 0.2059 |
| 27 | 1.5 | 3 | 50 | 1 | 0.2354 |

Main effects plot SN ratios

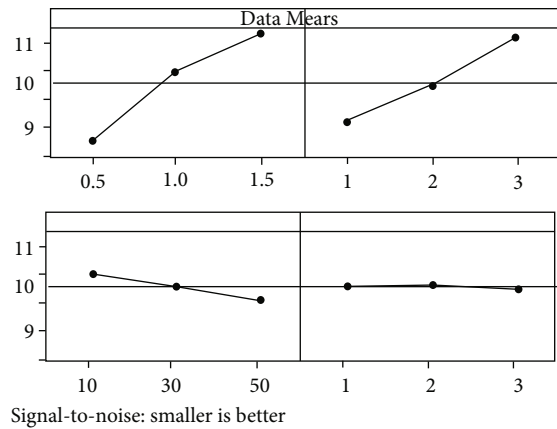


FIGURE 4: Key outcome plots of S/N ratios about the wear rate.

4.2. Influence of the Applied Load. Sliding wear is related to the applied force and the sliding distance and inversely proportional to the degraded surface's hardness. The shift in

TABLE 3: ANOVA observations of % contribution of inputs for the wear rate.

| Source | DF | Seq SS | F | P | Contribution % |
|-------------|----|---------|----------|---------|----------------|
| % HBN | 1 | 0.10125 | 82.13400 | 0.00171 | 55.749 |
| % CBN | 1 | 0.06167 | 4.69300 | 0.05113 | 33.957 |
| Load | 1 | 0.00550 | 2.67300 | 0.12802 | 3.028 |
| SS | 1 | 0.00038 | 0.00500 | 0.94500 | 0.206 |
| %HBN * %HBN | 1 | 0.00581 | 48.50900 | 0.00932 | 3.199 |
| %CBN * %CBN | 1 | 0.00002 | 0.16200 | 0.69404 | 0.010 |
| Load * load | 1 | 0.00000 | 0.02300 | 0.88262 | 0.002 |
| SS*SS | 1 | 0.00026 | 2.19100 | 0.16456 | 0.144 |
| %HBN * %CBN | 1 | 0.00135 | 7.01600 | 0.02122 | 0.744 |
| %HBN * load | 1 | 0.00133 | 6.58800 | 0.02469 | 0.730 |
| %HBN * SS | 1 | 0.00089 | 5.37900 | 0.03882 | 0.492 |
| %CBN * load | 1 | 0.00020 | 1.67800 | 0.21958 | 0.111 |
| %CBN * SS | 1 | 0.00082 | 6.85400 | 0.02247 | 0.452 |
| Load * SS | 1 | 0.00070 | 5.81100 | 0.03287 | 0.383 |
| Error | 12 | 0.00144 | | | 0.791 |
| Total | 26 | 0.18161 | | | 100.00 |

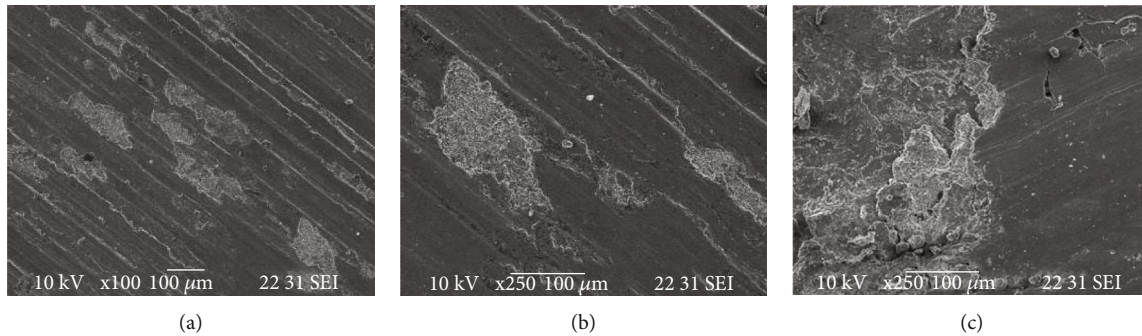


FIGURE 5: SEM image worn-out surface of experiments.

wear behavior with increasing load may be described using Archard's theory.

The observed increase in the wear rate was caused by the fact that as the applied stress rises, so does the permeation of stiff asperities of the counter exterior into the softer pin surface, as well as deformation and fracture of the softer surface asperities. As the load grows, thermal softening and plastic deformation tend to serve on the MMC. This might be due to the weight-bearing capacity of the reinforcements and base metal. As a result, at low speeds, the abrasive wear process takes over, in which the fracture strength exceeds the fracture strength, resulting in fracture owing to higher produced stresses. The material may be transported from the pin to the disc owing to the chafing action of broken reinforcing particles on the steel disc and the displacement of the matrix from the pin's surface. More energy is given as the load grows, and some of it is transformed to heat energy. The heating caused by friction increases as the applied load increases, resulting in localized adhesion of the pin surface

to the counter surface as the interface temperature rises. As the load rises, so does the pin's penetration into the composite surface, resulting in a quicker rate of wear.

4.3. Consequences of Sliding Speed. The results show that when a combination of percent HBN addition, percent CBN addition, and applied load is used, the frictional heat created between the pin and the steel disc is influenced by sliding speed. Where the reinforcements are penetrated from the pin to the counter plate, the degree of softening and frictional heat are directly proportional to each other. However, increasing the sliding speed reduces the wear rate, which is caused by reinforcement pulling due to thermal mismatch. When the drawn reinforcing particles come into contact with the steel disc, the wear rate is reduced at greater speeds.

4.4. Wear Surface Morphology of Aluminum Metal Matrix Composites by SEM Analysis. An SEM was used to examine the worn-out surface of selected specimens after the wear

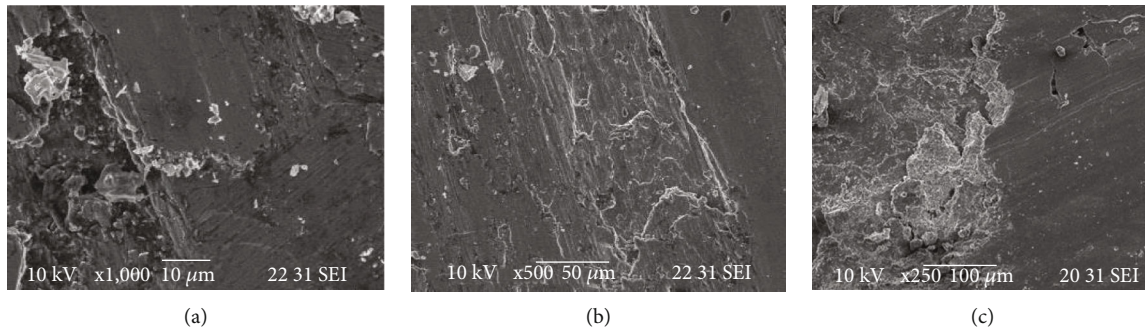


FIGURE 6: SEM image worn-out surface of experiments 2, 14, and 26.

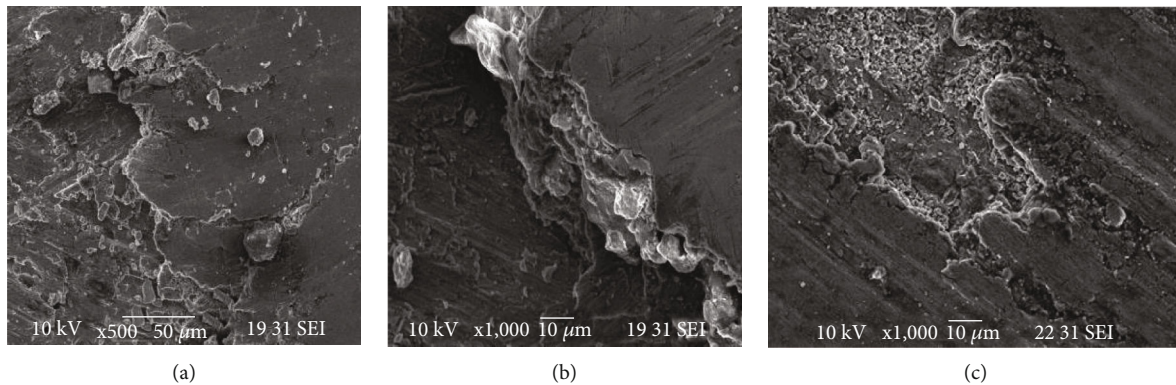


FIGURE 7: SEM image worn-out surface of experiments 9, 18, and 27.

test (SEM). Figures 5(a)–5(c) demonstrate the surface morphology of the hybrid composite for experiments 1, 4, and 7. It appears that cavities generated in the composite matrix have aligned parallel to the direction of sliding when tested at low load (10 N). During the scouring process, several particles were chopped off. In certain zones, the composite lattice has released smaller particles over the worn surface of the AA6061-HBN-CBN Hybrid composite. Deep and persistent grooves cause the oxide layer casting to fracture, resulting in increased wear loss. The two composites' worn surfaces had finer grooves and modest plastic distortion at the groove margins. The reinforcing also gives the surface a smooth appearance. Notably, fissures grow parallel to the sliding direction. When the applied load is low, the reinforcements fracture, fragment, or move along the crack lines. Although cavitations appear to be modest, deep cracks and grooves are plainly seen with increasing applied force.

SEM images for experimental conditions 2, 14, and 26 are depicted in Figures 6(a)–6(c). The worn surface changes appearance when subjected to 30 N of force. The cavitations are greater in this example than in the previous one. Some substructures run in the same direction as the sliding direction. The worn surface had resulted in subtle grooves and minor scratches. The ploughing effect of the counter disc's strong asperities and hardened worn detritus creates the grooves. Wear would be reduced if the tungsten carbide content was increased. The structures of worn surfaces change depending on the sliding speed and applied force. When

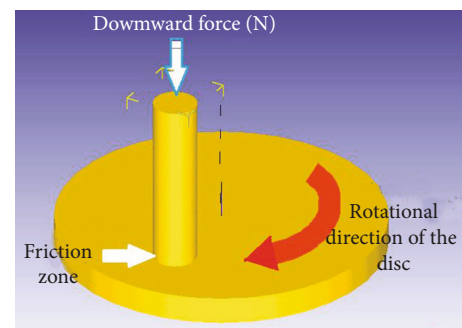


FIGURE 8: Modeling and assemblage of the pin-on-disc wear test in DEFORM 3D.

the sample is rubbed on a steel disc at a low sliding speed and applied force, the aluminum matrix appears to expand along the sliding direction. Cavitations have also increased. The hard particles seem to have fashioned a few holes (for example, HBN and CBN particulates)

Figures 7(a)–7(c) show SEM images for experimental conditions 9, 18, and 27. During sliding, hard particles dissolve the steel counter face, forming a thin coating of oxidized iron that acts as an ointment. Hard particles at grain boundaries would reduce particle breakage. Massive plastic strains in the composite network can cause subsurface breaks and delamination when in close contact with the steel counter face. Figure 7(a) depicts fractures occurring at

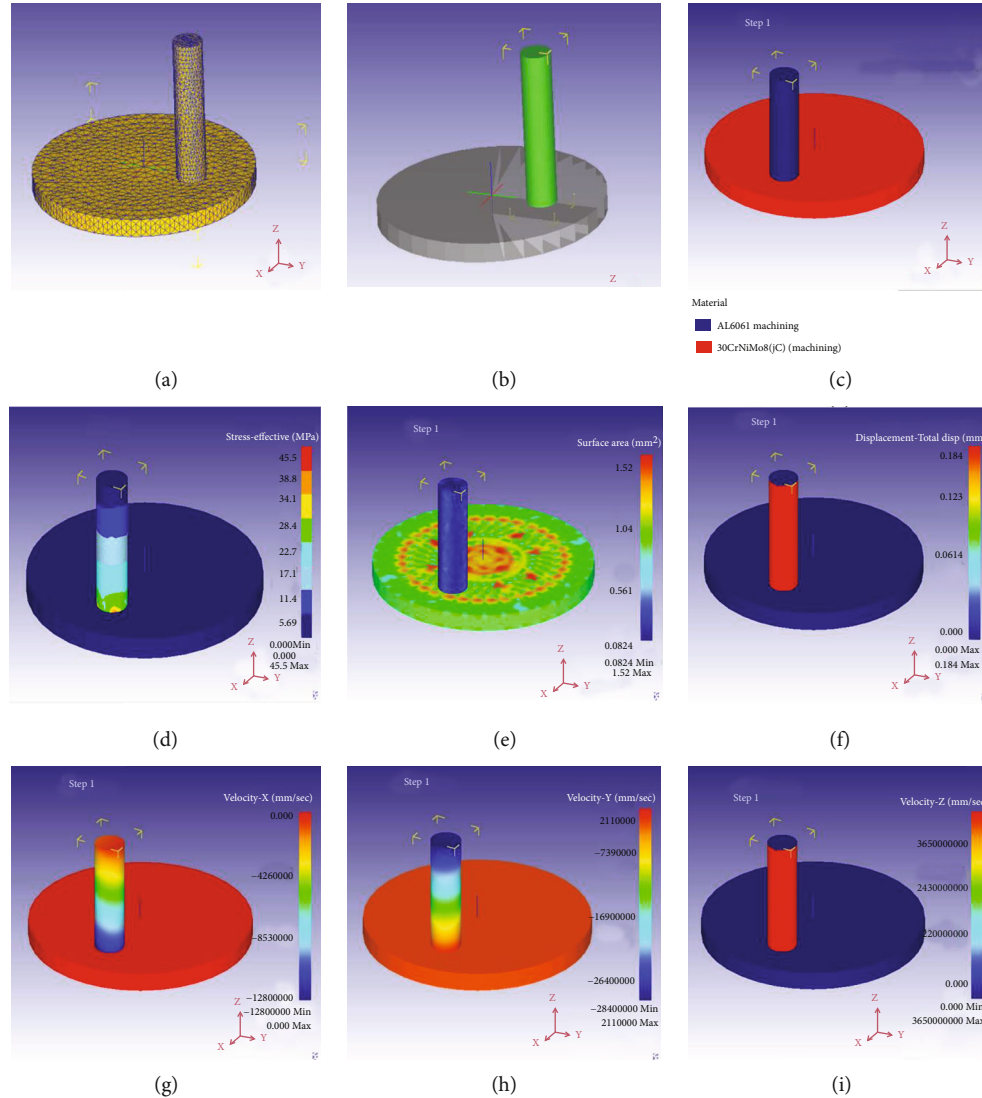


FIGURE 9: Simulation results of wear behavior.

aluminum grain boundaries as a result of strain hardening of aluminum during sliding with increasing stress and reinforcement explosion from aluminum grain boundaries as a result of increasing load. The wear rate reduces at 3 m/s, suggesting less material loss from the surface. Figure 7(c) shows a lot of grooves on the surface.

4.5. Validation of Wear Test through Simulation. The multi-directional simulation tool DEFORM 3D is used for all dynamically oriented analysis, especially used for the 3-dimensional analysis and simulation of all metal forming and machining techniques. We can easily predict the properties of all domain-related elements. As mentioned in the previous experimental stage, using the pin-on-disc apparatus, the friction level and the wear rates can be easily calculated by this simulation procedure. Based on this, the simulation procedures have been originated for the bid of comparing the stress, velocity, and displacement for the highlighted value which has been arrived from the experimental part. The clockwise rotation of the disc can be mod-

elled and located in the simulation platform with the vertical placement of the pin model. For both the pin and disc models, the material attributes were picked from the materials library.

The boundary conditions have been specified based on its rotation about the rotating disc assembly's center axis; similarly, a vertical downward force of 50 N can be applied over the pin in the DEFORM 3D simulation tool's z-axis as shown in Figure 8. The DEFORM 3D platform can simulate the frictional contact in a wear test.

The convergence relative mesh size was preferred in this case, and it was applied to both the friction plate and the pin element's surface. Both are in their correct positions, as revealed in Figures 9(a) and 9(b), with physical contact between the pin and the disc. Figure 9(c) shows the material properties of Al6061 for the pin element and 30CrNiMo8 steel for the revolving disc, which are labelled with distinct colors. As illustrated in Figure 9(d), the von Mises or effective stress was achieved in one of the experimental steps between the pin and the rotating disc. Here, the tension is

largest at the contact surface due to the gradually imposed load; it decreases lower along the vertical z -axis in DEFORM 3D. Figure 9(e) depicts the frictional impact on a disc with a surface area of 1.52 mm^2 . The dynamics simulation tool measured the displacement at 0.184 mm throughout the pin length. When there is a condition of friction between the mating surfaces, this approach can be utilized to anticipate stresses and displacements. Figures 9(g) and 9(h) and I demonstrate how the velocities on both the x -, y -, and z -axes can be anticipated in Figure 9(i). The y - and z -axis velocities are only active in this case. There was no velocity value obtained along the x -axis direction.

5. Conclusion

The addition of hexagonal boron nitride and cubic boron nitride improves the wear resistance of aluminum AA6061. Among these two, hexagonal boron nitride contributes more than its cubic structured counterpart. Wear resistance decreases as the load increases, independent of the composition, and mass loss increases. A thin tribo film is formed by the HBN reinforcements that have been removed. It keeps metal from coming into direct contact with the sliding surface, as well as CBN particles from fracturing. These reinforcements also serve as a barrier, inhibiting dislocation movement, which manifests as little patches. The greatest weight percent of HBN and CBN resulted in the least amount of material loss during wear. The deformation resistance given by CBN, which breaks into little pieces to produce wear debris particles, is a noteworthy component of this wear research. This garbage keeps the plate from penetrating the metal, securing the delicate aluminum structure and enhancing wear blockage. Affirmation experiments were communicated using the empirical equation. The discrepancy between the actual and expected readings was less than 5%. Better comparison has been created for the sake of prediction utilizing DEFORM 3D and can be taken as a future scope of work in the same operating conditions.

Data Availability

The data used to support the findings of this study are included in the article. Should further data or information be required, these are available from the corresponding author upon request.

Disclosure

This research was performed as part of the employment in Hawassa University, Ethiopia.

Conflicts of Interest

The authors declare that there are no conflicts of interest regarding the publication of this paper.

Acknowledgments

The authors appreciate the technical assistance to complete this experimental work from the department of mechanical engineering, Saveetha University, Chennai, Tamil Nadu, India.





References

- [1] N. Natarajan, S. Vijayarangan, and I. Rajendran, "Wear behaviour of A356/25SiC_p aluminium matrix composites sliding against automobile friction material," *Wear*, vol. 261, no. 7-8, pp. 812-822, 2006.
- [2] J. Singh, "Fabrication characteristics and tribological behaviour of Al/SiC/gr hybrid aluminum metal matrix composites: a review," *Friction*, vol. 4, pp. 1-17, 2016.
- [3] J. M. Mistry and P. P. Gohli, "An overview of diversified reinforcement on aluminium metal matrix composites: tribological aspects," *Journal of Indian tribology*, vol. 231, pp. 399-421, 2016.
- [4] A. E. Baradeswaran and A. E. Perumal, "Influence of B₄C on the tribological and mechanical properties of Al 7075-B₄C composites," *Composites Part B: Engineering*, vol. 54, pp. 146-152, 2013.
- [5] K. R. Padmavathi and R. Ramakrishnan, "Tribological behaviour of aluminium hybrid metal matrix composite," *Procedia Engineering*, vol. 97, pp. 660-667, 2014.
- [6] N. S. Prabhakar, N. Radhika, and R. Raghu, "Analysis of tribological behavior of aluminium/B₄C composite under dry sliding motion," *Procedia Engineering*, vol. 97, pp. 994-1003, 2014.
- [7] N. S. Kumar, V. M. Ravindranath, and G. S. Shankar, "Mechanical and wear behaviour of aluminium metal matrix hybrid composites," *Procedia Materials Science*, vol. 5, pp. 908-917, 2014.
- [8] P. Sharma, D. Khanduja, and S. Sharma, "Dry sliding wear investigation of Al6082/Gr metal matrix composites by response surface methodology," *Journal of Materials Research and Technology*, vol. 5, no. 1, pp. 29-36, 2016.
- [9] A. R. Riahi and A. T. Alpas, "The role of tribo-layers on the sliding wear behavior of graphitic aluminum matrix composites," *Wear*, vol. 251, no. 1-12, pp. 1396-1407, 2001.
- [10] P. Bindumadhavan, H. Wah, and O. Prabhakar, "Dual particle size (DPS) composites: effect on wear and mechanical properties of particulate metal matrix composites," *Wear*, vol. 248, no. 1-2, pp. 112-120, 2001.
- [11] R. Praveenkumar, P. Periyasamy, V. Mohanavel, and M. M. Ravikumar, "Mechanical and tribological behavior of Mg-matrix composites manufactured by stir casting," *International Journal of Vehicle Structures and Systems*, vol. 11, pp. 117-120, 2019.
- [12] P. Periyasamy, B. Mohan, and V. Balasubramanian, "Effect of heat input on mechanical and metallurgical properties of friction stir welded AA6061-10% SiCp MMCs," *Journal of Materials Engineering and Performance*, vol. 21, no. 11, pp. 2417-2428, 2012.
- [13] R. Praveenkumar, P. Periyasamy, V. Mohanavel, and D. Chandramohan, "Microstructure and mechanical properties of mg/WC composites prepared by stir casting method," *International Journal of Mechanical Engineering and Technology (IJMET)*, vol. 9, no. 10, pp. 1504-1511, 2018.

- [14] L. Natrayan and M. Senthil Kumar, "Optimization of wear parameters of aluminium hybrid metal matrix composites by squeeze casting using Taguchi and artificial neural network," in *Sustainable Manufacturing and Design*, vol. 10, pp. 223–234, Woodhead Publishing, 2021.
- [15] L. Natrayan and M. Senthil Kumar, "Influence of silicon carbide on tribological behaviour of AA2024/Al₂O₃/SiC/Gr hybrid metal matrix squeeze cast composite using Taguchi technique," *Materials Research Express*, vol. 6, no. 12, article 1265f9, 2019.
- [16] L. Natrayan, V. Sivaprakash, and M. S. Santhosh, "Mechanical, microstructure and wear behavior of the material AA6061 reinforced SiC with different leaf ashes using advanced stir casting method," *International Journal of Engineering and Advanced Technology*, vol. 8, pp. 366–371, 2018.

Review Article

Additive Manufacturing for Aerospace from Inception to Certification

Devarajan Balaji ¹, **Jarabala Ranga**,² **V. Bhuvaneshwari**,¹ **B. Arulmurugan** ¹,
L. Rajeshkumar ¹, **Mohan Prasad Manimohan**,³ **G. Ramya Devi**,⁴ **G. Ramya**,⁵
and Chandran Masi ⁶

¹Department of Mechanical Engineering, KPR Institute of Engineering and Technology, Tamilnadu, India

²Department of Electrical and Electronics Engineering, Ramachandra College of Engineering, India

³Mechanical Engineering, M.Kumarasamy College of Engineering (Autonomous), Karur, Tamilnadu, India

⁴Department of Mechanical Engineering, Saveetha School of Engineering, SIMATS, Chennai, 602105 Tamilnadu, India

⁵Department of Mechanical Engineering, Rajalakshmi Engineering College, Chennai, Tamilnadu, India

⁶Department of Biotechnology, College of Biological & Chemical Engineering, Addis Ababa Science & Technology University, Addis Ababa, Ethiopia

Correspondence should be addressed to Chandran Masi; chandran.chandran@aastu.edu.et

Received 25 February 2022; Revised 4 April 2022; Accepted 7 April 2022; Published 21 May 2022

Academic Editor: V. Vijayan

Copyright © 2022 Devarajan Balaji et al. This is an open access article distributed under the Creative Commons Attribution License, which permits unrestricted use, distribution, and reproduction in any medium, provided the original work is properly cited.

Metal additive manufacturing (MAM) does not require any preface for its potential applications in various engineering and technological sectors. This article comprehensively discusses about the application of additive manufacturing technique specifically aerospace components. The structure of this article begins with an introduction to the current state-of-the-art MAM technologies with the aid of patent landscape analysis. Any manufacturing starts with understating of the manufacturing cycle, so herein, the aerospace manufacturing cycle has been discussed commencing from the design phase and followed by the process parameters selection. The immediate effect after printing is the selection of evaluation parameters, wherein the surface texture analysis of AM printed components is discussed. This paves to discuss about the specific alloys such as titanium alloy and Inconel alloys which are widely used in the aerospace industry. This analysis paves a path for the utilization of these materials to manufacture specific aerospace components which are also discussed. Thereby, the impact of MAM over the aerospace sector and the guidelines to decision making on the suitable variant of MAM has been discussed clearly with the help of earlier literatures. Finally, the qualification and certification procedure are discussed therein, leading to the conclusion about the future scope of MAM in the aerospace sector.

1. Introduction

For decades, the fundamental concept of additive manufacturing had already persisted. It is explained as the method of building three-dimensional components progressively therein through computer model data, layer-by-layer [1, 2]. The very first efforts related to additive manufacturing occurred during the late 1960s by American Battelle Memorial Institute [3], wherein research teams were using laser beams as well as

photopolymers to construct solid artifacts in a liquid resin [4]. Developing the feasible marketable practice of SLA, stereolithography technology that took place during 1987 by Charles Hull as a patent holder is being introduced in the market which paves a path to develop the other variants, including FDM (fused deposition modeling), SLS (Selective Laser Sintering), EBM (Electron Beam Melting), and multijet printing, along with other variants that are being in usage today [5]. The initial applications of AMT

(additive manufacturing technology) include the machine for Rapid Prototyping (RP) to develop the models and tools for another conventional machining, and eventually, it is effectively grown and reached the stage wherein the complete product developed is reached. Its potential does not stop at that point further accelerating to have a functional product development.

Even so, steadily for the past decade, AM had already made rapid technological breakthroughs as well as has become an increasingly popular method of the research design method. AM is already used in conjunction with conventional manufacturing (CM), such as subtractive manufacturing (SM), that either depends on material removal to create a final product, in niche sectors such as biomedical, aviation, as well as automotive [6]. It has contributed to an increase in the number of start-up companies specializing in Rapid Manufacturing (RM) of components [7, 8]. In the aerospace industry, AM is particularly prevalent in the construction of different individual aircraft components, accounting for 16.6% and 18.2% of the world manufacturing share of the market in 2016 and 2017, correspondingly [9, 10]. One of the primary causes for the same is the requirement for redesigning and part production with reasonable mass and savings in cost but not at the cost of mechanical characteristics of AM parts. A unique characteristic of the FDM used for the manufacture of aerospace parts is its rapid melting and solidification phases which results in faster cooling time and very fine grains when compared with the material characteristics of traditionally machined components. [11–15].

In accumulation, the easy-off processing of these fusion-based ATMs permits for good microstructural topographies such as topology texture along with the grain structure, to be managed through the manipulation over the processing parameters while at the manufacturing stage [16]. This freedom allows for not just the development of sophisticated attributes that would be impossible to machine or fabricate using conventional manufacturing methods, as well as the customizing of microstructures, that are crucial for the construction of high-performance aerospace applications that are frequently utilized in extreme environments, such as higher temperatures, adverse weather, and extended life cycles [17]. Moreover, the economic status of AM variants comprehensively favours the low-volume manufacture of parts for aerospace. A significant factor in the significant expense of manufacturing aerospace parts using existing subtractive manufacturing processes is about their high buy over fly ratio, which is characterized as that of the volume proportion of the main raw material to the finished product. This ratio varies among 10:1 as well as 15-20:1 in the aviation industry and therefore can reach 40:1 besides increasingly complicated part [10, 18].

Advantageous in terms of AM in creating nearly net-shaped products, the buy-over-fly ratio can indeed be significantly reduced and sometimes even close to 1 is to 1 [7]. With the advancement of intrinsic microstructures, increased input material utilization as well as associated material waste, faster processing times, and 3D printing technology is therefore no longer recognized as a prototyp-

ing alternative though as a direct production process capable of producing near net-shaped high-quality products [7]. This innovative additive manufacturing technology gives end users increased control over part specific requirements including incurred costs, geometric constraints, and mass [19]. Additionally, MAM's prosperous transformation in the aviation industry creates additional possibilities for sustainable development as well as accompanying supply chain frameworks in the long term. While also additive manufacturing is gaining traction throughout the medical, aerospace, and automotive sectors, it would still be regarded as an emerging technology. Due to the absence of defined procedures as well as certification for AM-developed components, the majority of recent AM utilization in the aviation industry has already been limited to nonmission-specific applications [20]. To tackle these issues, producers, as well as governmental aerospace bodies, are growingly collaborating to innovate novel benchmarks that are compatible with AM's actual abilities [21].

Besides, they were acknowledged by academic researchers and industrialists which specifically use AMT for the part production. Such acknowledgments may reduce the ambiguities and contradictions in various 3D printing technologies and terminologies [22]. Numerous standards have indeed been established to date concerning metal additive manufacturing in summary; these standards have included the ISO/ASTM52900-15 guidelines for AM nomenclature, the ASTM F3122-14 standard for evaluating the material characteristics of MAM parts, and the ASTM F3049-14 standard for categorization of powder metallurgy being used AM systems [1, 23]. Nevertheless, hardly very few guidelines, as well as certifications, have been created in the sense of metal additive manufacturing mostly in the aerospace sector; instances involve MSFC-STD-3716 for spacecraft hardware designed and manufactured using laser powder bed fusion metal additive manufacturing techniques and SAE AS9100 for quality management framework necessities in aerospace, aviation, and defensive system associations. Various attempts are thus expected to properly incorporate metal additive manufacturing standards and, more particularly, to fulfil the criteria of aerospace industries, which have been presently being spearheaded by National Aeronautics and Space Administration (NASA) [1, 23].

Nonetheless, those same defined standards seem to be extremely beneficial to decision-makers as well as the 3D printing community in general and also have served as fundamental guidelines for developing additional aerospace-specific standards along with guidelines. Numerous works have been published that review on state-of-the-art metal 3D printing in a comprehensive way. For instance, Frazier [24] analyzed the diverse metal additive manufacturing classifications and concentrated on the material research, methodologies, company, and environmental challenges associated with MAM. Beyer [25] discussed the potential significance of mass acceptance of additive manufacturing, significantly about creating the required mind-frame between many engineers and producers to fully utilize the benefits of AM throughout a variety of industrial uses,

TABLE 1: Landscape analysis of MAM in aerospace [30].

| S. no | Country | No of patents | Major applicants | No of patents | Year-wise count | No of patents |
|-------|-----------|---------------|---|---------------|-----------------|---------------|
| 1 | USA | 42 | The Boeing Company | 5 | 2013 | 1 |
| 2 | PCT* | 23 | California institute of tech. | 4 | 2014 | 1 |
| 3 | China | 13 | The curators of the University of Missouri | 4 | 2015 | 1 |
| 4 | EPO** | 6 | Ebullient LLC | 3 | 2016 | 6 |
| 5 | UK | 4 | HRL laboratories LLC | 3 | 2017 | 13 |
| 6 | India | 4 | Lincoln global Inc. | 3 | 2018 | 14 |
| 7 | Australia | 1 | Mat solutions ltd. | 3 | 2019 | 26 |
| 8 | | | Nanocore tech. | 3 | 2020 | 22 |
| 9 | | | Shanghai aerospace equipment manufacturer co ltd. | 3 | 2021 | 9 |
| 10 | | | United tech co. | 3 | | |

including medical, engineering, consumer products, aerospace, and automotive industries. Additionally, Seifi et al. [26, 27] had also concentrated their attention on creating guidelines to aid in the credential and certification of metal additive manufacturing, particularly concerning material, microstructure, and mechanical properties. Additionally, additional investigators examined the application and enormous prospects of metal additive manufacturing in aerospace engineering. For instance, Uriondo et al. [22] described the utilization of metal additive manufacturing and material modeling in the manufacturing and as repair of aerospace components, emphasizing the critical role of regulatory frameworks, airworthiness, and air transport safety in accomplishing such two goals. In this way, Liu et al. [17] have emphasized the specific core competence of nonmetal and metal AM production along with repair of aerospace components and the upcoming trends of prospective AM technology in the business along with the academic perspective of the aerospace industries. Kinsella [28] explains that while metal additive production techniques may still not entirely substitute the conventional manufacturing techniques for manufacturing aviation components, those that may provide a reduction in costs as well as the manufacturing capability for creative features leveraging super-alloys, of that kind as dual-alloy accumulation as well as FGM - Functional Graded Materials, for such USAF - United States Air Force as well as DoD - Department of Defense. Additionally, Nickels [29] stated that perhaps the unresolved challenges of functional integration, geometric freedom, energy consumption, waste reduction, and machine constraints might well slow metal additive manufacturing's adoption for large-scale manufacturing in the aviation industry.

The MAM gained better acceleration in various domains, and specifically, the aerospace industry owing to its costlier metal parts is being predominantly used. So, it is necessary to understand clearly the entire process starting from MAM initial stage up to the product certification stage, based on this article, walkthrough is structured. The progress of the MAM can be revealed by the understand growth curve over the years, at least data of the decade owing to the expiration of Selective Laser Sintering (SLS) patent during 2014. The SLS is one of the pioneers in the MAM technique

in the AM variant, in place of searching the broad database wherein converging is harder. In the existing literature, patent databases are considered to be the latest and get updated every minute along with that consolidation related to specific domains is easier than other article clusters. So, the patent landscape analysis is taken as a core identity to understand the growth profile of the MAM variant of AM specifically in the aerospace domain.

The following Table 1 reveals 3 factors that are country, major players, and year versus a corresponding number of patents filed. The inference revealed out the USA is the dominating country in this variant of AM, might be owing to the fact they want to reduce the import of final finished products, and in lieu they can import only raw materials. So, they accelerate the product development within their country leads to reducing the manufacturing cost and time. The major player in this technology is "The Boeing Company" occupying the top of the table. The country of origin of Boeing is the USA, where remarkable industry in the aerospace can be found, considering the growth year was quite good numbers during the last 5 years that is in double digit. All these data depict that this MAM variant of AM has a good scope shortly at least for a decade. AM technique provides greater flexibility in manufacturing opens up a better forum for metal components to be manufactured. The total count is 93 as per the record for the keyword EN_ALL: ("Metal Additive Manufacturing" "Aerospace"). The analysis is made by selecting the option "Single-family member," which means that the same patent filed in multiple countries is considered as one patent.

Every 3D printing technique has its own unique set of material properties, treatment processes, as well as abilities. Nonetheless, the majority of them operate on a point-by-point basis and can use powdered material as more than just a raw resource. Industries such as Solidica in the United States manufacture components using an ultrasonic accumulation methodology [31]. Only Laser Metal Deposition (LMD), Selective Laser Melting (SLS), and Electron Beam Melting (EBM), as well as Wire Arc Additive Manufacturing (WAAM), have been regarded and explained in summary even if they are currently perceived as the four additive manufacturing processes another very acceptable towards the aviation industry, since they are capable of producing

nearly completely high-density parts without the use of post-processing (near to 99.9 percentage of density) while comparing over the conventional technique corresponding to their mechanical and electrochemical characteristics [32, 33].

There have been numerous classification schemes for these techniques. Those certain techniques were categorized according to the method by which the resource was available. On this same, yet another side, powder bed integration processing technologies include one or maybe more high-temperature resources for melting the powder, a technique for directing the fusion of the particles to a specific area within each layer, as well as a mechanism for prespreading a seamless layer of powder. MD procedures, from the other side, disintegrate the substance as it has been laid down. SLM and LMD both make use of a high-power laser. EBM, on the other hand, employs an electron beam wherein, WAAM uses plasma arc. Laser-based technology has advanced significantly over the years [34, 35], with smaller intensive areas and increased laser power, as well as wavelengths that are more tuned to the absorption characteristics of metal powder [36, 37]. At present, in every additive manufacturing technique, the laser is utilized in all the variants, therein, they use fiber lasers as a substitute over the carbon dioxide and Nd: YAG lasers. The subsequent sector offers some specific characteristics of LMD, SLM, and EBM through which the ability of an AMT to manufacture high performance parts through laser energy can be fabricated through particle embodiment on the surface [38]. Such embodiments can be made through a coaxial powder feeding system via nozzle and can be synchronized with the laser scanning [39, 40]. They can also be materialized through the tailoring of processing conditions, rate of deposition, scanning method, and materials. As a final point, it is indeed critical to keep in mind that the nomenclature used to describe LMD, SLM, and EBM techniques tend to vary between various organizations.

Additive manufacturing (AM) has the prospects to significantly reduce production time as well as the cost, particularly for aviation parts manufactured of expensive titanium alloys. It is looking to attract widespread interest owing to its outstanding capacity to establish complex components, including fine microstructure, better surface quality, and excellent properties. Significant work has indeed been accomplished in recent decades, which includes fabricating facility development, manufacturing technology development, and specification development. It summarizes the advancement and the status of AM technology and the underlying conditions and the potential applications on civilian aviation in this section. Only with constant ought to reduce the overall weight of airplane, as well as the expense of production titanium alloy parts, involvement in nontraditional 3D printing has increased, whether for a significant portion or tiny portion fabrication. It is assumed that 3D printing technology will provide a strategic vision for something like the production specialized field, including its radically different concept of fast evolution compared to traditional disposal forming, as well as pressured forming, to particularly emphasize the investigation as well as utiliza-

tion in the aviation industry. At almost the same moment, the advancement of process innovation encourages the emancipation of structural engineering notion and growth. All these mutual advancements will have a considerable impact on long-term aviation production technologies [41]. Let us move forward with the article that MAM has a scope, so it has to be understood from the manufacturing cycle till the certificate of metal products.

2. Manufacturing Cycle—MAM in Aerospace

3D Printing has been at the cutting edge of innovative production technology yet does have the same prospects to transform producing by radically altering design and endeavor belief systems. A concise evaluation of existing metal additive manufacturing procedures, producible materials, associated defects, and evaluation techniques (destructive and nondestructive) is described. Specifically, the AM structural optimization techniques are investigated, along with their associated risks and restrictions. Eventually, a research report from the aviation sector is introduced, along with several case studies. Figure 1 depicts the straightforward production cycle for additively manufactured metal components. The additive manufacturing market is rapidly expanding, and numerous AM machine providers have been accessible. While the mechanical and physical properties of something like the subsequent parts are occasionally superior to those of the started to bring contemporaries, reproducibility as well as standardization continues to be a challenge. Microstructural imperfections from either the resources or the procedures seem to be the consequence of the questionable reproducibility, and their characterization can always be accomplished using a variety of methods. To increase the growth of additive manufacturing, the technology cycle must be rethought. Although many instruments are already obtainable for its segments (design optimization and process simulation), this still simply lacks unification and competence. Additionally, the incorporation of production restrictions into design techniques is still very much in infant stages, even though other methods and techniques have also been reported. Strength analysis is a very important challenging issue caused by a variety of manifestations such as anisotropy, porosity, and residual stress. Numerous cost-effective examples exist in the aviation sector, where expense, as well as weight savings, has been validated. Due to the widespread acceptance of its prospects, endeavor requests are indeed being started opening to fund its further growth (namely, ESA Initiatives). Notwithstanding, their application would be limited to difficult components (concerning the material composition, shape, and/or weight) [42].

2.1. Parameters Selection for Invar 36 Processing. Owing to its poor correlation of thermodynamic enlargement, Invar 36 (I36) might have acquired tremendous prominence in a variety of industrial sectors, which include the aerospace industry. The goal of this article is to provide a summary of the study necessities in metal 3D printing. A comprehensive investigation of the effect of processing variables on the reliability of the components manufactured is introduced. This research is helpful for such additive manufacturing

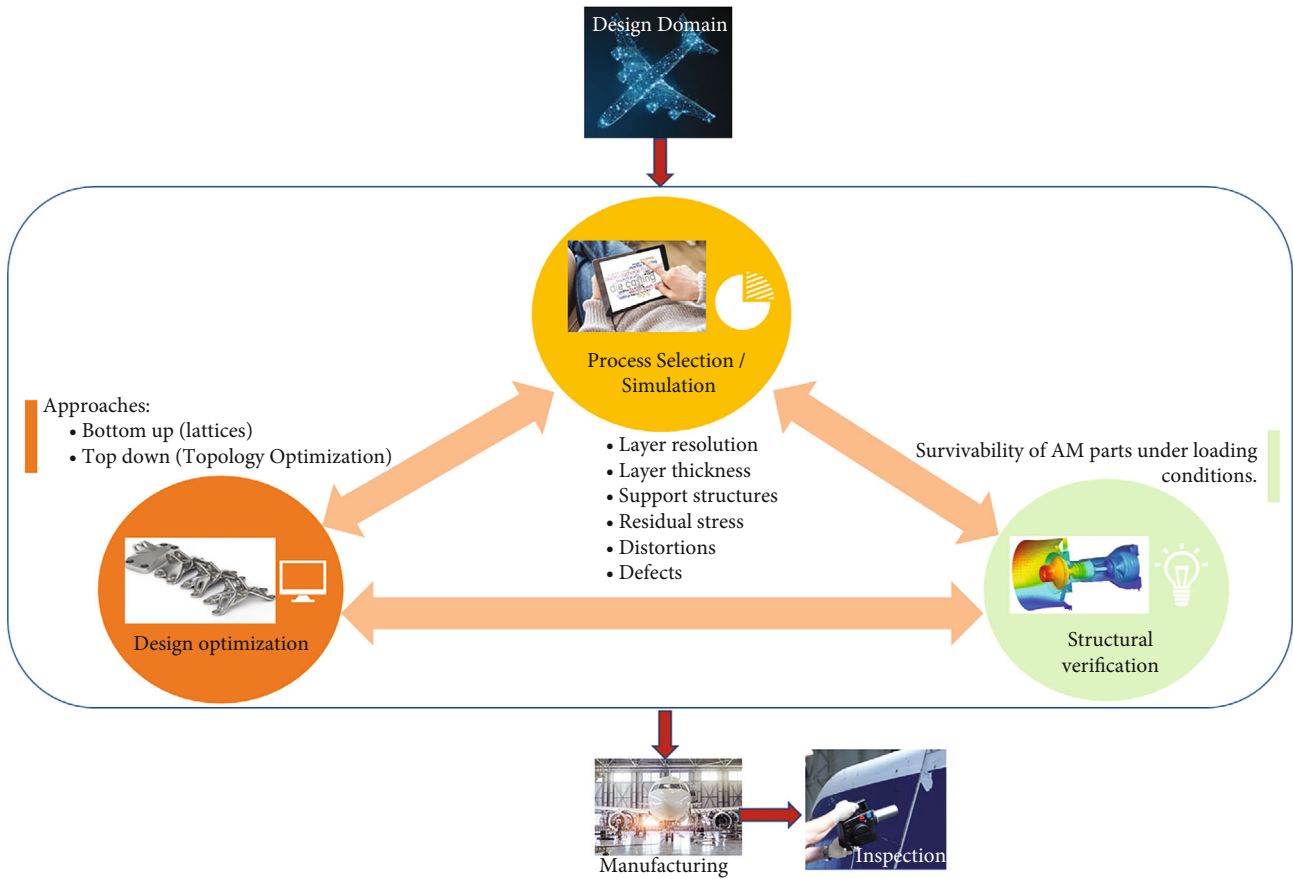


FIGURE 1: Manufacturing cycle.

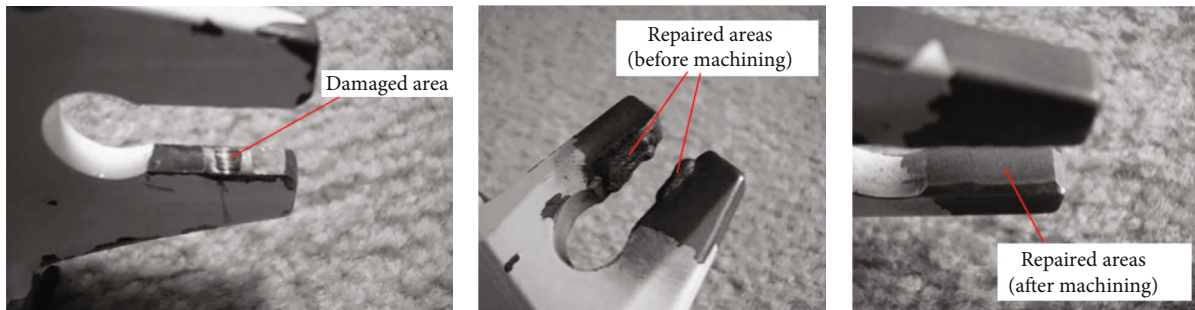


FIGURE 2: Repairing using direct energy deposition method [45].

company’s long-term development. The purpose of this article is to determine the processing variables necessary for fabricating dense components from I36 (UNS K93600) just using the selective laser melting method. Using only SLM equipment, an organization of cubes has been manufactured utilizing processing variables from I36 particles. Researchers evaluated the density, microstructures, and surface features among those cubes. Data gathering procedures were used to generate obtained data. The article discusses the effect of process variables upon this density of the components manufactured and establishes and suggests collections of SLM production variables for manufacturing high-density Invar 36 parts and structural features. Invar 36 is well-known in

the aviation sector for some of its minimal coefficients of thermodynamic development. It could be used in a variety of implementations requiring a high degree of strength properties. This comprehensive study conducts a thorough analysis of the effect of SLM processing conditions upon the density of components manufactured from I36.

For all of this research, the maraging steel 18Ni (300) is often been using factors that can explain a benchmark. The research reveals also that the density of something like the laser energy does indeed have a significant effect somewhat on the density of either the components manufactured. The density enhances proportionately to this same energy density till the reaches a certain point affiliated to melting.

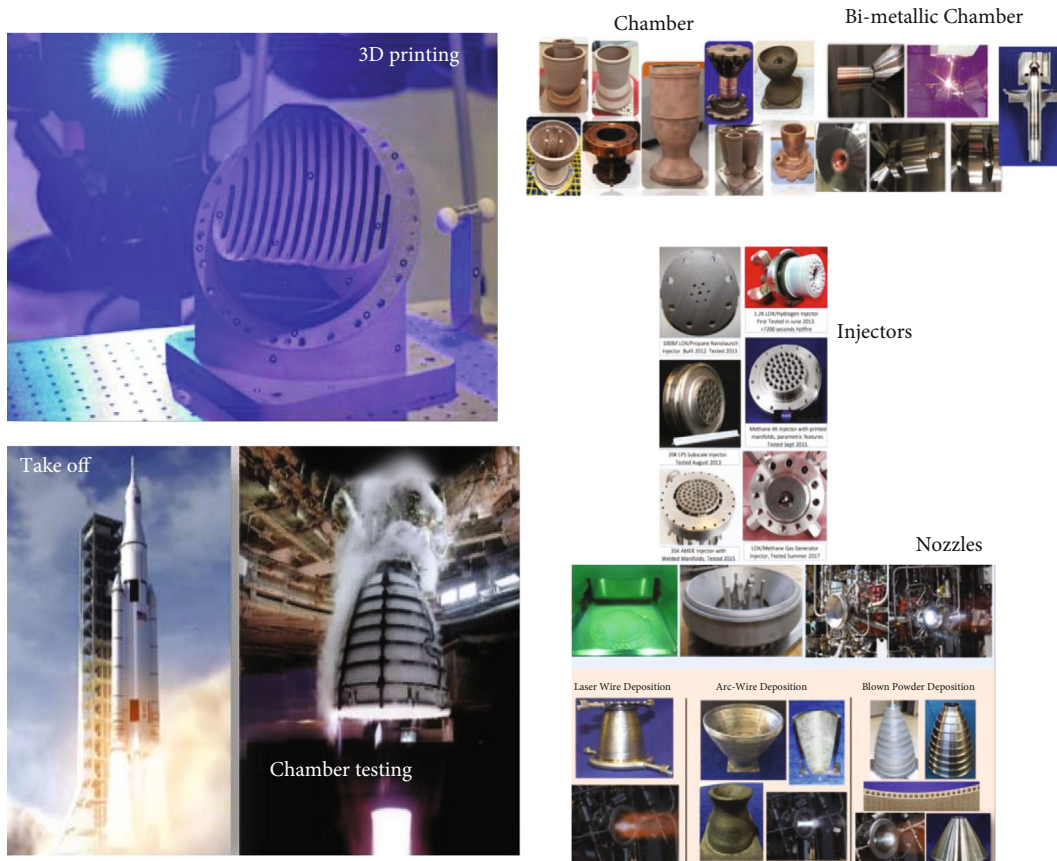


FIGURE 3: Engine parts are 3D printed [53]. (Courtesy: NASA).

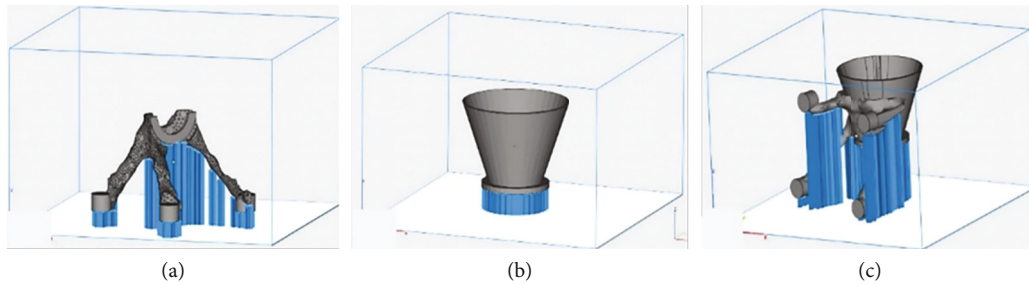


FIGURE 4: Antenna manufactured as 3 parts with topology optimized [54].

Following that, this same part is probably quality degrades as a result of thermal stresses and stimulated residual stresses. The assessment determined that I36 requires a sequence of SLM processing variables capable of generating roughly 60 to 75 J/mm³ of laser energy density to disintegrate completely (maraging steel requires approximately 67.5 J/mm³). Even though I36 seems to have a relatively low thermal conductivity compared to maraging steel, it does have an elevated energy density due to its relatively high thermal decomposition point. Thus, I36 requires a high amount of laser energy to melt completely. The proposed energy density variation may have an effect on other factors, such as component density and microstructure. Among those same

variables are percent elongation, tensile strength, hardness and residual stress. As a result, additional tests are required to analyze additional confounding variables. These experiments could perhaps establish the optimal range of laser energy densities necessary to completely melt I36 without impairing its efficiency [43].

3. Optimization and Characterization of Surface Texture

The discipline of additive manufacturing (AM) is accelerating its growth, to novel printing technologies and alterations to existing techniques being introduced daily. Powder bed

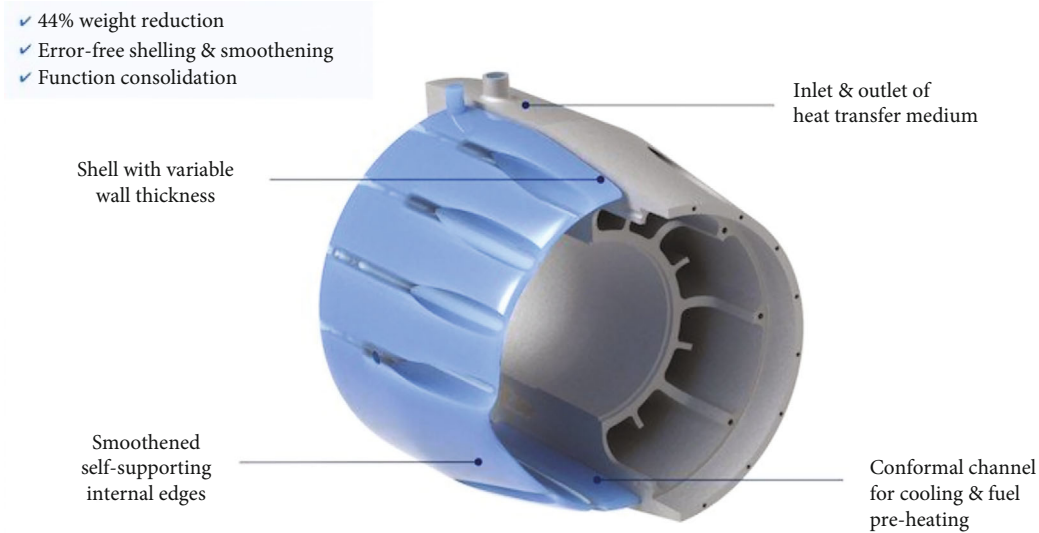


FIGURE 5: Optimized housing [55]



FIGURE 6: RF antenna [56]

fusion (PBF) needs to stand out among the numerous additive manufacturing (AM) technology solutions as the primary methodology for fabricating metallic parts for aircraft components. This article will discuss this same texture and modeling of metal part surfaces manufactured by PBF. Although the exterior texture among those parts is extremely complex and unique, it is necessary to understand their distinctive character to accurately characterize those. This section covers the best practices for determining the surface texture of PBF-built parts depending on the printed module's surface properties, optimizing the surface textures even during the construction phase and utilizing various surface modification methodologies (postprocessing) to

achieve smooth surfaces. For the aviation sector, additive manufacturing is an advisable method for producing sophisticated configurations with optimized weight reductions and economic viability. Nevertheless, the printing technology produces a considerable amount of surface roughness. Those certain surfaces seem to be extremely challenging to characterize and analyze. There has been a sequence of procedures that could be taken as the best techniques to ensure that surface roughness values have been reported adequately in the publications. Nonetheless, this outer layer can be optimized using a variety of surface modification methods; however, sacrificial metal should always be incorporated into the component to facilitate a surface smooth finish.

A surface treatment methodology's ability to remove surface stress growers including such notches and incompletely melted granules seems to be extremely coveted for outstanding mechanical efficiency. Numerous surface finishing techniques have been shown to significantly enhance the mechanical effectiveness of additively manufactured components. Nevertheless, the body of knowledge on this subject is extremely unpredictable, of research findings utilizing a variety of distinct fatigue tests on some kind of variety of distinctive materials for a variety of varying alloys with a wide assortment of various surface modification procedures. Additionally, the surface finish assessments disclosed in the publications are hard to comprehend leading to a shortage of sufficient data to assign a purposeful value toward the disclosed surface roughness criterion. Additionally, there may be an evident lack of available standardized data that provides an even more complete picture of the influence of surface modification on parts' mechanical characteristics [44].

4. Impact of MAM in Aerospace

MAM has progressed itself from early life in investigation towards the manufacturing of a diverse array of commercial

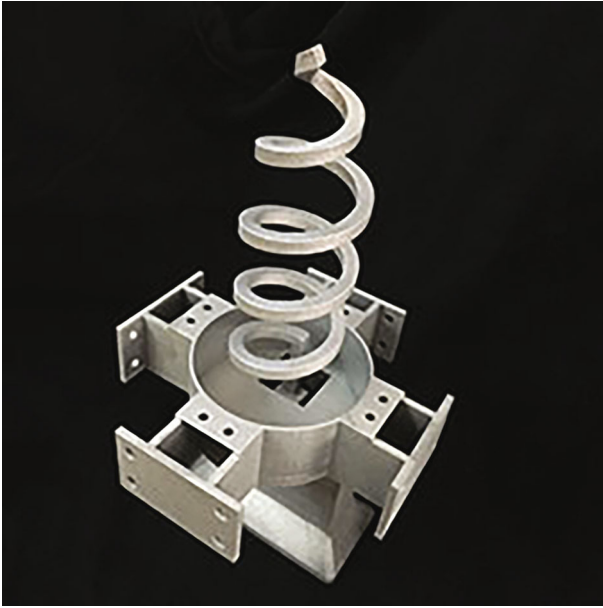


FIGURE 7: Antenna with feed [57]

application areas. Metal additive manufacturing is particularly famous in the aviation industrial sector at the moment for manufacturing and also repairing numerous parts for commercial and military airplanes and also external spacecrafts. To begin, the categories of additive manufacturing technologies some of which are frequently often used in fabricating metallic components. Whereupon, the transformation of metal additive manufacturing throughout the aviation sector is discussed, from designing to fabrication rocket engines as well as internal structures. Additionally, current unresolved issues preventing metal additive manufacturing from having entered widespread adoption in the aviation sector are explored, including standardization, sustainability, qualification, and also supply chain development.

Figure 2 reveals the repairing of a component using direct energy deposition additive manufacturing method. As MAM progresses to emerge, the aviation sector is preparing to ensure its success. While concerns about part certification, as well as sustainable development, persist, considerable advancement is anticipated in the coming years as governing agencies and business professionals collaborate to demonstrate guidelines and competencies for metal additive manufacturing. Major benefits of additive manufacturing, especially its design adaptability and a low waste of materials, had already resulted in the assimilation of metal AM in and out of numerous aviation producers' ongoing and prospective manufacturing lines. Looking at the latest manufacturing great successes, it has become clear that metal additive manufacturing will possess a lengthy influence somewhat on the aviation sector, laying the groundwork during the succeeding generation for designing products [45].

4.1. Design for Aerospace MAM. Our conversation will cover best practices for determining the surface texture of PBF-built

parts depending on the printed module's surface properties, optimizing the surface textures even during the construction phase and utilizing various surface modification methodologies (postprocessing) to achieve smooth surfaces. [46].

5. Aerospace Alloys

In the case of considering aerospace material, the list is very long, and in the survey, only a few alloys taken not on no specific options are chosen for the selection of the following alloys. One of the alloys used in aerospace is Inconel 625, while attempting for WAAM technique, and it reveals very fine columnar equiaxed grain formation and has no sign of secondary dendrites. So, this material shows the required strength which could be adopted for the aerospace industry [47]. Other than this alloy, titanium and nickel alloy is discussed.

5.1. Ti-6Al-4V. All microstructure simulation tools demonstrate the critical nature of developing an integrated and generalized concept for the MAM methodology as a feature of melt pool topography and resulting microstructure. To accomplish an exact simulation, establishing databases, respectively, and recognizing phenomena are the optimal methods for filling on some discrepancies at the moment. Additionally, it is critical to understand developing model because all anticipated outcome does not result in innovative perspectives. When simulating crystalline structure throughout MAM, it is preferable to create methods that contain essential guidelines or concept parts from whom the quite complicated crystalline structure, as well as texture, could indeed establish on their own. Alternatively, these same simulation models are just not suggestive and are mere representations of existing knowledge [48].

By utilizing additive manufacturing, researchers were prepared to create a versatile dimensional nanopositioning deformation to increase mechanical deformation and bandwidth encapsulated within a simple design. To begin, it characterized the material characteristics of EBM-printed Ti-6Al-4V bridges and especially compare them to the others of bulk metal bridges. Researchers discovered that, due to the porosity over surfaces, the printed bridges behaved like a smooth surface with such an estimated mean Young's modulus of 41 Giga Pascal since less than the uppermost dimensions were considered [49].

Various process specifications could be researched utilizing Ti6Al4V diamond-like formations and demonstrated heretofore unidentified data about the microstructure and mechanical characteristics of cellular structures. To begin, in the aspects of process parameters, lateral fasteners should indeed be avoided, except if the orientation of something like the force applied would be recognized and can be adequately substantiated by any of the other stiffeners. Furthermore, heat treatment methods had the same influence on all constructing orientations. It is recommended that the results, as well as conclusions from any of the actual work, be considered when developing additive manufacturing processes for metallic cellular structures for aviation applications [50].

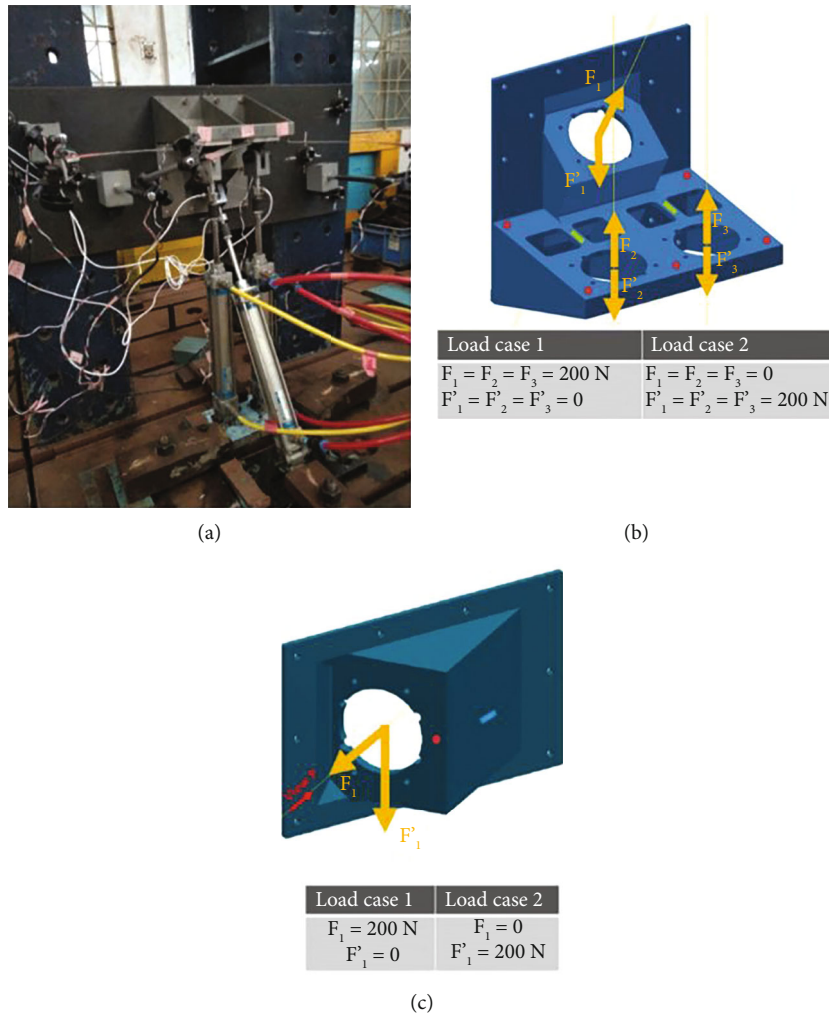


FIGURE 8: Brackets [58].

5.2. *Inconel 718*. Inconel 718 seems to be an extensively utilized alloy in metal additive manufacturing due to its broad scope of implementations in aerospace, gas turbines, and other high-temperature structural parts. Owing to its capacity to control microstructure, mechanical characteristics, and maintain high accuracy, the DED methodology had already been extensively used for aviation parts restoration. The findings manufactured while collaborating with DED on aviation parts repair were analyzed to determine the difficulties experienced throughout the methodology. Numerous issues have always been evidenced, including the appearance of micropores at the component’s edges and alteration inside the microstructure to increase diffusion height. As more than just a result, the research concentrated on demonstrating the DED process’s utility in repairing metallic aviation parts and recognizing the obstacles associated with the component’s geometric shapes and metallurgical characteristics [51].

6. Aerospace Components

6.1. *Flap Lever*. Weight enhancement and cost savings on build to fly ratio, fuel costs, and time-to-market, combined

with the convenience of personalization via additive manufacturing, could very well offer one such product an advantage. The generic remarks of numerous constraints and their potential implementation to an important system aviation part (flap lever) might very well pave the way for more practical deployment of crucial aviation components to comparable design purposes [52].

6.2. *Rocket Engine Parts*. Impactful hot-fire going to test of even a full-scale additive manufacturing component that will be airlifted on NASA’s (SLS (Space Launch System)) RS-25 Pogo Z-Baffle—reduced sophistication from 127 to 4 welds by utilizing an established DFAM [53]. Figure 3 shows the 3D-printed aerospace engine parts.

6.3. *Satellite Antenna*. Figure 4 compares the support structures created whenever the horn, as well as antenna bracket, has always been printed separately here to support structures produced even before their interfaces were indeed combined. Material utilization information for building parts and fabrication structural components could be estimated using software specific to the AM machine’s equipment set.

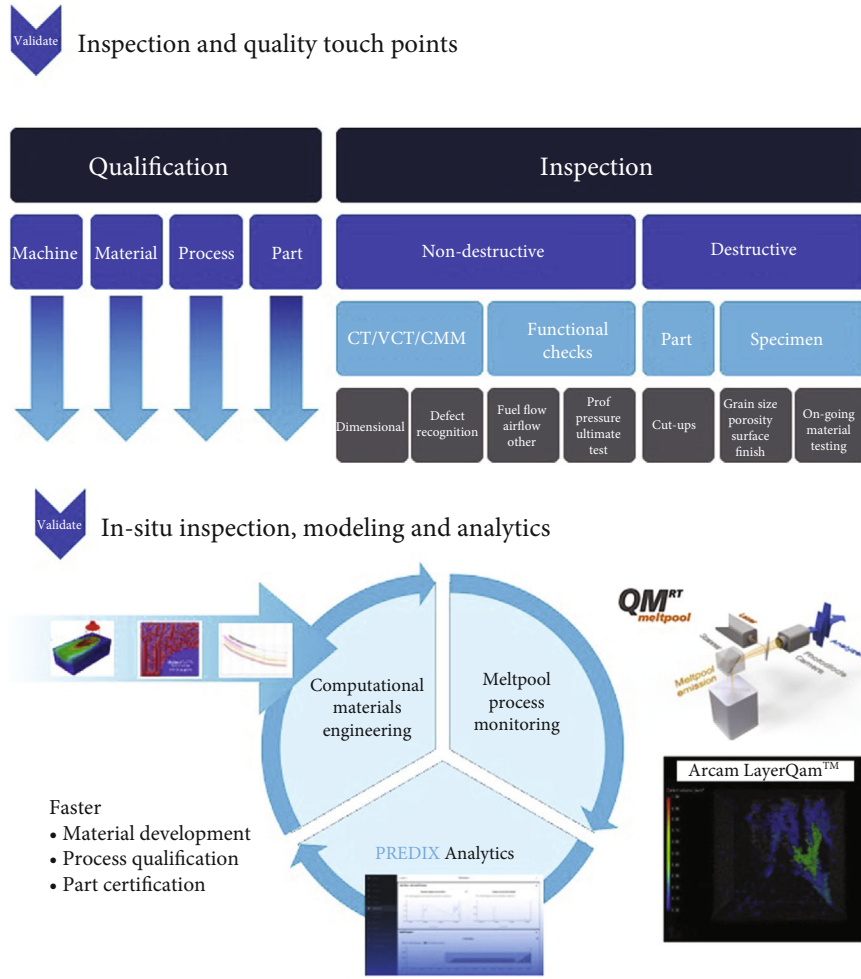


FIGURE 9: Certification cycle by GE [59].

Figures 4(a) and 4(b) illustrate the bracket and horn produced separately, with the required support structures indicated in blue. The horn and bracket are shown in Figure 4(c); within that configuration, the part has been positioned in the AM equipment of this same horn polishing prerequisites, as its reliability seemed to be crucial for the antenna’s core function. As a result, a significant portion of assistance must have been engendered during the bracket’s production process, influencing the quantity of material available for consumption, and, consequently, the weight starts changing feature [54].

6.4. Turbogenerator Casing. Enriquez, Chief Executive of KW MicroPower, begins to question just why someone might require to recognize any of it other than the 44 percent weight savings. This same newly configured housing of microturbine generator incorporates a conformal cooling channel established through differential shelling and automated smoothing. Figure 5 reveals the optimized housing [55].

6.5. RF Feed Antenna. The part seems to be an antenna based on RF feed something that was installed on the

GSAT-19 telecommunication satellite, which was launched by India’s largest launch vehicle forever, is GSLV Mk III D1 (Geosynchronous Satellite Launch Vehicle). Figure 6 represents the RF feed antenna [56].

6.6. Antenna Integrated Helix Feed. The “Antenna Incorporated Helix Feed” would be a component of a transmit antennas scheme that amplifies radio frequency signals. RF waves have always been typically carried by helical geometric shapes, and an electron beam has always been allowed to pass axial direction and segmentation-based helical configuration. There at the edge of the helical configuration, the RF wave and the electron beam converge, actually resulting inside of that this amplified RF wave. In summary, helical geometries do seem to be difficult to fabricate using traditional manufacturing methodologies without experiencing significant errors or waste. Anyway, to Additive Manufacturing’s freedom, helical frameworks also seem to be difficult to fabricate. Wipro 3D skilfully realized the “Antenna Incorporated Helix Feed” by leveraging its specialized powder bed method know-how. Figure 7 represents the antenna integrated helix feed [57].

TABLE 2: Major variants of MAM for aerospace.

| S. no | Technique | Parameters | Scale factor* | Reference |
|------------------------------|-----------|--|---------------|-----------|
| 1 | L-PBF | Part complexity | 10 | [60] |
| | | Accuracy | 10 | [61] |
| | | Surface finish | 9 | [62, 63] |
| | | Overall cost savings | 2.5 | [64, 65] |
| | | Material utilization | 3 | [64, 65] |
| | | Efficiency | 5 | [66] |
| | | Postprocessing requirements | 3 | [67, 68] |
| | | Mechanical properties | 5 | [69, 70] |
| | | Platform flexibility | 2 | [71, 72] |
| | | Maximum volume available | 5 | [73, 74] |
| | | Building rates | 2 | [60] |
| | | Defects | 9 | [75] |
| | | Contamination risk | 8 | [76] |
| | | Safety—prone to fire | 9 | [77] |
| | | Energy consumption | 5 | [78] |
| | | Dimensional accuracy | 10 | [63] |
| | | Build speed for Ti6Al4V | 10 | [78] |
| | | Maximum build volume | 6 | [78] |
| | | Minimum layer thickness | 10 | [63, 79] |
| | | Good surface roughness | 10 | [62] |
| | | Overall cost | 8 | [80] |
| | | Machinery cost | 7 | [81] |
| | | Raw material cost | 9 | [82] |
| | | Operational cost | 8 | [83] |
| | | Maintenance cost | 8 | [84] |
| | | Markforged; metal X (gen 2) 300 × 220 × 180 mm | — | [85] |
| | | Renishaw; RenAM 500 M— 250 mm × 250 mm × 350 mm | — | [86] |
| | | E.O.S; EOS M400 400 mm × 400 mm × 400 mm | — | [87] |
| | | AddUp; FormUp 350 350 mm × 350 mm × 350 mm | — | [88] |
| | | MetalFAB1 420 × 420 × 400 mm | — | [89] |
| | | XACT metal; XM300C (1118 × 711 × 1397 mm) | — | [90] |
| | | Part complexity | 9 | [60] |
| Accuracy | 9 | [61] | | |
| Surface finish | 8 | [62] | | |
| Overall cost savings | 2 | [64, 65] | | |
| Material utilization | 3 | [64, 65] | | |
| Efficiency | 5 | [66] | | |
| Post processing requirements | 3 | [67, 68] | | |
| Mechanical properties | 6 | [69, 70] | | |
| Platform flexibility | 2 | [71, 72] | | |
| Maximum volume available | 4 | [73, 74] | | |
| Building rates | 5 | [60] | | |
| Defects | 9 | [75] | | |

TABLE 2: Continued.

| S. no | Technique | Parameters | Scale factor* | Reference |
|-------|-----------|---|---------------|-----------|
| | | Contamination risk | 8 | [76] |
| | | Safety—prone to fire | 9 | [77] |
| | | Energy consumption | 8 | [91] |
| | | Dimensional accuracy | 9 | [92] |
| | | Build speed for Ti6Al4V | 9 | [93] |
| | | Maximum build volume | 3 | [78] |
| | | Minimum layer thickness | 9 | [94] |
| | | Good surface roughness | 8 | [62] |
| | | Overall cost | 10 | [80] |
| | | Machinery cost | 9 | [81] |
| | | Raw material cost | 7 | [82] |
| | | Operational cost | 6 | [95] |
| | | Maintenance cost | 8 | [96] |
| | | Arcam EBM spectra H 1,328 x 2,344 x 2,858 mm | — | [97] |
| | | Arcam EBM spectra L 1,328 x 2,344 x 2,858 mm | — | [98] |
| | | Freemelt ONE 100 mm H x 100 mm Dia | — | [99] |
| | | Tada electric EZ300 250 x 250 x 300 mm | — | [100] |
| | | Y150 China 150 x 150 x 180 mm | — | [101] |
| | | Part complexity | 8 | [60] |
| | | Accuracy | 6 | [61] |
| | | Surface finish | 7 | [63, 93] |
| | | Overall cost savings | 4 | [64, 65] |
| | | Material utilization | 6 | [64, 65] |
| | | Efficiency | 5 | [66] |
| | | Post processing requirements | 3 | [67, 68] |
| | | Mechanical properties | 7 | [69, 70] |
| | | Platform flexibility | 5 | [73, 74] |
| | | Maximum volume available | 8 | [73, 74] |
| | | Building rates | 5 | [60] |
| | | Defects | 9 | [75] |
| 3 | LMD | Contamination risk | 8 | [76] |
| | | Safety—prone to fire | 9 | [77] |
| | | Energy consumption | 7 | [102] |
| | | Dimensional accuracy | 7 | [66] |
| | | Build speed for Ti6Al4V | 10 | [93] |
| | | Maximum build volume | 8 | [103] |
| | | Minimum layer thickness | 6 | [93] |
| | | Good surface roughness | 7 | [63, 93] |
| | | Overall cost | 6 | [80] |
| | | Machinery cost | 5 | [104] |
| | | Raw material cost | 6 | [104] |
| | | Operational cost | 2 | [104] |
| | | Maintenance cost | 4 | [105] |
| | | | — | [106] |

TABLE 2: Continued.

| S. no | Technique | Parameters | Scale factor* | Reference |
|-------|-----------|------------------------------|---------------|------------|
| | | OPTOMECC; LENS CS 800 AM CA | | |
| | | 2997 × 2840 × 2662 mm | | |
| | | InssTek MX-standard | — | [107] |
| | | 800 × 1000 × 650 mm | | |
| | | Part complexity | 5 | [60] |
| | | Accuracy | 2 | [108, 109] |
| | | Surface finish | 3 | [110] |
| | | Overall cost savings | 8 | [64, 65] |
| | | Material utilization | 9 | [64, 65] |
| | | Efficiency | 9 | [111] |
| | | Post processing requirements | 6 | [67, 68] |
| | | Mechanical properties | 9 | [69, 70] |
| | | Platform flexibility | 8 | [73, 74] |
| | | Maximum volume available | 9 | [73, 74] |
| | | Building rates | 10 | [112] |
| | | Defects | 0 | [75] |
| | | Contamination risk | 0 | [66] |
| | | Safety on fire | 9 | [109] |
| 4 | WAAM | Energy consumption | 9 | [113] |
| | | Dimensional accuracy | 5 | [66] |
| | | Build speed for Ti6Al4V | 5 | [114] |
| | | Maximum build volume | 10 | [114] |
| | | Minimum layer thickness | 3 | [115] |
| | | Good surface roughness | 3 | [116] |
| | | Overall cost | 2 | [80] |
| | | Machinery cost | 2 | [117] |
| | | Raw material cost | 0 | [118] |
| | | Operational cost | 0 | [83] |
| | | Maintenance cost | 2 | [117] |
| | | AML3D ARCEMY | — | [119] |
| | | METAL XL | — | [120] |
| | | GEFERTEC-3DMP | — | [121] |

6.7. *Rocket Brackets.* Two different types of brackets for aviation implementations have always been created using LPBF/DMLS additive manufacturing process, pressure preheating, and meticulous categorization. Figure 8 represents the rocket brackets.

By having to add supplemental stock to relatively thin zones and attempting to remove in postprocessing, the deformation observed on relatively thin zones might have been prevented. Mechanical characteristics throughout the stress-relieved state encounter ASTM F 3184-16 requirements, as well as the obtained characteristics, are comparable to those of molded products. Sometimes in remedy strengthened conditions, the LPBF technique seems to provide superior mechanical characteristics to benchmark molded products. Structural experimentation established that sufficient margins seem to be obtainable inside the constructed brackets through the use of the LPBF AM pathway,

and supplemental weight savings have always been frequently accomplished across topology enhancement via DfAM (Design for Additive Manufacturing) [58].

7. Certification along with Qualification

Mostly in the aviation industry, additive manufacturing is progressively has been used to create novel metal goods. Nevertheless, as is the case with other commercial materials and processes, variability in component quality and mechanical characteristics owing to potential defects, insufficient control of dimensions, residual stress surface roughness, and microstructure could perhaps consequence in designs which thus preclude the utilization of a component in high-value or mission-critical applications. To guarantee quality and consistency and also to facilitate wider adoption, additively manufactured (AM) hardware requires vigorous

quality control and also qualification and certification (Q&C) methods. Unfortunately, there are few high-quality documents obtainable publicly, forcing aerospace companies and organizations to develop their standards. Additionally, where components and frameworks are required to be certified by regulators, requirement interpretations have all been even now progressing. This subsection discusses current quality and compliance standards for metal additive manufacturing hardware used for aviation applications from both an industry and government perspective. The existing state of Q&C standardization is summarized, and guidelines are managed to make to accelerate the adoption of metal additive manufacturing hardware in the aviation industry [59]. State-of-the-discipline quality assurance and control (Q&C) methodologies, utilized by the business sector and also government to regulate AM materials, procedures, and components, have indeed been summarized [122–125]. Figure 9 shows the certification cycle by GE.

Table 2 enlists the quality parameters considered for major variants of AM techniques which were used predominantly for manufacturing of aerospace components. Scale factor in Table 2 denotes the impact of the process parameter over the AM technique to render quality products.

8. Concluding Remarks

MAM in aerospace is a wider coverage from manufacturing a minor component to complete engine and further leads to building the aircraft. The trend is always positive despite pandemics, and the research in this domain is never been stopped at any phase. Future prediction is up to the complete manufacturing of aircraft, and the era of MAM continues therein the manufacturing augments to aerospace. It means that printing in space accelerates than manufacturing on the earth. This technique is another way to emphasize interplanetary movements. The scope of this article is initiated with the manufacturing cycle; thereby, the discussion about the aerospace manufacturing cycle, therein, flows through over the design phase and followed by the process parameter selection. The immediate effect after printing is evaluation parameters, therein surface texture analysis is discussed. Thereby, it kindles to discuss the specific alloys which are widely used in the aerospace industry, and titanium alloy and Inconel alloys are discussed. This analysis paves a path for the utilization of these characters into specific components that are being discussed in this segment. Therein, the impact of this MAM over the aerospace sector and the guidelines to decision making on a suitable variant of MAM are discussed. Finally, the qualification and certification procedures are discussed, thereby concluding with the future scope of MAM in the aerospace sector.

Data Availability

The data used to support the findings of this study are included in the article. Should further data or information be required, these are available from the corresponding author upon request.

Disclosure

This study was performed as a part of the employment of Hawassa University, Ethiopia.

Conflicts of Interest

The authors declare that there are no conflicts of interest regarding the publication of this paper.

Acknowledgments

The authors appreciate the technical assistance provided by the Department of Mechanical Engineering, KPR Institute of Engineering and Technology, Tamilnadu, India, to complete this review. Authors sincerely acknowledge the facilities provided by KPR Institute of Engineering and Technology, India, to complete the experimental work.

References

- [1] C. George, *Specification for Control and Qualification of Laser Powder Bed Fusion Metallurgical Processes; NASA Marshall Space Flight Center: Huntsville, MSFC Technical Standard MSFC-SPEC-3717, USA, 2017.*
- [2] J. Hart, "An introduction to additive manufacturing, mechanosynthesis group, MIT," 2021, <https://www.youtube.com/watch?v=ICjQ0UzE2Ao>.
- [3] T. E. Wohlers, "Research & Development," 2005, <http://www.wohlersassociates.com/history.pdf>.
- [4] T. Wohlers and T. Gornet, "History of additive manufacturing," *Wohlers Report*, vol. 24, article 118, 2014.
- [5] T. D. Ngo, A. Kashani, G. Imbalzano, K. T. Q. Nguyen, and D. Hui, "Additive manufacturing (3D printing): a review of materials, methods, applications and challenges," *Composites. Part B, Engineering*, vol. 143, pp. 172–196, 2018.
- [6] J. Coykendall, M. Cotteleer, J. Holdowsky, and M. Mahto, "3D opportunity in aerospace and defense: additive manufacturing takes flight," *Deloitte University Press: New York, NY, USA*, vol. 1, pp. 1–28, 2014.
- [7] S. Ford and M. Despeisse, "Additive manufacturing and sustainability: an exploratory study of the advantages and challenges," *Journal of Cleaner Production*, vol. 137, pp. 1573–1587, 2016.
- [8] "Process Steps in the Metal Additive Manufacturing Workflow, Digit. Alloy," 2021, <https://www.digitalalloys.com/blog/process-steps-metal-additive-manufacturing-workflow/>.
- [9] T. T. Wohlers, R. I. Campbell, and T. Caffrey, *3D Printing and Additive Manufacturing State of the Industry: Annual Worldwide Progress Report; Wohlers Associates: Fort Collins, Wohlers Associates, USA, 2016.*
- [10] J. C. Najmon, S. Raeisi, and A. Tovar, "Review of additive manufacturing technologies and applications in the aerospace industry," in *Additive Manufacturing for the Aerospace Industry*, pp. 7–31, Elsevier Inc., Amsterdam, Netherlands, 2019.
- [11] J. P. Oliveira, T. G. Santos, and R. M. Miranda, "Revisiting fundamental welding concepts to improve additive manufacturing: from theory to practice," *Progress in Materials Science*, vol. 107, article 100590, 2020.

- [12] W. J. Sames, F. A. List, S. Pannala, R. R. Dehoff, and S. S. Babu, "The metallurgy and processing science of metal additive manufacturing," *International Materials Review*, vol. 61, no. 5, pp. 315–360, 2016.
- [13] J. J. Lewandowski and M. Seifi, "Metal additive manufacturing: a review of mechanical properties," *Annual Review of Materials Research*, vol. 46, no. 1, pp. 151–186, 2016.
- [14] T. DebRoy, H. L. Wei, J. S. Zuback et al., "Additive manufacturing of metallic components - process, structure and properties," *Progress in Materials Science*, vol. 92, pp. 112–224, 2018.
- [15] T. A. Rodrigues, V. Duarte, R. M. Miranda, T. G. Santos, and J. P. Oliveira, "Current status and perspectives on wire and arc additive manufacturing (WAAM)," *Materials*, vol. 12, no. 7, p. 1121, 2019.
- [16] T. DebRoy, T. Mukherjee, J. O. Milewski et al., "Scientific, technological and economic issues in metal printing and their solutions," *Nature Materials*, vol. 18, no. 10, pp. 1026–1032, 2019.
- [17] R. Liu, Z. Wang, T. Sparks, F. Liou, and J. Newkirk, "Aerospace applications of laser additive manufacturing," in *Laser Additive Manufacturing: Elsevier*, pp. 351–371, Amsterdam, The Netherlands, 2017.
- [18] "Arcam. EBM in Aerospace—Additive Manufacturing Taken to Unseen Heights, Arcam AB," 2021, <http://www.arcam.com/solutions/aerospace-ebm/>.
- [19] Insight_08, "Additive Manufacturing—Applications in Aerospace. Aerosp. Inst. Technol," 2021, https://www.ati.org.uk/resource/insight_08-additive-manufacturing/insight08-additive-manufacturing/.
- [20] M. O. Brien and A. L. V. Alues, "Existing Standards as the Framework to Qualify Additive Manufacturing of Metals," in *Proceedings of the 2018 IEEE Aerospace Conference*, vol. 3–10, pp. 1–10, USA, March 2018.
- [21] D. Mies, W. Marsden, and S. Warde, "Overview of additive manufacturing informatics: "a digital thread"," *Integrating Materials and Manufacturing Innovation*, vol. 5, no. 1, pp. 114–142, 2016.
- [22] A. Uriondo, M. Esperon-Miguez, and S. Perinpanayagam, "The present and future of additive manufacturing in the aerospace sector: a review of important aspects," *Proceedings of the Institution of Mechanical Engineers, Part G: Journal of Aerospace Engineering*, vol. 229, pp. 2132–2147, 2015.
- [23] C. George, *Marshall Space Flight Center. Standard for Additively Manufactured Spaceflight Hardware by Laser Powder Bed Fusion in Metals*, NASA Marshall Space Flight Center, Huntsville, AL, USA, 2017.
- [24] W. E. Frazier, "Metal additive manufacturing: a review," *Journal of Materials Engineering and Performance*, vol. 23, no. 6, pp. 1917–1928, 2014.
- [25] C. Beyer, "Strategic implications of current trends in additive manufacturing," *Journal of Manufacturing Science and Engineering*, vol. 136, no. 6, article 064701, 2014.
- [26] M. Seifi, M. Gorelik, J. Waller et al., "Progress towards metal additive manufacturing standardization to support qualification and certification," *JOM*, vol. 69, no. 3, pp. 439–455, 2017.
- [27] M. Seifi, A. Salem, J. Beuth, O. Harrysson, and J. J. Lewandowski, "Overview of materials qualification needs for metal additive manufacturing," *JOM*, vol. 68, no. 3, pp. 747–764, 2016.
- [28] M. E. Kinsella, *Additive Manufacturing of Superalloys for Aerospace Applications; United States Air Force: Green and Montgomery*, Airforce Materials Laboratory, USA, 2008.
- [29] L. Nickels, "AM and aerospace: an ideal combination," *Metal Powder Report*, vol. 70, no. 6, pp. 300–303, 2015.
- [30] https://patentscope.wipo.int/search/en/result.jsf?_vid=P11-KREIX8-75337.
- [31] D. White, "Ultrasonic object consolidation," *Patent 6519500, US*, 2003.
- [32] J. Sun, Y. Yang, and D. Wang, "Mechanical properties of a Ti6Al4V porous structure produced by selective laser melting," *Materials and Design*, vol. 49, pp. 545–552, 2013.
- [33] S. Daniele, R. Chirone, P. Lettieri, D. Barletta, and M. Poletto, "Selective laser sintering of ceramic powders with bimodal particle size distribution," *Chemical Engineering Research and Design*, vol. 136, pp. 536–547, 2018.
- [34] W. M. Steen and J. Mazumder, *Laser Material Processing*, Springer, London; New York, 2010.
- [35] A. Otto and M. Schmidt, "Towards a universal numerical simulation model for laser material processing," *Physics Procedia*, vol. 5, pp. 35–46, 2010.
- [36] M. F. Zäh and S. Lutzmann, "Modelling and simulation of electron beam melting," *Production Engineering*, vol. 4, no. 1, pp. 15–23, 2010.
- [37] J. Zhou, Y. Zhang, and J. K. Chen, "Numerical simulation of laser irradiation to a randomly packed bimodal powder bed," *International Journal of Heat and Mass Transfer*, vol. 52, no. 13–14, pp. 3137–3146, 2009.
- [38] K. Brans and O. Ponfoort, "Strengthening the industries' competitive position by the development of a logistical and technological system for "spare parts" that is based on on-demand production," 2015.
- [39] S. Bontha, N. W. Klingbeil, P. A. Kobryn, and H. L. Fraser, "Effects of process variables and size-scale on solidification microstructure in beam-based fabrication of bulky 3D structures," *Materials Science and Engineering A*, vol. 513, pp. 311–318, 2009.
- [40] J. Sampedro, I. Pérez, B. Carcel, J. A. Ramos, and V. Amigó, "Laser cladding of TiC for better titanium components," *Physics Procedia*, vol. 12, pp. 313–322, 2011.
- [41] M. Q. Chu, L. Wang, H. Y. Ding, and Z. G. Sun, "Additive manufacturing for aerospace application," in *Applied Mechanics and Materials*, vol. 798, pp. 457–461, Trans Tech Publications Ltd., Switzerland, 2015.
- [42] B. Barroqueiro, A. Andrade-Campos, R. A. F. Valente, and V. Neto, "Metal additive manufacturing cycle in aerospace industry: a comprehensive review," *Journal of Manufacturing and Materials Processing*, vol. 3, no. 3, article 52, 2019.
- [43] M. Yakout, A. Cadamuro, M. Elbestawi, and S. Veldhuis, "The selection of process parameters in additive manufacturing for aerospace alloys," *International Journal of Advanced Manufacturing Technology*, vol. 92, no. 5–8, pp. 2081–2098, 2017.
- [44] A. Diaz, "Surface Texture Characterization and Optimization of Metal Additive Manufacturing-Produced Components for Aerospace Applications," in *Additive manufacturing for the aerospace industry*, pp. 341–374, Elsevier, Amsterdam, Netherlands, 2019.
- [45] S. Mohd Yusuf, S. Cutler, and N. Gao, "Review: the impact of metal additive manufacturing on the aerospace industry," *Metals*, vol. 9, no. 12, article 1286, 2019.

- [46] M. Kamal and G. Rizza, "Design for metal additive manufacturing for aerospace applications," in *Additive Manufacturing for the Aerospace Industry*, pp. 67–86, Elsevier, Amsterdam, Netherlands, 2019.
- [47] A. Chintala, M. T. Kumar, M. Sathishkumar, N. Arivazhagan, and M. Manikandan, "Technology development for producing Inconel 625 in aerospace application using wire arc additive manufacturing process," *Journal of Materials Engineering and Performance*, vol. 30, no. 7, pp. 5333–5341, 2021.
- [48] J. Li, X. Zhou, M. Brochu, N. Provatas, and Y. F. Zhao, "Solidification microstructure simulation of Ti-6Al-4V in metal additive manufacturing: a review," *Additive Manufacturing*, vol. 31, article 100989, 2020.
- [49] H. S. Fiaz, C. R. Settle, and K. Hoshino, "Metal additive manufacturing for microelectromechanical systems: titanium alloy (Ti-6Al-4V)-based nanopositioning flexure fabricated by electron beam melting," *Sensors and Actuators A: Physical*, vol. 249, pp. 284–293, 2016.
- [50] R. Wauthle, B. Vrancken, B. Beynaerts et al., "Effects of build orientation and heat treatment on the microstructure and mechanical properties of selective laser melted Ti6Al4V lattice structures," *Additive Manufacturing*, vol. 5, pp. 77–84, 2015.
- [51] A. Shrivastava, S. Rao, B. K. Nagesha, S. Barad, and T. N. Suresh, "Remanufacturing of nickel-based aero-engine components using metal additive manufacturing technology," *Materials Today: Proceedings*, vol. 45, pp. 4893–4897, 2021.
- [52] K. V. P. Reddy, I. M. Mirzana, and A. K. Reddy, "Application of additive manufacturing technology to an aerospace component for better trade-offs," *Materials Today: Proceedings*, vol. 5, no. 2, pp. 3895–3902, 2018.
- [53] P. Gradl, O. Mireles, and N. Andrews, "Intro to additive manufacturing for propulsion systems," in *AIAA Joint Propulsion Conference*, United States, July 2018.
- [54] O. Borgue, M. Panarotto, and O. Isaksson, "Modular product design for additive manufacturing of satellite components: maximising product value using genetic algorithms," *Concurrent Engineering*, vol. 27, no. 4, pp. 331–346, 2019.
- [55] <https://www.tctmagazine.com/additive-manufacturing-3d-printing-industry-insights/aerospace-insights/ntopology-redesign-3d-printed-aerospace-housing/>-accessed.
- [56] <https://wipro-3d.com/wp-content/uploads/2019/10/space-northwestfeedcluster.pdf>.
- [57] <https://wipro-3d.com/wp-content/uploads/2019/10/space-antenna-integrated-helix-feed.pdf>.
- [58] <http://www.objectify.co.in/legacy-components-for-indian-space-industry-isro-in-metal-additive-manufacturing/>.
- [59] R. Russell, D. Wells, J. Waller et al., "Qualification and certification of metal additive manufactured hardware for aerospace applications," *Additive Manufacturing for the Aerospace Industry*, pp. 33–66, 2019.
- [60] P. Colegrove and S. Williams, *High Deposition Rate High Quality Metal Additive Manufacture Using Wire+ Arc Technology*, Cranfield University, United Kingdom, 2013.
- [61] I. Gibson, D. Rosen, B. Stucker, I. Gibson, D. Rosen, and B. Stucker, "Extrusion-based systems," in *Additive Manufacturing Technologies*, pp. 147–173, Springer, New York, NY, 2015.
- [62] B. Vayre, F. Vignat, and F. Villeneuve, "Metallic additive manufacturing: state-of-the-art review and prospects," *Mechanics & Industry*, vol. 13, no. 2, pp. 89–96, 2012.
- [63] D. Gu and D. Gu, *Laser Additive Manufacturing (AM): Classification, Processing Philosophy, and Metallurgical Mechanisms*. In *Laser Additive Manufacturing of High-Performance Materials*, Springer, Berlin, Heidelberg, 2015.
- [64] S. Bremen, W. Meiners, and A. Diatlov, "Selective laser melting," *Laser Technik Journal*, vol. 9, no. 2, pp. 33–38, 2012.
- [65] B. Vandenbroucke and J. P. Kruth, "Selective laser melting of biocompatible metals for rapid manufacturing of medical parts," *Rapid Prototyping Journal*, vol. 13, no. 4, pp. 196–203, 2007.
- [66] D. Ding, Z. Pan, D. Cuiuri, and H. Li, "Wire-feed additive manufacturing of metal components: technologies, developments and future interests," *The International Journal of Advanced Manufacturing Technology*, vol. 81, no. 1-4, pp. 465–481, 2015.
- [67] Y. F. Shen, D. D. Gu, and P. Wu, "Development of porous 316L stainless steel with controllable microcellular features using selective laser melting," *Materials Science and Technology*, vol. 24, no. 12, pp. 1501–1505, 2008.
- [68] D. Gu and Y. Shen, "Processing conditions and microstructural features of porous 316L stainless steel components by DMLS," *Applied Surface Science*, vol. 255, no. 5, pp. 1880–1887, 2008.
- [69] G. Gagg, E. Ghassemieh, and F. E. Wiria, "Effects of sintering temperature on morphology and mechanical characteristics of 3D printed porous titanium used as dental implant," *Materials Science and Engineering: C*, vol. 33, no. 7, pp. 3858–3864, 2013.
- [70] J. Banhart, "Manufacture, characterisation and application of cellular metals and metal foams," *Progress in Materials Science*, vol. 46, no. 6, pp. 559–632, 2001.
- [71] B. Graf, A. Gumenyuk, and M. Rethmeier, "Laser metal deposition as repair technology for stainless steel and titanium alloys," *Physics Procedia*, vol. 39, pp. 376–381, 2012.
- [72] S. Liu and Y. Ding, "Wire-based direct metal deposition with Ti6Al4V," *Laser 3D Manufacturing VI*, vol. 10909, article 109090J, 2019.
- [73] C. Qiu, N. J. Adkins, and M. M. Attallah, "Microstructure and tensile properties of selectively laser-melted and of HIPed laser-melted Ti-6Al-4V," *Materials Science and Engineering: A*, vol. 578, pp. 230–239, 2013.
- [74] D. Manfredi, F. Calignano, M. Krishnan et al., "Additive manufacturing of Al alloys and aluminium matrix composites (AMCs)," *Light Metal Alloys Applications*, pp. 3–34, 2014.
- [75] A. Busachi, J. Erkoyuncu, P. Colegrove et al., "A system approach for modelling additive manufacturing in defence acquisition programs," *Procedia CIRP*, vol. 67, pp. 209–214, 2018.
- [76] F. Martina, J. Mehnen, S. W. Williams, P. Colegrove, and F. Wang, "Investigation of the benefits of plasma deposition for the additive layer manufacture of Ti-6Al-4V," *Journal of Materials Processing Technology*, vol. 212, no. 6, pp. 1377–1386, 2012.
- [77] V. Brøtan, O. Å. Berg, and K. Sørby, "Additive manufacturing for enhanced performance of molds," *Procedia Cirp*, vol. 54, pp. 186–190, 2016.
- [78] V. Bhavar, P. Kattire, V. Patil, S. Khot, K. Gujar, and R. Singh, *A Review on Powder Bed Fusion Technology of Metal Additive Manufacturing*. In *Additive Manufacturing Handbook*, CRC Press, United States, 2017.
- [79] W. Ruban, V. Vijayakumar, P. Dhanabal, and T. Pridhar, "Effective process parameters in selective laser sintering,"

- International Journal of Rapid Manufacturing*, vol. 4, no. 2-4, pp. 148–164, 2014.
- [80] I. Yadroitsev, P. Krakhmalev, I. Yadroitsava, S. Johansson, and I. Smurov, “Energy input effect on morphology and microstructure of selective laser melting single track from metallic powder,” *Journal of Materials Processing Technology*, vol. 213, no. 4, pp. 606–613, 2013.
- [81] M. T. Knothe, “The Value of Metal Additive Manufacturing with Diode Lasers,” *Laser Technik Journal*, vol. 15, no. 2, pp. 58–60, 2018.
- [82] D. D. Singh, T. Mahender, and A. R. Reddy, “Powder bed fusion process: a brief review,” *Materials Today: Proceedings*, vol. 46, pp. 350–355, 2020.
- [83] R. M. Mahamood, E. T. Akinlabi, M. Shukla, and S. L. Pityana, “Laser Metal Deposition of Ti6Al4V: A Study on the Effect of Laser Power on Microstructure and Microhardness,” 2013.
- [84] N. Kretzschmar, I. F. Ituarte, and J. Partanen, “A decision support system for the validation of metal powder bed-based additive manufacturing applications,” *The International Journal of Advanced Manufacturing Technology*, vol. 96, no. 9-12, pp. 3679–3690, 2018.
- [85] <https://s3.amazonaws.com/mf.product.doc.images/Datasheets/2021-docs-folder/F-PR-5000-gen2.pdf>.
- [86] 2021, <https://resources.renishaw.com/en/details/brochure:renam20500m-industrial-additive-manufacturing-system>.
- [87] <https://www.eos.info/en/additive-manufacturing/3d-printing-metal/eos-metal-systems/eos-m-400>.
- [88] <https://addupsolutions.com/machines/pbf/formup-350/>.
- [89] <https://www.additiveindustries.com/systems/metalfab1>.
- [90] <https://xactmetal.com/wp-content/uploads/2019/10/XM300C-1.pdf>.
- [91] M. Baumers, P. Dickens, C. Tuck, and R. Hague, “The cost of additive manufacturing: machine productivity, economies of scale and technology-push,” *Technological Forecasting and Social Change*, vol. 102, pp. 193–201, 2016.
- [92] C. Arnold and C. Körner, “In-situ electron optical measurement of thermal expansion in electron beam powder bed fusion,” *Additive Manufacturing*, vol. 46, article 102213, 2021.
- [93] B. Dutta and F. S. Froes, “The additive manufacturing (AM) of titanium alloys,” *Metal Powder Report*, vol. 72, no. 2, pp. 96–106, 2017.
- [94] L. E. Murr, E. Martinez, K. N. Amato et al., “Fabrication of metal and alloy components by additive manufacturing: examples of 3D materials science,” *Journal of Materials Research and Technology*, vol. 1, no. 1, pp. 42–54, 2012.
- [95] B. Alchikh-Sulaiman, *Powder Spreading and Tribocharging for Additive Manufacturing Powder Bed Fusion Processes*, McGill University, Canada, 2020.
- [96] I. Flores, N. Kretzschmar, A. H. Azman, S. Chekurov, D. B. Pedersen, and A. Chaudhuri, “Implications of lattice structures on economics and productivity of metal powder bed fusion,” *Additive Manufacturing*, vol. 31, article 100947, 2020.
- [97] https://www.ge.com/additive/sites/default/files/2020-07/ebm_spectra%25h_bro_4.
- [98] https://www.ge.com/additive/sites/default/files/2021-08/ebm_spectra%20l_bro_4_.
- [99] https://freemelt.com/app/uploads/FreemeltONE_brochure.pdf.
- [100] http://www.tadadenki.jp/english/welding_machines/metal_3d_printer/ez300.html.
- [101] <http://www.slmetal.com/en/index.php?m=Product&a=show&id=9>.
- [102] S. Cao and D. Gu, “Laser metal deposition additive manufacturing of TiC/Inconel 625 nanocomposites: relation of densification, microstructures and performance,” *Journal of Materials Research*, vol. 30, no. 23, pp. 3616–3628, 2015.
- [103] V. Bhuvanewari, M. Priyadharshini, C. Deepa, D. Balaji, L. Rajeshkumar, and M. Ramesh, “Deep learning for material synthesis and manufacturing systems: A review,” *Materials Today: Proceedings*, vol. 46, no. 9, pp. 3263–3269, 2021.
- [104] M. Cotteleer and J. Joyce, “3D opportunity: additive manufacturing paths to performance, innovation, and growth,” *Deloitte Review*, vol. 14, pp. 5–19, 2014.
- [105] S. Huang, L. Zhang, D. Li, W. Zhang, and W. Zhu, “Comparison of the microstructure and mechanical properties of FeCrNiBSi alloy fabricated by laser metal deposition in nitrogen and air,” *Surface and Coatings Technology*, vol. 381, article 125123, 2020.
- [106] https://optomec.com/wp-content/uploads/2019/02/LENS-800-600-AM-CA_WEB0119.
- [107] http://www.insstek.com/download/insstek_mx-standard_technicaldata_v1.0.pdf.
- [108] B. A. Szost, S. Terzi, F. Martina et al., “A comparative study of additive manufacturing techniques: residual stress and microstructural analysis of CLAD and WAAM printed Ti-6Al-4V components,” *Materials & Design*, vol. 89, pp. 559–567, 2016.
- [109] J. Zhang, X. Wang, S. Paddea, and X. Zhang, “Fatigue crack propagation behaviour in wire+arc additive manufactured Ti-6Al-4V: effects of microstructure and residual stress,” *Materials & Design*, vol. 90, pp. 551–561, 2016.
- [110] A. Paskual, P. Álvarez, and A. Suárez, “Study on arc welding processes for high deposition rate additive manufacturing,” *Procedia Cirp*, vol. 68, pp. 358–362, 2018.
- [111] S. Ríos, P. A. Colegrove, F. Martina, and S. W. Williams, “Analytical process model for wire + arc additive manufacturing,” *Additive Manufacturing*, vol. 21, pp. 651–657, 2018.
- [112] J. J. S. Dilip, G. D. Janaki Ram, and B. E. Stucker, “Additive manufacturing with friction welding and friction deposition processes,” *International Journal of Rapid Manufacturing*, vol. 3, no. 1, pp. 56–69, 2012.
- [113] G. Campatelli, F. Montevicchi, G. Venturini, G. Ingarao, and P. C. Priarone, “Integrated WAAM-subtractive versus pure subtractive manufacturing approaches: an energy efficiency comparison,” *International Journal of Precision Engineering and Manufacturing-Green Technology*, vol. 7, no. 1, pp. 1–11, 2020.
- [114] A. Garcia-Colomo, D. Wood, F. Martina, and S. W. Williams, “A comparison framework to support the selection of the best additive manufacturing process for specific aerospace applications,” *International Journal of Rapid Manufacturing*, vol. 9, no. 2-3, pp. 194–211, 2020.
- [115] D. H. Ding, Z. X. Pan, C. Dominic, and H. J. Li, “Process Planning Strategy for Wire and Arc Additive Manufacturing,” in *International Conference on Robotic Welding, Intelligence and Automation*, pp. 437–450, Springer, Cham, 2015.
- [116] J. Xiong, Y. J. Li, Z. Q. Yin, and H. Chen, “Determination of surface roughness in wire and arc additive manufacturing based on laser vision sensing,” *Chinese Journal of Mechanical Engineering*, vol. 31, no. 1, pp. 1–7, 2018.

- [117] S. Jhavar, "Wire arc additive manufacturing: approaches and future prospects," in *Additive Manufacturing*, pp. 183–208, Woodhead Publishing, United Kingdom, 2021.
- [118] S. C. Joshi and A. A. Sheikh, "3D printing in aerospace and its long-term sustainability," *Virtual and Physical Prototyping*, vol. 10, no. 4, pp. 175–185, 2015.
- [119] <https://aml3d.com/technology/>.
- [120] <https://mx3d.com/services/metalxl/>.
- [121] <https://www.gefertec.de/waam-technologie/>.
- [122] N. Anbuezhian, M. Priyadharshini, A. K. Balaji Devarajan, and L. R. Priya, "Machine learning frameworks for additive manufacturing – a review," *Solid State Technology*, vol. 63, no. 6, pp. 12310–12319, 2020.
- [123] M. Ramesh, L. Rajeshkumar, and D. Balaji, "Influence of process parameters on the properties of additively manufactured fiber-reinforced polymer composite materials: a review," *Journal of Materials Engineering and Performance*, vol. 30, no. 7, pp. 4792–4807, 2021.
- [124] L. Thijs, F. Verhaeghe, T. Craeghs, J. Van Humbeeck, and J. P. Kruth, "A study of the microstructural evolution during selective laser melting of Ti-6Al-4V," *Acta Materialia*, vol. 58, no. 9, pp. 3303–3312, 2010.
- [125] N. Hrabe, T. Gnäupel-Herold, and T. Quinn, "Fatigue properties of a titanium alloy (Ti-6Al-4V) fabricated via electron beam melting (EBM): effects of internal defects and residual stress," *International Journal of Fatigue*, vol. 94, pp. 202–210, 2017.

Research Article

Tribological Characteristics of GCI-EN31 Steel Surface Contact with Dry Sliding Condition

S. Ananth ¹, P. Sivaprakasam ², J. Udaya Prakash ³, B. Ravi ⁴, G. Kalusuraman ⁵,
and R. Sundarakannan ⁶

¹Department of Mechanical Engineering, Vardhaman College of Engineering, Shamshabad, Hyderabad, Telangana, India

²Department of Mechanical Engineering, College of Electrical and Mechanical Engineering, Addis Ababa Science and Technology University, Addis Ababa, Ethiopia

³Department of Mechanical Engineering, Vel Tech Rangarajan Dr. Sagunthala R&D Institute of Science and Technology, Chennai, Tamil Nadu, India

⁴Department of Mechanical Engineering, Swarna Bharathi Institute of Science and Technology, Khammam, Telangana, India

⁵Department of Agricultural Engineering, Kalasalingam Academy of Research and Education, Krishnankoil, Tamil Nadu, India

⁶Institute of Agricultural Engineering, Saveetha School of Engineering, SIMATS, Chennai, Tamil Nadu, India

Correspondence should be addressed to P. Sivaprakasam; shiva@aastu.edu.et

Received 19 March 2022; Accepted 22 April 2022; Published 11 May 2022

Academic Editor: V. Vijayan

Copyright © 2022 S. Ananth et al. This is an open access article distributed under the Creative Commons Attribution License, which permits unrestricted use, distribution, and reproduction in any medium, provided the original work is properly cited.

Grey cast iron (GCI) and steel contact surface application is an inevitable component and provides good wear resistance in several applications, not only in automobiles. Grey cast iron consists of a predominantly pearlitic/ferrite matrix or both with graphite flakes. The majority of previous research works were based on three different types of wear regimes. The wear regimes enumerate the wear track morphology, wear rate, and COF of the respective application. In this research work, dry sliding wear properties of GCI and EN31 pins were examined with different sliding parameters using pin on disc wear test. The weight loss, coefficient of frictions, and surface morphology were considered for experimental analysis. Due to the transfer of wear debris from the GCI disc, the counter steel pin surface experienced a progressive reduction in wear with increasing speed and load. With 30 N and 45 N contact loads and sliding speeds up to 1 m/sec, the GCI shows marginally positive wear. The surface textures were analyzed with the help of SEM and a surface roughness tester.

1. Introduction

Loss of material due to friction was encountered more often between two contact surfaces. Wear is the most commonly encountered in prime movers, particularly due to adhesion, leading to frequent replacement of components [1]. During dry sliding conditions, the observed wear normal modes are plowing, mild, and oxidative wear. This includes useful run-in wear as well. Adhesive wear is usually described as material transfer between two surfaces. Surface-to-surface contact, even though lubricated, can occur if the lubricant film has a discontinuity, resulting in material transfer and surface damage. Cold welding takes place in dry sliding wear between two surfaces, with one of the surfaces releasing

small particles which build up or agglomerate and transfer to another surface in layers. These built-up edges can be seen in cutting tools. Grey iron is used in a variety of engineering applications, including diesel engine components such as cylinder heads, piston rings, and engine blocks, where wear is a significant factor when using wet lubrication. Grey cast iron's properties are highly dependent on the graphite morphology and volume fraction (H. Mohamadzadeh et al., [2]). Response surface methodology was used to optimize the composites' tribological behaviour. According to the optimization results, the content of seashell powders increased the wear and frictional resistance of the composites, and it was the most influential factor (V. Bhuvaneshwari et al., [3]). The ball on disc sliding wear test was used to investigate the

tribological behaviour of the alumina coating. The alumina coating was shown to reduce the COF value and wear mass loss of the GCI substrate by at least ten percent and fifty percent, respectively [4]. Wear and scratch tests revealed that EN 36C steel coated with 75: 25 YSZ-Al₂O₃ exhibits superior wear and scratch resistance when compared to the other materials [5]. A. Saravanakumar et al., [6] investigated the wear characteristics of aluminium alloy AA2219-graphite (Gr) composites in dry sliding conditions. The effect of the initial deflection angle (IDA) on the tribological properties of grey cast iron (GCI) rings with curve distributed pits in the radial direction is investigated in this study (CDPRD). The antiwear performance of samples was determined using a pin-on-disc wear test rig with a normal load of 70 N and a rotating speed of 200 rpm [7].

Austempered grey cast iron is a material with solid, light, and wear-resistant qualities. It is also a good material for high design and production adaptability, as well as being cost effective [8]. Due to its high friction coefficient, low cost, good damping property, fine castability, machinability, and other properties, grey cast iron (GCI) is one of the most commonly used materials in industrial applications (N. Sun et al., [9]). According to literature surveys [10], a small amount of free ferrite is dispersed in the region of perlite matrix. Such a matrix composition provides good wear resistance between the two sliding surfaces and in similar applications like brakes, cylinder liners, and piston rings. Another investigation describes the association of two distinct regions of grey pearlitic cast iron that were exposed during the dry sliding wear experimentation [11, 12]. In the initial region of the crystal structure, the graphite dominates to mitigate the wear rate, and its graph has linear correlation. In the consequent portion crystal region, the loss of material due to friction was driven by two thermally simulated processes, namely, in the first case, the phenolic binder was degraded thermally, and in the next case, it was driven by tribooxidation. In the second case, specific wear rate was found to be better. Ghaderi et al. [13] examined three different materials of cast iron, including nodular, grey, and condensed iron, with different chemical conformations and subjected them to austempering (process carried out at 350°C). The investigation extended to find knowledge regarding graphite morphology and comparison with the pearlitic grey iron tested with the help of a block-on-ring wear tester. Austempered nodular iron shows high impact test results compared to austempered grey iron. Cast iron and Compacted Graphite Iron revealed higher wear resistance than other types of cast iron and lower wear resistance and lower impact test results due to the presence of graphite in the microstructure.

In the dry condition of surface contact, the normal wear that occurs in GCI is quite high, and the same was stated by Chawla et al. [14] in their experimentation. At an increasing sliding speed, wear was attributed more to stainless steel, and it was softened during its increasing load factor. It is vice versa in the case of GCI, and it happened due to the existence of graphite (ferrite), and decohesion was observed.

Cho et al. [15] observed the loss of material due to the sliding properties of grey iron by changing the carbon equiv-

TABLE 1: Process parameter and their levels.

| Levels | Parameters | | |
|--------|--------------|--------------------------|---------------------------|
| | Load L (N) | Sliding speed, S (m/s) | Sliding distance, D (m) |
| 1 | 15 | 0.5 | 300 |
| 2 | 30 | 1 | 600 |
| 3 | 45 | 1.5 | 900 |



FIGURE 1: Pin-on-disc set-up used for dry sliding test.

alent (CE). On all speeds of experimentation, the GCI of flake graphite dominates good wear resistance. On the other hand, the ferrite of GCI shows no change in coefficient of friction. Hirasata et al. [16] observed the wear rate, COF, and hardness in various ranges of cast iron under heavy range conditions. At the beginning stage of sliding distance, the hardness and COF show a lower hardness with a huge loss of material due to friction, and in the later stage of high sliding speed, there is a less amount of material loss due to the presence of stable graphite particles.

Wilson et al. [17] observed the reduced wear due to the influence of oxide particles and suggested another important oxidative wear model. Liu et al. [18] evaluated the hardness properties and variation of carbide grains due to the effect of shakeout time during the solidification process and found that at high hardness and strength, the cast iron shows increased wear rate due to oxidation. R. M. Galagali et al., [19] investigated the wear behaviour of austempered ductile iron against temperature and sliding speed. The wear rate was high up to a sliding speed of 2 m/s but significantly decreased above that speed. There is a work hardening effect at room temperature caused by the conversion of the remaining austenite to martensite. This makes the metal more durable. As with elevated temperatures, a constant rate of wear was observed with a dry sliding condition that increased significantly with speed. The temperature of the hands combined with the sliding speed has a greater effect on the rate of wear. Surface texturing of grey cast iron using femtosecond pulse duration improved wear resistance compared to untextured, millisecond, and nanosecond laser-textured surfaces [20]. Surface texturing research has exploded in recent years to improve lubrication in tribological applications [21]. The research activities in the field of tribology have grown rapidly in various sectors, in terms of both scope and depth recently, according to Meng et al. [22]. Despite its good features, it must withstand application settings such as dry and lubricated sliding, which have

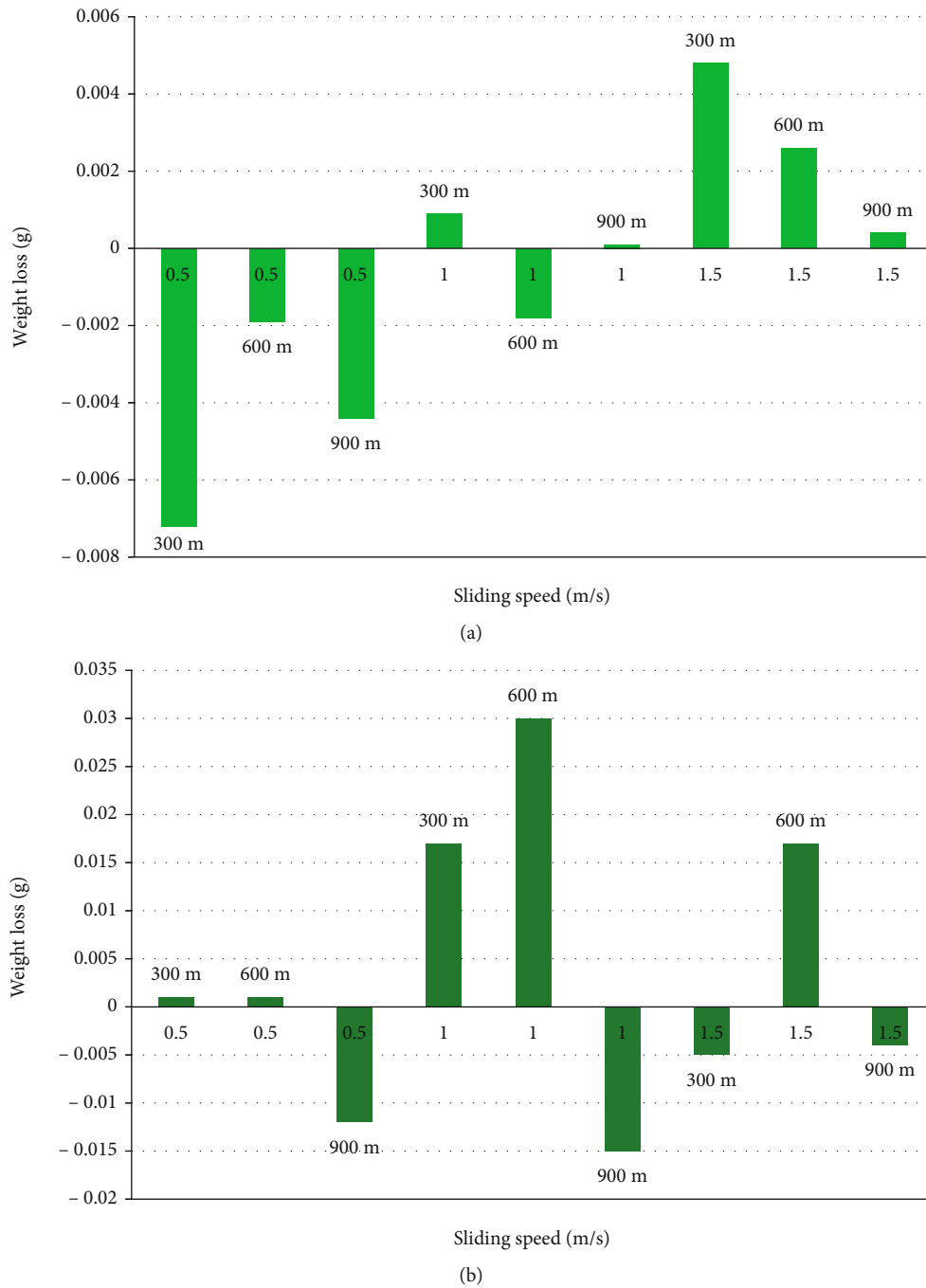


FIGURE 2: (a) Disc weight loss at 15 N and (b) pin weight loss at 15 N.

exposed positive and negative wear. Many researchers have tried to find out how grey cast iron wears. Only a few studies have talked about both the positive and negative wear behaviour of GCI.

2. Experimental Procedure

2.1. Sample Preparation and Test Parameters. In this experimentation, EN-31 is the counterpart material, and standard GCI test samples were machined to conduct the experiments [23]. Wear tests were carried out at three different param-

eters, and their levels are shown in Table 1. The test samples were prepared and experimented on the basis of the Taguchi Design of Experiment (DOE) with an Orthogonal Array (OA) of L_{27} .

2.2. Dry Wear Test. The wear test that is to be conducted in a normal atmospheric environment, and without lubrication is known as the “dry sliding wear test.” The pin-on-disc set-up used for experiments with dry sliding wear tests is shown in Figure 1. The sliding wear experiments were carried out under dry sliding conditions at room temperature

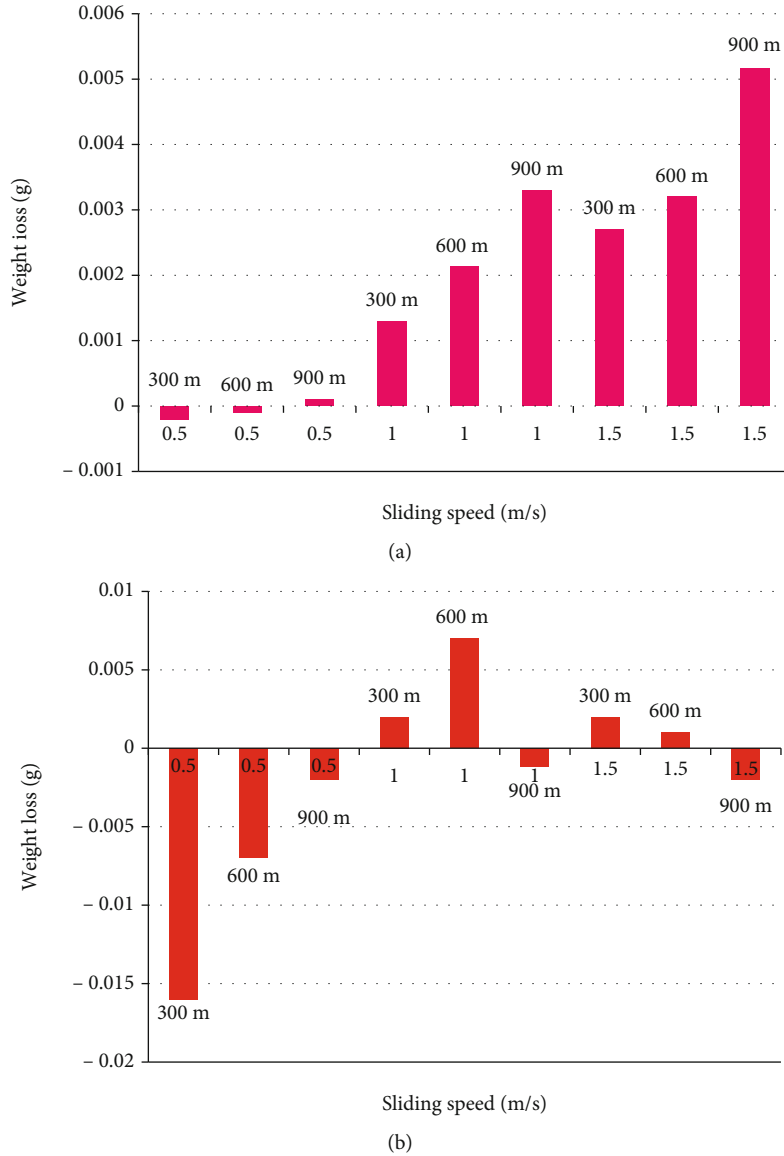


FIGURE 3: (a) Disc weight loss at 30 N and (b) pin weight loss 30 N.

in compliance with the ASTM standard G 99 [24, 25]. The EN31 pin was thoroughly cleaned using acetone. A pin was clamped at one end of the cantilever beam in a slot and tightened with the help of a screw. The cleaned disc specimen of grey cast iron was loaded on top of the circular column and tightened. To set the wear track on the disc, the pin was positioned over the disc at a 15 mm radius from the centre of the disc material.

The required weight was placed on the loading pan at the other end of the cantilever beam slowly without shaking. The wear test was started by pressing the push button on the controller panel. The necessary test parameter readings like coefficient of friction, speed, and load were noted and repeated the procedure for a suitable combination for the next test condition. The experiments were carried out on GCI discs with an outer diameter of 55 mm, an inner diameter of 6 mm, and a thickness of 10 mm. GCI has a surface hardness of 28 HRC. The counter specimen pin

EN31 was made of BS 970 steel and has a diameter of 6 mm and a length of 60 mm. Totally 27 experimental combination were performed using Taguchi-based design on experiments. The weights of pin and disc for each experiment before and after wear test measured using precision weighing machine.

3. Result and Discussion

3.1. Dry Slide Wear Study. Sliding wear tests have been conducted in a dry environment, and the test results are discussed as follows. Normally, the response of the contact surface under dry sliding depends on the material dependence PV (pressure P and sliding velocity V) factor. With increasing PV, the contact interface will be exposed to a rise in temperature and, accordingly, thermally influenced wear response will occur. Also, with heterogeneous structures such as CI, this response is more complex. This leads to

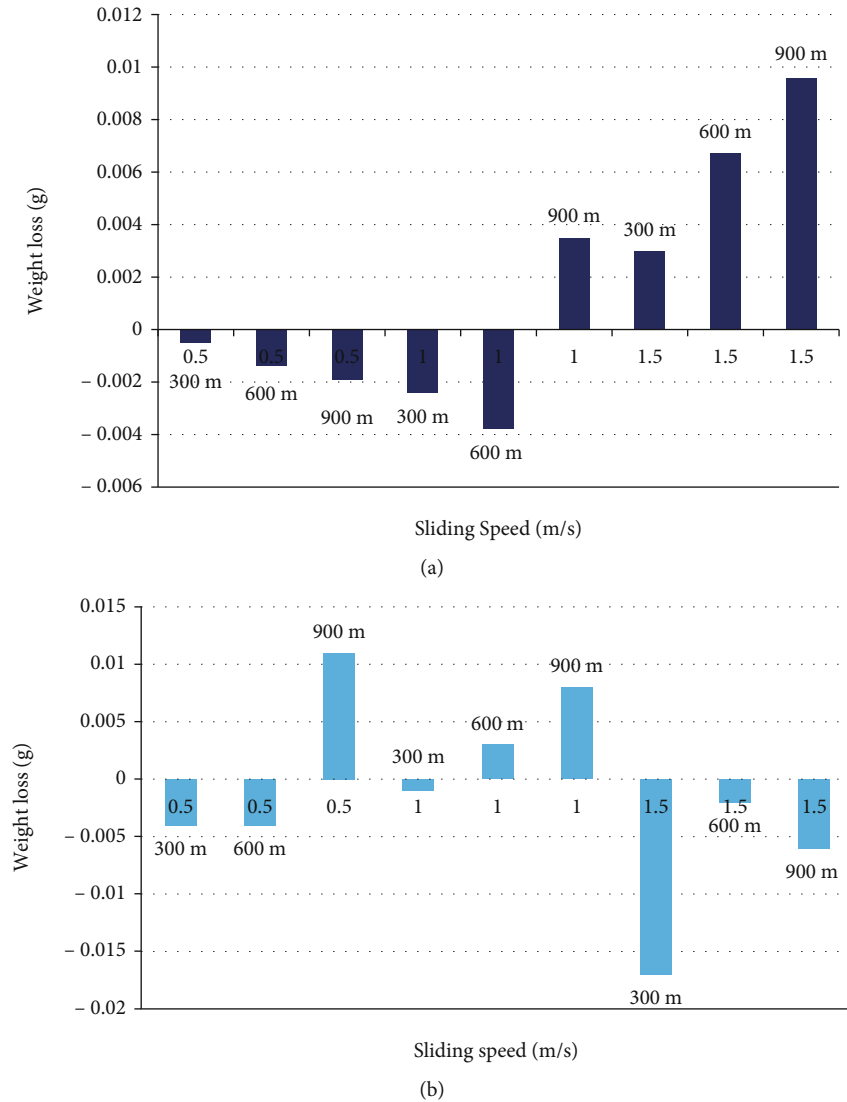


FIGURE 4: (a) Disc weight loss at 45 N and (b) pin weight loss at 45 N.

material transfer between contacting surfaces, resulting in condition-dependent -ve and +ve modes of wear.

Observation with 15 N with various sliding speeds and distances shows that while the GCI disc tends to display a reduced order of wear (due to run-in), the counter steel (pin) surface tends to show -ve approach of wear (alter suitable to transfer of wear particles) with 30 N and 45 N and both the CI disc and counter pin exhibit an increasing order of wear attributable to the significance of the PVT factor on wear.

Figure 2(a) describes the wear that occurs in both positive and negative modes with increasing sliding speed and sliding distance under a load of 15 N for the GCI disc. Figure 2(b) explains the variation of wear with increasing sliding speed and distance under load of 15 N for EN31 steel pins.

From Figure 2(a), it is evident that the GCI disc exhibits the negative wear at lower sliding speed. The wear tends to positive mode while at a sliding speed of 1 m/sec to 1.5 m/sec. It has been found that at low sliding speeds, the negative

mode of wear happens. At medium and high sliding speeds, mostly positive mode of wear has been found. The typical variation of wear of the counter steel surface at 15 N load is observed in Figure 2(b). Compared to the GCI wear track, the steel pin encounters relatively higher order wear. Mostly positive kinds of wear are observed. The observation of a +ve mode of wear for both the GCI disc and steel pin suggests little material transfer between the contacting surfaces.

Figures 3(a) and 3(b) show that with a 30 N load, the GCI disc has the least wear at 0.5 m/sec and tends to increase wear while sliding speed and distance (+ve mode). Whereas the counter steel pin's wear track begins in negative mode and tends to increase to positive mode (+ve mode) with increasing speed (i.e., greater sliding distance at 900 m), it may drop down (-ve mode), causing the graphite flakes of cast iron to be shifted to the steel's surface, resulting in the observed -ve wear.

Figure 4(a) implies that the GCI disc exhibits mild -ve wear with lower sliding velocity (0.5 m/sec) and up to 600 m of sliding distance with 1 m/sec. Then, it tends to

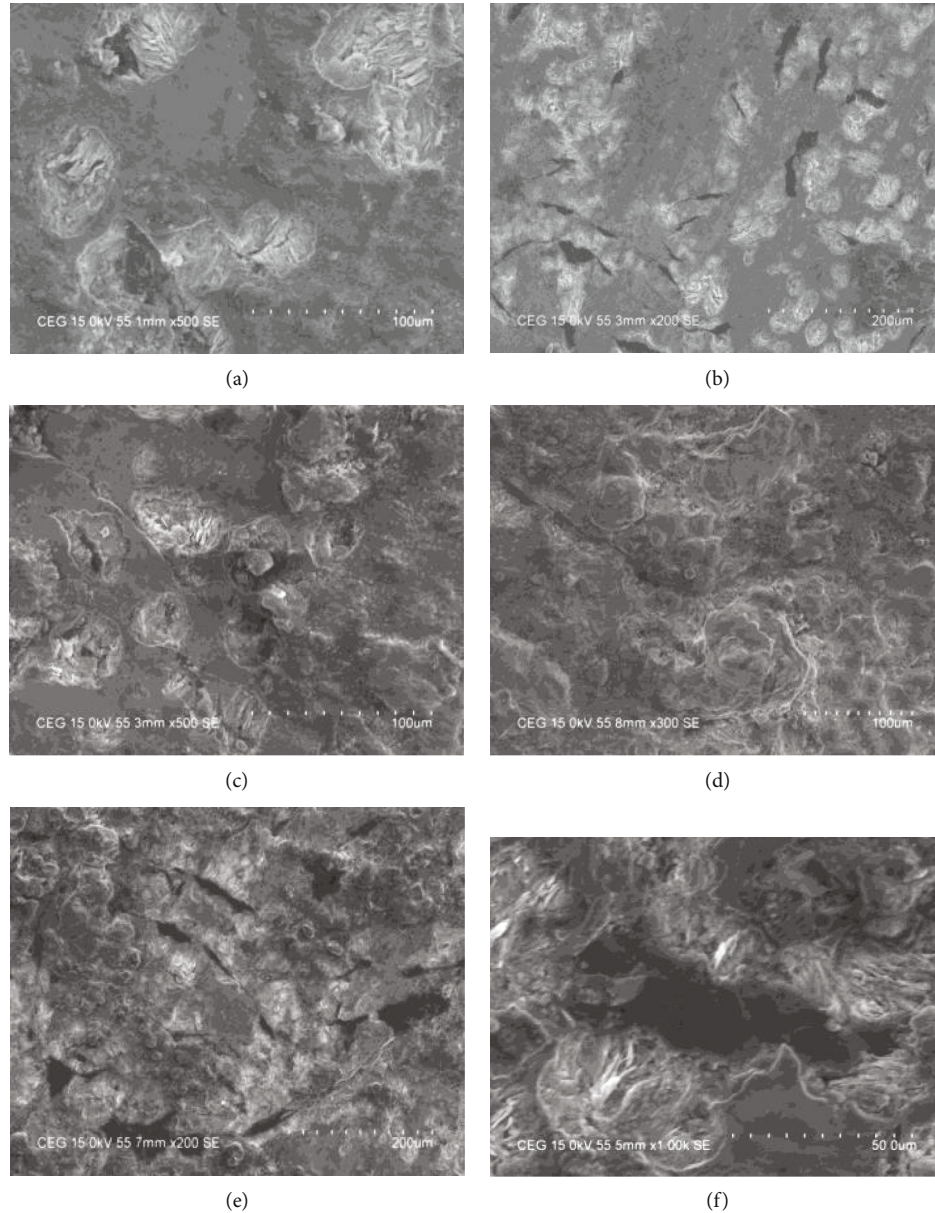


FIGURE 5: (a–f) Micrograph with dry sliding with 15 N load.

change its wear from $-ve$ to $+ve$ mode (it is known that normal GCI contains graphite, a layer lattice material, which on sliding contact pressure undergoes interplaner shear, forming a solid lubricant film for sliding). This is facilitated mostly with increased sliding speed and duration (distance traversed-PVT factor).

The typical wear of the counterpart (pin) surface is shown in Figure 4(b). It is seen that the pin surface exhibits mostly $+ve$ modes of wear (fluctuation) with a dominant $-ve$ mode of wear at higher contact load and sliding speed. Due to contact temperature, the steel surface would be oxidized, and there could also be unstable oxide film growth, and hence, the steel surface undergoes a fluctuating $+ve$ mode of wear. However, with a higher sliding speed (1.5 m/sec), the transfer of graphite from GCI results in the observed $-ve$ mode of wear.

3.2. SEM Observation. Figure 5(a) shows the contribution of material debris transfer for both the surface and the load of 15 N for the worn out portion of the GCI disc wear track. Discrete transfers of wear debris take place from the counter steel surface. Figure 5(b) shows how the GCI track is ploughed with dominant slide bands. The debris on the steel surface and how it is spread over the surface can be seen. Figure 5(c) depicts the graphite layer detaching and the transfer of steel surface debris embedded in the graphite flake.

A micrograph of the worn out GCI track under dry sliding with a 15 N load, 1.5 m/sec sliding speed, and a transverse distance of 900 m is shown in Figure 5(d). The micrograph depicts discrete pull out of graphite with the absence of any transferred particles ($+ve$ mode of wear). The micrograph's worn out GCI track (Figure 5(e)) shows

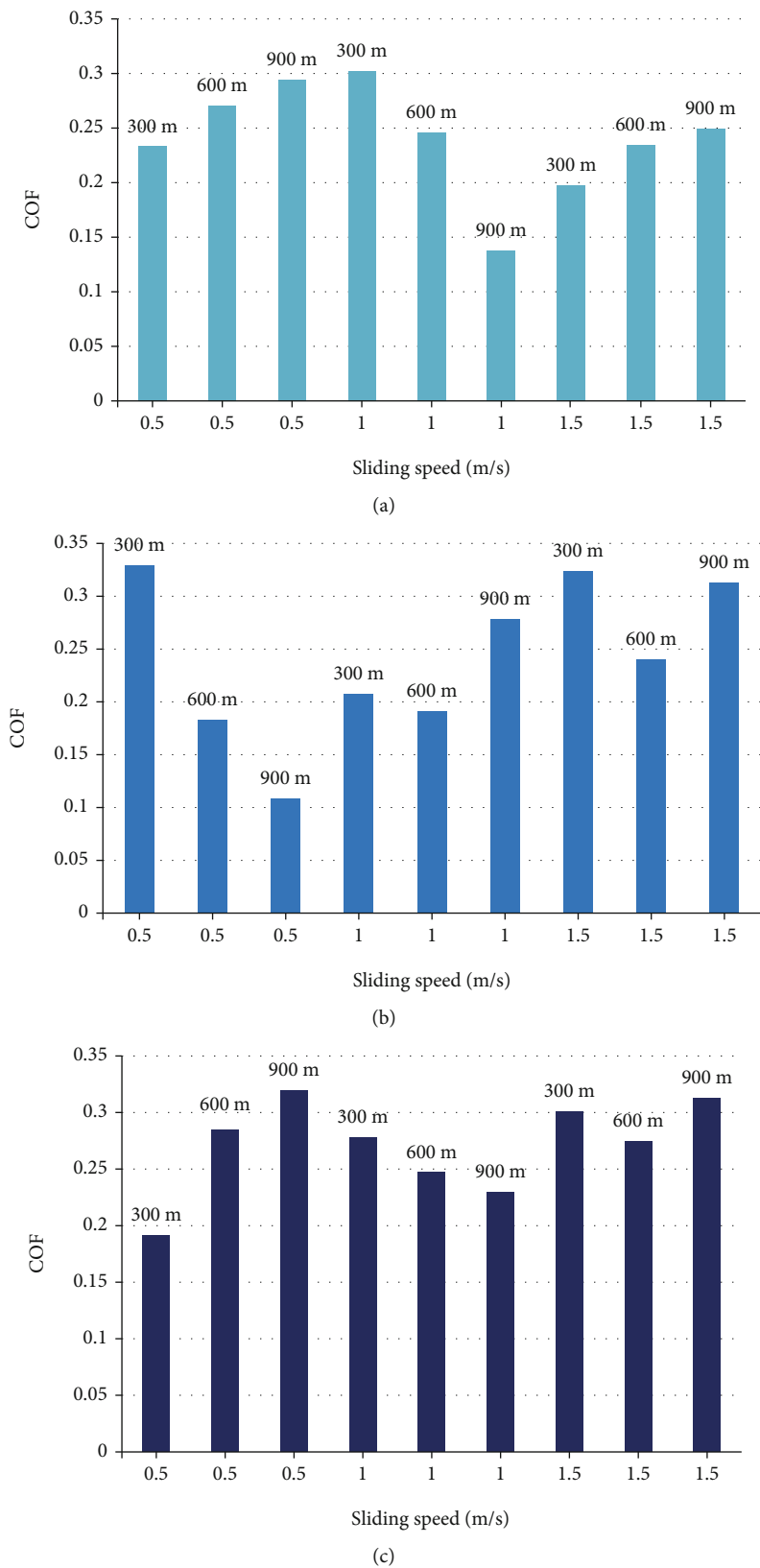
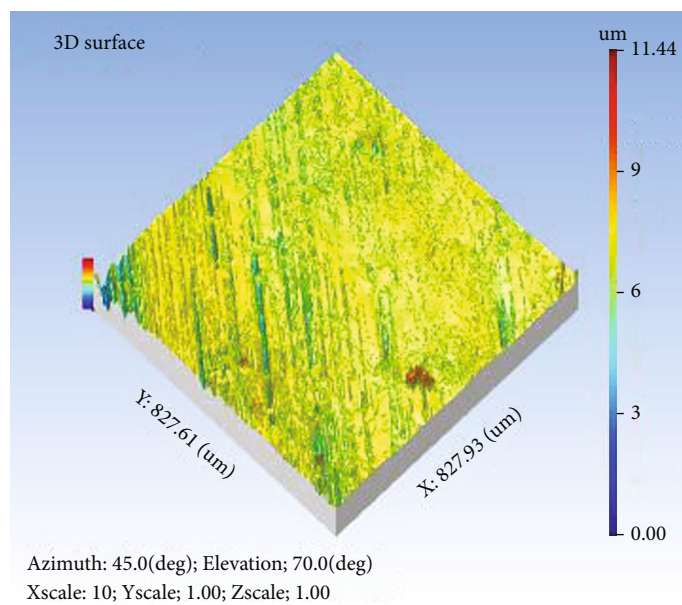
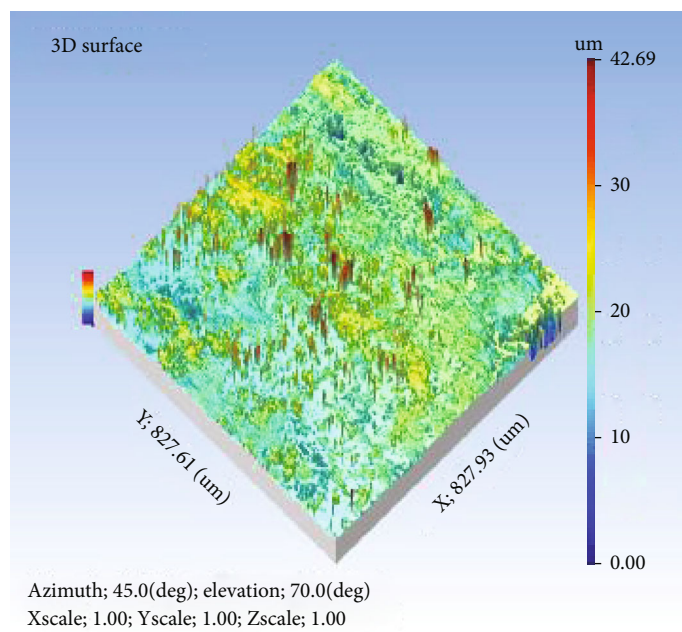


FIGURE 6: (a) Disc COF at 15 N, (b) disc COF at 30 N, and (c) disc COF at 45 N.

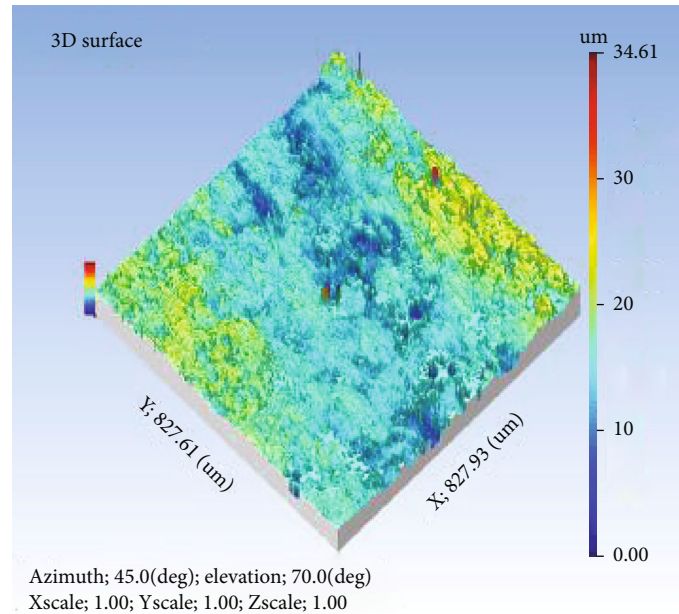


(a) 15 N, 1.5 m/sec, 900 m



(b) 30 N, 1.5 m/sec, 900 m

FIGURE 7: Continued.



(c) 45 N, 1.5 m/sec, 900 m

FIGURE 7: (a-c) 3D surface images.

flow of surface material with discrete ridges and surface cracks. Figure 5(d) depicts a micrograph of the worn out GCI track surface exhibiting discrete cleavage/surface fissures next portion of the worn out track describes the observation of the worn out transferred portion on GCI. The graphite layer is partly unpeeled, whereas ferrite structure exposed on substrate. Figure 5(f) depicts graphite flaking, revealing the texture beneath the ferrite structure.

3.3. Coefficient of Friction (COF). The typical observed variation of COF, with sliding speed at 15 N load, is illustrated in Figure 6(a). It is seen that with a lower speed of 0.5 m/sec, COF increases while increasing sliding distance. A mild rise in COF observed at the speed of sliding (1 m/sec) with a lower sliding distance of 300 m could be attributed to less transfer of graphite. The COF was reduced in (trials 5 and 6) with sliding speed of 1 m/sec and a sliding distance of 600 m and 900 m and a sliding speed of 1.5 m/sec and a sliding distance of 300 m, 600 m, and 900 m. The reason for the reduction in COF could be attributed to the transfer of graphite film.

The variation of COF in dry sliding with a load of 30 N is demonstrated in Figure 6(b). It is witnessed that COF drops down, which is attributed to the change for ploughing sliding. With increasing speed, a gradual increase of COF is observed. This may be attributed to increased contact area and interaction on account of higher speed/loads. Figure 6(c) depicts the variation of COF with sliding condition at 45 N load. The COF varied from 0.194 to 0.319, indicating relatively steadier sliding at 0.5 m/sec. It is seen that with sliding speeds of 1 m/sec and 1.5 m/sec, there is variation in COF. This could be attributed to increased contact area and consequent interaction. With a higher

sliding speed of 1.5 m/sec, the observed marginal variation in COF could be attributed to steadier sliding.

3.4. Surface Roughness. Figure 7(a) shows the 3D surface of the worn surface presents no visible lay pattern. In this case, positive wear mode appeared with a 15 N load, a 1.5 m/sec sliding speed, and 900 m sliding distance. The roughness parameters of this surface have Ra 0.182 μm , Rt 2.31 μm , and Rt/Ra > 10. It has been discovered that the mild crest flattened texture exists. Kurtosis is 26.1, and skewness is -2.54. Fine surface roughness values 180 nm were observed; also, there were no sticking and adhesion of another materials.

Figure 7(b) depicts the 3D surface with a 30 N load, a sliding speed of 1.5 m/sec, and a sliding distance of 900 m. The texture on a 3D surface is random, with no discernible lay pattern. The roughness parameters of this surface have Ra 1.70 μm , Rt 24.5 μm , Rt/Ra > 10, Rp 10.8 μm , and Rv 2.97 μm . Kurtosis is 14.3, and skewness is -1.29. An absence of crest flattening has been observed in a highly random and noncentric profile. It shows that more rough texture compared to load 15 N, and it has found that materials deposited on surfaces. At higher loads, more amounts of materials transformed between the materials and produced coarse surfaces. Figure 7(c) shows the 3D surface at 45 N load, 1.5 m/sec sliding speed, and 900 m sliding distance. The r. The roughness parameters of this surface have Ra 1.37 μm , Rt 15.8 μm , Rt/Ra > 10, kurtosis 4.38, skewness -0.45, mild wavy texture, and left centric profile.

4. Conclusions

Under dry sliding conditions, the GCI disc exhibits an increase in wear with increasing load. The counter steel pin

surface experienced a progressive reduction in wear with increasing speed and load, attributable to the transfer of wear debris from the GCI disc. The GCI exhibits marginal +ve wear with 30 N and 45 N contact load and sliding speeds of up to 1 m/sec. A micrograph of the worn out track of a GCI disc reveals the transfer of worn out debris (20 to 40 μm), from steel surface.

With a 15 N load, the COF increases while increasing the sliding distance at low and high levels of sliding speed, whereas at a medium sliding speed of 1 m/sec, it decreases from a higher to a lower value, indicating a transition from sliding form ploughing to stable mode. A mild rise in COF was observed at a higher speed of sliding (1 m/sec), attributable to less transfer of graphite.

The COF drops down initially at 30 N, lower sliding speeds, and with increasing speed, and a gradual increase of COF was observed. This may be attributable to an increase in contact area and interaction on account of higher speeds/loads.

At lower speeds, with a 45 N load, the COF is relatively steady, but at higher speeds, the COF gradually increases with increasing sliding speed.

At 15 N load, with a low initial stage of distance and sliding speed, the worn out surface presents an unsystematic surface texture with Ra 0.136 μm , while with medium speed of 1 m/sec, it presents a coarse texture with Ra value of 0.398 μm . At higher levels of sliding speed and distance, a mild wavy texture (Ra 1.37 μm) and a left centric profile were detected.

Data Availability

The data used to support the findings of this study are included within the article.

Conflicts of Interest

The authors declare that they have no conflicts of interest regarding the publication.

References

- [1] A. Renz, D. Kürten, and O. Lehmann, "Wear of hardfaced valve spindles in highly loaded stationary lean-burn large bore gas engines," *Wear*, vol. 376-377, pp. 1652–1661, 2017.
- [2] H. Mohamadzadeh, H. Saghafian, and S. Kheirandish, "Sliding wear behavior of a grey cast iron surface remelted by TIG," *Journal of Materials Science and Technology*, vol. 25, no. 5, pp. 622–628, 2009.
- [3] V. Bhuvanewari, L. Rajeshkumar, and K. N. S. Ross, "Influence of bioceramic reinforcement on tribological behaviour of aluminium alloy metal matrix composites: experimental study and analysis," *Journal of Materials Research and Technology*, vol. 15, pp. 2802–2819, 2021.
- [4] Z. A. Abd Halim, N. Ahmad, M. F. Hanapi, and M. F. Zainal, "Rapid surface treatment of grey cast iron for reduction of friction and wear by alumina coating using gas tunnel plasma spray," *Materials Chemistry and Physics*, vol. 260, article 124134, 2021.
- [5] M. Ramesh, K. Marimuthu, P. Karuppuswamy, and L. Rajeshkumar, "Microstructure and properties of YSZ-Al₂O₃ functional ceramic thermal barrier coatings for military applications," *Boletin de la Sociedad Espanola de Ceramica y Vidrio*, 2021.
- [6] A. Saravanakumar, L. Rajeshkumar, D. Balaji, and M. P. Jithin Karunan, "Prediction of wear characteristics of AA2219-Gr matrix composites using GRNN and Taguchi-based approach," *Arabian Journal for Science and Engineering*, vol. 45, no. 11, pp. 9549–9557, 2020.
- [7] S. Sun, R. Long, Y. Zhang, and M. Li, "The influence of initial deflection angle on the tribological properties of gray cast iron rings with curve distributed pits under dry sliding," *Proceedings of the Institution of Mechanical Engineers, Part J: Journal of Engineering Tribology*, vol. 235, no. 8, pp. 1659–1668, 2021.
- [8] S. K. Putatunda, "Austempering of silicon manganese cast steel," *Materials and Manufacturing Processes*, vol. 16, no. 6, pp. 743–762, 2001.
- [9] N. Sun, H. Shan, H. Zhou et al., "Friction and wear behaviors of compacted graphite iron with different biomimetic units fabricated by laser cladding," *Applied Surface Science*, vol. 258, no. 19, pp. 7699–7706, 2012.
- [10] V. Nayyar, J. Kaminski, A. Kinnander, and L. Nyborg, "An experimental investigation of machinability of graphitic cast iron grades; flake, compacted and spheroidal graphite iron in continuous machining operations," *Procedia CIRP*, vol. 1, pp. 488–493, 2012.
- [11] G. Straffellini and L. Maines, "The relationship between wear of semi metallic friction materials and pearlitic cast iron in dry sliding," *Wear*, vol. 307, no. 1-2, pp. 75–80, 2013.
- [12] E. E. Vera-Cardenas, R. Lewis, and T. Slatter, "Sliding wear study on the valve-seat insert contact", Open," *Journal of Applied Sciences*, vol. 7, no. 2, pp. 42–49, 2017.
- [13] A. R. Ghaderi, M. N. Ahmadabadi, and H. M. Ghasemi, "Effect of graphite morphologies on the tribological behavior of austempered cast iron," *Wear*, vol. 255, no. 1-6, pp. 410–416, 2003.
- [14] K. Chawla, N. Saini, and R. Dhiman, "Investigation of tribological behavior of stainless steel 304 and gray cast iron rotating against EN32 steel using pin on disc apparatus," *IOSR Journal of Mechanical and Civil Engineering (IOSR-JMCE)*, vol. 9, no. 4, pp. 18–22, 2013.
- [15] M. H. Cho, S. J. Kim, R. H. Basch, J. W. Fash, and H. Jang, "Tribological study of gray cast iron with automotive brake linings: the effect of rotor microstructure," *Tribology International*, vol. 36, no. 7, pp. 537–545, 2003.
- [16] K. Hirasata, K. Hayashi, and Y. Inamoto, "Friction and wear of several kinds of cast irons under severe sliding conditions," *Wear*, vol. 263, no. 1-6, pp. 790–800, 2007.
- [17] J. E. Wilson, F. H. Stott, and G. C. Wood, "The development of wear protective oxides and their influence on sliding friction," *Proceedings of the Royal Society of London. A. Mathematical and Physical Sciences*, vol. 369, no. 1739, pp. 557–574, 1980.
- [18] Y. C. Liu, J. M. Schissler, and T. G. Mathia, "The influence of surface oxidation on the wear resistance of cast iron," *Tribology International*, vol. 28, no. 7, pp. 433–438, 1995.
- [19] R. M. Galagali, M. H. Ashok, V. M. Khadakhbavi, J. Shivakumar, S. Malagi, and C. Patil, "Effect of speed and temperature on the tribological behaviour of ADI," in *Recent Advances in Mechanical Infrastructure. Lecture Notes in Intelligent Transportation and Infrastructure*, A. K. Parwani, P.

- Ramkumar, K. Abhishek, and S. K. Yadav, Eds., Springer, Singapore, 2022.
- [20] R. Bathe, V. Sai Krishna, S. K. Nikumb, and G. Padmanabham, "Laser surface texturing of gray cast iron for improving tribological behavior," *Applied Physics A: Materials Science & Processing*, vol. 117, no. 1, pp. 117–123, 2014.
- [21] L. R. R. da Silva and H. L. Costa, "Tribological behavior of gray cast iron textured by maskless electrochemical texturing," *Wear*, vol. 376-377, pp. 1601–1610, 2017.
- [22] Y. Meng, J. Xu, Z. Jin, B. Prakash, and Y. Hu, "A review of recent advances in tribology," *Friction*, vol. 8, no. 2, pp. 221–300, 2020.
- [23] S. Ananth, P. Sivaprakasam, J. Udaya Prakash, P. Maheandera Prabu, V. Perumal, and G. Kalusuraman, "Tribological behavior and surface characterization of gray cast iron-EN31 steel under lubricated sliding conditions," *Journal of Nanomaterials*, vol. 2021, Article ID 7725959, 9 pages, 2021.
- [24] P. Sivaprakasam, G. Elias, P. M. Prabu, and P. Balasubramani, "Experimental investigations on wear properties of AlTiN coated 316LVM stainless steel," *Materials Today: Proceedings*, vol. 33, pp. 3470–3474, 2020.
- [25] P. Sivaprakasam, A. Kirubel, G. Elias, P. Maheandera Prabu, and P. Balasubramani, "Mathematical modeling and analysis of wear behavior of AlTiN coating on titanium alloy (Ti-6Al-4V)," *Advances in Materials Science and Engineering*, vol. 2021, 9 pages, 2021.

Research Article

Analysis of Physical, Ocular, and Aquaphobic Properties of Zirconium Oxide Nanofilms by Varying Sputtering Pressure

Sujit Kumar,¹ Vikramaditya Dave,² Muthamil Bala Krishnan,³ V. Amudha,⁴ S. Gomathi,⁵ Sanjay Soni,⁶ Syed Hamim Jeelani,⁷ Ram Subbiah,⁸ and Kassu Negash ⁹

¹Department of Electrical and Electronics Engineering, Jain (Deemed-to-Be University), Bengaluru, Karnataka 560069, India

²Department of Electrical Engineering, College of Technology and Engineering, Udaipur, Rajasthan 313001, India

³Research Scholar, Department of Biomedical Engineering, SRM Institute of Science and Technology, Kattankulathur, Tamil Nadu 603203, India

⁴Department of Electronics and Communication Engineering, Saveetha School of Engineering, Saveetha Institute of Medical and Technical Sciences, Chennai, Tamil Nadu 602105, India

⁵Department of Electrical and Electronics Engineering, St. Joseph's Institute of Technology, Chennai, Tamil Nadu 600119, India

⁶Department of Industrial and Production Engineering, Jabalpur Engineering College, Jabalpur, Madhya Pradesh 482002, India

⁷Department of Civil Engineering, Koneru Lakshmaiah Education Foundation, Deemed to Be University, Andhra Pradesh 522502, India

⁸Department of Mechanical Engineering, Gokaraju Rangaraju Institute of Engineering and Technology, Hyderabad, Telangana 500090, India

⁹Department of Mechanical Engineering, Faculty of Manufacturing, Institute of Technology, Hawassa University, Hawassa, Ethiopia

Correspondence should be addressed to Kassu Negash; kassun@hu.edu.et

Received 23 February 2022; Accepted 2 April 2022; Published 6 May 2022

Academic Editor: V. Vijayan

Copyright © 2022 Sujit Kumar et al. This is an open access article distributed under the Creative Commons Attribution License, which permits unrestricted use, distribution, and reproduction in any medium, provided the original work is properly cited.

A thin coating of zirconium oxide (ZrO_2) is placed on outdoor high-voltage insulators to minimize air fouling. ZrO_2 thin film coatings were deposited on glass substrates using a DC sputtering (reactive magnetron) technique with sputtering pressures ranging from 5 to 25 mTorr. Characterization of the deposited films was carried out utilizing approaches such as XRD, AFM, CAG, and spectrophotometer. Following the XRD peaks, when 15 mTorr is reached, the average crystallite size increases, after which it begins to decline. The wettability of the deposited thin layer is associated with the coarseness calculated by AFM. At 15 mTorr pressure, maximum aquaphobic is achieved (107.45°). At this pressure, the transmittance and bandgap were similarly determined to be 90% and 5.43 eV, respectively.

1. Introduction

The ability of insulators to function in polluted environments is a critical aspect of the insulation of power transmission lines [1]. As a result, pollution flashover has emerged as a significant issue that electrical engineers must solve in their work. Outdoor high-voltage insulators are often made of porcelain or glass, which have been in use for more than a century [2], and have high surface energy between the atoms of the material [3, 4]. The above statement is due to the pow-

erful electrostatic interfaces between the substance's atoms, leading to an increase in impurity buildup, which results in a deterioration of the material's dielectric characteristics and a drop in the material's dielectric constant. A further risk is that the flashover conclusion might result in a catastrophic failure of the device, mainly if a contaminated layer builds [5–7]. In addition to the wind, pollution from nearby cement facilities, industrial smoke, and coastal salt [8] are all responsible for depositing contaminants on the surfaces of the insulators. Pollutants are classified as either soluble or

insoluble particles. A leakage current flows over the insulator surface when these pollutants conduct in fog, mist, or light rain, which causes it to overheat and fail [9]. Because of the leakage current, dry spots are observed on the outer part of the insulator. Due to their insulating properties, dry areas catch fire and ignite, leading to insulator surface flashover [8, 10]. Consequently, the whole power system that was interconnected with that insulating system went down.

Water spraying insulator is an expensive but frequently necessary approach that discloses the system operative to a potentially dangerous security state [11]. An aquaphobic coating was recommended to be applied to the surface to address these limitations. It was discovered that room temperature vulcanized (RTV) coating was the solution [12, 13]. Over the past two decades, it has been utilized to great success as an outdoor insulating material. Although it has good mechanical strength, it has poor wear and corrosion resistance due to its polymer makeup. Degradation of these coatings is significantly reduced due to this effect [14]. Recent research has focused on developing inorganic aquaphobic nanocoatings with superior mechanical, electrical, and thermal characteristics than organic coatings [15].

Zirconium oxide (ZrO_2) is a chemical compound that has applications in science and technology [16–21]. A wide variety of technical applications might benefit from ZrO_2 's chemical, electrical, and mechanical properties [16–18]. However, there are no many studies that have been done on the aquaphobic behavior of ZrO_2 . RF magnetron-sputtered ZrO_2 thin film was reported to have a maximum contact angle with water of 101° by Patel et al. [22]. By varying the sputtering pressure from 5 to 25 mTorr, the current work seeks to evaluate the physical, ocular, and aquaphobic characteristics of ZrO_2 surfaces, as well as their effect on surface coarseness.

Some deposition processes are employed to create ZrO_2 films, and these methods are discussed in detail in [23–31]. Each technique has its own set of benefits and drawbacks. When it comes to thin film deposition, DC reactive magnetron sputtering method stands out among the other methods because of its reproducibility, homogeneity, excellent adhesion, and convenience of usage [32, 33]. Because of this, the study concentrated on depositing thin films with varied sputtering pressures utilizing the DC reactive magnetron technique to achieve the desired results.

2. Experimentation Specifics

ZrO_2 films are generated by DC sputtering in a chamber mainly constructed for this purpose (Excel Instruments India), as shown in Figure 1. The target was made of pure zirconium metal and had a diameter of 2 inches and a thickness of 5 mm. Glass and silicon substrates were used in this experiment. After cleaning with an ultrasonic acetone solution and drying them for 2 minutes, the substrates were put on a glass substrate holder. The target-substrate distance was 41 mm in this case.

At the deposition, the chamber was expatriated with a vacuum pressure of 5×10^{-6} mTorr. With a fixed self-bias supply of 60 watt, a zirconium oxide target was sputtered

in an argon-oxygen gas combination. The pure argon (Ar) and oxygen (O) gas were separately injected into the chamber. Oxygen and argon gas flow was kept constant at 10 and 40 sccm, respectively, and pressure inside the chamber varied from 5 to 25 mTorr.

The microstructure of the films was examined through a “Bruker D8 advance diffractometer with Cu-K (40 kV, 20 mA) radiation at 20° – 80° .” The introductory study of the deposited film was carried out with the help of an energy dispersive X-ray (EDX) connected to a scanning electron microscope (SEM) (FEI, Quanta 200 F). Analysis of the surfaces of ZrO_2 films was carried out using atomic force microscopy (AFM) in the partial-contact method. A surface profilometer was used to measure the layer thickness. Contact angle goniometry measured the water droplet contact angles. By using a UV-NIR spectrophotometer, the ocular characteristics of ZrO_2 films were investigated.

3. Results and Discussion

Various XRD patterns of nanocrystalline ZrO_2 thin films were generated under multiple pressure ranges, as seen in Figure 2. It is confirmed by the existence of a big bump at $2\theta = 31.468^\circ$ in all deposited samples that there is a (111) plane of the monoclinic ZrO_2 structure present. This plane is indexed according to normal JCPDS (reference code: 00-037-1484) patterns for ZrO_2 lattice in all deposited samples. A less dominant peak is caused by the orientation (-111) of the monoclinic phase of ZrO_2 due to its exposure (-111).

In response to an increase in pressure (5–15 mTorr), the concentration of the emitted radiation rises (from 5 to 15 mTorr), implying a lessening in average crystallite size and, as a result, an increase in film crystallinity. In response to the rise in pressure between 15 and 25 mTorr, the (111) peak concentration declines correspondingly. The principal free path of the atoms is reduced when the deposition pressure is increased, which raises the possibility of particle collisions inside the gas environment. As a result, their kinetic energy is lowered when charged particles collide with a target surface [33–35]. Using the well-known Scherrer's formula [36], we were able to establish the average crystallite size “t.”

Figure 3 depicts the variability in average crystallite size regarding pressure during the sputtering process. The connection between MFP and the atomic diameter of the gas, which may be expressed mathematically as [37], explains why the size of crystallites increases with pressure increments up to 15 mTorr.

According to the equation [37], when pressure raises from 5 to 15 mTorr, the size of crystallites increases and decreases from 15 to 25 mTorr, respectively. The mobility of crystallites explains the previous argument.

With increasing sputtering pressure, the mobility of crystallites reduces. Collisions with Ar ions diminish the amount of ejected particles that reach the surface of the substrate when the pressure is greater than 15 mTorr. Because of this, surface diffusion requires less energy. Crystallite size is reduced due to decreased surface mobility of sprayed particles [37].

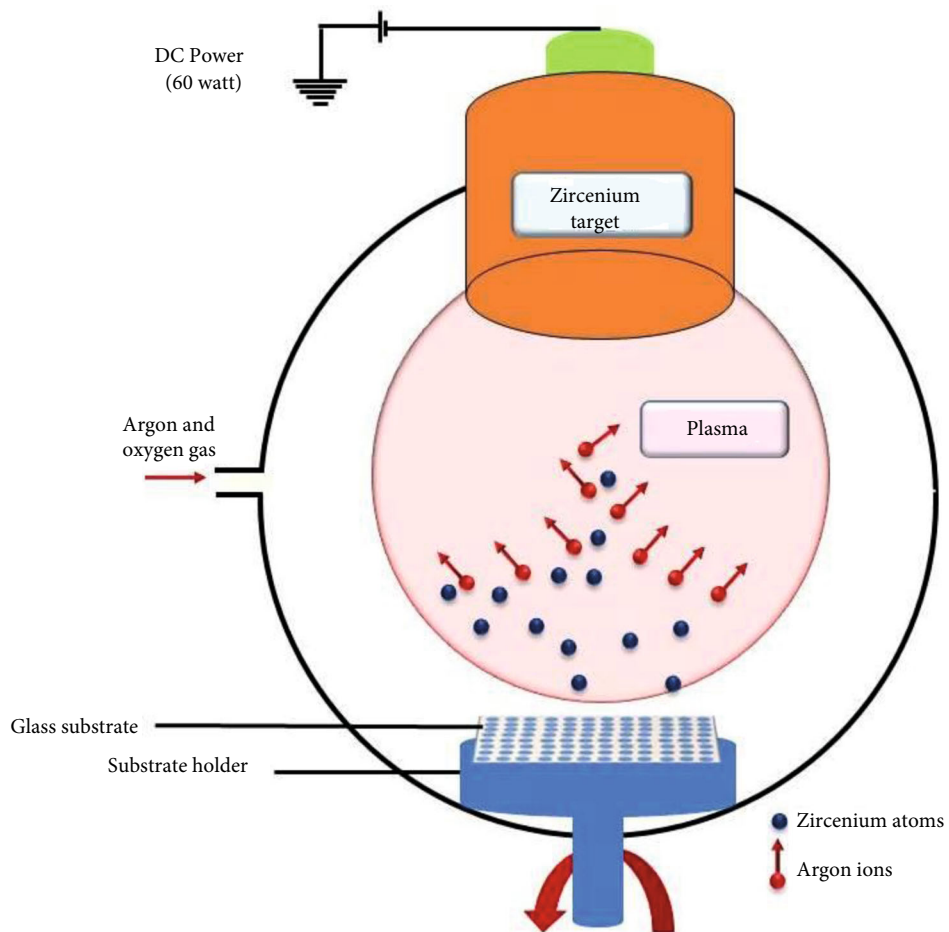


FIGURE 1: Schematic diagram of sputtering chamber.

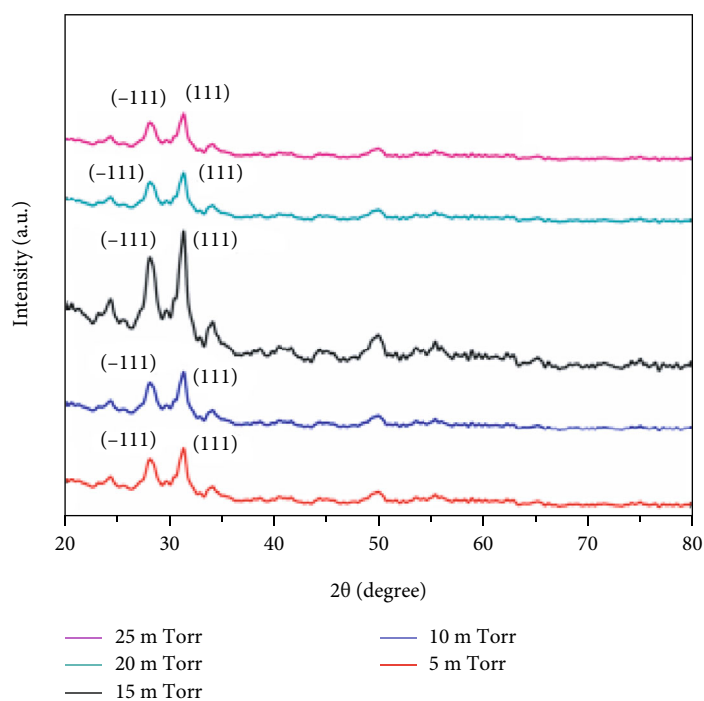


FIGURE 2: Intensity of deposited ZrO_2 XRD for the pressure ranges from 5 to 25 mTorr.

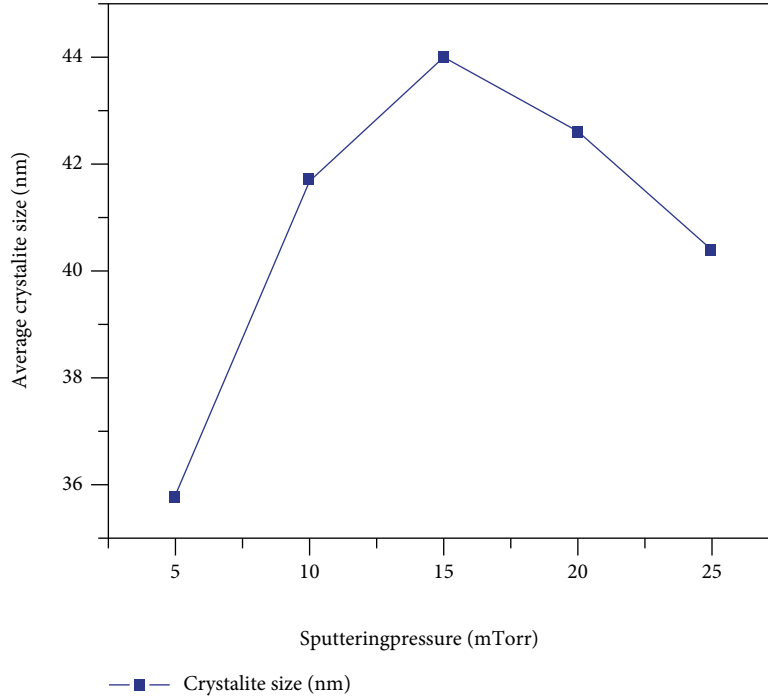


FIGURE 3: Average crystallite size varies with sputtering pressure.

TABLE 1: ZrO₂ film parameters at various pressures.

| Pressure (mTorr) | O (atomic weight %) | Zr (atomic weight %) | Average transmittance % | Extinction coefficient | Bandgap (eV) |
|------------------|---------------------|----------------------|-------------------------|------------------------|--------------|
| 5 | 72.62 | 27.38 | 98 | 0.22 | 5.33 |
| 10 | 72.89 | 27.11 | 96 | 0.28 | 5.35 |
| 15 | 72.02 | 27.98 | 94 | 0.31 | 5.43 |
| 20 | 72.08 | 27.92 | 95 | 0.26 | 5.41 |
| 25 | 73.21 | 26.79 | 97 | 0.23 | 5.39 |

EDX was used to determine the stoichiometry of crystalline films in the laboratory. Zirconium and oxygen atomic percentages are displayed in Table 1 at various pressures. The O/Zr ratio in all of the samples was deposited at 2:1.

Figure 4 depicts AFM micrographs of films formed at various pressures. The AFM micrographs show that the morphologies of the ZrO₂ films are pretty similar to one another. They are all composed of spherical particles that have been roughly compacted.

Even after increasing or decreasing the pressure used in sputtering, the particle size did not remain consistent. Using data analysis techniques, the AFM evaluates the surface coarseness of thin films that have been deposited. The root mean square (RMS) technique was used to determine the surface coarseness of each ZrO₂ film sample at five different locations on its surface. Figure 5 depicts the change in RMS surface coarseness in contrast with pressure.

Initially, the coarseness increases between 5 and 15 mTorr and subsequently reduces between 15 and 25 mTorr. At 15 mTorr pressure, the surface coarseness reaches its maximum (43.5 nm). From 5 to 15 mTorr, the pressure is raised, and the size of the crystallites and the

coarseness of the crystals both increase as the pressure is increased.

In response to increasing pressure (from 15 to 25 mTorr), the size of the crystallites is reduced, which results in a reduction in the coarseness of the films (from coarse to fine) [37, 38].

The aquaphobic of thin films was determined by measuring the angle they came into contact with water after being freshly formed. The contact angle was calculated using the sessile drop method. The contact angles of each sample were measured using a 3 μ L drop of the solution. The contact angle variation with pressure is shown in Figure 5. The contact angle (aquaphobic) rose as the pressure climbed from 5 to 15 mTorr, reaching a maximum of 107° at 15 mTorr. In this experiment, the contact angle decreased for increasing pressure from 15 to 25 mTorr; this contact angle measures how aquaphobic the material is. It was demonstrated that aquaphobic operate similarly to coarseness, and it further clarified the influence of coarseness on contact angle (aquaphobic) [38]. As a result, the coarseness of the surface increases, which increases its aquaphobic. Wenzel has also developed the following equation [39]. According

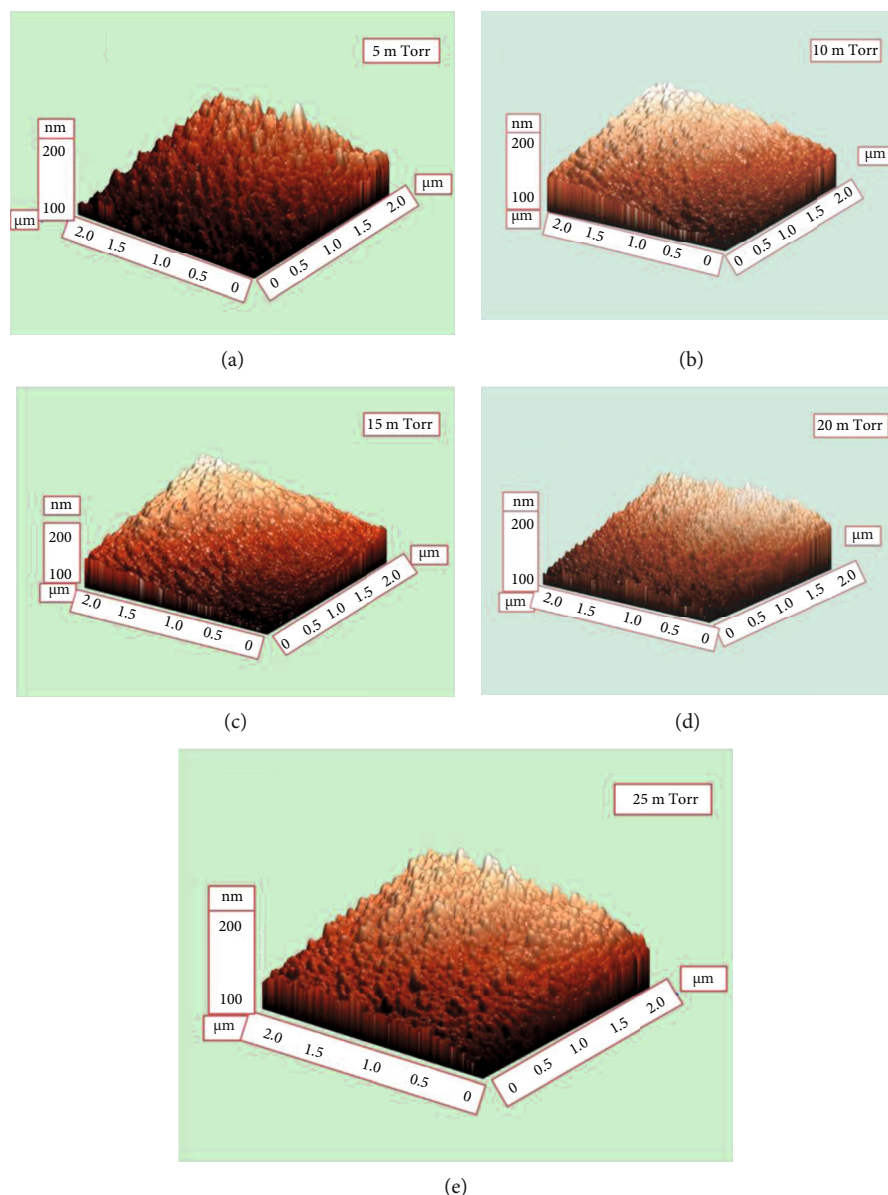


FIGURE 4: 3D pictures of ZrO_2 coating at numerous pressures using AFM.

to Wenzel's equation, a hydrophilic surface ($<90^\circ$) grows more hydrophilic, while an aquaphobic surface ($>90^\circ$) becomes more aquaphobic [40].

Figure 6 shows a plot of the transmittance band for all samples put on glass substrates in contrast with wavelength for all samples.

As a function of wavelength, the interference effect shows the oscillations in the spectrum due to the interaction. Table 1 depicts the average diffusion of each sample that has been placed. Although the intermediate diffusion level increases when the pressure exceeds 15 mTorr, the average transmission level falls when the pressure increases between 5 and 15 mTorr. Transparency and aquaphobic are inversely proportional to one another. As surface coarseness rises, so does aquaphobic, but this also results in light scattering sources [9]. As a result, the transparency of the deposited films is diminished. Even though the variation in the coarse-

ness of deposited films was minimal (less than 1 nm), it cannot be attributed to a single reason for the significant change in limpidity (5%). Numerous elements such as the extinction coefficient and defect density may be present in this adjustment [41]. In each sample, the average transmission rate was higher than 90 percent on average. As a result, the thin coatings that are deposited are transparent while also being aquaphobic.

Using the envelope approach, the diffusion data was utilized to compute the deposited samples' refractive index (RI) [42].

Using a wavelength of 550 nm, Figure 7 depicts the change in RI of films formed under different pressures and circumstances.

In this case, the refractive index ranges between 2.19 and 2.25, comparable to the bulk value [43]. While under pressure, the refractive index lowers from 5 to 15 mTorr,

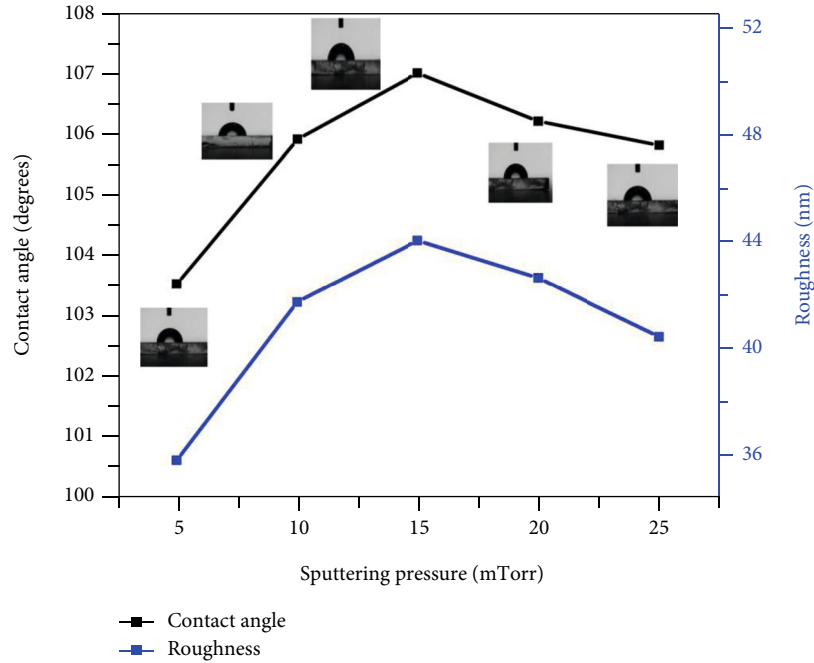


FIGURE 5: Contact angle and coarseness variation with sputtering pressure.

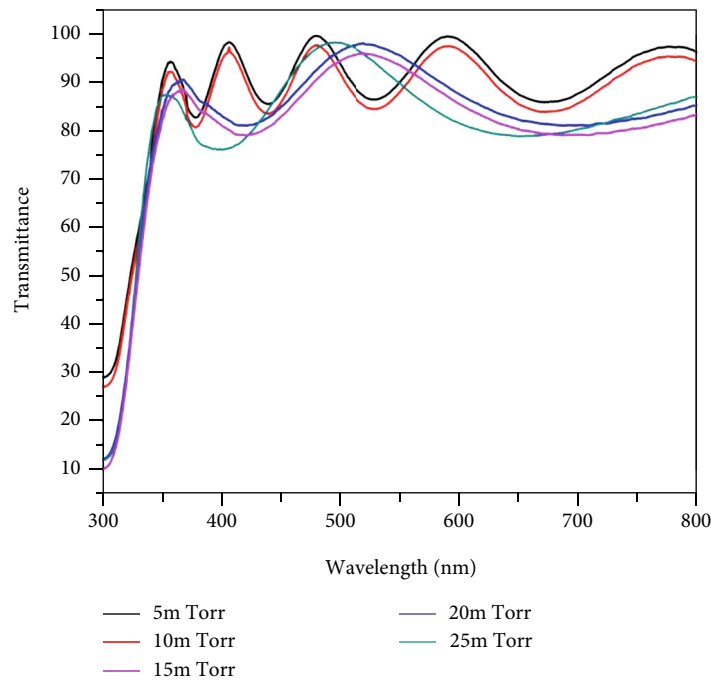


FIGURE 6: Ocular diffusion curve of deposited ZrO₂ thin film at varied pressures.

following which it starts to rise at 15 mTorr, and it continues to increase afterward. A variation in the transparency of the sampled film was determined to be the source of the variation in RI of ZrO₂ coating with raising sputtering pressure [44]. This change in transparency was a concerning coarseness of the sampled film. When comparing packing density to RI, the packing density of a film is highly significant [45].

The fluctuation in packing density concerning pressure is seen in Figure 7. Observation of substantial packing density in the deposited ZrO₂ thin film at 5 mTorr sputtering pressure indicated that the film had a densely packed structure.

The coating thickness was measured with the help of a surface profilometer. The diffusion statistics were too

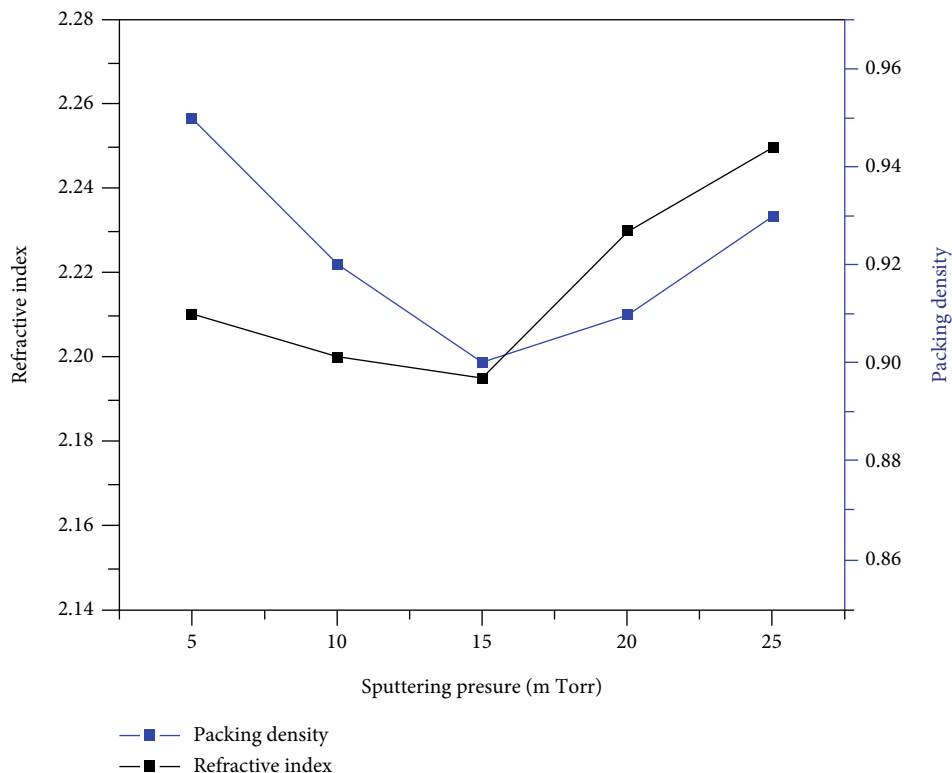


FIGURE 7: ZrO_2 thin film indicating RI and packing density at different pressures.

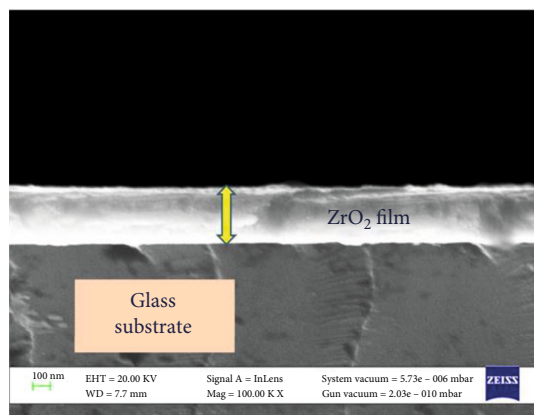


FIGURE 8: X-sectional SEM picture of ZrO_2 sample.

TABLE 2: Width of ZrO_2 films by SEM cross-section.

| Pressure (mTorr) | Width of ZrO_2 films (nm) | | |
|------------------|------------------------------------|----------------------|-------------------|
| | SEM image | Surface profilometer | Transmission data |
| 5 | 715 | 713 | 714 |
| 10 | 728 | 726 | 727 |
| 15 | 735 | 730 | 734 |
| 20 | 724 | 722 | 723 |
| 25 | 713 | 711 | 712 |

utilized to compute the layer width (d) using reference [40]. Using SEM cross-sectional images shown in Figure 8, the width of the film is validated even more precisely. The thickness of the films deposited using the procedures as mentioned earlier is depicted in Table 2.

It makes little difference whatever approach is employed because the breadth of each film is very near to the same. When the pressure is increased from 5 to 15 mTorr, the breadth of the ZrO_2 film grows and then begins to decrease. When particles are placed on the substrate, a loose packing arrangement results in higher film thickness for a given quantity of particles [9]. At 15 mTorr, the packing density was the highest (0.9). The maximum width (735 nm) was achieved using scanning electron microscope equipment at a pressure of 15 mTorr.

The visual immersion coefficient (α) was calculated from the relation [46]. The properties of inner reflections and typical incidence reflectance become less significant as the ocular density increases [40].

The extinction coefficient at 550 nm is seen in Table 1. The k value increases from 5 to 15 mTorr and then falls. Changes in film transparency are driven mainly by variations in the extinguishment coefficient. The extinction coefficient of deposited films is affected by the dispersion of the grains. A film's transparency decreases with increasing grain size because the impact of scattering increases with increasing grain size [47]. Pressure is raised from 5 to 15 mTorr, and the k value rises (0.22 to 0.31), resulting in a fall in average transparency from 97 to 90% when the pressure is increased. The increased pressure of more than

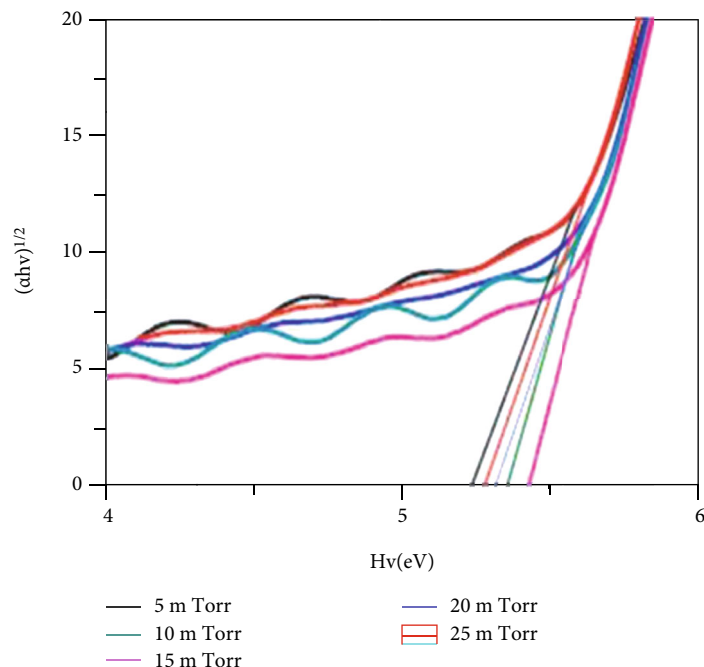


FIGURE 9: Ocular bandgap of ZrO_2 film at various sputtering pressure.

15 mTorr decreases grain size and boosts film transparency from 90 to 95%.

A thin layer of nanocrystalline zirconium oxide was investigated for its visual bandgap (E_g), which was calculated from immersion coefficient (α) employing the Tauc relation [48]. The value of n was set to $1/2$ [48] for transitions that were permitted directly. The ocular bandgap may be calculated from a graph of $(\alpha hv)^{1/2}$ vs hv . Figure 9 shows the relationship between $(\alpha hv)^{1/2}$ and photon energy hv for samples placed at various pressures.

Table 1 displays the bandgap values that were calculated at various pressures. The bandgap of ZrO_2 film produced varies between 5.23 and 5.43 eV, which is equivalent to the bandgap of ZrO_2 in bulk [49]. The largest bandgap (5.43 eV) was discovered at a pressure of 15 mTorr. ZrO_2 thin films have a bandgap that increases between 5 and 15 mTorr and decreases after 15 mTorr. The size of the crystallites affects the bandgap [48], and the size of crystallites explains the phenomenon described in [48].

4. Conclusions

The physical, optical, and aquaphobic properties of nanostructured ZrO_2 nanofilms were investigated on glass samples at various pressures and temperatures. A 15 mTorr pressure resulted in a monoclinic structure that was strongly oriented (111). The main objective of the work was to achieve a high aquaphobic coating (107°) with a large bandgap (5.43 eV) and a thin film (735 nm) using high sputtering pressure of 15 mTorr while using a thin film sputtering technique. On the other hand, the decreased sputtering pressure reduces transparency and refractive index, which might be missed owing to the enhanced aquaphobic of the material. The optimum sputtering pressure for generating dielectric

aquaphobic coatings for outdoor insulators was 15 mTorr, which was shown to be the case in this study. Additionally, when compared to HfO_2 coating over a glass substrate, ZrO_2 was shown to be the superlative coating since its aquaphobic was higher than that of HfO_2 .

Data Availability

The data used to support the findings of this study are included in the article. Should further data or information be required, these are available from the corresponding author upon request.

Disclosure

This study was performed as a part of the Employment Hawassa University, Ethiopia.

Conflicts of Interest

The authors declare that there are no conflicts of interest regarding the publication of this paper.

Acknowledgments

The authors appreciate the technical assistance to complete this experimental work from Department of Mechanical Engineering, St. Joseph's Institute of Technology, Chennai, Tamil Nadu, India. The authors are thankful for the technical assistance to complete this experimental work.

References

- [1] N. Dhahbi-Megrache, A. Beroual, and L. Krahenbuhl, "A new proposal model for flashover of polluted insulators," *Journal of Physics D: Applied Physics*, vol. 30, no. 5, pp. 889–894, 1997.
- [2] R. Hackam, "Outdoor HV composite polymeric insulators," *IEEE Transactions on Dielectrics and Electrical Insulation*, vol. 6, no. 5, pp. 557–585, 1999.
- [3] H. Deng, R. Hackam, and E. A. Cherny, "Influence of thickness, substrate type, amount of silicone fluid and solvent type on the electrical performance of RTV silicone rubber coatings," *Power Delivery*, vol. 11, no. 1, pp. 431–443, 1996.
- [4] R. S. Gorur, E. A. Chernry, and J. T. Burnham, *Outdoor Insulators*, Arizona, USA, Phoenix, 1st edn edition, 1999.
- [5] H. Su, Z. Jia, Z. Guan, and L. Li, "Mechanism of contaminant accumulation and flashover of insulator in heavily polluted coastal area," *IEEE Transactions on Dielectrics and Electrical Insulation*, vol. 17, no. 5, pp. 1635–1641, 2010.
- [6] B. S. Reddy and G. R. Nagabhushana, "Study of temperature distribution along an artificially polluted insulator String," *Plasma Science and Technology*, vol. 5, no. 2, pp. 1715–1720, 2003.
- [7] M. Farzaneh and J. F. Draupeau, "AC flashover performance of insulators covered with artificial ice," *Power Delivery*, vol. 10, no. 2, pp. 1038–1051, 1995.
- [8] P. J. Lambeth, "Effect of pollution on high voltage insulators proc," *IEE Review*, vol. 118, pp. 1107–1114, 1971.
- [9] S. Jain, A. Sanger, and R. Chandra, "Sputtering pressure dependent structural, optical and aquaphobic properties of DC sputtered Pd/WO₃ thin films for hydrogen sensing application," *Emerging Energy Technology perspectives-A Sustainable Approach*, vol. 549, pp. 146–154, 2014.
- [10] G. M. Tena, R. H. Corona, and I. R. Vazquez, "Experiences on pollution level measurement in Mexico," *Electric Power Systems Research*, vol. 76, no. 1-3, pp. 58–66, 2005.
- [11] K. F. Portella, F. Piazza, P. C. Inone et al., "Efeitos da poluição atmosférica (litorânea e industrial) em isoladores da rede elétrica da região metropolitana de Salvador," *Química Nova*, vol. 31, no. 2, pp. 340–348, 2008.
- [12] S. M. Gubanski, "Properties of silicone rubber housings and coatings," *IEEE Transactions on Electrical Insulation*, vol. 27, no. 2, pp. 374–382, 1992.
- [13] G. G. Karady, "Flashover mechanism of non-ceramic insulators," *IEEE Transactions on Dielectrics and Electrical Insulation*, vol. 6, no. 5, pp. 718–723, 1999.
- [14] D. Devendranath and A. D. Rajkumar, "Leakage current and charge in RTV coated insulators under pollution conditions," *IEEE Transactions on Dielectrics and Electrical Insulation*, vol. 2, pp. 294–301, 2002.
- [15] Y. Cao, P. C. Irwin, and K. Younsi, "The future of nanodielectrics in the electrical power industry," *IEEE Transactions on Dielectrics and Electrical Insulation*, vol. 11, no. 5, pp. 797–807, 2004.
- [16] M. L. Green, E. P. Gusev, R. Degraeve, and E. L. Garfunkel, "Ultrathin (<4 nm) SiO₂ and Si-O-N gate dielectric layers for silicon microelectronics: understanding the processing, structure, and physical and electrical limits," *Journal of Applied Physics*, vol. 90, no. 5, pp. 2057–2121, 2001.
- [17] D. Chi and P. C. McIntyre, "Germanium n-type shallow junction activation dependences," *Applied Physics Letters*, vol. 88, pp. 232901–232907, 2005.
- [18] C. M. Wang, S. Azad, S. Thevuthasan, V. Shutthanandan, D. E. Mc-Cready, and C. H. F. Peden, "Spectroscopic ellipsometry characterization of the optical properties and thermal stability of ZrO₂ films made by ion-beam assisted deposition," *Journal of Materials Research*, vol. 19, pp. 1315–1322, 2008.
- [19] W. L. Gong, W. Lutze, and R. C. Ewing, "Zirconia ceramics for excess weapons plutonium waste," *Journal of Nuclear Materials*, vol. 277, no. 2-3, pp. 239–249, 2000.
- [20] S. Venkataraj, O. Kappertz, R. Jayavel, and M. Wuttig, "Growth and characterization of zirconium oxynitride films prepared by reactive direct current magnetron sputtering," *Journal of Applied Physics*, vol. 92, no. 5, pp. 2461–2466, 2002.
- [21] S. Ramanathan and P. C. McIntyre, "Ultrathin zirconia/SiO₂-dielectric stacks grown by ultraviolet-ozone oxidation," *Applied Physics Letters*, vol. 80, no. 20, pp. 3793–3795, 2002.
- [22] U. S. Patel, K. H. Patel, K. V. Chauhan, A. K. Chawla, and S. K. Rawal, "Investigation of various properties for zirconium oxide films synthesized by sputtering," *Procedia Technology*, vol. 23, pp. 336–343, 2016.
- [23] S. Harasek, A. Lugstein, H. D. Wanzenboeck, and E. Bertagnolli, "Slow trap response of zirconium dioxide thin films on silicon," *Applied Physics Letters*, vol. 83, no. 7, pp. 1400–1402, 2003.
- [24] R. Puthenkovilakam and J. P. Chang, "Valence band structure and band alignment at the ZrO₂/Si Interface," *Applied Physics Letters*, vol. 84, no. 8, pp. 1353–1355, 2004.
- [25] A. Stesmans and V. V. Afanas'ev, "Si dangling-bond-type defects at the interface of (100)Si with ultrathin layers of SiO_x, Al₂O₃, and ZrO₂," *Applied Physics Letters*, vol. 80, no. 11, pp. 1957–1959, 2002.
- [26] T. Sikola, J. Spousta, L. Dittrichova, and L. Benes, "Deposition of magnetic thin films by IBAD," *Nuclear Instruments and Methods in Physics Research Section B: Beam Interactions with Materials and Atoms*, vol. 148, no. 1-4, pp. 907–911, 1999.
- [27] A. Meher, H. Klumper-Westkamp, F. Hoffmann, and P. Mayr, "Crystallization and residual stress formation of sol-gel-derived zirconia films," *Thin Solid Films*, vol. 308-309, pp. 363–368, 1997.
- [28] S. Kumar, K. Vikramaditya Dave, V. Velmurugan et al., "Analysis of structural, optical, and aquaphobic properties of zirconium oxide nanofilms by varying sputtering gas," *Advances in Materials Science and Engineering*, vol. 2022, Article ID 9968485, 2022.
- [29] J. M. Howard, V. Craciun, C. Essary, and R. K. Singh, "Interfacial layer formation during high-temperature annealing of ZrO₂ thin films on Si," *Applied Physics Letters*, vol. 81, no. 18, pp. 3431–3433, 2002.
- [30] J. S. Kim, H. A. Marzouk, and P. J. Reucroft, "Deposition and structural characterization of ZrO₂ and yttria-stabilized ZrO₂ films by chemical vapor deposition," *Thin Solid Films*, vol. 254, no. 1-2, pp. 33–38, 1995.
- [31] D. Ronnow, J. Isidorsson, and G. A. Niklasson, "Surface roughness of sputteredZrO₂films studied by atomic force microscopy and spectroscopic light scattering," *Physical Review E*, vol. 54, no. 4, pp. 4021–4028, 1996.
- [32] M. Ohring, *The Materials Science of Thin Films*, Academic Press, San Diego, 1992.
- [33] T. Kamohara, M. Akiyama, N. Ueno et al., "Influence of sputtering pressure on polarity distribution of aluminum nitride, thin films," *Applied Physics Letters*, vol. 89, no. 24, article 243507, 2006.

- [34] A. Ababneh, U. Schmid, J. Hernando, J. L. Sánchez-Rojas, and H. Seidel, "The influence of sputter deposition parameters on piezoelectric and mechanical properties of AlN thin films," *Materials Science and Engineering B*, vol. 172, no. 3, pp. 253–258, 2010.
- [35] X.-P. Kuang, H.-Y. Zhang, G.-G. Wang et al., "AlN films prepared on 6H-SiC substrates under various sputtering pressures by RF reactive magnetron sputtering," *Applied Surface Science*, vol. 263, pp. 62–68, 2012.
- [36] B. D. Cullity, *Elements of X-Ray Diffraction*, Addison-Wesley, London, 2nd edn edition, 1978.
- [37] R. Vipin Chawla and R. C. Jayaganthan, "Influence of sputtering pressure on the structure and mechanical properties of nanocomposite Ti-Si-N thin films," *Journal of Materials Science and Technology*, vol. 26, no. 8, pp. 673–678, 2010.
- [38] A. B. Cassie and S. Baxter, "Wettability of porous surfaces," *Transactions of the Faraday Society*, vol. 40, pp. 546–551, 1944.
- [39] R. N. Wenzel, "Resistance of solid surfaces to wetting by water," *Industrial and Engineering Chemistry*, vol. 28, no. 8, pp. 988–994, 1936.
- [40] K. R. Wu, J. J. Wang, W. C. Liu, Z. S. Chen, and J. K. Wu, "Deposition of graded TiO₂ films featured both hydrophobic and photo-induced hydrophilic properties," *Applied Surface Science*, vol. 252, no. 16, pp. 5829–5838, 2006.
- [41] H. N. Shah, R. Vipin Chawla, and D. K. Jayaganthan, "Microstructural characterizations and hardness evaluation of d.c. reactive magnetron sputtered CrN thin films on stainless steel substrate," *Bulletin of Materials Science*, vol. 33, no. 2, pp. 103–110, 2010.
- [42] J. C. Manifacier, J. Gasiot, and J. P. Fillard, "A simple method for the determination of the optical constants n, k and the thickness of a weakly absorbing thin film," *Journal of Physics E: Scientific Instruments*, vol. 9, no. 11, pp. 1002–1004, 1976.
- [43] M. Jerman, Z. Qiao, and D. Mergel, "Refractive index of thin films of SiO₂, ZrO₂, and HfO₂ as a function of the films mass density," *Applied Optics*, vol. 44, no. 15, pp. 3006–3012, 2005.
- [44] L. Zhang, D. Ouyang, and C. Mo, "Characterizations of optical absorption in porous Al₂O₃ / Cr₂O₃ nanocomposites," *Nanostructured Materials*, vol. 9, no. 1-8, pp. 563–566, 1997.
- [45] G. Bauer, "Absolutwerte der optischen Absorptionskonstanten von Alkalihalogenidkristallen im Gebiet ihrer ultravioletten Eigenfrequenzen," *Annalen der Physik*, vol. 411, no. 4, pp. 434–464, 1934.
- [46] Z. S. El Mandouh and M. S. Selim, "Physical properties of vanadium pentoxide sol gel films," *Thin Solid Films*, vol. 371, pp. 59–64, 2000.
- [47] G. He, L. Q. Zhu, M. Liu, Q. Fang, and L. D. Zhang, "Optical and electrical properties of plasma-oxidation derived HfO₂ gate dielectric films," *Applied Surface Science*, vol. 253, no. 7, pp. 3413–3418, 2007.
- [48] C. V. Ramana, R. S. Vemuri, I. Fernandez, and A. L. Campbell, "Size-effects on the optical properties of zirconium oxide thin films," *Applied Physics Letters*, vol. 95, no. 23, pp. 231905–231912, 2009.
- [49] J. G. Bendoraitis and R. E. Salomon, "Optical energy gaps in the monoclinic oxides of hafnium and zirconium and their solid Solutions¹," *The Journal of Physical Chemistry*, vol. 69, no. 10, pp. 3666–3667, 1965.

Research Article

Optimization of Cold Spray Process Inputs to Minimize Porosity and Maximize Hardness of Metal Matrix Composite Coatings on AZ31B Magnesium Alloy

Ashokkumar Mohankumar ¹, Thirumalaikumarasamy Duraisamy,¹
Deepak Sampathkumar,² Sathiyamoorthy Ranganathan,³ Guruprasad Balachandran,⁴
Murugan Kaliyamoorthy,⁵ Mathanbabu Mariappan,⁶ and Lijalem Mulugeta ⁷

¹Department of Manufacturing Engineering, Annamalai University, Annamalai Nagar, 608002 Tamil Nadu, India

²Department of Mechanical and Automation Engineering, Agni College of Technology, Thalambur, Chennai-600130, Tamilnadu, India

³Department of Mechanical Engineering, Institute of Road Transport Polytechnic College, Krishnagiri-635104, India

⁴Department of Mechanical Engineering, Alagappa Chettiar Government College of Engineering and Technology, Karaikudi, 630003 Tamil Nadu, India

⁵Department of Mechanical Engineering, Government Polytechnic College, Valangaiman, Thiruvavur, 612804 Tamil Nadu, India

⁶Department of Mechanical Engineering, Government College of Engineering, Bargur, Krishnagiri-635104, India

⁷Department of Mechanical Engineering, Faculty of Manufacturing Institute of Technology, Hawassa University, Ethiopia

Correspondence should be addressed to Lijalem Mulugeta; lijalem@hu.edu.et

Received 1 February 2022; Revised 7 March 2022; Accepted 30 March 2022; Published 30 April 2022

Academic Editor: V. Vijayan

Copyright © 2022 Ashokkumar Mohankumar et al. This is an open access article distributed under the Creative Commons Attribution License, which permits unrestricted use, distribution, and reproduction in any medium, provided the original work is properly cited.

In this investigation, the development of an empirical relationship to determine the porosity and microhardness of the coatings through low-pressure cold-sprayed (LPCS) aluminum alloy/alumina metal matrix composite (MMC) deposit. Spray parameters like temperature, standoff distance (SOD), and powder feed rate play an essential part in the determination of the coating effectiveness. In this study, 3 variables, 5 levels of central composite rotatable design (CCD) were used to decrease the total count of the experimentation. A mathematical model has been developed to evaluate the porosity and hardness of the coated samples along with LPCS spray parameters, and the model's applicability was inspected by ANOVA. Utilizing response surface methodology, spray parameter optimization was carried out. The deposit developed by optimal spray parameters produces the lowest surface porosity of 3.31 vol.% and a higher hardness of 137.21 HV compared with other coated samples. It is validated through the response graph. As a result, the optimized parameters for aluminum alloy/alumina metal matrix composite (MMC) coatings via LPCS are 500 degrees Celsius, 10 mm SOD, and 20 grams/min powder feed rate.

1. Introduction

Magnesium (Mg) and its alloys have received increased attention in a broad range of automobile and aerospace applications due to their high strength-to-weight ratio, higher stiffness, and lower density. Although in some applications, Mg alloys have excellent surface characteristics;

their tribological and electrochemical behavior is poor. Numerous coating processes, such as high velocity oxy fuel (HVOF) and atmospheric plasma spray (APS), can be used to enhance the surface characteristics of Mg alloys. However, the above processes are limited by their performance due to high amount of energy required to fabricate the coatings [1].

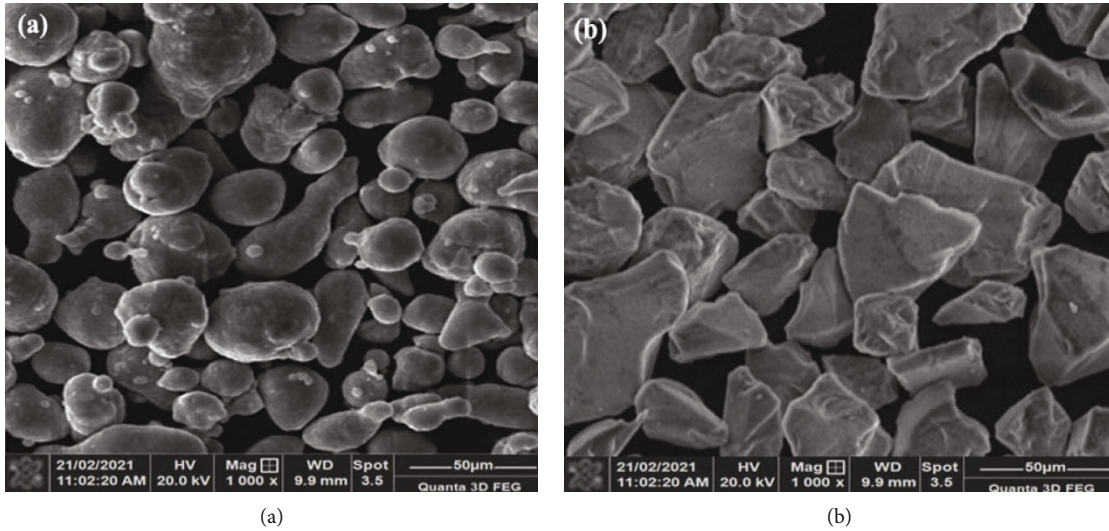
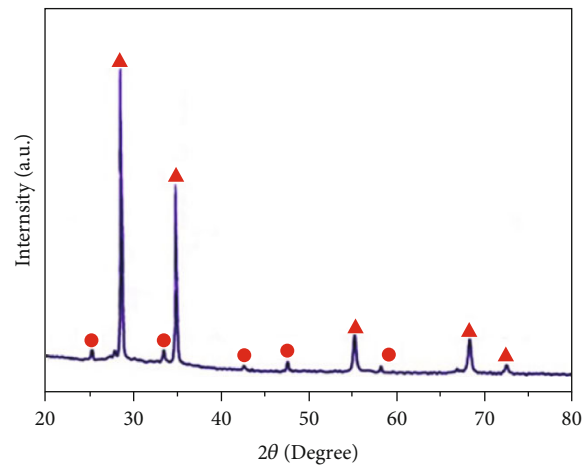
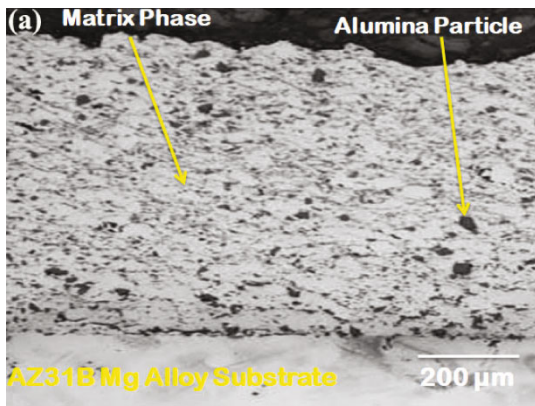


FIGURE 1: SEM morphology of coating material: (a) Al alloy powder; (b) alumina powder.

TABLE 1: LPCS spray parameters and their ranges.

| S. no | Parameter | Notation | Ranges | | | | |
|-------|--------------------------|----------|--------|--------|-----|--------|-------|
| | | | -1.682 | -1 | 0 | +1 | 1.682 |
| 1 | Temperature (degree) | <i>T</i> | 450 | 470.27 | 500 | 529.73 | 550 |
| 2 | Standoff distance (mm) | <i>D</i> | 5 | 7.02 | 10 | 12.97 | 15 |
| 3 | Powder feed rate (g/min) | <i>P</i> | 15 | 17.02 | 20 | 22.97 | 25 |



▲ Aluminium
● Alumina

FIGURE 2: (a) Cross-sectional optical microstructural view. (b) XRD of the LPCS MMC coatings.

Low-pressure cold spray (LPCS) is a solid form of depositing process that accelerates the coating material with a high impact on a substratum to produce a deposit. In the cold spray (CS), the coating powder is fed into a convergent-divergent nozzle to generate a supersonic flow. When the

coating powder reaches above the critical velocity, the coating material is deposited on the substratum owing to extreme plastic deformation of the impacting powder materials. In this technique, the temperature of the coating material should be kept below the melting temperature [2–5]. It

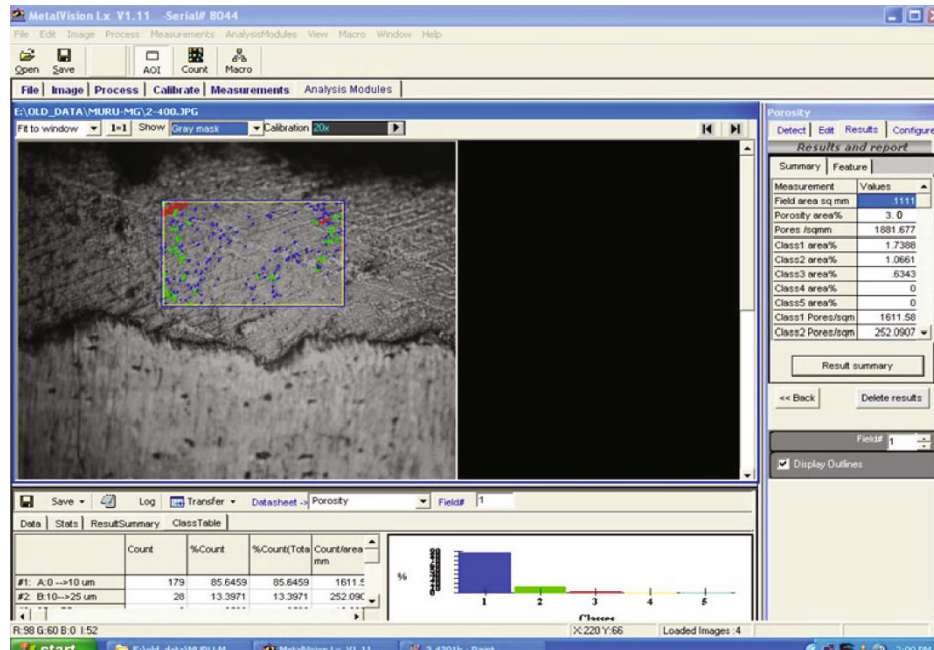


FIGURE 3: Porosity measurement through image analysing software.

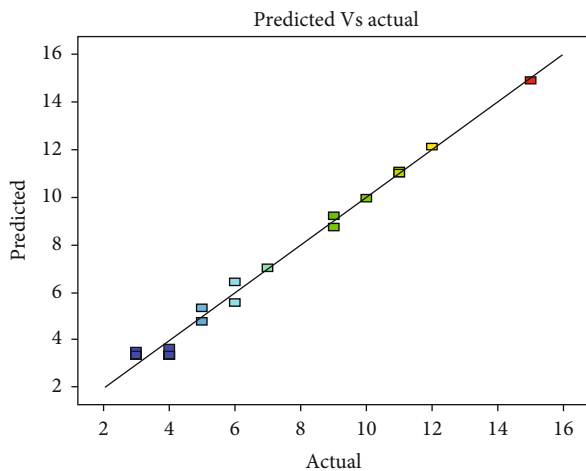


FIGURE 4: Correlation graph (porosity).

has been widely employed in the production of a wide range of metallic deposits like Cu, Al, Ni, and Ti [6, 7].

In order to enhance the properties of the metallic deposit, reinforced ceramic particles were added into the metallic powder to generate the MMC deposit. Aluminum oxide/alumina/ Al_2O_3 is the most popular reinforced ceramic powder for the CS process [8–10]. The wear and porosity behavior of the bronze/alumina MMC coatings is fabricated through atmospheric plasma spray and the CS process. The findings revealed that increasing the alumina concentration in MMC coatings manufactured using plasma and CS processes improved the tribological properties of the coatings, with CS coatings significantly outperforming plasma spraying [11]. The same results have been obtained for copper-

alumina-based MMC deposits with varying sizes and alumina volume percentages. According to the findings, the tribological characteristics of all MMC deposits, including varied volume fractions and sizes of alumina powder, were less compared with the Cu coating. The wear resistance is highly improved when the reinforcement particles have a smaller size of 2–12 microns compared with a larger particle size of 15–45 microns [12]. Other studies on aluminum/alumina, 6061-aluminum/alumina coated on AZ91E Mg alloy substratum by the LPCS process have been reported [10]. They discovered decrease in wear rate when comparing MMC deposits to solid aluminum with 12 weight percent silicon, 356.0 aluminum, and AZ91E T6. Few research studies have shown that mixing alumina particles with metallic powder in CSed composite deposits results in superior hardness compared with raw metallic deposits.

Qui et al. investigated the cold-sprayed A380 Al alloy, discovering that due to their higher strength, the A380 splats deformed remarkably little by the LPCS process. As a result, the surface porosity of the deposit was considerably high [12]. They revealed that the presence of ceramic elements in metallic powder creates a peening impact in cold spray, which has a direct impact on coating characteristics and deposit effectiveness [13, 14]. As a theory, the presence of alumina particles in the metal powder will improve the degree of deformation of A380 metal elements, resulting in less porosity in the coated sample. This will improve the hardness of the coatings, resulting in higher wear resistance [15]. From this is the recalibration or repair of a variety of aluminum and magnesium alloy parts [16]. Nevertheless, magnesium has a hexagonal, close-packed crystalline structure, so any type of magnesium alloy particle does not take deformation sufficiently to form dense coatings. As a result,

TABLE 2: DOE and outcomes.

| Exp. condition | Actual values | | | Outcomes | |
|----------------|------------------|------------------------|--------------------------|------------------|---------------|
| | Temperature (°C) | Standoff distance (mm) | Powder feed rate (g/min) | Porosity (vol.%) | Hardness (HV) |
| 1 | 470.27 | 7.02 | 17.02 | 9 | 93 |
| 2 | 529.73 | 7.02 | 17.02 | 5 | 128 |
| 3 | 470.27 | 12.97 | 17.02 | 11 | 88 |
| 4 | 529.73 | 12.97 | 17.02 | 4 | 129 |
| 5 | 470.27 | 7.02 | 22.97 | 7 | 109 |
| 6 | 529.73 | 7.02 | 22.97 | 6 | 122 |
| 7 | 470.27 | 12.97 | 22.97 | 15 | 83 |
| 8 | 529.73 | 12.97 | 22.97 | 10 | 99 |
| 9 | 450 | 10 | 20 | 11 | 91 |
| 10 | 550 | 10 | 20 | 3 | 132 |
| 11 | 500 | 5 | 20 | 6 | 120 |
| 12 | 500 | 15 | 20 | 12 | 98 |
| 13 | 500 | 10 | 15 | 5 | 115 |
| 14 | 500 | 10 | 25 | 9 | 101 |
| 15 | 500 | 10 | 20 | 3 | 140 |
| 16 | 500 | 10 | 20 | 4 | 135 |
| 17 | 500 | 10 | 20 | 3 | 138 |
| 18 | 500 | 10 | 20 | 4 | 134 |
| 19 | 500 | 10 | 20 | 3 | 137 |
| 20 | 500 | 10 | 20 | 3 | 139 |

repair or reprocessing of defected AZ31 Mg alloys with the same coating material becomes a difficult task as a result of poor wear resistance in the movable components. The coating characteristics of this LPCS MMC coating (including low-weight aluminum alloy with alumina powder) are significantly improved [17]. Hence, it is necessary to improve the Mg alloy product in order to extend its serviceability for industrial applications.

According to the literature review, no study was conducted on the LPCS technique for coating the MMC coating (aluminum alloy/alumina) on AZ31B magnesium alloy. From this, an attempt was made to acquire the best process parameters for MMC deposits to attain higher hardness and low porosity in the coatings. Then, response surface methodology (RSM) was used to optimize the hardness and porosity of the coatings.

2. Experimentation

The LPCS system (mode: Dymet 423, Russia) was employed for this experiment to fabricate the MMC coatings (Al alloy (4.6 wt.% of Cu and 1.4% Mg and Mn of 0.2 wt.)/alumina). The coating materials are as shown in Figures 1(a) and 1(b). Al alloy powder has a size of 6–58 μm and alumina has a size of 20–45 μm . Coating powder was blended with a weight percentage of 80 wt.% of Al alloy and 20 wt.% of alumina using ball milling (VB ceramics, Chennai, India). Before coating, grit blasting was done on the base material surface using corundum grits with a size of $500 \pm 350 \mu\text{m}$ to enhance

the adhesive behavior between the deposit and the base material. The substratum was washed using propanone. The coating was produced on the 5 mm thick AZ31B magnesium alloy substrate. During the coating process, the air pressure of 10 bar is kept constant, and other spray parameters are illustrated in Table 1.

2.1. Coating Characterization. Figure 2 illustrates the XRD and cross-sectional microstructure (optical microscope) (Mitutoyo, Japan; model: AE120) view of the LPCSed Al alloy/alumina coating through optimized spray parameters. From this figure, the interfacial bonding between the deposit and the base material is free of porosity, and good adhesion takes place between the base materials. The cold spray process has a feature that allows for excellent adherence and density deposit, which aids in the production of high-density coatings [12]. The alumina seems to be well retained in the deposit; nevertheless, the alumina phase appears to be dispersed unevenly. This results in the varied hardness in various regions of the deposit; the hardness was measured in 10 various regions of the coating. As a result, the optimized spray parameter hardness of the deposit is about 140 HV_{0.03} measured by the Vickers microhardness tester (Mitutoyo; model: HM-200 system D). Several authors have discovered the same microstructure characteristics for cold-sprayed deposits [8, 10, 13].

As shown in Figure 3, the porosity of the optimized parameters of the coatings for the surface was about 3%, measured using an optical microscope with image analysis

TABLE 3: Porosity and hardness images for experimental condition.

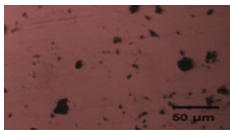
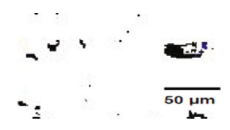
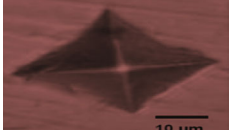
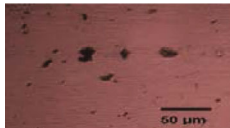

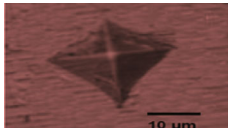
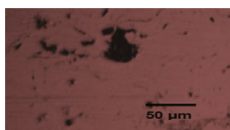
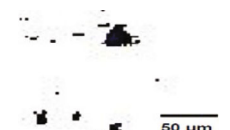
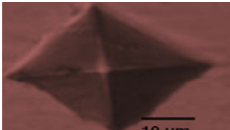
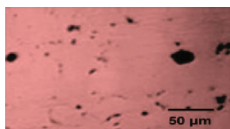

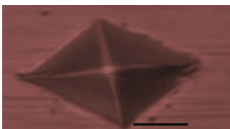



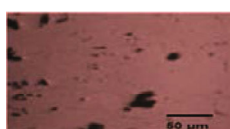

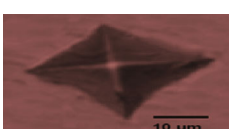
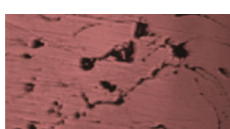

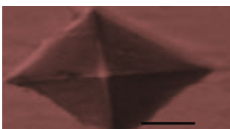


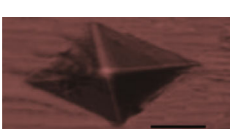

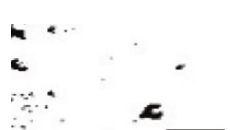




| No. of experiments | Microstructure of porosity analysis | Binary images of the porosity analysis | Hardness indentation |
|--|---|--|---|
| Exp. no: 01 <i>T</i> : 470.27 <i>D</i> : 7.02 <i>P</i> : 17.02 |  |  |  |
| Exp. no: 02 <i>T</i> : 529.73 <i>D</i> : 7.02 <i>P</i> : 17.02 |  |  |  |
| Exp. no: 03 <i>T</i> : 470.27 <i>D</i> : 12.97 <i>P</i> : 17.02 |  |  |  |
| Exp. no: 04 <i>T</i> : 529.73 <i>D</i> : 12.97 <i>P</i> : 17.02 |  |  |  |
| Exp. no: 05 <i>T</i> : 470.27 <i>D</i> : 7.02 <i>P</i> : 22.97 |  |  |  |
| Exp. no: 06 <i>T</i> : 529.73 <i>D</i> : 7.02 <i>P</i> : 22.97 |  |  |  |
| Exp. no: 07 <i>T</i> : 470.27 <i>D</i> : 12.97 <i>P</i> : 22.97 |  |  |  |
| Exp. no: 08 <i>T</i> : 529.73 <i>D</i> : 12.97 <i>P</i> : 22.97 |  |  |  |
| Exp. no: 09 <i>T</i> : 450 <i>D</i> : 10 <i>P</i> : 20550 |  |  |  |
| Exp. no: 10 <i>T</i> : 550 <i>D</i> : 10 <i>P</i> : 20 |  |  |  |

TABLE 3: Continued.

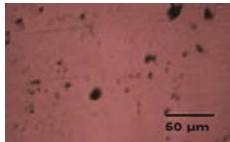
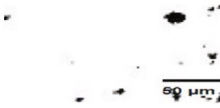
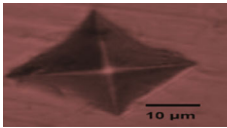
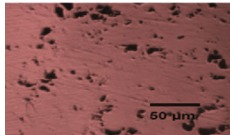
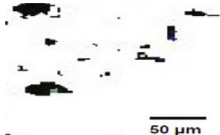
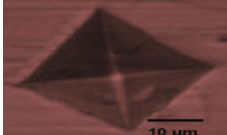
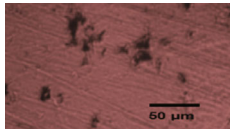
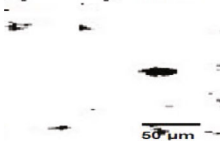
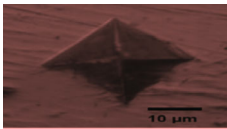
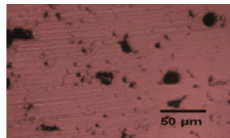
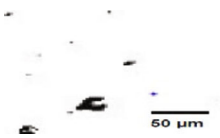
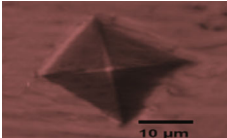
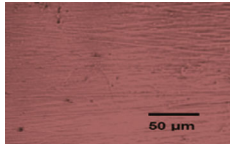
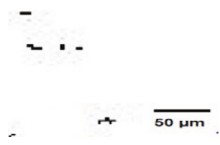
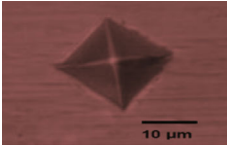
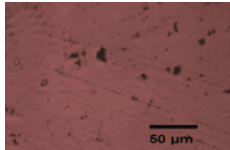
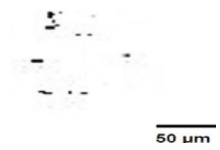
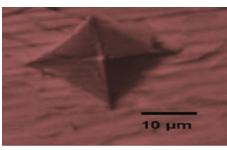
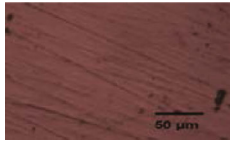
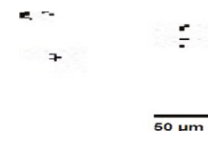
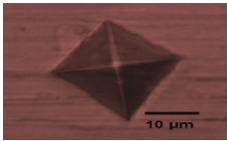
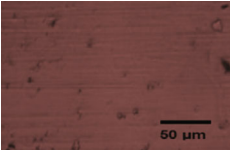
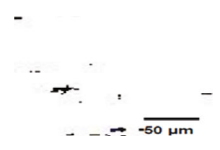
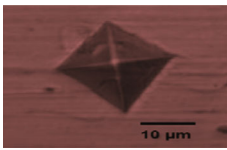
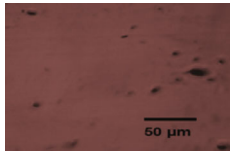

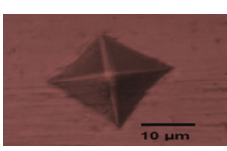
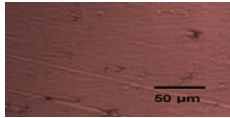
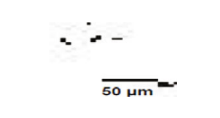
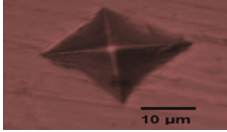
| No. of experiments | Microstructure of porosity analysis | Binary images of the porosity analysis | Hardness indentation |
|---|---|--|---|
| Exp. no: 11 <i>T</i> : 500 <i>D</i> : 5 <i>P</i> : 20 |  |  |  |
| Exp. no: 12 <i>T</i> : 500 <i>D</i> : 15 <i>P</i> : 20 |  |  |  |
| Exp. no: 13 <i>T</i> : 500 <i>D</i> : 10 <i>P</i> : 15 |  |  |  |
| Exp. no: 14 <i>T</i> : 500 <i>D</i> : 10 <i>F</i> : 25 |  |  |  |
| Exp. no: 15 <i>T</i> : 500 <i>D</i> : 10 <i>P</i> : 20 |  |  |  |
| Exp. no: 16 <i>T</i> : 500 <i>D</i> : 10 <i>P</i> : 20 |  |  |  |
| Exp. no: 17 <i>T</i> : 500 <i>D</i> : 10 <i>P</i> : 20 |  |  |  |
| Exp. no: 18 <i>T</i> : 500 <i>S</i> : 10 <i>P</i> : 20 |  |  |  |
| Exp. no: 19 <i>T</i> : 500 <i>D</i> : 10 <i>P</i> : 20 |  |  |  |
| Exp. no: 20 <i>T</i> : 500 <i>D</i> : 10 <i>P</i> : 20 |  |  |  |

TABLE 4: ANOVA result for porosity.

| Source | Sum of squares | Df | Mean square | F value | p value prob > F | |
|-----------------------|----------------|----|-------------|---------|------------------|-----------------|
| Model | 250.15 | 9 | 27.79 | 115.71 | <0.0001 | Significant |
| T (temperature) | 67.91 | 1 | 67.91 | 282.71 | <0.0001 | |
| D (standoff distance) | 39.04 | 1 | 39.04 | 162.53 | <0.0001 | |
| P (powder feed rate) | 18.11 | 1 | 18.11 | 75.40 | <0.0001 | |
| TD | 6.13 | 1 | 6.13 | 25.50 | 0.0005 | |
| TP | 3.13 | 1 | 3.13 | 13.01 | 0.0048 | |
| DP | 15.13 | 1 | 15.13 | 62.96 | <0.0001 | |
| T ² | 27.86 | 1 | 27.86 | 115.97 | <0.0001 | |
| D ² | 63.40 | 1 | 63.40 | 263.93 | <0.0001 | |
| P ² | 27.86 | 1 | 27.86 | 115.97 | <0.0001 | |
| Residual | 2.40 | 10 | 0.2402 | | | |
| Lack of fit | 1.07 | 5 | 0.2138 | 0.8016 | 0.5929 | Not significant |
| Pure error | 1.33 | 5 | 0.2667 | | | |
| Cor. total | 252.55 | 19 | | | | |

TABLE 5: ANOVA result for hardness.

| Source | Sum of squares | Df | Mean square | F value | p value prob > F | |
|-----------------------|----------------|----|-------------|---------|------------------|-----------------|
| Model | 7203.82 | 9 | 800.42 | 194.60 | <0.0001 | Significant |
| T (temperature) | 2215.72 | 1 | 2215.72 | 538.68 | <0.0001 | |
| D (standoff distance) | 593.10 | 1 | 593.10 | 144.19 | <0.0001 | |
| P (powder feed rate) | 172.56 | 1 | 172.56 | 41.95 | <0.0001 | |
| TD | 10.13 | 1 | 10.13 | 2.46 | 0.1477 | |
| TP | 276.12 | 1 | 276.12 | 67.13 | <0.0001 | |
| DP | 253.13 | 1 | 253.13 | 61.54 | <0.0001 | |
| T ² | 1267.92 | 1 | 1267.92 | 308.25 | <0.0001 | |
| D ² | 1518.14 | 1 | 1518.14 | 369.09 | <0.0001 | |
| P ² | 1624.53 | 1 | 1624.53 | 394.95 | <0.0001 | |
| Residual | 41.13 | 10 | 4.11 | | | |
| Lack of fit | 14.30 | 5 | 2.86 | 0.5329 | 0.7468 | Not significant |
| Pure error | 26.83 | 5 | 5.37 | | | |
| Cor. total | 7244.95 | 19 | | | | |

software based on ASTM B 276. At the time of the coating process, when the coating material feed rate increases, the harder elements (alumina) rebound from the coated surface, which causes the deposit flaws that lead to the coating porosity.

In this investigation, alumina blending of 20 wt.% with Al alloy powder was kept constant because increasing the hard element percentage in the coating will decrease the deposition efficiency owing to the hard particle rebound while spraying against the substrate, as acknowledged by Spencer et al. [10].

2.2. Identification of Process Parameters. The initial step in the design of the experiment is to select the spray parameters that will be explored. In general, all parameters impact on the characteristics of the deposit. The prominent parameters

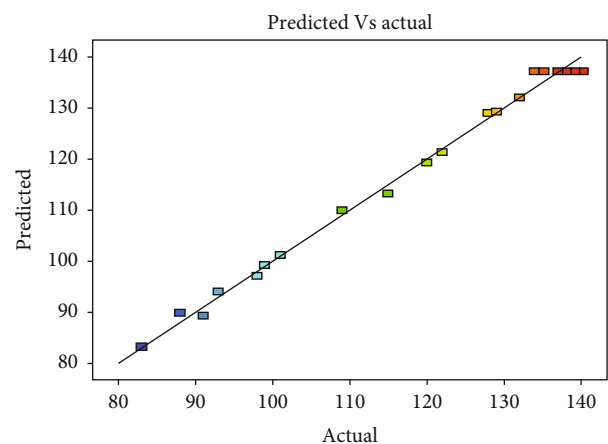


FIGURE 5: Correlation graph (hardness).

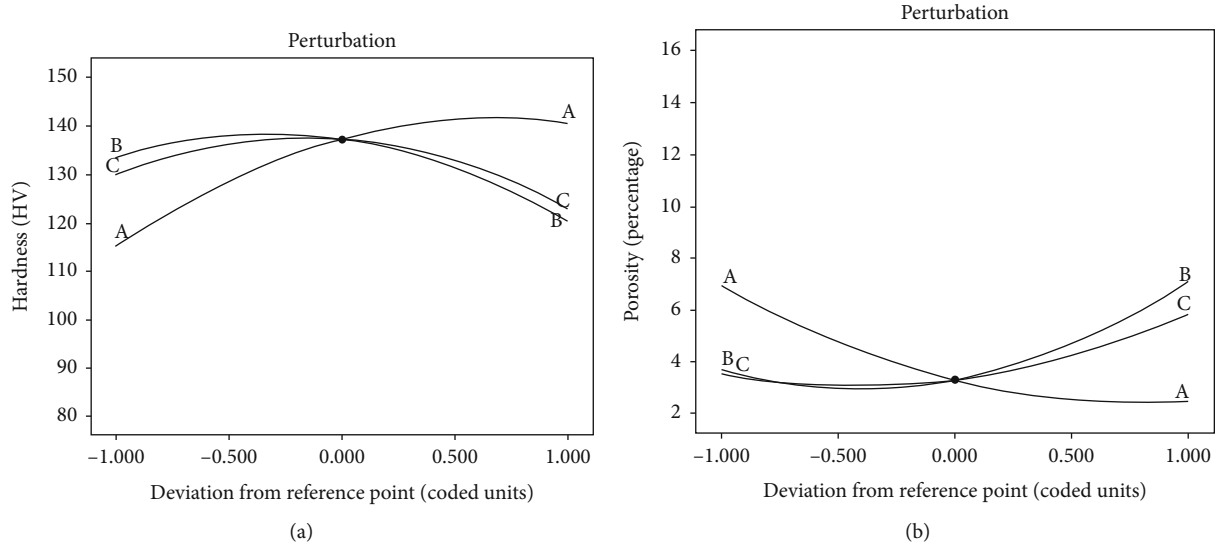


FIGURE 6: Perturbation plots: (a) hardness; (b) porosity.

that had a higher impact on the deposit were chosen based on previously published work [18, 19]. The selected factors are temperature, SOD, and powder feed rate. A higher number of experimental tests were conducted to identify the possible operating ranges for LPCS.

2.3. Identifying the Parameter's Operational Limits. To determine the feasible operational range of the aforesaid parameters, a vast number of tests are carried out on the AZ31B Mg alloy substratum by changing one of the LPCS process variables and maintaining the other parameters intact. Numerous tests were carried out by varying the variables of the LPCS, and the findings during coating are depicted in Figure 4.

If the temperature was below 500°C, the coating powder heating and softening do not take place, and the adhesive properties between the substrate and the coating are very poor. If the temperature is above 550°C, the melting of coating powder affects the coating principle of CS. Nozzle blocking occurs because of melting. The maximum possible temperature is 600°C (restriction in the temperature supply of the Dymet 423 LPCS process).

If the SOD was below 5 mm, the coating material does not stick to the substrate; it bounces back, so the deposition rate is very low. Above 15 mm, the spray plume becomes unstable and not able to reach the substrate. Deposition does not take place.

If the feed rate of the coating material is below 15 g/min, uniform deposition does not take place because the flow of coating powder is less. Above 25 g/min, the coating thickness increases dramatically, and the cohesive properties of the deposit are very poor.

2.4. Development of DOE Matrix. Depending on the conditions listed in the previous section, the feasible working range of the LPCS process parameters was determined by the spraying being completed without substratum faults

and the coated sample exhibiting excellent adherence and cohesion behavior. RSM is employed to determine the relationship between the major input parameters and output responses (porosity and hardness). DOE and optimization were conducted through "Design Expert Software 11" with 3 variables, and a 5-level CCD matrix was selected. Table 2 shows the coating factor levels. Table 3 shows the total 20 experiment parameters and their responses by means of microstructural, binary images of porosity and hardness indentation images of the coated sample. Then, the high and low range of the variables was +1.682 and -1.682. Equation (1) is used to determine the coded values of any intermediate value.

$$Y_i = 1.682 [2Y - (Y_{\text{maximum}} + Y_{\text{minimum}}) / (Y_{\text{maximum}} + Y_{\text{minimum}})], \quad (1)$$

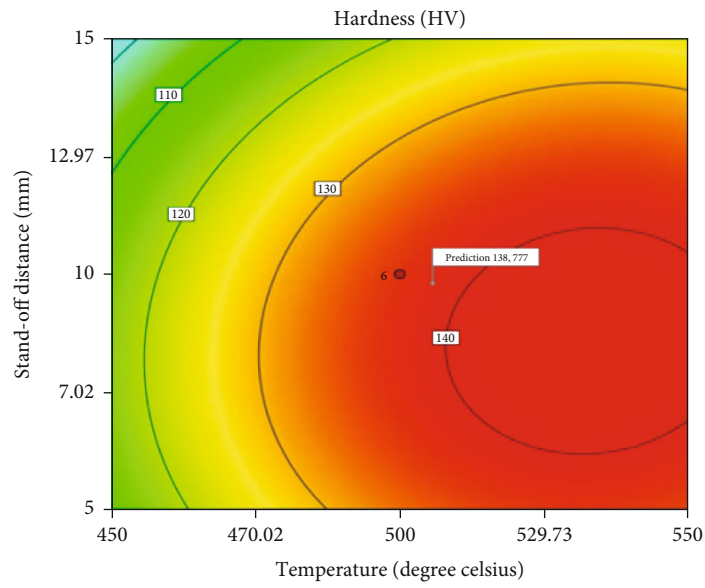
where Y_i is the coded value essential for the Y variable, Y represents any variable value between Y_{minimum} and Y_{maximum} , and the smaller range and higher range of the variables were indicated through Y_{minimum} and Y_{maximum} .

2.5. Development of Empirical Relationships. In the current study, in order to relate the coating parameters to the outcomes of LPCS coatings, a 2nd order polynomial function was constructed to determine the outcome of the experimentally obtained values. It is illustrated below.

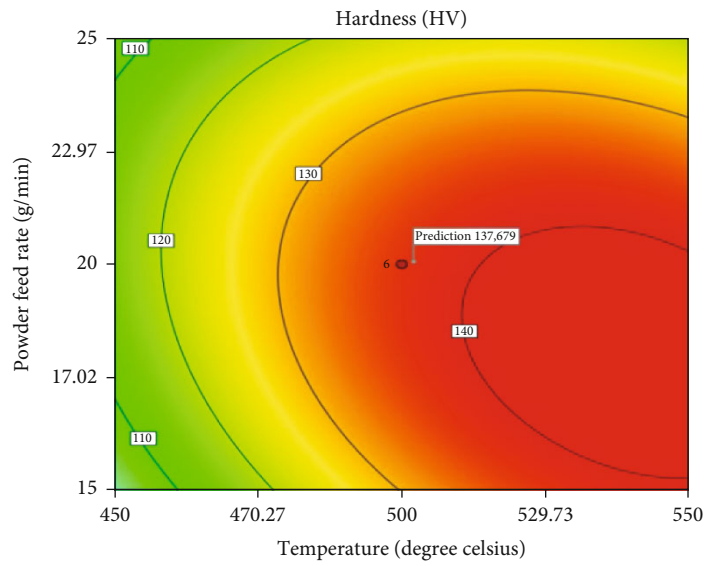
$$Z = a_0 + \sum a_i x_i + \sum a_{ii} x_i^2 + \sum a_{ij} x_i x_j. \quad (2)$$

The outcome (porosity and microhardness) is a function of temperature (T), standoff distance (D), and powder feed rate (P), and it can be indicated as

$$\text{Responses} = f(T, D, P). \quad (3)$$

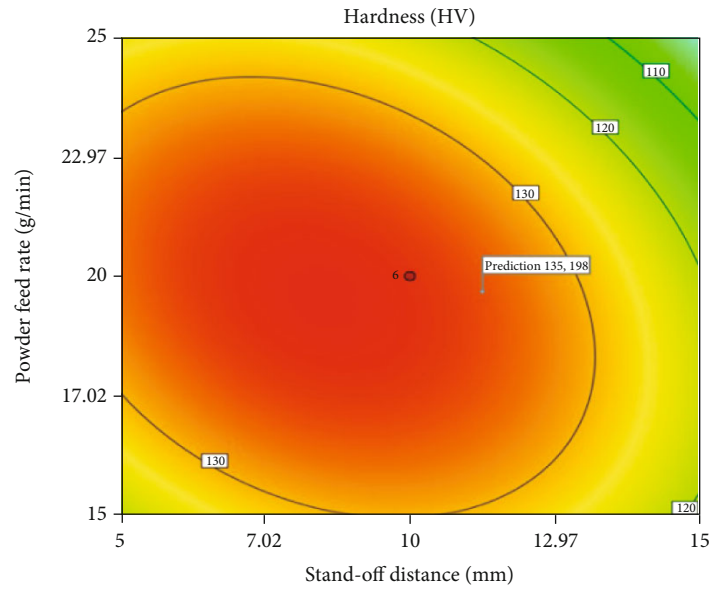


(a)

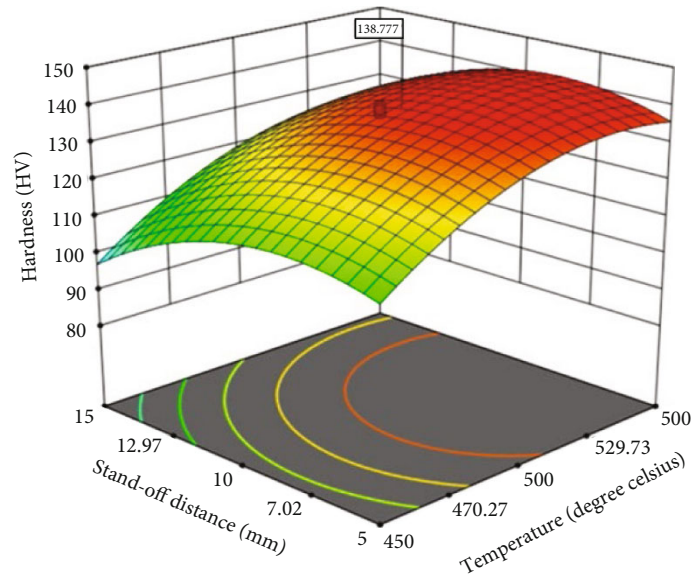


(b)

FIGURE 7: Continued.

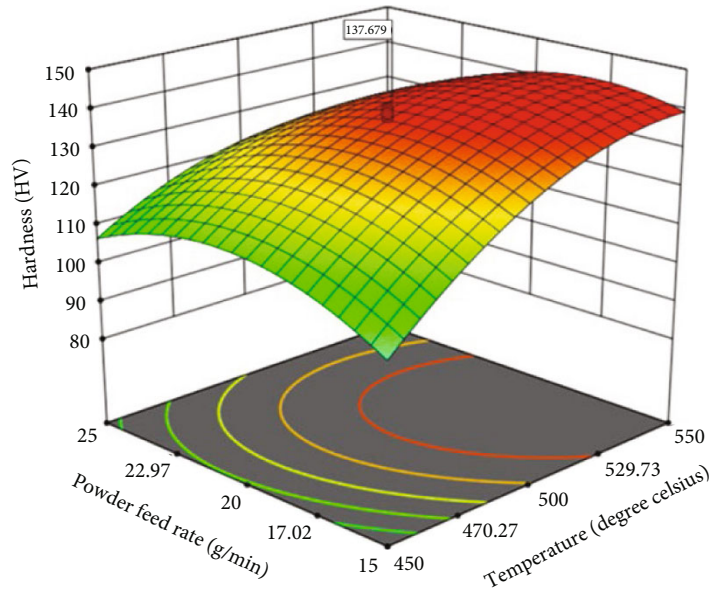


(c)

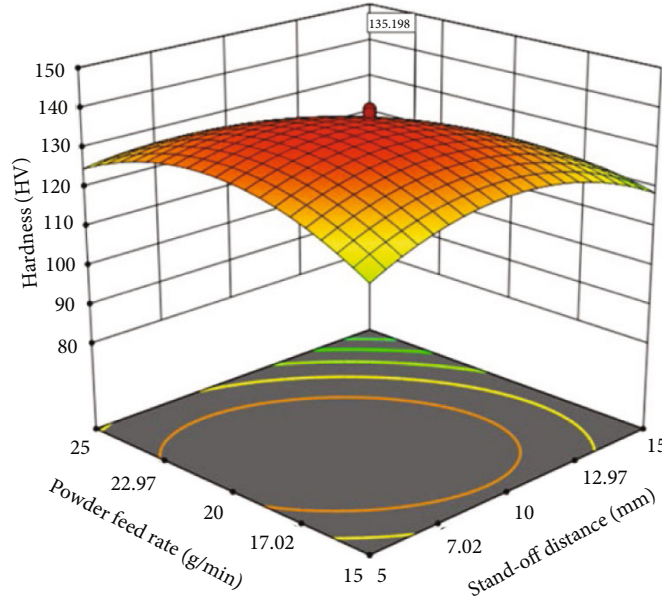


(d)

FIGURE 7: Continued.



(e)



(f)

FIGURE 7: (a–c) Contour graph and (d–f) response graph for hardness.

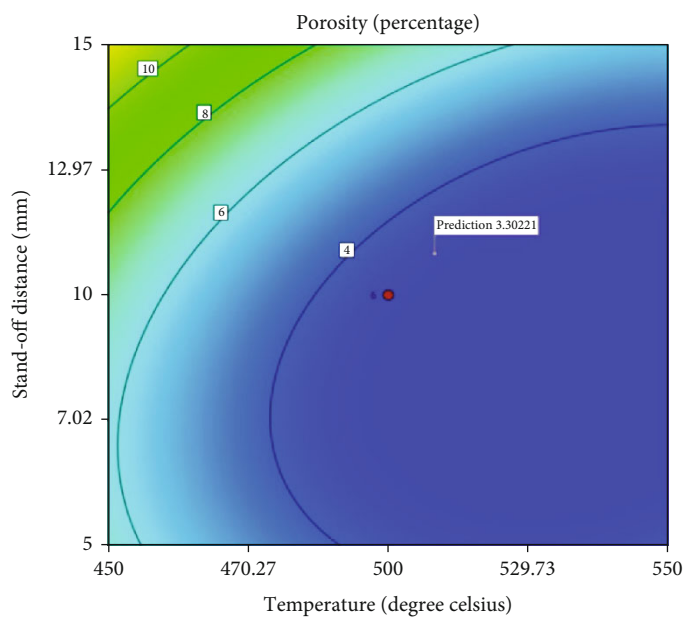
For three factors, the chosen polynomial was indicated as

$$Z = a_0 + a_1(T) + a_2(D) + a_3(P) + a_{11}(T^2) + a_{22}(D^2) + a_{33}(P^2) + a_{12}(TD) + a_{13}(TP) + a_{23}(DP), \quad (4)$$

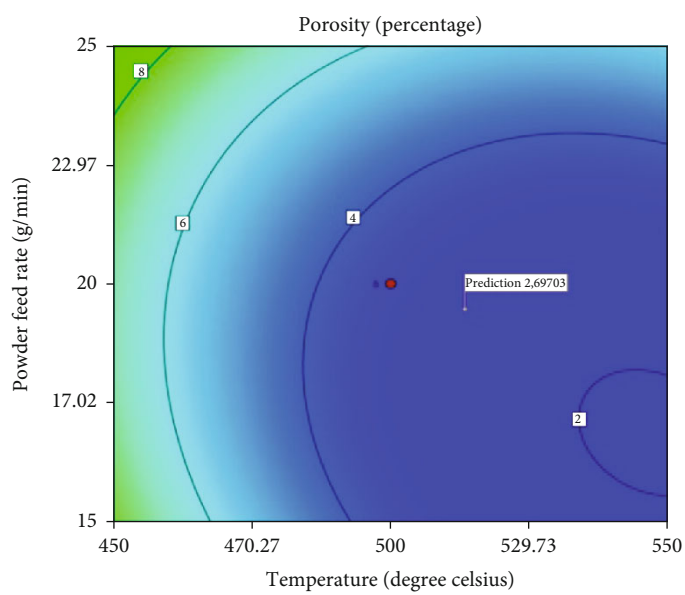
where a_0 is the average response value; the coefficients a_1, a_2, \dots, a_{23} are based on the linear, interactive, and square terms of factors. In this study, design expert software was utilized to compute the coefficients. The Student t -test and p values were adopted to know about the needs

of each coefficient and are illustrated in Tables 4 and 5. The following empirical relations were generated through these coefficients, which include important factors on their own.

$$\begin{aligned} \text{Porosity (volume\%)} = & 3.32 - 2.23(T) + 1.69(D) \\ & + 1.15(P) - 0.87(TD) + 0.62(TP) \\ & + 1.38(DP) + 1.39(T)^2 + 2.10(D)^2 \\ & + 1.39(C)^2, \end{aligned} \quad (5)$$



(a)



(b)

FIGURE 8: Continued.

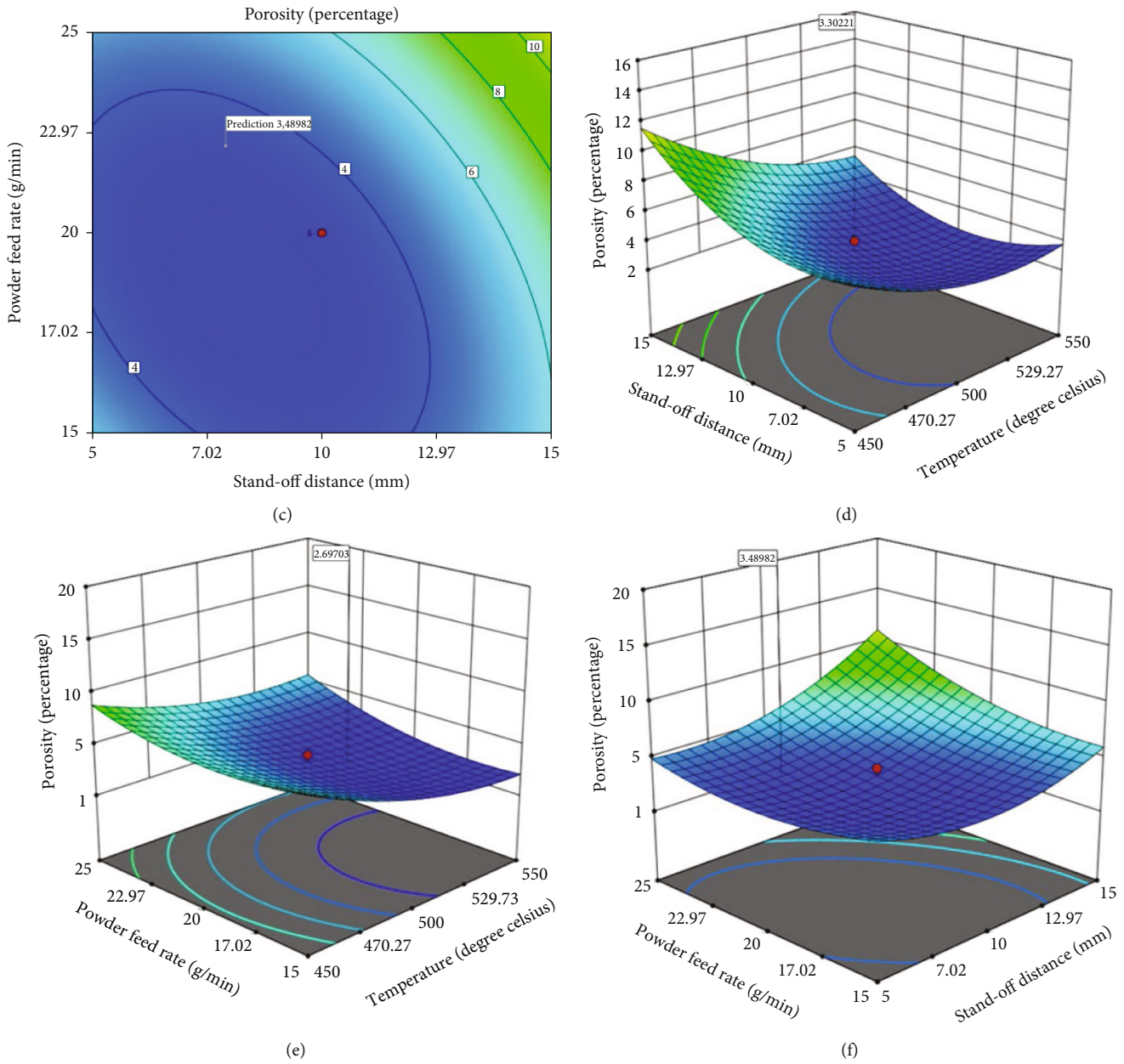


FIGURE 8: (a-c) Contour graph and (d-f) response graph for porosity.

$$\begin{aligned}
 \text{Hardness (HV}_{0.03}) &= 137.21 + 12.74 (T) + 6.59 (D) \\
 &\quad - 3.55 (P) + 1.13 (TD) - 5.87 (TP) \\
 &\quad - 5.62 (DP) - 9.38 (T)^2 - 10.26 (D)^2 \\
 &\quad - 10.26 (P)^2.
 \end{aligned}
 \tag{6}$$

The probability greater than F less than 0.05 denotes that the model is highly significant. R^2 values were determined to be 0.9951 and 0.9946, respectively. This means that 99.51% and 99.46% of the experimental outcomes accord with the proof anticipated through the known observational relationship. R^2 ranging between 0 and 1

indicates that the empirical relation developed is appropriate. The R^2 value must be near to 1.0, indicating that the statistical model generated is more accurate. The figure suggests that the residual fall of the straight line represents the flaws. The distribution of the flaws is normal. Figures 4 and 5 illustrate that the value obtained closely correlates with the experimental results.

3. Results and Discussion

In this investigation, a numerically and graphically optimized approach was used to determine the porosity and hardness of the LPCS deposit. Because the inverse correlation between porosity and hardness was well established in

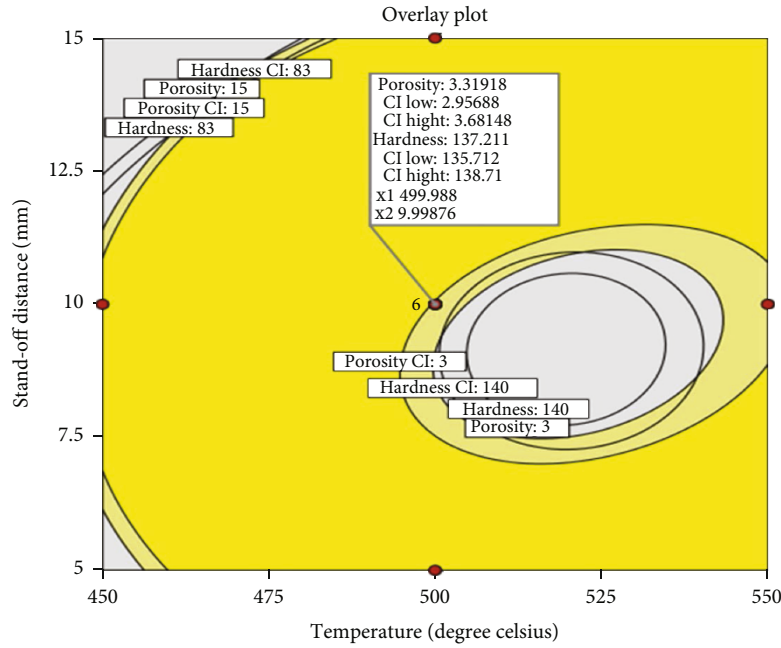


FIGURE 9: Overlay plot.

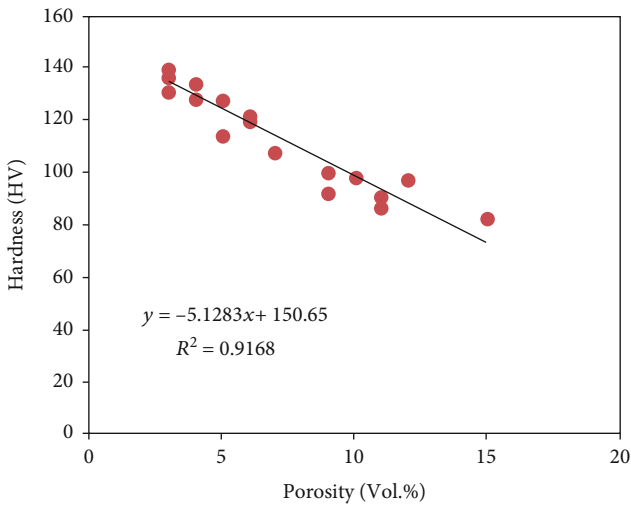


FIGURE 10: Relationship between porosity and hardness.

the LPCS deposit, the choice was made to improve hardness and reduce porosity. The best condition was obtained by setting constraints on output responses and on the process parameters. As indicated in Figure 6, the level of porosity of the deposit was predicted and exhibited based on the obtained regression equation.

As illustrated in Figure 7, the powder feed rate is the most important coating parameter because it reveals the greatest variation in coating properties. According to Figure 7 and Table 2, it is noticed that the hardness of the deposit raises remarkably when the powder feed rate is increased to the level of 20 g/min. At 20 g/min of powder feed rate, the alumina particles in the deposit also rise as large amounts of elements are distributed in the LPCS

plume. The presence of ceramic elements in the deposit gives better load distribution ability between the matrix phase and the ceramic elements, resulting in improved hardness. The presence of ceramic particles in the deposit raises the interface region accessible to distribute the load from the matrix phase when loads are applied. Finally, a higher concentration of ceramic elements reduces the mean free route among the ceramic elements, which prevents plastical distortion of the deposit in load state by preventing void nucleation, resulting in improved deposit hardness.

The coating properties show better results with the optimized standoff distance of 10 mm as shown in Figure 7. Therefore, by raising the standoff distance above 10 mm, the properties of coatings go down. The variance in coating properties as the standoff distance increases is based on the impact velocity of the coating material. At 10 mm of SOD, the powder elements' impact in flight velocity is raised; thus, the impact velocity of the elements is very high. Therefore, very high impacting velocity causes a peening reaction in the deposit, which causes it to consolidate and form a very dense coating. It results in the improved hardness of the deposit. Previously, we stated that by raising the standoff distance, the elements' dwell time in the spray plume increases, resulting in higher element temperature. Nevertheless, raising the standoff distance after reaching an optimum level leads to lowering the element temperature as the isothermic in the plume starts to decompose. As a result, raising the standoff distance beyond a particular level causes a reduction in the deposition efficiency and coating hardness. The hardness of the deposit is afflicted by the massive number of reinforcement particles (alumina) in the deposit, despite the fact that the presence of alumina particles in the coating material mixture was kept constant for this investigation. As a result, it is possible to infer that the alumina

TABLE 6: Validation results for optimization.

| Exp. no. | Temperature (degree) | Cold spray parameters | | Porosity (vol.%) | | | Microhardness (HV) | | |
|----------|----------------------|------------------------|--------------------------|------------------|----------|---------------|--------------------|----------|---------------|
| | | Standoff distance (mm) | Powder feed rate (g/min) | By experiment | By modal | Variation (%) | By experiment | By modal | Variation (%) |
| 1 | 510 | 11 | 19 | 4.3 | 4.5 | +3.77 | 128 | 134 | +4.47 |
| 2 | 513 | 13 | 22 | 5 | 4.6 | -2.56 | 126 | 132 | +4.54 |
| 3 | 520 | 12 | 23 | 5.3 | 5 | -4.63 | 135 | 130 | -3.38 |

TABLE 7: Validation outcomes for developed empirical relationships.

| Exp. no. | Temperature (degree) | Cold spray parameters | | Coatings | |
|----------|----------------------|------------------------|-------------------------|------------------|--------------------|
| | | Standoff distance (mm) | Powder federate (g/min) | Porosity (vol.%) | Microhardness (HV) |
| 1 | 560 | 16 | 27 | 7 | 110 |
| 2 | 440 | 8 | 12 | 13 | 97 |
| 3 | 460 | 9 | 18 | 11 | 90 |

presence in the deposit is maximized when the SOD is 10 mm, resulting in increased hardness as illustrated in Figure 7 and Table 2. The surface hardness of the deposit increases as the temperature rises to 500°C.

Figure 8 illustrates that the porosity of the coating is greatly influenced by powder feed rate and SOD. The deposit's porosity decreases dramatically as the SOD increases to 10 mm. From that, the optimal SOD of 10 mm increases the coating powder dwell span in the plume, resulting in higher particle temperatures. At a temperature of 500°C, the coating powder temperatures promote thermal softening, resulting in flattening the particles that are easy to bind with the early deposited particles. This leads to the pores in the deposits being closed. The porosity of the MMC coatings shows better results at a powder feed rate of 20 g/min, but when the powder feed rate is below 20 and or above 20 g/min, the porosity level in the coatings increases, as presented in Figure 8 and Table 2. Thus, hard particle rebounding will increase with the rising powder feed rate, causing porosity in the rebounded region. Raising the powder feed rate results in a thicker deposit, but the deposit has a higher level of pores owing to particle rebounding, which leads to the porosity level rising in the coating surface.

The multiple-objective optimization concept must be discovered where the criterion fulfills the desirable characteristics simultaneously. As a result, there is a balance between the conditions that must be met by the two techniques. To achieve the objective, the multiple objective optimization method is employed with a specific end aim. The various outcomes were attained through graphical optimization. In the contour graph, the best imposed or highly critical response contours are used to highlight the areas that can meet the stated requirements. It is feasible to visibly verify a good conciliation at this stage. Owing to the handling of many answers, it is recommended that an analytic form of optimization be performed first; otherwise, determining the possible zone could be problematic. Graphical optimization is most

commonly found in the sector of viable areas in the factor zone. The areas shaded are really not suitable for the optimization approach. The next step was to overlap the indicated regions of every outcome to create an intriguing location or a huge plot. Figure 9 depicts the predicted outcomes of the overlay patterning of outcomes (porosity and hardness). For concepts of better hardness and lower porosity, the light-reduced shadow is still used.

As illustrated in Figure 10, the hardness and porosity of the MMC deposit arising from the experimentation data are connected. The experimentation values are best suited by a single straight line.

The regression equation will be used to depict the straight line.

$$\text{Hardness (HV)} = -5.128x + 150.65 \text{ porosity (vol.\%)}. \quad (7)$$

The slope of the approximated regression model (-5.128) is negative, indicating that hardness values rise as porosity falls. The determination coefficient $R^2 = 92\%$. It could be expressed as a percent of the overall sum of squares that can be defined using the approximation regression models. The determination coefficient R^2 is a fit-goodness estimate of the predicted regression model.

The built regression line (Equation (7)) is frequently utilized for two reasons:

- (i) To calculate the hardness standard in relation to the porosity of the deposit
- (ii) Estimating the specific hardness for a particular degree of porosity for the deposit

The confidence and probabilistic intervals indicate if the regression outcomes shorter spacing provides greater precision (Figure 10). The confident interval is an approximated range among the mean value of Y 's and the X 's. PI is an approximation of the individualized value interval of y for

a specified x value. The developed regression model provides a point to determine the mean hardness value for a specified value of porosity. The differentiation among the confident and probabilistic intervals is due to the reason that the mean value of hardness can be measured more precisely than the individualized hardness value. The higher the probabilistic interval, the greater the uncertainty formed by predicted randomized variable value than that of estimated mean value.

3.1. Validation. It is essential to evaluate the determined relationship developed was correct for prediction of the responses in the formation of empirical relations. The prediction ability of the empirical relation developed was examined by running three more experimentation with coating process parameters.

Tables 6 and 7, demonstrate the experimental and expected findings. The anticipated porosity and hardness values estimated from present relation are similar to the experimentation findings and which is 5% of the deviation.

Depending on the results of the investigation, the proposed optimal parameters are provided in Table 6. Cold spray experiments were prepared and carried out with these variables, and other three sets of trials with higher and lower levels of optimum condition outcomes were also carried out, as shown in Table 7.

From this investigation, deviation from the optimized spray parameters results in a rise in porosity as well as a decrease in hardness. This is due to the higher temperature softening of the coating material, variations in SOD, and the time it takes for the coating plume to reach the substrate.

4. Conclusions

A central composite rotatable design was utilized to investigate the effect of coating parameters on the microhardness and porosity of the LPCS aluminum alloy/alumina metal matrix composite (MMC) deposit. The following results were obtained with the goal of improving the coating parameters to enhance coating hardness and reduce the porosity of the deposit.

Empirical relations were generated from the experimentation results that will be utilized to examine the correlation between the variables of the LPCS method and the quality properties of the deposit, such as the porosity and hardness of the MMC deposit by RSM.

According to ANOVA, graphical and numerical study outcomes, powder feed rate and standoff distance were found to be the most predominant factors affecting the porosity and hardness of the deposits, followed by temperature.

The optimum process parameters were determined to be 20 g/min feed rate, 500°C temperature, and 10 mm SOD. By using the above process parameters, the actual value (experimental) coating microhardness was 140 HV, and the porosity was 3 vol.%. The predicted value (contour, response, and overlay plot) coating microhardness was 137.21 HV and porosity was 3.31 vol.%.

Data Availability

The data used to support the findings of this study are included in the article. Should further data or information be required, these are available from the corresponding author upon request.

Disclosure

The study was performed as a part of the employment at Hawassa University, Ethiopia.

Conflicts of Interest

The authors declare that there are no conflicts of interest regarding the publication of this paper.

Acknowledgments

The authors are grateful to the Department of Science and Technology (DST)-Science and Engineering Research Board (SERB), Government of India, New Delhi, for providing financial support for this study under the Empowerment and Equity Opportunities for Excellence in Science (EMEQ) scheme, R&D project file no. EEQ/2018/000472. The project assistant of DRDO Mr. A. Arunkumar is greatly acknowledged for technical support.

References

- [1] J. E. Gray and B. Luan, "Protective coatings on magnesium and its alloys – a critical review," *Journal of alloys and compounds*, vol. 336, no. 1-2, pp. 88–113, 2002.
- [2] H. Assadi, F. Gartner, T. Stoltenhoff, and H. Kreye, "Bonding mechanism in cold gas spraying," *Acta Materialia*, vol. 51, no. 15, pp. 4379–4394, 2003.
- [3] T. Peat, A. Galloway, A. Toumpis, P. McNutt, and N. Iqbal, "The erosion performance of particle reinforced metal matrix composite coatings produced by co-deposition cold gas dynamic spraying," *Applied Surface Science*, vol. 396, pp. 1623–1634, 2017.
- [4] T. Stoltenhoff, H. Kreye, and H. J. Richter, "An analysis of the cold spray process and its coatings," *Journal of Thermal Spray Technology*, vol. 11, no. 4, pp. 542–550, 2002.
- [5] Y. L. Liang, Z. B. Wang, J. Zhang, J. B. Zhang, and K. Lu, "Enhanced bonding property of cold-sprayed Zn-Al coating on interstitial-free steel substrate with a nanostructured surface layer," *Applied Surface Science*, vol. 385, pp. 341–348, 2016.
- [6] T. Suhonen, T. Varis, S. Dosta, M. Torrell, and J. M. Guilemany, "Residual stress development in cold sprayed Al, Cu and Ti coatings," *Acta Materialia*, vol. 61, no. 17, pp. 6329–6337, 2013.
- [7] H. Koivuluoto, J. Lagerbom, and P. Vuoristo, "Microstructural studies of cold sprayed copper, nickel, and nickel-30% copper coatings," *Journal of Thermal Spray Technology*, vol. 16, no. 4, pp. 488–497, 2007.
- [8] Y. Tao, T. Xiong, C. Sun, H. Jin, H. Du, and T. Li, "Effect of α -Al₂O₃ on the properties of cold sprayed Al/ α -Al₂O₃ composite coatings on AZ91D magnesium alloy," *Applied Surface Science*, vol. 256, no. 1, pp. 261–266, 2009.

- [9] E. Irissou, J.-G. Legoux, B. Arsenault, and C. Moreau, "Investigation of Al-Al₂O₃ cold spray coating formation and properties," *Journal of Thermal Spray Technology*, vol. 16, no. 5-6, pp. 661–668, 2007.
- [10] K. Spencer, D. M. Fabijanac, and M. X. Zhang, "The use of Al-Al₂O₃ cold spray coatings to improve the surface properties of magnesium alloys," *Surface and Coating Technology*, vol. 204, no. 3, pp. 336–344, 2009.
- [11] J. M. Miguel, J. M. Guilemany, and S. Dosta, "Effect of the spraying process on the microstructure and tribological properties of bronze-alumina composite coatings," *Surface and Coating Technology*, vol. 205, no. 7, pp. 2184–2190, 2010.
- [12] K. I. Triantou, D. I. Pantelis, V. Guipont, and M. Jeandin, "Microstructure and tribological behavior of copper and composite copper+alumina cold sprayed coatings for various alumina contents," *Wear*, vol. 336-337, pp. 96–107, 2015.
- [13] H. Koivuluoto, J. Lagerbom, M. Kylvälähti, and P. Vuoristo, "Microstructure and mechanical properties of low-pressure cold-sprayed (LPCS) coatings," *Journal of Thermal Spray Technology*, vol. 17, no. 5-6, pp. 721–727, 2008.
- [14] H. Koivuluoto and P. Vuoristo, "Effect of powder type and composition on structure and mechanical properties of Cu +Al₂O₃ coatings prepared by using low-pressure cold spray process," *Journal of Thermal Spray Technology*, vol. 19, no. 5, pp. 1081–1092, 2010.
- [15] S. B. Dayani, S. K. Shaha, R. Ghelichi, J. F. Wang, and H. Jahed, "The impact of AA7075 cold spray coating on the fatigue life of AZ31B cast alloy," *Surface and Coating Technology*, vol. 337, pp. 150–158, 2018.
- [16] N. H. Tariq, L. Gyansah, J. Q. Wang et al., "Cold spray additive manufacturing: a viable strategy to fabricate thick B₄C/Al composite coatings for neutron shielding applications," *Surface and Coating Technology*, vol. 339, pp. 224–236, 2018.
- [17] M.-Z. Ge, J.-Y. Xiang, Y. Tang et al., "Wear behavior of Mg-3Al-1Zn alloy subjected to laser shock peening," *Surface and Coating Technology*, vol. 337, pp. 501–509, 2018.
- [18] W. Jibrán, J. Hogan, and A. McDonald, "Towards optimization of thickness, hardness, and porosity of low-pressure cold sprayed WC-Ni coatings," *International Journal of Advanced Manufacturing Technology*, vol. 116, no. 7-8, pp. 2149–2160, 2021.
- [19] J. Pattison, S. Celotto, A. Khan, and W. O'neill, "Standoff distance and bow shock phenomena in the cold spray process," *Surface and Coating Technology*, vol. 202, pp. 1443–1454, 2018.

Research Article

Surface Roughness Evaluation in Turning of Nimonic C263 Super Alloy Using 2D DWT Histogram Equalization

S. Lakshmana Kumar ¹, M. Thenmozhi ², R. M. Bommi ³,
Chakaravarthy Ezilarasan ⁴, V. Sivaraman ⁵ and Sivaprakasam Palani ⁶

¹Department of Mechanical Engineering, Sona College of Technology, Salem, India

²Department of Computer Science, Sona College of Arts and science, Salem, India

³Institute of ECE, Saveetha School of Engineering, SIMATS, Chennai, India

⁴Center for Applied Research, Chennai Institute of Technology, Chennai, India

⁵Department of Mechanical Engineering, Dr. N.G.P. Institute of Technology, Coimbatore, India

⁶Department of Mechanical Engineering, College of Electrical and Mechanical Engineering, Addis Ababa Science and Technology University, Addis Ababa, Ethiopia

Correspondence should be addressed to S. Lakshmana Kumar; lakshmana@gmail.com and Sivaprakasam Palani; shiva@aastu.edu.et

Received 24 February 2022; Accepted 9 April 2022; Published 28 April 2022

Academic Editor: V. Vijayan

Copyright © 2022 S. Lakshmana Kumar et al. This is an open access article distributed under the Creative Commons Attribution License, which permits unrestricted use, distribution, and reproduction in any medium, provided the original work is properly cited.

Surface roughness of specimens is an important area of research since it influences the performance of machined parts. Meanwhile, employing a vision system to judge the roughness of the machined surface of specimens via captured images acquired from the specimen is an innovative and extensively used method. In this investigation, a vision system is used to capture the SEM images of the machined surface. The two-dimensional images of the machined surface of the Nimonic263 alloy are used to approximate the profile of the surface of specimens in finish turning. Surface roughness was detected in simulated images of specimens in a variety of machining conditions using the imaging technology. In this research work, the surface texture is extracted using a technique that combines 2D surface images and wavelet transform approach. The 2D wavelet transform has the capability to disintegrate a machined surface image into multiresolution depiction for several surface characteristics and can be utilized for surface evaluation. The difference in the histogram frequency of an illuminated region of interest (ROI) from turned surface images was analyzed to aid in the evaluation of surface roughness with an average prediction error of less than 3.2%.

1. Introduction

In the production and development of industrial parts, both the microstructure of the surface on a μm -scale and integrity strongly influence the characteristics and functions of components, such as wear, precision, anticorrosion, fitting, friction, and antifatigue attributes. Direct methods and indirect methods are the two types of techniques available for surface roughness evaluation. Using a toolmaker's microscope, 3D surface profiler, optical microscope, or SEM (off-line method) or a CCD camera, significant procedures evaluate the surface profile of machined surfaces. These

observing systems are often based on a comparison of an optimum cutting process reference signal with the actual process signal [1, 2]. Electrical discharge machining was recently used to machine Nimonic super alloy (EDM) [3]. The measurement scale (L) and root mean squared roughness (R_q) are determined to comprehend the surface property based on scaling analysis [4]. Researchers have developed a method to determine the degree of tool wear by evaluating the machined surfaces' texture using an image processing methodological approach to the image of the machined surface to overcome these limitations. Tool wear measurement, surface quality control, workpiece surface

texture measurements, and other machining processes can all benefit from digital image processing (DIP) with machine vision. Image processing techniques were used to determine the surface roughness of large-scale SEM images [5, 6].

Response surface methodology (RSM) was employed to do mathematical modelling of surface roughness and flank wear. ANOVA is assessing the impact of each individual parameter on responses. Between the simulated and experimental data, there was a maximum inaccuracy of 13% and 7% in flank wear and roughness of the surface, respectively [7]. Machining of Nimonic alloy and Inconel alloy is regarded as critical, and it is necessary to investigate the impact of machining factors on machining responses in order to identify the best machining/control factors and their levels in order to improve the machined surface's integrity/machinability [8–10]. The majority of image processing-based machined surface roughness evaluation approaches depend on feature extraction processes [11].

A review of tool condition monitoring based on image processing approaches was presented by Dutta et al. The findings of Dutta et al. suggest that in a single experimental setup, direct approaches will be employed to validate the outcomes of indirect procedures. The tool wear was evaluated based on the workpiece's rough surface. The gray-level cooccurrence matrix (GLCM) is an efficient technique for selecting the best texture based on entropy metric [12]. Shahabi and Ratnam [13] proposed surface roughness evaluation by capturing the images of the machined surface in cycle using computer vision in this investigation. Grayscale imaging was used to detect simulated pictures of specimens in a variety of machining conditions. The results demonstrated that this method may be utilized to mimic and analyze a specimen's surface profile in finish lathe machining as a tool tip fingerprint.

Dutta et al. [14] designed an improvised GLCM algorithm to monitor the tool condition with an offset parameter. According to the findings, the GLCM analysis focussed on the pixel pair spacing (PPS) value selection that is entirely reliant on the variances of feed marks having been turned [15]. Using response surface methodology, the impact of drilling parameters like tool rotational speed, geometrical parameters, flank wear, and feed rate on surface roughness was investigated. GLCM-based texture analysis of workpiece surface images was employed to obtain waviness information through spatial correlation of pixels [16]. DWT-based texture analysis has also been used to machine surface images to gather information on modification in surface texture due to the increase in tool flank wear via G_a , GRMS, and energy in space-frequency localization.

Liu et al. [17] investigated the explored flank face surface texturing on the WC/Co carbide tools with various geometrical features. The tools with microscale grooves parallel to the primary cutting edge on the flank face had the best flank wear resistance. The tool wear was assessed using the DWT method on machined surface images [18]. The DWT was used to perform a microscale study of a turned surface with average coefficient of determination values of 0.957 and 0.953, respectively; an exponential association of GRMS and energy values with progressing flank wear of the tool

is discovered. Illumination-compensated pictures were suggested by John and Arunachalam to evaluate the surface roughness of turned surfaces in the grinding process [19].

Gandla et al. investigated surface roughness using incremental forming [20]. Taylor Hobson Talysurf is used to measure the surface roughness of manufactured parts, which varies from 0.61 to 3.61 mm. Few images were acquired from each formed part and saved in an image dataset for machine vision-based surface roughness evaluation. The wavelet transform method, Euclidean distance method, and Hamming distance approach were used to classify these images into three classes predicated on the range of surface roughness. The wavelet-based technique has a maximum classification performance of 95.4 percent, according to the results. The classifying effectiveness of the Hamming and Euclidean distance approaches is 78.39 percent and 81.48 percent, respectively. Ali and Dhar [21] proposed an ANN technique for forecasting surface roughness in turning. This model may be used to optimize the cutting process for efficient and economical manufacturing by predicting tool wear and surface roughness in the turning process. CNN algorithms have gained popularity in the assessment of surface roughness in recent years [22–25]. Because feature extraction is included into the network during the convolution phase, this technique eliminates it. Five loss functions are selected and evaluated for the prediction models based on their potential application and accuracy. The actual and expected surface roughness values are compared using a stylus-based profilometer.

The vibration and communication particle swarm optimization (VCPSO) algorithm, developed by Xu et al., included self-random vibration and interparticle communication processes [26]. When estimating tool wear, the ANFIS learned by the VCPSO algorithm (ANFIS-VCPSO) outperformed other intelligent models. The VCPSO algorithm was tested using benchmark functions, and the results showed that it is capable of global optimization. All the while, the VCPSO algorithm was used to determine the best milling parameter combinations under a variety of tool wear conditions. The technique proposed in this article extracts the surface texture by combining two-dimensional surface photography and a wavelet approach. Then, the future surface roughness is predicted by extracting the time delay parameters, the embedding dimension, and the false nearest neighbour of the produced surface texture. All offline and online approaches can estimate surface roughness parameters based on evidence from the surface image [27]. The stylus tracing (ST) technique became the most widely known way of evaluating the surface properties of components in recent decades, due to the implementation of tactile profilometers [24, 25]. The ST involves measuring the texture of the surface and calculating the R_a roughness parameter but in contact with the surface. The noncontact approach provided in this work, on the other hand, can predict surface texture and roughness characteristics more precisely and with less prediction error by using DWT histogram equalization and Laplacian filtering. This technology represents a significant advancement in the development of smart surface roughness measuring devices that may be used in the smart manufacturing sector in the near future.

2. Experimental Setup

In this experiment, a super alloy Nimonic C263 workpiece was machined in dry cutting mode with CBN inserts. After cutting the entire length of the workpiece, the machined surfaces were imaged as 640×480 -pixel gray-level image data using a CCD camera connected to a personal computer with machine vision capacity at 5 different locations on the surface of the workpiece. The photos were taken with a diffused lighting setup online. With relation to the workpiece, the camera and lighting source were put in place. For the most part, the illumination source was managed to hold at a 30-degree angle. The average flank wear of the insert (V_B average) was also determined using a Leica S6D microscope at 10 magnification and Leica QWin-V3 image capturing software.

Simultaneously, the surface roughness of the turned surface (R_a) was measured at the appropriate locations, where R_a stands for average surface roughness. Table 1 summarises the cutting conditions of turning operations performed on Nimonic 263. For each of the machining conditions, three sets of experiments were carried out (as listed in Table 1). Table 2 summarises the camera setup and surface roughness tester specifications. Each image was cropped to 210×210 pixels before processing. The MATLAB® environment was used for all image processing (version 7.8.0.347 R2021).

2.1. Materials. Nimonic C263 alloy with 150 mm length and 70 mm diameter with hardness of 32 HRC was considered the work material. It is a material with good resistance to high temperature and oxidation owing to its Ni, Cr, and cobalt content. The following are the chemical components of the workpiece material (in % weight): 0.48 Al, 2.94 Ti, 0.15 W, 0.04 Nb, 0.02 C, 0.02 V, 0.007 Ta, 0.001 S, 0.19 Si, 52.49 Ni, 20 Cr, 0.46 Mn, 0.07 Cu, 6.29 Mo, 16.7 Co, 1.0 Fe, 0.48 Al, and 1.94 Ti.

2.2. Methods. The experimental study was carried out on a NAGMATI175 lathe. Figures 1(a)–1(d) show the experimental setup, insert, tool holder, and flank wear. The Sandvik makes Cubic Boron Nitride (CBN) inserts to the specifications of CNGA 120 408S01030A, 7025 grade was chosen as the insert for the tests, and a PCLNR 2020 K12 tool holder was being used to fix the insert. Back rake angle (BRA) (6°), side rake angle (SRA) (6°), end relief angle (ERA) (6°), side relief angle (SRA) (6°), end cutting edge angle (ECEA) (5°), side cutting angle (SCEA) (5°), and nose radius (NR) (0.8 mm) are the tool signatures of the insert. The cutting parameter's effect on surface roughness in turning the Nimonic C-263 alloy was investigated. All turning trials were carried out by a new cutting edge. The experiment was carried out using an L_9 orthogonal array. The machining factors such as feed rate, cutting speed, and depth of cut were considered, and their ranges are listed in Table 3.

A tool maker's microscope was used to measure the surface roughness offline at regular intervals. The measuring range is X-200 mm and Y-100 mm, the microscope stand tilting range is 12, the maximum distance between centres is 700 mm, the maximum diameter accommodating between

TABLE 1: Machining Nimonic C263—experimental setup.

| | |
|---------------|--|
| | NAGMATI175: lathe |
| | H : 165 mm |
| | S : 305 mm |
| Machine tool | Speed: 54–1200 rpm |
| | Feed: 0.048–0.716 mm/rev |
| | Power: 1 HP |
| Insert | PVD-coated carbide insert |
| Cutting speed | 80 m/min, 125 m/min, 195 m/min |
| Feed | 0.055 mm/rev, 0.096 mm/rev, 0.159 mm/rev |
| Depth of cut | 0.25 mm, 0.50 mm, 0.75 mm |

TABLE 2: Machining Nimonic C263—imaging setup.

| Equipment | Specifications |
|------------------------------|--|
| Scanning electron microscopy | Imaging module: 17" touch screen monitor rotary knob, magnification range: 120x to 24,000x |
| | Cutoff: 0.8 mm |
| | Filter: Gauss |
| Surface roughness tester | I : 0.8 mm |
| | Evaluation "I": 4.00 mm |
| | Measuring speed: 0.5 mm/s |

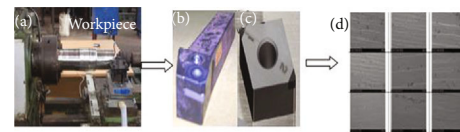


FIGURE 1: (a) Experimental setup, (b) tool holder, (c) insert, and (d) SEM image of flank wear.

TABLE 3: Machining parameters and assigned levels.

| S. no | Factors | Unit | L1 | L2 | L3 |
|-------|------------------------|--------|-------|-------|-------|
| 1 | Speed (S) | mm/rev | 0.055 | 0.096 | 0.159 |
| 2 | Feed (F) | m/min | 80 | 125 | 195 |
| 3 | Depth of cut (a_p) | mm | 0.25 | 0.50 | 0.75 |

centres is 100 mm, the plane stage area is $260 \text{ mm} \times 270 \text{ mm}$, and the resolution is 0.2 μm (linear) (1 minute). Table 4 shows the L_9 orthogonal array and surface roughness measured using conventional and unconventional methods.

3. Methodology

Machine vision systems by default initiate with the image acquisition stage. Machine vision-based methods are extremely recommended for safe evaluation in in situ investigation of machined surfaces. Turned surface images are captured utilizing a high-end vision camera to evaluate the surface texture. The machine vision camera acquires the machined surface images after turning operation, to examine the surface texture. The captured machined surface images undergo normalization to cope up with lighting changes that might affect the image quality. The overall process is encapsulated in the block diagram as shown in Figure 2.

TABLE 4: L_9 orthogonal array, experimental trail results, and unconventional method results.

| Exp. trail no. | Coded values | | | Actual setting values | | | Surface roughness (experimental values) (R_a) | Unconventional measured values (R_a) |
|----------------|--------------|---|-------|-----------------------|-------|-------|---|--|
| | S | F | a_p | S | F | a_p | | |
| 1 | 1 | 1 | 1 | 80 | 0.055 | 0.25 | 3.3057 | 1.25 |
| 2 | 1 | 2 | 2 | 80 | 0.096 | 0.50 | 3.55 | 1.75 |
| 3 | 1 | 3 | 3 | 80 | 0.159 | 0.75 | 2.43 | 2.10 |
| 4 | 2 | 1 | 2 | 125 | 0.055 | 0.50 | 4.89 | 1.50 |
| 5 | 2 | 2 | 3 | 125 | 0.096 | 0.75 | 3.77 | 1.10 |
| 6 | 2 | 3 | 1 | 125 | 0.159 | 0.25 | 2.73 | 1.50 |
| 7 | 3 | 1 | 3 | 195 | 0.055 | 0.75 | 0.844 | 1.075 |
| 8 | 3 | 2 | 1 | 195 | 0.096 | 0.25 | 2.27 | 0.90 |
| 9 | 3 | 3 | 2 | 195 | 0.159 | 0.50 | 3.65 | 0.85 |

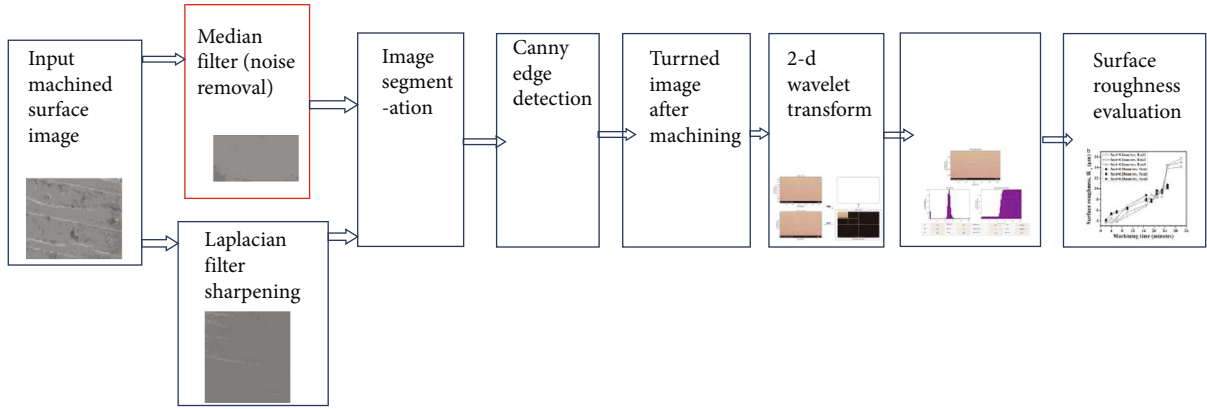


FIGURE 2: DWT histogram equalization.

Normalization is performed as given below:

$$s(m, n) = \frac{r(p, q) - \min(r)}{\max(r) - \min(r)} * 255. \quad (1)$$

The normalized image matrix is represented by $s(m, n)$. The intensity of each pixel in the image matrix is represented by $r(p, q)$. The image matrix's minimum and maximum pixel intensity values are denoted as $\min(r)$ and $\max(r)$, respectively. The machined surface images obtained after turning operation at varied cutting conditions had an enormous flank wear resulting in variation in workpiece textures. This increased flank wear (V_B) reduces the cutting insert noise radius, which affects the machined surface. Machine vision system-refined machined surface images contain flaws such as nanoparticle settlements and feed marks.

The digital camera output is

$$p(m, n) = b(m, n) + \varepsilon(m, n), \quad (2)$$

where $b(m, n)$ is the original image and $\varepsilon(m, n)$ is the added noise.

Wiener filtering is utilized to retrieve the images $b(m, n)$ disrupted by noise.

$$\lambda = \frac{1}{MN} \sum_{p_1, p_2 \in p} b(p_1, p_2), \quad (3)$$

where λ is the local mean intensity surrounding every pixel. Also, p denotes M -by- N neighborhood of every pixel, and $b(p_1, p_2)$ is the location of every pixel in the local neighborhood mask p . Also, variance of intensity surrounding every pixel is obtained by

$$\sigma^2 = \frac{1}{MN} \sum_{p_1, p_2 \in p} b^2(p_1, p) - \lambda^2. \quad (4)$$

The Wiener filter reduces the noise depending upon the statistical variables by lowering the variance of the neighboring pixels. In stage 3, the image segmentation is performed to segment the object from its surrounding pixels. This is utilized to set the cutting tool pixel intensity to 0 and the background to 1; it is explained in the below equation:

$$f_1(m, n) = \{1 \text{ if } f(m, n) \geq T, 0 \text{ if } f(m, n) \leq T\}, \quad (5)$$

TABLE 5: Machining parameters to examine the effect of surface roughness.

| Lathe machine | Nagamathi lathe machine |
|---------------|-------------------------|
| Specimen | Nimonic C263 |
| Cutting speed | 498 m/min |
| Feed rate | 0.1 mm/rev |
| Time | 5, 7, and 9 min |
| Cooling agent | Air |
| Depth of cut | 0.2 mm |

where $f(m, n)$ denotes the actual image of the tool tip after noise removal in the algorithm step 2 and $f_1(m, n)$ denotes the tool tip image after segmenting the cutting tool image. Also, T is the threshold value set by default utilizing the MATLAB command. The machine details and machining conditions considered for the study are given in Table 5.

Preprocessing is required to improve image quality through contrast stretching, histogram equalization, noise reduction through filtering, and inhomogeneous illumination compensation, among other things. Low-pass filtering (median filter) is very effective at reducing noise in machined surface images, particularly cutting tool images, because noise can occur due to dirt, oils, and precision machining dust and dirt on the surface of an object. The Laplacian filter is a second-order temporal high-pass filter that is used to sharpen machined surface images so that the feed marks can be seen clearly. The segmentation method and feature extraction are carried out after preprocessing. By calculating the image gradient and direction, the feature extraction ensures the information of the edges of the workpiece surface images. Because of its noise immunity and ability to detect actual edges with minimal flaws, the Canny edge detector is used in the field of machine vision. Convolution is performed between both the machined surface image and a Gaussian smoothing filter with a standard deviation of s in the Canny edge identification technique. The gradient computation for the smoothed image is the next step. This technique can be used to fetch the edges of a workpiece surface texture. To capture turned images with good contrast, a dispersed lighting prototype such as fibre optic-guided light with a DC-regulated light source and infrared interference filter is used. Segmentation is the process of dividing an image into multiple sections according to a set of rules. The feature-state method collects pixel characteristics into feature vectors, which are then used to assign pixels to classes by selecting a threshold value. Because the 2D wavelet transform can disintegrate a workpiece surface impression into multiresolution depictions for several surface morphologies, it can be used to evaluate surfaces. Signal vectors derived from feed mark images are used to represent the image's grayscale intensity. Use the 2D wavelet transform and the key local intensity variation technique to decompose the image signal vector. Wavelet transform is a time-frequency-conversion mathematical

procedure that is frequently used. The frequency analysis of the signal into scalar analysis is dealt with by wavelet analysis.

$$\Phi_{i,j}(y) = \frac{1}{\sqrt{i}} \varphi \left[\frac{y-j}{i} \right], \quad (6)$$

where i seems to be the scale parametric quantity for varying frequency and “ j ” is the interpretation parametric quantity and $i, j(x)$ is the wave function. Surface roughness is an important parameter for evaluating and controlling manufacturing quality because it can affect the friction coefficient, creep life, and fatigue strength of a machined part. Surface roughness results due to enhanced tool wear; it serves as an indication to replace the tool. Surface roughness evaluation procedures based on image processing can be performed online through E-evaluation. However, this facility is not available in traditional procedures. A rough surface tends to scatter more quantity of light. This causes larger dark regions to form that result in decrease in the image signal RMS value. A rough surface ends up with huge speckle patches that in turn reduce the variance, within the fixed evaluation length. The histogram mapping of an illuminated area of interest (ROI) from machined surface photographs was studied to see if there was any fluctuation in histogram frequency, which helps with surface roughness evaluation [28].

3.1. Evaluation Parameters. The roughness average, also known as the arithmetic average height (R_a), is a roughness parametric parameter that is often used in quality control.

$$R_a = \frac{1}{N} \sum_{i=1}^N |y_i|. \quad (7)$$

“ N ” is the number of samples for a certain evaluation duration and y_i denotes how far the profile deviates from the average line. The root mean square slope (R_{dq}) and arithmetic mean slope (R_{da}) hybrid parametric quantities are used.

$$R_{da}, \text{ Arithmetic Mean Slope} = \sum_{i=1}^N \frac{|\delta_i|}{N}. \quad (8)$$

δ_i is the slope at point “ i ” and “ N ” is the total number of points.

$$R_{dq}, \text{ Root Mean Square Slope} = \sqrt{\sum_{i=1}^N \frac{\delta_i^2}{N}}. \quad (9)$$

4. Results and Discussion

4.1. Characterization of the Machined Surface Utilizing Image Histogram. The surface profile of the workpiece surface is used to measure surface roughness in this paper. The MATLAB software is used to create an intensity

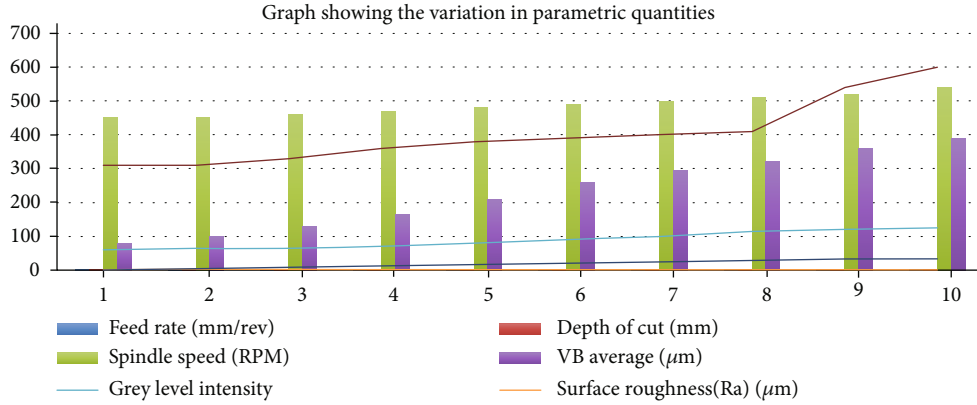


FIGURE 3: Graphical representation of the variations in parametric quantities.

TABLE 6: Evaluation parameters in DWT histogram equalization.

| Feed rate (mm/rev) | Depth of cut (mm) | Spindle speed (rpm) | V_B average (μm) | Gray-level intensity | Surface roughness (R_a) (μm) | Machining time (minutes) | Histogram frequency (Hz) |
|--------------------|-------------------|---------------------|---------------------------------|----------------------|---|--------------------------|--------------------------|
| 0.05 | 0.25 | 450 | 80 | 60 | 1.25 | 0 | 310 |
| 0.07 | 0.50 | 450 | 100 | 65 | 1.75 | 4 | 310 |
| 0.2 | 0.75 | 460 | 130 | 65 | 2.10 | 8 | 330 |
| 0.25 | 0.75 | 470 | 165 | 70 | 1.50 | 12 | 360 |
| 0.26 | 0.25 | 480 | 210 | 80 | 1.10 | 16 | 380 |
| 0.28 | 0.50 | 490 | 260 | 90 | 1.50 | 20 | 390 |
| 0.28 | 0.50 | 500 | 295 | 100 | 1.075 | 24 | 400 |
| 0.28 | 0.75 | 510 | 320 | 115 | 0.90 | 28 | 410 |
| 0.28 | 0.25 | 520 | 360 | 120 | 0.85 | 32 | 540 |
| 0.28 | 0.25 | 540 | 390 | 125 | 0.5 | 33 | 600 |

histogram for the workpiece surface image. The histogram is a visual representation of how the intensity of gray levels increases as the surface quality of the machined surface changes. The left portion of histogram denotes small intensity values, and the right portion denotes larger intensity values. The machined metal surface has high reflectivity; hence, it is convenient to monitor the right side of the histogram. Therefore, gray level of 125 is taken as the reference to evaluate the number of histogram frequency. The reflectivity is enhanced if the machined surface is smooth, thereby resulting in greater frequency values. The histogram for the machined surface is obtained by taking the gray-level intensity values on the x -axis and surface roughness R_a values taken on the y -axis. The machined surface is smooth possessing a surface roughness value of $R_a = 0.5 \mu\text{m}$ and gray-level intensity of 125, at a frequency of 600 Hz. In the second case, the machined surface is coarse possessing a surface roughness value of $R_a = 1.075 \mu\text{m}$ and gray-level intensity value of 100 at a frequency of 400 Hz. By analyzing the histogram of the machined surface image, it enables one to determine if a given machine surface is coarse or smooth. The work involves observing and inspecting the machined surface while turning the Nimonic 263 material with coated carbide inserts at various spindle speeds and feed combinations. Variations in the histogram statistical characteristics that aid in evaluating the surface finish were explored in the his-

toqram form of an illuminated area of interest (ROI) from turning machine surface images. The results clearly show that the turning procedure's cutting specifications have no effect on surface roughness. Figure 3 shows the relationship between machining time and histogram frequency for various feed rates and a steady depth of cut of 0.2 mm at 450 and 510 rpm spindle speeds. The graphs displayed give a general sense of the machined surface's histogram frequency. Only the lowest and maximum feeds at two different speeds are shown in the graphs. Again for entire cutting considerations, the machined surface's surface roughness remains constant. Many investigations have determined that the R_a value changes in a stable range, just as the histogram frequencies of the machined surface obtained with a machine vision system do. The results in Table 6 show that, while the cutting speed and feed rate vary, they have no effect on the machined surface's histogram frequency. For a consistent change in the histogram profile, changing the feed rate causes a change in the form of the feed marks over the machined surface. Various cutting speeds and feed rates were used in the technique.

Figure 4 depicts the original machined surface image and its histogram equivalent. The histogram graph is fetched by taking the surface roughness values on the y -axis and feed rate on the x -axis. An image histogram is a graphical representation of a digital image's tonal distribution. It assigns a

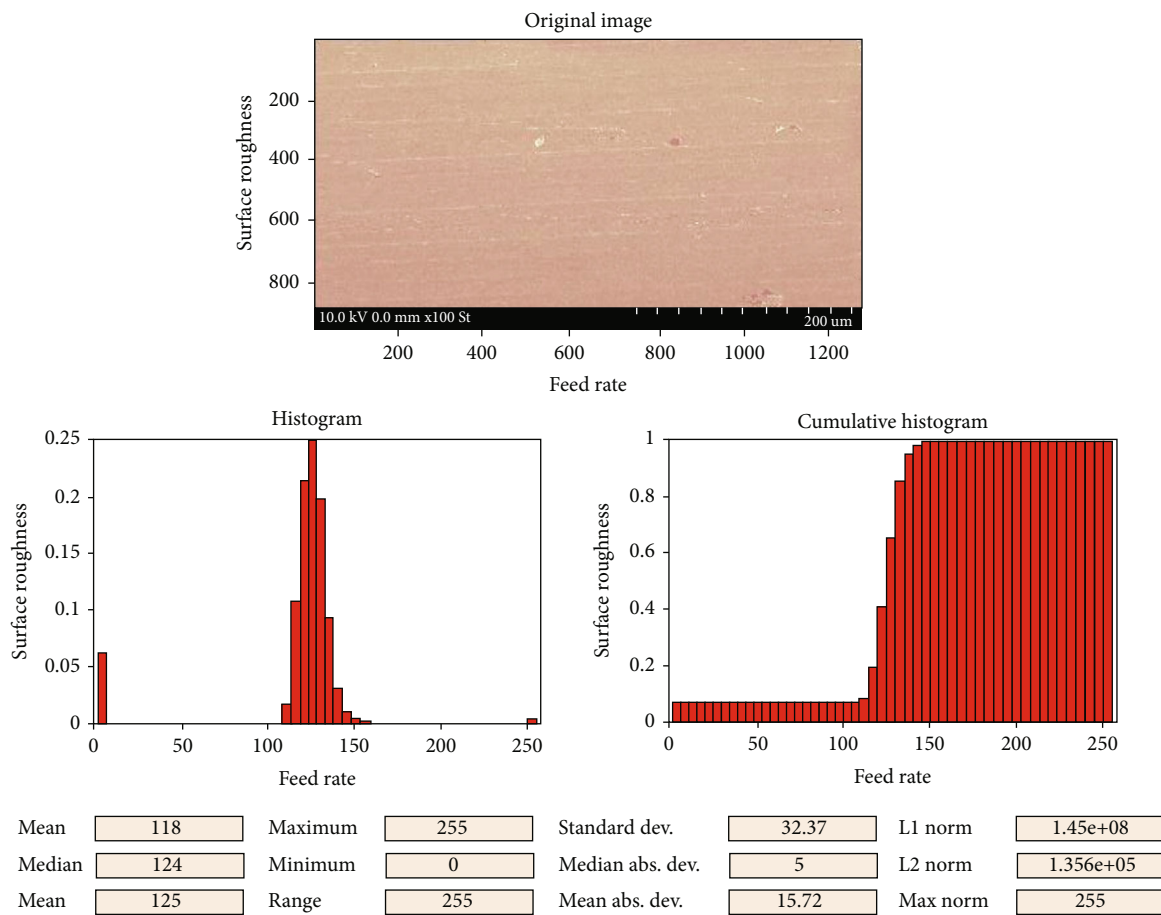


FIGURE 4: Original image and its histogram equivalent.

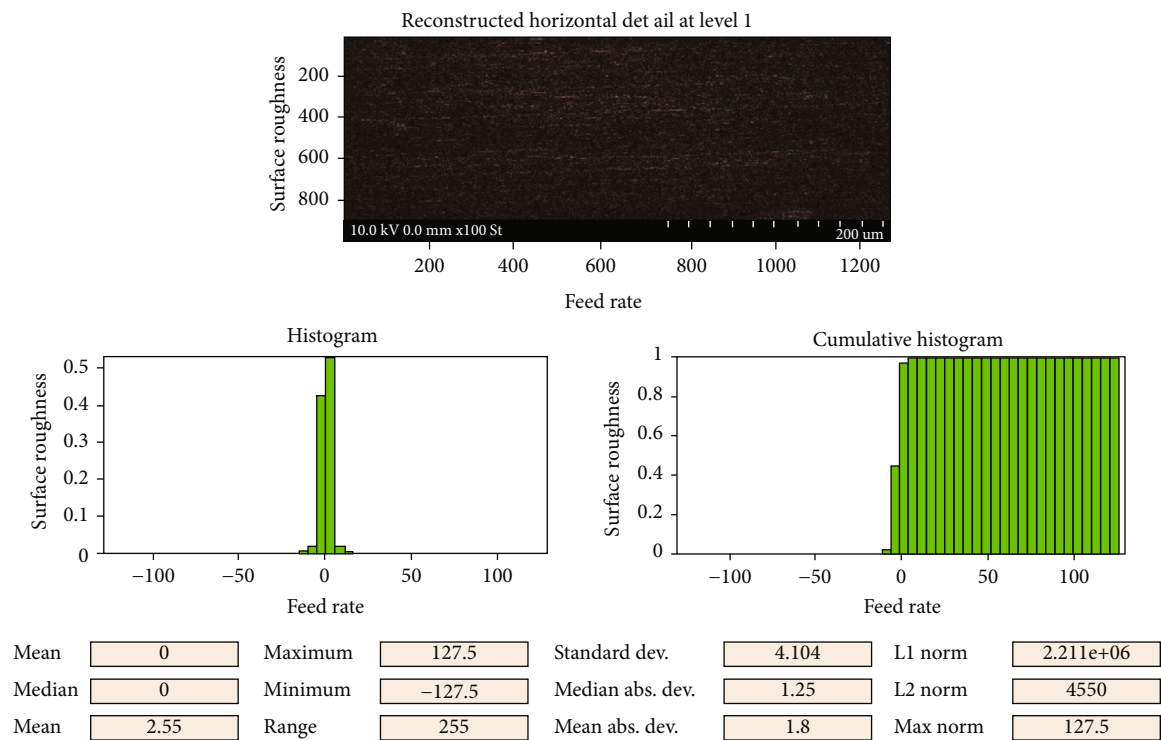


FIGURE 5: Reconstructed image and its histogram equivalent.

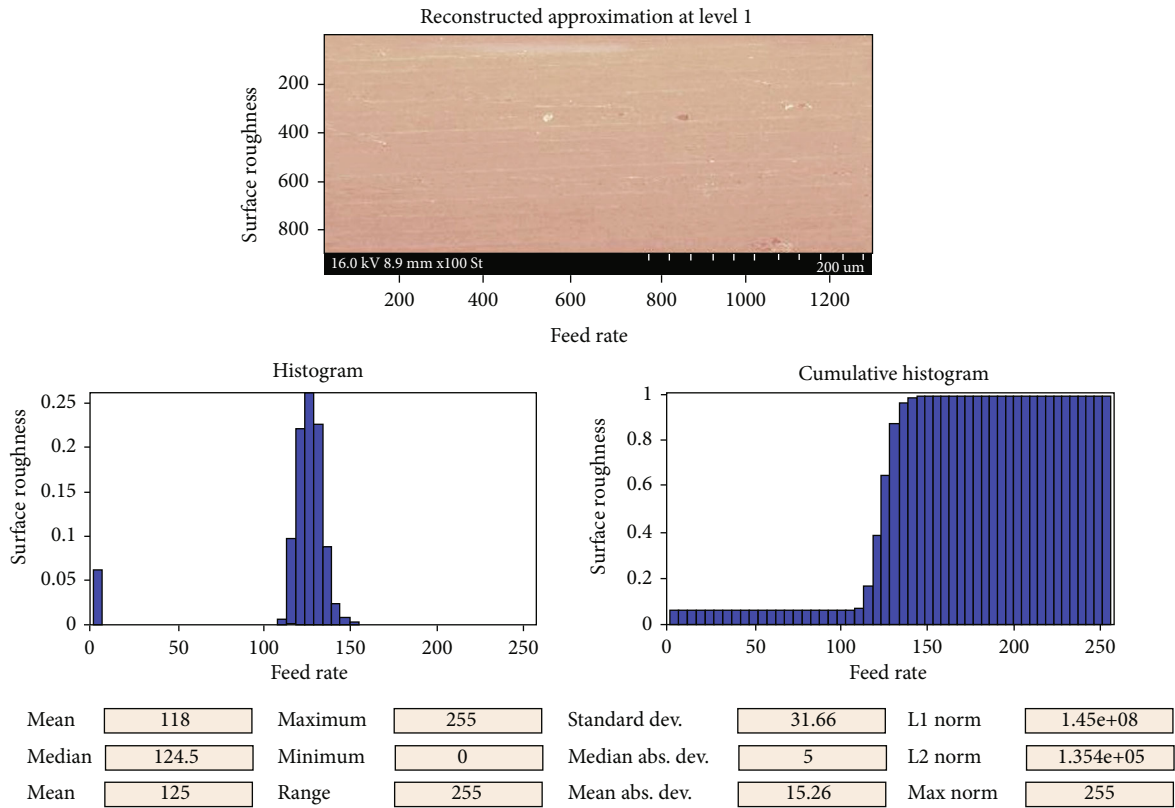


FIGURE 6: Reconstructed approximation and its histogram.

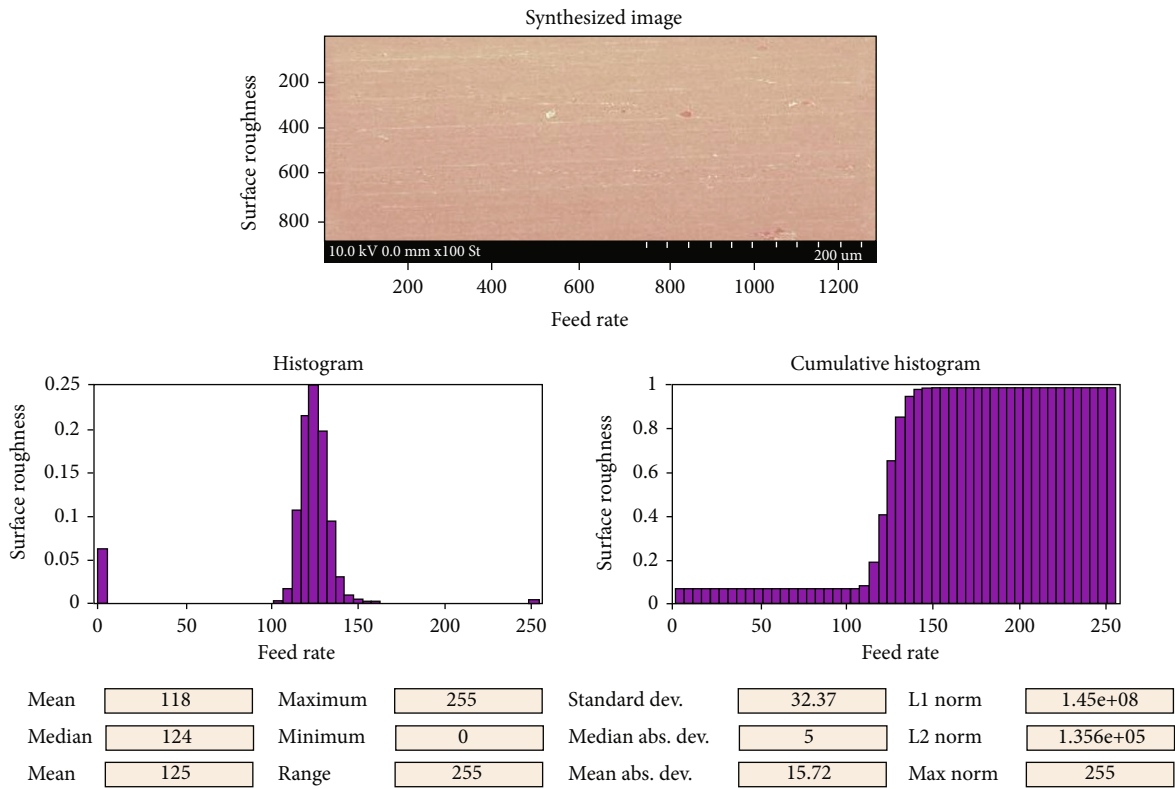


FIGURE 7: Synthesized image and its histogram equivalent.

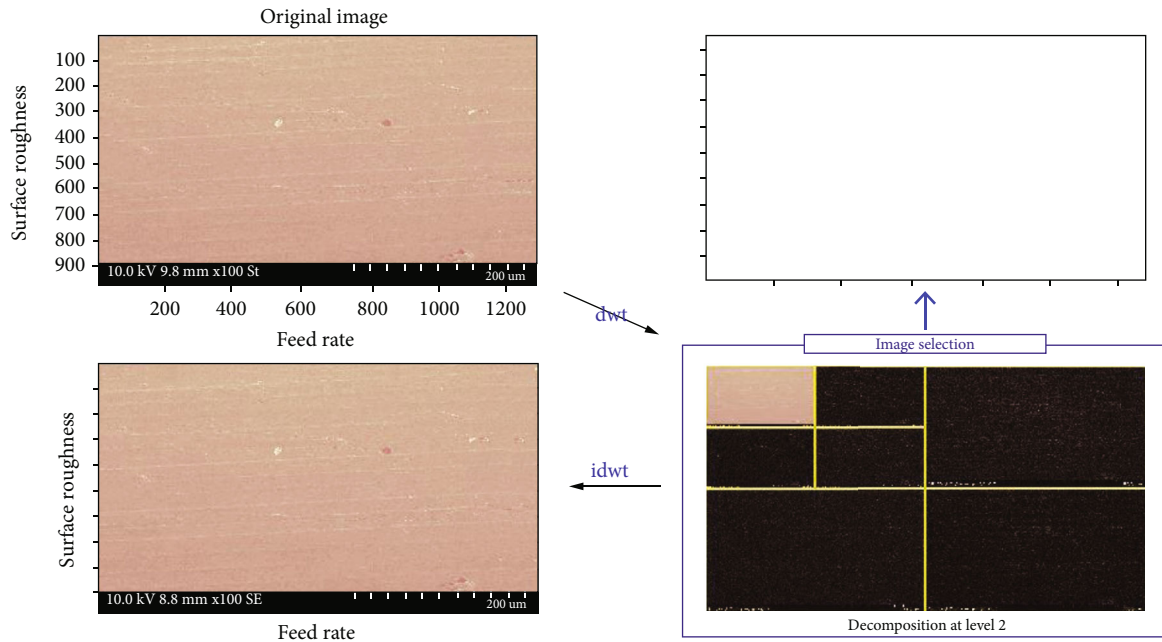


FIGURE 8: Decomposition using discrete wavelet transform.

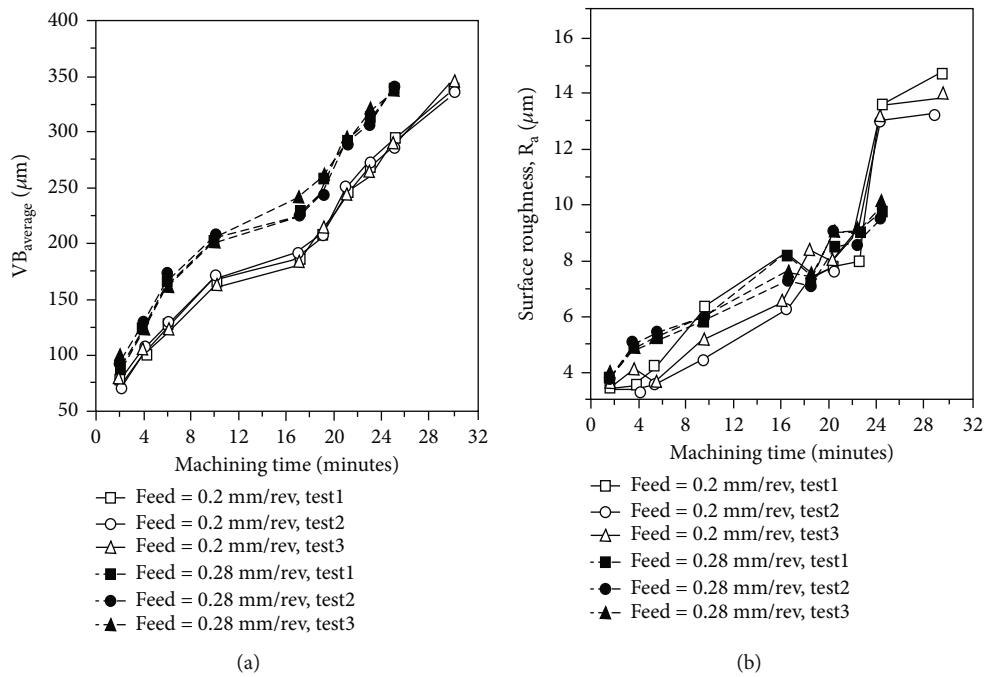


FIGURE 9: (a) Average flank wear vs. machining time. (b) Average surface roughness (R_a) vs. machining time.

pixel value to each tonal value. A viewer can quickly assess the entire tonal distribution by looking at the histogram for a specific image.

Figure 5 depicts the reconstructed machined surface image and its corresponding histogram equivalent. The histogram graph is fetched by taking the surface roughness values on the y-axis and the feed rate on the x-axis. Image reconstruction is the process of putting together 2D and 3D images from scattered or insufficient data.

Figure 6 depicts the reconstructed approximation at level 1 and its corresponding histogram equivalent. The histogram graph is fetched by taking the surface roughness values on the y-axis and the feed rate on the x-axis. The cumulative histogram is a histogram in which the vertical axis displays not only the number for a single bin but also the number for that bin and all bins with lower response variable values.

Figure 7 depicts the synthesized image at level 1 and its corresponding histogram equivalent. Image synthesis is the

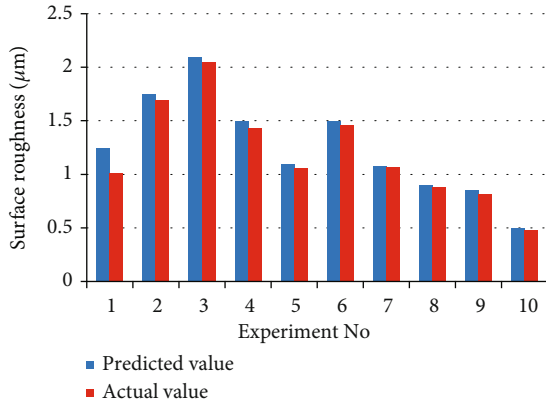


FIGURE 10: Graph showing the variation in measured and predicted values.

technique to create novel images from the image specifications. The histogram graph is fetched by taking the surface roughness values on the y -axis and the feed rate on the x -axis.

Figure 8 shows the decomposition of the original machined surface image and the equivalent generated image using discrete wavelet transform (DWT). Image decomposition segregates an input image as structural and textual components.

The average flank wear enhances with cutting time, as depicted in Figure 9(a), and the surface roughness is depicted in Figure 9(b). It demonstrates that, under the similar machining conditions, increasing cutting speed increases flank wear progressively. Higher cutting speeds cause the material to pass away in a short period of time, allowing the machining interface to become an adiabatic system. The cutting tool softens even as temperature increases, resulting in increased tool wear. The influence of feed rate on flank wear was measured using a 498 m/min cutting speed and a 0.1 mm cut depth.

$$\text{Prediction Error} = \frac{\text{Predicted value} - \text{Measured value}}{\text{Measured value}} * 100. \quad (10)$$

The predicted value is obtained by utilizing discrete wavelet transform (DWT) and the measured value from experimental investigation.

As seen in Figure 10 and Table 7 from the above analysis, it is clear that the average prediction error obtained using discrete wavelet transform is 3.16% which is very less when compared to conventional algorithms and techniques.

5. Conclusion

In this research, noncontact surface roughness estimation method has been proposed and investigated. This unconventional method involves steps of noise removal (median filtering), sharpening using the Laplacian filter, image segmentation, Canny edge detection, 2D wavelet transform, and histogram equalization. An improved DWT-combined histogram equalization is used to evaluate the surface roughness with minimum complexity and high accuracy. The fol-

TABLE 7: Prediction error based on experimental values and DWT histogram equalization.

| S. no | Surface roughness (R_a) (μm) | | Prediction error |
|-------|---|----------------|------------------|
| | Predicted value | Measured value | |
| 1 | 1.25 | 1.01 | 3.3057 |
| 2 | 1.75 | 1.69 | 3.55 |
| 3 | 2.10 | 2.05 | 2.43 |
| 4 | 1.50 | 1.43 | 4.89 |
| 5 | 1.10 | 1.06 | 3.77 |
| 6 | 1.50 | 1.46 | 2.73 |
| 7 | 1.075 | 1.066 | 0.844 |
| 8 | 0.90 | 0.88 | 2.27 |
| 9 | 0.85 | 0.82 | 3.65 |
| 10 | 0.5 | 0.48 | 4.16 |

lowing are the significant findings of this experimental study and analysis:

- (i) Histogram equalization has been shown to be a reliable method for determining surface roughness
- (ii) The proposed method is noncontact, with no additional surface damage to the work item and less complexity than standard surface roughness assessment methods
- (iii) Surface texture estimation on machined surfaces is used to verify the effectiveness of the suggested new method
- (iv) The results show that this approach predicts surface roughness with a 3.16 percent average prediction error

Abbreviations

| | |
|-------------|---|
| SEM: | Scanning electron microscopy |
| CCD: | Charge coupled device |
| EDM: | Electrical discharge machining |
| DIP: | Digital image processing |
| RSM: | Response surface methodology |
| ANOVA: | Analysis of variance |
| GCLM: | Gray-level cooccurrence matrix |
| PPS: | Pixel pair spacing |
| DWT: | Discrete wavelet transform |
| G_{RMS} : | Root mean square acceleration |
| ANN: | Artificial neural network |
| CNN: | Convolutional neural network |
| VCPSO: | Vibration and communication particle swarm optimization |
| ANFIS: | Adaptive neuro fuzzy inference system |
| ROI: | Region of interest. |

Data Availability

The data used to support the findings of this study are included within the article.

Conflicts of Interest

The authors declare that they have no conflicts of interest regarding the publication.

References

- [1] J. Mahashar Ali, H. Siddhi Jailani, and M. Murugan, "Surface roughness evaluation of electrical discharge machined surfaces using wavelet transform of speckle line images," *Measurement*, vol. 149, article 107029, 2020.
- [2] T. Pfeifer and L. Wieggers, "Reliable tool wear monitoring by optimized image and illumination control in machine vision," *Measurement*, vol. 28, no. 3, pp. 209–218, 2000.
- [3] R. K. Shastri and C. P. Mohanty, "Sustainable electrical discharge machining of Nimonic C263 superalloy," *Arabian Journal for Science and Engineering*, vol. 46, no. 8, pp. 7273–7293, 2021.
- [4] W. Zhou, X. Li, F. Feng et al., "Robustness of surface roughness against low number of picture elements and its benefit for scaling analysis," *Coatings*, vol. 10, no. 8, p. 776, 2020.
- [5] N. A. Hameed, I. M. Ali, and H. K. Hassun, "Calculating surface roughness for a large scale SEM images by mean of image processing," *Energy Procedia*, vol. 157, pp. 84–89, 2019.
- [6] T. Jeyapooan and M. Murugan, "Surface roughness classification using image processing," *Measurement*, vol. 46, no. 7, pp. 2065–2072, 2013.
- [7] A. Kumar Parida and K. Maity, "Modeling of machining parameters affecting flank wear and surface roughness in hot turning of Monel-400 using response surface methodology (RSM)," *Measurement*, vol. 137, pp. 375–381, 2019.
- [8] S. S. Kumar, M. P. Sudeshkumar, C. Ezilarasan, S. Palani, and J. Veerasundaram, "Modelling and simulation of machining attributes in dry turning of aircraft materials Nimonic C263 using CBN," *Manufacturing Review*, vol. 8, p. 30, 2021.
- [9] P. Sivaprakasam and P. Hariharan, "Surface characteristics of nano powder mixed micro-wire electrical discharge machining on Inconel alloy," *Materials Today: Proceedings*, vol. 38, pp. 494–498, 2021.
- [10] P. Sivaprakasam, P. Hariharan, and G. Elias, "Experimental investigations on magnetic field-assisted micro-electric discharge machining of Inconel alloy," *International Journal of Ambient Energy*, pp. 1–8, 2020.
- [11] S. Dutta, S. K. Pal, S. Mukhopadhyay, and R. Sen, "Application of digital image processing in tool condition monitoring: a review," *CIRP Journal of Manufacturing Science and Technology*, vol. 6, no. 3, pp. 212–232, 2013.
- [12] L. Li and Q. An, "An in-depth study of tool wear monitoring technique based on image segmentation and texture analysis," *Measurement*, vol. 79, pp. 44–52, 2016.
- [13] H. H. Shahabi and M. M. Ratnam, "Simulation and measurement of surface roughness via grey scale image of tool in finish turning," *Precision Engineering*, vol. 43, pp. 146–153, 2016.
- [14] S. Dutta, A. Datta, N. Das Chakladar, S. K. Pal, S. Mukhopadhyay, and R. Sen, "Detection of tool condition from the turned surface images using an accurate grey level co-occurrence technique," *Precision Engineering*, vol. 36, no. 3, pp. 458–466, 2012.
- [15] M. Balaji, K. Venkata Rao, N. Mohan Rao, and B. S. N. Murthy, "Optimization of drilling parameters for drilling of TI-6Al-4V based on surface roughness, flank wear and drill vibration," *Measurement*, vol. 114, p. 332, 2018.
- [16] S. Dutta, S. K. Pal, and R. Sen, "On-machine tool prediction of flank wear from machined surface images using texture analyses and support vector regression," *Precision Engineering*, vol. 43, pp. 34–42, 2016.
- [17] Y. Liu, J. Deng, F. Wu, R. Duan, X. Zhang, and Y. Hou, "Wear resistance of carbide tools with textured flank-face in dry cutting of green alumina ceramics," *Wear*, vol. 372–373, pp. 91–103, 2017.
- [18] S. Dutta, S. K. Pal, and R. Sen, "Progressive tool flank wear monitoring by applying discrete wavelet transform on turned surface images," *Measurement*, vol. 77, pp. 388–401, 2016.
- [19] J. G. John and N. Arunachalam, "Illumination compensated images for surface roughness evaluation using machine vision in grinding process," *Procedia Manufacturing*, vol. 34, pp. 969–977, 2019.
- [20] P. K. Gandla, V. Inturi, S. Kurra, and S. Radhika, "Evaluation of surface roughness in incremental forming using image processing based methods," *Measurement*, vol. 164, article 108055, 2020.
- [21] S. M. Ali and N. R. Dhar, "Tool wear and surface roughness prediction using an artificial neural network (ANN) in turning steel under minimum quantity lubrication (MQL)," *World Academy of Science, Engineering and Technology*, vol. 62, pp. 830–839, 2010.
- [22] G. Martínez-Arellano, G. Terrazas, and S. Ratchev, "Tool wear classification using time series imaging and deep learning," *International Journal of Advanced Manufacturing Technology*, vol. 104, no. 9–12, pp. 3647–3662, 2019.
- [23] H. Chen, A. Chen, L. Xu et al., "A deep learning CNN architecture applied in smart near-infrared analysis of water pollution for agricultural irrigation resources," *Agricultural Water Management*, vol. 240, article 106303, 2020.
- [24] A. P. Rifai, H. Aoyama, N. H. Tho, S. Z. Md Dawal, and N. A. Masruroh, "Evaluation of turned and milled surfaces roughness using convolutional neural network," *Measurement*, vol. 161, article 107860, 2020.
- [25] Y. He, W. Zhang, Y. F. Li, Y. L. Wang, Y. Wang, and S. L. Wang, "An approach for surface roughness measurement of helical gears based on image segmentation of region of interest," *Measurement*, vol. 183, article 109905, 2021.
- [26] L. Xu, C. Huang, C. Li, J. Wang, H. Liu, and X. Wang, "Estimation of tool wear and optimization of cutting parameters based on novel ANFIS-PSO method toward intelligent machining," *Journal of Intelligent Manufacturing*, vol. 32, no. 1, pp. 77–90, 2021.
- [27] S. Nouhi and M. Pour, "Prediction of surface roughness of various machining processes by a hybrid algorithm including time series analysis, wavelet transform and multi view embedding," *Measurement*, vol. 184, article 109904, 2021.
- [28] J. Xiong, D. Yu, Q. Wang et al., "Application of histogram equalization for image enhancement in corrosion areas," *Shock and Vibration*, vol. 2021, Article ID 8883571, 13 pages, 2021.

Research Article

Multiparametric Optimization on Influence of Ethanol and Biodiesel Blends on Nanocoated Engine by Full Factorial Design

A. P. Venkatesh,¹ T. P. Latchoumi,² S. Chezhan Babu,³ K. Balamurugan,⁴ S. Ganesan,⁵ M. Ruban ,⁶ and Lijalem Mulugeta ⁷

¹Department of Automobile Engineering, Vel Tech Rangarajan Dr Sagunthala R&D Institute of Science and Technology, Chennai, India

²Department of Computer Science and Engineering, SRM Institute of Science and Technology, Ramapuram Campus, Chennai, India

³Department of Mechanical Engineering, Panimalar Engineering College, Chennai, India

⁴Department of Mechanical Engineering, VFSTR (Deemed to be University), Guntur, Andhra Pradesh, India

⁵Department of Mechanical Engineering, Sathyabama Institute of Science and Technology, Chennai, India

⁶Department of Automobile Engineering, Vels Institute of Science, Technology & Advanced Studies, Chennai, India

⁷Department of Mechanical Engineering, Faculty of Manufacturing Institute of Technology, Hawassa University, Ethiopia

Correspondence should be addressed to M. Ruban; ruban.se@velsuniv.ac.in

Received 22 March 2022; Accepted 11 April 2022; Published 22 April 2022

Academic Editor: V. Vijayan

Copyright © 2022 A. P. Venkatesh et al. This is an open access article distributed under the Creative Commons Attribution License, which permits unrestricted use, distribution, and reproduction in any medium, provided the original work is properly cited.

Energy conservation and management have become critical industrial activities, since energy expenses account for a significant portion of production costs. This proactive strategy has had an effect on worldwide energy consumption trends. Integration of thermal barrier coatings into engine design is necessary to solve efficiency concerns, and this coating technology has the potential to increase engine power while lowering specific fuel consumption. In a similar line, biodiesel has been presented as a possible substitute to diesel since it is nontoxic and sourced from renewable energy sources. The present study aims to enhance the performance of a diesel engine via the use of a thermal barrier-coated piston that works on biodiesel mixes. Due to its outstanding thermal insulation qualities, yttria-stabilized zirconia is the preferred material for thermal barrier coatings. Brake thermal efficiency for B20E15 is about 4% better than diesel and for B20E05 and B20E15 is about 4.6% and 13.5% less fuel consumption. CO and HC emissions were reduced by 6% to 8% on average with the B20 blends. Biodiesel blends were compared to pure diesel in terms of performance and emissions, and the blend ratio was improved using a design of experiment tool.

1. Introduction

In today's rapidly evolving technological world, energy is vital to a country's growth. It is also used to measure economic and social progress. In particular, per capita energy consumption is used to assess a country's wealth. Globally, most issues of careless energy use have been tackled by the industrial revolution in the last century. Most nations' technological advancement is linked to increased energy consumption, industrial development, and less efficient use of energy sources [1]. Energy conservation and management have become essential industrial activities since energy is a

substantial component of production costs. This constructive approach has impacted global energy use patterns. Thus, rich nations' production has increased, but their energy consumption has remained stable. Finally, renewable energy sources are equally relevant and significant in today's fast-growing globe, particularly since they are local and create fewer emissions. Using these resources to their full potential may significantly reduce pollution [2].

Studies on internal combustion engines are ongoing to reduce fuel and operational expenses as well as fuel consumption. With the advent of advanced ceramics technology, one of the methods to improve engine efficiency is via

structural alterations. These coatings were first used on gas turbines and aeronautical engines [3]. Improved ceramic coatings may improve engine performance and reduce emissions by reducing heat rejection from the combustion chamber. Aside from that, as much fuel energy as feasible should be turned into useable mechanical energy. To attain these outcomes, the engine combustion chamber must be covered with low-heat-transmitting modern ceramic materials that may enhance cylinder temperature and pressure [4].

Alternative fuels for I.C. engines have been studied globally. Performance studies have proven the appropriateness of hydrogen, alcohols, biogas, producing gas, and different edible and nonedible oils. However, in India, bio-based fuels including vegetable oils, bio-alcohols, and biogas may be widely employed to alleviate fuel shortage issues [5]. Many different biodiesel blends are being developed and utilized in diesel engines to enhance performance and emissions. Linseed oil, rubber seed oil, and ternary biodiesel mixes are among the mixtures being tried in diesel engines. Diesel engines emit more carbon and nitrogen than gasoline engines [6].

Vegetable oils may be used in diesel engines without any changes by just mixing them with the fuel. Density, viscosity, volatility, and heating value are all improved by the process of blending. Counter flow heat exchangers may be used to preheat rubber seed oil by capturing the heat from exhaust gases. Preheated rubber seed oil improved engine analysis and exhaust emissions, according to the researchers. At all loads, warmed mixes had greater nitrogen emissions than plain rubber seed oil [7]. The performance and emissions of biodiesel made from rubber seed oil will be put to the test in a diesel engine using calcined eggshells as a heterogeneous catalyst, and their performance and emissions will be evaluated. The emissions of a diesel engine employing synthetic biodiesel were studied [2].

The combustion parameters affect power output, exhaust emissions, fuel consumption, engine vibration, and noise. The temperature and pressure of compressed air influence the ignition delay. While compression is occurring, the cooling system absorbs a lot of heat. Thermal barrier-coated engines may reduce heat loss and increase workable output with low heat conduction and high temperature resistance materials covering the combustion chambers [8].

Coating engine components with zirconia reduces heat conductivity. In conclusion, using ethanol as a fuel with a glow plug reduces exhaust pollutants but reduces efficiency compared to using diesel fuel. However, the engine's thermal efficiency improves somewhat with delayed injection timing. This improves thermal efficiency and decreases carbon monoxide and unburned hydrocarbon emissions while increasing nitrogen oxide emissions due to greater combustion temperatures [9]. Thermal barrier coatings on different engine components have gained traction in recent years because of their enhanced thermal and mechanical efficiency, reduced pollutants, and reduced fuel consumption. Soot precursors in hydrocarbon combustion may be oxidized using the waste heat that is rejected from the engine via insulation, thereby reducing emissions [10]. High melting points, strong adhesion, and wear resistance proper-

ties make ceramic materials ideal for use in high-temperature applications. On the basis of their qualities, ceramics may be used to cover combustion chamber components. In the combustion chamber, a covered engine retains heat better than a naked engine. As a result, less pollution and less fuel are produced [11].

When utilizing diesel and palm oil biodiesel, the impact of a thermal barrier coating including zirconia and aluminum silicate in conjunction with a NiCrAl bond coat on engine performance and emission analyses was investigated. Coated engines were found to have the lowest emissions of both diesel and biodiesel fuels [12]. A study compared two coated pistons with two coating thicknesses against a noncoated piston. The impact of biofuel was seen by comparing the results of experiments done using diesel as a fuel for coated and noncoated pistons, respectively. As coating thickness increases, thermal efficiency, fuel consumption, and pollutants decrease [13]. In grey relational analysis optimization approach, a copper alloy-coated diesel engine has been improved to improve performance and reduce emissions. When compared to an uncoated piston type engine, the improved copper chromium zirconium catalytic-coated piston generates fewer emissions and enhances performance [14].

The purpose of this research is to explore the effects of ethanol on rubber seed biodiesel blends with pure diesel at concentrations of 20% and 30%. In this study, a single-cylinder diesel engine is subjected to various load circumstances in order to determine its performance and emissions. The findings of the experiment tool "full factorial design" were optimized for mixes of biodiesel and ethanol in terms of fuel consumption, hydrocarbon emissions, and carbon monoxide emissions.

2. Material and Methods

Biodiesel offers a number of advantages over other alternative fuels due to its similarity to petroleum-derived diesel fuel. Many oil companies utilize biodiesel instead of diesel, which is equivalent to conventional petroleum fuels in engine efficiency, power production, uphill climbing, and hauling. In cold weather, biodiesel will fog and gel like regular diesel [15].

Natural rubber production in India ranks fourth in the world. Rubber latex, a valuable plantation commodity for the Indian economy, is harvested from the rubber tree. Rubber seed oil is an important byproduct of the rubber tree and is obtained by crushing and filtering the rubber seeds. In addition to natural rubber, the rubber tree produces a wide range of other goods. Rubber seed oil content varies from region to region, but on average, the oil output is 40%. Some businesses, such as soap and lubricating oil, are allowed to use rubber seed oil commercially, but most are prohibited. Rainfall, moisture, and bright sunlight are the primary reasons for its high demand. Unsaturated fatty acids make up about 75 to 85 percent of the rubber seed oil's composition [6].

Rubber seed oil has a calorific value of 39,800 KJ/kg, equal to diesel fuel. Rubber seed oil has a higher flash point

than diesel but a viscosity ten times that of diesel. Finally, most research shows that rubber seed oil may be utilized as a substitute for petroleum diesel in a compression ignition engine. For CI engines, the higher the amount of carbon and hydrogen, the better the fuel quality and calorific value. The lower the sulfur concentration, the fewer sulfur oxides are formed, resulting in less pollution from exhaust fumes and fewer corrosive effects on engine components [5].

Rubber seed oil has a greater calorific value than other biofuels because it contains more carbon and hydrogen. There is no deposit and little heat loss due to the high calorific value. Rubber seed oil also has a high oxygen concentration, which minimizes CO emissions and unburned hydrocarbons. Because of its natural qualities, rubber seed oil may be used as a diesel engine replacement. It is utilized as an alternative fuel in rural regions, particularly for agricultural activities and irrigation equipment operation, apart from its principal use in engines. Overall, rubber seed oil is a simple and easy-to-utilize renewable energy source. It is also a low-cost fuel that is simply deployed and is environmentally friendly [7]. Table 1 displays the properties of rubber seed biodiesel and ethanol.

The piston coating is significant because its thermal expansion rate is different from other ceramic materials. Materials that provide good results include ZrO_2 stabilized with Y_2O_3 and ceramic coatings. ZrO_2 stabilized with MgO may be used safely in cylinder heads and intake exhaust valves. The composition of the binding layer is also critical in ceramic coatings, bonding materials to avoid hot corrosion and resistance. The use of NiCrAlY as a binding layer improves coating durability [16].

Thermal conductivity and expansion coefficient of ceramic materials are all poor at elevated temperatures. This means that less heat is dissipated from the combustion chamber components than with metals or metal alloys. Thermal barrier materials for covering combustion chamber components may be chosen from a small number of ceramic substances depending on their noteworthy qualities. Because heat loss is slowed, the coated engine will be capable of retaining the most heat at high combustion chamber temperatures. Using a high temperature will aid in full combustion, decrease emissions, and reduce the amount of fuel used [17].

The features of these materials, such as melting points, temperature transition minima, coefficients of thermal expansion, chemical composition, and compatibility with metallic substrates, all played a role in their selection. Thermal insulation for an internal combustion engine is provided by yttria-stabilized zirconia (YSZ) coated to a thickness of 200 μ m in the present experiment. There are a variety of ways to insulate a surface. The plasma spraying is used to coat YSZ, in which powdered YSZ enters as the phase, melts, and steers toward the piston, where it coagulates as a thick coating [8].

3. Experimental Details

Diesel engines are more efficient and utilize less fuel than gasoline engines owing to greater compression ratios, leaner

air-fuel combinations, and reduced pumping losses. Developing nations like India increasingly depend on diesel engines to move people and products. This increases fuel usage, foreign currency outflows, and environmental concerns. Biofuels that are renewable and have characteristics similar to diesel might solve these issues [1].

A single-cylinder, constant-speed direct-injection engine was used to evaluate rubber seed biodiesel with ethanol blends. The results are displayed in Figure 1. The speed of the diesel engine is maintained independent of the load and the proportion of biodiesel in the fuel. The engine was connected to an eddy current dynamometer, which varied the loads from 0% to 100%. Every testing mixture is subjected to an additional 25% load increase in accordance with the engine power output of 4.2 kW. An eddy current dynamometer is used in order to manually alter the engine loads. In this experiment, a calibrated orifice on an air drum and a calibrated burette were used to monitor airflow and fuel flow rates, respectively. Both diesel and an esterified rubber seed biodiesel/ethanol mix were used to measure the flow of fuel, with the flow of each being recorded, in order to get different readings and results while the test rig was in use, with AVL software.

This study focuses on the influence of an ethanol additive on nanocoated pistons fuelled with rubber seed biodiesel. Biodiesel obtained from the transesterification process of rubber seed biodiesel was blended with diesel at different ratios of 20% and 30% on a volume basis, along with oxygenated additives of ethanol at 5% and 15% as B20E05, B20E15, B30E05, and B30E15. The biodiesel fuel named for the nanocoated low heat rejection engine (LHR) as LHRB20E05 is formed by the blend of 20% rubber seed biodiesel (B20), 5% ethanol on a volume basis, and mixed with pure diesel of 75%. The biodiesel fuel blends are prepared as LHRB20E15 (65% diesel + 20% rubber seed biodiesel + 15% ethanol), LHRB30E05 (65% diesel + 30% rubber seed biodiesel + 5% ethanol), and LHRB30E15 (55% diesel + 30% rubber seed biodiesel + 15% ethanol).

4. Results and Discussion

4.1. Performance Characteristics. When tested under maximum load conditions, the brake thermal efficiency (BTE) of B20E15 was found to be about 4% higher than that of pure diesel. A higher oxygen concentration in ethanol means that it will burn more efficiently, resulting in increased thermal performance. Because of the higher viscosity and resulting lower combustion rate caused by the high content of ethanol in the mix, the BTE is lower than that of B40E15 as shown in Figure 2. When compared to diesel, rubber seed biodiesel has greater viscosity and density, causing slower heat release during the first combustion phase [18]. This results in a decrease in the brake thermal efficiency. As the proportion of ethanol in the fuel mix increases, the thermal efficiency of the brakes improves. Due to the latent heat of ethanol and its high volatility, which tend to increase the blend density, the temperature of the air-fuel mixture decreases as the ethanol energy share increases. Premixed combustion is made better by the lower temperature of the

TABLE 1: Properties of rubber seed biodiesel and ethanol.

| Sl. no | Property | Diesel | Rubber seed biodiesel | Ethanol | ASTM standards |
|--------|--------------------------------------|--------|-----------------------|---------|----------------|
| 1 | Density, at 15°C (g/m ³) | 0.843 | 0.882 | 0.720 | D 4052 |
| 2 | Viscosity, at 40°C (cSt) | 2.72 | 5.96 | 1.52 | D 445 |
| 3 | Lowest heating value (MJ/kg) | 42.31 | 35.82 | 26.92 | D240 |
| 4 | Flash point (°C) | 60 | 140 | 13 | D 93 |
| 5 | Oxygen(wt%) | 0 | 11 | 21 | E385 |
| 6 | Cetane index | 54 | 49 | 8 | D 613 |

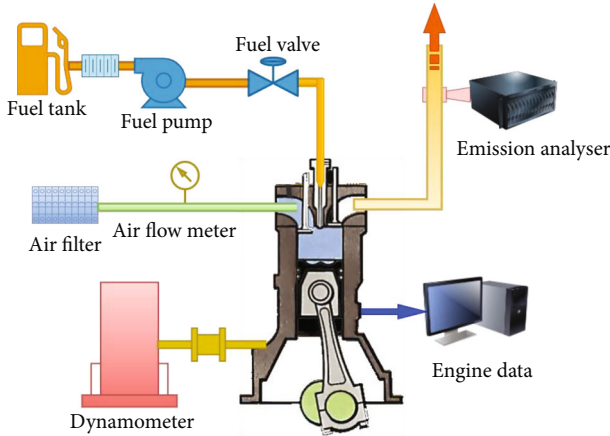


FIGURE 1: Experimental engine setup.

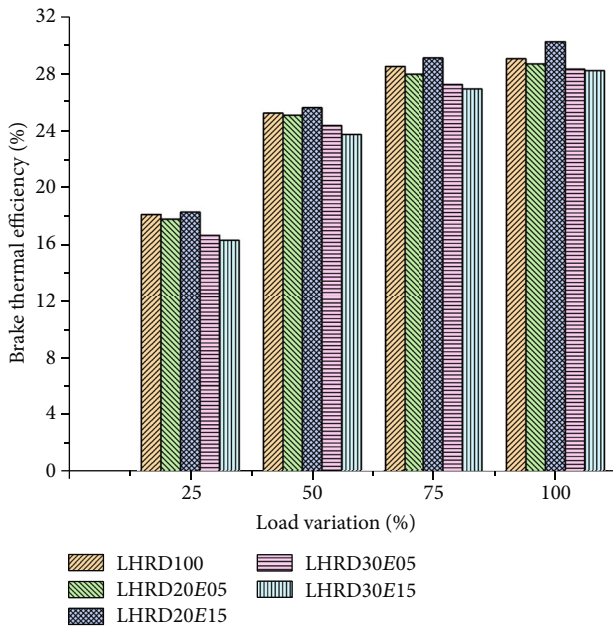


FIGURE 2: Variation of brake thermal efficiency with ethanol blends.

air and the longer time it takes for the fire to start because of this [1].

The thermal efficiency of the low heat rejection engine with partially stabilized zirconia coating was higher than that of the other engines because the ceramic coating acts

as a heat barrier between the engine and the surrounding environment. The reduction of heat loss is allowed for an increase in engine power and thermal efficiency. [9].

Specific fuel consumption (SFC) was ascribed to the increase in injected fuel that occurred in tandem with the rise in load. The SFC decreases as the engine load increases with ethanol ratios, as shown in Figure 3. Compared to diesel, B20E05 and B20E15 blends achieved 4.6% and 13.5% lower SFC, respectively, whereas B30E15 blends achieved 8% higher fuel consumption, respectively, when compared with diesel. Because biodiesel blends have a lower calorific value and a greater density than conventional diesel, their fuel consumption is higher than that of conventional diesel while running an engine using biodiesel blends compared to traditional diesel. Fuel consumption rises as the calorific value and density of the fuel mixture decrease when the biodiesel blend ratio is increased [2].

Because of the superior heat retention qualities provided by the YSZ coating, greater in-cylinder temperatures are possible owing to better oxidation of the biodiesel mix, resulting in better atomization and vaporization, and therefore reduced fuel consumption while the engine speed is kept constant.

4.2. Emission Characteristics. When full combustion occurs at low loads, diesel emits less carbon monoxide (CO). It has lower CO emissions and more biodiesel blends than diesel. The addition of biodiesel to gasoline blends has affected CO and CO₂ emissions, the researchers found. This is because biodiesel has more oxygen. As a result, CO is reduced, and CO₂ is the larger load mass, which is related to chemical processes that enhance CO production [6].

As shown in Figure 4, B20E05 and B20E15 blends decreased CO emissions by 6.8% and 9.6%, respectively, compared to pure diesel, whereas B30 blends produced higher CO emissions than diesel. The thermal barrier coatings also had an impact on CO emissions, with covered engines emitting fewer emissions than untreated engines. Nanocoated thermal insulation is activated by late-phase combustion and CO oxidation. The CO emission dropped with increasing speed, and when the engine was operating at its optimal speed, the CO emission was reduced to virtually nothing. This test also shows that CO emission is substantially controlled independent of piston coating [19].

Fuel efficiency is improved because hydrocarbon (HC) emissions are reduced, and the oxidation of atmospheric hydrocarbons is enhanced because of the oxygen present in

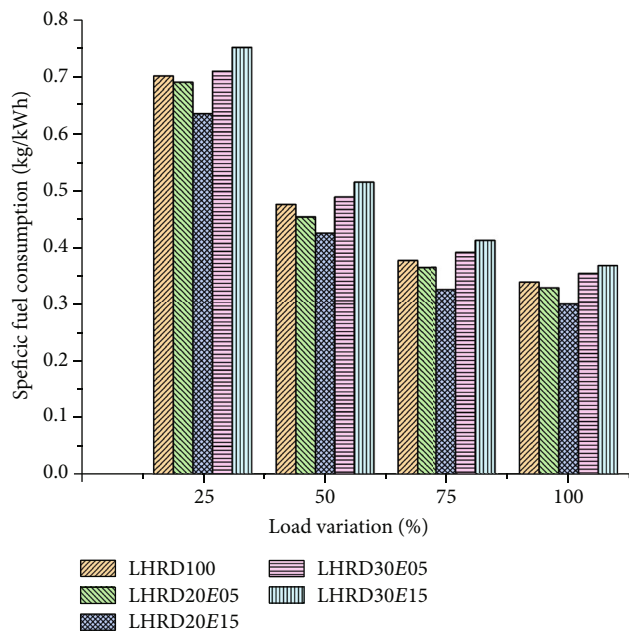


FIGURE 3: Variation of fuel consumption with ethanol blends.

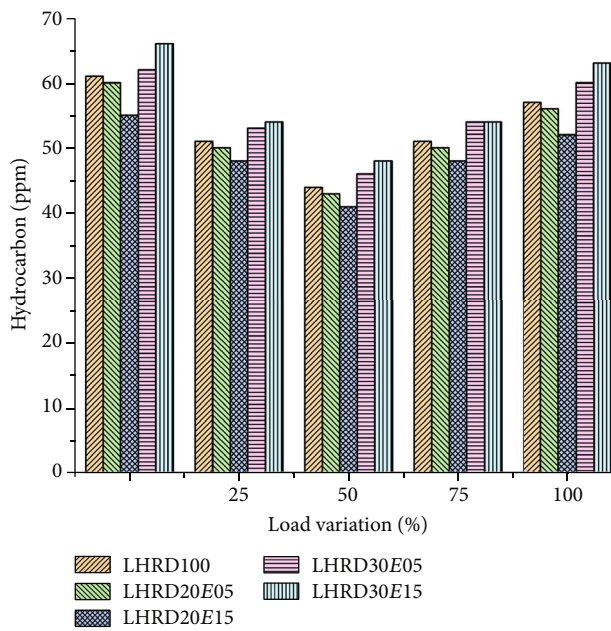


FIGURE 5: Variation of hydrocarbon emission with ethanol blends.

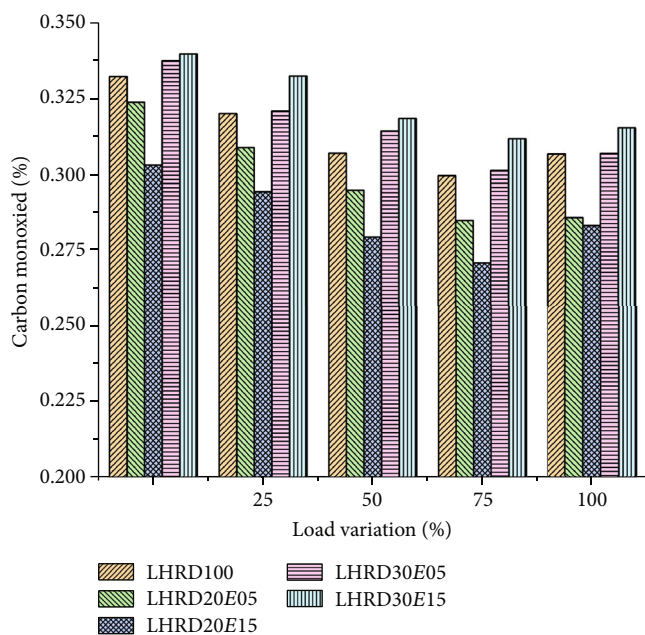


FIGURE 4: Variation of carbon monoxide emission with ethanol blends.

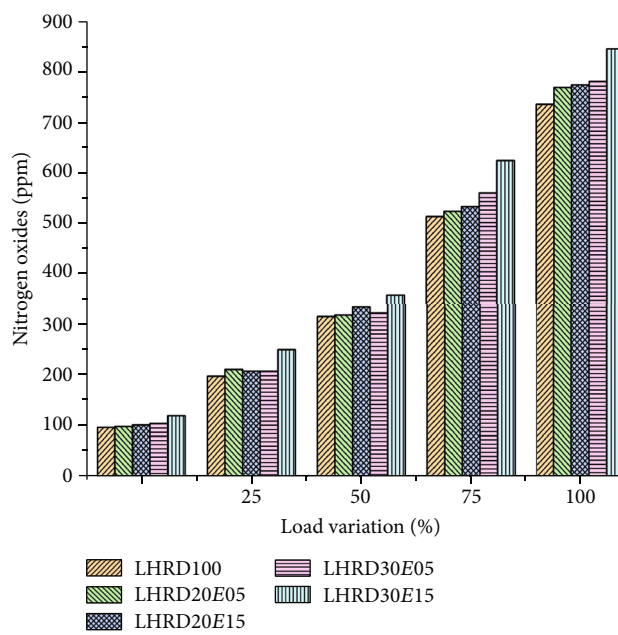


FIGURE 6: Variation of nitrogen oxides emission with ethanol blends.

ethanol. The higher HC emissions are caused by the lower combustion pressure and temperature achieved in ethanol combustion compared to hydrogen lead combustion, which results in less oxidation of hydrocarbons [7]. As shown in Figure 5, B20E05 and B20E15 blends reduced HC emissions by 2.5% and 8.6%, respectively, when compared to pure diesel, while B30E15 blends increased hydrocarbon emissions by 10% when compared to diesel.

A higher temperature in the combustion chamber and a coated piston crown improved fuel evaporation rates. The thermal barrier coating's greater combustion temperature facilitates and improves fuel combustion. Reduced hydrocarbon emissions were observed for coated pistons due to the thermal barrier coating's increased rate of hydrocarbon breakdown into hydrogen and oxygen in the combustion chamber. Reducing hydrocarbon emissions from heat barrier

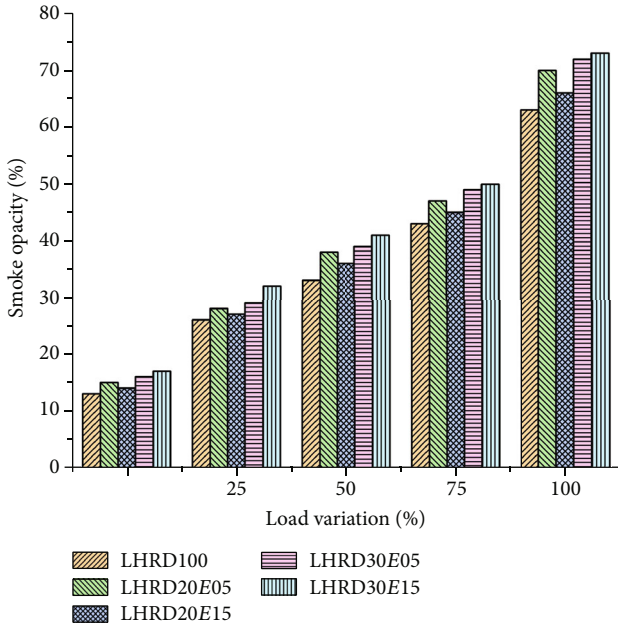


FIGURE 7: Variation of smoke emission with ethanol blends.

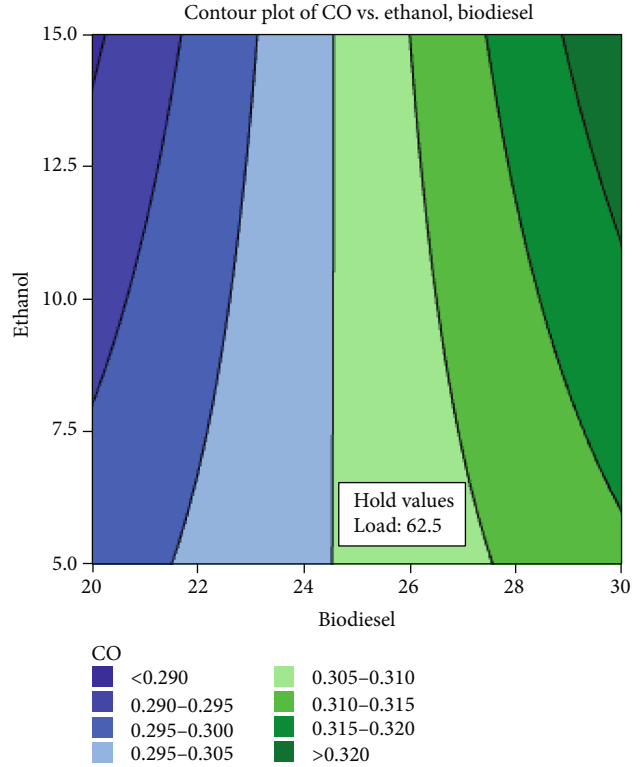


FIGURE 9: Influence of biodiesel and ethanol blends on CO emission.

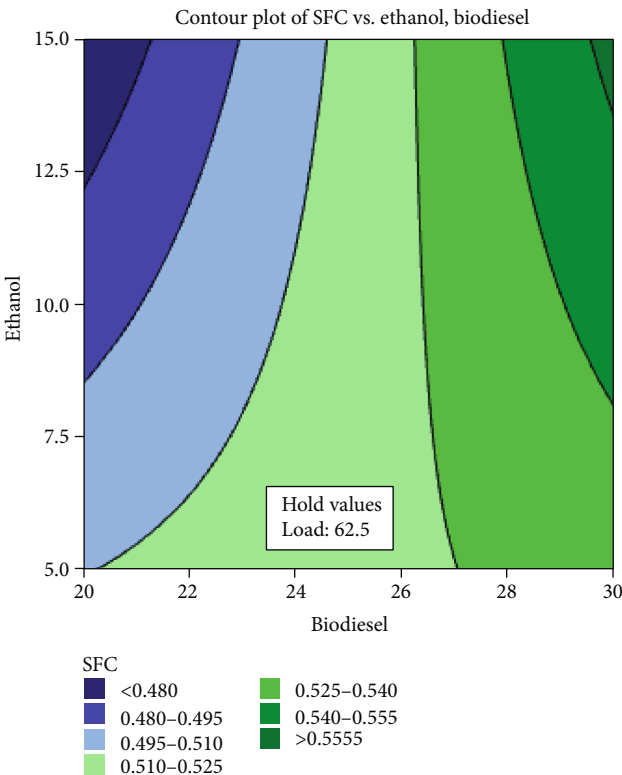


FIGURE 8: Influence of biodiesel and ethanol blends on SFC.

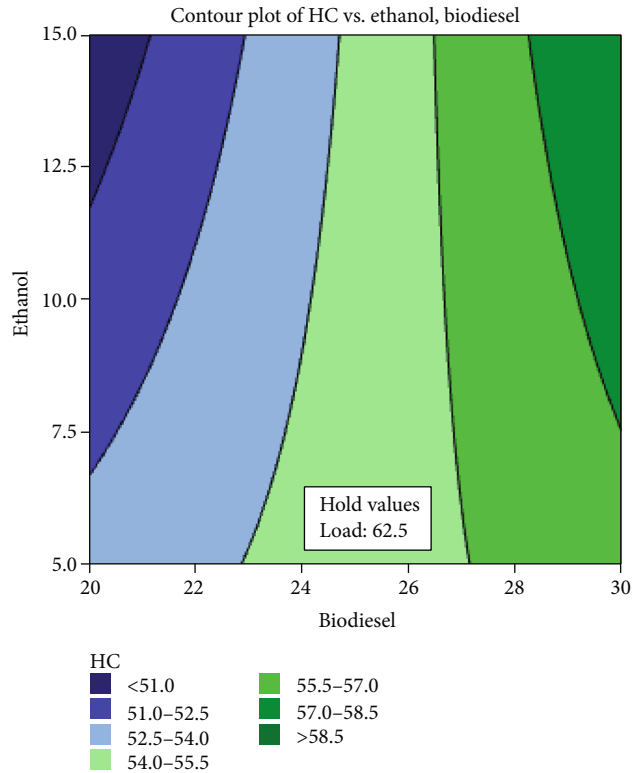


FIGURE 10: Influence of biodiesel and ethanol blends on CO emission.

coatings requires consideration of other aspects such as quenching distance and flammability threshold [20].

Reducing the premixed burning rate reduces nitrogen oxide (NOx) emissions while releasing heat more slowly. As ethanol's energy share rises, NOx emissions rise across the

TABLE 2: Parametric results on biodiesel and ethanol blends.

| Solution | Load | Biodiesel | Ethanol | HCFit | SFCFit | COFit | Composite desirability |
|----------|---------|-----------|---------|---------|----------|----------|------------------------|
| 1 | 100.000 | 20.0000 | 15 | 52.0000 | 0.301000 | 0.283396 | 0.966458 |
| 2 | 99.999 | 20.0000 | 15 | 51.9999 | 0.301006 | 0.283396 | 0.966458 |
| 3 | 99.999 | 20.0000 | 15 | 51.9999 | 0.301006 | 0.283396 | 0.966458 |

board. Many factors influence NO_x generation in ethanol biodiesel dual-fuel engines. As the flame temperature and burning velocity decrease, the generation of NO_x is reduced [1]. As a consequence of the higher fuel use, increased engine load was blamed for the spike in NO_x emissions. At maximum load conditions, B20E05, B2015, B30E05, and B30E15 blends produce NO_x at a rate of 4.5%, 5.2%, 6.2%, and 14.9% greater than diesel, as shown in Figure 6.

There is just one issue with the coated engine that has to be addressed: the emission of NO. The NO emission of a coated piston engine is higher than that of a noncoated piston engine and may be higher in temperature, resulting in an earlier start of combustion that transfers pressure and temperature. Premixed biofuels are mostly burned during the premixing phase, which reduces NO_x emissions [10].

The increase in the temperature of the combustion chamber and the wall temperature of the LHR engines are the two most important factors in reducing smoke. In general, nano-coating increases the proportion of pre-premixed fuel in the combustion chamber, boosts evaporation as a consequence of the very high combustion chamber temperatures, and lowers the diffusion burn, resulting in a reduction in the generation of smoke [21]. B20E05, B2015, B30E05, and B30E15 blends produce smoke at a rate of 11%, 4.8%, 14.3%, 9%, and 15.9% greater than diesel at maximum load conditions as shown in Figure 7.

The creation of smoke happens when the burning of the fuel occurs in an inefficient manner. The decrease in latent heat of vaporization and the delay in ignition that occur as the engine load increases also have an effect on the reduction in smoke emissions. When nano-coating is applied to engine components, high combustion temperatures are obtained, which has the effect of burning the fuel entirely. As a result, smoke emissions for the coated pistons at high compression ratios are decreased, as can be recorded [16].

5. Multiparametric Optimization

The design of experiment is often used in the process improvement to determine the most exhaustive solution to a solvable issue. In contrast to the conventional approach, this method makes use of statistical data acquired from a limited number of trials to forecast the understanding and repercussions of a complicated and multivariable process that is now underway. In comparison to any other research strategy, it is the most often used numerical technique for optimizing results. The number of process parameters and their levels has been needed to design a full factorial model for the research investigation. The full factorial design is a methodological and analytical process for evaluating the key effects and interactions of research projects. Even if the

design is solid, giving a single element or combination of variables additional prominence results in an increase in the overall number of test points [22]. The number of process parameters and their levels were necessary for the development of a comprehensive factorial model for the study inquiry. The effect of biodiesel and ethanol blends on fuel consumption, CO, and HC emissions were examined in this study. In this research, biodiesel and ethanol blends were analyzed for their influence on fuel consumption, CO, and HC emissions.

The contour plots (Figures 8–10) demonstrate that the highest ethanol mix and the lowest biodiesel blend have the greatest impact on the engine's capacity to run at the lowest potential emissions and fuel consumption. Additionally, ethanol has a beneficial effect on fuel consumption and emissions, with the lowest values obtained at a 15% mix, which is thought to be related to a quicker combustion rate owing to the increased oxygen content. Additionally, since biodiesel has a greater viscosity, emissions rose as the mix ratio was raised, resulting in a decrease in the burning effect [23]. When a 20% biodiesel blend is utilized, the quantity of CO and HC generated is decreased because the mixture is more oxygenated, which aids in full combustion [24–26]. With an increase in the ethanol ratio, emissions fall, with the lowest amounts of carbon monoxide and hydrocarbon emissions occurring at 15% of the ethanol ratio, which is mostly due to a faster rate of combustion.

5.1. Parametric Optimization of Emission and Fuel consumption. Response optimization identifies the variables that jointly optimize a response or group of answers. This is helpful for comparing the effects of many factors on a response [27–29]. To maximize the effectiveness of response optimization, it should be understood in combination with appropriate subject matter expertise. An optimal solution for the variable input combinations is provided by the response optimizer function in statistical analysis software, as well as a visual optimization plot.

An “optimizer” is a tool that recorded the optimized results in Table 2, and Figure 11 shows that the lowest blend ratio of biodiesel at the highest ethanol additive is best for getting low exhaust emissions and the lowest fuel consumption under the most extreme conditions. This conclusion is backed up by the results. This happens because of faster combustion and a more oxygenated mixture, which leads to complete combustion at these blend ratios. The best load to get these results is when the engine is fully loaded with a B20E15 fuel blend. When the B20E15 is running at full power, the ideal CO and HC emissions are 0.283 percent and 52 ppm, and the lowest possible fuel consumption of 0.301 kg/kWh was achieved.

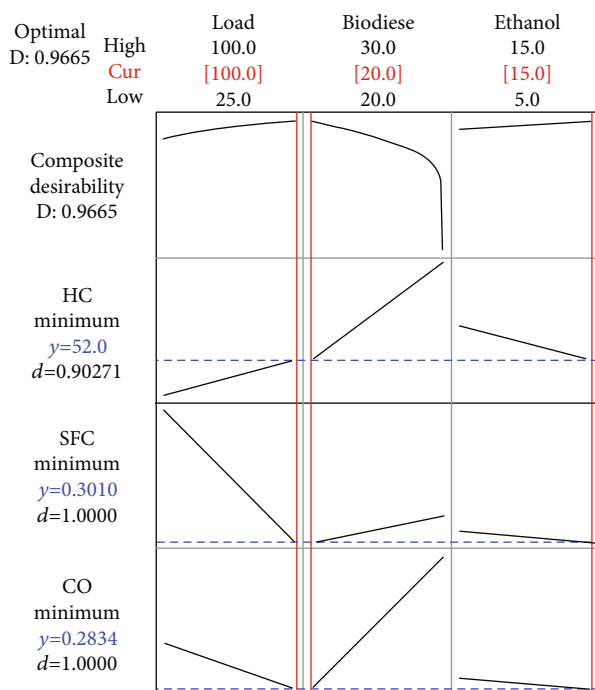


FIGURE 11: Optimization plot for emission and fuel consumption.

6. Conclusion

Diesel engines are becoming more common in developing countries like India and are used to move people and goods. This leads to more fuel use, more cars on the road, and more environmental concerns. These problems could be solved by biofuels that are made from plants and have the same properties as diesel, which could solve these problems. This study is going to look at how rubber seed biodiesel and ethanol blends work in a diesel engine. Different amounts of biodiesel and ethanol were used in a single-cylinder diesel engine with a nanocoated piston, which improves the combustion. Brake efficiency for B20E15 is about 4% better than diesel. For B20E05 and B20E15, there is a lot more oxygen in ethanol than in gasoline. This means that when comparing the specific fuel consumption of these two types of fuel, they will get about 4.6% and 13.5% less fuel consumption, respectively. CO emissions were cut by up to 6% to 8% on average with the B20 blends. At 2.5 to 8.6 percent, ethanol blends with a lot of oxygen are better for the environment than diesel because they make the combustion more efficient. When the B20E15 is running at full power, the best CO and HC emissions are 0.283 percent and 52 ppm, and the best fuel consumption is 0.301 kg/kWh.

Data Availability

The data used to support the findings of this study are included in the article. Should further data or information be required, these are available from the corresponding author upon request.

Disclosure

This study was performed as a part of the Employment Hawassa University, Ethiopia.

Conflicts of Interest

The authors declare that there are no conflicts of interest regarding the publication of this paper.

Acknowledgments

The authors would like to thank the Vels Institute of Science, Technology and Advance Studies (VISTAS), Chennai, for their excellent support for the submission of their papers.

References

- [1] V. E. Geo, A. Sonthalia, G. Nagarajan, and B. Nagalingam, "Studies on performance, combustion and emission of a single cylinder diesel engine fuelled with rubber seed oil and its biodiesel along with ethanol as injected fuel," *Fuel*, vol. 209, pp. 733–741, 2017.
- [2] S. B. Sai, N. Subramaniapillai, M. S. B. Khadhar Mohamed, and A. Narayanan, "Effect of rubber seed oil biodiesel on engine performance and emission analysis," *Fuel*, vol. 296, article 120708, 2021.
- [3] P. Sambandam, H. Venu, and B. K. Narayanaperumal, "Effective utilization and evaluation of waste plastic pyrolysis oil in a low heat rejection single cylinder diesel engine," *Energy Sources, Part A: Recovery, Utilization, and Environmental Effects*, pp. 1–17, 2020.
- [4] L. Urtekin and S. Bayaçoğlu, "Investigation of the wear characteristics of thermal barrier coating in a biodiesel engine," *Surface Review and Letters*, vol. 27, article 1950158, 2020.
- [5] M. Morshed, K. Ferdous, M. R. Khan, M. S. I. Mazumder, M. A. Islam, and M. T. Uddin, "Rubber seed oil as a potential source for biodiesel production in Bangladesh," *Fuel*, vol. 90, no. 10, pp. 2981–2986, 2011.
- [6] K. Sudalaiyandi, K. Alagar, R. Vignesh Kumar, V. J. Manoj Praveen, and P. Madhu, "Performance and emission characteristics of diesel engine fueled with ternary blends of linseed and rubber seed oil biodiesel," *Fuel*, vol. 285, article 119255, 2021.
- [7] V. Edwin Geo, G. Nagarajan, B. Nagalingam, F. Aloui, and M. Tazerout, "A comparative analysis of different methods to improve the performance of rubber seed oil fuelled compression ignition engine," *Fuel*, vol. 280, article 118644, 2020.
- [8] M. M. Musthafa, "Thermal barrier coated diesel engine running on biodiesel: a review," *International Journal of Sustainable Engineering*, vol. 11, no. 3, pp. 159–166, 2018.
- [9] P. Balu, P. Saravanan, and V. Jayaseelan, "Effect of ceramic coating on the performance, emission, and combustion characteristics of ethanol di diesel engine," *Materials Today: Proceedings*, vol. 39, pp. 1259–1264, 2021.
- [10] M. Selvam, S. Shanmugan, and S. Palani, "Performance analysis of IC engine with ceramic-coated piston," *Environmental Science and Pollution Research*, vol. 25, no. 35, pp. 35210–35220, 2018.
- [11] V. Dananjayakumar, M. B. Sanjeevannavar, S. M. Golabhanvi, and M. A. Kamoji, "Experimental analysis of CI engine using zirconia ceramic powder coated piston fuelled with Karanja

- biodiesel," *Materials Today: Proceedings*, vol. 42, pp. 1387–1392, 2021.
- [12] N. Ramasamy, M. A. Kalam, M. Varman, and Y. H. Teoh, "Comparative studies of piston crown coating with YSZ and $\text{Al}_2\text{O}_3\text{-SiO}_2$ on engine out responses using conventional diesel and palm oil biodiesel," *Coatings*, vol. 11, no. 8, p. 885, 2021.
- [13] A. M. Narad and M. P. Joshi, "Experimental analysis of CI engine using titanium oxide and aluminum oxide alloy coated piston fuelled with biofuel made up of agricultural waste," *Results in Materials*, vol. 8, article 100140, 2020.
- [14] S. Yessian and P. A. Varthanan, "Optimization of performance and emission characteristics of catalytic coated IC engine with biodiesel using Grey-Taguchi method," *Scientific Reports*, vol. 10, no. 1, pp. 1–13, 2020.
- [15] S. Ganesan, S. Padmanabhan, J. Hemanandh, and S. P. Venkatesan, "Influence of substrate temperature on coated engine piston head using multi-response optimisation techniques," *International Journal of Ambient Energy*, vol. 43, no. 1, pp. 610–617, 2022.
- [16] S. R. K. Valiveti, H. Shaik, and K. V. K. Reddy, "Analysis on impact of thermal barrier coating on piston head in CI engine using biodiesel," *International Journal of Ambient Energy*, pp. 1–18, 2020.
- [17] P. Sambandam, K. Giridharan, B. Stalin et al., "Sustainability and environmental impact of ethanol and oxyhydrogen addition on nanocoated gasoline engine," *Bioinorganic Chemistry and Applications*, vol. 2022, Article ID 1936415, 12 pages, 2022.
- [18] L. Geng, L. Bi, Q. Li, H. Chen, and Y. Xie, "Experimental study on spray characteristics, combustion stability, and emission performance of a CRDI diesel engine operated with biodiesel-ethanol blends," *Energy Reports*, vol. 7, pp. 904–915, 2021.
- [19] N. Ramasamy, M. A. Kalam, M. Varman, and Y. H. Teoh, "Effect of thermal barrier coating on the performance and emissions of diesel engine operated with conventional diesel and palm oil biodiesel," *Coatings*, vol. 11, no. 6, p. 692, 2021.
- [20] S. Padmanabhan, C. Joel, L. Joel, O. Y. Reddy, K. G. D. S. Harsha, and S. Ganesan, "Evaluation of waste plastic pyrolysis oil performance with diethyl ether additive on insulated piston diesel engine," *Nature, Environment and Pollution Technology*, vol. 20, no. 5, pp. 2079–2086, 2021.
- [21] V. K. Kumaraswamy, G. Purushotham, and R. Suresh, "Thermal analysis of nickel ALLOY/ $\text{AL}_2\text{O}_3/\text{TIO}_2$ hybrid metal matrix composite in automotive engine exhaust valve using FEA method," *Journal of Thermal Engineering*, vol. 7, no. 3, pp. 415–428, 2021.
- [22] L. Karikalan, M. Chandrasekaran, S. Venugopal, S. Jacob, and S. Baskar, "Investigations on diesel engine characteristics with Pongamia biodiesel at dissimilar compression ratios," *International Journal of Ambient Energy*, vol. 42, no. 9, pp. 1005–1008, 2021.
- [23] K. Jayappa, V. Kumar, and G. G. Purushotham, "Effect of reinforcements on mechanical properties of nickel alloy hybrid metal matrix composites processed by sand mold technique," *Applied Science and Engineering Progress*, vol. 14, no. 1, pp. 44–51, 2020.
- [24] J. Kumaraswamy, V. Kumar, and G. Purushotham, "Evaluation of the microstructure and thermal properties of (ASTM A 494 M grade) nickel alloy hybrid metal matrix composites processed by sand mold casting," *International Journal of Ambient Energy*, pp. 1–10, 2021.
- [25] S. Ramasubramanian, S. Santhosh Kumar, L. Karikalan, and S. Baskar, "Performances emissions behaviors of compression ignition engine by mahua oil," *Materials Today: Proceedings*, vol. 37, pp. 982–985, 2021.
- [26] L. Karikalan, S. Jacob, S. Baskar, and S. Venugopal, "Analyzing the influence of varied fuel injection pressure on diesel engine fueled with Karanja biodiesel," *Materials Today: Proceedings*, vol. 21, pp. 291–294, 2020.
- [27] V. R. Gangula, G. R. Nandhana Gopal, and H. Tarigonda, "Investigation on different thermal barrier-coated piston engines using Mahua biodiesel," *Journal of The Institution of Engineers (India): Series C*, vol. 102, no. 1, pp. 131–144, 2021.
- [28] M. Bhargavi, T. Vinod Kumar, R. Ali Azmath Shaik, S. Kishore Kanna, and S. Padmanabhan, "Effective utilization and optimization of waste plastic oil with ethanol additive in diesel engine using full factorial design," *Materials Today: Proceedings*, vol. 52, pp. 930–936, 2022.
- [29] I. Veza, A. D. Karaoglan, E. Ileri et al., "Grasshopper optimization algorithm for diesel engine fuelled with ethanol-biodiesel-diesel blends," *Case Studies in Thermal Engineering*, vol. 31, article 101817, 2022.

Research Article

Adiabatic CMOS-Based Electrostatic MEMS Actuation for Reduced Dynamic Power and Switching Activity

P. Muthu ¹, P. T. Vasanth Raj ², R. M. Bommi ³, M. Baskar ⁴, S. Selvaganapathi ⁵
and P. Sivaprakasam ⁶

¹ECE, Narayana Engineering College, Gudur, India

²Centre for System Design, Chennai Institute of Technology, Chennai, India

³Institute of ECE, Saveetha School of Engineering, SIMATS, India

⁴Mechatronics Engineering, Chennai Institute of Technology, Chennai, India

⁵EEE, C. Abdul Hakeem College of Engg & Tech, Vellore, Melvisharam, India

⁶Department of Mechanical Engineering, College of Electrical and Mechanical Engineering, Addis Ababa Science and Technology University, Addis Ababa, Ethiopia

Correspondence should be addressed to R. M. Bommi; rmbommi@gmail.com and P. Sivaprakasam; shiva@aastu.edu.et

Received 11 February 2022; Accepted 10 March 2022; Published 8 April 2022

Academic Editor: V. Vijayan

Copyright © 2022 P. Muthu et al. This is an open access article distributed under the Creative Commons Attribution License, which permits unrestricted use, distribution, and reproduction in any medium, provided the original work is properly cited.

The basic purpose of MEMS actuation is to miniaturize the actuators and sensors for applications in nanoelectronics. The transistor switching current and power supply noises due to voltage drops across the metal lines can impair circuit timing and performance, posing a continuing problem for high-performance chip designers. This work presents an empirical concept of a reconfigurable charge pump based on FPGA for electrostatic actuation of the Microelectromechanical System (MEMS). The goal of the design is to produce enough on-chip voltages for actuating the MEMS that are continuously adaptive and reconfigurable. In this proposed method, pumping capacitors lying in the range of 1-pF have been deployed to decrease the area of design concerned. The various voltages are programmable digitally and created by dynamically altering the number of phases as well as the clock drive levels. The dynamic model is designed by adjusting the number of stages to produce on-chip voltages including clock drive speeds, assuming a purely capacitive load. The proposed model's power consumption can be lowered in the steady state by lowering its clock frequency and electrostatic MEMS actuators with capacitive load. An average of 0.62 W is dissipated by the circuit when the eight stages are triggered. Consequently, with adiabatic and without adiabatic architecture, 0.0186 mW of minimum power difference is obtained.

1. Introduction

In recent years, new adiabatic MEMS actuation paradigms have contributed to an exponential growth in microelectronics. The most important obstacle in designing high performance microelectronic systems is the dissipation of energy. CMOS technology is one of the most prominent technologies in the field of computer chip design and is extensively used today in numerous and varied applications to construct integrated circuits. Due to several main benefits, today's computer memories, CPUs, and cellular phones make use of this technology. Both P channel and

N channel semiconductor devices make use of this technology. Similarly, it is proposed to design low-power circuits employing dynamic logic families, but after each test period, the circuit must be precharged [1, 2]. As an alternate, [3] suggested energy recovery circuits called adiabatic circuits to design electronic circuits. But change in voltage levels is sufficiently slow in adiabatic circuits in which no heat loss or gain occurs. A node's charge and discharge are rendered sufficiently slow to make it equal to a current source's charge/discharge. To accomplish the purpose, the power clocks are used in place of DC power supply as implemented in traditional circuits [4].

MEMS technology or Microelectromechanical Systems can be described at its most basic context as electromechanical devices and structures as scaled up elements manufactured through micromanufacturing techniques. MEMS devices can vary in critical physical properties from less than one micron dimension to many millimeters. A key criterion of MEMS is that, whether or not these elements can move, there are at the minimum some elements which have mechanical functionality. In various parts of the world, the definition used to describe MEMS varies. They are primarily called MEMS in the United States, although they are called “Microsystems Technology” or “micromachined machines” in some other parts of the globe.

This paper provides a comprehensive investigation of the actions of the suggested adiabatic electrostatic MEM actuation. As a result of the previous research, MEMS have a higher temperature drift, which can be a problem for those without temperature compensation or heating capabilities. The current design has one of the lowest supply voltages, as well as a low voltage gain per step [i.e., (V/V)/stage] while prior works use either more steps or a higher supply voltage than the current design, which results in an accumulation of voltage from an 8-stage 1.2 V supply. Since the circuit is not connected to any recycling equipment, energy cannot be recycled. The voltage phase size will not be consistently tuned. Hence, the proposed work recycles energy in a more efficient way with lower supply voltage. This facilitates the implementation of energy efficient gates in the design of reversible logic circuits.

2. Dynamic Power and Switching Activity

Dynamic, sometimes referred to as switching power and static, and sometimes referred to as leakage power, are two forms of power consumed in a system. Leakage power has been the dominant power user in geometries smaller than 90 nm, while switching is the greater contributor for larger geometries. As shown in Figure 1, it is possible to use power reduction techniques to minimize both kinds of power. Total power, as shown in Figure 2, is a feature of the process of voltage, switching, capacitance, and transistor arrangement itself. Because switching activity and clock frequency influence output voltage, lowering capacitance and supply voltage can reduce dynamic power dissipation.

3. Background

The recent developments of M/NEMS logic devices based on resonator [5] are reviewed, experimental works in that area are explored, and logic circuits are designed based on cascability and frequency tuning of these digital logic circuits. An empirical model of the Stepwise Adiabatic Circuits (SAC) for energy consumption was proposed [6, 7] when discharge of the load capacitor is required. Another application for low-power was proposed ([8] which mathematically modeled an Adiabatic DCVSL. In terms of dissipation of power, the Adiabatic-DCVSL circuit performs better and could be modified suit low power implementation layout.

In the standard CMOS of 0.13 μm technology, an 8-stage reconfigurable charge pump was developed for Microelectromechanical system (MEMS) electrostatic actuation and also manufactured from a 1.2 V supply. The circuit achieves a calculated max *o/p* voltage of about 10 V [9]. The maximum output ripple for a 10 pF load is 1.1 V, meaning that MEMS electrostatic actuation can handle a 0.31% relative deviation. The circuit is made of CMOS technology with a 0.8 m high voltage and a 675 m X1100 m area [10]. The regulatory algorithm devised by [11] improves the power efficiency of a switched-capacitor DC-DC converter by automatically changing the voltage gain and switching frequency in response to input voltage and load current. The converter will produce a balanced 1.2 V output rail with an input of 0.5 V to 2.5 V and deliver a load capacity of 100A, according to simulation results. Most MEMS (Microelectromechanical Systems) actuators [12] need high control voltage, such as 20 V.

In [13], one of the major reasons for implementing MEMS on Si CMOS is that the control voltage approaches the knee voltage of the PN-junction diode. This work proposed an adiabatic charge pump, by adding sufficient bias voltages to both the back gate as well as deep-N-well of N-MOSFETs, and can produce greater output voltage than that of the breakdown voltage. Results reveal that perhaps the prototype can produce a 21 V DC voltage at 0.18 μm Si CMOS to 11 V but 15 V PN-junction breakdown voltage. MEMS have a higher temperature drift, which can be a problem for those without temperature compensation or heating capabilities. Prior works either used more steps or a greater supply voltage than the current design, which resulted in an accumulation of voltage from an 8-stage 1.2 V supply. Energy cannot be recycled since the circuit is not connected to any recycling equipment. The size of the voltage phase will not be consistent. As a result, with reduced supply voltage, the suggested work recycles energy more efficiently.

4. Nonadiabatic Electrostatic MEMS Actuation Using Charge Pump

The current system consists of different blocks and their functionalities in Figure 3. To regulate the clock at each point, a 4-to-8 thermometer decoder is incorporated to circuit in this block diagram, allowing the no/- of active clocks to be dynamically vary by changing the input signals, CTRL*i*. The actual circuit block diagram in Figure 3 is made up of a digital control circuit, a charge pump with its clock, and a discharge point.

The proposed work is aimed at achieving higher output voltage for the given supply voltage and moreover at also providing dynamic configurability of such a voltage, in contrast to traditional charge pumps. The charge pump circuit is designed specifically to dynamically configure a switched capacitor array through switches, which are conceptually seen from Figure 3. For each point, the capacitive array consists of 8 pairs of pumping capacitor, C_1 and C_2 . This is of greater significance if MEMSs that need many different actuation voltages concurrently need to be used on a multitude

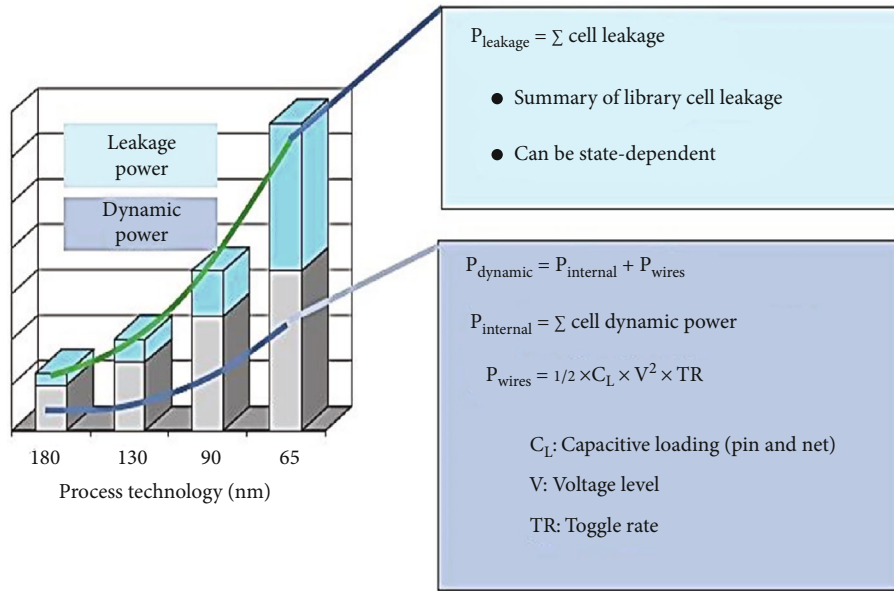


FIGURE 1: Leakage power and dynamic power.

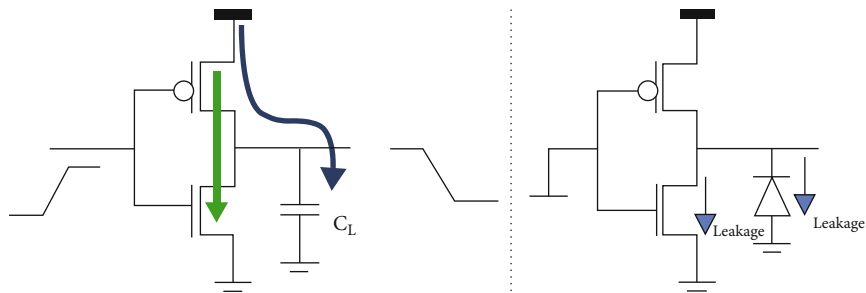


FIGURE 2: Power dissipation during charging and discharging.

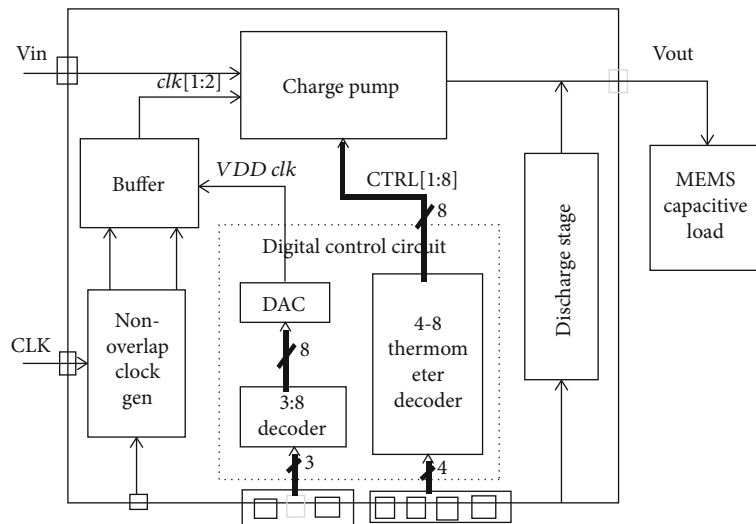


FIGURE 3: Charge pump-based electrostatic MEMS actuation.

of charge pumps. The top plate of pumping capacitor is connected to the *i/p* and *o/p* terminals via switches, and bottom plate connecting to a pair of CLK1-CTRL i and CLK2-CTRL i regulated nonoverlapping clock signals and CTRL i are control signals to activate each level.

A 4×8 decoder is incorporated into capacitor charge pump circuit. The capacitor charge pump works in all eight stages when CTRL1 to CTRL8 is high. For example, by making CTRL8 small, the number of points can be minimized to seven.

The stage is turned off, resulting in a charging pump with seven stages. In the same way, the number of stages is reduced: each stage is turned off one by one by lowering the CTRL i control signals, as shown in Table 1. The proposed design utilizes control parameters and 9-bit programming word as seen from Figure 4.

An adiabatic controller attached to MEMS overcomes the big downside of charge pump controller dependent MEMS actuation. Implementing an adiabatic controller in the proposed device would not only activate the MEMS for a short time, but it will also recycle the wasted energy and store it in micro capacitors, enabling a few digital circuits to be activated. The adiabatic theory also helps to minimize power consumption. The system's value is that it makes effective use of power and has small design architecture for such a large idea.

5. Adiabatic Controller-Based Electrostatic MEM Actuation

The major two blocks connected with proposed system are as follows:

- (i) Adiabatic logic controller
- (ii) Low power blocks

These two blocks are important in our project for recycling the circuit's dissipated power. Since it does not dissipate electricity, adiabatic activity offers significant reductions in power consumption. Unlike traditional logic switching, where only the input signals with different final logic states change, adiabatic circuits require all input signals to undergo a controlled transition in the form of a ramp [14]. Logic switching cannot be instantaneous in order to minimize energy dissipation; instead, it must be incremental.

Two main blocks have been included in the proposed block diagram, 4as shown in Figure 5, the adiabatic controller and the low power blocks that are related to the MEMS capacitive load. The buffer is used to provide enough drive power to transfer signals or data bits to the next level. Non-overlapping clock generation is used to prevent signal overlapping between circuits. DAC, 3:8 decoder, and 4-8 thermometer decoders make up the optical based control circuit. As illustrated in Figure 5, a DAC, Digital to Analog Converter, is a system that converts digital data into an analogue signal. The output of a thermometer decoder is similar to that of a thermometer.

TABLE 1: Array control scheme for switched capacitor.

| Active control signals | Active switches | Output |
|------------------------|------------------|-----------|
| CTRL | S_1 - S_4 | $2V_{in}$ |
| CTRL1-CTRL2 | S_1 - S_8 | $3V_{in}$ |
| CTRL1-CTRL3 | S_1 - S_{12} | $4V_{in}$ |
| CTRL1-CTRL4 | S_1 - S_{16} | $5V_{in}$ |
| CTRL1-CTRL5 | S_1 - S_{20} | $6V_{in}$ |
| CTRL1-CTRL6 | S_1 - S_{24} | $7V_{in}$ |
| CTRL1-CTRL7 | S_1 - S_{28} | $8V_{in}$ |
| CTRL1-CTRL8 | S_1 - S_{32} | $9V_{in}$ |

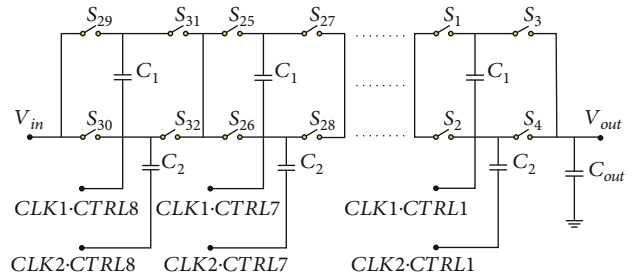


FIGURE 4: Schematic of reconfigurable switched capacitor array.

The architecture includes replicated output thermometer code to boost basic converter specifications. The signal of the thermometer decoder and buffer is provided to the charge pump, but these three signals control all of the signals from its outer circuit. The charge pump was used in the circuit raise voltage, and the discharge stage is coupled to the capacitive load. The small pumping stages are allowed by this stage. As compared to other related families, it used a special logic called Positive Feedback Adiabatic Logic employed in the adiabatic controller because it consumes minimum energy and a strong robustness to technical dynamic characteristics. The PFAL gate is depicted in general in Figure 6. 8:1 multiplexer controls the low-power blocks that feed the MEMS capacitive load.

In this design, a Multiplexer (MUX) is used as the key element in these low-power blocks, which should be operated by a 1.2V supply. The adiabatic controller's recycled energy is being used to drive another circuit, in which the energy is only useful for digital circuits. Low-power blocks perform these functions. As a result, get two types of recycled clock signals; CLK1 and CLK2 are obtained, based on the capacitance value, during charging and discharging. These dual clocks, start mux and start clk, are provided as inputs to another circuit. The capacitor has begun to charge after the start mux has been activated, and waste energy recycling has begun. As a result, this process will continue until the heat has dissipated. The dissipated energy can be recycled using adiabatic logic, and then, this energy could be used to drive another circuit. For storing thousands of capacitance values, the proposed device used digital MEM capacitance. Since there are so many reconfigurable pumping stages involved, the pace of operation is

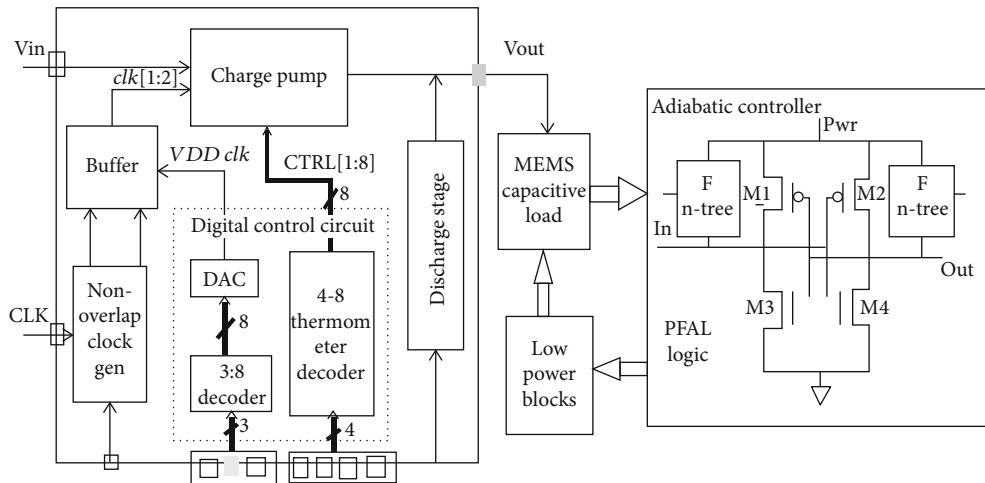


FIGURE 5: Block diagram of the proposed system.

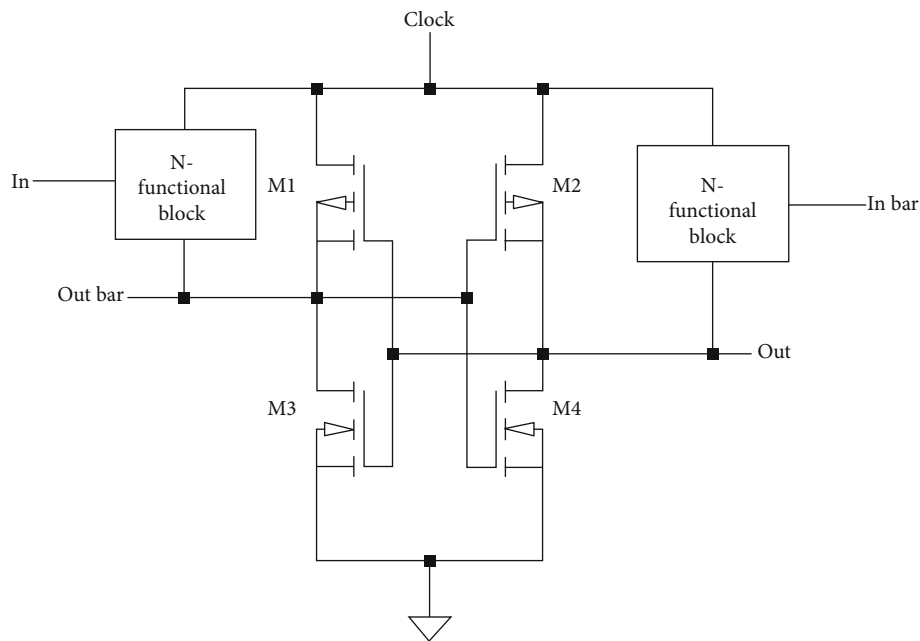


FIGURE 6: Schematic of PFAL gate.

increased. The use of a regulated clock frequency has decreased power consumption.

6. Results and Discussion

The complete system was created in a CPLD environment and then analysed with a DSO. Because the clock inverter's driving ability is reduced when the clock voltage is reduced, the rise time is affected. Furthermore, clock levels below 0.4 V significantly decrease output voltage because they are well below inverter's optimum operational threshold. This necessitates a 0.5 V minimum operating voltage for Vdd Clk. At a clock frequency of 40 MHz, the maximum output voltage ($V_{dd} = V_{ddClk} = 1.2 \text{ V}$) is developed and the dissipated power observed is 0.62 W. The power

consumption of the auxiliary electronics compensates for this scaling.

6.1. Multiplexer Design. As shown in Figure 7, this circuit has 2 blocks (i.e., mux0 and mux1). These circuits have 3 inputs and 2 outputs. In mux0 circuit, the involt input takes 4-bit value and generates output as 8-bit value adcout. This adcout is given as input to the mux1 circuit. Finally, we get the 32 combinations of memout values. Based on the input values, the memout value gets changed.

6.2. Control Signal Design. As shown in below design, the memout taken from the multiplexer design is given as the input to the digital circuit of 4 bits (deign) as shown in Figure 8. The clock and clear signal is given common to both the threshold_

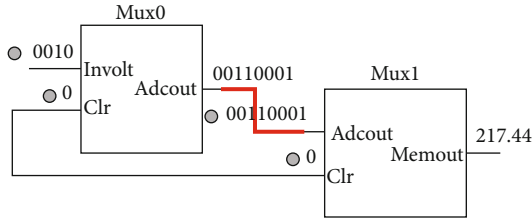


FIGURE 7: Memout design.

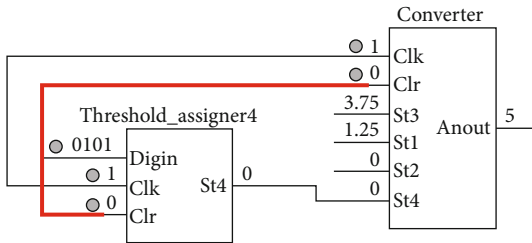


FIGURE 8: Analog output design.

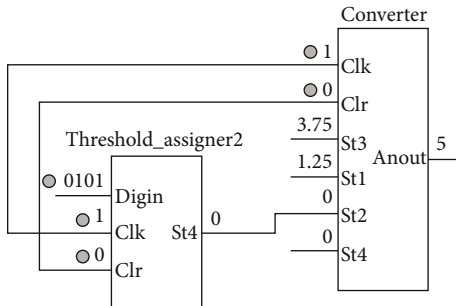


FIGURE 9: Digital converter design.

assigner4 and converter. Thus, the particular signal has been selected and delivers the anout in the converter.

6.3. DAC Design. In DAC design, the clock and clear input is given common to both the threshold_assigner2 and converter as the same to all the other three designs. The 4-bit digital input is converted into analogous output by using this design as shown in Figure 9.

6.4. Integration Design

- (i) From the above three designs such as multiplexer, control signal, and DAC design, these are integrated in a single integration design as shown in Figure 10
- (ii) The selected signal is given as common input to all the other four threshold assigners, and the 4-bit input values are given commonly and produce different single bit values

7. Simulation Results

The proposed model generates the range of voltages for an 8-stage 1.2 V supply. Since low supply voltage is beneficial because it lets an improved tuning of MEMS actuator's output voltage by increasing the tuning resolution obtained by adjusting the number of levels. To make up the difference for higher resolution, more bits can be used in VddClk, but balancing the range of drive levels in VddClk with the series of stages allows for well-spread tuning characteristics. The design is 0.0645 mm^2 in size, which is very thin. It is indeed important to note although the reported region encompasses the entire system (i.e., charge pump, control, and clocking).

- (i) The calculated output voltage reaches its full value with a 1-pF load, an electrostatic MEMS actuator, and an oscilloscope probe. The discharge transistors' size could be increased to improve release performance
- (ii) From the MEMS output as referenced with Figure 11, it is observed that based on the given input the charging and discharging amplitude values varied from one time period to another period

7.1. Control Signal

- (i) The stray capacitance and leakage current rise the dynamic power consumption of the circuit, explaining the difference between observed and calculated power consumption as shown in Figure 12
- (ii) These control signals are used as a reference signals to the overall circuit, and overlapping of signals can be prevented and controlled
- (iii) According to the selection line, the control signal can be varied from one clock to another clock

7.2. DAC. The DAC can be synthesized entirely in an FPGA and does not require the use of external components. Even though power consumption limits the maximum number of bits that can be used and that this DAC is not the most linear one, the FPGA-based DAC may be used in many applications.

- (i) Based on the given digital input, DC-DC level signal can be generated
- (ii) The required analog output is obtained, where the analogous output value depends upon the given digital input as highlighted in Figure 13
- (iii) Improve the resolution of the DAC to provide finer clock drive levels, particularly in the relatively high output voltage scale

7.3. Adiabatic Controller. As shown in Figure 14, a rise time of 80 ns and a fall time of 6.40 s are observed in this state. In an adiabatic controller, the capacitive load has

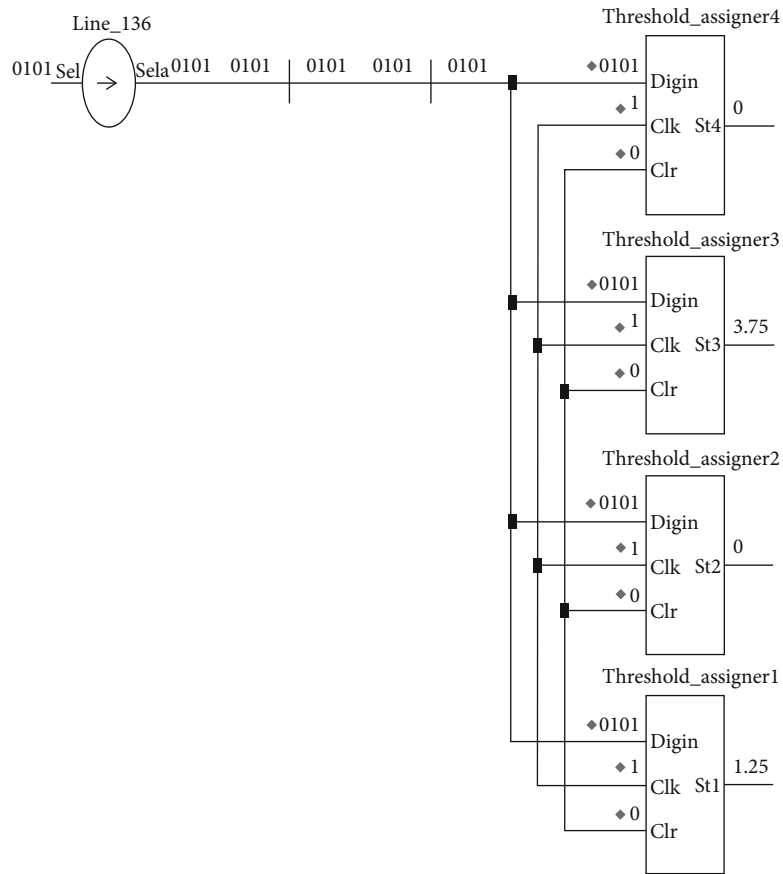


FIGURE 10: Integration design.

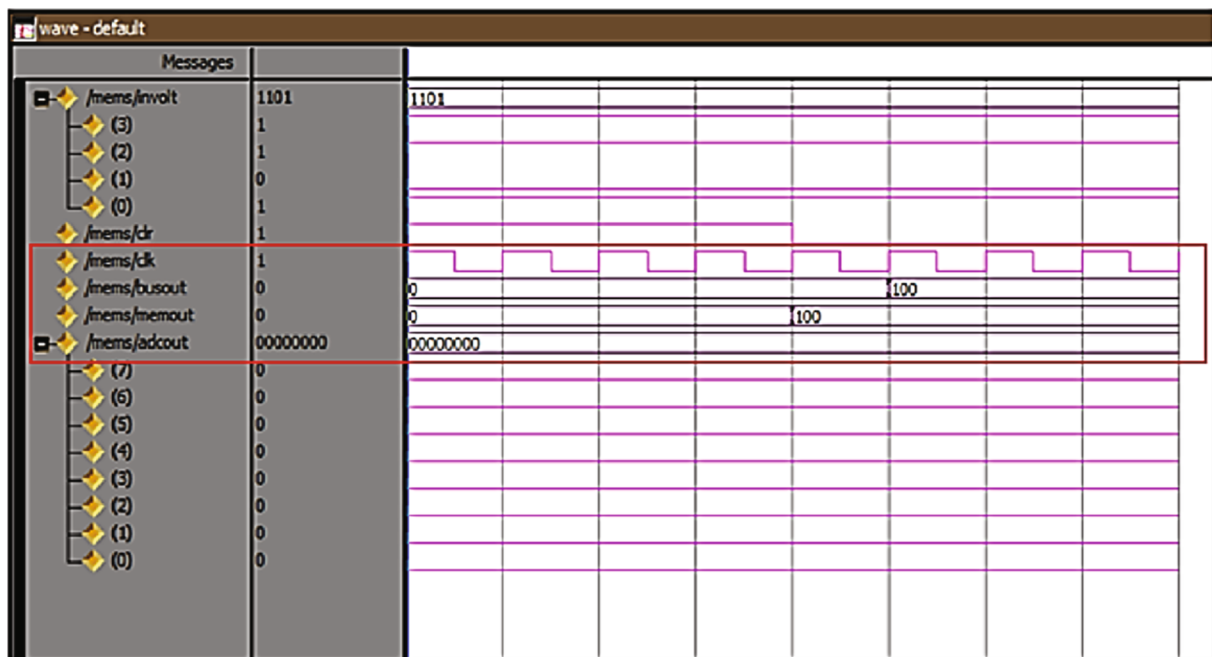


FIGURE 11: MEMS actuator with 1-pF load.

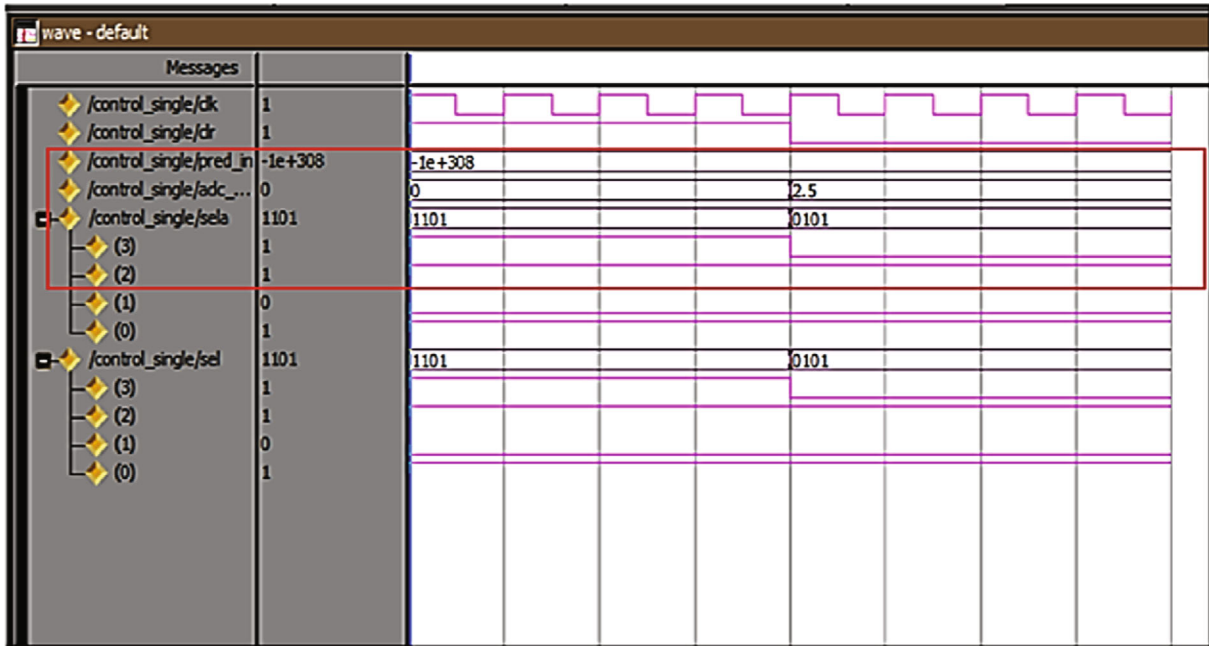


FIGURE 12: Control signal output.

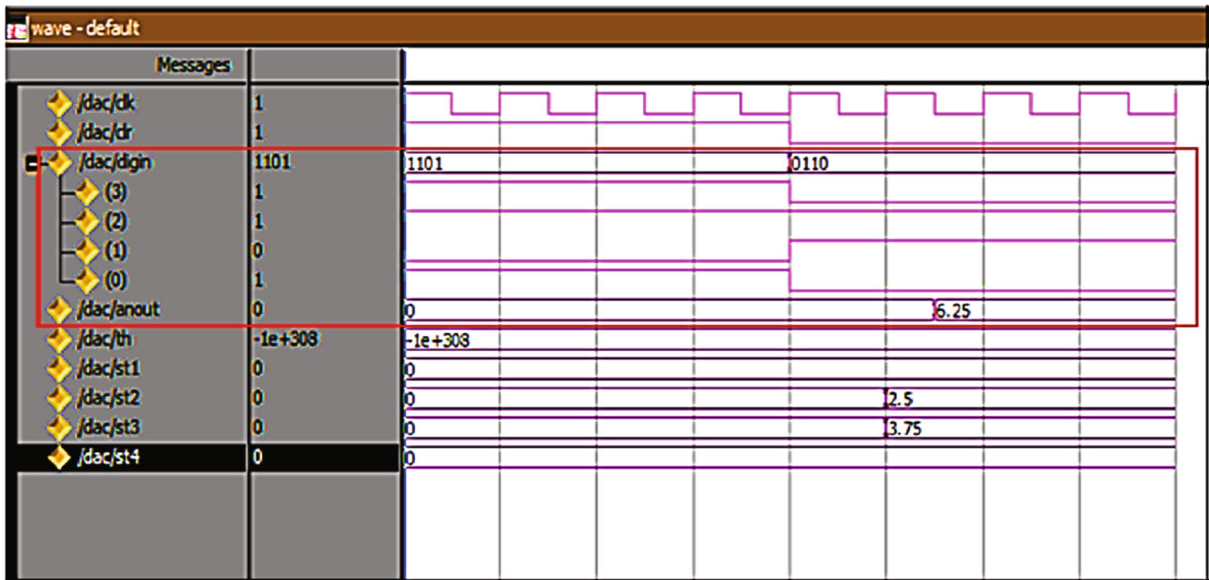


FIGURE 13: DAC output.

been stored as an energy and it can be recycled by decoder recycled count to enable the circuits, where the circuit does not work while giving 0's as an input and alternatively by giving 1's it works as indicated in Figure 15.

7.4. Integration

(i) By integrating the above three modules, we can get the final output as shown in Figure 16

- (ii) During charging and discharging, we get two types of recycled clock signals as CLK1 and CLK2 based on the capacitance value
- (iii) These two clocks are given as an input to another circuit (i.e., start_mux and start_clk)
- (iv) After enabling the start mux, the capacitor has been started to charge and recycling of wasted energy gets started

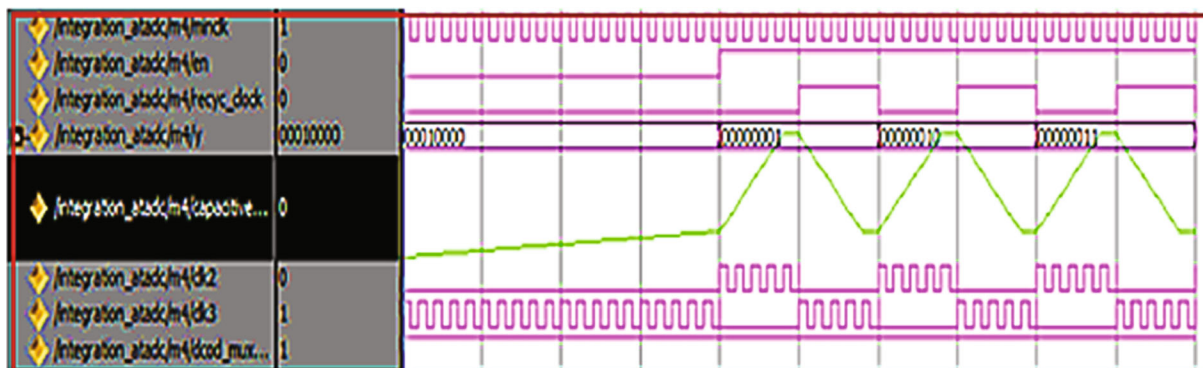


FIGURE 14: Integration output showing rise time and fall time.

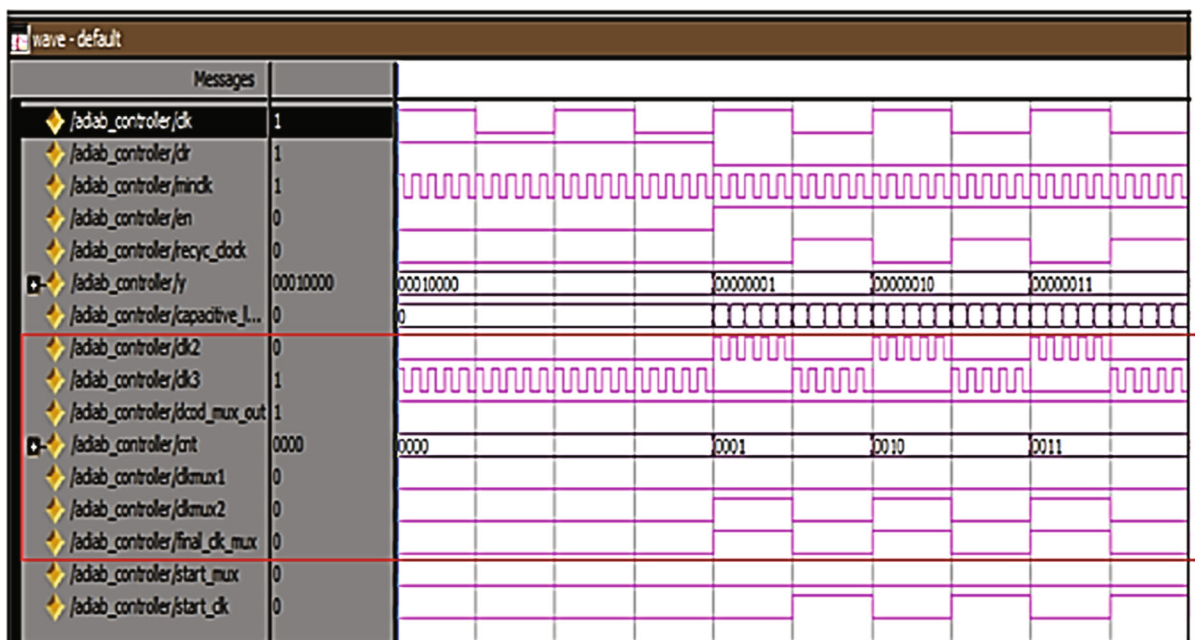


FIGURE 15: Adiabatic controller output.

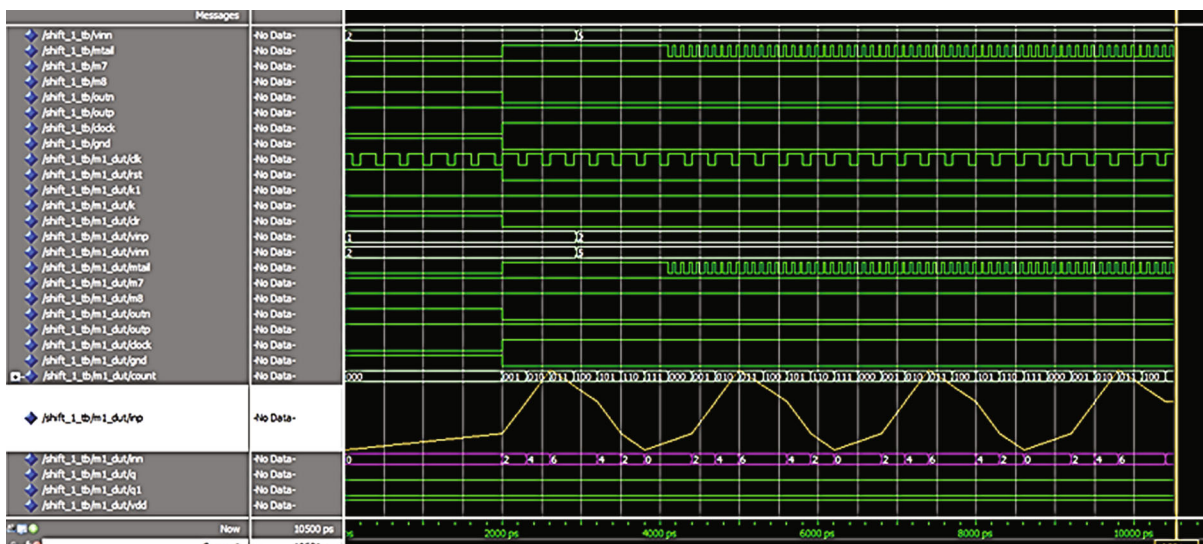


FIGURE 16: Integration output.

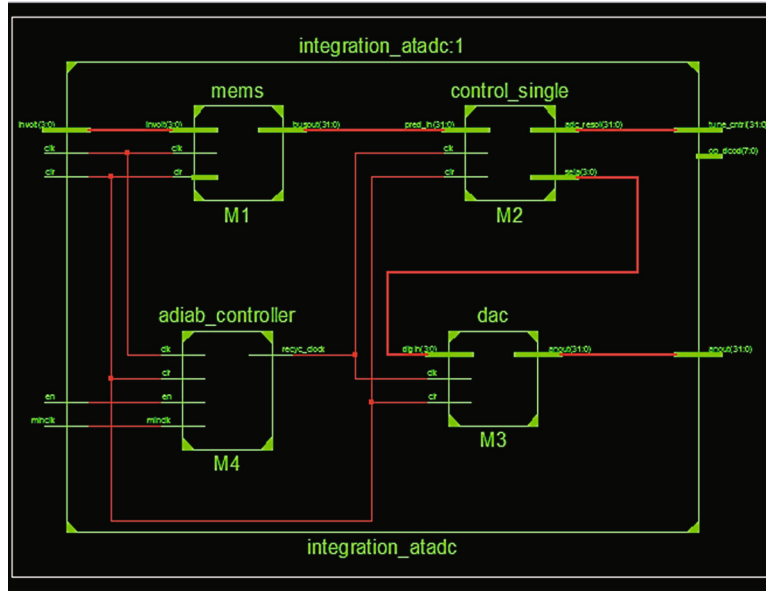


FIGURE 17: Architectural design of integration module.

(v) Finally, as more and more CMOS technologies progress to lower supply voltages, this makes the proposed circuit well-suited for this operation, with a comparatively low voltage

7.5. Architectural Circuit Design. The architectural design circuit of integration module is shown in Figure 17. The blocks present in the circuit are MEMS, control signal, DAC, and adiabatic controller. The integration modules integrate all these blocks, and then finally, it generates two types of recycled clock pulses CLK1 and CLK2 during charging and discharging of capacitive process. CLK1 and CLK2 are used to enable other circuits like AND and MUX. These clocks are only valid for 5 V DC circuits.

7.6. CPLD Implementation. In this work, we had done the partial configuration of FPGA design which is shown in Figure 18. From this board, we have used only few components such as input switches, output led L3, power supply, and ground pin. MEMS value was programmed by using 8 bits; this can be varied as 20 types of input combinations. First, SW16 was kept in LOW position, and according to the truth table, SW1-SW8 can be varied. Based on the input values, LED brightness and clock width of the signal also varied. If clock width increases, LED brightness will decrease. The rise time and fall time values are varied based on clock width.

8. Comparison

8.1. Area Utilization. The area utilized in this design is brought up in the table as device utilization summary. The number of usage of each logic, availability, and their utilization are clearly shown in Tables 2 and 3. The average area utilized in proposed versus existing is also indicated in the following tables.

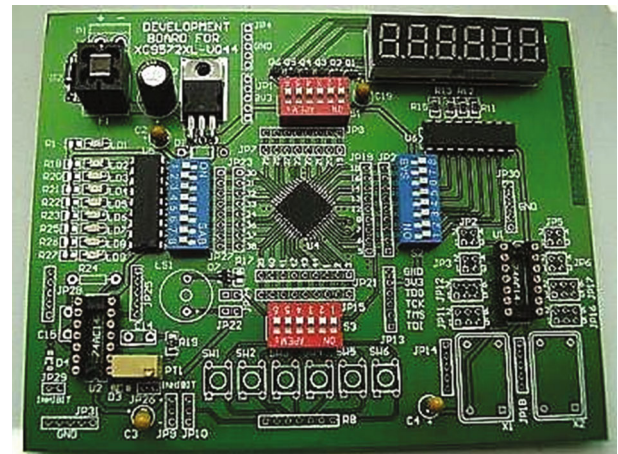


FIGURE 18: CPLD implementation.

Therefore, the average area utilized in this design is 2.95 which is 20% less than that of existing design, where the existing design occupied 3.31 which is 20% higher than that of proposed design.

8.2. Power Analysis. Finally, Figures 19 and 20 show the analysis of leakage power and the amount of power consumed with adiabatic and without adiabatic controller. In Table 2, the total utilization is 55% and 2% shown in the H column. So totally, 57% is occupied in the existing design, and the leakage power is about 0.62 W as shown in Figure 19.

$$0.62 \times (57\%) = 0.3534 \tag{1}$$

Thus, the required signal and logic power can be obtained by altering the signal rate in the navigator. In existing data, 0.00006 W out of 0.00154 W is obtained.

TABLE 2: Area utilization without energy recycling.

| Logic utilization | Used | Available | Utilization |
|--|------|-----------|-------------|
| No/- of slice flip flops | 26 | 7168 | 1% |
| No/- of 4 input LUTs | 131 | 7168 | 1% |
| No/- of occupied slices | 96 | 3584 | 2% |
| Number of slices containing only related logic | 96 | 96 | 100% |
| Number of slices containing only unrelated logic | 0 | 96 | 0% |
| Total number of 4 input LUTs | 157 | 7168 | 2% |
| Number of bonded IOBs | 78 | 141 | 55% |
| Average fan-out | 3.31 | | |

TABLE 3: Area utilization summary employing adiabatic controller.

| Logic utilization | Used | Available | Utilization |
|--|------|-----------|-------------|
| No/- of slice flip flops | 67 | 7168 | 1% |
| No/- of 4 input LUTs | 175 | 7168 | 2% |
| No/- of occupied slices | 124 | 3584 | 3% |
| Number of slices containing only related logic | 124 | 124 | 100% |
| Number of slices containing only unrelated logic | 0 | 124 | 0% |
| Total number of 4 input LUTs | 209 | 7168 | 2% |
| Number of bonded IOBs | 80 | 141 | 56% |
| Average fan-out | 2.95 | | |

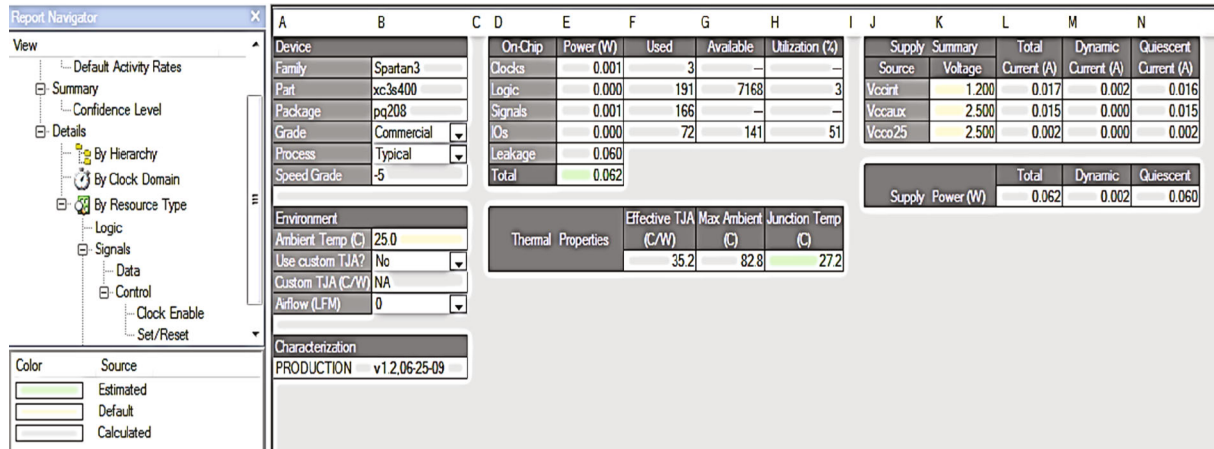


FIGURE 19: Leakage power without adiabatic architecture.

In Table 3, the total utilization is 51% and 2% shown in the H column. So in total, 53% is occupied in the proposed design and the leakage power is about 0.62 W as shown in Figure 20.

$$0.62 \times (53\%) = 0.3348 \quad (2)$$

Thus, the required signal and logic power can be obtained by altering the signal rate in the navigator. In existing data, 0.00006 W out of 0.00099 W is obtained (0.3534-0.3348 = 0.0186 MW). Therefore, 0.0186 MW of minimum

power difference is there in with adiabatic and without adiabatic designs.

By significantly reducing the clock frequency at steady state, as well as the power consumption of the circuits which are ancillary mostly to charging pump, it will greatly reduce dynamic power consumption as indicated in Table 4. When the 8 stages are powered, the circuit dissipates 0.62 W on average. As a result, the minimum power difference between adiabatic and adiabatic architecture is 0.0186 MW. The proposed circuit is a flexible bias circuit that is well suited to MEMS electrostatic actuation due to these requirements.

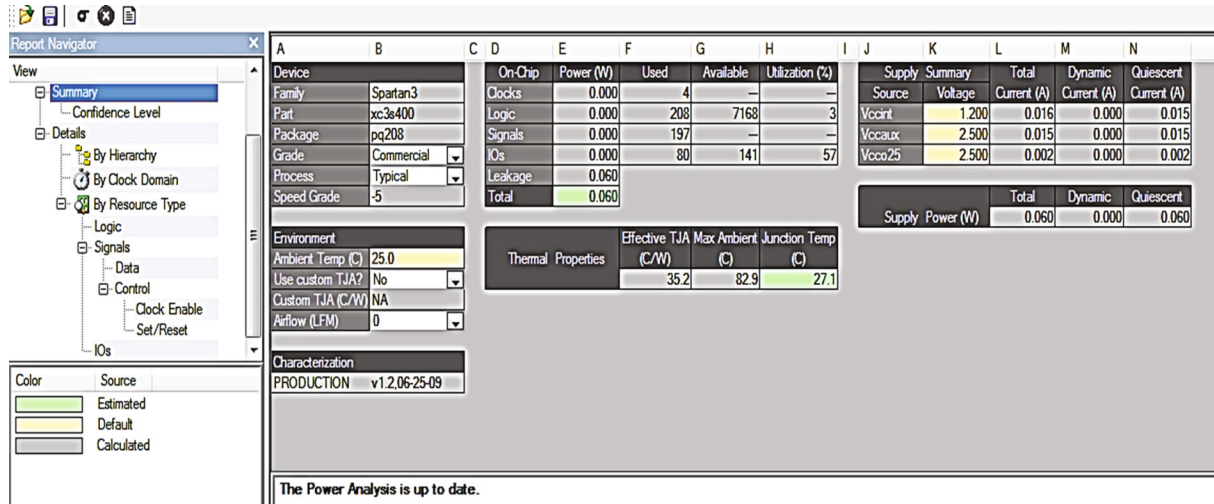


FIGURE 20: Leakage power with adiabatic architecture.

TABLE 4: Comparison of parameters.

| Parameters | Charge pump-based MEMS electrostatic actuator [8] | Adiabatic controller-based MEMS electrostatic actuator |
|-------------------------------|---|--|
| CMOS technology | 0.13 μm | 0.13 μm |
| Clock frequency | 50 MHz and 80 MHz | 40 MHz |
| Area (mm^2) | 0.0645 | 0.0645 |
| Load impedance | 1 pF | 1 pF |
| Rise time (ns) | 7 μs | 80 ns |
| Fall time (ns) | 6.11 μs | 6.40 μs |
| Nonclock sets of fan-out | 3.31 | 3.11 |
| Leakage power consumption (W) | 0.00006 | 0.00006 |
| Power consumption (W) | 0.00154 | 0.00099 |
| Supply voltage | 1.2 | 1.2 |
| Number of stages | 8 | 8 |
| Number of bonded IOBs | 55% | 51% |
| Total number of 4 LUTs | 2% | 2% |

9. Conclusion

This research work describes a nonconventional electrostatic MEMS-specific reconfigurable charge pump. In a steady state, the circuit's energy consumption can be reduced by lowering the clock frequency, which takes advantage of the solely capacitive load characteristics of MEMS electrostatic actuators. To allow for short output voltage rise times for stable MEMS actuation, a 50 MHz clock frequency was used, and the clock frequency was also decreased in steady-state operation to save power. A circuit that can be reconfigured to create a variety of voltage levels and dynamically changing output voltage is required for an ideal MEMS actuator. To reduce power dissipation, the adiabatic logic controller allows for dynamically altering output voltage. Reduced power consumption is achieved by using a variable fre-

quency clock. The major findings of the work are listed as follows:

- (1) A rising time of 80 ns and a fall time of 6.40s are accomplished with a 40 MHz clock. The circuit consumes 0.00099 W of power at the max output voltage for a 40 MHz clock. The output load of this circuit is a MEMS capacitive actuator; hence, no significant output DC current is delivered
- (2) By significantly reducing the clock frequency at steady state, as well as the power consumption of the circuits which are ancillary mostly to charging pump, it will greatly reduce dynamic power consumption. When the 8 stages are powered, the circuit dissipates 0.62 W on average. As a result, the minimum power

difference between adiabatic and adiabatic architecture is 0.0186 MW. The proposed circuit is a flexible bias circuit that is well suited to MEMS electrostatic actuation due to these requirements

- (3) Because of the circuit's small size, it can be integrated with MEMS in the same box, or multiple bias circuits can be used for MEMS that require multiple actuation voltages. In recent years, VLSI technology has been the most common and advanced technology. This technology could be able to reduce power consumption by using adiabatic logic and low power blocks. Power can be recycled and is used in portable wireless devices including pressure sensing, blood pressure measurement, and cell phones using the adiabatic circuit. Recycled power has been stored in devices for a long time and automatically withstands the capacity

Data Availability

The data used to support the findings of this study are included within the article.

Conflicts of Interest

The authors declare that they have no conflicts of interest regarding the publication.

Acknowledgments

This work is partially funded by Centre for System Design, Chennai Institute of Technology (funding number CIT/CSD/2022/006).

References

- [1] R. Uma, J. Ponnian, and P. Dhavachelvan, "New low power adders in self resetting logic with gate diffusion input technique," *Journal of King Saud University-Engineering Sciences*, vol. 29, pp. 118–134, 2017.
- [2] S. M. Kang and Y. Leblebici, *CMOS Digital Integrated Circuits Analysis & Design*, McGraw-Hill, New York, NY, USA, 2002.
- [3] W. C. Athas, J. Svensson, J. G. Koller, N. Tzartzanis, and Y. C. Chou, "Low-power digital systems based on adiabatic-switching principles," *IEEE Transactions on Very Large Scale Integration (VLSI) Systems*, vol. 2, no. 4, pp. 398–407, 1994.
- [4] S. Jain, S. Garg, N. Pandey, and K. Gupta, "Sinusoidal power clock based PFAL," *ICTACT Journal on Microelectronics*, vol. 5, pp. 801–806, 2019.
- [5] S. Ilyas and M. I. Younis, "Resonator-based M/NEMS logic devices: Review of recent advances," *Sensors and Actuators A: Physical*, vol. 302, article 111821, 2020.
- [6] A. Khorami and R. Saeidi, "Energy consumption analysis of the stepwise adiabatic circuits," *Microelectronics Journal*, vol. 104, article 104868, 2020.
- [7] R. M. Bommi and R. S. Selvakumar, "A survey on adiabatic logic families for implementing reversible logic circuits," in *2018 IEEE International Conference on Computational Intelligence and Computing Research (ICIC)*, pp. 1–4, Madurai, India, 2018.
- [8] K. Gupta and N. P. VishwasGosain, "Adiabatic Differential Cascode Voltage Switch Logic (A-DCVSL) for low power applications," *Journal of King Saud University - Engineering Sciences*, vol. 34, no. 3, pp. 180–188, 2022.
- [9] A. H. Alameh and F. Nabki, "A 0.13- μm CMOS dynamically reconfigurable charge pump for electrostatic MEMS actuation," *IEEE Transactions on Very Large Scale Integration (VLSI) Systems*, vol. 25, no. 4, pp. 1261–1270, 2017.
- [10] P. Beaulieu, A. H. Alameh, M. Menard, and F. Nabki, "A 360 V high voltage reconfigurable charge pump in 0.8 μm CMOS for optical MEMS applications," in *2016 IEEE International Symposium on Circuits and Systems (ISCAS)*, pp. 1630–1633, Montreal, QC, Canada, 2016.
- [11] I. Vaisband and E. G. Friedman, "Stability of distributed power delivery systems with multiple parallel on-chip LDO regulators," *IEEE Transactions on Power Electronics*, vol. 31, no. 8, pp. 5625–5634, 2016.
- [12] A. Shirane, H. Ito, N. Ishihara, and K. Masu, "A 21 V output charge pump circuit with appropriate well-bias supply technique in 0.18 μm Si CMOS," in *2011 International SoC Design Conference*, pp. 28–31, Jeju, Republic of Korea, 2011.
- [13] A. H. Alameh, A. Robichaud, and F. Nabki, "A reconfigurable charge pumps in 0.13 μm CMOS for agile MEMS actuation," in *2014 21st IEEE International Conference on Electronics, Circuits and Systems (ICECS)*, pp. 670–673, Marseille, France, 2014.
- [14] R. M. Bommi and M. S. Christo, "Adiabatic Configurable Reversible Synthesizer for 5G Applications," *Arabian Journal for Science and Engineering*, vol. 47, 2022.

Research Article

Analysis of Mechanical Properties for Al-MMC Fabricated through an Optimized Stir Casting Process

Bhiksha Gugulothu ¹, **N. Nagarajan**,² **A. Pradeep**,³ **G. Saravanan**,⁴ **S. Vijayakumar** ⁵,
and **Janardhana Rao**⁶

¹Department of Mechanical Engineering, Bule Hora University, Post box no-144, Ethiopia

²Department of Ancient Science, Tamil University, Thanjavur, India

³Department of Mechanical Engineering, Saveetha School of Engineering, SIMATS, Chennai, India

⁴Department of Mechanical Engineering, Kongunadu College of Engineering and Technology, Trichy, India

⁵Department of Mechanical Engineering, BVC Engineering College (Autonomous), Odalarevu-533210, Andhrapradesh, India

⁶Department of Electronics and Communications Engineering, BVC Engineering College (Autonomous), Odalarevu-533210, Andhrapradesh, India

Correspondence should be addressed to Bhiksha Gugulothu; bhikshamg@bhu.edu.et

Received 11 February 2022; Revised 4 March 2022; Accepted 8 March 2022; Published 29 March 2022

Academic Editor: V. Vijayan

Copyright © 2022 Bhiksha Gugulothu et al. This is an open access article distributed under the Creative Commons Attribution License, which permits unrestricted use, distribution, and reproduction in any medium, provided the original work is properly cited.

This work concentrated on preparation of Al-based composites through stir casting process. Al6082 was chosen as base material that is reinforced with zirconium silicate and titanium carbide. As per Taguchi design L16 orthogonal array, specimens are produced with variation of casting parameters for performing tensile and hardness test. In this process, ZrSiO₄ is kept constant to 10 wt%, whereas TiC concentration varied from 2.5 to 10wt%. For analyzing the properties of optimized stir cast samples for AA6082/ZrSiO₄/TiC, three input variables with four levels are taken such as Stir speed (SS) 300-750 rpm, Stir time (ST) 5-20 min, and Reinforcement (RI) 2.5-10 wt%. The Taguchi technique was used as an analyzer to determine optimal parameter on Tensile Strength (TS) and Hardness (HN). The Minitab-17 software is assisting to find analysis of variance (ANOVA), regression equation, and contour plots of the selected parameters. Finally, it is witnessed that SS (65.9%) is the maximum influenced factor that increases TS, followed by RI (23.1%) and ST (11%). The best combinations of parameters on TS and HN were found at SS2-ST1-RI2 (450 rpm, 5 min, and 5wt%) and SS3-ST2-RI4 (600 rpm, 10 min, and 10wt percent), respectively. From the contour plots, the casting variables SS (600-650 Rpm), ST (15-17.5 min), and RI (5-8wt%) were proposed for achieving excellent mechanical properties.

1. Introduction

Al matrix composites are frequently preferred in many applications to create various lightweight items [1]. Stir casting is one of the manufacture processes which makes effective components by pouring of molten metal in to standard dies [2]. These cast products minimize porosity and have a uniformly mixing of grain particles [3, 4]. Al

alloy properties were developed by choosing nano and microlevel reinforcements. Ceramic particles such as TiC, silicon carbide and alumina were mostly added with AL for improving microhardness and UTS [4–9]. Ravikumar et al. studied about behavior of AA 6082/TiC by execution of different examinations like SEM investigation, XRD, and destructive tests [10]. Rajaganapathy explained that the addition of both TiC and WC (3-10%) particles with

6082 alloy enhanced wear resistance at dry condition [11]. Zrsio4 is one of the greatest corrosion resistances which is contributed in several productions such as boilers and valve vessels [12–14]. Sharma et al. aimed to study the WEDM process parameter of AA6063/ZrSiO4 and optimization process and also carried out the Box-Behnken-RSM method [15]. Gurusami et al. selected three factors and prepare 15 composites (AA7068/B4C) by casting route, the outcome of ANOVA revealed that the most influenced optimal factor on wear resistance was at sample no. 10 (B4C-6%, speed of stirrer-750 rpm, and stir time-7minutes) [14]. Adeolu fabricated Al7075-TiO₂ composites through stir-casting way and detected that temperature (750°C) and stir speed (500 rpm) are premier significant variables which exhibited the best UTS [16]. Sathishkumar et al. have done microstructure study and material behavior and properties Mg matrix nanocomposites (MMNCs) [17]. Due to the increment of TiC particles from 0 to 12% in AA2014 matrix, ductility reduced around 45% and tensile strength and BHN are improved to 52% and 21%, respectively [18]. Talikoti et al. fabricated AA 7075 reinforced SiC/graphite hybrid composites by liquid metallurgy method, from optimization process, more contribution of silicon carbide increased yield strength and elongation about 68% and 51%, respectively [19]. The improvement of mechanical properties of AA6063/SiC/MoS₂ mainly depends on the grain size of abrasives and corrosion resistance which decreased due to raising of temperature [20]. The 5059-Al reinforced on 30lm size silicon carbide (5-15%) and molybdenum-disulphide (about 2%) hybrid compounds were made by stir casting. The metal removal rate (MRR) was examined with variation of voltage level, feed rate, and electrolyte quantity on the L27 Taguchi design [21]. Zhu established composite of Al6082 alloy with nanosize of SiC via gravity casting procedure. It was noticed that tensile (29%) and yield strength (43%) improved at T6 heat treatment [22]. The prepared composites mostly are used in many fields such high-stress applications, bridges, winches, transport applications, ore skips, beer barrels, and milk can.

In this research, optimal performance done for tensile strength (TS) and hardness (HN) is the prime concern. The measurements of TS and HN are needed to be analyzed, the main effort of research process is to determine optimal input considerations, improving output responses (TS) in the design of experiments.

2. Experiment Setup

Al alloy (6082) is one of the best 6xxx type alloys, with outstanding wear resistance, and is extensively used in machining. Strengthening materials ZrSiO₄ and TiC were added to Al 6082 at varied percent weights. To create a hybrid composite, 6082 was cast with Zrsio4/TiC. Stirrer was rotated at various rates by an electrical motor. To bring the stirrer into touch with the compound components, a safe lifting mechanism was used. Initially, Al alloy was put in a crucible and burned in an electric furnace at roughly 700°C. Heat the zirconium silicate (2.5 percent wt)

TABLE 1: Casting input parameters.

| Factors | Levels | | | |
|--------------------|--------|-----|-----|-----|
| | 1 | 2 | 3 | 4 |
| Stir speed (SS) | 300 | 450 | 600 | 750 |
| Stir time (ST) | 5 | 10 | 15 | 20 |
| Reinforcement (RI) | 2.5 | 5 | 7.5 | 10 |

and titanium carbide (5 wt percent) particles at 350°C simultaneously with the use of a second furnace after measuring with a digital weigh scale. Thereafter, molten Al alloy metals and reinforcements were combined and heated to roughly 750°C. For 5 minutes, the melt was continually agitated by a stirrer linked to the motor; then, the prepared melted particles were poured into the desired mold to generate Al-based composites. Variate the stirrer speed, mixing time, and weightiness % of reinforced materials to continue the procedure for creating many samples. With the help of grinding machine, remove unnecessary portion from the developed samples.

3. Result and Discussion

Four different levels of parameters mentioned in Table 1 were selected to find optimal outputs of hardness and tensile strength. The Taguchi is one of the finest approaches to be used as tool on optimization solution even though many methods like Box-Behnken exist. Conclusions of investigational examinations were scrutinized with the assistance of ANOVA 95% level [23]. The experimental and S/N ratio effects on both TS and BHN have been exposed in Table 2. It was witnessed that greatest and lowest optimum combinations of parameters on TS were identified at SS2-ST1-RI2 (450 rpm, 5 min, and 5 wt%) and SS1-ST1-RI1 (300 rpm, 5 min, and 2.5 wt%), respectively. Best and least for HN were also detected at SS3-ST2-RI4 (600 rpm, 10 min, and 10 wt%) and SS4-ST1-RI4 (750 rpm, 5 min, and 10 wt%). S/N ratios and means at all level parameters are displayed in Figures 1 and 2. RI and SS are peak-manipulating parameters, followed by ST as the lowest contribution to improve composite strengths. Optimized significance of every input consideration for both properties can be found according to signal and noise which is exposed in Tables 3 and 4. From tabulation effects, SS1 (-49.47) has been a chief influencing factor on tensile property tailed by RI2(-50.10) and ST2(-50.26). Likewise, RI4 (-38.29) has a primary factor which followed via ST4 and SS1.

4. Regression Equation

The correlation was recognized among input considerations of casting procedure which calculate the value of HN and TS and equations of regression analysis (Equations 1 and 2) which was symbolized from the Optimize software (Minitab-17 version).

TABLE 2: Experiment and S/N results.

| Experiment no. | Process parameters | | Experimental observations | | S/N ratio | |
|----------------|--------------------|----------|---------------------------|------|-----------|----------|
| | SS (Rpm) | ST (min) | TS (Mpa) | HN | TS(dB) | HN(dB) |
| L1 | 300 | 5 | 289.83 | 92 | -49.2429 | -39.2758 |
| L2 | 300 | 10 | 297.52 | 83 | -49.4703 | -38.3816 |
| L3 | 300 | 15 | 302.58 | 86 | -49.6168 | -38.6900 |
| L4 | 300 | 20 | 300.80 | 79 | -49.5656 | -37.9525 |
| L5 | 450 | 5 | 415.57 | 90 | -52.3729 | -39.0849 |
| L6 | 450 | 10 | 387.52 | 86.2 | -51.7659 | -38.7101 |
| L7 | 450 | 15 | 298.79 | 78.5 | -49.5073 | -37.8974 |
| L8 | 450 | 20 | 352.74 | 85.5 | -50.9491 | -38.6393 |
| L9 | 600 | 5 | 375.71 | 92 | -51.4971 | -39.2758 |
| L10 | 600 | 10 | 326.28 | 98.3 | -50.2718 | -39.8511 |
| L11 | 600 | 15 | 406.23 | 79.6 | -52.1754 | -38.0183 |
| L12 | 600 | 20 | 394.63 | 75.3 | -51.9238 | -37.5359 |
| L13 | 750 | 5 | 357.27 | 74.8 | -51.0599 | -37.4780 |
| L14 | 750 | 10 | 299.56 | 82.9 | -49.5297 | -38.3711 |
| L15 | 750 | 15 | 347.83 | 95 | -50.8273 | -39.5545 |
| L16 | 750 | 20 | 362.94 | 92.6 | -51.1967 | -39.3322 |

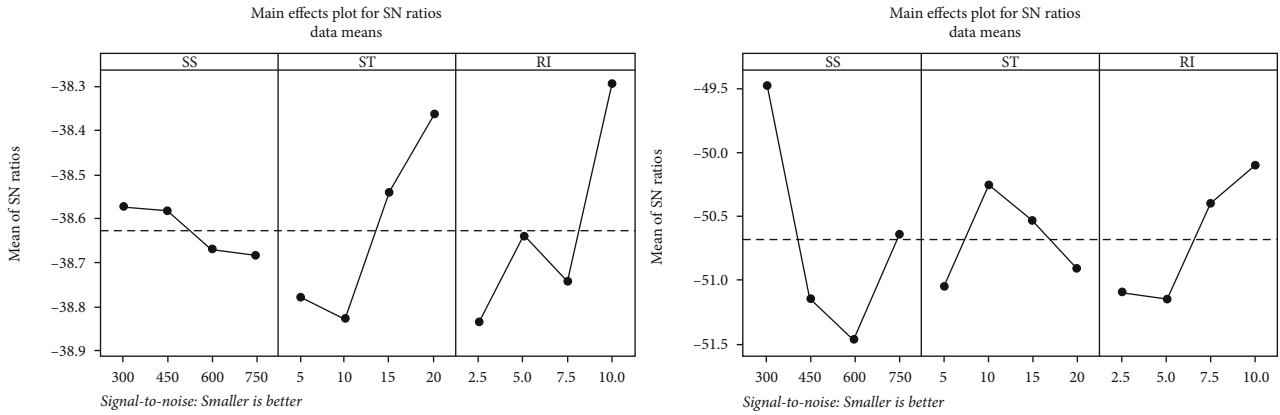


FIGURE 1: S/N ratio—TS and HN.

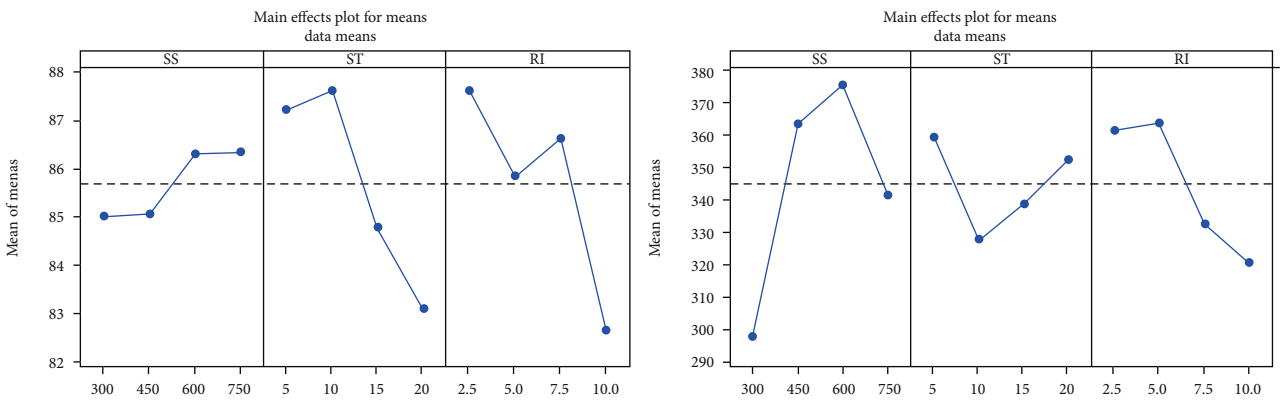


FIGURE 2: Means—TS and HN.

TABLE 3: S/N ratio response—TS.

| Level | SS | ST | RI |
|-------|--------|--------|--------|
| 1 | -49.47 | -51.04 | -51.10 |
| 2 | -51.15 | -50.26 | -51.15 |
| 3 | -51.47 | -50.53 | -50.40 |
| 4 | -50.65 | -50.91 | -50.10 |
| Delta | 1.99 | 0.78 | 1.05 |
| Rank | 1 | 3 | 2 |

TABLE 4: S/N ratio response—HN.

| Level | SS | ST | RI |
|-------|--------|--------|--------|
| 1 | -38.57 | -38.78 | -38.83 |
| 2 | -38.58 | -38.83 | -38.64 |
| 3 | -38.67 | -38.54 | -38.74 |
| 4 | -38.68 | -38.36 | -38.29 |
| Delta | 0.11 | 0.46 | 0.54 |
| Rank | 3 | 2 | 1 |

Tensile Strength = 334.9 + 0.0965 Stir speed – 0.19 Stir time – 6.15 Reinforcement(1)

Hardness = 91.14 + 0.0035 Stir speed – 0.303 Stir time – 0.563 Reinforcement(2)

5. ANOVA Analysis and Contour Graphs

The formulation of analysis of variance was done by mathematical statistical method (Minitab-17). Table 5 exposes that effect of each parameter contributed on the experimental

values of tensile strength and hardness. It was established that stir speed (65.9%) is the most significant factor that improves mechanical properties of AMC (Al6082-ZrSiO4-TiC) and reinforcement (23.1%) is considered as the next effective parameter followed by stir time (11%). Contour graphs attained for TS and HN against input process factors are shown in Figures 3 and 4. From the plotted observation, the ranges of casting factors SS (600-650 Rpm), ST (15-17.5 min), and RI (5-8 wt%) were recommended for attaining high tensile strength and hardness values.

TABLE 5: ANOVA result—TS.

| Source | DF | Sum of square (SOM) | Mean sum(MS) | F | P | Contribution (%) |
|--------|----|---------------------|--------------|------|-------|------------------|
| SS | 3 | 9.178 | 3.0593 | 4.79 | 0.049 | 65.9 |
| ST | 3 | 1.532 | 0.5106 | 0.80 | 0.538 | 11 |
| RI | 3 | 3.225 | 1.0751 | 1.68 | 0.269 | 23.1 |

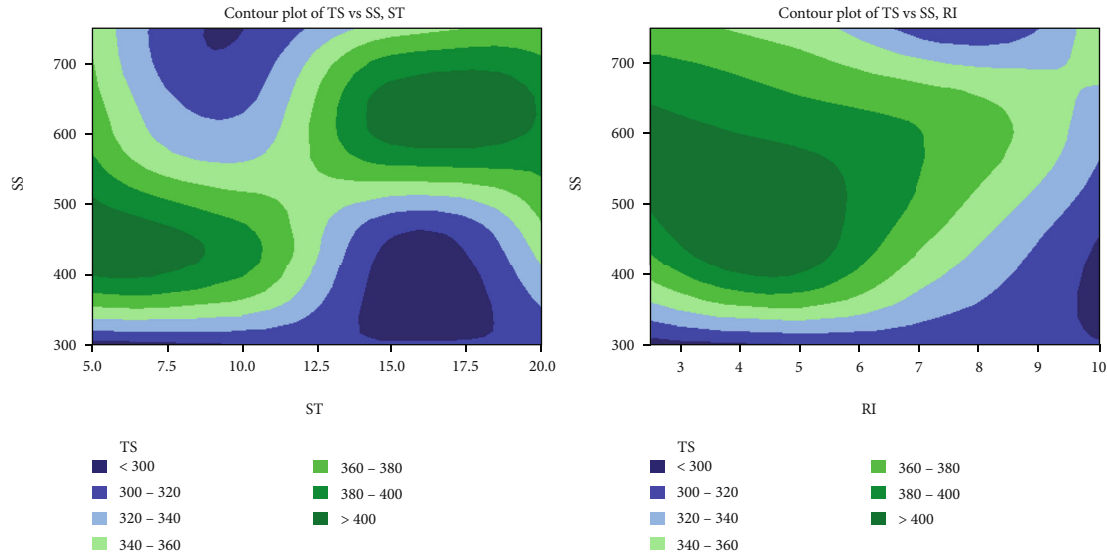


FIGURE 3: Contour plot on TS for casing variables.

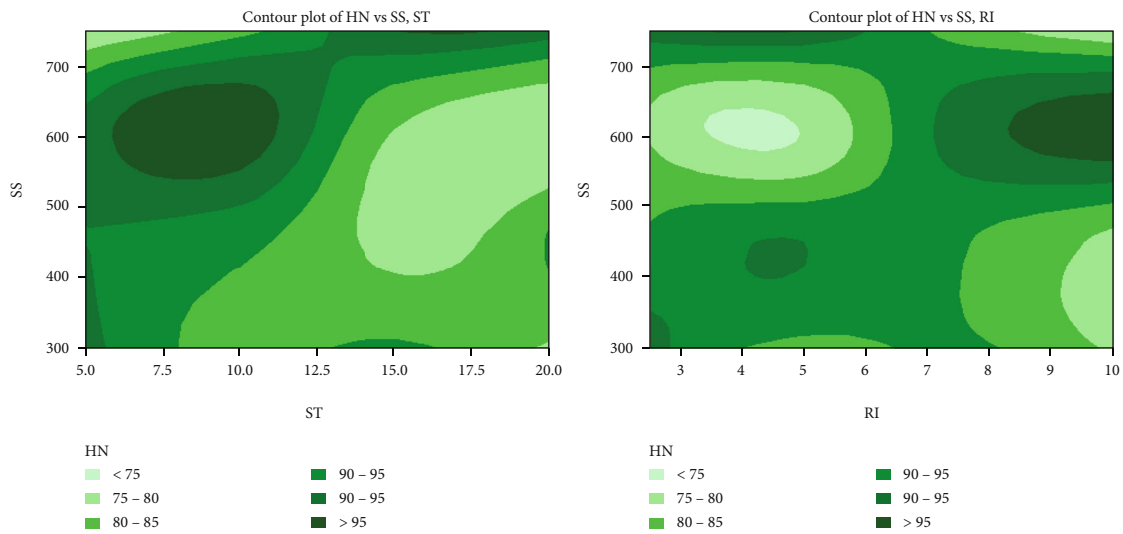


FIGURE 4: Contour plot—HN vs. stir parameters.

6. Conclusion

In this work, stir casting (SC) was used to make several AMC (Al6082-ZrSiO₄-TiC) samples. In Taguchi’s design, the orthogonal array (L16) has been effectively used to optimize the SC variables of stir speed (SS), stir time (ST), and reinforcements (RI). At L5, the maximum tensile strength

(TS) was achieved (SS:450 rpm, ST:5 min, and RI:5 wt%). When it came to hardness, the highest HN was found at L10 sample (SS-600 rpm, ST-10 min, and RI-10 wt%). The lowest TS and HN were reported at L1 and L13, respectively. According to the ANOVA results, the most important element in developing AMC characteristics was SS-65.9%, followed by RI-23.1% and ST-11%.

Data Availability

The data used to support the findings of this study are included in the article. Should further data or information be required, these are available from the corresponding author upon request.

Disclosure

This study was performed as a part of the Employment Bule Hora University, Ethiopia.

Conflicts of Interest

The authors declare that there are no conflicts of interest regarding the publication of this paper.

Acknowledgments

The authors appreciate the technical assistance to complete this experimental work from the Department of Mechanical Engineering, Bule Hora University, Ethiopia. The authors thank Department of Ancient Science, Tamil University, Thanjavur; Department of Mechanical Engineering, BVC Engineering College (Autonomous), Andhra Pradesh; Department of Mechanical Engineering, Saveetha School of Engineering, Chennai; and Department of Mechanical Engineering, Kongunadu College of Engineering, Trichy, India, for their support of draft writing.

References

- [1] J. V. Christy, R. Arunachalam, A. H. I. Mourad, P. K. Krishnan, S. Piya, and M. Al-Maharbi, "Processing, properties, and microstructure of recycled aluminum alloy composites produced through an optimized stir and squeeze casting processes," *Journal of Manufacturing Processes*, vol. 59, p. 287, 2020.
- [2] U. Arunachalam and J. Vairamuthu, "Tribological analysis on magnesium alloy AZ31B with reinforced ZrSiO₄ through Taguchi technique," *Materials Today: Proceedings*, vol. 37, pp. 2521–2528, 2021.
- [3] A. Karthik, R. Karunanithi, S. A. Srinivasan, and M. Prashanth, "The optimization of squeeze casting process parameter for AA2219 alloy by using the Taguchi method," *Materials Today: Proceedings*, vol. 27, pp. 2556–2561, 2020.
- [4] H. P. Pydi, A. Pradeep, S. Vijayakumar, and R. Srinivasan, "Examination of various weld process parameters in MIG welding of carbon steel on weld quality using radiography & magnetic particle testing," *Materials Today: Proceedings*, pp. 1–4, 2022.
- [5] B. Gugulothu, P. S. S. Kumar, B. Srinivas, A. Ramakrishna, and S. Vijayakumar, "Investigating the material removal rate parameters in ECM for Al 5086 alloy-reinforced silicon carbide / flyash hybrid composites by using Minitab-18," *Advances in Materials Science and Engineering*, 7 pages, 2021.
- [6] H. P. Pydi, A. P. Pasupulla, S. Vijayakumar, and H. A. Agisho, "Study on microstructure, behavior and Al₂O₃ content flux A-TIG weldment of SS-316L steel," *Materials Today: Proceedings*, vol. 51, pp. 728–734, 2022.
- [7] A. Prakash Pasupulla, H. Abebe Agisho, S. Seetharaman, and S. Vijayakumar, "Characterization and analysis of TIG welded stainless steel 304 alloy plates using radiography and destructive testing techniques," *Materials Today: Proceedings*, vol. 51, pp. 935–938, 2022.
- [8] S. Vijayakumar, N. Dhasarathan, P. Devabalan, and C. Jehan, "Advancement and design of robotic manipulator control structures on cyber physical production system," *Journal of Computational and Theoretical Nanoscience*, vol. 16, no. 2, pp. 659–663, 2019.
- [9] V. Preethi and A. D. Das, "Optimization of friction stir welding parameters for better hardness in weld nugget of hybrid aluminium composite," *Mater. Today Proc.*, vol. 37, pp. 723–727, 2021.
- [10] K. Ravikumar, K. Kiran, and V. S. Sreebalaji, "Characterization of mechanical properties of aluminium/tungsten carbide composites," *Meas. J. Int. Meas. Confed.*, vol. 102, pp. 142–149, 2017.
- [11] M. Ravichandran, M. Meignanamoorthy, G. P. Chellasivam, J. Vairamuthu, A. S. Kumar, and B. Stalin, "Effect of Stir Casting Parameters on Properties of Cast Metal Matrix Composite," *Materials Today: Proceedings*, vol. 22, pp. 2606–2613, 2020.
- [12] P. Paramasivam and S. Vijayakumar, "Mechanical characterization of aluminium alloy 6063 using destructive and non-destructive testing," *Materials Today: Proceedings*, 2021.
- [13] R. M. Badizi, A. Parizad, M. Askari-Paykani, and H. R. Shahverdi, "Optimization of mechanical properties using D-optimal factorial design of experiment: Electromagnetic stir casting process of A357–SiC nanocomposite," *Transactions of Nonferrous Metals Society of China*, vol. 30, no. 5, pp. 1183–1194, 2020.
- [14] K. Gurusami, S. Shalini, and T. Sathish, "Optimization of stir casting parameters for corrosion rate analysis of AA7068 - boron carbide composites," *Materials Today: Proceedings*, vol. 33, pp. 4650–4655, 2020.
- [15] A. Sharma, M. P. Garg, and K. K. Goyal, "Prediction of optimal conditions for WEDM of Al 6063 ZrSiO₄ p MMC Procedia," *Materials Science*, vol. 6, pp. 1024–1033, 2014.
- [16] A. A. Adediran, A. A. Akinwande, O. A. Balogun, and B. J. Olorunfemi, "Optimization studies of stir casting parameters and mechanical properties of TiO₂ reinforced Al 7075 composite using response surface methodology," *Scientific Reports*, vol. 11, no. 1, 2021.
- [17] P. Sathishkumar, V. Deepakaravind, P. Gopal, and P. Azhagiri, "Analysis the mechanical properties and material characterization on magnesium metal matrix nano composites through stir casting process," *Materials Today: Proceedings*, vol. 46, pp. 7436–7441, 2021.
- [18] P. Sharma, S. P. Dwivedi, R. Sharma, V. Dabra, and N. Sharma, "Microstructural and mechanical behavior of aluminium alloy reinforced with TiC," *Materials Today: Proceedings*, vol. 25, pp. 934–937, 2020.
- [19] B. H. Talikoti, H. N. Girisha, and L. Bharath, "Optimization of process parameter on yield strength and ductility on Al7075/SiC/Gr. Hybrid composite by using Taguchi's technique," *Materials Today: Proceedings*, vol. 47, pp. 2370–2375, 2021.
- [20] K. Umanath, K. Palanikumar, V. Sankaradass, and K. Uma, "Optimizations of friction stir welding process parameters of AA6063 Aluminium alloy by Taguchi technique," *Materials Today: Proceedings*, vol. 46, pp. 4008–4013, 2021.

- [21] S. A. A. Daniel, S. V. Ananth, A. Parthiban, and S. Sivaganesan, "Optimization of machining parameters in electro chemical machining of Al5059/SiC/MoS₂ composites using taguchi method," *Materials Today: Proceedings*, vol. 21, pp. 738–743, 2020.
- [22] J. Zhu, W. Jiang, G. Li, F. Guan, Y. Yu, and Z. Fan, "Micro-structure and mechanical properties of SiC_{np}/Al6082 aluminum matrix composites prepared by squeeze casting combined with stir casting," *Journal of Materials Processing Technology*, vol. 283, article 116699, 2020.
- [23] D. Pal, S. Vijayakumar, T. V. J. Rao, and R. S. R. Babu, "An examination of the tensile strength, hardness and SEM analysis of Al 5456 alloy by addition of different percentage of SiC/flyash," *Materials Today: Proceedings.*, 2022.

Research Article

Improvement Study on Blood Test Investigation by Nanoparticle-Coated Colour-Coded Sample Paper

P. Jayakumar ¹, **S. Padmanabhan** ², **B. Sheela Rani**,¹ **B. Balamugundan**,³
and **Lijalem Mulugeta** ⁴

¹*Sathyabama Institute of Science and Technology, Chennai, India*

²*School of Mechanical and Construction, Vel Tech Rangarajan Dr. Sagunthala R&D Institute of Science and Technology, Chennai, India*

³*Department of Mechanical Engineering, Panimalar Engineering College, Chennai, India*

⁴*Department of Mechanical Engineering, Faculty of Manufacturing Institute of Technology, Hawassa University, Ethiopia*

Correspondence should be addressed to P. Jayakumar; jaijat07@gmail.com

Received 24 February 2022; Accepted 12 March 2022; Published 25 March 2022

Academic Editor: V. Vijayan

Copyright © 2022 P. Jayakumar et al. This is an open access article distributed under the Creative Commons Attribution License, which permits unrestricted use, distribution, and reproduction in any medium, provided the original work is properly cited.

Nanobiotechnology is a growing branch of research that combines biology and nanotechnology to study and create unique, functionalized nanobiosystems. This interdisciplinary study subject has significant promise for improving medical engineering. Finding the exact blood category is a coercive test for blood transfer and other incalculable health checkups. The pandemic has accelerated these test frequencies in an exponential fashion. It is usually the job of the practitioners working in the laboratory to name the types of blood samples. Depending on the blood type and its cross-matching fitness, recommendations are offered for blood transfer. In many places, this type of testing is done manually, and it is done through a microplate and test tube. These tests usually take longer, and the chances of errors are high, which can lead to fatalities. Polymer-based paper sample collection has been shown to be ideal instruments for conducting blood tests in response to this requirement because of their capacity to do quick and low-cost diagnostics and analyses. In this paper, a novel nanocoated blood polymer sample paper with unique coding was proposed and investigated for its operational simplicity and effectiveness. A unique coded polymer sample paper has prevented complications during blood tests and provides expected results without errors.

1. Introduction

Nanotechnology, one of the most fascinating fields of science, provides scientists with the power to make, manipulate, and utilize materials on a nanoscale, making it one of the most exciting research areas. Biotechnology has aided in transmitting information about biological systems to the industrial sector. The various physicochemical and biological features of nanoparticles have also led to the use of nanotechnology in a variety of healthcare settings [1]. Nanobiotechnology is one of the most recent developing branches of research, and it is the interface between biology and nanotechnology, studying and designing unique functionalized nanobiosystems. This interdisciplinary study topic offers tremendous promise for advancing medical engineering technology [2].

In 1616, the English physician William Harvey discovered the existence of blood circulation in animals. He also discovered that blood could be transferred from one animal to another because it circulates here and there in an organism. In 1665, English physician Richard Lowe examined blood transfusions in dogs. In the nineteenth century, physician James proposed that humans donate blood to compensate the blood loss during surgery. During his study, physician Leonard Landois discovered that when red blood cells were transfused from one species of animal to another, they usually clumped and sometimes scattered. Further, he reported that injecting a person with a different type of red blood cell would cause his or her urine to turn black. Through this, he scientifically proved that transferring blood from one species to another could be harmful. In 1901, an

American biologist, Karl Landsteiner, discovered the presence of ABO blood groups in humans by birth in Austria. He also discovered the existence of antigens and antibodies in the blood. Further, when one type of blood mixes with another type of blood, these substances trigger the red blood cells to appear to merge [3].

A year later, some other researchers diagnosed a fourth type of AB blood type. Red blood cells combine when transfusing type B blood to a person with type A or transferring type A blood to a person with type B. The same result can be seen when injecting AB type blood into a person with type A or type B blood. Usually, when type O blood is mixed with other blood types, it does not coalesce and remains normal. This knowledge of blood types is essential because if mistakes are made, they can lead to loss of life. Blood cross-matching can be done to find out if a person's blood is suitable for another. Most people in Great Britain and Northern Ireland routinely donate blood voluntarily [4]. Moreover, an average of two million units of blood per year are used for transfusion. The blood should be used in an appropriate manner as it can be donated in small quantities by one person at a time. The use of blood transfusions can be best managed using the Maximum Surgical Blood Order Schedule (MSBOS) during surgery [5]. The number of required blood units for each operation is calculated according to the traditional analysis method. Before surgery, the quantity of blood units a patient needs can be booked on a cash basis in real time. It allows us to accurately calculate the number of blood units needed in an emergency [6]. The British Committee for Standards in Hematology has given the world the practical guidelines needed to perform blood transfusions properly [7]. It is necessary to verify that the blood transfusion is correctly done through a compatibility test based on a patient's past blood transfusion history, cross-match, ABO, Rh combination, and suitability of antibodies for both the blood giver and the patient. The blood level similarities and conflicts between the blood giver and patient can be identified through the cross-match test. Usually, this type of information is not available through blood group typing [8]. It was reported that, traditionally, the anti-IgG tests performed had been done in an unsafe manner compared to the computerized cross-match test. Further, all computer-assisted blood test results are stored on the computer, which reduces the possibility of human errors, and thus, the cost of the process is also reduced. At the University of Michigan Medical Center, the most notable event is the blood transfusion without any errors being found from the results of one lakh, 38 thousand cross-match tests conducted with the help of a computer [9].

The blood has the potential to be a window into one's health, and as a consequence, it is the human biofluid that has been researched the most. Blood tests may be used to diagnose disorders, evaluate the effectiveness of treatment medications, and gather information about a person's overall health. It is becoming more critical to do rapid reaction blood tests when following therapy is necessary. Paper-based devices have been shown to be ideal instruments for conducting blood tests in response to this requirement because of their capacity to do quick and low-cost diagnos-

tics and analyses in a nonlaboratory setting. In this perspective, we discuss recent advancements in paper-based blood testing, with a particular emphasis on the individual methodologies and assays that have been used in each case. Additional topics covered in this study include how to increase the signal intensity of these paper-based devices and leverage in situ synthesis of nanomaterial to improve the sensitivity, functionality, and operational simplicity of these devices in the future. As a result of these developments, paper-based devices are becoming more viable instruments for performing point-of-care blood tests in a variety of real-world situations. The purpose of this article is to look at the issues that may arise during blood grouping tests and cross-matching tests and how to deal with such problems effectively. The proposed method eliminates the complications that occur during manual blood grouping. In this research, the nanoparticle of titanium oxide- (TiO_2 -) coated blood sample polymer paper with unique coding was proposed and investigated for its operational simplicity and effectiveness on blood test investigations.

2. Blood Group Investigation

Before transfusing blood from one person to another, one needs to find out the blood types of the donor and receiver and then find out the cross-match between the two. Individuals who perform these experiments are certified in this domain and have experience in training. The practitioner will decide whether or not to use one's blood based on the results of the cross-match test. If the results of the cross-match test are appropriate, the blood transfusion between two people will be allowed; otherwise, it can cause the patient's immune system to fail to function appropriately and sometimes even result in loss [10]. This type of test is usually needed when the hemoglobin level in the blood is low, when there is a disease in the blood cells, or in cases where the blood is not stopping or going for tissue transplantation. In medical emergencies, doctors usually choose O type blood, also known as universal blood type, for blood transfusion. If it is entirely free of antibodies at the end of the cross-match test, then it will be selected as the best suitable blood. In a few cases, a low number of antibodies will be found at the end of the test, and it will be tested further to determine its suitability. It is completely eliminated when antibodies are found that usually cause side effects. Direct handling of blood samples should be minimized when performing these types of tests because sometimes there is a chance that some samples may have some pathogens, so the chances of the pathogen being infected are very, very high [11].

There are some flaws in the cross-match. There is no guarantee that the red blood cells that were first transplanted will enter the patient's body and live well. This test, performed on a patient's serum, does not detect unexpected red blood cell antibodies. An unknown drug injected into a patient's body will break down the patient's red blood cells and antibodies in the patient's body, which cannot be prevented by a cross-match test [12]. Furthermore, the test does not reveal any details about other diseases in the donor's

body or the recipient of the blood. Most importantly, these blood samples must be collected and tested within three days; otherwise, we will not be able to obtain accurate patient information. The room temperature of the laboratory where this test is being performed should not exceed 37 degrees Celsius so that we can easily see the clumping antibodies [13].

The donor's or recipient's serum is used to determine if there are any antibodies attached to the cells that are not appearing as a group. The cross-match test with the addition of polymerized albumin improves the performance. The computer-assisted cross-match test is performed on the serum and the donor's blood. This test requires only a small amount of blood [14]. During this test, the patient's blood must be in the laboratory [15–17].

Between December 2013 and December 2016, a study was conducted at the Indus Hospital Blood Centre, Pakistan, which showed 45,425 donors. Of these, a total of 413 blunders were detected. Here, human errors were spotted by computer-based blood bank management software that could run with the help of the website. Looking at the literature reports mentioned above confirms that the errors that occur in the laboratory persist. The primary purpose of this research is to look at how manual tests can be ruled out, such as naming blood groups, transfusions, and cross-match testing errors. It will save a great deal of time and human lives. Observational research was done at the Yazd Blood Transfusion Center between March 2010 and March 2017 and reported by Napier et al. [18]. The blood types of all the donors were tested by test tube and were considered the number of blood transfusions during the eight years mentioned above which was three lakh twenty two thousand, of which about 130 cases were misdiagnosed. The percentage of these errors is approximately 0.04% [18].

3. Existing Methodology

Many types of strategies and observations are employed for naming blood in general in medical laboratories. However, many of them are concerned with the appearance of test results. Here, we look at the pros and cons of the slide method.

3.1. Slide Method. The slide test has much lower sensitivity compared to other tests that detect blood types. However, this test is very effective in emergencies as it gives accurate results. A glass plate is divided into three regions during the test; one drop from the donor's blood and one drop from the recipient's blood are mixed with antigens A, B, and C separately. This test lasts five to ten minutes and can detect the formation or scattering of blood platelets by which blood type is determined. However, it is very difficult to diagnose blood types with blood samples that are less reactive to antigens. Slide tests are beneficial for detecting blood types outdoors, but blood transfusions based solely on the results obtained from slide tests may not be safe [6]. Beyond all of this, all the test results will be taken incorrectly if the technicians sometimes mistakenly put this glass plate upside down while performing this test. There are some new ideas

in this article to help with the problems that come up because of the changes.

3.2. Glass Slides with Colour Code Marking. During a blood type test, three drops of red blood cells are taken at different points on a piece of glass. The three antigens, A, B, and anti-D, will be added separately with the samples taken and observed in Figure 1. The antigen combined with blood cells reacts and turns into agglutination; otherwise, it remains the same. Blood types are classified according to this. Hundreds of samples of such blood types in laboratories are handled simultaneously, and laboratory assistants are more likely to place the plates in an upside down position when handling them. It will become erroneous when deciding the tests of the samples thus placed.

3.3. Error Data. Errors that occur when using this existing method are studied. For this purpose, three blood test laboratories in small towns near Madurai, India, were considered. The following is the study report taken from January 2019 to December 2019.

Table 1 shows the results of the blood test. The tests are conducted at three blood test centers. Table 1 covers all the results of tests conducted in those centers during 2019 that have been taken into account. Of these, 1348 tests were performed at Vickram labs (test lab I), 923 tests at the Siva X-ray Center (test lab II), and 2345 tests at Vaigai Raj Scan (test lab III). When you look at the results of this table, it is clear that something went wrong. The results of seven tests in the test conducted on the Vickram labs were incorrectly identified. Similarly, three tests were incorrectly reported at the end of one-year tests conducted at the Siva X-ray Center. In addition, out of 2345 tests conducted on the Vaigai Raj Scan, the results of about seven tests were incorrect. In particular, a test conducted at the Vickram lab misdiagnosed two people with A-ve blood types as O+ve and five people with B+ve blood types as AB-ve. In the same way, a test at the Siva X-ray Center misidentified three people with O+ve blood types as A-ve and one person with an AB-ve blood type as B+ve. Similar confusion occurred in the Vaigai Raj Scan as well, where four people with A-ve blood types were diagnosed as O+ve and three people with B+ve blood types were reported as AB-ve.

When examining how errors occurred in the results of these experiments, it became apparent that technical errors were the cause. These errors occurred while the test was being performed with the test microplate upside down. For example, if the plate with an AB-ve blood type shown in Figure 1 is turned upside down, it will be B+ve. A new attempt to fix this problem has been made, and its results have been successful. Figure 2 compares the error rates of the three selected blood test centers in 2019.

4. Nanocoated Paper with Colour Code Marking Method

There are several applications for titanium dioxide nanostructures, including medical, energy, and biosensing, to name a few. For biosensor applications, the use of TiO₂



FIGURE 1: Blood test samples for AB negative blood and B positive blood using glass plate.

TABLE 1: Comparison of blood test results (actual vs. reported) during 2019.

| Name of the lab | No. of blood tests in 2019 | Blood test types (actual) | | | | | | | | Blood test types (reported) | | | | | | | |
|-----------------|----------------------------|---------------------------|-----|----|-----|----|-----|-----|-----|-----------------------------|-----|----|-----|----|-----|-----|-----|
| | | O- | O+ | A- | A+ | B- | B+ | AB- | AB+ | O- | O+ | A- | A+ | B- | B+ | AB- | AB+ |
| Test lab I | 1348 | 13 | 535 | 5 | 342 | 3 | 356 | 2 | 92 | 13 | 537 | 3 | 342 | 3 | 351 | 7 | 92 |
| Test lab II | 923 | 2 | 395 | 1 | 241 | 0 | 202 | 1 | 81 | 2 | 392 | 4 | 241 | 0 | 203 | 0 | 81 |
| Test lab III | 2345 | 23 | 905 | 9 | 667 | 9 | 524 | 7 | 201 | 23 | 909 | 5 | 667 | 9 | 521 | 10 | 201 |

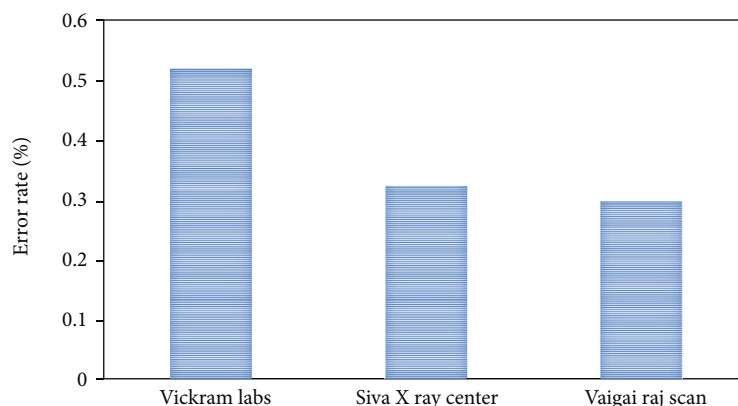


FIGURE 2: Comparison of error rate.

nanostructures has resulted in significant improvements in target detection. Titanium implants have poor contact with the surrounding tissues, and TiO_2 nanostructures are a good way to make up for this problem by making nanoporous surfaces and complex structures. Nanotechnology has produced a variety of valuable nanostructures for biotechnological purposes, the most common of which is nanosized titanium dioxide. Nanostructured TiO_2 can be used in a lot of different ways because of its low toxicity, good biocompatibility, and own properties [19].

Nanostructured TiO_2 seems to be inert and harmless when exposed to the human body. Biomedical device development will be aided by a thorough knowledge of nanoscale phenomena, which may be used to create antimicrobial surfaces, implants, and more. To better understand how TiO_2 nanoparticles are being used for biomedical purposes today, this study will concentrate on the most recent developments

in that field's utilization and the most critical aspects that impact TiO_2 's biocompatibility and the difficulties that lie ahead. Traditional disinfection techniques are not as successful as photocatalytic procedures. Therefore, TiO_2 -coated surfaces with antibacterial qualities might be used in the healthcare business. Because TiO_2 -coated catheters are safe and have the potential for light disinfection for clinical usage, they are another interesting use of TiO_2 in biomedicine [20].

During a blood type test, three drops of red blood cells are taken at different points on a piece of glass. The three antigens (A, B, and anti-D) will be added separately with the samples taken and observed. The antigen combined with blood cells reacts and turns into agglutination; otherwise, it remains the same. Blood types are classified according to this. Hundreds of samples of such blood types in laboratories are handled at one time, and laboratory

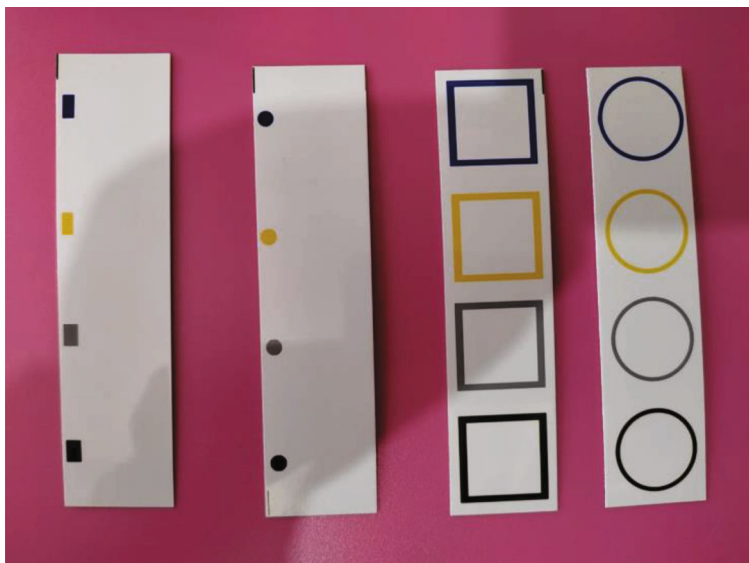


FIGURE 3: Nanocoated polymer-based sample paper with colour code marking.

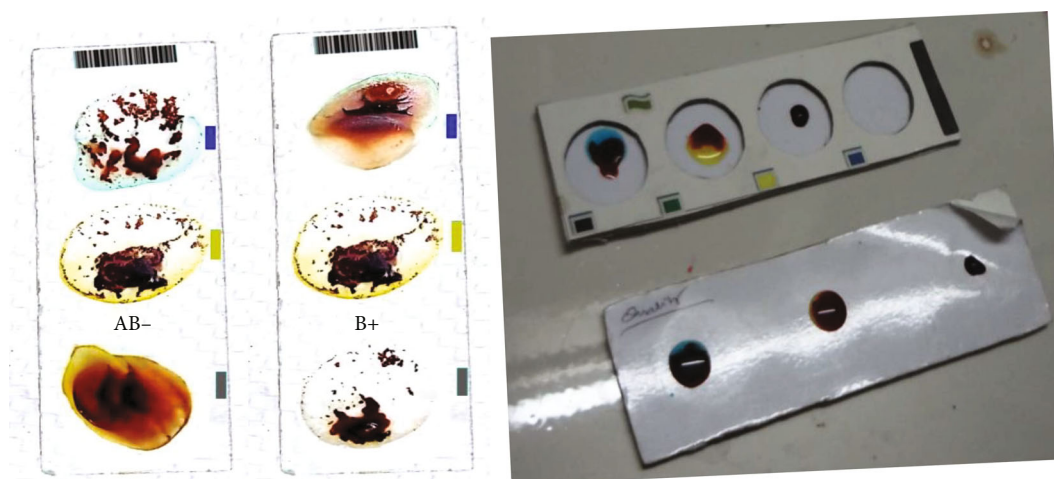


FIGURE 4: Blood samples on nanocoated polymer paper with bar code.

assistants are more likely to place the plates in an upside down position when handling them. It will become erroneous when deciding the tests of the samples thus placed [21].

A new colour-coding system has been introduced to eliminate such mistakes. That is, colour coding similar to the colours of the antigens is attached to the side of the nanocoated paper, as shown in Figure 3. This allows laboratory assistants to insert the exemplary antigens in the right place during the test to correctly record the results. A bar code is attached to the top of the blood sample polymer paper as shown in Figure 4.

Tests were performed at all three centers again for a period of six months by attaching colour coding to a microplate that can be used for blood type. The results of this test are shown in Table 2.

Many researchers [22–26] tried the sampling through paper-based biological tests and succeeded in their investiga-

tions. The blood paper slide is made of nanocoated paper with a thickness of 0.28 mm and is pasted on the card board pierced with a circular brim to prevent the blood dot from escaping sideways. The four coloured dots, as per the standard provided on the board, are to mix the blood with various antigens and to see the result. The gelatin-coated layer on the slide prevents blotting of the blood liquid. After usage, if the slide is incinerated, there are no harmful chemicals emanating through combustion, thus preventing pollution in the atmosphere. Each slide card is provided with a barcode to identify the particulars of the patient. The results show that errors are reduced with the help of the proposed colour-coding method. Blood type tests performed during the study period using the proposed colour-coding scheme proved that there were no technical errors. There is a small cost to driving the colour pieces on the microplate that can be used in a blood classification test using this method, but significant damage is avoided.

TABLE 2: Comparison of blood test results (actual vs. reported) during 2021.

| Name of the lab | No. of blood tests in 2021 | Blood test types (actual) | | | | | | | | Blood test types (reported) | | | | | | | |
|-----------------|----------------------------|---------------------------|-----|----|-----|----|-----|-----|-----|-----------------------------|-----|----|-----|----|-----|-----|-----|
| | | O- | O+ | A- | A+ | B- | B+ | AB- | AB+ | O- | O+ | A- | A+ | B- | B+ | AB- | AB+ |
| Test lab I | 533 | 9 | 207 | 5 | 138 | 4 | 127 | 1 | 42 | 9 | 207 | 5 | 138 | 4 | 127 | 1 | 42 |
| Test lab II | 412 | 3 | 169 | 2 | 111 | 1 | 103 | 1 | 22 | 3 | 169 | 2 | 111 | 1 | 103 | 1 | 22 |
| Test lab III | 1107 | 2 | 416 | 1 | 321 | 2 | 287 | 1 | 77 | 2 | 416 | 1 | 321 | 2 | 287 | 1 | 77 |

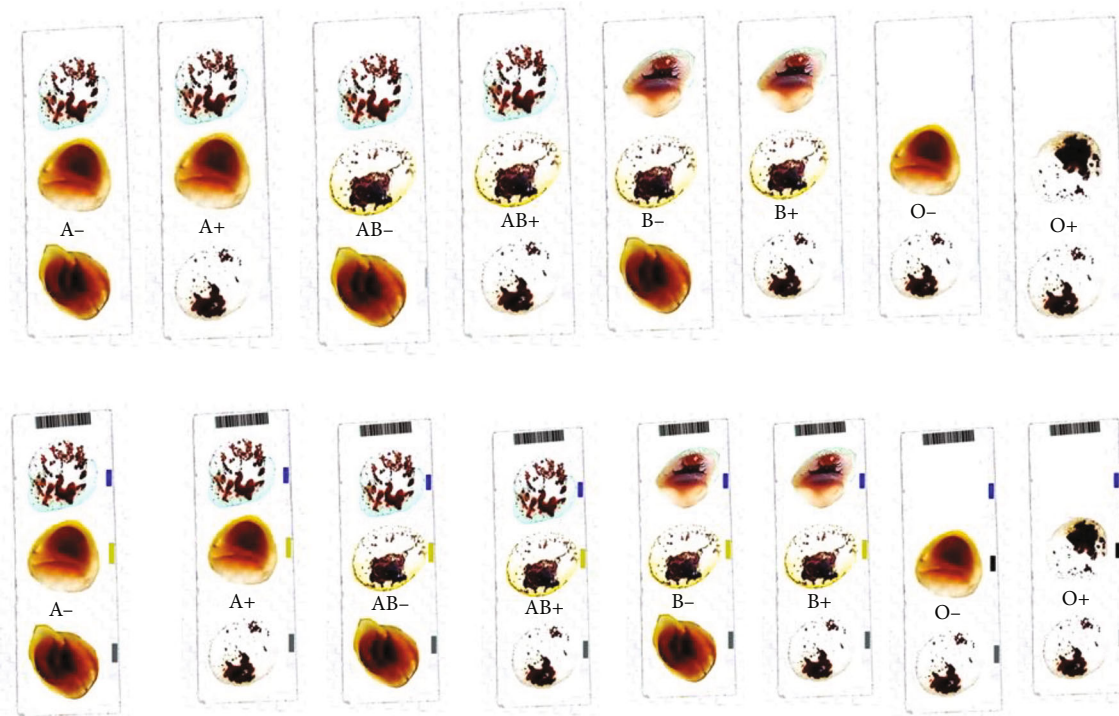


FIGURE 5: Blood group identification on nanocoated paper.

When supporting materials have adhered to a polymer paper sheet, nano-TiO₂ may be utilized as a retention agent to keep them in place. Concerning the retention agent, there are two possible mechanisms: coating with a nano-TiO₂ suspension on the sheet surface and wet end addition, in which nano-TiO₂ is deposited onto individual fibers prior to sheet formation, resulting in an even distribution of TiO₂ loading throughout the sheet [27]. For example, when nano-TiO₂ was combined with hexadecanoic acid, the surface characteristics of the combination revealed a significant improvement in wetting and dispersion. The polymer paper containing nano-TiO₂ showed a greater dynamic elastic modulus than the empty papers. There is a new way to make high-tech polymer paper with a superhydrophobic surface made by adding modified nano-TiO₂ to cellulosic fibers [28].

The absence of an evident agglomeration phenomenon between the coated particles suggests that the TiO₂ particles may be effectively coated on the blood sample polymer paper when the blood sample papering process was used. In this case, irregular morphologies of the coated TiO₂ particles might explain the uneven surface structure of the produced paper. The results of the blood being deposited on the surfaces of both uncoated blood sample paper and

TiO₂-coated polymer paper (Figure 5) for the creation of spots are remarkable in that a substantial difference was noticed between the top and rear surfaces of both paper substrates [29]. The blood sample paper demonstrated that the applied bovine blood penetrated consistently through the paper substrate. The diameters of the spots on the top and rear sides showed a similar value. The minimal variation between them reveals that the colour of the backside of the paper substrate inside the spot region was somewhat darker than the colour of the top surface. As shown in Figure 6, when blood was deposited on TiO₂-coated polymer paper, the blood sample was utterly blocked on the top side of the paper substrate, and there was no prominent blood sample visible on the backside of the paper substrate, which is in contrast to the performance of the commercially available polystyrene base paper [30].

To our understanding, the surface characteristics of the one-sided TiO₂-coated polymer paper might be responsible for this event. After the blood sample was placed on the coated paper, it would interact directly with the TiO₂ particles coated on the top side of the blood sample paper's cellulose fibers, therefore enhancing the experiment's effectiveness. This may be advantageous for the analysis of target

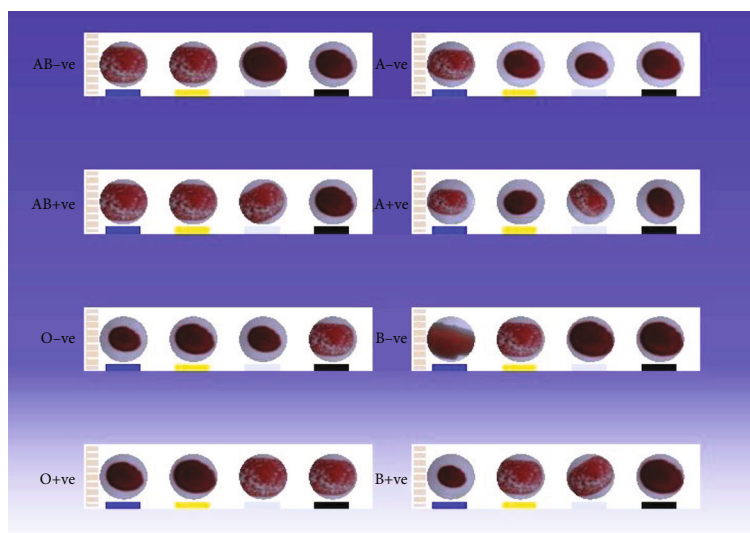


FIGURE 6: Blood identification on nanocoated paper [21].

chemicals in spots because of the high capacity of the coated TiO_2 particles, which adsorb blood onto the surfaces of these particles and make it difficult for the blood to pass through the paper substrate on the other side [31]. At the same time, higher concentrations of blood samples between the edge and the center of the spot were observed from the photographic image of the spot on the TiO_2 -coated polymer paper, which could be an issue when a subpunching strategy is used. A nonwhole spot is analyzed due to the nonuniform distribution of blood samples on the TiO_2 -coated polymer paper.

4.1. Environmental Impact of Bioclinical Waste. Bioclinical waste is a significant source of hazardous biomedical waste creation globally. The development and disposal of medical waste is an essential consideration, particularly in nations with poor hygiene and a large population. Medical facilities, such as hospitals, clinics, and other locations where diagnosis and treatment are provided, create hazardous trash and put individuals at risk of contracting life-threatening infections. Policies should be developed to prevent the spread of infectious diseases by specifying how waste should be handled throughout the stages of creation, segregation, collection, storage, transportation, and treatment. It is necessary to raise awareness at all levels of society, using various communication and educational tools, to reduce the likelihood of the health dangers spreading. Healthcare waste includes potentially hazardous bacteria that can potentially infect hospital patients, healthcare employees, and members of the public at large [32–34].

The most common issues associated with healthcare waste are a lack of awareness of the health risks associated with waste generated during medical procedures, insufficient training in proper waste management, a lack of waste management and disposal systems, a lack of financial and human resources, and a lack of priority given to the issue of waste generated during medical procedures. Many nations either do not have enough rules or do not enforce those that exist [35–38].

Safe and sustainable management of biological waste is the social and legal duty of everyone who participates in, supports, or provides financial support for healthcare operations. Effective biomedical waste management is essential for the health of individuals and the preservation of the environment. The blood sample paper is biodegradable. Biodegradation of biomedical waste is a more efficient and cost-effective procedure than any other traditional method of biowaste disposal. It is also more environmentally friendly [39, 40].

5. Conclusion

It is the social and legal responsibility of everyone involved in, supporting, or giving financial support for healthcare activities to ensure the safe and sustainable treatment of biomedical waste. This blood type test is essential today as the population increases and diseases are also on the rise. Especially in this pandemic period, many people around the world have been subjected to this blood type test. It is challenging to do many tests manually, so mistakes are severe. Laboratory assistants were employed over time in hospitals, in many laboratories, and in many places. From the study, it is proved that this novel attempt prevents complications during the blood test. Moreover, this system provides an accurate result, saves time, and slightly increases the cost. The next step in this endeavour is to test this nanocoated polymer paper with the help of a computer system. Also, by fitting the barcode on this polymer paper, the details about the patient can be known accurately. Nanocoated blood sample polymer papers avoid clerical errors that may occur during blood tests and save valuable human lives. This polymer-based paper also helps to preserve the environment by replacing glass slides as biomedical waste.

Data Availability

The data used to support the findings of this study are included in the article. Should further data or information

be required, these are available from the corresponding author upon request.

Disclosure

This study was performed as a part of the Employment Hawassa University, Ethiopia.

Conflicts of Interest

The authors declare that there are no conflicts of interest regarding the publication of this paper.

Acknowledgments

The authors would like to thank the Sathyabama Institute of Science and Technology for their excellent support for the submission of their papers.

References

- [1] R. K. Jha, P. K. Jha, K. Chaudhury, S. V. Rana, and S. K. Guha, "An emerging interface between life science and nanotechnology: present status and prospects of reproductive healthcare aided by nano-biotechnology," *Nano Reviews*, vol. 5, no. 1, p. 22762, 2014.
- [2] Z. Xu and X. Jiang, "Rapid fabrication of TiO₂ coatings with nanoporous composite structure and evaluation of application in artificial implants," *Surface and Coating Technology*, vol. 381, article 125094, 2020.
- [3] B. A. Friedman, H. A. Oberman, A. R. Chadwick, and K. I. Kingon, "The maximum surgical blood order schedule and surgical blood use in the United States," *Transfusion*, vol. 16, no. 4, pp. 380–387, 1976.
- [4] A. A. Milne, A. Gray, J. Clarke, and W. G. Murphy, "Surgical blood-ordering schedules for elective aortic aneurysm repair," *British Journal of Surgery*, vol. 84, no. 3, pp. 331–332, 1997.
- [5] D. Voak, J. A. F. Napier, F. E. Boulton et al., "Guidelines for implementation of a maximum surgical blood order schedule," *Clinical and Laboratory Haematology*, vol. 12, no. 3, pp. 321–327, 1990.
- [6] A. Gower, A. I. Hussein, P. J. Briggs, and M. S. Dewar, "Blood utilization in hip and knee arthroplasty: a cost-minimization study," *Journal of the Royal College of Surgeons of Edinburgh*, vol. 43, no. 6, pp. 397–399, 1998.
- [7] J. F. Chapman, K. Forman, P. Kelsey et al., "Guidelines for pre-transfusion compatibility procedures in blood transfusion laboratories," *Transfusion Medicine*, vol. 6, no. 3, pp. 273–283, 1996.
- [8] C. Milkins, J. Berryman, C. Cantwell et al., "Guidelines for pre-transfusion compatibility procedures in blood transfusion laboratories," *Transfusion Medicine*, vol. 23, no. 1, pp. 3–35, 2013.
- [9] O. Arslan, "Electronic crossmatching," *Transfusion Medicine Reviews*, vol. 20, no. 1, pp. 75–79, 2006.
- [10] J. F. Chapman, C. Milkins, and D. Voak, "The computer cross-match: a safe alternative to the serological cross-match," *Transfusion Medicine*, vol. 10, no. 4, pp. 251–256, 2000.
- [11] D. J. Triulzi, "Indirect and Direct Antiglobulin (Coombs) Testing and the Crossmatch," in *Transfusion medicine update*, Institute for Transfusion Medicine, 2000.
- [12] B. Jaffray, P. M. King, M. M. Basheer, and J. Gillon, "Efficiency of blood use and prospects for autologous transfusion in general surgery," *Annals of the Royal College of Surgeons of England*, vol. 73, no. 4, pp. 235–238, 1991.
- [13] E. C. Vamvakas and M. A. Blajchman, "Deleterious clinical effects of transfusion-associated immunomodulation: fact or fiction?," *Blood*, vol. 97, no. 5, pp. 1180–1195, 2001.
- [14] C. Rouault and J. Gruenhagen, "Reorganization of blood ordering practices," *Transfusion*, vol. 18, no. 4, pp. 448–453, 1978.
- [15] A. M. Fordyce, M. R. Telfer, and L. F. Stassen, "Cross-matched blood for major head and neck surgery: an analysis of requirements," *British Journal of Oral and Maxillofacial Surgery*, vol. 36, no. 2, pp. 103–106, 1998.
- [16] K. Z. Sivardeen, S. S. Kaleel, P. Weaver, and P. Chandran, "Total hip arthroplasty: to cross-match or not to cross-match an evidence-based, cost-effective and safe protocol," *European Journal of Orthopaedic Surgery & Traumatology*, vol. 18, no. 2, pp. 107–109, 2008.
- [17] D. P. Sarma, "Use of blood in elective surgery," *Journal of the American Medical Association*, vol. 243, no. 15, pp. 1536–1538, 1980.
- [18] J. A. Napier, A. H. Biffin, and D. Lay, "Efficiency of use of blood for surgery in south and mid Wales," *British Medical Journal*, vol. 291, no. 6498, pp. 799–801, 1985.
- [19] S. Khelge, V. Kumar, V. Shetty, and J. Kumaraswamy, "Effect of reinforcement particles on the mechanical and wear properties of aluminium alloy composites," *Materials Today: Proceedings*, vol. 52, pp. 571–576, 2022.
- [20] H. J. Shahshahani and A. Hayati, "Blood group discrepancies at a regional blood center," *International Journal of Hematology-Oncology and Stem Cell Research*, vol. 14, no. 1, pp. 38–44, 2020.
- [21] D. V. Bavykin, J. M. Friedrich, and F. C. Walsh, "Protonated titanates and TiO₂ nanostructured materials: synthesis, properties, and applications," *Advanced Materials*, vol. 18, no. 21, pp. 2807–2824, 2006.
- [22] P. Jayakumar, P. Sambandam, S. Kannan, Y. Kumar, and M. Sujith, "Identification and analysis of blood group with digital microscope using image processing," in *IOP Conference Series Materials Science and Engineering*, p. 12013, Chennai, India, 2020.
- [23] Y. Hao, P.-Y. Chiu, and C.-F. Chen, "Paper-based analytical devices for point-of-care blood tests," *Biomicrofluidics*, vol. 15, no. 4, article 041303, 2021.
- [24] L. Syedmoradi and F. A. Gomez, "Paper-based point-of-care testing in disease diagnostics," *Bioanalysis*, vol. 9, no. 11, pp. 841–843, 2017.
- [25] W.-C. Tai, Y.-C. Chang, D. Chou, and F. Lung-Ming, "Lab-on-paper devices for diagnosis of human diseases using urine samples—a review," *Biosensors*, vol. 11, no. 8, p. 260, 2021.
- [26] N. Grüner, O. Stambouli, and R. S. Ross, "Dried blood spots—preparing and processing for use in immunoassays and in molecular techniques," *Journal of Vision*, vol. 97, no. 97, article e52619, 2015.
- [27] J. Kumaraswamy, V. Kumar, and G. Purushotham, "Thermal analysis of nickel alloy/Al₂O₃/TiO₂ hybrid metal matrix composite in automotive engine exhaust valve using FEA method," *Journal of Thermal Engineering*, vol. 7, no. 3, pp. 415–428, 2021.

- [28] I. Chauhan, S. Chattopadhyay, and P. Mohanty, "Fabrication of titania nanowires incorporated paper sheets and study of their optical properties," *Materials Express*, vol. 3, no. 4, pp. 343–349, 2013.
- [29] R. H. Tang, H. Yang, J. R. Choi et al., "Advances in paper-based sample pretreatment for point-of-care testing," *Critical Reviews in Biotechnology*, vol. 37, no. 4, pp. 411–428, 2017.
- [30] R. Garimella and A. E. Eltorai, "Nanotechnology in orthopedics," *Journal of Orthopaedics*, vol. 14, no. 1, pp. 30–33, 2017.
- [31] S. Baskar, M. Chandrasekaran, T. Vinod Kumar, P. Vivek, and L. Karikalan, "Experimental studies on convective heat transfer coefficient of water/ethylene glycol-carbon nanotube nanofluids," *International Journal of Ambient Energy*, vol. 41, no. 3, pp. 296–299, 2020.
- [32] V. Shetty, B. Shabari Shedthi, and J. Kumaraswamy, "Predicting the thermodynamic stability of perovskite oxides using multiple machine learning techniques," *Materials Today: Proceedings*, pp. 1–7, 2022.
- [33] H. Hashemzadeh, A. Allahverdi, M. Ghorbani et al., "Gold nanowires/fibrin nanostructure as microfluidics platforms for enhancing stemcell differentiation: bio-AFM study," *Micro-machines*, vol. 11, no. 1, p. 50, 2020.
- [34] L. Sha and H. Zhao, "Preparation and properties of nano-TiO₂ photocatalytic silk respirator paper," *Fibers and Polymers*, vol. 13, no. 9, pp. 1159–1164, 2012.
- [35] S. Jafari, B. Mahyad, H. Hashemzadeh, S. Janfaza, T. Gholikhani, and L. Tayebi, "Biomedical applications of TiO₂ nanostructures: recent advances," *International Journal of Nanomedicine*, vol. 15, pp. 3447–3470, 2020.
- [36] S. Baskar and L. Karikalan, "Thermo-physical properties of Al₂O₃ and preparation technique," in *Advances in Industrial Automation and Smart Manufacturing, Lecture Notes in Mechanical Engineering*, Springer Singapore, 2020.
- [37] K. K. Padmanabhan and D. Barik, "Health hazards of medical waste and its disposal," in *Energy from Toxic Organic Waste for Heat and Power Generation*, Woodhead Publishing, 2019.
- [38] L. F. Diaz, G. M. Savage, and L. L. Eggerth, "Alternatives for the treatment and disposal of healthcare wastes in developing countries," *Waste Management*, vol. 25, no. 6, pp. 626–637, 2005.
- [39] E. Sannyasi, R. K. Gopal, D. K. Gunasekar, and P. P. Raj, "Biodegradation of low-density polyethylene (LDPE) sheet by microalga," *Scientific Reports*, vol. 11, no. 1, p. 17233, 2021.
- [40] M. Area and H. Cheradame, "Paper aging and degradation: recent findings and research methods," *BioResources*, vol. 6, pp. 5307–5337, 2011.

Research Article

Estimation of Entropy for Log-Logistic Distribution under Progressive Type II Censoring

M. Shrahili ¹, Ahmed R. El-Saeed,² Amal S. Hassan,³ Ibrahim Elbatal ⁴,
and Mohammed Elgarhy ⁵

¹Department of Statistics and Operations Research, College of Science, King Saud University, P. O. Box 2455 Riyadh 11451, Saudi Arabia

²Department of Basic Sciences, Obour High Institute for Management & Informatics, Egypt

³Faculty of Graduate Studies for Statistical Research, Cairo University, Giza 12613, Egypt

⁴Department of Mathematics and Statistics,

College of Science Imam Mohammad Ibn Saud Islamic University (IMSIU), Saudi Arabia

⁵The Higher Institute of Commercial Sciences, Al Mahalla Al Kubra, Algarbia 31951, Egypt

Correspondence should be addressed to Ibrahim Elbatal; iielbatal@imamu.edu.sa and Mohammed Elgarhy; m_elgarhy85@sva.edu.eg

Received 7 January 2022; Revised 3 March 2022; Accepted 8 March 2022; Published 23 March 2022

Academic Editor: V. Vijayan

Copyright © 2022 M. Shrahili et al. This is an open access article distributed under the Creative Commons Attribution License, which permits unrestricted use, distribution, and reproduction in any medium, provided the original work is properly cited.

Entropy is a useful indicator of information content that has been used in a number of applications. The Log-Logistic (LL) distribution is a probability distribution that is often employed in survival analysis. This paper addresses the problem of estimating multiple entropy metrics for an LL distribution using progressive type II censoring. We derive formulas for six different types of entropy measurements. To obtain the estimators of the proposed entropy measures, the maximum likelihood approach is applied. Approximate confidence intervals are calculated for the entropy metrics under discussion. A numerical evaluation is performed using various censoring methods and sample sizes to characterize the behavior of estimator's measures using relative biases, related mean squared errors, average interval lengths, and coverage probabilities. Numerical analysis revealed that the accuracy measures improve with sample size, and the suggested entropy estimates approach the genuine values as censoring levels decrease. Finally, an actual dataset was evaluated for demonstration purposes.

1. Introduction

Over the last few decades, log-logistic (or Fisk) distribution (LLD) has been frequently employed, notably in the areas of survival and reliability. The LLD is a popular alternative to the log-normal distribution because it has a failure rate function that grows with time, peaks after a certain period, and then gradually reduces [1]. Unlike the log-normal, the cumulative distribution function (CDF) of LLD has a closed form. For some parameter values, this distribution can have a monotonically declining failure rate function. In economics, the LLD is used to simulate wealth and income [2], while

in hydrology, the LLD is used to describe stream flow data [3]. For additional details on the significance and applications of a LLD, see Bennett [4], Ahmad et al. [5], and Robson and Reed [6].

A random variable (\mathbf{RVr}) X is said to have a LLD with the scale parameter α and the shape parameter β if its CDF is provided via

$$F(y) = \left(1 + \left(\frac{y}{\alpha}\right)^{-\beta}\right)^{-1}, y > 0, \alpha, \beta > 0. \quad (1)$$

TABLE 1: Removal patterns of units in numerous censoring schemes.

| (n, m) | Censoring schemes | | |
|----------|-------------------------------|-------------|-----------------|
| | Scheme I | Scheme II | Scheme III |
| (60,10) | $(0^{*9}, 50)$ | (5^{*10}) | $(50, 0^{*9})$ |
| (60,20) | $(0^{*19}, 40)$ | (2^{*20}) | $(40, 0^{*19})$ |
| (60,30) | $(0^{*29}, 30)$ | (1^{*30}) | $(30, 0^{*29})$ |
| (60,60) | Complete sample (0*60) | | |

For contrast, $(1*5, 0)$ denotes that the censoring scheme used is $(1, 1, 1, 1, 1, 0)$.

The probability density function (PDF) corresponding to (1) is then provided via

$$f(y) = \frac{\beta}{\alpha^\beta} y^{\beta-1} \left(1 + \left(\frac{y}{\alpha} \right)^\beta \right)^{-2}, \quad y > 0, \alpha, \beta > 0. \quad (2)$$

The hazard function of the LLD is either decreasing or inverted bath-tub, and the PDF is either reversed J shaped or unimodal, see Johnson et al. [7].

In reliability studies, researchers want to see how long it takes for units to fail. However, due to time and expense restrictions, as well as a variety of other factors, experimenters are unable to track the lifetime of all units. As a result, filtered data is available. The most frequent types are type I and type II. In the statistical literature, popular censoring techniques are explored. However, in medical/engineering survival analysis, units may be removed at intermediate phases for a variety of causes beyond the experimenter's control. In this case, progressive censoring (PC) system is an acceptable censoring strategy since it permits surviving items to be removed before the test ends. PC has the benefit of quickly terminating the test and including at least some extreme life periods in the sample data. Progressive type I censoring (PTIC) happens when the number of survivors reduces to predefined levels, whereas progressive type II (PT2C) occurs when the number of survivors drops to specified levels.

The following is how a PT2C sample is carried out: A life testing experiment with n units and the PC method $r_i, i = 1, 2, \dots, m$ is used. Units are randomly eliminated from the remaining $n - 1$ surviving units at the moment of the first failure y_1 . Similarly, units from the remaining $n - 2 - r_1$ units are randomly eliminated after the second failure y_2 . The test continues until the m^{th} failure occurs, at which point all remaining $n - m - r_1 - r_2 - \dots - r_{m-1}$ units are removed. The number of failures m as well as the progressive censoring design r_1, r_2, \dots, r_m is preset and fixed. Let $Y_{(1)} \leq Y_{(2)} \leq \dots \leq Y_{(m)}$ denote such a PT2C sample with (r_1, \dots, r_m) being the PC scheme. Balakrishnan and Aggrawala [8] provided some historical remarks and a good summary of progressive censoring. It really should be observed that this censorship is limited to the classical type II censoring (T2C) when $r_1 = r_2 = \dots = r_{m-1} = 0$ and $r_m = n - m$; further, it reduces to a complete sample having no censoring for $m = n$ and $r_i = 0, i = 1, 2, \dots, n$.

In information theory, entropy is a measure of uncertainty in a RVr that gauges the anticipated value of the information embodied in that RVr. Entropies are motivated by how receiving new information decreases uncertainty. Shannon's entropy is one of the earliest and most commonly used measurements of entropy. In the study of communication systems, this measure has proven to be effective. Let Y be a non-negative RVr with a continuous CDF; the formal measure of Shannon's entropy is characterized by:

$$S = - \int_{-\infty}^{\infty} f(y) \log(f(y)) dy. \quad (3)$$

One of the most significant disadvantages of Shannon's measure is that it may be negative for particular probability distributions, making it useless as a measure of uncertainty. Rényi [9] developed a new generalized entropy by studying the concepts of uncertainty and randomness. The Rényi entropy ($R\acute{e}$) is calculated as follows:

$$R_\gamma = (1-\gamma)^{-1} \log \left\{ \int_{-\infty}^{\infty} f(y)^\gamma dy \right\}, \quad \gamma > 0 \text{ and } \gamma \neq 1, \quad (4)$$

where the constant γ is conditional, leading to a positive entropy. Different generalizations of entropy were proposed by Havrda and Charvat [10], Arimoto [11], Awad et al. [12], and Tsallis [13].

Havrda and Charvat's (HC) entropy suggested extension of (3). This extension is called HC entropy of degree γ and is characterized with

$$HC_\gamma = \frac{1}{2^{1-\gamma}-1} \left[\int_{-\infty}^{\infty} f(y)^\gamma dy - 1 \right]. \quad (5)$$

Arimoto's (Ar) entropy measure (see [11]) is characterized with

$$A_\gamma = \frac{\gamma}{1-\gamma} \left[\left(\int_{-\infty}^{\infty} f(y)^\gamma dy \right)^{\frac{1}{\gamma}} - 1 \right]. \quad (6)$$

Awad et al. [12] suggested two types of entropy: an extension of Rényi entropy and Havrda and Charvat entropy. The first extension, denoted by $A1_\gamma$, and the second extension, denoted by $A2_\gamma$, are characterized with

$$A1_\gamma = \frac{1}{\gamma-1} \log \left[\int_{-\infty}^{\infty} \frac{f(y)^\gamma}{v} dy \right], \quad v = \left[\sup_{0 < y < \infty} f(y) \right]^{1-\gamma}, \quad (7)$$

$$A2_\gamma = \frac{1}{2^{1-\gamma}-1} \left[\left\{ \int_{-\infty}^{\infty} \frac{f(y)^\gamma}{v} dy \right\} - 1 \right]. \quad (8)$$

TABLE 2

(a) Rbias, MSE, AIL, and CP of different entropy estimates under PT2C schemes at $\gamma = 0.5$, and $(n, m) = (60, 10)$

| Scheme | | Entropy methods | | | | | |
|--------|--------------------|-----------------|---------------|---------------|---------------|---------------|----------------|
| | | R_γ | HC_γ | A_γ | T_γ | $A1_\gamma$ | $A2_\gamma$ |
| | Exact value | 2.2690 | 5.0930 | 8.6696 | 4.2192 | 1.1987 | -1.0884 |
| I | Estimate | 1.7878 | 4.3804 | 9.4136 | 3.6289 | 1.9795 | -1.2832 |
| | Rbias | 0.2121 | 0.1399 | 0.0858 | 0.1399 | 0.6514 | 0.1790 |
| | MSE | 1.3496 | 15.0356 | 166.7630 | 10.3188 | 2.5768 | 0.6486 |
| | AIL | 4.1469 | 14.9484 | 50.5619 | 12.3837 | 5.5007 | 3.0647 |
| | CP (%) | 95.20 | 94.60 | 94.70 | 94.60 | 95.90 | 94.00 |
| II | Estimate | 1.9068 | 4.4836 | 8.8110 | 3.7143 | 1.7539 | -1.2101 |
| | Rbias | 0.1596 | 0.1197 | 0.0163 | 0.1197 | 0.4632 | 0.1118 |
| | MSE | 0.9131 | 9.9744 | 87.5434 | 6.8453 | 1.8282 | 0.5637 |
| | AIL | 3.4680 | 12.1534 | 36.6908 | 10.0682 | 4.8351 | 2.9056 |
| | CP (%) | 95.30 | 94.50 | 94.40 | 94.50 | 95.60 | 94.40 |
| III | Estimate | 2.1477 | 5.0985 | 9.9041 | 4.2237 | 1.3879 | -1.0378 |
| | Rbias | 0.0535 | 0.0011 | 0.1424 | 0.0011 | 0.1578 | 0.0465 |
| | MSE | 0.5120 | 7.1138 | 67.2224 | 4.8822 | 1.1105 | 0.5405 |
| | AIL | 2.7655 | 10.4604 | 31.7887 | 8.6656 | 4.0658 | 2.8765 |
| | CP (%) | 95.90 | 95.60 | 94.90 | 95.60 | 95.10 | 95.70 |

(b) Rbias, MSE, AIL, and CP of different entropy estimates under PT2C schemes at $\gamma = 0.5$, and $(n, m) = (60, 20)$

| Scheme | | Entropy methods | | | | | |
|--------|--------------------|-----------------|---------------|---------------|---------------|---------------|----------------|
| | | R_γ | HC_γ | A_γ | T_γ | $A1_\gamma$ | $A2_\gamma$ |
| | Exact value | 2.2690 | 5.0930 | 8.6696 | 4.2192 | 1.1987 | -1.0884 |
| I | Estimate | 2.0413 | 4.6608 | 8.5353 | 3.8612 | 1.5384 | -1.1417 |
| | Rbias | 0.1004 | 0.0849 | 0.0155 | 0.0849 | 0.2834 | 0.0490 |
| | MSE | 0.4951 | 5.7061 | 42.4241 | 3.9160 | 1.1759 | 0.4370 |
| | AIL | 2.6111 | 9.2138 | 25.5393 | 7.6329 | 4.0389 | 2.5840 |
| | CP (%) | 95.70 | 96.30 | 95.00 | 96.30 | 95.40 | 95.70 |
| II | Estimate | 2.1097 | 4.8192 | 8.7517 | 3.9923 | 1.4324 | -1.1062 |
| | Rbias | 0.0702 | 0.0538 | 0.0095 | 0.0538 | 0.1950 | 0.0164 |
| | MSE | 0.3686 | 4.5905 | 35.1121 | 3.1504 | 0.8884 | 0.3822 |
| | AIL | 2.2978 | 8.3339 | 23.2371 | 6.9040 | 3.5810 | 2.4236 |
| | CP (%) | 95.40 | 95.70 | 95.50 | 95.70 | 95.40 | 95.50 |
| III | Estimate | 2.1680 | 4.9539 | 8.9216 | 4.1039 | 1.3719 | -1.0937 |
| | Rbias | 0.0445 | 0.0273 | 0.0291 | 0.0273 | 0.1445 | 0.0049 |
| | MSE | 0.2644 | 3.5581 | 27.6580 | 2.4419 | 0.6971 | 0.3048 |
| | AIL | 1.9773 | 7.3776 | 20.6019 | 6.1118 | 3.2033 | 2.1650 |
| | CP (%) | 95.60 | 96.20 | 95.30 | 96.20 | 95.70 | 96.30 |

(c) Rbias, MSE, AIL, and CP of different Entropy estimates under PT2C schemes at $\gamma = 0.5$, and $(n, m) = (60, 30)$

| Scheme | | Entropy methods | | | | | |
|--------|--------------------|-----------------|---------------|---------------|---------------|---------------|----------------|
| | | R_γ | HC_γ | A_γ | T_γ | $A1_\gamma$ | $A2_\gamma$ |
| | Exact value | 2.2690 | 5.0930 | 8.6696 | 4.2192 | 1.1987 | -1.0884 |
| I | Estimate | 2.1433 | 4.8692 | 8.6973 | 4.0338 | 1.3889 | -1.0901 |
| | Rbias | 0.0554 | 0.0439 | 0.0032 | 0.0439 | 0.1587 | 0.0016 |

TABLE 2: Continued.

| Scheme | | Entropy methods | | | | | |
|--------|----------|-----------------|-------------|------------|------------|-------------|-------------|
| | | R_γ | HC_γ | A_γ | T_γ | $A1_\gamma$ | $A2_\gamma$ |
| | MSE | 0.2798 | 3.5222 | 25.7945 | 2.4172 | 0.7902 | 0.3600 |
| | AIL | 2.0151 | 7.3078 | 19.9183 | 6.0540 | 3.4055 | 2.3530 |
| | CP (%) | 95.30 | 95.50 | 95.10 | 95.50 | 94.99 | 95.89 |
| II | Estimate | 2.1675 | 4.9167 | 8.7186 | 4.0732 | 1.3572 | -1.0943 |
| | Rbias | 0.0447 | 0.0346 | 0.0057 | 0.0346 | 0.1322 | 0.0054 |
| | MSE | 0.2291 | 2.9321 | 21.1112 | 2.0123 | 0.6348 | 0.2711 |
| | AIL | 1.8345 | 6.6799 | 18.0189 | 5.5338 | 3.0622 | 2.0417 |
| | CP (%) | 95.40 | 95.40 | 95.40 | 95.40 | 94.40 | 95.40 |
| | Estimate | 2.2079 | 5.0444 | 9.0077 | 4.1789 | 1.2861 | -1.0521 |
| III | Rbias | 0.0269 | 0.0095 | 0.0390 | 0.0095 | 0.0729 | 0.0334 |
| | MSE | 0.1969 | 2.7007 | 20.2460 | 1.8535 | 0.5708 | 0.2822 |
| | AIL | 1.7238 | 6.4423 | 17.5969 | 5.3370 | 2.9431 | 2.0787 |
| | CP (%) | 94.90 | 94.80 | 94.50 | 94.80 | 94.90 | 95.10 |
| | Estimate | 2.2079 | 5.0444 | 9.0077 | 4.1789 | 1.2861 | -1.0521 |
| | Rbias | 0.0269 | 0.0095 | 0.0390 | 0.0095 | 0.0729 | 0.0334 |

Tsallis [13] generalized Shanon's entropy and defined the measure as

$$T_\gamma = \frac{1}{\gamma - 1} \left[1 - \int_{-\infty}^{\infty} f(y)^\gamma dy \right]. \quad (9)$$

Many researchers have worked on entropy estimates for various life distributions. Cramer and Bagh [14] used progressive censoring to investigate entropy in the Weibull distribution. Kang et al. [15] used doubly type II censored data to construct entropy estimators for a double exponential distribution. Using record values from the generalized half-logistic distribution, Seo et al. [16] calculated an entropy estimate. Cho et al. [17] addressed entropy estimates for Rayleigh distribution using doubly generalized type II hybrid censoring. Cho et al. [18] used generalized type II hybrid censored samples to derive estimators for the entropy function of a Weibull distribution. Dey et al. [19] studied the loss of entropy for a truncated Rayleigh distribution using different entropy measures. Chacko and Asha [20] investigated entropy estimation in generalized exponential distribution. Bantan et al. [21] considered the entropy estimators for inverse Lomax via the multiple censored scheme. The dynamic cumulative residual Ré for the Lomax distribution was estimated using Bayesian and maximum likelihood (ML) techniques by Al-Babtain et al. [22]. Entropy estimator of Lindley was prepared by Almarashi et al. [23]. Helmy et al. [24] investigated Shannon entropy estimation of Lomax distribution using unified hybrid censored data. Bayesian and non-Bayesian estimation of the Nadarajah-Haghighi distribution using progressive Type-1 censoring scheme studied by Elbatal et al. [25].

In this paper, we are inspired to investigate six possible entropy estimators for log-logistic distributions in the presence of T2PC data. We construct analytical formulas for the entropy measurements proposed. The ML and two-sided approximate confidence intervals of several entropy

estimators are calculated. Numerical comparisons for various sample sizes are presented to identify which entropy estimator outperforms the others.

The paper is broken down into five sections. Section 2 presents expressions for the recommended entropy measures based on LLD. PT2C is used in Section 3 to give several entropy estimators as well as their estimated confidence intervals. In Section 4, numerical comparisons of different entropy estimators and data analysis are examined. Finally, in Section 5, there are some conclusions and a summary of the study.

2. Expressions of Entropy Measures

Statistical entropy measures the amount of uncertainty or variability in a RVr. The higher the value of entropy leads to more variability in the data. This section focuses on obtaining the expression for various entropy measurements of LLD.

2.1. Rényi Entropy. The Ré of LLD is obtained by replacing (1) in (3) as follows:

$$R_\gamma = (1 - \gamma)^{-1} \log \left\{ \frac{\beta^\gamma}{\alpha^{\beta\gamma}} \int_0^\infty y^{\beta\gamma-\gamma} \left(1 + \left(\frac{y}{\alpha} \right)^\beta \right)^{-2\gamma} dy \right\}. \quad (10)$$

Write $I = \beta^\gamma / \alpha^{\beta\gamma} \int_0^\infty y^{\beta\gamma-\gamma} (1 + (y/\alpha)^\beta)^{-2\gamma} dy$, and assume that $z = (y/\alpha)^\beta$, $y = \alpha z^{1/\beta}$, $dy = (\alpha/\beta) z^{1/\beta-1} dz$, thus the integral I will be written as

$$\begin{aligned} I &= \frac{\beta^{\gamma-1}}{\alpha^{\beta\gamma-1}} \int_0^\infty \alpha^{\beta\gamma-\gamma} z^{\gamma-\frac{\gamma}{\beta}-1} (1+z)^{-2\gamma} dz \\ &= \beta^{\gamma-1} \alpha^{1-\gamma} B \left(\gamma - \frac{\gamma}{\beta} + \frac{1}{\beta}, \gamma + \frac{\gamma}{\beta} - \frac{1}{\beta} \right), \end{aligned} \quad (11)$$

TABLE 3

(a) Rbias, MSE, AIL, and CP of different Entropy estimates under PT2C schemes at $\gamma = 1.5$, and $(n, m) = (60, 10)$

| Scheme | | Entropy methods | | | | | |
|--------|--------------------|-----------------|---------------|---------------|---------------|---------------|-----------------|
| | | R_γ | HC_γ | A_γ | T_γ | $A1_\gamma$ | $A2_\gamma$ |
| | Exact value | 0.5601 | 0.8339 | 0.5109 | 0.4885 | 2.9076 | -11.1963 |
| I | Estimate | 0.3186 | 0.3469 | 0.2329 | 0.2032 | 3.3739 | -17.4037 |
| | Rbias | 0.4312 | 0.5840 | 0.5441 | 0.5840 | 0.1604 | 0.5544 |
| | MSE | 1.0201 | 1.0552 | 0.3681 | 0.3621 | 1.5820 | 16.4038 |
| | AIL | 3.8461 | 3.5471 | 2.1151 | 2.0778 | 4.5814 | 8.7875 |
| | CP (%) | 99.90 | 95.30 | 95.40 | 95.30 | 98.00 | 94.90 |
| II | Estimate | 0.3901 | 0.4935 | 0.3156 | 0.2891 | 3.2303 | -15.4706 |
| | Rbias | 0.3034 | 0.4082 | 0.3823 | 0.4082 | 0.1110 | 0.3818 |
| | MSE | 0.6745 | 0.6767 | 0.2438 | 0.2322 | 1.1372 | 9.5542 |
| | AIL | 3.1511 | 2.9370 | 1.7784 | 1.7205 | 3.9863 | 6.8951 |
| | CP (%) | 99.70 | 95.20 | 95.30 | 95.20 | 98.30 | 94.50 |
| III | Estimate | 0.4853 | 0.6819 | 0.4254 | 0.3994 | 3.0255 | -12.8624 |
| | Rbias | 0.1335 | 0.1823 | 0.1674 | 0.1823 | 0.0406 | 0.1488 |
| | MSE | 0.1656 | 0.3220 | 0.1247 | 0.1105 | 0.4050 | 3.0465 |
| | AIL | 1.5689 | 2.1440 | 1.3435 | 1.2559 | 2.4526 | 4.1274 |
| | CP (%) | 95.10 | 95.10 | 95.20 | 95.10 | 94.80 | 96.30 |

(b) Rbias, MSE, AIL, and CP of different Entropy estimates under PT2C schemes at $\gamma = 1.5$, and $(n, m) = (60, 20)$

| Scheme | | Entropy methods | | | | | |
|--------|--------------------|-----------------|---------------|---------------|---------------|---------------|-----------------|
| | | R_γ | HC_γ | A_γ | T_γ | $A1_\gamma$ | $A2_\gamma$ |
| | Exact value | 0.5601 | 0.8339 | 0.5109 | 0.4885 | 2.9076 | -11.1963 |
| I | Estimate | 0.4796 | 0.6946 | 0.4292 | 0.4069 | 3.0801 | -13.3805 |
| | Rbias | 0.1437 | 0.1671 | 0.1600 | 0.1671 | 0.0593 | 0.1951 |
| | MSE | 0.1048 | 0.2064 | 0.0801 | 0.0708 | 0.4507 | 3.6689 |
| | AIL | 1.2295 | 1.6960 | 1.0624 | 0.9935 | 2.5447 | 4.4314 |
| | CP (%) | 95.40 | 95.60 | 95.90 | 95.60 | 95.00 | 95.30 |
| II | Estimate | 0.4936 | 0.7208 | 0.4442 | 0.4223 | 3.0513 | -12.8807 |
| | Rbias | 0.1188 | 0.1356 | 0.1306 | 0.1356 | 0.0494 | 0.1505 |
| | MSE | 0.0810 | 0.1554 | 0.0609 | 0.0533 | 0.3152 | 2.3936 |
| | AIL | 1.0853 | 1.4813 | 0.9317 | 0.8677 | 2.1286 | 3.6029 |
| | CP (%) | 95.30 | 95.30 | 95.10 | 95.30 | 95.20 | 95.40 |
| III | Estimate | 0.4997 | 0.7270 | 0.4485 | 0.4259 | 3.0106 | -12.4840 |
| | Rbias | 0.1079 | 0.1282 | 0.1221 | 0.1282 | 0.0354 | 0.1150 |
| | MSE | 0.0864 | 0.1642 | 0.0645 | 0.0563 | 0.2711 | 1.9416 |
| | AIL | 1.1280 | 1.5327 | 0.9652 | 0.8978 | 2.0016 | 3.3053 |
| | CP (%) | 94.60 | 94.70 | 94.80 | 94.70 | 94.30 | 95.80 |

(c) Rbias, MSE, AIL, and CP of different entropy estimates under PT2C schemes at $\gamma = 1.5$, and $(n, m) = (60, 30)$

| Scheme | | Entropy methods | | | | | |
|--------|--------------------|-----------------|---------------|---------------|---------------|---------------|-----------------|
| | | R_γ | HC_γ | A_γ | T_γ | $A1_\gamma$ | $A2_\gamma$ |
| | Exact value | 0.5601 | 0.8339 | 0.5109 | 0.4885 | 2.9076 | -11.1963 |
| I | Estimate | 0.5081 | 0.7498 | 0.4606 | 0.4392 | 3.0397 | -12.7520 |
| | Rbias | 0.0928 | 0.1008 | 0.0985 | 0.1008 | 0.0454 | 0.1389 |

TABLE 3: Continued.

| Scheme | | Entropy methods | | | | | |
|--------|----------|-----------------|-------------|------------|------------|-------------|-------------|
| | | R_γ | HC_γ | A_γ | T_γ | $A1_\gamma$ | $A2_\gamma$ |
| | MSE | 0.0510 | 0.0944 | 0.0375 | 0.0324 | 0.2928 | 2.2382 |
| | AIL | 0.8622 | 1.1591 | 0.7337 | 0.6790 | 2.0582 | 3.5045 |
| | CP (%) | 95.20 | 95.40 | 95.40 | 95.40 | 94.90 | 96.10 |
| II | Estimate | 0.5195 | 0.7656 | 0.4704 | 0.4485 | 2.9842 | -12.1793 |
| | Rbias | 0.0725 | 0.0819 | 0.0792 | 0.0819 | 0.0263 | 0.0878 |
| | MSE | 0.0484 | 0.0873 | 0.0350 | 0.0299 | 0.2182 | 1.4672 |
| | AIL | 0.8479 | 1.1271 | 0.7163 | 0.6602 | 1.8073 | 2.9039 |
| | CP (%) | 95.60 | 96.50 | 96.10 | 96.50 | 94.60 | 95.70 |
| III | Estimate | 0.5081 | 0.7498 | 0.4606 | 0.4392 | 3.0397 | -12.7520 |
| | Rbias | 0.0928 | 0.1008 | 0.0985 | 0.1008 | 0.0454 | 0.1389 |
| | MSE | 0.0510 | 0.0944 | 0.0375 | 0.0324 | 0.2928 | 2.2382 |
| | AIL | 0.8622 | 1.1591 | 0.7337 | 0.6790 | 2.0582 | 3.5045 |
| | CP (%) | 95.20 | 95.40 | 95.40 | 95.40 | 95.00 | 96.00 |

TABLE 4: Rbias, MSE, AIL, and CP of different Entropy estimates under PT2C schemes at $\gamma = (0.5, 1.5)$, and $(n, m) = (60, 30)$.

| Scheme | | Entropy methods | | | | | |
|--------|--------------------|-----------------|---------------|---------------|---------------|---------------|-----------------|
| | | R_γ | HC_γ | A_γ | T_γ | $A1_\gamma$ | $A2_\gamma$ |
| 0.5 | Exact value | 2.2690 | 5.0930 | 8.6696 | 4.2192 | 1.1987 | -1.0884 |
| | Estimate | 2.2430 | 5.0925 | 8.9237 | 4.2188 | 1.2379 | -1.0622 |
| | Rbias | 0.0115 | 0.0001 | 0.0293 | 0.0001 | 0.0327 | 0.0240 |
| | MSE | 0.1039 | 1.4883 | 11.0349 | 1.0214 | 0.3110 | 0.1533 |
| | AIL | 1.2601 | 4.7846 | 12.9899 | 3.9637 | 2.1816 | 1.5323 |
| | CP (%) | 95.50 | 95.50 | 95.00 | 95.50 | 95.80 | 94.80 |
| 1.5 | Exact value | 0.5601 | 0.8339 | 0.5109 | 0.4885 | 2.9076 | -11.1963 |
| | Estimate | 0.5461 | 0.8069 | 0.4955 | 0.4727 | 2.9603 | -11.8045 |
| | Rbias | 0.0249 | 0.0324 | 0.0302 | 0.0324 | 0.0181 | 0.0543 |
| | MSE | 0.0277 | 0.0478 | 0.0195 | 0.0164 | 0.1186 | 0.7083 |
| | AIL | 0.6510 | 0.8507 | 0.5441 | 0.4983 | 1.3346 | 2.0323 |
| | CP (%) | 95.40 | 95.50 | 95.30 | 95.50 | 94.90 | 95.10 |

where $B(\cdot, \cdot)$ is the beta function. As a result of inserting (11) into (10), LLD's Ré entropy takes the form

$$R_\gamma = (1 - \gamma)^{-1} \log \left(\beta^{\gamma-1} \alpha^{1-\gamma} B \left(\gamma - \frac{\gamma}{\beta} + \frac{1}{\beta}, \gamma + \frac{\gamma}{\beta} - \frac{1}{\beta} \right) \right), \tag{12}$$

Hence, (12) is the necessary formulation of LLD Ré entropy.

2.2. *Havrda and Charvat Entropy.* The HC of the LLD is obtained by replacing (1) in (4) as follows:

$$HC_\gamma = \frac{1}{2^{1-\gamma} - 1} \left[\frac{\beta^\gamma}{\alpha^{\beta\gamma}} \int_0^\infty y^{\beta\gamma-\gamma} \left(1 + \left(\frac{y}{\alpha} \right)^\beta \right)^{-2\gamma} dy - 1 \right]. \tag{13}$$

As a result, we get the HC of LLD by inserting (11) in (4) as follows

$$HC_\gamma = \frac{1}{2^{1-\gamma} - 1} \left[\beta^{\gamma-1} \alpha^{1-\gamma} B \left(\gamma - \frac{\gamma}{\beta} + \frac{1}{\beta}, \gamma + \frac{\gamma}{\beta} - \frac{1}{\beta} \right) - 1 \right]. \tag{14}$$

Hence, (14) is the necessary formulation of LLD HC entropy.

2.3. *Arimoto Entropy.* The Ar entropy of LLD is obtained by replacing (1) in (5) as follows:

$$A_\gamma = \frac{\gamma}{1 - \gamma} \left[\left(\frac{\beta^\gamma}{\alpha^{\beta\gamma}} \int_0^\infty y^{\beta\gamma-\gamma} \left(1 + \left(\frac{y}{\alpha} \right)^\beta \right)^{-2\gamma} dy \right)^{\frac{1}{\gamma}} - 1 \right]. \tag{15}$$

TABLE 5: Estimates of different entropy measures under PT2C schemes for the given real data, where $\gamma = (0.5, 1.5)$, and $(n, m) = (128, 30)$.

| Scheme | $(\hat{\alpha}, \hat{\beta})$ | R_γ | HC_γ | Entropy methods | | | |
|----------------|--|------------|-------------|-----------------|------------|-------------|-------------|
| | | | | A_γ | T_γ | $A1_\gamma$ | $A2_\gamma$ |
| $\gamma = 0.5$ | | | | | | | |
| I | $\hat{\alpha} = 6.9409 \hat{\beta} = 1.4379$ | 4.6318 | 22.0524 | 101.7061 | 18.2688 | 1.3603 | -1.1913 |
| II | $\hat{\alpha} = 6.0531 \hat{\beta} = 1.6856$ | 4.2481 | 17.7813 | 68.9778 | 14.7305 | 1.9920 | -1.5225 |
| III | $\hat{\alpha} = 6.2489 \hat{\beta} = 1.5729$ | 4.3961 | 19.3326 | 80.1414 | 16.0157 | 1.7126 | -1.3888 |
| Complete | $\hat{\alpha} = 6.0962 \hat{\beta} = 1.7160$ | 4.2227 | 17.5263 | 67.2218 | 14.5193 | 2.0659 | -1.5548 |
| $\gamma = 1.5$ | | | | | | | |
| I | $\hat{\alpha} = 6.9409 \hat{\beta} = 1.4379$ | 3.2140 | 2.7297 | 1.9723 | 1.5990 | 2.7781 | -10.2809 |
| II | $\hat{\alpha} = 5.3452 \hat{\beta} = 1.6388$ | 2.8755 | 2.6034 | 1.8496 | 1.5251 | 3.1745 | -13.2824 |
| III | $\hat{\alpha} = 4.7569 \hat{\beta} = 1.6371$ | 2.7595 | 2.5550 | 1.8042 | 1.4967 | 3.1715 | -13.2575 |
| Complete | $\hat{\alpha} = 6.0962 \hat{\beta} = 1.7160$ | 2.9766 | 2.6434 | 1.8877 | 1.5484 | 3.3120 | -14.4713 |

We obtain the Ar entropy of LLD by putting (11) into (15) as follows

$$A_\gamma = \frac{\gamma}{1-\gamma} \left[\beta^{1-\frac{1}{\gamma}} \alpha^{\frac{1}{\gamma}-1} \left(B \left(\gamma - \frac{\gamma}{\beta} + \frac{1}{\beta}, \gamma + \frac{\gamma}{\beta} - \frac{1}{\beta} \right) \right)^{\frac{1}{\gamma}} - 1 \right]. \tag{16}$$

Thus, the formula for Ar entropy found in equation (16).

2.4. *A-entropies.* To get (6) and (7), we must obtain $\sup_{0 < y < \infty} f(y)$, by getting the maximum value of $f(y)$ as below:

$$y^{\beta-2} \left(1 + \left(\frac{y}{\alpha} \right)^\beta \right)^{-3} \left\{ (\beta-1) \left(1 + \left(\frac{y}{\alpha} \right)^\beta \right) - 2 \frac{\beta}{\alpha^\beta} y^\beta \right\} = 0. \tag{17}$$

After simplification, then (17) is written as follows

$$\frac{\beta+1}{\alpha^\beta} y^\beta = \beta-1, \tag{18}$$

which leads to the following

$$y = \alpha \left(\frac{\beta-1}{\beta+1} \right)^{\frac{1}{\beta}}. \tag{19}$$

Using (17), we get $\sup_{0 < y < \infty} f(y)$, as

$$\begin{aligned} \sup_{0 < y < \infty} f(y) &= \frac{\beta}{\alpha^\beta} \left\{ \alpha \left(\frac{\beta-1}{\beta+1} \right)^{\frac{1}{\beta}} \right\}^{\beta-1} \left(1 + \left(\left(\frac{\beta-1}{\beta+1} \right)^{\frac{1}{\beta}} \right)^\beta \right)^{-2} \\ &= \frac{(\beta-1)^{1-1/\beta} (\beta+1)^{1+(1/\beta)}}{4\alpha\beta}. \end{aligned} \tag{20}$$

Using (11) and (19), hence the A-entropies can be expressed as

$$A1_\gamma = \frac{1}{\gamma-1} \log \left[\left[\frac{(\beta-1)^{1-1/\beta} (\beta+1)^{1+(1/\beta)}}{4\alpha\beta} \right]^{1-\gamma} \beta^{\gamma-1} \alpha^{1-\gamma} B \left(\gamma - \frac{\gamma}{\beta} + \frac{1}{\beta}, \gamma + \frac{\gamma}{\beta} - \frac{1}{\beta} \right) \right], \tag{21}$$

$$A2_\gamma = \frac{1}{2^{1-\gamma}-1} \left\{ \left[\frac{(\beta-1)^{1-1/\beta} (\beta+1)^{1+(1/\beta)}}{4\alpha\beta} \right]^{1-\gamma} \beta^{\gamma-1} \alpha^{1-\gamma} B \left(\gamma - \frac{\gamma}{\beta} + \frac{1}{\beta}, \gamma + \frac{\gamma}{\beta} - \frac{1}{\beta} \right) \right\} - 1. \tag{22}$$

Thus, (20) and (21) provide essential expressions of A-entropy.

2.5. *Tsallis Entropy.* The Tsallis entropy of LLD is obtained by replacing (1) in (9) as follows:

$$T_\gamma = \frac{1}{\gamma-1} \left[1 - \frac{\beta^\gamma}{\alpha^{\beta\gamma}} \int_0^\infty y^{\beta\gamma-\gamma} \left(1 + \left(\frac{y}{\alpha} \right)^\beta \right)^{-2\gamma} dy \right]. \tag{23}$$

Thus, using (11) in (23), then the Tsallis entropy of LLD is obtained as follows

$$T_\gamma = \frac{1}{\gamma-1} \left[1 - \beta^{\gamma-1} \alpha^{1-\gamma} B \left(\gamma - \frac{\gamma}{\beta} + \frac{1}{\beta}, \gamma + \frac{\gamma}{\beta} - \frac{1}{\beta} \right) \right]. \tag{24}$$

Thus, the formula of Tsallis entropy of LLD is provided in equation (24).

3. Estimation of Different Entropies

Using the ML method and T2PC data, we get estimators for the various entropies metrics provided in the preceding section. To construct entropies estimators, we start with the ML estimator of population parameters. The invariance property of ML estimators may then be used to determine the ML of the recommended entropies measurements. Furthermore, we obtain the approximate confidence intervals of the suggested entropy measures.

Assume that $Y_{(1)} \leq Y_{(2)} \leq \dots \leq Y_{(m)}$ be a PT2C sample of size m from a sample of size n drawn from CDF (1) and PDF (2) with censoring scheme r_1, r_2, \dots, r_m . The likelihood (L) function based on the PT2C sample is given by

$$L(\alpha, \beta) = c \prod_{i=1}^m f(y_{(i)}) [1 - F(y_{(i)})]^{r_i} = c \prod_{i=1}^m \frac{\beta}{\alpha^\beta} y_{(i)}^{\beta-1} \cdot \left(1 + \left(\frac{y_{(i)}}{\alpha}\right)^\beta\right)^{-2} \left[1 - \left(1 + \left(\frac{y_{(i)}}{\alpha}\right)^{-\beta}\right)^{-1}\right]^{r_i}, \quad (25)$$

where $c = n(n - r_1 - 1)(n - r_1 - r_2 - 2) \dots n - m + 1 - \sum_{i=1}^{m-1} r_i$. Thus, the constant is the number of ways in which the m PT2C order statistics may occur if the observed failure times are $Y_{(1)}, Y_{(2)}, \dots, Y_{(m)}$. The log- L function of (25), say $\ln L^*$, is then provided via

$$\ln L^* \propto m(\ln \beta - \beta \ln \alpha) + (\beta - 1) \sum_{i=1}^m \ln y_i - 2 \sum_{i=1}^m \ln \left(1 + z_i^\beta\right) + \sum_{i=1}^m r_i \ln \left[1 - \left(1 + z_i^{-\beta}\right)^{-1}\right]. \quad (26)$$

where we write $z_i = (y_i/\alpha)$, and $z_i = z_{(i)}$ for simplified forms. Form (26), we derive the L equation for α and β as

$$\frac{\partial \ln L^*}{\partial \alpha} = -\frac{m\beta}{\alpha} + \frac{2\beta}{\alpha} \sum_{i=1}^m \frac{z_i^\beta}{1 + (z_i)^\beta} + \alpha\beta \sum_{i=1}^m r_i \frac{\left(1 + (z_i)^{-\beta}\right)^{-2} (z_i)^{-\beta}}{1 - \left(1 + (z_i)^{-\beta}\right)^{-1}}, \quad (27)$$

$$\frac{\partial \ln L^*}{\partial \beta} = \frac{m}{\beta} - m \ln \alpha + \sum_{i=1}^m \ln y_i - 2 \sum_{i=1}^m \frac{(z_i)^\beta \ln(z_i)}{1 + (z_i)^\beta} - \sum_{i=1}^m r_i \frac{\left(1 + (z_i)^{-\beta}\right)^{-2} (z_i)^{-\beta} \ln(z_i)}{1 - \left(1 + (z_i)^{-\beta}\right)^{-1}}. \quad (28)$$

The ML estimator of α and β can be obtained using the numerical method by solving the non-linear Equations (27) and (28) after setting them with zero. Once the ML estimator of α and β , say $\hat{\alpha}$ and $\hat{\beta}$, is computed, we can obtain the ML estimator of entropy measures provided in (12), (14), (16), (20), (21), and (24). Consequently, the ML estimator

of Ré entropy, denoted by \hat{R}_γ , is obtained by inserting $\hat{\alpha}$ and $\hat{\beta}$ in (11) as follows

$$\hat{R}_\gamma = (1 - \gamma)^{-1} \log \left(\hat{\beta}^{\gamma-1} \hat{\alpha}^{1-\gamma} B \left(\gamma - \frac{\gamma}{\hat{\beta}} + \frac{1}{\hat{\beta}}, \gamma + \frac{\gamma}{\hat{\beta}} - \frac{1}{\hat{\beta}} \right) \right). \quad (29)$$

The other entropy estimators, indicated by $H\hat{C}_\gamma, \hat{A}_\gamma, \hat{T}_\gamma, \hat{A}1_\gamma$, and $\hat{A}2_\gamma$, may be obtained in a similar fashion.

The preceding theoretical results may be specialized in two cases; firstly, ML estimators of $\alpha, \beta, R_\gamma, HC_\gamma, A_\gamma, T_\gamma, A1_\gamma$, and $A2_\gamma$ are produced when $r_1 = r_2 = \dots = r_{m-1} = 0$ and $r_m = n - m$, via T2C. Second, for $r_1 = r_2 = \dots = r_{m-1} = 0$ and $r_m = 0$, we get the ML estimators of population parameters as well as the proposed entropy measures.

The asymptotic normality of ML estimation may be used to determine the asymptotic 100(1- ν) confidence intervals (**CIn**) for the parameters as

$$\hat{\alpha} \pm Z_{\nu/2} \sqrt{\text{var}(\hat{\alpha})}, \hat{\beta} \pm Z_{\nu/2} \sqrt{\text{var}(\hat{\beta})}. \quad (30)$$

Also, the asymptotic 100(1- ν) CIn for entropy measures are given by

$$\begin{aligned} & \hat{R}_\gamma \pm Z_{\nu/2} \sqrt{\text{var}(\hat{R}_\gamma)}, H\hat{C}_\gamma \pm Z_{\nu/2} \sqrt{\text{var}(H\hat{C}_\gamma)}, \hat{A}_\gamma \\ & \pm Z_{\nu/2} \sqrt{\text{var}(\hat{A}_\gamma)}, \hat{T}_\gamma \pm Z_{\nu/2} \sqrt{\text{var}(\hat{T}_\gamma)}, \\ & \hat{A}1_\gamma \pm Z_{\nu/2} \sqrt{\text{var}(\hat{A}1_\gamma)}, \hat{A}2_\gamma \pm Z_{\nu/2} \sqrt{\text{var}(\hat{A}2_\gamma)}, \end{aligned} \quad (31)$$

where $Z_{\nu/2}$ is standard normal and (1- ν) is the confidence coefficient.

4. Simulation and Real Data Outcomes

The challenge in this section is to analyze the outcomes of the numerous entropy estimations stated before. To evaluate the behavior of the suggested entropy measures and to analyze the statistical performances of the estimators under PT2C, a Monte Carlo study is used. An actual data is also examined for demonstration purposes. For calculations, the statistical programming language R will be used in this study.

4.1. Simulation Study. The effectiveness of the approaches recommended of entropy estimation using Monte Carlo is compared using a simulated exercise. Six entropy estimates are calculated using the Monte Carlo process. For the ML estimates (MLEs), one may generate 1000 data from the LLD with the following assumptions:

- (1) Presume the parameters of the LLD in the coming situations: $\alpha = 0.5, \beta = 1.5$
- (2) Assume two values for the constant $\gamma = (0.5, 1.5)$

- (3) Sample size is $n=60$ and number of observed failures are $m=10, 20, 30$.
- (4) Removed items r_j are assume the accompanying:

Scheme I: $r_1 = r_2 - \dots = r_{m-1} = 0, r_m = n - m$.

Scheme II: $r_1 = r_2 - \dots = r_{m-1} = r_m = n - m/m$.

Scheme III: $r_1 = n - m, r_2 - \dots = r_m = 0$.

Table 1 shows the patterns that were eliminated for each suggested schemes. Note that the first scheme (Scheme I) is a particular instance of PT2C, which is the most common T2C. Another, particular case is considered when $n = m = 60$ which leads to a complete sample.

According to the generated data, MLEs are computed under the above assumptions using PT2C. When getting MLEs, keep in mind that the initial estimate values are treated the same as the real parameter values. These values, MLEs, are then plugged-in to calculate the desired entropy estimates.

All the average entropy estimates, relative biases (**Rbias**), associated mean squared errors (**MSEs**), corresponding average interval lengths (**AIL**), and coverage probabilities (**CPs**) for all six entropy methods are reported in Table 2 for $\gamma = 0.5$ and in Table 3 for $\gamma = 1.5$. Also, the results of the complete sample case are reported in Table 4 for both values of γ .

From tabulated values, it can be noticed that:

- (i) Higher values of m lead to a decrease in Rbias, MSE, and AIL for all different schemes of removing items and all different entropy methods.
- (ii) All CPs are greater than 93% for all different schemes of removing items and all different entropy methods.
- (iii) The increase in the constant term γ leads to a decrease in estimates of all different entropy methods.

4.2. Real Data Application. A real data set is analyzed for illustrative purposes as well as to assess the statistical performances of the MLEs for different entropy estimates in the case of the LLD under different PT2C schemes.

The uncensored data set below corresponds to the remission periods (in months) of a random sample of 128 bladder cancer patients reported in Lee and Wang [26]. The following are the bladder cancer remission times:

0.08, 2.09, 3.48, 4.87, 6.94, 8.66, 13.11, 23.63, 0.20, 2.23, 3.52, 4.98, 6.97, 9.02, 13.29, 0.40, 2.26, 3.57, 5.06, 7.09, 9.22, 13.80, 25.74, 0.50, 2.46, 3.64, 5.09, 7.26, 9.47, 14.24, 25.82, 0.51, 2.54, 3.70, 5.17, 7.28, 9.74, 14.76, 26.31, 0.81, 2.62, 3.82, 5.32, 7.32, 10.06, 14.77, 32.15, 2.64, 3.88, 5.32, 7.39, 10.34, 14.83, 34.26, 0.90, 2.69, 4.18, 5.34, 7.59, 10.66, 15.96, 36.66, 1.05, 2.69, 4.23, 5.41, 7.62, 10.75, 16.62, 43.01, 1.19, 2.75, 4.26, 5.41, 7.63, 17.12, 46.12, 1.26, 2.83, 4.33, 7.66, 11.25, 17.14, 79.05, 1.35, 2.87, 5.62, 7.87, 11.64, 17.36, 1.40, 3.02, 4.34, 5.71, 7.93, 11.79, 18.10, 1.46, 4.40, 5.85, 8.26, 11.98, 19.13, 1.76, 3.25, 4.50, 6.25, 8.37, 12.02, 2.02, 3.31, 4.51, 6.54, 8.53, 12.03, 20.28, 2.02, 3.36, 6.76, 12.07, 21.73, 2.07, 3.36, 6.93, 8.65, 12.63, 22.69, 5.49.

We first check whether the LLD is suitable for analyzing this data set. We report the MLEs of the parameters and the value of the Kolmogorov–Smirnov (**K–S**) test statistic to judge the goodness of fit. The calculated K-S distance between the empirical and fitted LLD distribution is 0.0440 and its p -value is 0.9667 where $\hat{\alpha} = 6.0978$ and $\hat{\beta} = 1.7160$ which indicate that this distribution can be considered an adequate model for the given data set.

From the original data, one can generate, e.g., three PT2C samples with a number of stages $m = 30$ and removed items r_j are assumed to be as follows:

Scheme I: $r_1 = r_2 - \dots = r_{m-1} = 0, r_m = n - m$.

Scheme II: $r_1 = r_2 - \dots = r_{m-1} = r_m = n - m + 1/m$.

Scheme III: $r_1 = n - m, r_2 - \dots = r_m = 0$.

Also, we consider the complete case as $n = m = 128$. Two different values of the constant are proposed: 0.5 and 1.5. In Table 5, the MLEs of the parameters have been calculated and then plugged into different entropy methods in the proposed schemes for PT2C samples as in the given real data set.

5. Summary and Conclusion

In this paper, we look at the estimation problem of certain entropy measures for log-logistic distribution under the PT2C scheme. Rényi entropy, Havrda and Charvat entropy, Arimoto entropy, A-entropies, and Tsallis entropy are the six entropy measures considered. The recommended entropy measurement expressions are computed. The point and two-sided approximate confidence intervals for the recommended entropy measures are obtained using the maximum likelihood procedure. To describe and compare the behavior of estimator's measures, a numerical evaluation is done in terms of relative biases, associated mean squared errors, average interval lengths, and coverage probabilities under different censoring schemes as well as different sample sizes. The suggested entropy estimates approach the real values with decreasing censoring levels, as well as the accuracy of measurements increases with sample sizes. Finally, an actual dataset was analyzed for demonstration purposes.

Data Availability

If you would like to get the numerical dataset used to conduct the study reported in the publication, please contact the appropriate author.

Conflicts of Interest

The authors state that they have no conflicts of interest to disclose in relation to this work.

Acknowledgments


This work was supported by Researchers supporting project number RSP2022R464, King Saud University, Riyadh, Saudi Arabia.

References

- [1] D. Collet, *Modelling Survival Data in Medical Research*, Chapman and Hall, London, 2003.
- [2] C. Kleiber and S. Kotz, *Statistical Size Distributions in Economics and Actuarial Sciences*, John Wiley, New York, 2003.
- [3] F. Ashkar and S. Mahdi, "Fitting the log-logistic distribution by generalized moments," *Journal of Hydrology*, vol. 328, no. 3-4, pp. 694-703, 2006.
- [4] S. Bennett, "Log-logistic regression models for survival data," *Journal of the Royal Statistical Society: Series C*, vol. 32, no. 2, pp. 165-171, 1983.
- [5] M. I. Ahmad, C. D. Sinclair, and A. Werritty, "Log-logistic flood frequency analysis," *Journal of Hydrology*, vol. 98, no. 3-4, pp. 205-224, 1988.
- [6] A. Robson and D. Reed, *Flood Estimation Handbook Volume 3: Statistical Procedures for Flood Frequency Estimation*, Institute of Hydrology, Wallingford, 1999.
- [7] N. L. Johnson, S. Kotz, and N. Balakrishnan, *Continuous Univariate Distribution, 2-nd Edition*, vol. 1, Wiley and Sons, New York, 1995.
- [8] N. Balakrishnan and R. Aggrawala, *Progressive Censoring, Theory, Methods and Applications*, Birkhauser, Boston, 2000.
- [9] A. Rényi, "On measures of entropy and information," in *Proc. 4th Berkeley Symposium on Mathematical Statistics and Probability*, pp. 547-561, University of California Press, 1960.
- [10] J. Havrda and F. S. Charvat, "Quantification method of classification processes: concept of structural-entropy," *Kybernetika*, vol. 3, pp. 30-35, 1967.
- [11] S. Arimoto, "Information-theoretical considerations on estimation problems," *Information and Control*, vol. 19, no. 3, pp. 181-194, 1971.
- [12] A. M. Awad, M. Azzam, and D. Hussein, "SUP-entropy of degree-alpha," *Arabian Journal for Science and Engineering*, vol. 12, no. 4, pp. 473-480, 1987.
- [13] C. Tsallis, "Possible generalization of Boltzmann-Gibbs statistics," *Journal of Statistical Physics*, vol. 52, no. 1-2, pp. 479-487, 1988.
- [14] E. Cramer and C. Bagh, "Minimum and maximum information censoring plans in progressive censoring," *Communication in Statistics Theory & Methods*, vol. 40, no. 14, pp. 2511-2527, 2011.
- [15] S. B. Kang, Y. S. Cho, J. T. Han, and J. Kim, "An estimation of the entropy for a double exponential distribution based on multiply type-II censored samples," *Entropy*, vol. 14, no. 2, pp. 161-173, 2012.
- [16] J. I. Seo, H. J. Lee, and S. B. Kang, "Estimation for generalized half logistic distribution based on records," *Journal of the Korean Data and Information Science Society*, vol. 23, no. 6, pp. 1249-1257, 2012.
- [17] Y. Cho, H. Sun, and K. Lee, "An estimation of the entropy for a Rayleigh distribution based on doubly-generalized Type-II hybrid censored samples," *Entropy*, vol. 16, no. 7, pp. 3655-3669, 2014.
- [18] Y. Cho, H. Sun, and K. Lee, "Estimating the entropy of a Weibull distribution under generalized progressive hybrid censoring," *Entropy*, vol. 17, no. 1, pp. 102-122, 2015.
- [19] S. Dey, S. S. Maiti, and M. Ahmad, "Comparison of different entropy measures," *Pakistan Journal of Statistics*, vol. 32, no. 2, pp. 97-108, 2016.
- [20] M. Chacko and P. Asha, "Estimation of entropy for generalized exponential distribution based on record values," *Journal of the Indian Society for Probability and Statistics*, vol. 19, no. 1, pp. 79-96, 2018.
- [21] R. A. R. Bantan, M. Elgarhy, C. Chesneau, and F. Jamal, "Estimation of entropy for inverse Lomax distribution under multiple censored data," *Entropy*, vol. 22, no. 6, p. 601, 2020.
- [22] A. A. Al-Babtain, A. S. Hassan, A. N. Zaky, I. Elbatal, and M. Elgarhy, "Dynamic cumulative residual Rényi entropy for Lomax distribution: Bayesian and non-Bayesian methods," *AIMS Mathematics*, vol. 6, no. 4, pp. 3889-3914, 2021.
- [23] A. M. Almarashi, A. Algarni, A. S. Hassan, A. N. Zaky, and M. Elgarhy, "Bayesian analysis of dynamic cumulative residual entropy for Lindley distribution," *Entropy*, vol. 23, no. 10, p. 1256, 2021.
- [24] B. A. Helmy, A. S. Hassan, and A. K. El-Kholy, "Analysis of uncertainty measure using unified hybrid censored data with applications," *Journal of Taibah University for Science*, vol. 15, no. 1, pp. 1130-1143, 2021.
- [25] I. Elbatal, N. Alotaibi, S. A. Alyami, M. Elgarhy, and A. R. el-Saeed, "Bayesian and non-Bayesian estimation of the Nadarajah-Haghighi distribution: using progressive Type-1 censoring scheme," *Mathematics*, vol. 10, no. 5, p. 760, 2022.
- [26] E. T. Lee and J. W. Wang, *Statistical Methods for Survival Data Analysis*, John Wiley & Sons, Inc, Third edition edition, 2003.

Review Article

Nanomaterials: A Promising Therapeutic Approach for Cardiovascular Diseases

Hitesh Chopra ¹, **Shabana Bibi**,^{2,3} **Awdhesh Kumar Mishra** ⁴, **Vineet Tirth**,^{5,6} **Sree Vandana Yerramsetty**,⁷ **Sree Varshini Murali**,⁷ **Syed Umair Ahmad** ⁸, **Yugal Kishore Mohanta** ⁹, **Mohamed S. Attia** ¹⁰, **Ali Algahtani** ^{5,6}, **Fahadul Islam**,¹¹ **Abdul Hayee** ¹², **Saiful Islam**,¹³ **Atif Amin Baig** ¹⁴, and **Talha Bin Emran** ¹⁵

¹Chitkara College of Pharmacy, Chitkara University, Punjab 140401, India

²Yunnan Herbal Laboratory, College of Ecology and Environmental Sciences, Yunnan University, Kunming, 650091 Yunnan, China

³The International Joint Research Center for Sustainable Utilization of Cordyceps Bioresources in China and Southeast Asia, Yunnan University, Kunming, 650091 Yunnan, China

⁴Department of Biotechnology, Yeungnam University, Gyeongsan, Gyeongsangbuk-do, Republic of Korea

⁵Mechanical Engineering Department, College of Engineering, King Khalid University, Abha, 61421 Asir, Saudi Arabia

⁶Research Center for Advanced Materials Science (RCAMS), King Khalid University, Guraiger, Abha, 61413 Asir, P.O. Box No. 9004, Saudi Arabia

⁷Department of Chemical and Biotechnology, SASTRA Deemed University, Thanjavur, Tamil Nadu 613402, India

⁸Department of Bioinformatics, Hazara University, Mansehra, Pakistan

⁹Department of Applied Biology, University of Science and Technology Meghalaya, Ri-Bhoi 793101, India

¹⁰Department of Pharmaceutics, Faculty of Pharmacy, Zagazig University, Zagazig 44519, Egypt

¹¹Department of Pharmacy, Faculty of Allied Health Sciences, Daffodil International University, Dhaka 1207, Bangladesh

¹²Department of Immunology, Faculty of Medicine, Academic Assembly, University of Toyama, Toyama, Japan

¹³Civil Engineering Department, College of Engineering, King Khalid University, Abha, 61421 Asir, Saudi Arabia

¹⁴Unit of Biochemistry, Faculty of Medicine, Universiti Sultan Zainal Abidin, Malaysia

¹⁵Department of Pharmacy, BGC Trust University Bangladesh, Chittagong 4381, Bangladesh

Correspondence should be addressed to Atif Amin Baig; atifameen01@gmail.com and Talha Bin Emran; talhabmb@gmail.com

Received 22 January 2022; Accepted 5 February 2022; Published 23 February 2022

Academic Editor: N Senthilkumar

Copyright © 2022 Hitesh Chopra et al. This is an open access article distributed under the Creative Commons Attribution License, which permits unrestricted use, distribution, and reproduction in any medium, provided the original work is properly cited.

Cardiovascular diseases (CVDs) are a primary cause of death globally. A few classic and hybrid treatments exist to treat CVDs. However, they lack in both safety and effectiveness. Thus, innovative nanomaterials for disease diagnosis and treatment are urgently required. The tiny size of nanomaterials allows them to reach more areas of the heart and arteries, making them ideal for CVDs. Atherosclerosis causes arterial stenosis and reduced blood flow. The most common treatment is medication and surgery to stabilize the disease. Nanotechnologies are crucial in treating vascular disease. Nanomaterials may be able to deliver medications to lesion sites after being infused into the circulation. Newer point-of-care devices have also been considered together with nanomaterials. For example, this study will look at the use of nanomaterials in imaging, diagnosing, and treating CVDs.

1. Introduction

Cardiovascular diseases (CVDs) are the leading cause of death worldwide. CVD was responsible for the deaths of

around 18.6 million persons globally in 2019 [1]. Heart disease and related disorders, such as atherosclerosis, arrhythmia, coronary heart disease, peripheral arterial disease, rheumatic heart disease, congenital heart disease, deep vein

thrombosis, and pulmonary embolism, are all caused by changes in the normal functioning of the heart and its associated structures. The major explanation for these reported ailments is a sedentary lifestyle of living with little or no physical exercise, which has been identified as the leading cause of the CVD in humans. Moreover, the lockdown and work-from-home lifestyle have minimized physical movement, adding more to the sedentary lifestyle. However, various options are available for preventing and treating CVDs, such as regular exercise and physical activity to reduce CVDs [2]. Other factors aggregating the CVDs include smoking, hypertension, and hyperlipidemia. However, exercising can minimize CVD and help reduce the body mass index to normal [3, 4]. Traditional treatment options include operating the affected part for thrombosis and placing the artificial pacemaker for arrhythmia. However, they were adequate to some extent of the population, but they are associated with lower patient compliance, including discomfort for a lifetime. Then, the role of nanotechnology comes into the limelight. Owing to their small size, they can easily be penetrated inside the tight junctions. Due to the small size, the surface area of entities increased, thus providing more comprehensive options for surface modification and binding. The knowledge and utilization of innovative technology shall provide a safe and effective platform for the controlled, targeted delivery of actives that shall lower the incidences of lipid disorders and other diseases [5]. Nanomaterials showed the way forward to overcome the limits arising from using conventional biomaterials [6, 7]. Moreover, new technologies can be coupled with nanotechnology that will revolutionize the treatment of CVDs. Many researchers had prepared nanomaterials mimicking the extracellular matrix and accelerating the healing mechanism [8–10]. The final value of nanoparticulate imaging media is determined by their pharmacokinetics and biodistribution. To provide therapeutically effective tissue imaging, particles must accumulate in target tissues quickly, with little nonspecific uptake. Importantly, these pharmacokinetic requirements for image generation vary by modality. Particles may cause false-positive detection in ultrasensitive modes. Small changes in nanoparticle (NP) size, shape, or surface chemistry may often enhance particle pharmacokinetics, but at a cost. For example, polyethylene glycol is often added to NP surfaces to enhance circulation [11]. This speeds up molecule binding and therapeutic delivery but delays image collecting and bioelimination. Amplification of background signals by larger particles with lower renal clearance [12]. Making nanoparticulate imaging agents safe and effective may be tricky. Longer circulation times and slower tissue absorption rates may need longer decay half-lives, resulting in higher radiation exposure [13–15]. After imaging for 24 hours, diagnostic NPs must be totally removed or biodegraded without producing harm or immunogenicity. Renal filtration is the quickest and most direct way to remove NPs, lowering the danger of biological interactions. Fast renal filtration (4 hours) restricts targeting to certain organs and NP design [16]. Larger nanoparticles are retained in MPS organs until broken down into smaller components and excreted in bile or urine. This method increases exposure due to its slowness and inaccuracy. Larger NPs

(250 nm) were cleared quickly in rats, but not in large animals or humans [17]. Organic or iron nanoparticles that can be appropriately eliminated or digested have been authorized by the Food and Drug Administration (FDA) [18]. However, despite their increased extravasation rate, tiny molecules enter tissues more deeply and wash out more rapidly than larger molecules. The endothelium of healthy, nonfenestrated endothelium is often too small to allow considerable extravasation of intermediate-sized NPs, such as those seen in the sinusoidal capillaries of the liver and spleen, as well as those found in tumors and areas of inflammation [19, 20]. For this reason, NPs are more prone to collect in the perivascular gaps of permeable tissues because of their comparatively large size. The enhanced permeability and retention effect (EPR) describes the passive accumulation of NPs in tissues with higher vascular permeability, and it has been used in several medicinal and imaging applications [21, 22]. EPR may be beneficial for detecting pathological tissues, but it is necessary to keep in mind that the effect often occurs over longer time periods (hours) that may not be suitable for clinical diagnostic imaging [20]. Because it generates nonspecific background signals that may obscure or confuse desirable signals from molecular binding events, EPR-based NP accumulation is unfavorable for molecular imaging applications because it inhibits particle removal [12].

Nanomaterials can help in achieving therapeutic functions that are difficult to achieve with traditional biomaterials. Nanomaterials can act as a carrier and can travel through the endothelium of blood vessels also, and they can interfere with the internalization step involved in the delivery of preloaded drugs [23–25]. Developed during the last two decades, there are several distinct types of nanotechnologies for biomedicine with their own distinct features and benefits. Liposomes, NPs, and the application of nanocoating techniques are all considered nanomaterials. The treatment of disease with nanotechnology is currently being concentrated on cancer, specifically on curing and diagnosing cancer. However, it is beginning to move to other treatment areas, specifically to managing CVDs. Current therapies for CVDs are concentrated on restoring normal blood flow through or around the damaged vasculature and the avoidance of repeated cardiovascular shocks. Reduction in subsequent build up and thickness of atherosclerotic plaques, as well as impacts on exterior elastic membranes and fibrous and dense calcium volumes, is obtained by statin treatment [26]. Dual antiplatelet therapy utilizing cyclooxygenase inhibitors such as aspirin and P2Y₁₂ inhibitor such as clopidogrel is first-line treatments for prevention of CVDs, which seek to minimize clot formation and platelet aggregation [27]. There is a necessity for improvement in these therapies, particularly owing to the hazards involved with taking antiplatelet medication having considerably unfavorable side effect profiles, and poor patient compliance [28]. In addition to this, some patients may not react well to antiplatelet medication, which has a detrimental influence on their long-term prognosis. Studies have revealed that individuals who have experienced an acute myocardial infarction but have a poor response to clopidogrel are at greater risk of recurrent cardiovascular events during

follow-up [29]. This underscores the demand for developments in technology and a potential for nanomedicine. This review summarizes the key technologies that are being explored in this field.

2. Why There Is Need for a Nanocardiovascular Targeting Approach

Restoring normal blood flow and preventing repeated cardiovascular shocks are the primary goals of current therapy for CVDs. Statin treatment reduces the growth and thickness of atherosclerotic plaques and the effects on external elastic membranes and fibrous and dense calcium volumes [26]. Aspirin and clopidogrel are first-line antiplatelet medications to prevent cardiovascular disease, which attempt to minimize clot formation and platelet aggregation [27]. It has been reported that administration of clopidogrel and aspirin to minor ischemic stroke patients had a lower risk of major ischemic events in comparison to patients with aspirin alone [30]. It has also been reported that ethidium bromide gets bound to calf thymus DNA signal that indicated clopidogrel bisulphate thus displacing ethidium bromide from its binding site of DNA [31]. Moreover, aspirin, being weaker acid, depresses the availability of clopidogrel bisulphate in basic media [32]. Antiplatelet therapy has high detrimental side effect profiles and low patient compliance, which necessitates improvement in these therapies [33]. In addition, some patients fail to react effectively to antiplatelet medication, which severely impacts their long-term prognosis. Following an acute myocardial infarction, individuals who show limited response to clopidogrel are at greater risk of recurrent cardiovascular events. This finding is consistent with previous research [29]. This demonstrates the need for technological improvements and the potential for nanomedicine.

3. Nanotechnology-Based Approaches

3.1. Liposomes. Liposomes are the uni or multilamellar lipid membrane carriers that can entrap both hydrophilic and lipophilic drugs for the targeted delivery at distant organs. The spherical shape of the vesicle closely resembles the structure of the cell membrane. Liposomes are biocompatible, biodegradable, and lower the toxicity arising after entrapment [34].

In myocardial infarction, reperfusion is an essential step in restoring the circulation to the ischemic myocardium. An improper way may lead to reperfusion injury, decreased cardiac functioning, and scar formation at last. It is a complex phenomenon and comprises multiplayers such as inflammatory cells and cardiac fibroblasts. Researchers identified some specific peptides for infarct and border zone using the *in vivo* phage display and optical imaging methods [35]. The cardiomyocytes, endothelial cells, myofibroblasts, and ckit+ cells were present in border zones of remodeled infarcts. Researchers prepared site-specific liposomes, i.e., cardiomyocyte-specific (I-1) liposomes, for the targeted delivery of Poly (ADP-ribose) polymerase-1 inhibitor after myocardial reperfusion. With the use of liposomes, the

AZ7379 (PARP-1 (poly [ADP-ribose] polymerase 1) inhibitor) concentration increased in the border zone at 24 h post-administration compared to control AZ7379, freely administered. About a 3-fold increase in inhibitory therapeutic efficiency was observed due to entrapment of PARP-1 inhibitor.

Berberine has also been reported to reduce the negative impact on cardiac functions after myocardial infarction [36]. Formulators developed liposomes using ethanol injection technique using dipalmitoylphosphatidylcholine, 1,2-distearoyl-sn-glycero-3-phosphoethanolamine-N-[amino (polyethylene glycol)-2000] (DSPE-PEG2000), and cholesterol as lipoids and dissolved them in HEPES [(4-(2-hydroxyethyl)-1-piperazineethanesulfonic acid)] buffered saline and berberine. Macrophages infiltrate into the heart during and after infarction and cause inflammation [37]. During this event, the capillary permeability increases. It was hypothesized that encapsulating the liposomes shall enrich the berberine. Berberine in the heart tissue shall help to extravagate by the locally enhanced permeability and thus improve the local delivery and overall treatment. Practically, after intravenous administration, the berberine liposomes got accumulated at infarcted heart tissue after 3 days of myocardial infarction. It was indicating the successful integration of liposomes for delivery to the target site. Moreover, the macrophages infiltrated into infarcted heart tissue, suggesting the release of preloaded berberine at the target site by liposomes and improving the anti-inflammatory response [38–40].

MicroRNA-21 are short regulatory RNA acting as down-regulators for gene expression by inhibiting mRNA translation and promoting mRNA degradation [41]. Many researchers suggested using microRNA (miRNA) in cardiac hypertrophy and other associated cardiac disorders [42, 43]. It has been observed that the expression of levels of mir-21 in cardiac cells gets upregulation with oxygen-glucose deprivation. Depletion of miR-21 causes the enhancement in fibroblast activation and promotes the cardiomyocytes against oxidative stress. Researchers prepared miR-21 liposomes as a promising strategy for treating acute myocardial infarction [44]. The process of liposomes was chosen owing to poor stability and insufficient cellular uptake that acted as a significant hurdle for miR-21. Formulators developed miR-21 mimics into liposomes modified with the cardiac troponin T antibody to target the miR-21 to the myocardium. The liposomes showed enhanced targeting efficiency to hypoxia primary cardiomyocytes. The liposomes were administered via the tail vein and got accumulated inside the ischemic heart. The liposomes improved cardiac functions and a decrease in infarct size after acute myocardial infarction and maintained cardiac cells' viability. Darraji et al. prepared azithromycin's liposomal preparation to reduce its cytotoxicity and enhance its immunotherapeutic efficacy [45].

The liposomes were prepared by using the DSPC (distearoylphosphatidylcholine), DSPG (distearoylphosphatidylglycerol), and cholesterol via the thin-film hydration method. The liposomal formulation showed a reduction in cytotoxicity and mortality rate by 50% in mice. Also, the

liposomes decreased the cardiac inflammatory neutrophils and infiltration of inflammatory monocytes while angiogenesis got enhanced. Wei et al. administered Lipo-prostaglandin E1 (Lipo-PGE1) before primary percutaneous coronary intervention (PCI), and improvement in myocardial microcirculation in reperfusion injury was observed [46]. During acute myocardial infarction, damage to the microvascular is observed, limiting the completeness of tissue perfusion [47]. The intravenous administration of Lipo-PGE1 causes a decrease in cTFC (corrected thrombolysis in myocardial infarction frame count) and increased myocardial blush grade. After 6 months of follow-up, it was found that the patients with Lipo-PGE1 have fewer major adverse cardiac events. Atherosclerosis is a disease characterized by the deposition of plaque inside the blood vessels. The extravasation of liposomes to plaque can be carried out using the injured endothelium's enhanced permeability and retention effect in atherosclerosis. The damaged vessels have been found to overexpress some molecules that can target the liposomes and thus permit liposomes' entry. The molecules such as vascular cell adhesion molecule 1 (VCAM1), intercellular adhesion molecule-1 (ICAM-1), P-selectin, E-selectin, and alpha V beta three integrins are generally found at luminal endothelium or newly formed endothelium. Even the noncellular components of plaques could also act as the target for liposomal entry [48].

The clinical trial was conducted with liposomes encapsulating the prednisolone for use in atherosclerosis [49]. The liposomes were found to increase the plasma half-life to 63 hours. The macrophages isolated from iliofemoral plaques showed appearance in 75% of macrophages isolated. However, the liposomes were not able to reduce the arterial wall permeability in infected patients. Later, it was confirmed that liposomal prednisolone showed accumulation in low-density lipoprotein receptor knockout mice. The liposome enhanced the recruitment of monocytes at plaque position [50].

The choice of therapeutic drug for treatment has been under discussion for many years as angiogenesis also constitutes a potential target for the treatment of atherosclerosis [51]. Fumagillin has been shown to possess antiangiogenic effects in tumor therapies [52]. Also, the water-soluble analog of Fumagillin, TNP-470, has been shown to lower plaque growth in the case of atherosclerosis [53]. Pont et al. prepared liposomes of the antiangiogenic drug Fumagillin derived from *Aspergillus fumigatus* [54]. Fumagillin is a selective inhibitor of endothelium cell proliferation and migration. The liposomes consisted of 1-palmitoyl-2-oleoyl-sn-glycero-3-phosphocholine (POPC), 1, 2-dipalmitoyl-sn-glycero-3-phosphoethanolamine-N-7-nitro-2-1, 3-benzoxadiazol-4-yl (DPPE-NBD), 1, 2-dipalmitoyl-sn-glycero-3-phosphoethanolamine-N-biotinyl (DPPE-Biotin), and Tween 80, and the drug was incorporated using the thin-film hydration method. The liposomes were labile, and biotin-phospholipid was attached as conjugation between biotinylated antibodies via Avidin Bridge. An antibody-targeted macrophage scavenger receptor B (CD-36) was attached to the liposome, causing an enhancement in signals from MRI and fluorescence. Also, the CD-36 is

being a glycoprotein and is present in membranes of macrophages. Therefore, the anti-CD36 targets the macrophages scavenger receptor B facilitating the *in vivo* imaging in atherosclerosis plaques. The liposomes showed a reduction in plaque development by 23.7%. The liposome administration decreased the fatty streaks that started to appear normal at 8-20 weeks of administration in mice fed with an atherogenic diet. Fluorescence imaging and histochemical analysis reported the accumulation of liposomes. To exploit the role of macrophages, another group prepared liposomes consisted of decoration of phosphatidylserine and DSPE-PEG2000 onto the surface of liposome encapsulating pioglitazone [55]. Pioglitazone is a peroxisome proliferator-activated receptor γ agonist for atherosclerosis macrophages. The surface decorated liposomes showed more penetration efficiency towards activated vascular endothelial monolayers and suppressed the inflammatory cytokines *in vitro*.

Thrombosis is one of the significant contributors to CVDs. Many antithrombosis drugs have been effective but showed lower limited efficacy due to lower shorter half-life in plasma and associated side effects. The liposomes functionalized with cyclic RGD encapsulating urokinase were found to be effective in thrombosis [56].

The liposomes could bind to activated platelets, and the *in vitro* pattern showed a release plateau in 5 h with 60% release for urokinase. As a result, the dose of urokinase decreased by 75%, as evidenced by the mouse mesenteric thrombosis model. Interleukin-10 (IL10) acts to alleviate the inflammation arising from atherosclerosis plaque, using cRGD conjugated liposomes and IL10 [57]. The liposomes with the size of 180 nm and PDI 0.14 were prepared. The liposome administration *in vitro* showed sustained release of IL10 and reduced the ROS and NO. The IL-1 β and TNF- α were downregulated with administration in RAW 264.7 cells apart from drug delivery applications; liposomes have also been utilized in imaging applications. Liposomal nanoparticles were utilized in positron emission tomography (PET) [58]. The liposomal NPs were decorated with Zirconium-89. After 15 days of administration, the positron emission tomography/computed tomography and PET/MRI showed their biodistribution and vessel wall targeting in the rabbit atherosclerosis model. The liposomes showed biodistribution patterns like long-circulating NPs and accumulated in atherosclerosis lesions confirmed by imaging techniques. Many other researches have been tabulated in Table 1.

The main advantage of using liposomes for cardiac applications includes encapsulating and targeting high payload on lipoidal vesicles. However, liposome components' interaction with the immune system has contributed to the difficulties encountered during their translation into therapeutic application. Antibodies may be produced against their different components and/or the enclosed payload when they are subjected to synthetic changes in order to improve their usability as drug delivery vehicles. According to Dams et al. [65], repeated injection of PEGylated liposomes has been related with a loss of their long circulating characteristics and a subsequent clearance from the circulation. The "accelerated blood clearance" (ABC) phenomenon

TABLE 1: Literature view of liposomal preparation for cardiovascular diseases.

| Name of drug/active | Constituents of liposomes | Animal model/ cell lines | Particle size | Outcome of study | References |
|--|---|--|--------------------|---|------------|
| Ameliorated sirolimus | Dioleytrimethylammonium propane (DOTAP), dimyristoylphosphatidylglycerol (DMPG), distearoylphosphatidylethanolamine polyethylene glycol 2000 (DSPE-PEG) | Balloon injured rats | 100 nm | As with decrease in size of liposomal vesicles and change in ionic strength resulted in variation in antirestenosis efficacy of liposomes | [59] |
| Human vascular endothelial growth factor-165 | Cholesterol (Chol) + DOTAP liposome (CD liposome) | Rat heart | 50-150 nm | It was observed that the liposomes caused a reduction in apoptosis and improvement in angiogenesis. Also, the study showed gene transfection efficiency using cyclodextrin liposomes medicated hVEGF165 gene transfer | [60] |
| α -Tocopherol | Egg lecithin, cholesterol, sodium deoxycholate | Sprague Dawley rats | 231.1 \pm 6.1 nm | The hydrogels showed a highly porous structure interconnected throughout and liposomes distributed uniformly. The liposomes showed delayed-release and excellent biocompatibility in cardiomyocytes. The formulation was able to resist oxidative stress and improve the survival of cardiomyocytes | [61] |
| Indium | Phosphatidylserine and PEG2000; PEG5000 | ddY mice | 200 nm | The PEGylated liposomes showed slow uptake in comparison to non-PEGylated liposomes. Also, the <i>in vivo</i> results showed slower blood clearance in PEGylated liposomes | [62] |
| Atorvastatin calcium and curcumin | Mal-PEG2000-DSPE and cholesterol | ApoE knockout (ApoE ^{-/-}) mice | 190 nm | Targeted liposomes transported atorvastatin calcium and curcumin to defective endothelial cells, leading in synergistic reduction of adhesion molecules (E-selectin and ICAM-1) and plasma lipid levels | [63] |
| Fluocinolone acetonide | DMPC (1,2-dimyristoyl-sn-glycero-3-phosphocholine), DPPC, and DSPC | Apolipoprotein E-knockout (ApoE ^{-/-}) mouse model | 100 nm | <i>In vivo</i> studies carried out with an apolipoprotein E-knockout (ApoE ^{-/-}) mouse model of atherosclerosis show accumulation of liposomes in atherosclerotic plaques, colocalization with plaque macrophages, and antiatherogenic effect over 3 weeks of treatment | [64] |

is the term used to describe these phenomena. When it comes to the therapeutic use of PEGylated formulations that need numerous dosage regimens, the ABC phenomenon is a significant source of worry. Also, these systems have inability to maintain long-term stability, which results in the release of drugs at an inopportune time. In addition, greater excipient-to-drug ratios are often needed, making them costlier and less effective than some of the polymer-based systems available on the market today.

3.2. Nanoparticles (NPs). NPs are characterized by smaller sizes and can be surface functionalized with new side chains. Their smaller size presents a large surface area for interaction and binding. The NPs can permeate easily through the tight junctions, as they can be prepared both as hydrophilic

and hydrophobic. NPs can be conjugated with d- and f-block elements and targeted from macrophage scavenger receptors, thus improving the cardiac magnetic resonance that can help diagnose atherosclerosis [66].

Natural agents such as curcumin can also be entrapped inside the NPs and targeted to treat Ehrlich ascites carcinoma cardiac toxicity. The treatment with NPs resulted in a reduction in volume and tumor cells with a marked increase in apoptotic cell numbers in ascites fluid. The treatment also decreased the cardiac markers [67].

Cerium oxide, also known as Ceria, has also been reported to show cardioprotective effects. Pagliari et al. reported the use of Ceria NPs (nanoceria) in controlling the ROS-induced cell damage on the cardiac progenitor cells (CPCs). CPCs are an autologous source of cells and needed

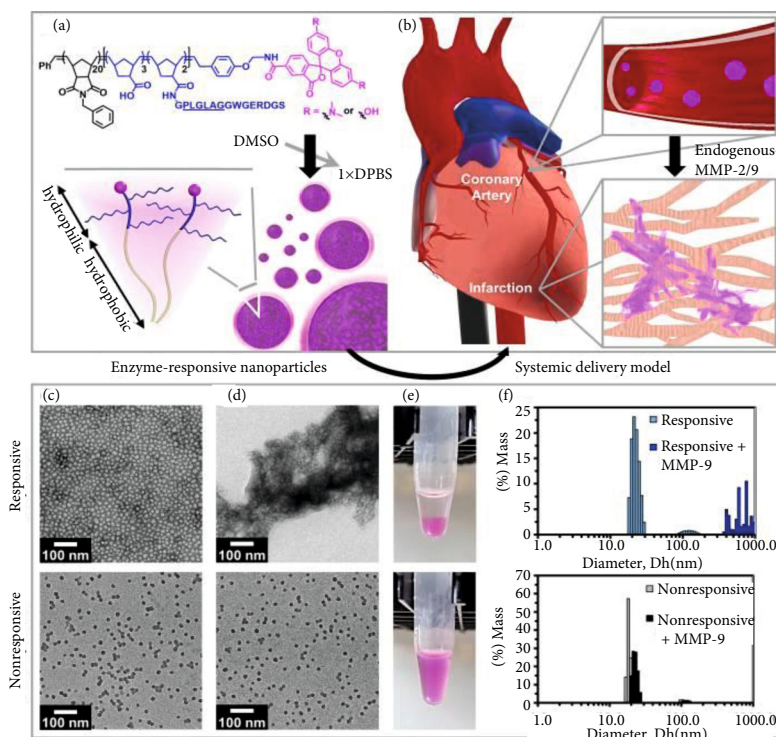


FIGURE 1: (a) Representation of enzyme responsive nanoparticles for use in myocardial infarction. (b) Representation of nanoparticles freely in the bloodstream and later getting settled at the infarcted vessel. (c) *In vitro*: responsive and nonresponsive nanoparticles. (d) Responsive and nonresponsive behavior of nanoparticles on activation. (e) Images of nanoparticle solution after activation. (f) DLS pattern of nanoparticles after and before activation. Reproduced with permission from reference [73].

microenvironmental conditions for preparing them in *in vitro* conditions. Findings showed that CPCs resident in the heart were quickly exposed to uptake the nanoceria, as they were present in the cytosol. Even after 7 days, no evidence of encapsulation and particle translocation was seen and prevented the progenitor cells from hydrogen peroxide-induced injury and nanoceria acting as an antioxidant [68].

Similarly, mesoporous silica-based nanoparticles prepared showed detection ability for hydrogen peroxide, the selective drug released and controlled treatment toward heart failure. The peroxide sensing probes were functionalized on the surface for detection and captopril as the drug was loaded inside the NP. The hydrogen peroxide present in tissue could react with the probe causing dissociation of cyclodextrin present on the surface, causing drug release at the site. This occurs as a turn-on and turn-off mechanism [69].

Researchers prepared inhalable peptide-based calcium phosphate NPs for the treatment of CVDs [70]. The particles of <50 nm size, with excellent biocompatibility and biodegradability option, allow rapid translocation of NPs from pulmonary system to the bloodstream and heart, where peptides are released. The rodent model and porcine with diabetic cardiomyopathy showed improvement in myocardial contraction, resulting in everyday functioning. However, this approach was based on the pathophysiological conditions of the lungs. Thus, this may affect the persistence of nanoparti-

cles targeted to the myocardium. It has already been reported that macrophages' role in inflammation-related mutations in patients with myocardial infarction [71]. During ischemia, inflammatory macrophages get accumulated in the arterial wall and heart muscles, causing tissue destruction and death. Therefore, there is a need to evaluate the positioning of macrophages to prevent further destruction. Keliher et al. described the use of ^{18}F -Macroflor (modified poly glucose nanoparticles with high avidity for macrophages). Owing to its smaller size, the NP can be excreted renally. Macroflor is enriched in cardiac, and plaque macrophages can direct the PET signals as evidenced in mouse and rabbit atherosclerotic plaques. Positron emission tomography (PET) imaging helps detect the macrophage population, while MRI reports the extent of inflammation [72].

Similarly, Nguyen et al. reported enzyme-responsive NPs for the increased retention and accumulation in the myocardial infarcted heart via IV injection. The NPs were designed to respond to enzymatic stimuli (matrix metalloproteinases), causing the morphological changes in the discrete NPs into network-like scaffolds (Figure 1). The IV administration causes enzyme-responsive NPs to circulate in the bloodstream and reaches the infarcted point in vasculature. At the injured site, NPs were found to remain for about 28 days' postadministration. Reducing the degree of polymerization of hydrophilic block and degree of conjugation of hydrophilic peptides increased the responsiveness of NPs [73].

TABLE 2: Literature overview of nanoparticle-based study done by other researchers, where n.m. is not mentioned.

| Active ingredient | Disease targeted | Type of nanoparticle | Particle size | Outcome of study | References |
|---|-------------------------|--|---------------|--|------------|
| Atrial natriuretic peptide (ANP) | Ischemic heart disease | Biodegradable porous silicon (PSi) nanoparticle | 168-230 nm | ANP-PSi nanoparticles loaded with a unique cardioprotective small molecule attenuate hypertrophic signaling in the endocardium, signifying their cardioprotective potential | [77] |
| Vascular endothelial growth factor | Ischemic heart disease | Pluronic F-127 (poly(ethylene oxide)-poly(propylene oxide)-poly(ethylene oxide) triblock copolymer-based nanoparticles | n.m. | The VEGF-loaded nanoparticles and their gel formulation improved heart functions such as improved ejection fraction and cardiac output | [78] |
| Exosomes | Ischemic heart disease | Fe ₃ O ₄ core and a silica shell | 200 nm | The introduction of a magnetic field resulted in the accumulation and cleavage of hydrazone bonds between acidic pH of injured cardiac tissue, causing exosomes to release, leading to a reduction in infarct size and improved ejection fraction and angiogenesis | [79] |
| Atorvastatin and rapamycin | Valvular heart disease | PLGA nanoparticles | 99-103 nm | The modified valves showed a reduction in levels of TNF- α levels and increased IL-10. Further results showed resistance of valves to the calcification after implantation due to the release of drugs | [80] |
| Atrial natriuretic peptide (ANP) and linTT1 | Atherosclerotic plaques | Acetylated dextran | 100-200 nm | The results demonstrated that the nanosystem has the potential to exploit the "hitchhike" effect on M2-like macrophages and thereby improving the ability of the ANP peptide to target infarcted heart in a dual-targeting strategy | [81] |

Vascular endothelial growth factor (VEGF) chemically is a proangiogenic cytokine that promotes neovascularization in patients' hearts with ischemic heart. However, VEGF has a shorter half-life and rapid renal clearance rate. Oduk et al. [74] prepared VEGF-based nanoparticles (average size 113 nm diameter) for repairing the heart after myocardial infarction. The VEGF was encapsulated in the PLGA NPs, and increased the exposure time for VEGF (31 days exposure time), improved cardiac functions (after exposure of 4 weeks), protected the heart against the left ventricular remodeling were its pharmacological actions.

Simdax (levosimendan) is the most common and effective inotropic agent reported for improvement in myocardial contractility in heart failure patients [75]. Spivak et al. conjugated gold nanoparticles with the Simdax to evaluate the targeted delivery of the drug and the effect of sonoporation on nanoparticles [76]. The nanoparticles conjugated with the Simdax were administered to Wistar rats (chosen as a model for heart failure with doxorubicin-induced failure). However, the administration does not induce any changes in the liver, and no ascites were observed. However, the conjugated formulation showed higher hydrothorax reduction, but no significant difference was observed in recovery. Sonoporation enhanced the transfer of gold nanoparticles into the cell, and significant localization was observed in the mito-

chondria region. The work done by other researchers has been tabulated in Table 2.

A platform for inflammatory macrophage theranostics was developed by Qin et al. using gold nanorods (Au-NRs) [82]. Micro-CT (computed tomography) imaging of macrophages showed that the signal intensity increased with increasing concentration. Au-NRs intravenously injected into Apo E mutant mice elicited a little increase in CT intensity in the inflamed femoral artery. Laser therapy also increased the temperature of the irritated femoral artery by up to 50.5°C (808 nm). In the femoral artery restenosis, CD68-stained histology data demonstrated that macrophages had been damaged. As a novel theranostic platform treating atherosclerosis, this nanosystem seems to be non-toxic and promising. Detection of atherosclerosis might be improved by using computed tomography agents, such as gold. CNR (contrast-to-noise ratio) of Au-NPs is greater than the commercially available iodinated agent Visipaque™ [83]. However, CT imaging equipment itself entails radiation exposure, and numerous scans in a short period of time are unlikely to be therapeutically feasible. Radiation-related harm may be reduced in the future by using more sensitive CT agents. Phosphatidylserine and oxidized cholesterol ester derivative cholesterol-9-carboxynonanoate nanoparticles were synthesized by

Bagalkot et al. to target macrophages of the M1 inflammatory phenotype [84].

This nanosystem also includes gadolinium (Gd) and fluorescein isothiocyanate (FITC) for MRI detection and optical screening. Noninvasive MR imaging of atherosclerotic plaques in ApoE^{-/-} mice was made possible by combining nanoparticles Gd-FITC-LiLa. Inflammatory adipose tissue macrophages might potentially be used as a medicine carrier for them. In order to give a therapeutic anti-inflammatory effect, this nanocarrier was loaded with rosiglitazone (Rosi). Atherosclerosis imaging and treatment might benefit from LiLa NPs, according to the study's findings. A polyacrylic acid-coated magnetic nanoparticle conjugated with rtPA was developed by Ma et al. for use in thrombolysis and thrombosis diagnosis (PAA-MNP-rtPA). While free rtPA demonstrated no appreciable thrombolysis in rat right iliac arteries after 25 minutes of PAA-MNP-rtPA treatment, the 0.2 mg/kg dose of PAA-MNP-rtPA could efficiently dissolve the thrombus [85]. There was no MRI in this trial. MRI contrast agents PAA-MNP-rtPA might be tested in follow-up investigations because of the nanosystem's iron core. When Yang and colleagues synthesized core-shell NPs with Fe₃O₄ magnetic NPs for thrombolysis, they created a comparable NP [86]. For the breaking of blood clots, the NPs had 276 g of active rtPA per milligram. Magnetic guiding lowered clot disintegration time from 39.2 ± 3.2 to 10.8 ± 4.2 minutes. In rats, this nanosystem's biodistribution was studied using SPECT/computed tomography techniques (CT). The Fe₃O₄-PLGA-rtPA/CS-cRGD NP (Fe₃O₄-PLGA-rtPA/CS-cRGD) was synthesized by Zhou et al. in another study, which included the development of the Fe₃O₄-PLGA-rtPA nanoparticle with a core of rtPA and an outer shell of Fe₃O₄ and poly (lactic-co-glycolic acid) [87]. Fe₃O₄-PLGA-rtPA/CS-cRGD NPs dissolved clots three times faster than free rtPA did after 60 minutes of administration. Researchers found that CS-cRGD coating did not alter the MRI signal, and the NPs displayed a significant T2 signal in the rats' abdomens with thrombus. The precise targeting function of Arg-Gly-Asp (RGD) peptides was critical to the success of therapy and imaging. RGD might bind to active platelets at thrombus sites as a receptor antagonist of platelet membrane glycoprotein GP IIb/IIIa [88].

Using tagged mitochondria, Cowan et al. devised a method of cardioprotection [89]. Iron oxide NPs were used to identify mitochondria such that they could be detected by PET, fluorescence imaging, magnetic resonance imaging (MRI), and micro-CT. As predicted, fluorescence pictures of iron oxide NPs and Fluorine-18-rhodamine 6G are attached to mitochondrial amine groups through transmission electron microscopy. In order to lessen the extent of the infarct, mitochondrial transplantation was employed in the ischemic regions to enhance ATP content in the tissues. The infarct size of the rabbit ischemic hearts was significantly reduced following treatment with these tagged mitochondria. T2-weighted images of the ischemic left ventricle showed a strong signal from 18F-R6G-labeled mitochondria. Signals from the MRI and PET scanners were absent from the typical right ventricle. Infarct size could be reduced, and cell loss could be minimized using this method [90,

91]. This strategy might be used to safeguard the heart. Mitochondria-transplanted hearts exhibited a substantial decrease in infarct size compared to the control group of normal hearts. Iron oxide NPs are the most extensively utilized image contrast agents for magnetic resonance imaging (MRI), which is used to diagnose a variety of CVDs. For MRI and CT, perfluorocarbon and gadolinium NPs, as well as gold nanoparticles, have been developed for the detection of vascular damage and atherosclerosis. Atherosclerosis may also be seen with photoacoustic imaging agents such as copper sulphide, which provide a strong photoacoustic signal. Fluorescent dye and polymer are used in another theranostic device to monitor and evaluate treatment effects in the ex vivo environment. Because the human body has a far greater level of fluorescence than cells or mice, fluorescent drugs are unlikely to be used in clinical studies. Polymeric NPs can change and resorb in the body, making them prominent in cardiovascular nanomedicine. Oral, cutaneous, mucosal, or transdermal delivery of these NPs is possible [92].

PEG, PGA, and PLA are the most often utilized biodegradable polymeric nanocarriers (PLA). They are biodegradable because they are readily excreted as CO₂. PLGA has been widely explored as a CVD medication carrier [93]. Both SB431542 and CHIR99021 (model drugs) were given as dextran-coated nanoparticles to convert fibroblasts into cardiomyocytes. To administer the medicines, AcDX (acetaled dextran) nanoparticles functionalized with spermine were used. It is always attractive to reprogramme myofibroblasts and fibroblasts into healthy myocytes to replace lost cardiac cells [94]. The polymeric NPs containing quercetin increased water solubility and stability. This halted atherosclerosis and to boost medication effectiveness and minimize ROS generation; this antioxidant was encapsulated on PLGA nanoparticles [95]. Polymeric nanocarriers deliver antiproliferative drugs to injured vasculature [96].

ROS plainly damage heart cells and induce thrombosis (e.g., hydrogen peroxide). They have delayed medication release and fast blood circulation. As a consequence, thrombo-occluded vein clots disintegrate faster. These NPs include antioxidant (glutathione) and anticoagulant (heparin) properties. Controlled and targeted medication administration proved efficient in treating vascular disorders in two hours [97].

Quantum dots (QDs) are semiconductor nanocrystals with a 10 nm average diameter. They have varying luminescence qualities depending on their size, as well as different energy levels. There have been recent efforts to create heavy metal-free QDs that are less toxic since QDs have clinical safety restrictions due to the usage of heavy metals that may produce toxicity or other adverse effects [98]. Immunosensors for detecting cardiac myoglobin (cMyo), a significant biomarker for the diagnosis of MI, have been developed by Tuteja and colleagues. An immobilized template of GQDs was created by hydrothermally synthesizing and implanting them on screen-printed electrodes (SPEs). Finally, SPEs were treated with anti-cMyo antibodies to detect cMyo more precisely. Compared to the usual enzyme-linked immunosorbent assay (ELISA) tests,

modified SPEs showed a broad range of 0.01–100 ng mL⁻¹ and a detection limit of 0.01 ng mL⁻¹ (i.e., more than 400-fold in comparison) [99].

Silica NPs were recently employed to transport adenosine, a prototype cardioprotective drug, into I/R heart tissue [100]. Silica NPs can generate ROS, which can cause cytokine release and apoptosis [101]. IT injection of silica NPs raises hs-CRP levels in rats in a size-dependent way, as well as TNF- α , IL-6, and IL-1 levels. These particles promote inflammation in the cardiovascular system. After being exposed to silica nanoparticles, the levels of ET-1, D-dimer, LDH, and CK-MB rose. Following exposure to these particles, there was an increase in vascular permeability [102]. Another investigation found a small alteration in cell viability and genetic content [103, 104]. When BALB/c mice were given 10 mg/kg polyacrylic acid coated-Fe₂O₃ NPs, their heart rate was reduced acutely [104]. Sun et al. investigated the effect of Fe₂O₃ and Fe₃O₄ NPs (0.001–100 g/mL) on endothelial cells of the heart microvascular. Their findings demonstrated that these particles had no significant effect on plasma membrane permeability or inflammatory markers [102].

Superparamagnetic iron oxide NPs were found in the heart, lung, kidney, liver, and spleen after subcutaneous administration [105]. Iron oxide NPs cause oxidative damage due to ROS production. As a result, cytoskeletal disruption, decreased proliferation, and cell death ensued [106]. On the contrary, using confocal microscopy, it was also observed that negatively charged superparamagnetic iron oxide NPs had no significant effect on the actin cytoskeleton of heart cells while dramatically disrupting the actin cytoskeleton of kidney cells.

3.3. Nanofibers. Nanofibers can be defined as fibers with a small diameter of range 1–1000 nm. The nanofibers can be employed for cardiac tissue engineering and regeneration purpose. Many researchers have combined nanofibers with drug elution or embedded cells for regenerative engineering and treatment of dilated cardiomyopathy. The human inducible pluripotent stem cell-derived cardiomyocytes (hiPSC-CMs) were cultured on the cardiac patch using PLGA-based nanofiber scaffolds [107]. The patch showed >90% parallel alignment with ECM of the animal model myocardium and showed more calcium cycling. The high calcium cycling enables the cells to get contracted at a higher frequency. The presence of actinin and connexin-43 confirmed the maturity and terminal differentiation of cardiomyocytes. Another study also confirmed the use of PLGA in seeding embryonic stem cell-derived ventricular cardiomyocytes for regular electrical stimulation and was resistant to arrhythmogenesis [108].

Wu et al. prepared a 3D cellular anisotropic cardiac structure for tissue regeneration. The nanofiber yarn is made of polycaprolactone, silk fibroin, and carbon nanotubes. The yarn enhanced the cardiomyocyte's maturation. The three-dimensional hydrogel provided an environment for endothelialization and shown their potential to be used in 3D cardiac anisotropy [109].

Ischemia causes gradual loss to ECM, after MI causing the heart failure later. To combat this, Lakshamanan et al. prepared a nanofibrous scaffold using poly (1-lactide-co-caprolactone) (PLCL) and poly (2-ethyl-2-oxazoline) (PEOz) via electrospinning technique with a diameter of size 500 nm [110]. Due to the presence of both hydrophilic and hydrophobic polymers, both types of drugs/growth factors can be entrapped inside the scaffold. The scaffold fiber was loaded with VEGF and bFGF as the matrix, and their bioactivity towards the human umbilical vein endothelial cells (HUVECs) was evaluated. The scaffolds showed the release of growth factors from the matrix activating the signal molecules for HUVECs. *In vivo* results showed the initiation of angiogenesis and mimicked the ECM. Microscopic results confirmed the structural changes in cell morphology, such as the formation of lamellipodia and filopodia. Similarly, for heart failure, cardiac progenitor cells (CPCs), which can differentiate themselves into various other cell types such as cardiomyocytes, endothelial cells, and smooth cells, were immobilized on the 3D culture conjugated with nanofiber scaffolds. Scaffold showed environment mimicking the ECM and improved the differentiation of iPSC-CPCs forming the cardiomyocytes and increased number of cardiac troponin R positive cells [111].

Congenital heart disease is by birth type of defect causing failure in the right ventricular of the heart. Researchers reported the preparation of cardiac patches containing child c-Kit+ progenitor cells in polycaprolactone nanofibers [112]. The presence of gelatin caused the increase in the metabolism of neonatal and child CPC. The extract collected from the patch showed a reduction of fibrotic gene expression in rat cardiac fibroblasts. Also, the extract showed a positive effect of tube formation of HUVECs, showing the angiogenesis nature of the patch. Similarly, Kang et al. reported immobilization of umbilical cord blood-derived mesenchymal stem cells seeding fibronectin on the polycaprolactone nanofibers and coating with poly (glycidyl methacrylate) [113]. The nanofibers stabilized cardiac function and inhibited left ventricle modeling in an animal model with MI. The scaffold promoted cell elongation and adhesion efficiency while angiogenesis and mesenchymal differentiation activities were also reported. The electrocardiogram (ECG) showed an increase in LV ejection fraction in the animal group treated. Also, the reduction in the size of MI and fibrosis was reported with an increase in scar thickness. PCL-based nanoscaffolds with thymosin β 4 coating functionalized with murine-derived cardiomyocytes to improve cardiac functions were also reported [114].

Silk is one of the older biopolymers and has been extensively used in various medical applications. Researchers exploited silk fibroin to prepare a PVA/silk fibroin-based nanofibrous heart patch using an electrospinning technique with the size of 228 nm [115]. The fiber was cross-linked via glutaraldehyde and prevented its degradation. Due to the presence of silk fibroin, the mechanical properties got enhanced with a minimal rate of degradation. The patch acted as excellent homing material for human cardiac fibroblast cells showing good cellular proliferation. Another group of researchers reported the trilayered patch consisting

TABLE 3: Nanofiber-based approaches for cardiovascular disease treatment.

| Name of polymers used | Cells/drug entrapped | Diameter of fiber | Outcome of study | References |
|--|---|----------------------------|---|------------|
| Molybdenum disulfide, reduced graphene oxide, and silk fibroin | TBX18-hiPSCs | 450 nm | Scaffolds were able to induce cardiac differentiation and controlled self-renewal potency | [121] |
| Silk-fibroin, superparamagnetic iron oxide nanoparticles | Mouse embryonic cardiac cells | 250 nm | The presence of silk fibroin supported cardiac differentiation; upregulation of cardiac genes such as GATA-4, cardiac troponin T, Nkx 2.5, and alpha-myosin heavy chain | [122] |
| Polyethylene terephthalate/graphene oxide | Human umbilical vein endothelial cells | 147 ± 38 and 253 ± 67 nm | Improvement in cardiac electroconductivity, the substrate could support HUVECs; improved cardiac cell attachment and proliferation | [123] |
| Poly(L-lactic acid) and polyurethane | Rat cardiomyoblasts (H9C2 line), human and rat cardiomyocytes | 178 ± 32 nm to 367 ± 66 nm | Prepared nanofibrous mats using solution blow spinning method; mats showed proliferation activity for reported cells | [123] |
| Peptide amphiphile | Fractalkine | n.m. | Targeted the fractalkine in carotid artery balloon injured model and showed 4.2-fold enhancement in fluorescence and increased dose-dependent manner | [124] |
| Poly(L-lactide-cocaprolactone) | Fibroblast-derived ECM | 500 to 900 nm | Improvement in cell viability, molecular diffusion, and cell maturation | [124] |
| Polyvinyl alcohol, methylacrylate grafted lignin | Betulinic acid | ~1 μm | Formulation proved to be noncytotoxic on normal endothelial cells, inhibited cytokine levels, increased vasodilators, and prevented myocardial cells from degeneration | [125] |

of silk fibroin and PVA forming the middle layer as hydrophilic while the top and bottom layers were made from PCL and polylactic acid (PLA) using layer-by-layer technology. The patch showed biocompatibility against the human endothelial cells. SEM results confirmed the property of endothelial cells to get dispersed and get themselves adhere to the surface of patch forming endothelial cell layer [116].

Rufaihah et al. reported a nanofiber scaffold made of glycosaminoglycan mimetic peptide, capable of inducing angiogenesis after MI without any stem cells. Injecting nanofibrous gels increased VEGF-A expression and deployment of vascular cells for better cardiac performance [117]. Survival of cardiac performance could be accounted for by the overexpression of Ang-1 that activates the prosurvival pathway via interaction with integrin receptors of muscle cells and promotes survival [118]. Also, the presence of Ang-1 prevented the loss of cardiac myocytes. Overexpression of VEGF might be a reason for the activation and migration of the cardiac stem cell population for repairing MI [119].

Shojaie et al. prepared an on-demand drug release-based patch of gelatin and oligoaniline/PVA via electrospinning technique [120]. Owing to the hydrophobic nature of aniline oligomer, the increasing concentration decreased the diameter from 300 to 150 nm. Also, the increase in aniline oligomer increased conductivity, controlled thermal properties, and sustained drug released with a low degradation rate. The lower diameter of fibers exposed a high surface area to surroundings, and degradation is enhanced. However, due to the presence of oligoaniline, the penetration of media is restricted and repels the aqueous media, thus lowering the degradation rate. Work done by other researchers has been cited in Table 3.

Polyvinyl alcohol (PVA)/chitosan nanofibers electrospun using MWCNT-incorporated polyvinyl alcohol (PVA) were made by Liao et al. Microwave carbon nanotubes (MWCNTs) were introduced into PVA and chitosan fiber blends (160 nm diameter) [126]. MWCNTs (7-15 nm in diameter) were attached to hydrophobic polycaprolactone (PCL) sheets and nanofiber meshes by Wickham and colleagues using thiophene. Mechanical strength might be increased without altering mesh shape in this group. Increased cardiac progenitor cell (CPC) proliferation was also seen when thiophene-conjugated CNTs were added to PCL polymers [127].

The alignment, mechanical toughness, and electrical conductivity of fibers were significantly improved when CNTs were incorporated into other materials, including gelatin nanofibers and poly (glycerol sebacate) (PGS). The cardiomyocytes were able to beat strongly and synchronized because to the improved substance. An increase in Cx43 expression and a decrease in the excitation threshold were achieved by adding CNTs. Aside from that, CNTs enhance the scaffold's ability to imitate the left ventricle's anisotropic structure [128]. PLGA and CNF composites were studied by Stout et al. for cardiomyocyte function. They found that CNFs improved the conductivity and cytocompatibility of PLGA, which in turn boosted the adhesion and proliferation of cardiomyocytes. CNFs also boosted the density of cardiomyocytes (up to 25:75 wt percent PLGA:CNFs). The addition of CNFs of any diameter improved the electrical conductivity of PLGA/CNF composites [129]. A new injectable scaffold for cardiac tissue engineering was developed by Meng et al. [130] by combining CNFs, self-assembling rosette nanotubes (RNTs), and poly (2-hydroxyethyl

methacrylate) (pHEMA) hydrogel. The density of cardiomyocytes in the pHEMA hydrogel rose when more CNFs and RNTs were introduced into the matrix. CNFs enhanced conductivity and surface roughness but decreased tensile modulus and contact angle when added to composites. Patterns of aligned CNFs (100 nm in diameter) were produced on the surface of PLGA by Asiri et al. to replicate the anisotropy of the myocardium (50:50 PGA:PLA weight ratio). According to the findings, CNF alignment enhanced the scaffold's cardiomyocyte density. Comparing a vertical (0.1 S/m) and horizontal (0.0025 S/m) conductivity of the PLGA scaffold with that of genuine heart tissue revealed that aligning the CNFs improved both the vertical and horizontal (0.0025 S/m) conductivities.

To imitate the ECM, various synthetic biomaterials were designed with a nanoscale level of detail. Cardiac tissue may be formed by using the 3D growth and differentiation of cardiomyocytes in the NF poly (L-lactic acid) matrix [131]. Structures with varied PCL/PGA proportions in the PCL and poly glycolic acid NF scaffolds maintained live cells that expressed the major cell marker proteins of cardiomyocytes, smooth muscle cells, and endothelial cells (ECs) inside the subcutaneous tissue of mice [132]. It is generally accepted that synthetic or biological polymeric biomaterials, like cardiac patches, may aid cell organization but, owing to their inherent weak conductivity, restrict the patch's capacity to contract, in general. In order to do this, a polymeric patch must be strengthened or implanted with conductive nanoparticles utilizing several ways [133]. Cardiac tissue engineering scaffolds and patches may be made from electroactive materials, including polypyrrole, polyaniline, and polythiophene, which have been shown to be effective. Biocompatibility and biodegradability are two of the most pressing issues that need to be addressed, but the ability of biomaterials to be changed is also a concern. Since electrically conductive nanostructured materials may be used in cardiac tissue engineering, additional research is needed to understand their potential usage [134]. Polymeric nanoparticles may be used to change cardiac patches, but their usefulness as drug delivery methods to treat myocardial infarction must not be overlooked. NPs made from deblock copolymers of poly (ethylene glycol) and poly (propylene sulphide) (PPS), loaded with ginsenoside Rg3, have been shown in a rat ischemia-reperfusion model to enhance heart function and decrease infarct size by decreasing oxidative stress, inflammation, and fibrosis [135].

Myocardial ischemia-reperfusion may be treated effectively and efficiently by infusing appropriate dosages of anti-inflammatory medication (adenosine) into multilayered scaffolds with cardio-inductive effects on stem cells [136]. There is an improved therapy for reperfusion damage using polymeric core shell polymeric nucleic acids with adenosine-core shell polymeric NPs [137]. To improve cardiac scaffolds after an AMI, polymeric nanoparticles capable of recognizing particular ECM metalloproteinase have also been tested [138].

3.4. Carbon Nanomaterials. Carbon being the eternal element has shown its good nature in the medical field also.

Carbon not only forms strong bonds but is also nontoxic to normal cells. Due to its nanoscaling, high thermal conductivity, and high affinity towards interaction with proteins, carbon nanomaterials (CNMs) prepare a 3D environment for the growth of cardiac cells [125]. CNMs have also been reported as proliferation, differentiation, and maturation medium for various cardiac cells [139–142].

Based on novel properties of CNMs, Tashakori et al. prepared CNM-based collagen scaffold for repairing the myocardial-based injury [143]. The collagen-CNM scaffolds impregnated into damaged heart tissue were able to improve the repair of the heart, and no toxic response was visible. The material also induced neovascularization. Stout et al. [129] prepared PLGA and carbon nanofiber-based material for cardiac application. The presence of CNM caused the increase in conductivity, and cytocompatibility in a dose-dependent manner also promoted the adhesion and proliferation of cardiomyocytes.

Ataei et al. [144] used CNMs in the preparation of heart valves. The researchers functionalized a carbon nanotube with heparin and combined heparin functionalized carbon nanotube (HCNT) with plasma-treated polyurethane using the solvent casting method. The presence of heparin resulted in surpassing the dispersal and calcification resistance for CNMs. Also, the addition of CNT to the matrix caused enhancement in modulus. The initial results with L929 cells showed no cytotoxicity and were more blood compatible. The contact angle increased remarkably with the introduction of OVS. Also, the adhesion increased towards the L929 fibroblast cells. Similar results were reported for the platelet adhesion test. Pyrolytic carbon is a common material used for biomedical engineering but is prone to microbial attack. Silver nanoparticle (Ag-NP) deposition used the pulsed laser deposition technique. Ag-NPs have proven activity against gram-positive and gram-negative bacteria; thus, the microbial load can be reduced [145].

Ahadian et al. [146] reported the use of CNMs for cardiac tissue engineering. Researchers combined CNTs with poly (octamethylene maleate (anhydride) 1,2,4-butanetricarboxylate) using UV light as a crosslinker for preparing elastomeric scaffold. With the increase in CNT content, surface moduli of scaffold increased while bulk moduli decreased. The decrease in CNT content resulted in a significant reduction in tissue maturity. The scaffolds also showed coordinated beating with the cardiomyocyte cells. Chitosan is one of the most reported biopolymers for biomedical applications. Chitosan has been coupled with carbon nanomaterial for cardiac tissue engineering. Martins et al. reported the formation of composite scaffolds with carbon nanofibers dispersed in chitosan solution. The scaffolds showed a seeding nature for neonatal rat heart cells; after 2 weeks, the pores of scaffolds were filled with cells. The presence of carbon nanofibers caused enhancement in the expression of cardiac-specific genes required for contraction and electrical coupling [147].

Hybrid hydrogels of reduced graphene oxide and gelatin methacryloyl were reported for cardiac tissue engineering [148]. The hydrogel thus formed has enhanced electrical conductivity and mechanical properties. The hydrogel

TABLE 4: Tabulated literature citing carbon nanomaterials for cardiovascular diseases, where n.m. is not mentioned.

| Type of carbon nanomaterial | Name of polymer | <i>In vivo</i> studies | Electrical interpretation | Size | Biological interpretation | References |
|---|--|-----------------------------------|---|---------------------------|--|------------|
| Carbon quantum dots (CQD) | Poly glycerol sebacate; polycaprolactone | n.m. | The presence of QD, increased electrical conductivity | 376.82 ± 150 nm | 1% CQD, decreased cell viability; 0.5% CQD, persisted cell viability | [149] |
| Carbon nanotubes (CNT) | Polyurethane, chitosan | H9C2 cells | Increase in electrical conductivity | n.m. | Biocompatible with H9C2 cells | [150] |
| P-Phenylenediamine surface-functionalized CQD | Silk fibroin/ polylactic acid | Rat cardiomyocytes | Improved electrical conductivity among cardiomyocytes | n.m. | Increased cardiac marker gene expression | [151] |
| Carbon nanotubes (CNT) | Polyvinyl alcohol, chitosan | Rat mesenchymal stem cells | The presence of large quantities of CNT, decreased electrical conductivity | 255 ± 3.5 to 307 ± 5.9 nm | Expression of Nkx2.5, Troponin I, and β-MHC cardiac marker increased significantly | [152] |
| Carbon nanotubes (CNT) | Gelatin with methacrylate anhydride | Neonatal rat ventricular myocytes | Showed apparent spontaneous electrical conductivity; Beta1-integrin pathway was involved in modulation of electrical impulses | n.m. | Increase in expression of p-FAK and RhoA in cardiac constructs | [153] |
| SWCNTs | Gelatin | Rat H9c2 cells | n.m. | n.m. | Increased expression, proliferation, and differentiation | [154] |
| MWCNTs functionalized with carbodihydrazide | n.m. | HL-1 cardiomyocytes | The electrical conductivity of the scaffold was 0.015 S/cm | 166 nm | Improved heartbeat and cellular viability | [155] |
| MWCNTs | PCL | Rat H9c2 cells | Conductivity increased with PCL content | n.m. | Myoblast cells showed adherence for 4 days | [156] |

supported cellular differentiation and proliferation of NIH-3T3 cells. Also, the cardiomyocytes showed contractility and a faster heartbeat. The scaffold has a mechanism for electrical current flow, thus reducing charge distribution and potential propagation impedance. Work done by other researchers has been cited in Table 4.

Research by Kaya et al. used an electroconductive hydrogel created by reinforcing reduced graphene oxide (rGO) into an acid-gelatin-poly (ethylene oxide) (PEO) hydrogel in order to evaluate the kinetics of irbesartan's drug release. Angiotensin receptor blockers (ARBs) are used to treat excessive blood pressure in individuals with CVD. Irbesartan belongs to this family. Models of irbesartan kinetics from electroconductive hydrogel are used in this work to mimic and analyze release kinetics. According to the study, the hydrogel that contained 20% rGO successfully released irbesartan over the course of 10 days. As a medication carrier for treating CVDs, this composite demonstrates the effectiveness of rGO in hydrogel [157]. The release kinetics of diltiazem were studied in a work by Sarkar et al. using a drug carrier membrane made from GO and methylcellulose (MC). Diltiazem, a calcium channel blocker, is used to treat arrhythmias and high blood pressure. To ensure effective

and regulated drug release, the researchers in this work used a GO/MC composite matrix [158].

CNTs functionalized with PEI/polyamidoamine dendrimer (PAMAM) were used to deliver miR-503 oligonucleotides to increase angiogenesis during CVD in another investigation. CNTs have been shown to be effective in delivering miR-503 and promoting angiogenesis [159]. The use of CNTs in stent coating has also been shown to inhibit in-stent restenosis by delivering angiogenic chemicals. Endothelial dysfunction and enhanced smooth muscle cell proliferation surrounding the stent may develop after stent implantation in the coronary artery. There is an increased risk of heart attacks and other symptoms as a consequence of this fast reocclusion of the coronary artery, which may be connected with recurring heart attacks. Polyacrylic acid (PAA) coated SWCNT in a fibrin hydrogel containing angiopoietin-1 and VEGF was designed by Paul et al. to address this issue. A canine model was used to evaluate the effectiveness of this mixture. Biohybrid stents like this one increased reendothelialization, reduced necrosis development, and avoided stenosis in the wounded arterial segment [160]. It has been shown that MWCNTs, GO, and carbon black can be used as drug transporters in research by

Renyun et al. According to this research, GO had the largest loading capacity among the CNMs studied (i.e., there are additional parameters, such as pH and functionalization, that have a role in the release profile of medication, according to this research) [161].

Graphene's toxicity in biological systems is mediated by its planar dimensions, particle concentration, and surface characteristics [162, 163]. Long-term graphene exposure and buildup in cells produces inflammation, lasting genetic damage, and cell death [164]. The size and dispersion of graphene nanosheets are key challenges that must be addressed in order to reduce toxicity in a biological system. GO and hydrophobic graphene generated oxidative stress in the lungs, while hydrophobic graphene dispersed in pluronic was biocompatible and evoked no toxicity *in vivo*, according to Duch et al. This work emphasized the significance of surface functionalization and dispersion in improving graphene biocompatibility [165]. Chen et al. used different diameters of GO (50–200 nm, 500 nm, and >500 nm) at varied doses (0.1, 1, 10, and 100 mg/L) to evaluate their impact on embryonic zebrafish development. According to this study, GO at 100 mg/L concentration resulted in a longer hatching time for zebrafish embryos, shorter body length, changes in heart rate and blood flow, and an increase in apoptotic gene expression. When the concentration of GO exceeded 10 mg/L, the toxicity was not dependent on the size of the GO [166]. As a result, selecting the size and dosage of CNMs is critical for their safety and effectiveness in therapeutic applications.

Conjugating harmless chemical groups or eliminating reactive functional groups on the surface of graphene-based composites is commonly used to make them biocompatible. The toxicity of SWCNTs and acid functionalized SWCNTs was assessed in mice using oropharyngeal aspiration in one research. Acid functionalized SWCNTs were found to promote neutrophil and edoema production in the lungs in a dose-dependent manner [167]. Because of its bulky and massive size, CNTs tend to cluster in aqueous solutions compared to smaller CNMs that can be readily dispersed. This is the primary cause of CNM-mediated cell toxicity [168].

3.5. Dendrimers. An adequate description of dendrimers' structure may be found in the Greek word for "tree," dendron, which translates to "branch" [169]. With their multi-branched, three-dimensional structure, and low polydispersity, dendrimers are really unusual [170]. Dendrimers, as nonviral vectors for therapeutic applications, seem to have numerous benefits over other nanotechnologies. They are superior to other viral and nonviral equivalents because of their high solubility, higher stability, low immunogenicity, and capacity to support the successful transport of therapeutic molecules, DNA, and RNAs [171]. Due to the nanoscale environment provided by considerable branching, the focal core of a dendrimer has been used to host chemical species. The perimeter of dendrimers may show a variety of functional groups, enabling them to interact with the surrounding molecular environment and with other dendrimers. Additionally, the dendrimer's repeating

units enable the modification and encapsulation of pharmacological molecules inside the dendrimer [172].

To prevent atherosclerosis, it has these properties; thus, it may be crucial [173]. For injured tissue, NO encapsulation inside dendrimers has been found to be an effective treatment option. Poly (propylene imine) dendrimers have been shown to successfully release NO, suggesting that they might be used as drug delivery systems in the future [174]. Attempts have been made to regulate the elevation of inflammation at specific areas inside injured vasculature using dendrimers with promise as gene delivery vehicles for treating CVDs. Dendrimers containing DNA plasmids have been demonstrated to boost the gene's survival, stability, and vitality in the nucleus indicating that they might be used as potential therapeutic agents [175].

Overstimulating, the heart and blood vessels may lead to fibrosis and vascular and cardiac hypotrophy. Overexpression of angiotensin II, a peptide implicated in the RAAS, may lead to heart disease and cardiac remodeling. Cardiovascular disease may be prevented and treated by the reduction of its activation. The angiotensin II receptor type 1 is responsible for the majority of angiotensin II's harmful effects (AT1R). To lower AT1R expression in an ischemia-reperfusion paradigm, PAMAM dendrimers were utilized as siRNA carriers [176]. Nifedipine has a limited bioavailability in the human body because of its low water solubility throughout a pH range of 4–13. A pH of 7 improved the water solubility of nifedipine in amine or ester-functionalized PAMAM dendrimers G0 to G3. It was found that the ester functional groups were more effective than the amine ones on the surface. PAMAM dendrimers may solubilize nifedipine in order to enhance its therapeutic properties [176].

To combat CVD, researchers have turned to gene therapy, and as a result, several have investigated ways to better deliver genetic material to the desired locations, as well as ways to control the upregulation of inflammatory genes using nanocarriers such as cationic liposomes. Cationic liposomes, like dendrimers, bind polyanionic DNA and deliver it to cells. Gene transfer into mouse cardiac grafts was studied using a G5 dendrimer with an ethylenediamine core. X-Gal labeling revealed a 1000-fold increase in G5 dendrimer expression in both myocytes and graft filtering cells over the course of seven to 28 days. Dendrimers were found to improve plasmid survival rates [177–180].

In the nucleus, dendrimer improved gene stability and viability. Higher transfection and viability may be achieved by lowering the charge ratio of DNA to dendrimer [181]. The same was done by Turunen et al., who compared the transfection efficiency of different lipids and fractured PAMAM and poly ethylenimine (PEI) dendrimer *in vitro* against smooth muscle cells (SMC) as well as endothelial cells (ECV 304) and chose fractured G6 PAMAM dendrimer and PEI dendrimer with 25 kDa and 800 kDa for *in vivo* studies. They stated that transfection was dependent on charge ratio and observed that the highest transfection efficiency was shown by fractured dendrimer at charge ratio 6, and as the charge ratio increased, cell survival rate decreased for fractured dendrimer as well as PEI dendrimer, but the

survival rate was higher in fractured dendrimer between both dendrimers. In vivo experiments indicated that β -galactosidase activity with a broken dendrimer at a charge ratio of 3 was the most effective transfection method. It was shown that the transfection effectiveness of PEI and fragmented dendrimer was greater than that of liposomes and cationic-plasmid liposomes [182]. Gene transfer and expression in the mouse vascularized transplant model may be improved using the G5 EDA core dendrimer. β -Galactose expression was monitored for 7 to 14 days after the plasmid pMP6A β -gal expressing β -galactose was combined with dendrimer and perfused into coronary arteries. They also found a charge ratio of 1:20, and serotonin incubation for two hours increased the expression [183]. The electroporation and DNA/dendrimer combination improved gene transfer in a mouse heart transplant study by Wang et al. Electroporation of β -galactosidase reporter gene and starburst PAMAM dendrimer into live human myocardium resulted in a 10- to 45-fold increase in gene expression [184]. By connecting mAb to PAMAM dendrimer in tissue that expresses overexpressed adhesion molecule P- and E-selectin on activated endothelial cells, it is possible to increase the effectiveness of transfection. They employed avidin and biotin to cross-link anti-E/P selectin antibody to a premade superfect DNA complex, which was then used to transfect a reporter gene into the E-selectin-expressing cells of CHO cells [185].

One disadvantage of dendrimers is that they frequently have highly charged exteriors due to their high number of branches at their surface, each with their own surface charge; this can often result in either a highly cationic or highly anionic nature, which can lead to toxicity issues if not fully addressed [186].

3.6. Cell Membrane Coated Particles. As an alternative to PEGylation, cell membrane coating technology relies on natural cell membranes to protect manufactured NPs. Coating NPs with functional membrane proteins on their surface helps them escape the body's immune system and prolong their circulation (better biocompatibility), but it also provides them with numerous cell-like biofunctions because of their ability to mimic cell membrane proteins (cell-mimicking properties). Hu et al. were the first to cover PLGA nanoparticles with an erythrocyte membrane [187]. Their work employed hypotonic medium hemolysis to remove the RBC membrane, which was then fused with PLGA NPs to produce RBC membrane camouflaged NPs (RBC-NPs). In addition, they demonstrated that the RBC membrane proteins were transferred onto PLGA NPs effectively. As a further bonus, the RBC membrane-coated NPs remained stable even after six hours of coculture with HeLa cells. Consequently, a nanoplateform has an exceptional potential to evade immune clearance, allowing it to remain in the body for an extended period of time. This nanostructure might be used as a generally effective medication delivery platform against CVD if small-molecule medicines are placed into the inner PLGA core. PLGA NPs encased in RBC membranes (RBC/RAP@PLGA) have been described by Wang et al. After treatment with this nanoplateform, the average area

ratio of plaque to vascular lumen dropped from 47.95 percent to 31.34 percent, which was superior to the free medication group in terms of advancement of atherosclerosis (from 47.95 percent to 42.42 percent) [188].

Platelet membrane-coated PLGA NPs produced by Hu et al. were the first to show preferential attachment to injured human and rodent vascular tissue and MRSA252 [189]. With the right loading agents, these platelet membrane-coated nanoformulations might be used to treat thrombosis, arterial damage, and sepsis. Platelet membrane-coated PLGA nanoparticles (PNPs/LBK) were manufactured by Wang et al. in order to combat the formation of thrombus [190]. Consequently, PNP/LBK has a greater potential to target thrombuses while reducing the danger of hemorrhagic complications.

In the event of a thrombus, a hypoxic environment increases the formation of ROS and tissue destruction in the affected area. Platelet membrane-encased argatroban-loaded polymeric nanoparticles (PNPArg) were recently produced by Zhao et al. to treat thrombus. An anticoagulant medication known as argatroban has been shown to have excellent therapeutic benefits on many thrombotic illnesses, and the inner core of their method is poly (vanillyl alcohol-cooxalate) (PVAX), an H₂O₂ degradable polymer that is capable of scavenging excess ROS [191].

Virus-like particles (VLPs) are naturally occurring viral genome encapsulators. To a growing degree, theranostic platforms using VLPs are becoming more popular due to their many advantages over traditional theranostic platforms. Examples of VLP cargo molecules include chemotherapeutic medicines, small interfering RNAs (siRNAs), RNA aptamers, proteins, and other peptides and proteins, among others [192–194]. A targeting function may be added to VLPs by genetic engineering. Insertions or extensions of peptides and proteins may be directly inserted into the main amino acid sequences of the coat proteins (CPs), allowing their presentation on either the interior or outer surface of the VLP [195–197].

Trifunctional SV40-based NPs were produced by Sun and colleagues to transport Hirulog peptide. Near-infrared quantum dots (CGNKRTRGC) and cyclic peptides (CGNKRTRGC) were put into the nanosystem for targeting the p32 protein on macrophages. NPs that were specifically targeted by ApoE(-/-) mice produced a fluorescent signal in the plaques that was three times brighter than that of untargeted particles. In ApoE knockout mice, SV40 NPs delivered Hirulog to atherosclerotic plaques. Mice injected with SV40 NPs had more antithrombin activity in their aortae than those injected with SV40 NPs that were not treated. Atherosclerosis medication delivery and molecular targeting will both benefit from this novel kind of NP [198].

4. Challenges for Nanomedicines for CVD

It is impossible to tell how long a nanomaterial has been present in a biological cell. There is insufficient long-term evidence to provide an accurate approximation of a definitive response. The possible negative consequences of a foreign body inside a live cell are also up in the air at this

point. The negative impacts of nanomedicines at the cellular level may express themselves as symptoms at the level of the patient's body. However, there is no consistent evidence available on the biological safety of NPs at the current time. Although safety guidelines and tests have been created, hazard and risk identification is now done on a case-by-case basis, rather than in bulk. The chemical composition of the nanoparticle has the potential to produce direct toxicity inside a live cell. The chemical structure of the particles determines the toxicity of nanoparticles. For example, the toxicity of carbon nanotubes is a direct result of the mechanical structure, size, kind of carbon isotope employed, surface coating, and relative carbon concentrations of the nanotubes in question.

The protein corona formation is a major issue in focused nanomedicine. Once in the bloodstream, the nanocarriers are opsonized, meaning they are phagocytized by MPS and subsequently expelled. The protein in question has been widely investigated for a decade and is called protein corona [199]. In interaction with biological fluids, proteins create protein coronas on NPs. The protein corona may influence the biological destiny of nanocarriers by enhancing mononuclear phagocyte system absorption [200, 201]. Protein corona has been found to be deleterious to active targeting techniques as well as MPS absorption [202]. The biological corona coating reduces the selectivity of the targeted ligand [203]. For example, following incubation with plasma, transferrin-modified silica NPs lost their targeting capacity [204]. Despite considerable attempts, few viable solutions have been developed to reduce corona-induced mistargeting. One method involves coating NPs with zwitterionic chemicals. For example, zwitterionic coatings have produced corona-free Au-NPs [205].

Recent research has demonstrated that iron compounds may cause ferroptosis, a novel kind of programmed cell death linked to I/R damage [206]. The Fenton reaction/iron metabolism leads to excessive ROS generation, resulting in regulatory cell death [207]. These results question the usage of iron-based NPs and advice professionals to choose NP composition carefully. Long-term usage of nondegradable inorganic NPs requires evaluation of their biological destiny and safety. The liver proteolytic enzymes may destroy polymeric-coated Au-NPs. This shows that the NP physicochemical qualities may change *in vivo*, causing unwanted toxicity, aggregation, or immunological activation. The altered physical and chemical features of NPs complicate the inflammatory response of the human immune system, causing greater unfavorable consequences on the heart failure process. Thus, additional research on NP biological destiny is required [208].

The nanobiointeraction is one of the primary hurdles in translating theranostic nanomedicine to clinics. When nanomedicine interacts with biological material, it may cause immune reactions, inflammation, or other illnesses. The hazardous impact of nanoformulations is highly dependent on size, zeta-potential, and solubility [209]. When nanoparticles enter a biological system, they interact with proteins, forming a surface "corona." It also changes their size, stability, dispersibility, pharmacokinetics, biodistribution, and

toxicity [210]. Also, several nanoplatforms elicit an immediate adverse immunological response called complement activation-related pseudo allergy [211, 212]. Thus, studying nanomedicines' physicochemical properties in relation to pathophysiology and disease heterogeneity is vital. Furthermore, theranostic nanomedicine is not a one-size-fits-all notion, since therapy differs from person to person [213]. Theranostic nanomedicines are also challenging to synthesize in a controlled and repeatable manner. Large-scale nanoparticle production has poor batch-to-batch repeatability, variable physical and chemical properties, and low yield. Due to the difficulty imposed to pharmaceutical firms, nanoplatforms with arduous and sophisticated production procedures seldom make it into the clinic [213, 214]. Since theranostic nanoparticles are multifunctional units, more accurate chemistry, manufacture, and control are required, coupled with excellent manufacturing practice.

A third key problem is the large gulf between scientists and regulatory bodies. Many government rules regulate the commercialization of nanomedicine based on quality control, manufacturing methods, safety profile, and patent protection. The lack of clear regulatory and safety requirements hinders timely and successful theranostics market translation [215].

Determining the relationship between patient biology and disease heterogeneity and nanomedicine can help overcome the biological limitations of nanotheranostics. Before starting clinical trials, nanoformulations must be thoroughly tested in several preclinical animal model systems. For treating and imaging human patient groups, preclinical investigations in animal models are often beneficial [216]. The early phases of clinical development need the use of nanotoxicology profiles consisting of standardised laboratory procedures for assessing patient risk [211, 217]. Noncancer disorders have normal vascular architecture; thus, developing nanotheranostics for them is important. Making biomimetic NPs that mimic natural cell functions (such as secretory chemicals, cell surface markers, and extracellular matrix) has a lot of promise for theranostic use. Using stimuli-based smart nanoparticles to deliver therapeutic loads selectively at the site of action may enhance theranostics' real-world effectiveness. Personalized treatment plans for illnesses with heterogeneity, malignancy, and adaptability may benefit from real-time monitoring and provision of this kind. Academia is the source of nanoparticle-based medicinal delivery methods. They often understand the technological problems encountered by industry in commercializing techniques. To close this gap, increased coordination between labs and drug firms is needed. GMP modifications for large-scale theranostic NP production are required.

5. Future Perspective

The status of nanomaterials is midway. Though nanomaterials had been exploited to some extent, some groundbreaking research is still on its way. The use of three-dimensional printing is not new in the pharmaceutical world. It has been used in various applications, such as dosage form

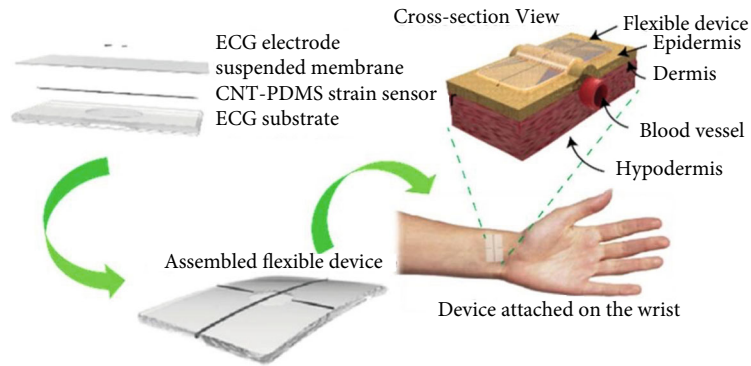


FIGURE 2: Schematic of the CNT-PDMS wearable device structure for measurement of wrist pulse pressure and ECG. Here, the ECG signal was captured by the flexible CNT-PDMS ECG electrodes. The shape change of blood vessels during a wrist pulse induced the resistance change of the CNT-PDMS strain sensor. Reproduced with permission from reference [222].

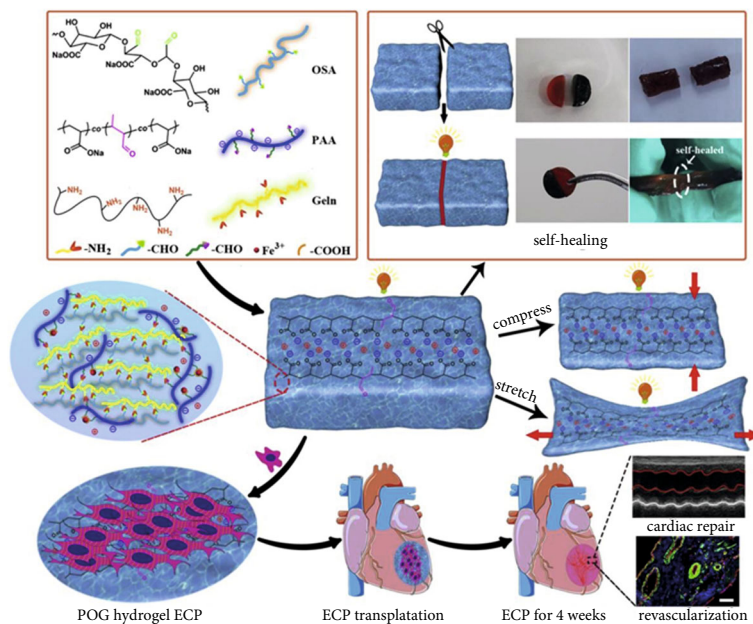


FIGURE 3: Schematic illustration about the tunable self-healing POG1 hydrogel fabrication and its application in myocardial infarction repair. Reproduced with permission from reference [223].

preparation to complex tissue recreation. It consisted of bioink (material containing active or cells), printer, and substrate [218]. Ho et al. reported the fabrication of cardiac tissue scaffolds using PCL and CNTs supported the proliferation of H9C2 cells [156]. Kanawati et al. reported the fabrication of a heartbeat synchronization device for a 76-year-old patient with congenitally corrected transposition of the great arteries (ccTGA) [219]. A precise 3D model with anatomic specification, same as that of the patient body, was printed. 3D printed heart models can also help understand the patient's status better and help find the solution for surgery procedures [220].

Apart from 3D printing, now sensors are also conjugated as point-of-care devices. Rezaei et al. reported the fabrication of sandwich-type immunosensor-based carboxylated multi-walled carbon nanotube for detecting the cardiac Troponin

I. These nanofibers were fabricated in carbon electrode and utilized enzyme-labeled amperometric immunoassay and immobilized horseradish peroxidase enzyme. The detection limit ranged from 0.5 to 2 ng mL⁻¹ in the case of the average person, while in the case of an infarcted patient, > 20 ng mL⁻¹ was the limit [221].

Su et al. reported a wearable device measuring CNT and polydimethylsiloxane's electrical impulses based on piezoresistance and voltage sensing phenomenon [222]. The device measured wrist pulse pressure and cardiac electrical signal based on the change in resistance and pressure with device sensitivity of 0.01 Pa⁻¹. The device can be worn on the wrist, and ECG signals after physical activity are transmitted using Bluetooth, and data is captured on a mobile phone and analyzed as an early warning (Figure 2). Due to regular movement of the heart and associated parts,

extensive wear and tear are observed; these polymer patches and scaffolds have lower life. To solve this problem, Song et al. prepared self-healing ionic hydrogel made of polyacrylic acid and oxidized alginate (OA)/gelatin (POG) (as shown in Figure 3) [223]. The hydrogel showed super stretchability (>500% strain) and compressive strength (>85% strain). The hydrogel showed more oriented sarcomeres than the control group after *in vivo* results showed robust left ventricular remodeling and restoring heart functionality.

Initially, percutaneous coronary lumen enlargement was treated with balloon angioplasty, also known as plain old balloon angioplasty. Though this technique persisted in the market for many decades, the risk of abrupt closure and nondurability and restenosis decreased its trend [224–226]. Later, the metallic stents took their place and shown remarkable results in improving procedural success, but they were costly [227–229]. However, they were considered as standards in their use and rule market for many years. Plastic stents and metallic stents had similar output; no significant difference was observed [230]. Later, drug-eluting stents come into play. A clinical trial comparing metal stents and drug-eluting stents on patients with antiplatelet therapy showed drug-eluting stents better with low mortality, MI, and stroke [231]. In a clinical trial conducted on biodegradable drug-eluting stent containing sirolimus and everolimus, a total of 1300 patients participated [232]. The stent with sirolimus elution showed better results due to lower lesions of the ischemic heart observed. Three-dimensional printing can also be hyphenated with the stent preparation [233]. Thus, there is still a way ahead in terms of clinical trials and its usefulness in regular day life.

6. Conclusions

As theranostic agents, nanotechnology and nanomedicine may be utilized to detect and treat cardiovascular problems. To distribute drugs to injured regions, small particles act as nanodevices or nanotransporters. Nanocarriers offer promise for effective, tailored medicine, and gene delivery that overcomes challenges of solubility, bioavailability, and other pharmacokinetic aspects. Many CVDs, treatment choices, and current medical breakthroughs are discussed in this paper. It highlights the progress made in the administration of drugs to cardiovascular tissues with greater precision. Studies in the lab and in the animal model of several cardiovascular nanoformulations have yet to be translated into the clinic. It handles pharmaceutical scale-up, release efficiency, important regulatory constraints, and Good Manufacturing Practice (GMP). *In vivo* and clinical studies are required to determine the full effect of nanoparticles on the human body and cardiac tissues. Future CVD nanocarrier designs and advancements will require additional investigation. Cardio-protective characteristics of a number of natural substances are awaiting further research and clinical translation. Several challenges hinder the practical application of nanomedicine in CVDs. Institutional and industrial interests, lack of sufficient infrastructure and skills to prepare patients for treatment, efficient monitoring of patient outcomes, registration

of patients in clinical trials, and country-specific remuneration and cost are among the difficulties. Thus, nanoparticle translational medicine in CVDs should encompass bioengineers, pharmacists, chemists, biologists, and clinicians. Future investigation will leverage peptides and antibodies to detect CVD markers and build personalized nanodelivery systems. Future nanocardio medicine will research novel nanosystem clinical implications to promote quality of life.

Conflicts of Interest

We wish to confirm that there are no known conflicts of interest associated with this publication, and there has been no significant financial support for this work that could have influenced its outcome.

Authors' Contributions

Hitesh Chopra, Shabana Bibi, and Awdhesh Kumar Mishra contributed equally to this work.

Acknowledgments

The authors gratefully acknowledge the Deanship of Scientific Research, King Khalid University (KKU), Abha-61421, Asir, Kingdom of Saudi Arabia, for funding this research work under the grant number R.G.P1./291/43.

References

- [1] S. S. Virani, A. Alonso, H. J. Aparicio et al., "Heart Disease and Stroke Statistics-2021 Update A Report from the American Heart Association," *Circulation*, vol. 143, no. 8, pp. E254–E743, 2021.
- [2] R. S. Paffenbarger, R. Hyde, A. L. Wing, and C. Hsieh, "Physical activity, all-cause mortality, and longevity of college alumni," *The New England Journal of Medicine*, vol. 314, no. 10, pp. 605–613, 1986.
- [3] J. Stevens, J. Cai, K. R. Evenson, and R. Thomas, "Fitness and fatness as predictors of mortality from all causes and from cardiovascular disease in men and women in the Lipid Research Clinics Study," *American Journal of Epidemiology*, vol. 156, no. 9, pp. 832–841, 2002.
- [4] F. B. Hu, W. C. Willett, T. Li, M. J. Stampfer, G. A. Colditz, and J. E. Manson, "Adiposity as compared with physical activity in predicting mortality among women," *The New England Journal of Medicine*, vol. 351, no. 26, pp. 2694–2703, 2004.
- [5] J. W. Rhee and J. C. Wu, "Advances in nanotechnology for the management of coronary artery disease," *Trends in Cardiovascular Medicine*, vol. 23, no. 2, pp. 39–45, 2013.
- [6] W. Jiang and H. Liu, "Nanocomposites for bone repair and osteointegration with soft tissues," in *Nanocomposites for Musculoskeletal Tissue Regeneration*, Woodhead Publishing, 2016.
- [7] H. Liu and T. J. Webster, "Nanomedicine for implants: a review of studies and necessary experimental tools," *Biomaterials*, vol. 28, no. 2, pp. 354–369, 2007.
- [8] O. Pagliarosi, V. Picchio, I. Chimenti, E. Messina, and R. Gaetani, "Building an artificial cardiac microenvironment:

- a focus on the extracellular matrix,” *Frontiers in Cell and Development Biology*, vol. 8, p. 8, 2020.
- [9] R. Ravichandran, V. Seitz, J. Reddy Venugopal et al., “Mimicking native extracellular matrix with phytic acid-crosslinked protein nanofibers for cardiac tissue engineering,” *Macromolecular Bioscience*, vol. 13, no. 3, pp. 366–375, 2013.
 - [10] C. M. Kelleher and J. P. Vacanti, “Engineering extracellular matrix through nanotechnology,” *Journal of the Royal Society Interface*, vol. 7, suppl_6, pp. S717–S729, 2010.
 - [11] J. Hrkach, D. Von Hoff, M. M. Ali et al., “Preclinical development and clinical translation of a PSMA-targeted docetaxel nanoparticle with a differentiated pharmacological profile,” *Science Translational Medicine*, vol. 4, no. 128, p. 128ra39, 2012.
 - [12] H. S. Choi, W. Liu, F. Liu et al., “Design considerations for tumour-targeted nanoparticles,” *Nature Nanotechnology*, vol. 5, no. 1, pp. 42–47, 2010.
 - [13] Y. Liu, E. D. Pressly, D. R. Abendschein et al., “Targeting angiogenesis using a C-type atrial natriuretic factor-conjugated nanoprobe and PET,” *Journal of Nuclear Medicine*, vol. 52, no. 12, pp. 1956–1963, 2011.
 - [14] M. D. Majmudar, J. Yoo, E. J. Keliher et al., “Polymeric nanoparticle PET/MR imaging allows macrophage detection in atherosclerotic plaques,” *Circulation Research*, vol. 112, no. 5, pp. 755–761, 2013.
 - [15] H. P. Luehmann, E. D. Pressly, L. Detering et al., “Pet/ct imaging of chemokine receptor CCR5 in vascular injury model using targeted nanoparticle,” *Journal of Nuclear Medicine*, vol. 55, 2014.
 - [16] H. Soo Choi, W. Liu, P. Misra et al., “Renal clearance of quantum dots,” *Nature Biotechnology*, vol. 25, 2007.
 - [17] J. W. M. Bulte, A. H. Schmieder, J. Keupp, S. D. Caruthers, S. A. Wickline, and G. M. Lanza, “MR cholangiography demonstrates unsuspected rapid biliary clearance of nanoparticles in rodents: implications for clinical translation,” *Nanomedicine: Nanotechnology, Biology and Medicine*, vol. 10, 2014.
 - [18] H. S. Choi and J. V. Frangioni, “Nanoparticles for biomedical imaging: fundamentals of clinical translation,” *Molecular Imaging*, vol. 9, 2010.
 - [19] S. Mitragotri and J. Lahann, “Physical approaches to biomaterial design,” *Nature Materials*, vol. 8, 2009.
 - [20] F. Kiessling, M. E. Mertens, J. Grimm, and T. Lammers, “Nanoparticles for imaging: top or flop?,” *Radiology*, vol. 273, 2014.
 - [21] A. N. Lukyanov, W. C. Hartner, and V. P. Torchilin, “Increased accumulation of PEG-PE micelles in the area of experimental myocardial infarction in rabbits,” *Journal of Controlled Release*, vol. 94, 2004.
 - [22] H. Hwang, J. Kwon, P. S. Oh et al., “Peptide-loaded nanoparticles and radionuclide imaging for individualized treatment of myocardial ischemia,” *Radiology*, vol. 273, 2014.
 - [23] G. Fullstone, J. Wood, M. Holcombe, and G. Battaglia, “Modelling the transport of nanoparticles under blood flow using an agent-based approach,” *Scientific Reports*, vol. 5, 2015.
 - [24] H. Ye, Z. Shen, L. Yu, M. Wei, and Y. Li, “Manipulating nanoparticle transport within blood flow through external forces: an exemplar of mechanics in nanomedicine,” *Proceedings of the Proceedings of the Royal Society A: Mathematical, Physical and Engineering Sciences*, vol. 474, p. 20170845, 2018.
 - [25] S. Barua and S. Mitragotri, “Challenges associated with penetration of nanoparticles across cell and tissue barriers: a review of current status and future prospects,” *Nano Today*, vol. 9, 2014.
 - [26] M. Banach, C. Serban, A. Sahebkar et al., “Impact of statin therapy on coronary plaque composition: a systematic review and meta-analysis of virtual histology intravascular ultrasound studies,” *BMC Medicine*, vol. 13, 2015.
 - [27] N. Kapil, Y. H. Datta, N. Alakbarova et al., “Antiplatelet and anticoagulant therapies for prevention of ischemic stroke,” *Clinical and Applied Thrombosis/Hemostasis*, vol. 23, pp. 301–318, 2017.
 - [28] R. A. Harrington, P. K. Hodgson, and R. L. Larsen, “Antiplatelet therapy,” *Circulation*, p. 108, 2003.
 - [29] T. Geisler, H. Langer, M. Wydymus et al., “Low response to clopidogrel is associated with cardiovascular outcome after coronary stent implantation,” *European Heart Journal*, vol. 27, 2006.
 - [30] S. C. Johnston, J. D. Easton, M. Farrant et al., “Clopidogrel and aspirin in acute ischemic stroke and high-risk TIA,” *The New England Journal of Medicine*, vol. 379, pp. 215–225, 2018.
 - [31] S. Malini, K. Raj, and M. Sennappan, “Electrochemical and spectroscopic studies of interaction of clopidogrel bisulphate with calf thymus DNA,” *Asian Journal of Chemistry*, vol. 30, pp. 129–132, 2018.
 - [32] K. Raj and S. Malini, “Cyclic voltammetric studies of invitro interaction of clopidogrel bisulphate and aspirin,” *Materials Today: Proceedings*, vol. 5, pp. 22390–22398, 2018.
 - [33] D. A. Tonetti, B. T. Jankowitz, and B. A. Gross, “Antiplatelet therapy in flow diversion,” *Neurosurgery*, p. 86, 2020.
 - [34] P. Stano, S. Bufali, C. Pisano et al., “Novel camptothecin analogue (gimatecan)-containing liposomes prepared by the ethanol injection method,” *Journal of Liposome Research*, vol. 14, 2004.
 - [35] S. S. K. Dasa, R. Suzuki, M. Gutknecht et al., “Development of target-specific liposomes for delivering small molecule drugs after reperfused myocardial infarction,” *Journal of Controlled Release*, vol. 220, 2015.
 - [36] I. E. Allijn, B. M. S. Czarny, X. Wang et al., “Liposome encapsulated berberine treatment attenuates cardiac dysfunction after myocardial infarction,” *Journal of Controlled Release*, vol. 247, 2017.
 - [37] L. Timmers, J. P. G. Sluijter, J. K. Van Keulen et al., “Toll-like receptor 4 mediates maladaptive left ventricular remodeling and impairs cardiac function after myocardial infarction,” *Circulation Research*, vol. 102, 2008.
 - [38] A. Kumar, V. Hasija, A. Sudhaik et al., “Artificial leaf for light-driven CO₂ reduction: basic concepts, advanced structures and selective solar-to-chemical products,” *Chemical Engineering Journal*, vol. 430, p. 133031, 2022.
 - [39] H. N. Cuong, S. Pansambal, S. Ghotekar et al., “New frontiers in the plant extract mediated biosynthesis of copper oxide (CuO) nanoparticles and their potential applications: a review,” *Environmental Research*, vol. 203, p. 111858, 2022.
 - [40] R. Kumar, P. Raizada, A. A. P. Khan et al., “Recent progress in emerging BiPO₄-based photocatalysts: synthesis, properties, modification strategies, and photocatalytic applications,” *Journal of Materials Science and Technology*, vol. 108, pp. 208–225, 2022.

- [41] C. Courts and B. Madea, "Micro-RNA-a potential for forensic science?," *Forensic Science International*, vol. 203, 2010.
- [42] J. Wang, W. Huang, R. Xu et al., "MicroRNA-24 regulates cardiac fibrosis after myocardial infarction," *Journal of Cellular and Molecular Medicine*, vol. 16, 2012.
- [43] R. J. Perera and A. Ray, "MicroRNAs in the search for understanding human diseases," *BioDrugs*, vol. 21, 2007.
- [44] M. Li, X. Tang, X. Liu et al., "Targeted miR-21 loaded liposomes for acute myocardial infarction," *Journal of Materials Chemistry B*, vol. 8, 2020.
- [45] A. Al-Darraj, R. R. Donahue, H. Tripathi et al., "Liposomal delivery of azithromycin enhances its immunotherapeutic efficacy and reduces toxicity in myocardial infarction," *Scientific Reports*, vol. 10, 2020.
- [46] L. Y. Wei, X. H. Fu, W. Li et al., "Effect of intravenous administration of liposomal prostaglandin E1 on microcirculation in patients with ST elevation myocardial infarction undergoing primary percutaneous intervention," *Chinese Medical Journal*, vol. 128, 2015.
- [47] T. Reffelmann and R. A. Kloner, "Microvascular reperfusion injury: rapid expansion of anatomic no reflow during reperfusion in the rabbit," *American Journal of Physiology. Heart and Circulatory Physiology*, vol. 283, 2002.
- [48] A. Nakhband, M. Eskandani, Y. Omid et al., "Combating atherosclerosis with targeted nanomedicines: recent advances and future prospective," *BioImpacts: BI*, vol. 8, 2018.
- [49] F. M. van der Valk, D. F. van Wijk, M. E. Lobatto et al., "Prednisolone-containing liposomes accumulate in human atherosclerotic macrophages upon intravenous administration," *Nanomedicine: Nanotechnology, Biology and Medicine*, vol. 11, 2015.
- [50] F. M. van der Valk, D. M. Schulte, S. Meiler et al., "Liposomal prednisolone promotes macrophage lipotoxicity in experimental atherosclerosis," *Nanomedicine: Nanotechnology, Biology and Medicine*, vol. 12, 2016.
- [51] "Does the role of angiogenesis play a role in atherosclerosis and plaque instability?," *Anatomy and Physiology*, vol. 4, 2013.
- [52] E. A. Kruger and W. D. Figg, "TNP-470: an angiogenesis inhibitor in clinical development for cancer," *Expert Opinion on Investigational Drugs*, vol. 9, 2000.
- [53] K. S. Moulton, E. Heller, M. A. Konerding, E. Flynn, W. Palinski, and J. Folkman, "Angiogenesis inhibitors endostatin or TNP-470 reduce intimal neovascularization and plaque growth in apolipoprotein E-deficient mice," *Circulation*, vol. 99, 1999.
- [54] I. Pont, A. Calatayud-Pascual, A. López-Castellano et al., "Anti-angiogenic drug loaded liposomes: nanotherapy for early atherosclerotic lesions in mice," *PLoS One*, vol. 13, 2018.
- [55] Y. Wu, Y. Zhang, L. L. Dai et al., "An apoptotic body-biomimic liposome in situ upregulates anti-inflammatory macrophages for stabilization of atherosclerotic plaques," *Journal of Controlled Release*, vol. 316, 2019.
- [56] N. Zhang, C. Li, D. Zhou et al., "Cyclic RGD functionalized liposomes encapsulating urokinase for thrombolysis," *Acta Biomaterialia*, vol. 70, 2018.
- [57] J. Li, F. Ding, X. Qian et al., "Anti-inflammatory cytokine IL10 loaded cRGD liposomes for the targeted treatment of atherosclerosis," *Journal of Microencapsulation*, vol. 38, 2020.
- [58] M. E. Lobatto, T. Binderup, P. M. Robson et al., "Multimodal positron emission tomography imaging to quantify uptake of ^{89}Zr -labeled liposomes in the atherosclerotic vessel wall," *Bioconjugate Chemistry*, vol. 31, 2020.
- [59] A. Haeri, S. Sadeghian, S. Rabbani, S. Shirani, M. S. Anvari, and S. Dadashzadeh, "Physicochemical characteristics of liposomes are decisive for their antirestenosis efficacy following local delivery," *Nanomedicine*, vol. 12, pp. 131–145, 2017.
- [60] L. Ye, H. K. Haider, R. Tan et al., "Angiomyogenesis using liposome based vascular endothelial growth factor-165 transfection with skeletal myoblast for cardiac repair," *Biomaterials*, vol. 29, pp. 2125–2137, 2008.
- [61] Y. Qu, J. Tang, L. Liu, L. L. Song, S. Chen, and Y. Gao, " α -Tocopherol liposome loaded chitosan hydrogel to suppress oxidative stress injury in cardiomyocytes," *International Journal of Biological Macromolecules*, vol. 125, pp. 1192–1202, 2019.
- [62] M. Ogawa, R. Uchino, A. Kawai, M. Kosugi, and Y. Magata, "PEG modification on ^{111}In -labeled phosphatidyl serine liposomes for imaging of atherosclerotic plaques," *Nuclear Medicine and Biology*, vol. 42, pp. 299–304, 2015.
- [63] X. Li, H. Xiao, C. Lin et al., "Synergistic effects of liposomes encapsulating atorvastatin calcium and curcumin and targeting dysfunctional endothelial cells in reducing atherosclerosis," *International Journal of Nanomedicine*, vol. 14, p. 649, 2019.
- [64] A. Darwitan, Y. S. Wong, L. T. H. Nguyen et al., "Liposomal nanotherapy for treatment of atherosclerosis," *Advanced Healthcare Materials*, vol. 9, 2020.
- [65] E. T. M. Dams, P. Laverman, W. J. G. Oyen et al., "Accelerated blood clearance and altered biodistribution of repeated injections of sterically stabilized liposomes," *The Journal of Pharmacology and Experimental Therapeutics*, vol. 292, no. 3, pp. 1071–1079, 2000.
- [66] M. J. Lipinski, J. C. Frias, V. Amirbekian et al., "Macrophage-specific lipid-based nanoparticles improve cardiac magnetic resonance detection and characterization of human atherosclerosis," *JACC: Cardiovascular Imaging*, vol. 2, pp. 637–647, 2009.
- [67] B. Alotaibi, E. Tousson, T. A. El-Masry, N. Altwajry, and A. Saleh, "Ehrlich ascites carcinoma as model for studying the cardiac protective effects of curcumin nanoparticles against cardiac damage in female mice," *Environmental Toxicology*, vol. 36, pp. 105–113, 2021.
- [68] F. Pagliari, C. Mandoli, G. Forte et al., "Cerium oxide nanoparticles protect cardiac progenitor cells from oxidative stress," vol. 6, no. 5, pp. 3767–3775, 2012.
- [69] S. Y. Tan, C. Teh, C. Y. Ang et al., "Responsive mesoporous silica nanoparticles for sensing of hydrogen peroxide and simultaneous treatment toward heart failure," *Nanoscale*, vol. 9, pp. 2253–2261, 2017.
- [70] M. Miragoli, P. Ceriotti, M. Iafisco et al., "Inhalation of peptide-loaded nanoparticles improves heart failure," *Science Translational Medicine*, vol. 10, p. 6205, 2018.
- [71] S. Kathiresan, B. F. Voight, S. Purcell et al., "Genome-wide association of early-onset myocardial infarction with single nucleotide polymorphisms and copy number variants," *Nature Genetics*, vol. 41, pp. 334–341, 2009.
- [72] F. K. Swirski and M. Nahrendorf, "Leukocyte behavior in atherosclerosis, myocardial infarction, and heart failure," *Science*, vol. 339, no. 6116, pp. 161–166, 2013.
- [73] M. M. Nguyen, A. S. Carlini, M. P. Chien et al., "Enzyme-responsive nanoparticles for targeted accumulation and

- prolonged retention in heart tissue after myocardial infarction,” *Advanced Materials*, vol. 27, 2015.
- [74] Y. Oduk, W. Zhu, R. Kannappan et al., “VEGF nanoparticles repair the heart after myocardial infarction,” *American Journal of Physiology. Heart and Circulatory Physiology*, vol. 314, pp. 278–284, 2018.
- [75] A. Levin and G. Paret, “Levosimendan,” *Journal of Pediatric Intensive Care*, vol. 2, no. 3, pp. 095–103, 2013.
- [76] M. Y. Spivak, R. V. Bubnov, I. M. Yemets, L. M. Lazarenko, N. O. Tymoshok, and Z. R. Ulberg, “Development and testing of gold nanoparticles for drug delivery and treatment of heart failure: a theranostic potential for PPP cardiology,” *The EPMA Journal*, vol. 4, 2013.
- [77] M. P. A. Ferreira, S. Ranjan, S. Kinnunen et al., “Drug-loaded multifunctional nanoparticles targeted to the endocardial layer of the injured heart modulate hypertrophic signaling,” *Small*, vol. 13, p. 1701276, 2017.
- [78] K. S. Oh, J. Y. Song, S. J. Yoon, Y. Park, D. Kim, and S. H. Yuk, “Temperature-induced gel formation of core/shell nanoparticles for the regeneration of ischemic heart,” *Journal of Controlled Release*, vol. 146, no. 2, pp. 207–211, 2010.
- [79] S. Liu, X. Chen, L. Bao et al., “Treatment of infarcted heart tissue via the capture and local delivery of circulating exosomes through antibody-conjugated magnetic nanoparticles,” *Nature Biomedical Engineering*, vol. 4, no. 11, pp. 1063–1075, 2020.
- [80] C. Hu, R. Luo, and Y. Wang, “Heart valves cross-linked with erythrocyte membrane drug-loaded nanoparticles as a biomimetic strategy for anti-coagulation, anti-inflammation, anti-calcification, and endothelialization,” *ACS Applied Materials & Interfaces*, vol. 12, no. 37, pp. 41113–41126, 2020.
- [81] G. Torrieri, F. Fontana, P. Figueiredo et al., “Dual-peptide functionalized acetalated dextran-based nanoparticles for sequential targeting of macrophages during myocardial infarction,” *Nanoscale*, vol. 12, no. 4, pp. 2350–2358, 2020.
- [82] J. Qin, Z. Peng, B. Li et al., “Gold nanorods as a theranostic platform for in vitro and in vivo imaging and photothermal therapy of inflammatory macrophages,” *Nanoscale*, vol. 7, no. 33, pp. 13991–14001, 2015.
- [83] H. Taghavi, M. Bakhshandeh, A. Montazerabadi, H. N. Moghadam, S. B. M. Shahri, and M. Keshtkar, “Comparison of gold nanoparticles and iodinated contrast media in radiation dose reduction and contrast enhancement in computed tomography,” *Iranian Journal of Radiology*, vol. 17, no. 1, 2020.
- [84] V. Bagalkot, M. A. Badgeley, T. Kampfrath, J. A. Deiuliis, S. Rajagopalan, and A. Maiseyeu, “Hybrid nanoparticles improve targeting to inflammatory macrophages through phagocytic signals,” *Journal of Controlled Release*, vol. 217, pp. 243–255, 2015.
- [85] Y. H. Ma, S. Y. Wu, T. Wu, Y. J. Chang, M. Y. Hua, and J. P. Chen, “Magnetically targeted thrombolysis with recombinant tissue plasminogen activator bound to polyacrylic acid-coated nanoparticles,” *Biomaterials*, vol. 30, no. 19, pp. 3343–3351, 2009.
- [86] H. W. Yang, M. Y. Hua, K. J. Lin et al., “Bioconjugation of recombinant tissue plasminogen activator to magnetic nanocarriers for targeted thrombolysis,” *International Journal of Nanomedicine*, vol. 7, pp. 5159–5173, 2012.
- [87] J. Zhou, D. Guo, Y. Zhang, W. Wu, H. Ran, and Z. Wang, “Construction and evaluation of Fe₃O₄-based PLGA nanoparticles carrying rtPA used in the detection of thrombosis and in targeted thrombolysis,” *ACS Applied Materials & Interfaces*, vol. 6, no. 8, pp. 5566–5576, 2014.
- [88] G. Huang, Z. Zhou, R. Srinivasan et al., “Affinity manipulation of surface-conjugated RGD peptide to modulate binding of liposomes to activated platelets,” *Biomaterials*, vol. 29, no. 11, pp. 1676–1685, 2008.
- [89] D. B. Cowan, R. Yao, V. Akurathi et al., “Intracoronary delivery of mitochondria to the ischemic heart for cardioprotection,” *PLoS One*, vol. 11, no. 8, p. e0160889, 2016.
- [90] J. D. McCully, D. B. Cowan, C. A. Pacak, I. K. Toumpoulis, H. Dayalan, and S. Levitsky, “Injection of isolated mitochondria during early reperfusion for cardioprotection,” *American Journal of Physiology. Heart and Circulatory Physiology*, vol. 296, no. 1, pp. H94–H105, 2009.
- [91] A. Masuzawa, K. M. Black, C. A. Pacak et al., “Transplantation of autologously derived mitochondria protects the heart from ischemia-reperfusion injury,” *American Journal of Physiology. Heart and Circulatory Physiology*, vol. 304, no. 7, pp. H966–H982, 2013.
- [92] M. Chandarana, A. Curtis, and C. Hoskins, “The use of nanotechnology in cardiovascular disease,” *Applied Nanoscience*, vol. 8, no. 7, pp. 1607–1619, 2018.
- [93] S. Katsuki, T. Matoba, J. I. Koga, K. Nakano, and K. Egashira, “Anti-inflammatory nanomedicine for cardiovascular disease,” *Frontiers in Cardiovascular Medicine*, vol. 4, 2017.
- [94] M. P. A. Ferreira, V. Talman, G. Torrieri et al., “Dual-drug delivery using dextran-functionalized nanoparticles targeting cardiac fibroblasts for cellular reprogramming,” *Advanced Functional Materials*, vol. 28, no. 15, 2018.
- [95] M. Giannouli, V. Karagkiozaki, F. Pappa, I. Moutsios, C. Gravalidis, and S. Logothetidis, “Fabrication of quercetin-loaded PLGA nanoparticles via electrohydrodynamic atomization for cardiovascular disease,” *Proceedings of the Materials Today: Proceedings*, vol. 5, no. 8, pp. 15998–16005, 2018.
- [96] B. L. Banik, P. Fattahi, and J. L. Brown, “Polymeric nanoparticles: the future of nanomedicine,” *Wiley Interdisciplinary Reviews. Nanomedicine and Nanobiotechnology*, vol. 8, no. 2, pp. 271–299, 2016.
- [97] P. C. Lee, B. S. Zan, L. T. Chen, and T. W. Chung, “Multifunctional PLGA-based nanoparticles as a controlled release drug delivery system for antioxidant and anticoagulant therapy,” *International Journal of Nanomedicine*, vol. 14, pp. 1533–1549, 2019.
- [98] A. Jayagopal, P. K. Russ, and F. R. Haselton, “Surface engineering of quantum dots for in vivo vascular imaging,” *Bioconjugate Chemistry*, vol. 18, no. 5, pp. 1424–1433, 2007.
- [99] S. K. Tuteja, R. Chen, M. Kukkar et al., “A label-free electrochemical immunosensor for the detection of cardiac marker using graphene quantum dots (GQDs),” *Biosensors & Bioelectronics*, vol. 86, pp. 548–556, 2016.
- [100] M. Galagudza, D. Korolev, V. Postnov et al., “Passive targeting of ischemic-reperfused myocardium with adenosine-loaded silica nanoparticles,” *International Journal of Nanomedicine*, vol. 7, 2012.
- [101] J. M. Hamilton, D. P. Salmon, D. Galasko et al., “Visuospatial deficits predict rate of cognitive decline in autopsy-verified dementia with Lewy bodies,” *Neuropsychology*, vol. 22, no. 6, pp. 729–737, 2008.

- [102] J. Sun, S. Wang, D. Zhao, F. H. Hun, L. Weng, and H. Liu, "Cytotoxicity, permeability, and inflammation of metal oxide nanoparticles in human cardiac microvascular endothelial cells: cytotoxicity, permeability, and inflammation of metal oxide nanoparticles," *Cell Biology and Toxicology*, vol. 27, no. 5, pp. 333–342, 2011.
- [103] S. C. Hong, J. H. Lee, J. Lee et al., "Subtle cytotoxicity and genotoxicity differences in superparamagnetic iron oxide nanoparticles coated with various functional groups," *International Journal of Nanomedicine*, vol. 6, 2011.
- [104] N. K. Iversen, S. Frische, K. Thomsen et al., "Superparamagnetic iron oxide polyacrylic acid coated γ -Fe₂O₃ nanoparticles do not affect kidney function but cause acute effect on the cardiovascular function in healthy mice," *Toxicology and Applied Pharmacology*, vol. 266, no. 2, pp. 276–288, 2013.
- [105] S. Liu, Y. Han, L. Yin, L. Long, and R. Liu, "Toxicology studies of a superparamagnetic iron oxide nanoparticle <i>In Vivo</i>," *Proceedings of the Advanced Materials Research*, vol. 47-50, PART 2, pp. 1097–1100, 2008.
- [106] M. Mahmoudi, H. Hofmann, B. Rothen-Rutishauser, and A. Petri-Fink, "Assessing the in vitro and in vivo toxicity of superparamagnetic iron oxide nanoparticles," *Chemical Reviews*, vol. 112, no. 4, pp. 2323–2338, 2012.
- [107] M. Khan, Y. Xu, S. Hua et al., "Correction: Evaluation of changes in morphology and function of human induced pluripotent stem cell derived cardiomyocytes (hiPSC-CMs) cultured on an aligned-nanofiber cardiac patch," *PLoS One*, vol. 10, no. 10, p. e0141176, 2015.
- [108] S. Pok, J. D. Myers, S. V. Madhally, and J. G. Jacot, "A multilayered scaffold of a chitosan and gelatin hydrogel supported by a PCL core for cardiac tissue engineering," *Acta Biomaterialia*, vol. 9, no. 3, pp. 5630–5642, 2013.
- [109] Y. Wu, L. Wang, B. Guo, and P. X. Ma, "Interwoven aligned conductive nanofiber yarn/hydrogel composite scaffolds for engineered 3D cardiac anisotropy," *ACS Nano*, vol. 11, no. 6, pp. 5646–5659, 2017.
- [110] R. Lakshmanan, P. Kumaraswamy, U. M. Krishnan, and S. Sethuraman, "Engineering a growth factor embedded nanofiber matrix niche to promote vascularization for functional cardiac regeneration," *Biomaterials*, vol. 97, pp. 176–195, 2016.
- [111] M. Ding, H. Andersson, S. Martinsson et al., "Aligned nanofiber scaffolds improve functionality of cardiomyocytes differentiated from human induced pluripotent stem cell-derived cardiac progenitor cells," *Scientific Reports*, vol. 10, no. 1, p. 13575, 2020.
- [112] B. W. Streeter, J. Xue, Y. Xia, and M. E. Davis, "Electrospun nanofiber-based patches for the delivery of cardiac progenitor cells," *ACS Applied Materials & Interfaces*, vol. 11, no. 20, pp. 18242–18253, 2019.
- [113] B. J. Kang, H. Kim, S. K. Lee et al., "Umbilical-cord-blood-derived mesenchymal stem cells seeded onto fibronectin-immobilized polycaprolactone nanofiber improve cardiac function," *Acta Biomaterialia*, vol. 10, no. 7, pp. 3007–3017, 2014.
- [114] A. Kumar, A. Patel, L. Duvalsaint, M. Desai, and E. D. Marks, "Thymosin β 4 coated nanofiber scaffolds for the repair of damaged cardiac tissue," *Journal of Nanobiotechnology*, vol. 12, no. 1, p. 10, 2014.
- [115] M. M. Sayed, H. M. Mousa, M. R. El-Aassar et al., "Enhancing mechanical and biodegradation properties of polyvinyl alcohol/silk fibroin nanofibers composite patches for cardiac tissue engineering," *Materials Letters*, vol. 255, p. 126510, 2019.
- [116] H. M. Mousa, K. H. Hussein, M. M. Sayed et al., "Development of biocompatible tri-layered nanofibers patches with endothelial cells for cardiac tissue engineering," *European Polymer Journal*, vol. 129, p. 109630, 2020.
- [117] A. J. Rufaihah, I. C. Yasa, V. S. Ramanujam et al., "Angiogenic peptide nanofibers repair cardiac tissue defect after myocardial infarction," *Acta Biomaterialia*, vol. 58, pp. 102–112, 2017.
- [118] S. M. Dallabrida, N. Ismail, J. R. Oberle, B. E. Himes, and M. A. Rupnick, "Angiopoietin-1 promotes cardiac and skeletal myocyte survival through integrins," *Circulation Research*, vol. 96, no. 4, pp. e8–24, 2005.
- [119] J. M. Tang, J. N. Wang, L. Zhang et al., "VEGF/SDF-1 promotes cardiac stem cell mobilization and myocardial repair in the infarcted heart," *Cardiovascular Research*, vol. 91, no. 3, pp. 402–411, 2011.
- [120] S. Shojaie, M. Rostamian, A. Samadi et al., "Electrospun electroactive nanofibers of gelatin-oligoaniline/Poly (vinyl alcohol) templates for architecting of cardiac tissue with on-demand drug release," *Polymers for Advanced Technologies*, vol. 30, no. 6, pp. 1473–1483, 2019.
- [121] H. Nazari, A. Heirani-Tabasi, M. Hajiabbas et al., "Incorporation of two-dimensional nanomaterials into silk fibroin nanofibers for cardiac tissue engineering," *Polymers for Advanced Technologies*, vol. 31, no. 2, pp. 248–259, 2020.
- [122] H. Nazari, A. Heirani-Tabasi, M. Hajiabbas et al., "Incorporation of SPION-casein core-shells into silk-fibroin nanofibers for cardiac tissue engineering," *Journal of Cellular Biochemistry*, vol. 121, no. 4, pp. 2981–2993, 2020.
- [123] A. Ghasemi, R. Imani, M. Yousefzadeh, S. Bonakdar, A. Solouk, and H. Fakhrazadeh, "Studying the potential application of electrospun polyethylene terephthalate/graphene oxide nanofibers as electroconductive cardiac patch," *Macromolecular Materials and Engineering*, vol. 304, no. 8, p. 1900187, 2019.
- [124] H. A. Kassam, D. C. Gillis, B. R. Dandurand et al., "Development of fractalkine-targeted nanofibers that localize to sites of arterial injury," *Nanomaterials*, vol. 10, no. 3, p. 420, 2020.
- [125] M. Suhaeri, R. Subbiah, S. H. Kim et al., "Novel platform of cardiomyocyte culture and coculture via fibroblast-derived matrix-coupled aligned electrospun nanofiber," *ACS Applied Materials & Interfaces*, vol. 9, no. 1, pp. 224–235, 2017.
- [126] H. Liao, R. Qi, M. Shen et al., "Improved cellular response on multiwalled carbon nanotube-incorporated electrospun polyvinyl alcohol/chitosan nanofibrous scaffolds," *Colloids and Surfaces. B, Biointerfaces*, vol. 84, no. 2, pp. 528–535, 2011.
- [127] A. M. Wickham, M. M. Islam, D. Mondal et al., "Polycaprolactone-thiophene-conjugated carbon nanotube meshes as scaffolds for cardiac progenitor cells," *Journal of Biomedical Materials Research – Part B: Applied Biomaterials*, vol. 102, no. 7, pp. 1553–1561, 2014.
- [128] M. Kharaziha, S. R. Shin, M. Nikkiah et al., "Tough and flexible CNT-polymeric hybrid scaffolds for engineering cardiac constructs," *Biomaterials*, vol. 35, no. 26, pp. 7346–7354, 2014.
- [129] D. A. Stout, B. Basu, and T. J. Webster, "Poly (lactic-co-glycolic acid): carbon nanofiber composites for myocardial tissue engineering applications," *Acta Biomaterialia*, vol. 7, no. 8, pp. 3101–3112, 2011.

- [130] X. Meng, D. A. Stout, L. Sun, R. L. Beingessner, H. Fenniri, and T. J. Webster, "Novel injectable biomimetic hydrogels with carbon nanofibers and self assembled rosette nanotubes for myocardial applications," *Journal of Biomedical Materials Research Part A*, vol. 101A, no. 4, pp. 1095–1102, 2013.
- [131] Q. Liu, S. Tian, C. Zhao et al., "Porous nanofibrous poly (l-lactic acid) scaffolds supporting cardiovascular progenitor cells for cardiac tissue engineering," *Acta Biomaterialia*, vol. 26, pp. 105–114, 2015.
- [132] R. M. Aghdam, S. Shakhesi, S. Najarian, M. M. Mohammadi, S. H. Ahmadi Tafti, and H. Mirzadeh, "Fabrication of a nanofibrous scaffold for the in vitro culture of cardiac progenitor cells for myocardial regeneration," *International Journal of Polymeric Materials and Polymeric Biomaterials*, vol. 63, no. 5, pp. 229–239, 2014.
- [133] R. Amezcua, A. Shirolkar, C. Frazee, and D. A. Stout, "Nanomaterials for cardiac myocyte tissue engineering," *Nanomaterials*, vol. 6, no. 7, p. 133, 2016.
- [134] K. Ashtari, H. Nazari, H. Ko et al., "Electrically conductive nanomaterials for cardiac tissue engineering," *Advanced Drug Delivery Reviews*, vol. 144, pp. 162–179, 2019.
- [135] L. Li, Y. Wang, R. Guo et al., "Ginsenoside Rg3-loaded, reactive oxygen species-responsive polymeric nanoparticles for alleviating myocardial ischemia-reperfusion injury," *Journal of Controlled Release*, vol. 317, pp. 259–272, 2020.
- [136] C. Cristallini, G. Vaccari, N. Barbani et al., "Cardioprotection of PLGA/gelatin cardiac patches functionalised with adenosine in a large animal model of ischaemia and reperfusion injury: a feasibility study," *Journal of Tissue Engineering and Regenerative Medicine*, vol. 13, no. 7, pp. 1253–1264, 2019.
- [137] C. Cristallini, C. Giachino, N. Barbani, E. C. Rocchietti, M. Gagliardi, and P. Pagliaro, "A polymeric scaffold for cardiac regeneration and protection from reperfusion injury-WO2014108814A1," Google Patent.
- [138] C. Cristallini, M. Gagliardi, N. Barbani, D. Giannessi, and G. D. Guerra, "Novel biodegradable, biomimetic and functionalised polymer scaffolds to prevent expansion of post-infarct left ventricular remodelling," *Journal of Materials Science. Materials in Medicine*, vol. 23, no. 1, pp. 205–216, 2012.
- [139] P. C. Sherrell, A. Ciešlar-Pobuda, M. S. Ejneby et al., "Rational design of a conductive collagen heart patch," *Macromolecular Bioscience*, vol. 17, no. 7, 2017.
- [140] B. Peña, S. Bosi, B. A. Aguado et al., "Injectable Carbon Nanotube-Functionalized Reverse Thermal Gel Promotes Cardiomyocytes Survival and Maturation," *ACS Applied Materials & Interfaces*, vol. 9, no. 37, pp. 31645–31656, 2017.
- [141] J. Ren, Q. Xu, X. Chen et al., "Superaligned carbon nanotubes guide oriented cell growth and promote electrophysiological homogeneity for synthetic cardiac tissues," *Advanced Materials*, vol. 29, no. 44, 2017.
- [142] M. D. McCauley, F. Vitale, J. S. Yan et al., "In vivo restoration of myocardial conduction with carbon nanotube fibers," *Circulation. Arrhythmia and Electrophysiology*, vol. 12, no. 8, p. e007256, 2019.
- [143] M. Tashakori-Miyanroudi, K. Rakhshan, M. Ramez et al., "Conductive carbon nanofibers incorporated into collagen bio-scaffold assists myocardial injury repair," *International Journal of Biological Macromolecules*, vol. 163, pp. 1136–1146, 2020.
- [144] B. Ataei, M. T. Khorasani, M. Karimi, and M. Daliri-Joupari, "Plasma modification of heparinised CNT/PU nanocomposite and measuring of mechanical, calcification and platelet adhesion properties for application in heart valve," *Plastics, Rubber and Composites*, vol. 49, no. 7, pp. 289–299, 2020.
- [145] J. T. T. Angelina, S. Ganesan, T. M. R. Panicker, R. Narayani, M. Paul Korath, and K. Jagadeesan, "Pulsed laser deposition of silver nanoparticles on prosthetic heart valve material to prevent bacterial infection," *Materials and Technologies*, vol. 32, no. 3, pp. 148–155, 2017.
- [146] S. Ahadian, L. Davenport Huyer, M. Estili et al., "Moldable elastomeric polyester-carbon nanotube scaffolds for cardiac tissue engineering," *Acta Biomaterialia*, vol. 52, pp. 81–91, 2017.
- [147] A. M. Martins, G. Eng, S. G. Caridade, J. F. Mano, R. L. Reis, and G. Vunjak-Novakovic, "Electrically conductive chitosan/carbon scaffolds for cardiac tissue engineering," *Biomacromolecules*, vol. 15, no. 2, pp. 635–643, 2014.
- [148] S. R. Shin, C. Zihlmann, M. Akbari et al., "Reduced graphene oxide-GelMA hybrid hydrogels as scaffolds for cardiac tissue engineering," *Small*, vol. 12, no. 27, pp. 3677–3689, 2016.
- [149] S. Rastegar, M. Mehdikhani, A. Bigham, E. Poorazizi, and M. Rafienia, "Poly glycerol sebacate/polycaprolactone/carbon quantum dots fibrous scaffold as a multifunctional platform for cardiac tissue engineering," *Materials Chemistry and Physics*, vol. 266, p. 124543, 2021.
- [150] P. Ahmadi, N. Nazeri, M. A. Derakhshan, and H. Ghanbari, "Preparation and characterization of polyurethane/chitosan/CNT nanofibrous scaffold for cardiac tissue engineering," *International Journal of Biological Macromolecules*, vol. 180, pp. 590–598, 2021.
- [151] C. Yan, Y. Ren, X. Sun et al., "Photoluminescent functionalized carbon quantum dots loaded electroactive silk fibroin/PLA nanofibrous bioactive scaffolds for cardiac tissue engineering," *Journal of Photochemistry and Photobiology B: Biology*, vol. 202, p. 111680, 2020.
- [152] S. Mombini, J. Mohammadnejad, B. Bakhshandeh et al., "Chitosan-PVA-CNT nanofibers as electrically conductive scaffolds for cardiovascular tissue engineering," *International Journal of Biological Macromolecules*, vol. 140, pp. 278–287, 2019.
- [153] H. Sun, J. Tang, Y. Mou et al., "Carbon nanotube-composite hydrogels promote intercalated disc assembly in engineered cardiac tissues through $\beta 1$ -integrin mediated FAK and RhoA pathway," *Acta Biomaterialia*, vol. 48, pp. 88–99, 2017.
- [154] M. Cabiati, F. Vozi, F. Gemma et al., "Cardiac tissue regeneration: a preliminary study on carbon-based nanotubes gelatin scaffold," *Journal of Biomedical Materials Research – Part B: Applied Biomaterials*, vol. 106, no. 8, pp. 2750–2762, 2018.
- [155] K. Roshanbinfar, J. Hilborn, O. P. Varghese, and O. P. Oommen, "Injectable and thermoresponsive pericardial matrix derived conductive scaffold for cardiac tissue engineering," *RSC Advances*, vol. 7, no. 51, pp. 31980–31988, 2017.
- [156] C. M. B. Ho, A. Mishra, P. T. P. Lin et al., "3D printed polycaprolactone carbon nanotube composite scaffolds for cardiac tissue engineering," *Macromolecular Bioscience*, vol. 17, no. 4, 2017.
- [157] D. Kaya, K. Küçükada, and N. Alemdar, "Modeling the drug release from reduced graphene oxide-reinforced hyaluronic acid/gelatin/poly (ethylene oxide) polymeric films," *Carbohydrate Polymers*, vol. 215, pp. 189–197, 2019.
- [158] G. Sarkar, N. R. Saha, I. Roy et al., "Cross-linked methyl cellulose/graphene oxide rate controlling membranes for:

- in vitro and ex vivo permeation studies of diltiazem hydrochloride," *RSC Advances*, vol. 6, no. 42, pp. 36136–36145, 2016.
- [159] A. Masotti, M. R. Miller, A. Celluzzi et al., "Regulation of angiogenesis through the efficient delivery of microRNAs into endothelial cells using polyamine-coated carbon nanotubes," *Nanomedicine: Nanotechnology, Biology and Medicine*, vol. 12, no. 6, pp. 1511–1522, 2016.
- [160] A. Paul, W. Shao, D. Shum-Tim, and S. Prakash, "The attenuation of restenosis following arterial gene transfer using carbon nanotube coated stent incorporating TAT/DNAAng1 +Vegf nanoparticles," *Biomaterials*, vol. 33, no. 30, pp. 7655–7664, 2012.
- [161] R. Zhang and H. Olin, "Carbon nanomaterials as drug carriers: real time drug release investigation," *Materials Science and Engineering: C*, vol. 32, no. 5, pp. 1247–1252, 2012.
- [162] A. B. Seabra, A. J. Paula, R. De Lima, O. L. Alves, and N. Durán, "Nanotoxicity of graphene and graphene oxide," *Chemical Research in Toxicology*, vol. 27, no. 2, pp. 159–168, 2014.
- [163] T. P. Dasari Shareena, D. McShan, A. K. Dasmahapatra, and P. B. Tchounwou, "A review on graphene-based nanomaterials in biomedical applications and risks in environment and health," *Nano-Micro Letters*, vol. 10, no. 3, p. 53, 2018.
- [164] H. B. Bostan, R. Rezaee, M. G. Valokala et al., "Cardiotoxicity of nano-particles," *Life Sciences*, vol. 165, pp. 91–99, 2016.
- [165] M. C. Duch, G. R. S. Budinger, Y. T. Liang et al., "Minimizing oxidation and stable nanoscale dispersion improves the biocompatibility of graphene in the lung," *Nano Letters*, vol. 11, no. 12, pp. 5201–5207, 2011.
- [166] Z. Chen, C. Yu, I. A. Khan, Y. Tang, S. Liu, and M. Yang, "Toxic effects of different-sized graphene oxide particles on zebrafish embryonic development," *Ecotoxicology and Environmental Safety*, vol. 197, p. 110608, 2020.
- [167] H. Tong, J. K. McGee, R. K. Saxena, U. P. Kodavanti, R. B. Devlin, and M. I. Gilmour, "Influence of acid functionalization on the cardiopulmonary toxicity of carbon nanotubes and carbon black particles in mice," *Toxicology and Applied Pharmacology*, vol. 239, no. 3, pp. 224–232, 2009.
- [168] V. M. Harik, "Geometry of carbon nanotubes and mechanisms of phagocytosis and toxic effects," *Toxicology Letters*, vol. 273, pp. 69–85, 2017.
- [169] H. L. Crampton and E. E. Simanek, "Dendrimers as drug delivery vehicles: non-covalent interactions of bioactive compounds with dendrimers," *Polymer International*, vol. 56, no. 4, pp. 489–496, 2007.
- [170] A. P. Sherje, M. Jadhav, B. R. Dravyakar, and D. Kadam, "Dendrimers: a versatile nanocarrier for drug delivery and targeting," *International Journal of Pharmaceutics*, vol. 548, no. 1, pp. 707–720, 2018.
- [171] L. P. Mendes, J. Pan, and V. P. Torchilin, "Dendrimers as nanocarriers for nucleic acid and drug delivery in cancer therapy," *Molecules*, vol. 22, no. 9, p. 1401, 2017.
- [172] W. D. Jang and T. Aida, "Dendritic physical gels: structural parameters for gelation with peptide-core dendrimers," *Macromolecules*, vol. 36, no. 22, pp. 8461–8469, 2003.
- [173] C. Napoli, F. de Nigris, S. Williams-Ignarro, O. Pignalosa, V. Sica, and L. J. Ignarro, "Nitric oxide and atherosclerosis: an update," *Nitric Oxide: Biology and Chemistry*, vol. 15, no. 4, pp. 265–279, 2006.
- [174] Y. Lu, B. Sun, C. Li, and M. H. Schoenfisch, "Structurally diverse nitric oxide-releasing poly (propylene imine) dendrimers," *Chemistry of Materials*, vol. 23, no. 18, pp. 4227–4233, 2011.
- [175] A. Gothwal, P. Kesharwani, U. Gupta et al., "Dendrimers as an effective nanocarrier in cardiovascular disease," *Current Pharmaceutical Design*, vol. 21, no. 30, pp. 4519–4526, 2015.
- [176] H. Türk, A. Shukla, P. C. A. Rodrigues, H. Rehage, and R. Haag, "Water-soluble dendritic core-shell-type architectures based on polyglycerol for solubilization of hydrophobic drugs," *Chemistry - A European Journal*, vol. 13, no. 15, pp. 4187–4196, 2007.
- [177] N. K. Egilmez, Y. Iwanuma, and R. B. Bankert, "Evaluation and optimization of different cationic liposome formulations for in vivo gene transfer," *Biochemical and Biophysical Research Communications*, vol. 221, no. 1, pp. 169–173, 1996.
- [178] H. San, Z. Y. Yang, V. J. Pompili et al., "Safety and short-term toxicity of a novel cationic lipid formulation for human gene therapy," *Human Gene Therapy*, vol. 4, no. 6, pp. 781–788, 1993.
- [179] E. G. Nabel, G. Plautz, and G. J. Nabel, "Site-specific gene expression in vivo by direct gene transfer into the arterial wall," *Science*, vol. 249, no. 4974, pp. 1285–1288, 1990.
- [180] H. Lin, M. S. Parmacek, G. Morle, S. Bolling, and J. M. Leiden, "Expression of recombinant genes in myocardium in vivo after direct injection of DNA," *Circulation*, vol. 82, no. 6, pp. 2217–2221, 1990.
- [181] L. Qin, D. R. Pahud, Y. Ding et al., "Efficient transfer of genes into murine cardiac grafts by starburst polyamidoamine dendrimers," *Human Gene Therapy*, vol. 9, no. 4, pp. 553–560, 1998.
- [182] M. P. Turunen, M. O. Hiltunen, M. Ruponen et al., "Efficient adventitial gene delivery to rabbit carotid artery with cationic polymer-plasmid complexes," *Gene Therapy*, vol. 6, no. 1, pp. 6–11, 1999.
- [183] Y. Wang, P. Boros, J. Liu et al., "DNA/dendrimer complexes mediate gene transfer into murine cardiac transplants ex vivo," *Molecular Therapy*, vol. 2, no. 6, pp. 602–608, 2000.
- [184] Y. Wang, Y. Bai, C. Price et al., "Combination of electroporation and DNA/dendrimer complexes enhances gene transfer into murine cardiac transplants," *American Journal of Transplantation*, vol. 1, no. 4, pp. 334–338, 2001.
- [185] S. Theoharis, U. Krueger, P. H. Tan, D. O. Haskard, M. Weber, and A. J. T. George, "Targeting gene delivery to activated vascular endothelium using anti E/P-Selectin antibody linked to PAMAM dendrimers," *Journal of Immunological Methods*, vol. 343, 2009.
- [186] K. Jain, P. Kesharwani, U. Gupta, and N. K. Jain, "Dendrimer toxicity: let's meet the challenge," *International Journal of Pharmaceutics*, vol. 394, no. 1–2, pp. 122–142, 2010.
- [187] C. M. J. Hu, L. Zhang, S. Aryal, C. Cheung, R. H. Fang, and L. Zhang, "Erythrocyte membrane-camouflaged polymeric nanoparticles as a biomimetic delivery platform," *Proceedings of the National Academy of Sciences of the United States of America*, vol. 108, no. 27, pp. 10980–10985, 2011.
- [188] Y. Wang, K. Zhang, X. Qin et al., "Biomimetic nanotherapies: red blood cell based core-shell structured nanocomplexes for atherosclerosis management," *Advancement of Science*, vol. 6, no. 12, 2019.
- [189] C. M. J. Hu, R. H. Fang, K. C. Wang et al., "Nanoparticle biointerfacing by platelet membrane cloaking," *Nature*, vol. 526, no. 7571, pp. 118–121, 2015.

- [190] S. Wang, R. Wang, N. Meng et al., "Platelet membrane-functionalized nanoparticles with improved targeting ability and lower hemorrhagic risk for thrombolysis therapy," *Journal of Controlled Release*, vol. 328, pp. 78–86, 2020.
- [191] Y. Zhao, R. Xie, N. Yodsanit et al., "Hydrogen peroxide-responsive platelet membrane-coated nanoparticles for thrombus therapy," *Biomaterials Science*, vol. 9, no. 7, pp. 2696–2708, 2021.
- [192] P. Y. Fang, L. M. G. Ramos, S. Y. Holguin et al., "Functional RNAs: combined assembly and packaging in VLPs," *Nucleic Acids Research*, vol. 45, no. 6, pp. 3519–3527, 2017.
- [193] B. K. Gan, C. Y. Yong, K. L. Ho, A. R. Omar, N. B. Alitheen, and W. S. Tan, "Targeted delivery of cell penetrating peptide virus-like nanoparticles to skin cancer cells," *Scientific Reports*, vol. 8, no. 1, pp. 1–3, 2018.
- [194] H. Kim, H. Choi, Y. Bae, and S. Kang, "Development of target-tunable P22 VLP-based delivery nanoplatforms using bacterial superglue," *Biotechnology and Bioengineering*, vol. 116, no. 11, pp. 2843–2851, 2019.
- [195] L. Zhao, M. Kopylov, C. S. Potter, B. Carragher, and M. G. Finn, "Engineering the PP7 virus capsid as a peptide display platform," *ACS Nano*, vol. 13, no. 4, pp. 4443–4454, 2019.
- [196] Y. Ren, Y. Mu, L. Jiang et al., "Multifunctional TK-VLPs nanocarrier for tumor-targeted delivery," *International Journal of Pharmaceutics*, vol. 502, no. 1-2, pp. 249–257, 2016.
- [197] J. S. Santillán-Uribe, J. Valadez-García, A. C. Morán-García, H. C. Santillán-Uribe, and I. Bustos-Jaimes, "Peptide display on a surface loop of human parvovirus B19 VP2: assembly and characterization of virus-like particles," *Virus Research*, vol. 201, pp. 1–7, 2015.
- [198] X. Sun, W. Li, X. Zhang et al., "In vivo targeting and imaging of atherosclerosis using multifunctional virus-like particles of Simian virus 40," *Nano Letters*, vol. 16, no. 10, pp. 6164–6171, 2016.
- [199] M. Mahmoudi, I. Lynch, M. R. Ejtehad, M. P. Monopoli, F. B. Bombelli, and S. Laurent, "Protein-nanoparticle interactions: opportunities and challenges," *Chemical Reviews*, vol. 111, no. 9, pp. 5610–5637, 2011.
- [200] M. P. Monopoli, D. Walczyk, A. Campbell et al., "Physical-chemical aspects of protein corona: relevance to in vitro and in vivo biological impacts of nanoparticles," *Journal of the American Chemical Society*, vol. 133, no. 8, pp. 2525–2534, 2011.
- [201] W. Xiao and H. Gao, "The impact of protein corona on the behavior and targeting capability of nanoparticle-based delivery system," *International Journal of Pharmaceutics*, vol. 552, no. 1-2, pp. 328–339, 2018.
- [202] M. P. Monopoli, C. Åberg, A. Salvati, and K. A. Dawson, "Biomolecular coronas provide the biological identity of nanosized materials," *Nature Nanotechnology*, vol. 7, no. 12, pp. 779–786, 2012.
- [203] V. Mirshafiee, M. Mahmoudi, K. Lou, J. Cheng, and M. L. Kraft, "Protein corona significantly reduces active targeting yield," *Chemical Communications*, vol. 49, 2013.
- [204] A. Salvati, A. S. Pitek, M. P. Monopoli et al., "Transferrin-functionalized nanoparticles lose their targeting capabilities when a biomolecule corona adsorbs on the surface," *Nature Nanotechnology*, vol. 8, 2013.
- [205] D. F. Moyano, K. Saha, G. Prakash et al., "Fabrication of corona-free nanoparticles with tunable hydrophobicity," *ACS Nano*, vol. 8, 2014.
- [206] S. J. Dixon, K. M. Lemberg, M. R. Lamprecht et al., "Ferroptosis: an iron-dependent form of nonapoptotic cell death," *Cell*, vol. 149, no. 5, pp. 1060–1072, 2012.
- [207] S. J. Dixon and B. R. Stockwell, "The role of iron and reactive oxygen species in cell death," *Nature Chemical Biology*, vol. 10, no. 1, pp. 9–17, 2014.
- [208] W. G. Kreyling, A. M. Abdelmonem, Z. Ali et al., "In vivo integrity of polymer-coated gold nanoparticles," *Nature Nanotechnology*, vol. 10, 2015.
- [209] F. Dilnawaz, S. Acharya, and S. K. Sahoo, "Recent trends of nanomedicinal approaches in clinics," *International Journal of Pharmaceutics*, vol. 538, no. 1-2, pp. 263–278, 2018.
- [210] K. Riehemann, S. W. Schneider, T. A. Luger, B. Godin, M. Ferrari, and H. Fuchs, "Nanomedicine-challenge and perspectives," *Angewandte Chemie, International Edition*, vol. 48, no. 5, pp. 872–897, 2009.
- [211] J. A. Jackman, T. Mészáros, T. Fülöp, R. Urbanics, J. Szebeni, and N. J. Cho, "Comparison of complement activation-related pseudoallergy in miniature and domestic pigs: foundation of a validatable immune toxicity model," *Nanomedicine: Nanotechnology, Biology and Medicine*, vol. 12, 2016.
- [212] J. Szebeni and G. Storm, "Complement activation as a bio-equivalence issue relevant to the development of generic liposomes and other nanoparticulate drugs," *Biochemical and Biophysical Research Communications*, vol. 468, 2015.
- [213] S. Hua, M. B. C. de Matos, J. M. Metselaar, and G. Storm, "Current trends and challenges in the clinical translation of nanoparticulate nanomedicines: pathways for translational development and commercialization," *Frontiers in Pharmacology*, vol. 9, 2018.
- [214] V. Sainz, J. Conniot, A. I. Matos et al., "Regulatory aspects on nanomedicines," *Biochemical and Biophysical Research Communications*, vol. 468, no. 3, pp. 504–510, 2015.
- [215] R. Gaspar, "Regulatory issues surrounding nanomedicines: setting the scene for the next generation of nanopharmaceuticals," *Nanomedicine*, vol. 2, 2007.
- [216] J. I. Hare, T. Lammers, M. B. Ashford, S. Puri, G. Storm, and S. T. Barry, "Challenges and strategies in anti-cancer nanomedicine development: an industry perspective," *Advanced Drug Delivery Reviews*, vol. 108, pp. 25–38, 2017.
- [217] L. Accomasso, C. Cristallini, and C. Giachino, "Risk assessment and risk minimization in nanomedicine: a need for predictive, alternative, and 3Rs strategies," *Frontiers in Pharmacology*, vol. 9, p. 228, 2018.
- [218] H. Chopra, S. Kumar, and I. Singh, "Bioinks for 3D printing of artificial extracellular matrices," in *Advanced 3D-Printed Systems and Nanosystems for Drug Delivery and Tissue Engineering*, pp. 1–37, Elsevier, 2020.
- [219] J. Kanawati, A. J. Kanawati, M. K. Rowe, H. Khan, W. K. Chan, and R. Yee, "Utility of 3-D printing for cardiac resynchronization device implantation in congenital heart disease," *Heart. Case Reports*, vol. 6, 2020.
- [220] N. Tiwari, H. R. Ramamurthy, V. Kumar, A. Kumar, B. Dhanalakshmi, and G. Kumar, "The role of three-dimensional printed cardiac models in the management of complex congenital heart diseases," *Medical Journal, Armed Forces India*, vol. 77, no. 3, pp. 322–330, 2021.
- [221] B. Rezaei, A. M. Shoushtari, M. Rabiee, L. Uzun, W. C. Mak, and A. P. F. Turner, "An electrochemical immunosensor for cardiac Troponin I using electrospun carboxylated multi-

- walled carbon nanotube-whiskered nanofibres,” *Talanta*, vol. 182, 2018.
- [222] L. Wang, W. Dou, J. Chen et al., “A CNT-PDMS wearable device for simultaneous measurement of wrist pulse pressure and cardiac electrical activity,” *Materials Science and Engineering: C*, vol. 117, 2020.
- [223] X. Song, X. Wang, J. Zhang et al., “A tunable self-healing ionic hydrogel with microscopic homogeneous conductivity as a cardiac patch for myocardial infarction repair,” *Biomaterials*, vol. 273, 2021.
- [224] D. R. Holmes, R. E. Vlietstra, H. C. Smith et al., “Restenosis after percutaneous transluminal coronary angioplasty (PTCA): a report from the PTCA registry of the national heart, lung, and blood institute,” *The American Journal of Cardiology*, vol. 53, 1984.
- [225] M. Nobuyoshi, T. Kimura, H. Nosaka et al., “Restenosis after successful percutaneous transluminal coronary angioplasty: serial angiographic follow-up of 229 patients,” *Journal of the American College of Cardiology*, vol. 12, 1988.
- [226] A. Grüntzig, “Transluminal dilatation of coronary-artery stenosis,” *Lancet*, vol. 311, 1978.
- [227] E. Eeckhout, L. Kappenberger, and J. J. Goy, “Stents for intracoronary placement: current status and future directions,” *Journal of the American College of Cardiology*, vol. 27, 1996.
- [228] G. S. Roubin, A. D. Cannon, S. K. Agrawal et al., “Intracoronary stenting for acute and threatened closure complicating percutaneous transluminal coronary angioplasty,” *Circulation*, vol. 85, 1992.
- [229] J. Iqbal, J. Gunn, and P. W. Serruys, “Coronary stents: historical development, current status and future directions,” *British Medical Bulletin*, vol. 106, 2013.
- [230] J. Y. Bang, U. Navaneethan, M. K. Hasan, B. Sutton, R. Hawes, and S. Varadarajulu, “Non-superiority of lumen-apposing metal stents over plastic stents for drainage of walled-off necrosis in a randomised trial,” *Gut*, vol. 68, 2019.
- [231] O. Varenne, S. Cook, G. Sideris et al., “Drug-eluting stents in elderly patients with coronary artery disease (SENIOR): a randomised single-blind trial,” *Lancet*, vol. 391, 2018.
- [232] J. F. Iglesias, O. Muller, D. Heg et al., “Biodegradable polymer sirolimus-eluting stents versus durable polymer everolimus-eluting stents in patients with ST-segment elevation myocardial infarction (BIOSTEMI): a single-blind, prospective, randomised superiority trial,” *Lancet*, vol. 394, no. 10205, pp. 1243–1253, 2019.
- [233] A. J. Guerra, P. Cano, M. Rabionet, T. Puig, and J. Ciurana, “3D-printed PCL/PLA composite stents: towards a new solution to cardiovascular problems,” *Materials*, vol. 11, 2018.